NASA Conference Publication 3248
Part 1

Orbiter Experiments (OEX) Aerothermodynamics Symposium

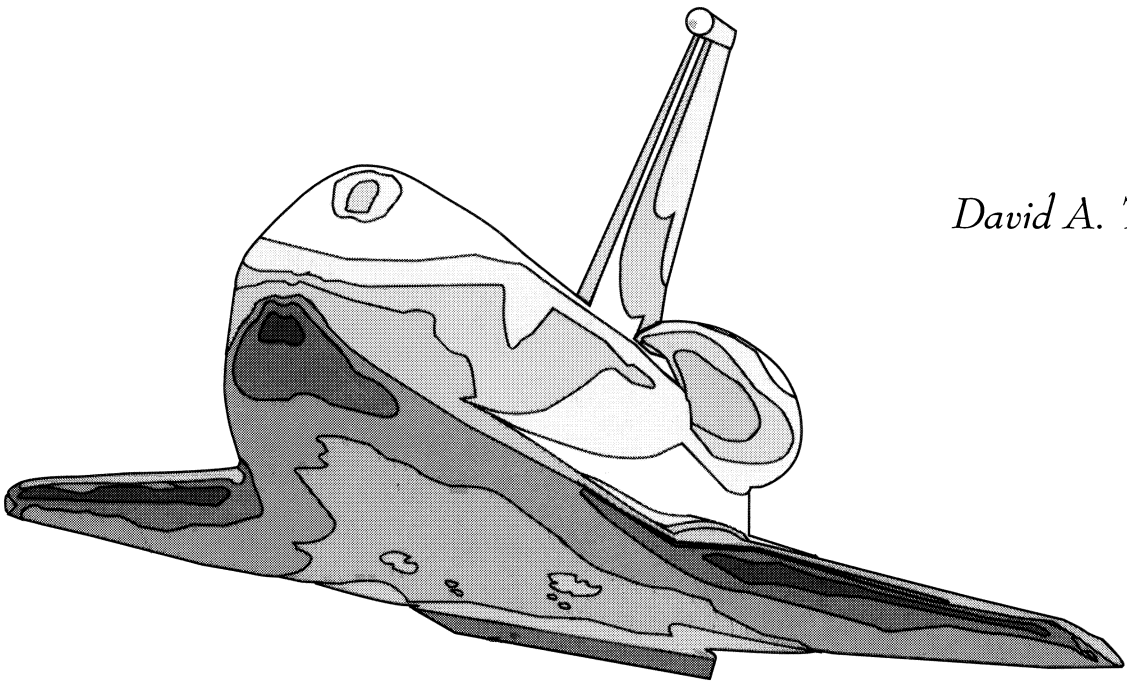

Edited by
David A. Throckmorton

Proceedings of a symposium sponsored by the
National Aeronautics and Space Administration
Washington, DC, and held in
Williamsburg, Virginia
April 27-30, 1993

April 1995

NASA Conference Publication 3248
Part 1

Orbiter Experiments (OEX) Aerothermodynamics Symposium

Edited by
David A. Throckmorton
Langley Research Center • Hampton, Virginia

Proceedings of a symposium sponsored by the
National Aeronautics and Space Administration,
Washington, D.C., and held in
Williamsburg, Virginia
April 27–30, 1993

National Aeronautics and Space Administration
Langley Research Center • Hampton, Virginia 23681-0001

April 1995

This publication is available from the following source:

NASA Center for AeroSpace Information
800 Elkridge Landing Road
Linthicum Heights, MD 21090-2934
(301) 621-0390

ERRATA

NASA Conference Publication 3248, Part 1

ORBITER EXPERIMENTS (OEX) AEROTHERMODYNAMICS SYMPOSIUM

David A. Throckmorton

April 1995

Page 247, figures 7 and 8: See the color versions of figures 7 and 8, page 496 for complete figure data.

Page 248, figure 9: See the color version of figure 9, page 497 for complete figure data.

Issued April 1995

PREFACE

Operations of the Nation's Space Transportation System (STS) have provided recurring opportunities for the aerothermodynamicist to study entry aerothermal phenomena unique to lifting vehicles in hypersonic flight. Initiated in the mid-1970s, the NASA Orbiter Experiments (OEX) Program provided a mechanism for utilization of the Shuttle Orbiter as an entry aerothermodynamic flight-research vehicle, as an adjunct to its normal operational missions.

Under the auspices of the OEX Program, various elements of aerothermodynamic research instrumentation flew aboard the Orbiters *Columbia* and *Challenger*. These OEX experiment instrumentation packages obtained in-flight measurements of the requisite parameters for (1) determination of Orbiter aerodynamic characteristics (both static and dynamic) over the entire entry flight regime, and (2) determination of the aerodynamic heating rates imposed upon the vehicle's thermal protection system during the hypersonic portion of atmospheric entry.

The data derived from the OEX complement of experiments represent benchmark hypersonic flight data heretofore unavailable for a lifting entry vehicle. These data are being used in a continual process of validation of state-of-the-art methods, both experimental and computational, for simulating/predicting the aerothermodynamic characteristics of advanced space transportation vehicles.

The ***Orbiter Experiments (OEX) Aerothermodynamics Symposium*** provided a forum for dissemination of OEX experiment flight data and for demonstration of the manner in which these data are being used for validation of advanced vehicle aerothermodynamic design tools. The Symposium's invited speakers included both OEX experiment Principal Investigators and other researchers who have been active users and analysts of the Orbiter entry flight data. This NASA Conference Publication comprises a compendium of the papers presented at the Symposium.

CONTENTS

PART 1

Part 2**

---

*Retired.
**Part 2 is presented under separate cover.

---

*Retired.

Part 1
WELCOME AND OPENING REMARKS

H. Lee Beach, Jr.
Deputy Director
NASA Langley Research Center
Hampton, VA

I would like to welcome all of you who have come long distances to participate in what I hope will be a very dynamic and productive Symposium over the next four days. Let me start with an apology. As your Program indicates, Paul Holloway, the Director of the Langley Research Center, had planned to be here this morning. Paul is very disappointed that he was unable to do so because he had been planning for some time to be here to welcome you and provide the opening remarks for the Symposium. He was informed on Friday that he would be needed in Washington both yesterday and today. So he asked me to express his sincere apologies for not being here, and I know that is an apology that is very heartfelt. Paul has a strong association with the Orbiter Experiments (OEX) Program. He, along with many of you in this room, invested a tremendous amount of energy getting this program started a number of years ago, and I know he is extremely disappointed that he could not be here to share in this occasion with you. In any case, I'm glad to be able to express a few thoughts that I think Paul would have shared had he been able to be here.

Why did we have an OEX program to begin with? In my opinion, having been an outsider looking in, it was the result of both the foresight and very aggressive advocacy efforts of some specific individuals from across the Agency. In the early 1970s, during the Phase B portion of the Shuttle program, significant uncertainties and concerns existed with regard to our ability to accurately predict the entry aerothermodynamic environment of the Shuttle Orbiter. Specifically, concerns existed relative to phenomena such as leeside heat transfer, lower-surface boundary-layer transition, and the vehicle's hypersonic aerodynamic characteristics. (These, of course, were only a few of the many vehicle design concerns.) Leeside heat transfer and boundary-layer transition issues would influence thermal protection system requirements heavily and, therefore, total vehicle weight, payload mass-fraction, and other important aspects of the transportation system. Uncertainties in extrapolating wind-tunnel-derived hypersonic aerodynamics to flight would influence the vehicle's flight-control system design and robustness, as well as safety-of-flight issues. Of course, all these issues would be "solved," in some sense of the word, for the orbiter design. However, they would be solved through inclusion of significant design conservatism, *not* by improved predictive capabilities at the time. So the early flights of the Shuttle would be performed in a highly constrained flight envelope, and that envelope would be incrementally expanded as flight experience and data were obtained. It was in this environment that the Orbiter Experiments Program was born (as I have indicated, not without significant difficulty) to take advantage of the anticipated "regular" flights of the Shuttle to gather flight data which could be used to improve and validate the aerothermodynamic predictive techniques which will be used for the design of other vehicles for future space transportation systems.

Where do we stand today? The aerothermodynamic design process for the Shuttle Orbiter required more than 100,000 hours of wind-tunnel occupancy in facilities all over the country. Even today, the operational flight envelope of the orbiter, specifically its cross-range capability, is constrained relative to what had been initially planned, as a direct result of under-prediction of certain aspects of the entry aeroheating environment of the orbiter. The Orbiter Experiments Program has enabled us to better understand which flight parameters *really* require accurate simulation in our ground-test facilities and how to more accurately extrapolate wind-tunnel results to the flight environment. One would think, therefore, that "better, faster, and cheaper" development of future space transportation vehicles could be achieved through more efficient utilization of our ground-based facilities than was the case for the Shuttle Orbiter.

After almost twenty years since the beginning of the Shuttle Orbiter design process and the birth of the OEX program, we have computational fluid dynamic (CFD) capabilities which were not dreamed-of in the time frame of Shuttle development. A lot of modeling work has gone on. We still do wind-tunnel testing, of course, and in my judgment will continue to do so for the remainder of our careers and probably the careers of our children. But, we have greatly improved our predictive capabilities, and the OEX Program has provided significant amounts of data that have helped us and will continue to help us understand how we can better use the tools of today to design the vehicles of tomorrow.

It's our hope at Langley that this Symposium will be a good mechanism to sum up what we have learned and hopefully to point the way to those future vehicles that I sincerely hope will be coming down the pike for our country in the years to come. I hope that you will have a very productive four days here, as I am sure you will. I invite you to participate aggressively and vigorously, in the hope that we'll come out of these four days with a much better understanding of where the technology stands, and we can take this information and look forward to the future.

Again let me say, welcome to each of you, and have a very productive and enjoyable Symposium.

ORBITER EXPERIMENTS (OEX) PROGRAM OBJECTIVE AND EXPERIMENT COMPLEMENT

David A. Throckmorton
NASA Langley Research Center
Hampton, VA

SUMMARY

Routine operations of the Nation's Space Transportation System (STS) have provided recurring opportunities for the aerothermodynamicist to study entry aerothermal phenomena unique to lifting entry vehicles in hypersonic flight. Initiated in the mid-1970s, the Orbiter Experiments (OEX) Program provided a mechanism for utilization of the shuttle orbiter as an entry research vehicle as an adjunct to its normal operational mission. OEX Program experiments were unique among orbiter payloads, as the research instrumentation for these experiments were carried as integral parts of the orbiter vehicle's structure, rather than being placed in the orbiter's payload bay as mission cargo.

The data derived from the OEX experiments represent benchmark hypersonic flight results heretofore unavailable for a lifting entry vehicle. These data are being used in a continual process of validation of state-of-the-art methods, both experimental and computational, for simulating and/or predicting the aerothermodynamic flight characteristics of advanced space transportation vehicles. This paper summarizes the aerothermodynamic research objectives of the OEX Program and the flight data requirements of such research. The OEX Program complement of aerothermodynamic research experiments and the synergy among these experiments are described.

INTRODUCTION

The NASA Orbiter Experiments (OEX) Program had its genesis in the early days of the Space Shuttle Program's Phase C/D, design and development of the shuttle orbiter. Development of the orbiter represented the first attempt to design a reusable vehicle capable of controlled aerodynamic entry from low-Earth orbit to a horizontal landing at a predetermined landing site. The operational requirements of this vehicle presented significant challenges to its aerothermodynamic designers. The vehicle was required to be aerodynamically controllable across the speed-regime, from Earth-orbital, hypersonic entry velocities to low-subsonic landing speeds; and the vehicle's thermal protection system (TPS) was required to protect the vehicle's structure from the extreme levels of aerodynamic heating which would accompany the hypersonic entry, yet be reusable for many additional missions.

The aerothermodynamic design process required a high degree of integration among the disciplines of aerodynamics, aeroheating, and guidance, navigation, and control. The aerodynamic performance, and stability and control characteristics, of the orbiter configuration had to be adequately defined over the entire entry flight regime in order to enable design of the guidance, navigation, and flight control systems. The vehicle's aerodynamic heating environment had to be adequately predicted in order to enable design of the thermal protection system, as well as definition of the thermal flight envelope constraints which would influence entry trajectory design.

An extensive program of ground-based testing was undertaken in order to generate the database required for the aerothermodynamic design of the orbiter vehicle. This test program, which required tens of thousands of hours of testing in the nation's hypersonic wind tunnel facilities, included aerodynamic performance, stability and control, and aerodynamic heat-transfer testing. This expansive ground-test program notwithstanding, it was recognized that prior to the orbiter's first flight, significant uncertainties would exist in predictions of both the vehicle's aerodynamic characteristics and its aerodynamic heating environment. These uncertainties resulted from inherent limitations in the ability of ground-test facilities to adequately simulate the full-scale flight environment. While existing test facilities could, in some instances, replicate certain of the relevant parameters (e.g., Mach number or Reynolds number), no facility could provide simultaneous simulation of the relevant parameters. More importantly, no facilities existed which could replicate the "real-gas" aspects of the flight environment. Additionally, since no data existed for a lifting vehicle in the actual flight environment, methodologies for extrapolation of ground-test results to the flight environment could not be validated.

The vehicle's flight control and thermal protection system designs were required to be sufficiently robust to assure fail-safe operation of the orbiter during entry in the face of these uncertainties. Systems robustness would be obtained through the application of significant factors of conservatism in the systems designs. This conservatism would result in a highly-constrained aerodynamic flight envelope, in severe limitations on allowable vehicle center-of-gravity variation, and most probably in an overweight thermal protection system.

The conservatism in the orbiter's aerothermodynamic design was known to be significant, and the research community recognized the importance of eliminating this conservatism in the design of future entry vehicles. Members of this community also recognized the unique opportunity which Shuttle operations might provide: to routinely gather hypersonic aerothermodynamic flight data with which to enhance understanding of the real-gas, hypersonic flight environment, and to enable improvement and validation of ground-to-flight data extrapolation techniques. Thus the concept of the Orbiter Experiments (OEX) Program was born.

NOMENCLATURE

ACIP	Aerodynamic Coefficient Identification Package
AIP	Aerothermal Instrumentation Package
ALT	Approach and Landing Test
BET	Best Estimate of Trajectory
c.g.	center of gravity
CSE	Catalytic Surface Effects
DFI	Development Flight Instrumentation
GN&C	guidance, navigation, and control
HiRAP	High-Resolution Accelerometer Package
IMU	Inertial Measurement Unit
IRIS	Infrared Imagery of Shuttle
L/D	lift-to-drag ratio
NASA	National Aeronautics and Space Administration
OARE	Orbital Acceleration Research Experiment
OAST	Office of Aeronautics and Space Technology
OEX	Orbiter Experiments
OFT	Orbital Flight Test
PCM	pulse code modulation

RCG	reaction cured glass
RCS	reaction control system
SEADS	Shuttle Entry Air Data System
SILTS	Shuttle Infrared Leeside Temperature Sensing
SUMS	Shuttle Upper-Atmosphere Mass Spectrometer
TACAN	tactical air navigation
TGH	Tile Gap Heating
TPS	thermal protection system
x/L	non-dimensional vehicle length (L=32.77m)

OEX PROGRAM GENESIS

The concept of utilizing the shuttle orbiter as a flight research vehicle, as an adjunct to its normal operational mission, was a topic of discussion within the research community circa 1974. In this time frame, the idea received programmatic attention in deliberations of the NASA Research and Technology Advisory Council's (RTAC) Panel on Space Vehicles. Meetings of this Panel in March and October of 1975 resulted in recommendations to the NASA Office of Aeronautics and Space Technology (OAST), that it pursue development and implementation of expanded flight test instrumentation to be flown aboard the shuttle orbiter.

Potential flight investigations were identified and/or documented during a Space Technology Workshop sponsored by the NASA OAST in August 1975 (ref. 1). This workshop was intended: (1) to foster identification of areas of needed technology development which required, or could substantially benefit from, space flight experimentation; and (2) to define candidate flight research experiments which would address those technology development needs, by taking advantage of the ready access to space which was to become possible with the advent of Shuttle operations. Entry technology was one of eleven research areas addressed at this workshop. The report of the Workshop's Entry Technology Panel (ref. 2) included recommendations of specific flight instrumentation concepts which, if implemented, would enable collection of aerothermodynamic flight research data during atmospheric entry of the shuttle orbiter. A subsequent Mini-Workshop on Entry Technology, in March 1976, provided for more detailed definition of candidate flight experiments.

These preliminary planning activities, as well as the deliberations and recommendations of the RTAC Panel on Space Vehicles, led to the establishment, in July 1976, of the Orbiter Experiments (OEX) Program. Initial funding for the Program was provided, for Fiscal Year 1977, from discretionary funds of the Associate Administrator of OAST. The OEX Program was an integral part of the proposed NASA Budget for Fiscal Year 1978. As such, the Program was discussed in testimony (see ref. 3 as example) before Congressional Committees with NASA oversight, during the Fiscal Year 1978 Budget Authorization process. The OEX Program was approved as part of the NASA Budget and began to receive yearly funding allocations in Fiscal Year 1978.

AEROTHERMODYNAMIC FLIGHT RESEARCH DATA REQUIREMENTS

Performing aerothermodynamic research in the hypersonic flight environment is not unlike the process of conducting similar research in ground-based wind-tunnel facilities. The generic data requirements of both are identical, although the manner in which those data are obtained may differ. In both instances, the freestream environment in which the test is being conducted must be characterized, and the vehicle's attitude with respect to the freestream must be accurately known. For aerodynamic testing, the aerodynamic forces acting on the vehicle must be determined; and for aerothermal testing, aerodynamic surface pressure, temperature, and heat-transfer-rate data must be obtained. Of course, in both instances, the vehicle's aerodynamic configuration (i.e., control surface deflection positions) must also be known.

Table I presents a summary list of the classes of data required for the determination of hypersonic vehicle aerothermodynamic characteristics, whether testing is performed in ground-based wind-tunnel facilities or in flight. The measurement techniques used to obtain these data in flight are compared with those used to obtain similar data in the wind tunnel. The following subsections contain more in-depth discussions of these data classes, and the flight data-measurement techniques.

Freestream Environment and Vehicle Attitude Data

In flight testing, freestream environmental definition is typically achieved by the measurement of appropriate flight-test variables, which enable determination of the pertinent freestream flow parameters. Normally, a calibrated "air data" probe is mounted at the end of a long boom attached to the nose of a flight-test vehicle to enable direct, in-situ measurements of freestream dynamic and static pressures, freestream total temperature, and vehicle attitude during flight testing. If for some reason an air-data boom cannot be used, alternate (less accurate) approaches may be implemented to infer the required environmental data. Atmospheric properties of static temperature, pressure, density, and winds may be determined as a function of altitude by balloon-borne measurement devices; and vehicle position (altitude) and velocity (ground-relative) may be determined by ground-based radar tracking. Inertial measurement devices onboard the test vehicle may also be used for the determination of vehicle velocity and attitude (relative to an inertial reference, without respect to winds).

Aerodynamic Force and Moment Data

Flight test determinations of aerodynamic forces and moments are accomplished by measurement of the three-axis linear accelerations, and angular accelerations and rates, experienced by the vehicle in flight. These data, when combined with appropriate vehicle mass, center-of-gravity, and moments-of-inertia information enable determination of the in-flight aerodynamic forces and moments.

Aerodynamic stability and control derivatives are determined from flight-measured dynamic data using a process known as "maximum-likelihood estimation." In the maximum-likelihood estimation process (ref. 4), the six-degree-of-freedom equations of motion are formulated with vehicle aerodynamic coefficients, and stability and control derivatives, as independent model variables. In flight, a precisely-defined, vehicle aerodynamic control input is commanded and measured, and the resulting small-perturbation vehicle dynamic response data are recorded. The vehicle's estimated (expected) response to the control input (based upon the pre-flight aerodynamic model) is then compared to the actual measured response. Based upon this comparison, the aerodynamic model is updated, and a new vehicle response estimate is generated, which is again compared to the measured response. This process is performed iteratively until the differences between the estimated and actual response data are statistically minimized. The resulting aerodynamic model then represents the "maximum-likelihood estimate" of the vehicle's in-flight aerodynamic characteristics.

Aerodynamic Surface Pressure and Heat Transfer Data

Methods used to obtain aerodynamic surface data in flight are fundamentally identical to those used in hypersonic wind tunnels. The specific implementation approaches differ somewhat, however, because of the unique characteristics of the flight environment.

In-flight measurements of surface pressure are normally obtained using small pressure orifices normal to the aerodynamic surface, through which the static pressure may be sensed. Each orifice is typically connected, by tubing, to an individual pressure transducer. Because the flight-test environment (certainly that of the shuttle orbiter) is by its very nature a transient environment, care must be taken in the implementation of a flight pressure-sensing system to minimize measurement sensitivity to transient phenomena and pressure losses due to tube length. Good engineering practice demands that tube lengths between orifices and sensors be minimized. This is accomplished by simply locating the pressure transducers as close as is *practically* possible to their orifice location. Thus, the influences of both pressure transients and tube losses are minimized.

Techniques for flight measurement of aerodynamic heat-transfer rates are analogous to those used in hypersonic wind tunnels. On the shuttle orbiter, temperatures within the orbiter's thermal protection materials were measured at discrete locations by means of in-situ thermocouples and/or resistance-temperature-devices (RTD's). Where installation of these devices was incompatible with the material in which the measurement was to be made, or where spatially-continuous temperature distribution data were desired and where a vantage point for surface viewing was available, radiometers provided for non-intrusive measurement of temperature levels. These temperature data, when combined with proper modeling of the heat conduction process within the thermal protection materials and reradiation of energy into space (unique to the flight case), enabled determination of aerodynamic heat-transfer rates to the orbiter surfaces.

Vehicle Configuration Data

Proper interpretation of aerothermodynamic flight test data obviously requires accurate knowledge of the aerodynamic configuration under test. In the context of this discussion, configuration data refers not simply to the geometric shape of the configuration, but, more specifically, refers to the control-surface position configuration. In flight, control surface positions may or may not be controllable test variables. Specifically in the shuttle orbiter case, control-surface deflections are first dictated by vehicle trim requirements, and the guidance and navigation requirements of the entry trajectory. Variability of the orbiter's control surface configuration about the nominal is severely limited, constrained by the energy management requirements of the specific entry (the orbiter is an unpowered glider) and possible thermal constraints on control surface deflection or vehicle attitude. Additionally, nominal control surface positions may differ from mission-to-mission as a result of mission-dependent vehicle center-of-gravity variations. Nonetheless, control-surface position data are measured during orbiter entry.

As a hybrid spacecraft and aircraft, the shuttle orbiter has not only aerodynamic control surfaces, but also a reaction control system (RCS) which provides on-orbit vehicle attitude control. The RCS includes some 19 primary and 4 vernier pitch-axis thrusters, and 12 primary and 2 vernier yaw-axis thrusters. The reaction control system is active during much of the hypersonic portion of atmospheric entry, providing attitude control at flight conditions where the dynamic pressure is insufficient for effective attitude control by the aerodynamic control surfaces. Reaction control system operation data are also measured during entry.

OEX EXPERIMENT COMPLEMENT AND SYNERGY

Under the auspices of the Orbiter Experiments (OEX) Program, various experiment systems were designed, developed, and integrated aboard the Shuttle Orbiter *Columbia* to enable collection of research-quality aerothermodynamic flight data. Unique OEX experiment instrumentation augmented existing orbiter instrumentation systems. The total complement of orbiter instrumentation and OEX experiments comprised a comprehensive instrumentation system for the determination of orbiter aerodynamic and aerothermal flight characteristics across the entire entry flight regime.

Several early papers (refs. 5-7) documented the planning for utilization of the orbiter as an entry flight-research vehicle. Reference 5 provides an excellent presentation of the data requirements for orbiter aerodynamic testing, as well as descriptions of the orbiter baseline and OEX measurement systems which were to be implemented to enable orbiter aerodynamic research. A summary discussion of the more significant orbiter entry aerothermodynamic problems, and short, overview descriptions of the proposed OEX experiments are contained in reference 6. Lastly, planned aerothermodynamic flight research analyses, to be conducted by NASA Langley Research Center staff members, using data obtained during the Orbital Flight Test missions of the Orbiter *Columbia*, are described in reference 7. Reference 8 is a contemporary paper which, like the current paper, presents a retrospective overview of the OEX aerothermodynamic experiments. It also presents typical OEX-experiments flight data and examples, drawn from the literature, of utilization of that data for validation of advanced vehicle aerothermodynamic design tools.

The following subsections contain discussions of both the orbiter baseline and OEX-unique experiment systems which were incorporated (and/or used) for the purpose of obtaining orbiter entry aerothermodynamic flight research data. These discussions are organized by data type, in the same manner as the foregoing section entitled *Aerothermodynamic Flight Research Data Requirements*.

Freestream Environment and Vehicle Attitude Data

The Shuttle Orbiter Enterprise was equipped with an air data boom to obtain freestream environment and vehicle attitude data during the Orbiter's Approach and Landing Test Program (Fig. 1). At hypersonic speeds, however, utilization of an air-data boom is not practical because of the extreme aerodynamic heating environment which accompanies hypersonic flight. Consequently, a non-intrusive method of measuring air-data parameters is required for a hypersonic flight test vehicle. The challenge of obtaining air data on a hypersonic flight vehicle was first faced during the X-15 program. That vehicle incorporated a spherical "ball-nose" flow direction sensor (ref. 9). This sensor used differential pressure measurements from orifices located on opposite sides of a sphere at the vehicle's nose to drive a hydraulic actuator which rotated the sphere so as to null the pressure differential. The resulting position of the sphere relative to the vehicle centerline provided a direct indication of angles-of-attack and -sideslip. The ball-nose also contained a stagnation-point pressure orifice. Although not used for the purpose at the time, this pressure measurement could have been used for accurate determination of freestream dynamic pressure.

For shuttle orbiter operational purposes, inertial measurement techniques are used to infer the air-data parameters required for vehicle guidance, navigation, and control (GN&C) during hypersonic flight. The inertially-derived parameters are sufficiently accurate to enable the GN&C system to guide the vehicle to the vicinity of the landing site, where data from other sources (e.g., TACAN, beginning at about 49 km altitude) provide updates to the vehicle state vector and enable the vehicle to be flown to a precise landing. The inertially-derived air data parameters are not sufficiently accurate, however, for research flight data analyses. Consequently, the OEX Program provided for the development and implementation of both in-situ measurement systems, and post-flight data analysis methods, to enable "research-quality" determination of vehicle freestream environmental and attitude information.

Shuttle Entry Air Data System (SEADS)

The Shuttle Entry Air Data System (refs. 10-12) was designed to provide "across-the-speed-range" air data from approximately 90 km altitude, when the orbiter vehicle is traveling in excess of Mach 25, through the supersonic, transonic, and subsonic portions of the entry, to landing. This system might be viewed as conceptually similar to the X-15 "ball-nose"; however, its implementation approach was substantially different from, and its air data parameter determination capability far exceeded, that of the X-15 "ball-nose." The SEADS system comprised a specially-designed orbiter nose-cap, which incorporated 14 pressure orifice assemblies through which the aerodynamic surface pressure could be measured during entry (Fig. 2). Measurement of the magnitude and distribution of aerodynamic pressure acting on the orbiter's nosecap in flight enabled accurate post-flight determination of vehicle angles-of-attack and -sideslip, as well as freestream dynamic pressure.

The SEADS pressure orifices were arranged in a cruciform array (Fig. 2) with eight orifices in the plane of symmetry and six orifices in the transverse plane. The symmetry-plane orifice array contributed primarily to determination of stagnation point location and pressure, and vehicle angle-of-attack. The transverse orifice array contributed primarily to determination of angle-of-sideslip. Each orifice assembly was connected, through internal nosecap "plumbing," to two pressure transducers -- one with a measurement range of 0-1 psia, and one with a measurement range of 0-20 psia. Dual-range measurements at each orifice assured accurate determination of pressure level for the entire altitude regime over which the system was designed to operate. Temperatures of the pressure transducer banks (of which there were two) were measured in order to account for the temperature-dependence of transducer calibrations. Analog-to-digital conversions of transducer output signals were performed by a 12-bit pulse-code-modulation (PCM) unit. The data were sampled at a rate of 28 hertz, and were recorded on an OEX-dedicated flight data recorder.

The 14 nosecap orifices were augmented by six supplementary orifices located on the orbiter forebody aft of the nosecap (Fig. 2). Four of these measurements were obtained at locations around the periphery and just aft of the nosecap: two, located windward and leeward, on the plane of symmetry; and one each located on either side of the fuselage. Two additional pressure orifices, located well aft of the nose, one on either side of the fuselage, provided static pressure data which were of particular importance for low supersonic and subsonic air data parameter determination.

Air data parameters were determined from the SEADS pressure data post-flight, by application of a unique data processing algorithm. This algorithm incorporated a mathematical model of the pressure distribution about the orbiter forebody as a function of an "aerodynamic state vector" which had elements of total and static pressure, and angles-of-attack and -sideslip. The mathematical model was constructed based upon a combination of theoretical considerations and the results of extensive wind tunnel tests. The flight-observed pressures were smoothed, with respect to time, and then "fit" to the model pressures using a digital batch filter process which optimized the "aerodynamic state vector" by minimizing, in a weighted-least-squares sense, the differences between the flight-observed and model pressures. The resulting "aerodynamic state vector," containing the basic air data information, was derived at an effective data rate of four hertz.

The SEADS was installed in place of the baseline nosecap on the Orbiter *Columbia* during that orbiter's modification period in 1984-85. The SEADS was subsequently operated successfully on five *Columbia* missions: STS-61C, -28, -32, -35, and -40.

Shuttle Upper-Atmosphere Mass Spectrometer (SUMS)

The Shuttle Upper Atmosphere Mass Spectrometer experiment (refs. 13 and 14) was intended to supplement the SEADS by providing atmospheric density data at altitudes above 90 km. Just as SEADS would provide flight environmental information in the continuum flow flight regime, the SUMS would provide similar data to enable aerodynamic research in the transitional and free-molecular flow flight regimes. At these extreme altitudes, aerodynamic surface pressures are too low to be accurately sensed by conventional pressure transducers such as those used by the SEADS. The SUMS instrument, instead, utilized a mass spectrometer, operating as a pressure-sensing device, to determine orbiter stagnation-region surface pressure, and thence infer the atmospheric density in this high-altitude, rarefied-flow flight regime.

The SUMS mass spectrometer was originally spare flight equipment developed for the Viking Mars Lander. This mass spectrometer was modified to enable it to operate in the entry flight environment of the shuttle orbiter. The SUMS sampled atmospheric gases through an orifice on the orbiter's lower surface centerline, just aft of the orbiter nosecap; this orifice was shared with the SEADS experiment. The mass spectrometer was connected to the gas-sampling orifice by a unique inlet system comprised of tubing, operation control valves, and a pressure transducer. The SUMS instrument assembly was mounted on the forward bulkhead of the orbiter's nose wheel well (Fig. 3), with the inlet system connected to the orifice plumbing.

SUMS data were sampled at an effective rate of 0.2 hertz, and recorded on the OEX recorder for post-flight processing. The processed SUMS data were combined with computational modeling of the rarefied flow, within both the inlet system and the orbiter's forebody flowfield (ref. 15), to enable determination of the freestream atmospheric density.

The SUMS was initially installed aboard the Orbiter *Columbia* following its 1984-85 modification period. The experiment was subsequently flown on STS-61C. Unfortunately, a "protection" valve, designed to prevent atmospheric-pressure gases from entering the mass spectrometer during ground operations, failed to open as planned when the vehicle reached orbit, and remained stuck in the closed position throughout the mission. Consequently, no freestream gases were able to reach the mass spectrometer during entry and thus no science data were obtained on the STS-61C mission. The SUMS was next flown on mission STS-35, during which the system operated properly, gathering data over the altitude range from orbit to 87 km. Useful science data were obtained over the approximate altitude range of 172-87 km. Science data for altitudes in excess of 172 km were masked by a "background" signal which resulted from gas molecules trapped in the SEADS and SUMS pressure transducers connected to the SUMS inlet system. The last flight of SUMS was on mission STS-40. On this mission, the instrument experienced an automatic shutdown immediately upon experiment initiation. The shutdown occurred (to protect the mass spectrometer from damage) when an excessive pressure level was detected in the mass spectrometer. The excessive pressure was attributed to the vapor pressure of water, which was present in the inlet system at launch. No science data were obtained on the STS-40 flight.

Best Estimate of Trajectory (BET)

In the absence of the SEADS and SUMS instruments to provide in-situ measurements of flight environmental information, these data were determined through processes of "reconstruction" of both the orbiter entry trajectory and the atmosphere at the time of entry, and correlation of these two data sets to provide an analytically and physically consistent "best-estimate" of the entry flight environmental parameters.

The trajectory reconstruction process (ref. 16) utilizes ground tracking data and onboard measurements of orbiter inertial attitude, linear accelerations, and angular rates to determine the vehicle inertial state vector (inertial position, velocity, and attitude) from near-orbital altitude to landing (Fig. 4).

Linear acceleration and angular rate information, derived from orbiter inertial measurement unit data, are used to deterministically integrate the six-degree-of-freedom equations of motion in time, from a known initial condition (shortly after the de-orbit burn) through orbiter landing, to define a first estimate of the history of the inertial state vector. These inertial position and velocity estimates are then constrained to fit, in a weighted least-squares of residuals sense, the observed position and velocity data measured by the ground-based tracking. The result is a statistically-best estimate of the vehicle entry trajectory (position, velocity, and attitude) in an inertial reference space.

Consideration of the rotation and oblate shape of the Earth allows the trajectory information to be transformed into an Earth/atmosphere referenced system. The final product of the trajectory reconstruction process is then a "best estimate" of the time-history of orbiter position (altitude above an oblate spheroid, latitude, and longitude), and atmosphere-relative (no winds) velocity and attitude (angles-of-attack and -sideslip), from near-orbital altitude to touchdown.

Definition of the state of the atmosphere through which the orbiter has flown is accomplished by a process (ref. 17) which combines atmospheric modeling with direct measurements of atmospheric profiles of pressure, temperature, density, and winds (Fig. 5). Atmospheric soundings made near the time of entry provide the measured atmospheric profiles. However, the soundings are made at only a few locations. These locations may not be along the orbiter's entry ground-track, and the time at which the soundings are made may not correspond well with that of orbiter entry. Additionally, the soundings only provide measured data to an altitude of approximately 90 km. Atmospheric data above 90 km are estimated using upper atmospheric models to propagate the pressure, temperature, density, and winds data to higher altitudes.

The measured and estimated data are then used to define freestream pressure, temperature, density, and winds along the orbiter entry corridor. The reconstructed trajectory defines the time of day, and corresponding latitude, longitude, and altitude of the orbiter's entry; atmospheric modeling is used to define the time-of-day and latitude variations in atmospheric properties. The measured atmospheric data are extrapolated to the orbiter entry corridor, in a manner which accounts for the time-of-day and latitude differences between the orbiter entry and the atmospheric soundings.

The results of the trajectory and atmospheric reconstruction processes are melded together to provide the "Best Estimate of Trajectory," which is an analytically- and physically-consistent definition of the freestream flight environment (i.e., freestream pressure, temperature, and density, wind-relative velocity, and angles-of-attack and -sideslip) from near-orbital altitude to landing.

Aerodynamic Force and Moment Data

Inertial Measurement Units (IMU)

The inertial measurement units are part of the orbiter's operational instrumentation system. The triply-redundant IMUs comprise all-attitude, four-gimbal, inertially-stabilized platforms, upon which are mounted two mutually-perpendicular linear accelerometers. In addition to the inertial acceleration data, primary outputs of the IMUs are vehicle velocity and attitude in the inertial reference space. Angular rate data may be inferred from the IMU attitude outputs.

Detailed descriptions of the IMU and other orbiter operational systems can be found in reference 18.

Aerodynamic Coefficient Identification Package (ACIP)

Although the orbiter's operational instrumentation system includes instruments which measure each of the vehicle motion parameters required for in-flight aerodynamic coefficient determination, these components were designed to meet only the operational requirements of vehicle guidance, navigation, and control. The measurement resolution and the data sampling rates of these instruments are not sufficient for accurate, research-quality determination of in-flight aerodynamic stability and control characteristics. Consequently, the Aerodynamic Coefficient Identification Package experiment (refs. 19 and 20) was designed specifically to enable collection of vehicle motion information with the resolution and data sampling rates required for accurate flight determination of orbiter aerodynamic characteristics.

The ACIP includes three-axis, orthogonal sets of linear accelerometers, angular accelerometers, and rate gyros. The ACIP linear accelerometers operate over a measurement range of ±3 g, with a measurement resolution of 300 micro-g, which enables the ACIP to accurately measure vehicle motion data at altitudes below approximately 80 km. Thus, the ACIP experiment obtains data which are synergistic with that of the SEADS.

In addition to processing data from its own sensors, ACIP data handling electronics also process control-surface-position sensor information for the orbiter's four elevons and rudder, as well as operation data for a single aft RCS yaw thruster. These data are routed through the ACIP data handling electronics to assure that they are recorded with proper time correlation, relative to the ACIP data, and at data rates which are sufficient to enable post-flight estimation of vehicle stability and control characteristics. ACIP data are digitized to 14-bit resolution, and recorded on the OEX recorder at a sampling rate of 174 hertz, as compared to the 1-25 hertz sampling-rate range for similar operational instrumentation data.

The ACIP is mounted on the orbiter keel (Fig. 6), in the wing carrythrough structure beneath the payload bay, at a longitudinal position of approximately 76 percent of vehicle length. This location is about 315 cm aft (10 percent of vehicle length), and 216 cm below the orbiter's entry center of gravity (c.g.). Proximity to the center of gravity minimizes the significance of correction factors associated with translation of the information for reference to the vehicle c.g. The ACIP is precisely aligned with respect to the orbiter's body-axis coordinate system.

Two ACIP flight units were fabricated for use on the Orbiters *Columbia* and *Challenger*. An ACIP has flown on every flight of these two vehicles.

High Resolution Accelerometer Package (HiRAP)

The High-Resolution Accelerometer Package experiment (refs. 21 and 22) comprises a three-axis, orthogonal set of high-resolution linear accelerometers. The HiRAP instrument operates over a range of ±8000 micro-g, with a measurement resolution of one micro-g, and data sampling rate of 174 hertz. The measurement range of the HiRAP enables it to sense aerodynamic forces acting on the orbiter from approximately 80 km to near orbital altitudes. HiRAP data were intended to be obtained in conjunction with SUMS freestream density data, enabling direct determination (based solely upon in situ measurements) of the aerodynamic performance characteristics of the orbiter in the rarefied flow flight regime.

The HiRAP (Fig. 7) is located beside the ACIP in the orbiter's wing carrythrough structure, approximately 330 cm aft and 188 cm below the orbiter's c.g., and is precisely aligned with respect to the orbiter's body-axis coordinate system.

As with ACIP, two HiRAP flight units were fabricated for flight on the Orbiters and *Challenger*. A HiRAP unit was flown on eight missions of *Challenger*, beginning with its first flight (STS-6), and four missions of *Columbia* beginning with STS-9. (See ref. 23.)

Orbital Acceleration Research Experiment (OARE)

The Orbital Acceleration Research Experiment (refs. 24 and 25) complements the ACIP and HiRAP instruments by extending the altitude range over which vehicle aerodynamic acceleration data may be obtained to orbital altitudes. Like the HiRAP, the OARE instrument comprises a three-axis, orthogonal set of extremely sensitive linear accelerometers. The OARE instrument can be operated over three auto-selected, or pre-programmed, measurement ranges. The least-sensitive measurement range envelopes that of the HiRAP instrument; the most-sensitive range (±150 micro-g) is almost two orders-of-magnitude more sensitive than the HiRAP. On the most-sensitive range, the measurement resolution of the OARE instrument is less than five nano-g. The operational range of the OARE is at such a low acceleration level that the sensors cannot be accurately calibrated in the one-g ground environment. Consequently, the instrument sensors are mounted, within the OARE, on a rotary calibration table which enables an accurate calibration to be performed on orbit, in the absence of Earth's gravity.

The OARE instrument produces acceleration data at an effective data rate of 10 hertz. These raw data may be recorded on an onboard tape recorder for post-flight processing and analysis. However, because the OARE was intended to measure the low-frequency, aerodynamic accelerations over long orbital time periods, the instrument has its own internal data processing and storage capability. The internal data processing software, which may be modified from flight-to-flight, currently uses a trimmed-mean filter algorithm to extract the "steady-state" acceleration signal. The processed data are then recorded on an internal solid-state memory device at a sampling rate of 1/25 hertz.

Unlike other OEX experiments, the OARE is carried as orbiter payload. It is mounted at the bottom of the payload bay envelope (Fig. 8) on a carrier plate attached to the orbiter's keel. This places the instrument approximately 165 cm aft and 137 cm below the orbiter's entry center-of-gravity. It is, of course, precisely aligned with respect to the orbiter's body axes.

On its first flight, on STS-40 in June 1991, the OARE experienced significant hardware anomalies which limited the accuracy of the data collected. On STS-50, the OARE successfully obtained measurements of aerodynamic drag on orbit. The OARE is currently manifested for reflight on STS-58 in the Summer of 1993.

Aerodynamic Surface Data

Development Flight Instrumentation (DFI)

During the Orbital Flight Test missions (STS-1 thru -5), the Orbiter *Columbia* was equipped with a large complement of diagnostic instrumentation which was referred to as the Development Flight Instrumentation. DFI measurements were intended to provide the requisite data for postflight certification of orbiter subsystems designs, prior to the start of orbiter operational missions. The DFI system was comprised of over 4500 sensors, associated data handling electronics, and data recorder.

Included among the DFI, and of particular interest to aerothermodynamic researchers, were measurements of the orbiter's aerodynamic surface temperature at over 200 surface locations (Fig. 9). These measurements were obtained using thermocouples mounted within the thermal protection system (TPS) materials, in thermal contact with the TPS surface coatings (ref. 26). The DFI also included temperature measurements in-depth, within the TPS materials, at some 19 locations, and along TPS tile sidewalls within the gaps between tiles at 16 locations. Aerodynamic surface pressure measurements were also made in numbers and distribution similar to the surface temperature measurements.

The Development Flight Instrumentation was aboard *Columbia* on missions STS-1 thru -5. However, mission unique circumstances limited the amount of hypersonic entry temperature and pressure data collected on these flights. On missions STS-1 and -4, failures of the onboard flight data recorder precluded collection of data when the orbiter was not in communications contact with a ground telemetry station. Consequently, data from these flights are available only for flight conditions of approximately Mach 12 and below. On STS-2, the pressure instrumentation was not "powered-up" during entry. This was due to a constrained orbiter entry power budget on this mission, which resulted from an in-flight failure of one of the orbiter's three fuel cells. Pressure data were obtained over the complete entry trajectory only on missions STS-3 and -5; and temperature data were obtained over the complete entry trajectory only on missions STS-2, -3, and -5.

The DFI-derived surface temperature data from STS-2, -3, and -5 have been processed to infer aerodynamic heat-transfer rates, using the methodology described in reference 27. The resulting orbiter flight heat-transfer data are contained in references 28-30.

Catalytic Surface Effects (CSE) Experiment

Early arc-jet testing of orbiter thermal protection materials indicated that the reaction cured glass (RCG) coating of the TPS tiles was non-catalytic to the recombination of dissociated air (specifically oxygen). Were this to be the case in flight, substantially reduced heat-transfer levels could be expected, when compared to those which would be experienced if the surface were fully catalytic. Prior to the advent of shuttle flights, however, this non-catalytic surface phenomenon had not been demonstrated to occur in the flight environment. Consequently, the shuttle TPS design was predicated on the conservative assumption that the gas chemistry at the TPS surface would be in chemical equilibrium. The Catalytic Surface Effects experiment (refs. 31 and 32) was conceived to provide direct confirmation of the non-catalytic nature of the TPS tile surface in flight, and provide information with which to estimate, quantitatively, the catalytic efficiency of the RCG material.

The CSE experiment would provide an "inverse" demonstration of the non-catalytic nature of the baseline tile surface material. The implementation of this experiment involved coating selected orbiter lower surface TPS tiles, which contained DFI surface temperature sensors, with a material which was known (based upon arc-jet tests) to be highly catalytic to the recombination of dissociated air. By comparing the flight-measured temperatures of the coated tiles and nearby baseline tiles, the relative catalytic efficiency of the baseline tile coating material would be demonstrated.

CSE experiment data were obtained on missions STS-2, -3, and -5 (refs. 33 and 34). On STS-2, two individual tiles on the lower surface centerline at 15- and 40-percent of vehicle length were coated (Fig. 10). For STS-3, individual tiles at 30- and 40-percent of vehicle length were coated. On STS-5, the catalytic coating was applied to individual tiles on the centerline at 10-, 15-, 20-, 30-, and 60-percent, and continuously along a centerline strip from 35- to 40-percent, of vehicle length. Two additional tiles located at 76- and 82-percent of vehicle length along the 60-percent semispan chord of the wing were also coated.

Tile Gap Heating (TGH) Experiment

The Tile Gap Heating experiment (ref. 35) was intended to obtain entry flight data with which to investigate the phenomenon of aerodynamic heating in the gaps between adjacent thermal protection system tiles. The experiment hardware consisted of a carrier panel of tiles which was installed on the orbiter's lower surface, near the centerline, at approximately 27-percent of vehicle length. This carrier panel was bolted directly to the orbiter structure and carried eleven tiles. At three locations on the array, tiles were instrumented with thermocouples in-depth, on the outer tile surface, and along the sidewalls of the tile-to-tile gaps. Data from these thermocouples was recorded as part of the DFI system.

The experiment tiles were fabricated and installed with exacting specifications applied to the values of tile edge radius and gap width. The experiment plan was to systematically vary these parameters over multiple flights of the experiment panel to gain an understanding of the effects of these variables on tile gap heating, and ultimately to determine optimum values of these parameters in order to minimize gap heating.

The TGH experiment was only flown on the STS-2 mission. Results from that flight are reported in reference 35.

Infrared Imagery of Shuttle (IRIS) Experiment

The objective of the Infrared Imagery of Shuttle experiment (refs. 36 and 37) was determination of the temperature distribution over the orbiter's lower surface at a *single* entry flight condition, at greater spatial resolution than would be achieved with the DFI measurements. This measurement was to be made remotely by underflying the entering orbiter with the NASA Kuiper Airborne Observatory (KAO) C-141 aircraft. An infrared image of the orbiter was to be obtained as it passed through the field-of-view of the KAO's astronomical telescope, which was equipped with two linear, focal-plane arrays of infrared detectors.

The IRIS experiment was successful in obtaining a partial image of the orbiter on STS-3. Unfortunately, the image was found to be severely spatially and thermally distorted, and efforts to accurately resolve the image were unsuccessful. As a result of extensive image-data and experiment-system analyses, the most-likely cause of the distortion was determined to be atmospheric density gradients which existed in the open telescope cavity of the KAO aircraft. Consequently, it was concluded that a spatially-resolvable image of the orbiter could not be attainable using this experimental technique.

Shuttle Infrared Leeside Temperature Sensing (SILTS) Experiment

The Shuttle Infrared Leeside Temperature Sensing experiment (refs. 38 and 39) was designed to obtain high-spatial-resolution temperature measurements of the leeside (wing and fuselage) of the orbiter during entry. These measurements were obtained by means of an imaging, infrared radiometer (camera) located in a unique experiment pod atop the vertical tail of the Orbiter *Columbia* (Fig. 11). The SILTS camera contained a single infrared detector element and dual, rotating scanning-prisms (one horizontal and one vertical), which enabled the detector to scan the field-of-view, producing two-dimensional imagery. The experiment could be configured to view the orbiter leeside surfaces through either of two infrared-transparent windows: one of which enabled viewing of the left wing, the other enabled viewing of the fuselage.

The SILTS experiment pod also contained a data and control electronics module, and a pressurized nitrogen system. Window protection plugs protected the viewport windows during orbiter ground handling, launch, and orbital operations. At experiment initiation, the window protection plugs were ejected, allowing the camera to "see" the orbiter surfaces. The viewport windows were transpiration-cooled, during experiment operation, by the injection of gaseous nitrogen over the external window surfaces. Active cooling of the windows was required to prevent window temperatures from increasing to levels at which the windows themselves would become radiators in the infrared, thus "fogging" the data images.

On a normal mission, the SILTS experiment was initiated at the time the orbiter reached the "entry interface" altitude of 122 km, and infrared imagery were collected throughout the hypersonic portion of atmospheric entry. A data image was obtained approximately every 8.6 seconds during experiment operation. SILTS data were recorded on the OEX flight data recorder.

The SILTS experiment was flown on five orbiter missions. Significant SILTS hardware anomalies prevented useful data from being obtained on its first flight on STS-61C (ref. 40). Useful data were obtained, however, on four subsequent flights. Flights of the SILTS experiment on STS-28 (ref. 41) and -32 provided temperature data for the orbiter's left wing throughout the hypersonic portion of entry. The experiment was configured to view the leeside fuselage on the STS-35 and -40 missions. Unique operational anomalies occurred on each of these flights (different for each flight) which limited the quantity of data obtained (see ref. 42).

Aerothermal Instrumentation Package (AIP)

The Aerothermal Instrumentation Package comprised some 125 measurements of aerodynamic surface temperature and pressure at discrete locations on the leeside of the orbiter's left wing, side and upper fuselage, and vertical tail (Fig. 12). AIP temperature sensors provided in-situ measurements which comprised both "ground-truth" and corollary information for the SILTS experiment. The AIP pressure sensors were intended to provide data to support investigations of reaction control system jet interactions with the aerodynamic flowfield.

All of the AIP sensors were originally elements of the Development Flight Instrumentation system. They were reactivated through implementation of new orbiter wire harnesses which connected the sensors to an AIP-unique data handling system. AIP temperature data were recorded at a sampling rate of 5.3 hertz on the OEX flight data recorder.

The AIP obtained data throughout the hypersonic portion of atmospheric entry on shuttle missions STS-28, -32, and -40. Only limited data (below about 73 km altitude) were obtained on STS-35 as a result of a ground telemetry failure, which also affected the SILTS experiment. As with the DFI data, the AIP temperature data have been processed to infer aerodynamic heat-transfer rates, using the methodology of reference 27. The flight heat-transfer rate data are contained in references 43-45.

Vehicle Configuration Data

Orbiter control surface position data are measured and recorded in-flight by elements of the orbiter's operational instrumentation system. As was discussed in the preceding section on the ACIP, certain of these data are also processed, in parallel, by the ACIP data handling electronics. Operational measurements of control surface positions are recorded at rates of 1-25 hertz.

Reaction control system thruster firing data are inferred by measurements of pressure in the jet combustion chambers. These data are recorded at the rate of 25 hertz.

Vehicle mass, center-of-gravity, and moments of inertia are determined analytically by means of a complex mass accounting system. Each orbiter was weighed to establish a baseline set of mass and center-of-gravity information. A database of mass and location information is maintained for all additional orbiter hardware, and other elements (e.g., payloads), which may be installed on, or removed from, the orbiter vehicle during ground processing. In-flight, consumables are continually monitored. Using this mass accounting system, a vehicle mass properties history is produced following each flight.

CONCLUDING REMARKS

The Orbiter Experiment (OEX) Program successfully utilized the shuttle orbiters *Columbia* and *Challenger* to gather research-quality aerodynamic and aeroheating flight data during atmospheric entry of these vehicles as an adjunct to their normal operational missions. OEX Program experiments were unique among orbiter payloads, as the research instrumentation for these experiments was carried as integral parts of the orbiter vehicle's structure, rather than being placed in the orbiter's payload bay as mission cargo. Detailed descriptions of each of these experiments and their operational flight history are contained in subsequent papers herein.

The data derived from the OEX experiments represent benchmark hypersonic flight results heretofore unavailable for a lifting entry vehicle. These data are being used in a continual process of validation of state-of-the-art methods, both experimental and computational, for simulating and/or predicting the aerothermodynamic flight characteristics of advanced space transportation vehicles. The validation and advancements of state-of-the-art design methodologies, made possible by the availability of the OEX flight data, are also demonstrated in additional papers contained in this symposium-proceedings document.

ACKNOWLEDGMENTS

Although those individuals responsible for the OEX experiments described herein have, by and large, been recognized by reference to their published work, the author wishes to specifically recognize each of the past and present Principal (or Co-) Investigators for the OEX aerothermodynamic experiments:

Experiment	Principal Investigator(s)
SEADS	P. M. Siemers III NASA Langley Research Center
SUMS	R. C. Blanchard NASA Langley Research Center
ACIP	D. R. Cooke D. B. Kanipe NASA Johnson Space Center
HiRAP OARE	R. C. Blanchard NASA Langley Research Center
CSE	D. A. Stewart NASA Ames Research Center
TGH	W. C. Pitts NASA Ames Research Center
IRIS	W. C. Davy M. J. Green B. L. Swenson NASA Ames Research Center
SILTS	J. C. Dunavant D. A. Throckmorton E. V. Zoby NASA Langley Research Center
AIP	D. A. Throckmorton NASA Langley Research Center

No OEX experiment could have been successfully flown were it not for the untiring efforts of the personnel of the OEX Project Office at the NASA Johnson Space Center. The OEX Project Office was responsible for: overall OEX Project management, management and engineering interfaces with the Shuttle Orbiter Project, provision of an OEX data handling/recording system, assurance of OEX experiment flight operational planning and control, and integration of all OEX experiment systems aboard the orbiter. The personnel of the OEX Project Office, who were a part of the OEX Team during the 15-year lifespan of this project, are no less deserving of recognition than the experiment Principal Investigators and their hardware support teams. However, the numbers of people involved preclude their individual acknowledgment. Nevertheless, they know who they are! They should know that they have the gratitude of this author and each of the Principal Investigators whose research benefited substantially as a result of their efforts.

REFERENCES

1. NASA Langley Research Center and Old Dominion University: Executive Summary, *NASA Office of Aeronautics and Space Technology Summer Workshop,* NASA TM X-73960, 1975.
2. NASA Langley Research Center and Old Dominion University: Entry Technology, *NASA Office of Aeronautics and Space Technology Summer Workshop, Vol. 9,* NASA TM X-73969, 1975.
3. Hayes, W. C., Jr.: OAST Shuttle Orbiter Experiments Program. Testimony before the Subcommittee on Space Science and Applications, Committee on Science and Technology, United States House of Representatives, February 9, 1977.
4. Iliff, K. W.: Parameter Estimation for Flight Vehicles. *Journal of Guidance, Control, and Dynamics,* Vol. 12, No. 5, September-October 1989, pp. 609-622 (1987 AIAA Dryden Research Lectureship).
5. Siemers, P. M. III, and Larson, T. J.: Space Shuttle Orbiter and Aerodynamic Testing. *Journal of Spacecraft and Rockets,* Vol. 16, No. 4, July-August 1979, pp. 223-231.
6. Jones, J. J.: OEX - Use of the Shuttle Orbiter as a Research Vehicle. AIAA Paper 81-2512, November 1981.
7. Throckmorton, D. A.: Research Analysis of Space Shuttle Orbiter Entry Aerothermodynamic Flight Data at the NASA Langley Research Center. AIAA Paper 81-2429, November 1981.
8. Throckmorton, D. A.: Shuttle Entry Aerothermodynamic Flight Research: The Orbiter Experiments Program. *Journal of Spacecraft and Rockets*, Vol. 30, No. 4, July-August 1993, pp. 449-465.
9. Cary, J. P., and Keener, E. R.: *Flight Evaluation of the X-15 Ball-Nose Flow-Direction Sensor as an Air Data System.* NASA TN D-2923, July 1965.
10. Siemers, P. M. III: Shuttle Entry Air Data System (SEADS) -- Advanced Air Data System Results: Air Data Across the Entry Speed Range. *Orbiter Experiments (OEX) Aerothermodynamics Symposium*, NASA CP-3248, 1995.
11. Pruett, C. D., Wolf, H., Heck, M. L., and Siemers, P. M. III: Innovative Air Data System for the Space Shuttle Orbiter. *Journal of Spacecraft and Rockets,* Vol. 20, No. 1, January-February 1983, pp. 61-69.
12. Siemers, P. M. III, Wolf, H., and Henry, M. W.: Shuttle Entry Air Data System (SEADS) -- Flight Verification of an Advanced Air Data System Concept. AIAA Paper 88-2104, May 1988.

13. Blanchard, R. C., Ozoroski, T. A., and Nicholson, J. Y.: Shuttle Upper-Atmosphere Mass Spectrometer (SUMS) Flight Results on STS-35. *Orbiter Experiments (OEX) Aerothermodynamics Symposium*, NASA CP-3248, 1995.

14. Blanchard, R. C., Duckett, R. J., and Hinson, E. W.: The Shuttle Upper Atmosphere Mass Spectrometer Experiment. *Journal of Spacecraft and Rockets,* Vol. 21, No. 2, March-April 1984, pp. 202-208.

15. Moss, J. N., and Bird, G. A.: Monte Carlo Simulations in Support of the Shuttle Upper Atmosphere Mass Spectrometer Experiment. *Journal of Thermophysics and Heat Transfer,* Vol. 2, No. 2, April 1988, pp. 138-144.

16. Compton, H. R., Findlay, J. T., Kelly, G. M., and Heck, M. L.: Shuttle (STS-1) Entry Trajectory Reconstruction. AIAA Paper 81-2459, November 1981.

17. Price, J. M.: Atmospheric Definition for Shuttle Aerothermodynamic Investigations. *Journal of Spacecraft and Rockets,* Vol. 20, No. 2, March-April 1983, pp. 133-140.

18. Anon.: *National Space Transportation Reference*, NASA TM-101,877, June 1988.

19. Giesecke, R. L., and Romere, P. O: Aerodynamic Coefficient Identification Package (ACIP). *Orbiter Experiments (OEX) Aerothermodynamics Symposium*, NASA CP-3248, 1995.

20. Anon.: End Item Specification -- Aerodynamic Coefficient Identification Package (ACIP) and High Resolution Accelerometer Package (HiRAP) for Shuttle Orbiter Experiments. Contract NAS9-15588, Specification 3291583, The Bendix Communications Division, 1981.

21. Blanchard, R. C., Larman, K. T., and Borchardt, R. P. Jr.: High-Resolution Accelerometer Package (HiRAP). *Orbiter Experiments (OEX) Aerothermodynamics Symposium*, NASA CP-3248, 1995.

22. Blanchard, R. C., and Rutherford, J. F.: Shuttle Orbiter High-Resolution Accelerometer Package Experiment: Preliminary Flight Results. *Journal of Spacecraft and Rockets,* Vol. 22, No. 4, July-August 1985, pp. 474-480.

23. Blanchard, R. C., Larman, K. T., and Barrett, M.: The High Resolution Accelerometer Package (HiRAP) Flight Experiment Summary for the First Ten Flights. NASA RP-1267, March 1992.

24. Blanchard, R. C., Nicholson, J. Y., and Ritter, J. R.: Orbital Acceleration Research Experiment (OARE). *Orbiter Experiments (OEX) Aerothermodynamics Symposium*, NASA CP-3248, 1995.

25. Blanchard, R. C., Hendrix, M. K., Fox, J. C., Thomas, D. J., and Nicholson, J. Y.: Orbital Acceleration Research Experiment. *Journal of Spacecraft and Rockets,* Vol. 24, No. 6, November-December 1987, pp. 504-507.

26. Stoddard, L. W., and Draper, H. L.: Development and Testing of Development Flight Instrumentation for the Space Shuttle Orbiter Thermal Protection System. *Proceedings of the 24th International Symposium,* Instrument Society of America, 1978.

27. Throckmorton, D. A.: Benchmark Determination of Shuttle Orbiter Entry Aerodynamic Heat-Transfer Data. *Journal of Spacecraft and Rockets,* Vol. 20, No. 3, May-June 1983, pp. 219-224.

28. Hartung, L. C., and Throckmorton, D. A.: *Space Shuttle Entry Heating Data Book, Volume 1 - STS-2, Parts 1 and 2.* NASA RP-1191, May 1988 (ITAR Restricted Distribution).

29. Hartung, L. C., and Throckmorton, D. A.: *Space Shuttle Entry Heating Data Book, Volume 2 - STS-3, Parts 1 and 2.* NASA RP-1192, May 1988 (ITAR Restricted Distribution).

30. Hartung, L. C., and Throckmorton, D. A.: *Space Shuttle Entry Heating Data Book, Volume 3 - STS-5, Parts 1 and 2.* NASA RP-1193, May 1988 (ITAR Restricted Distribution).

31. Stewart, D. A.: Catalytic Surface Effects (CSE) Experiment for Space Shuttle. *Orbiter Experiments (OEX) Aerothermodynamics Symposium*, NASA CP-3248, 1995.

32. Stewart, D. A., Rakich, J. V., and Lanfranco, M. J.: Catalytic Surface Effects Experiment on the Space Shuttle. *Thermophysics of Atmospheric Entry, Progress in Astronautics and Aeronautics,* Vol. 82, 1982, pp. 248-272.

33. Rakich, J. V., Stewart, D. A., and Lanfranco, M. J.: Results of a Flight Experiment on the Catalytic Efficiency of the Space Shuttle Heat Shield. AIAA Paper 82-944, June 1982.

34. Stewart, D. A., Rakich, J. V., and Lanfranco, M. J.: Catalytic Surface Effects on Space Shuttle Thermal Protection System During Earth Entry of Flights STS-2 Through STS-5. *Shuttle Performance: Lessons Learned,* NASA CP-2283, Part 2, March 1983, pp. 827-845.

35. Pitts, W. C., and Murbach, M. S.: *Flight Measurements of Tile Gap Heating on the Space Shuttle.* AIAA Paper 82-0840, June 1982.

36. Davy, W. C., and Green, M. J.: A Review of the Infrared Imagery of Shuttle (IRIS) Experiment. *Orbiter Experiments (OEX) Aerothermodynamics Symposium*, NASA CP-3248, 1995.

37. Green, M. J., Budnik, M. P., Yang, L., and Chaisson, M. P.: *Supporting Flight-Data Analysis for Space-Shuttle Orbiter Experiments at NASA Ames Research Center.* NASA Technical Memorandum 84345, April 1983.

38. Throckmorton, D. A.: Shuttle Infrared Leeside Temperature Sensing (SILTS) Experiment. *Orbiter Experiments (OEX) Aerothermodynamics Symposium*, NASA CP-3248, 1995.

39. Throckmorton, D. A., Zoby, E. V., and Kantsios, A. G.: The Shuttle Infrared Leeside Temperature Sensing (SILTS) Experiment. AIAA Paper 85-0328, January 1985.

40. Dunavant, J. C., Myrick, D. L., Zoby, E. V., and Throckmorton, D. A.: *Shuttle Infrared Leeside Temperature Sensing (SILTS) Experiment - STS 61-C Final Results.* NASA TP-2958, December 1989.

41. Throckmorton, D. A., Zoby, E. V., Dunavant, J. C., and Myrick, D. L.: Shuttle Infrared Leeside Temperature Sensing (SILTS) Experiment - STS-28 Preliminary Results. AIAA Paper 90-1741, June 1990.

42. Throckmorton, D. A., Zoby, E. V., Dunavant, J. C., and Myrick, D. L.: Shuttle Infrared Leeside Temperature Sensing (SILTS) Experiment - STS-35 and STS-40 Preliminary Results. AIAA Paper 92-0126, January 1992.

43. Throckmorton, D. A., and Hartung, L. C.: *Space Shuttle Orbiter Entry Lee-Side Heat-Transfer Data -- STS-28.* NASA RP-1306, September 1993 (ITAR Restricted Distribution).

44. Throckmorton, D. A., and Hartung, L. C.: *Space Shuttle Orbiter Entry Lee-Side Heat-Transfer Data -- STS-32*. NASA RP-1307, September 1993 (ITAR Restricted Distribution).

45. Throckmorton, D. A., and Hartung, L. C.: *Space Shuttle Orbiter Entry Lee-Side Heat-Transfer Data -- STS-40*. NASA RP-1308, September 1993 (ITAR Restricted Distribution).

Table I -- Aerothermodynamic Data Classes and Measurement Techniques

Data Class	Measurement Technique	
	Wind Tunnel	Flight
Freestream Environment Definition	Facility Calibration Total and/or Static Pressure and Temperature Measurements	Atmospheric Soundings Air Data System
Vehicle Attitude	Specified and Controlled	Air Data System Inertial Data
Aerodynamic Forces and Moments	Force Balance	Linear and Angular Acceleration and Rate Measurements Mass and Moments-of-Inertia Tracking
Surface Conditions	Direct Measurement	Direct Measurement
Control Configuration	Specified and Controlled	Direct Measurement

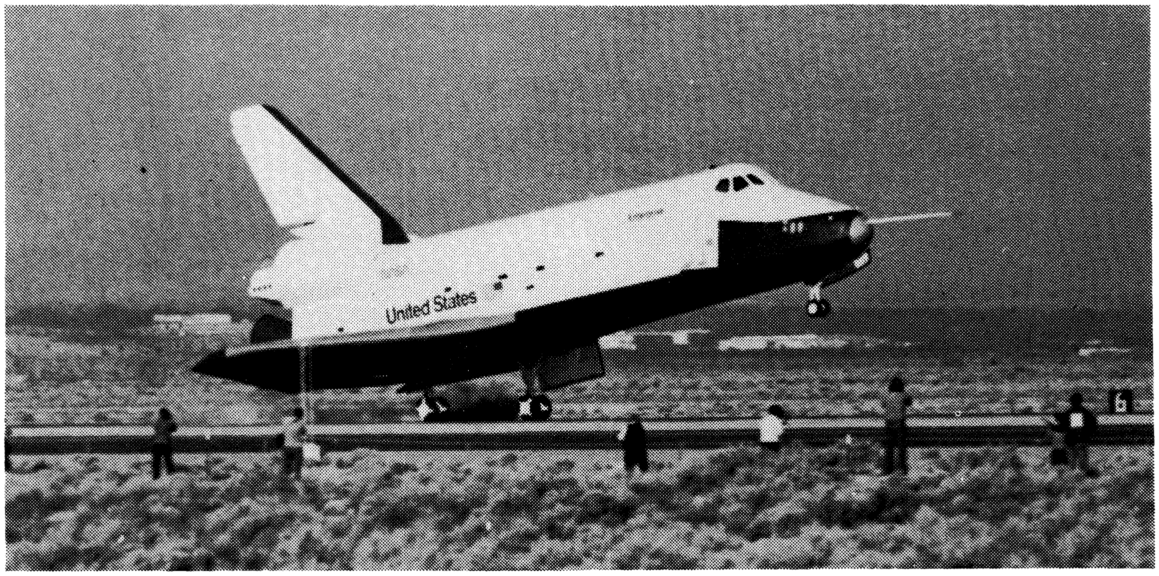

Figure 1 -- Orbiter *Enterprise* during approach and landing test flight.

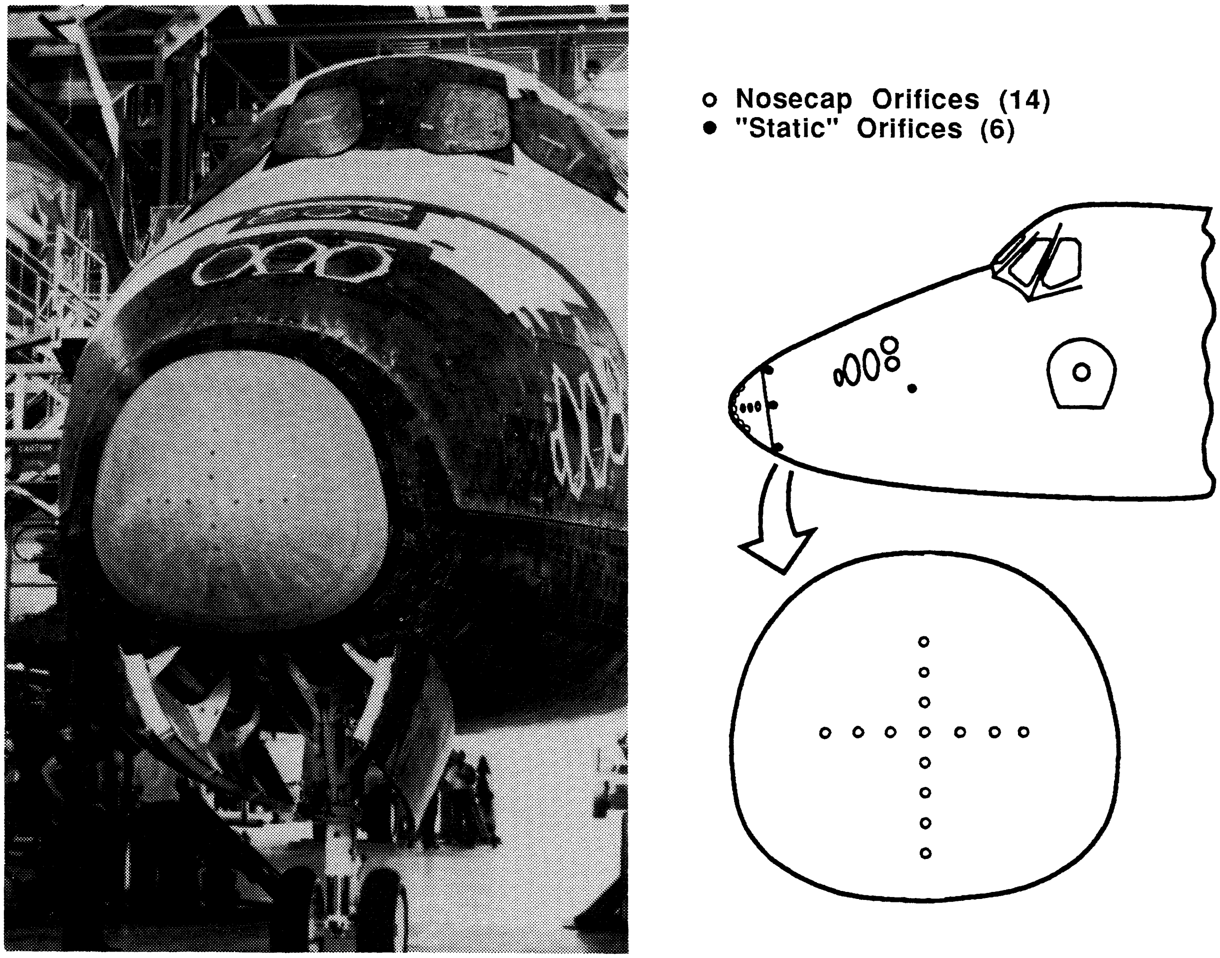

(a) Photograph.

(b) Orifice location schematic.

Figure 2 -- SEADS installation on Orbiter *Columbia*.

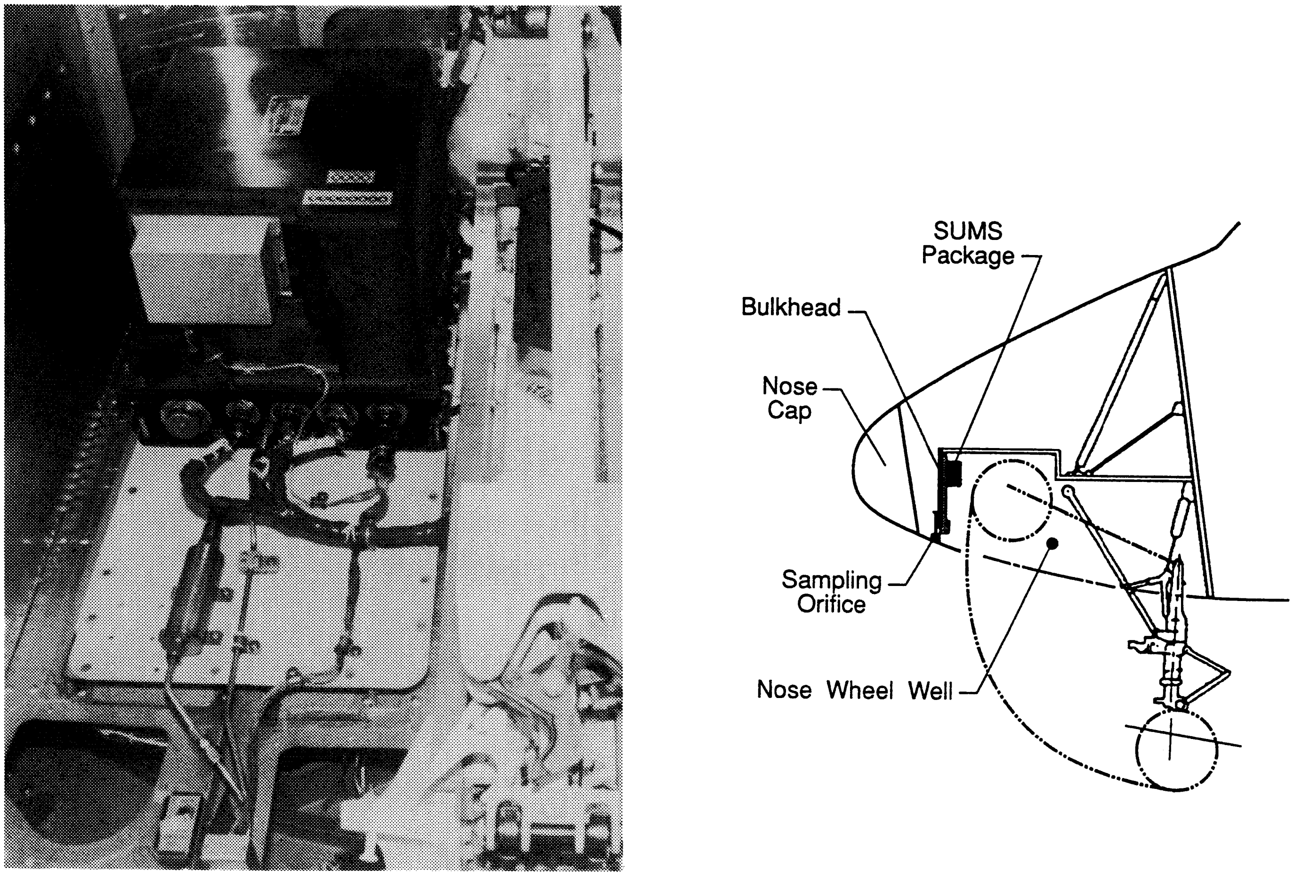

(a) Photograph.

(b) Schematic.

Figure 3 -- SUMS installation on Orbiter *Columbia.*

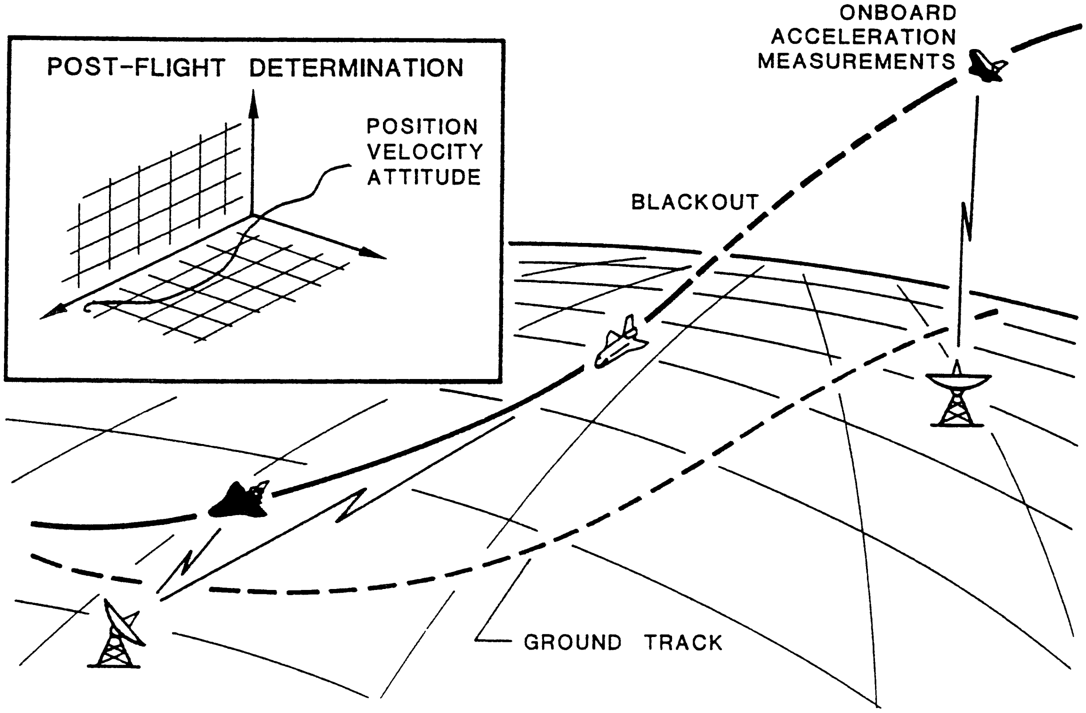

Figure 4 -- Entry trajectory reconstruction.

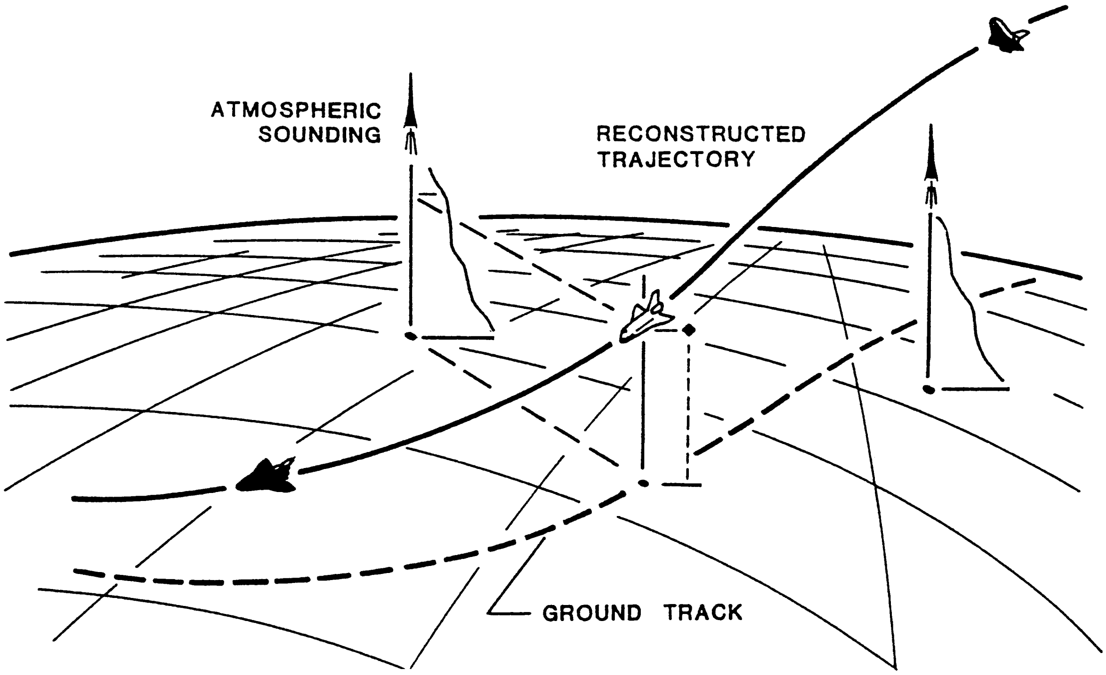

Figure 5 -- Entry atmospheric reconstruction.

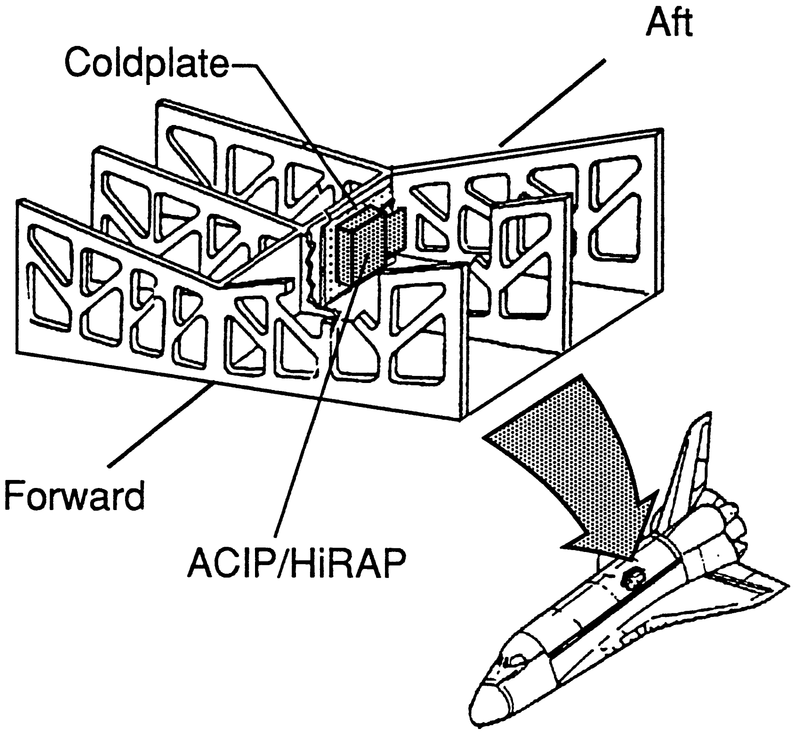

Figure 6 -- ACIP installation schematic.

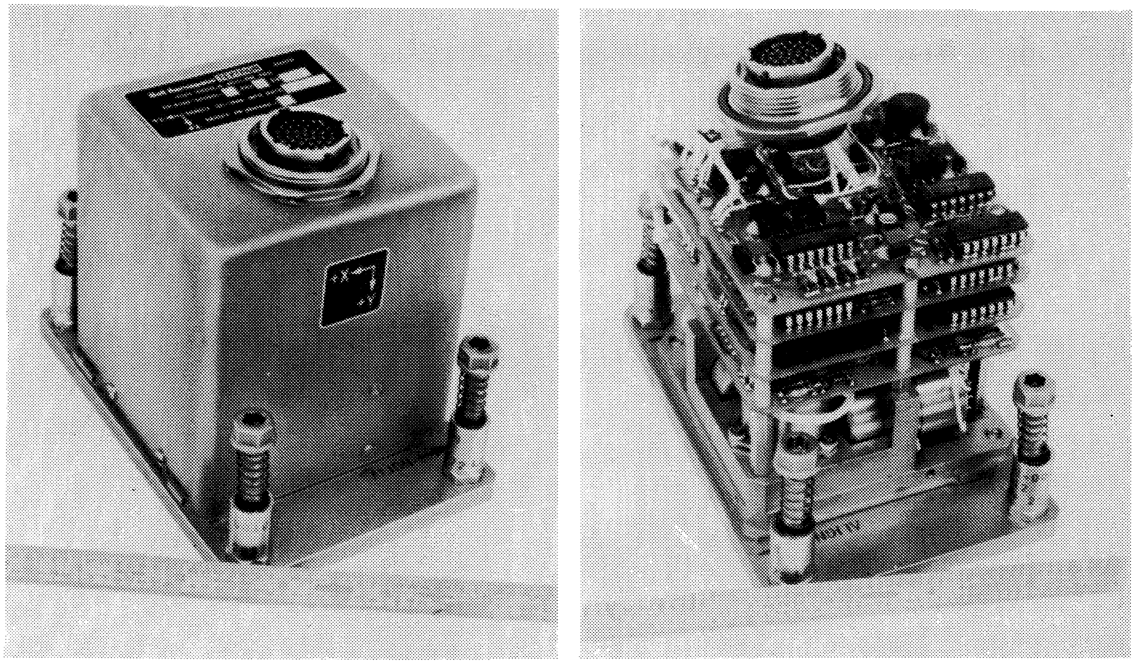

Figure 7 -- HiRAP flight unit.

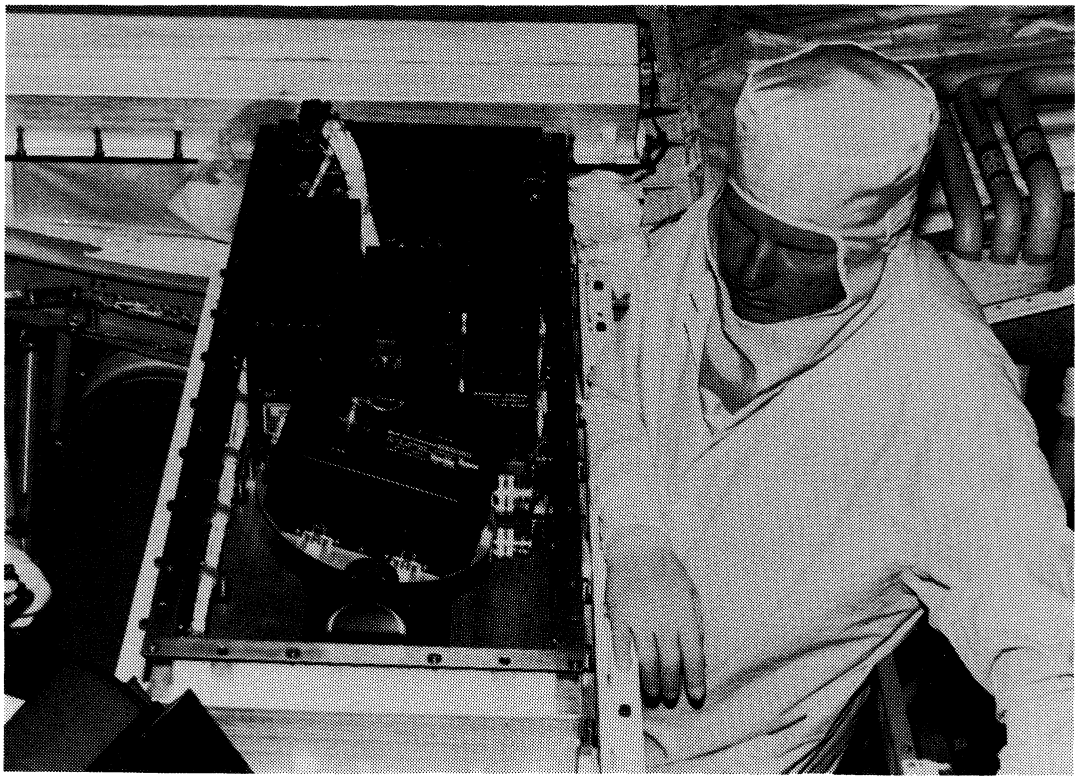

Figure 8 -- OARE installed on *Columbia* for STS-40.

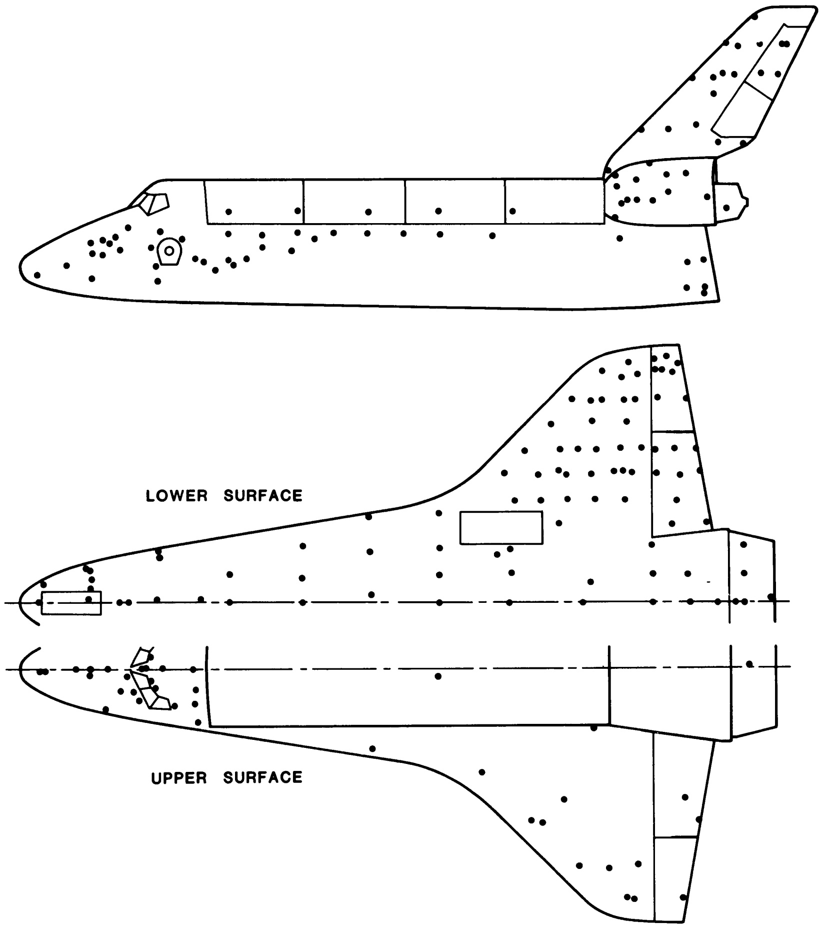

Figure 9 -- DFI surface temperature-measurement locations.

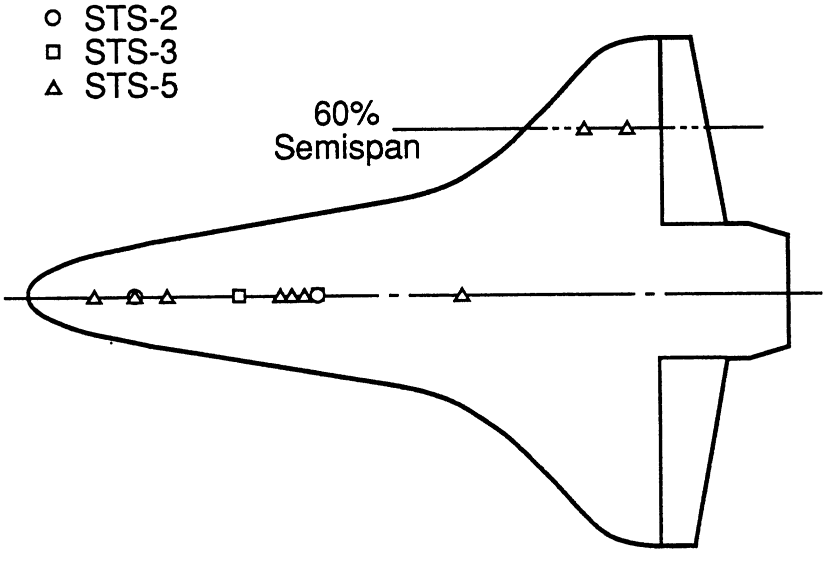

Figure 10 -- CSE experiment coated-tile locations.

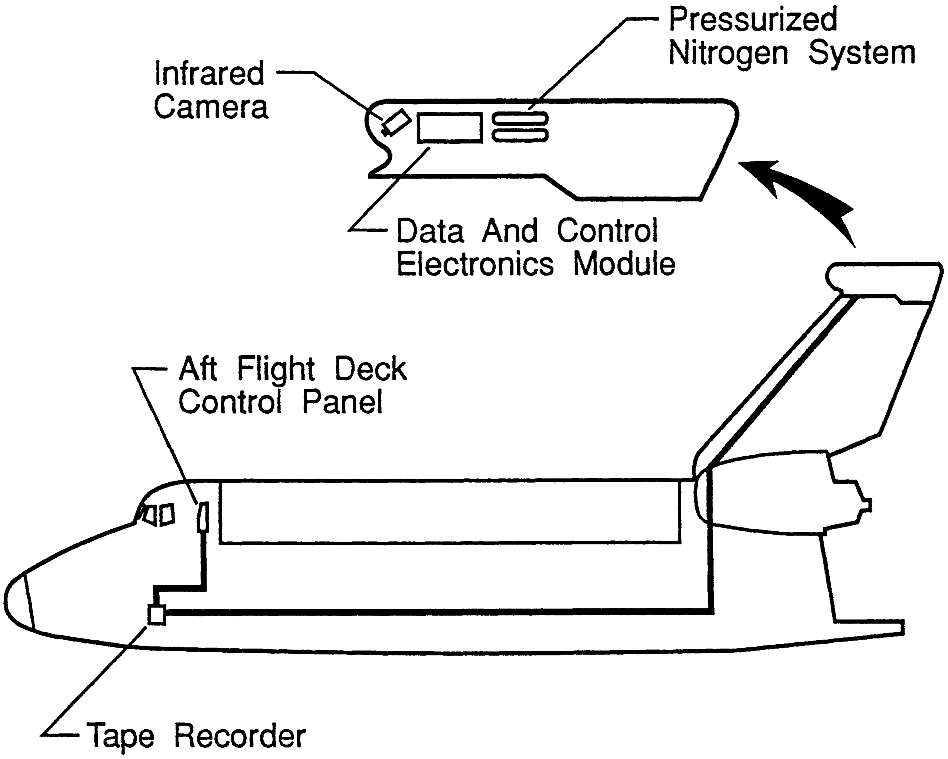
Pressurized Nitrogen System
Infrared Camera
Data And Control Electronics Module
Aft Flight Deck Control Panel
Tape Recorder

(a) Schematic.

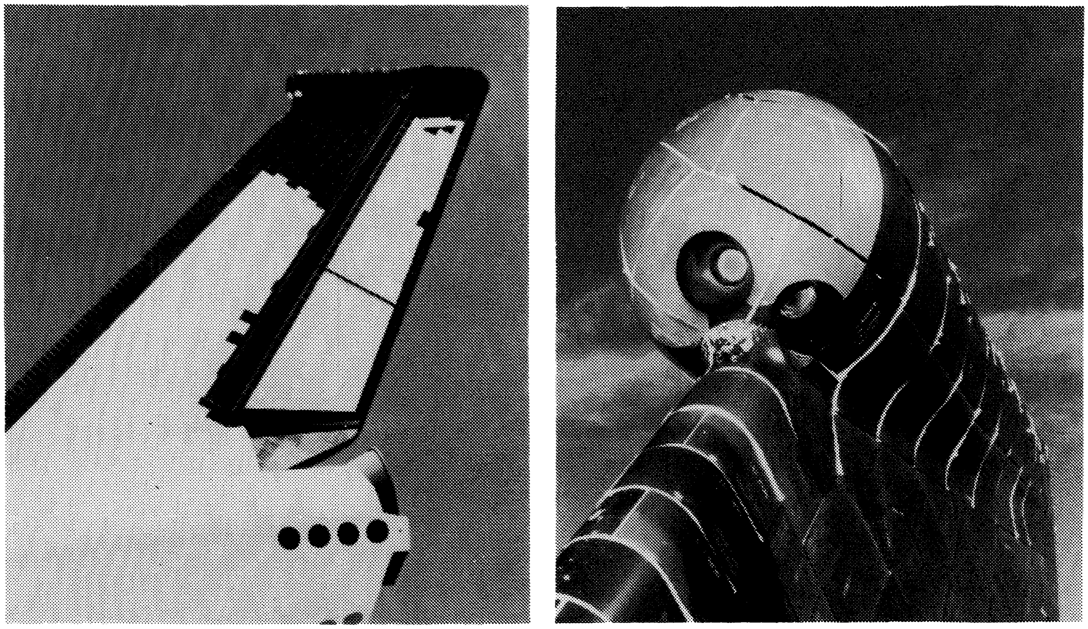

(b) Pod atop vertical tail.

Figure 11 -- SILTS experiment system installation on Orbiter *Columbia.*

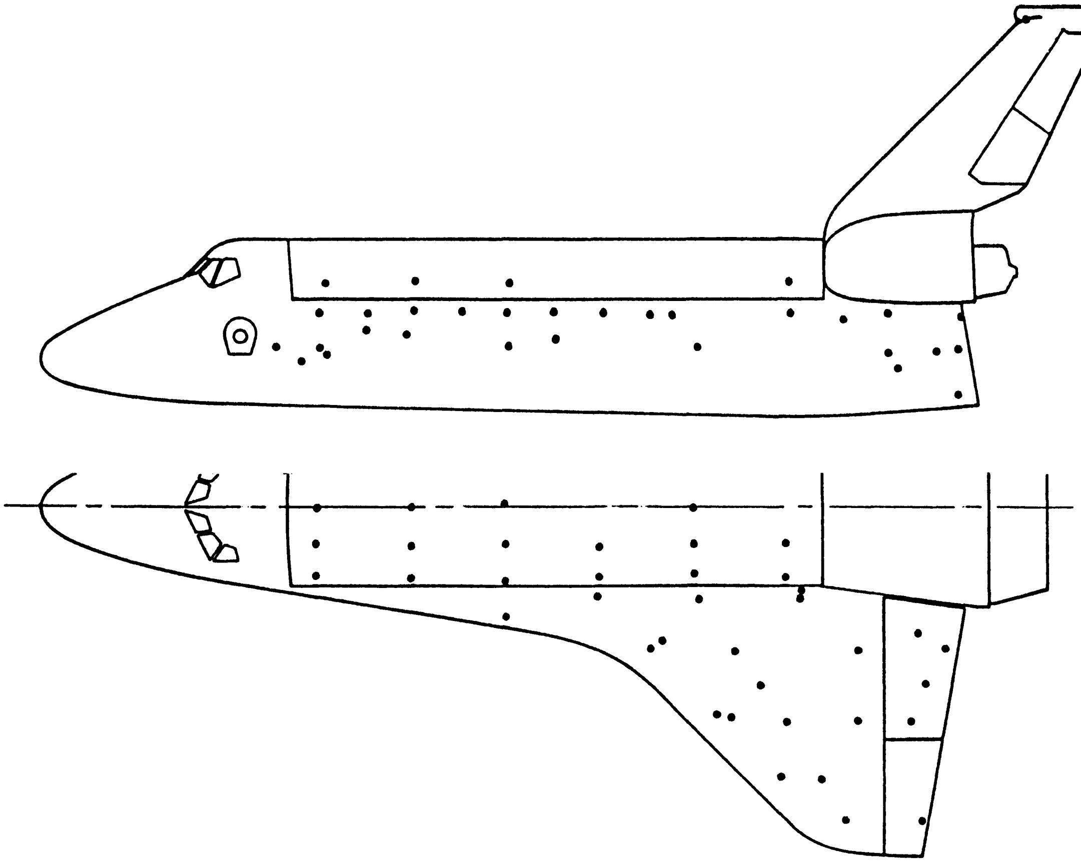

Figure 12 -- AIP surface-temperature-measurement locations.

ORBITER EXPERIMENTS (OEX) PROGRAM/PROJECT MANAGEMENT APPROACH AND EXPERIENCE

Robert L. Spann and Robert L. Giesecke
NASA Johnson Space Center
Houston, TX

A written version of this paper was not provided by the authors.

Copies of presentation materials used at the Symposium are presented herein.

OEX Project Flow - From Concept To Applications

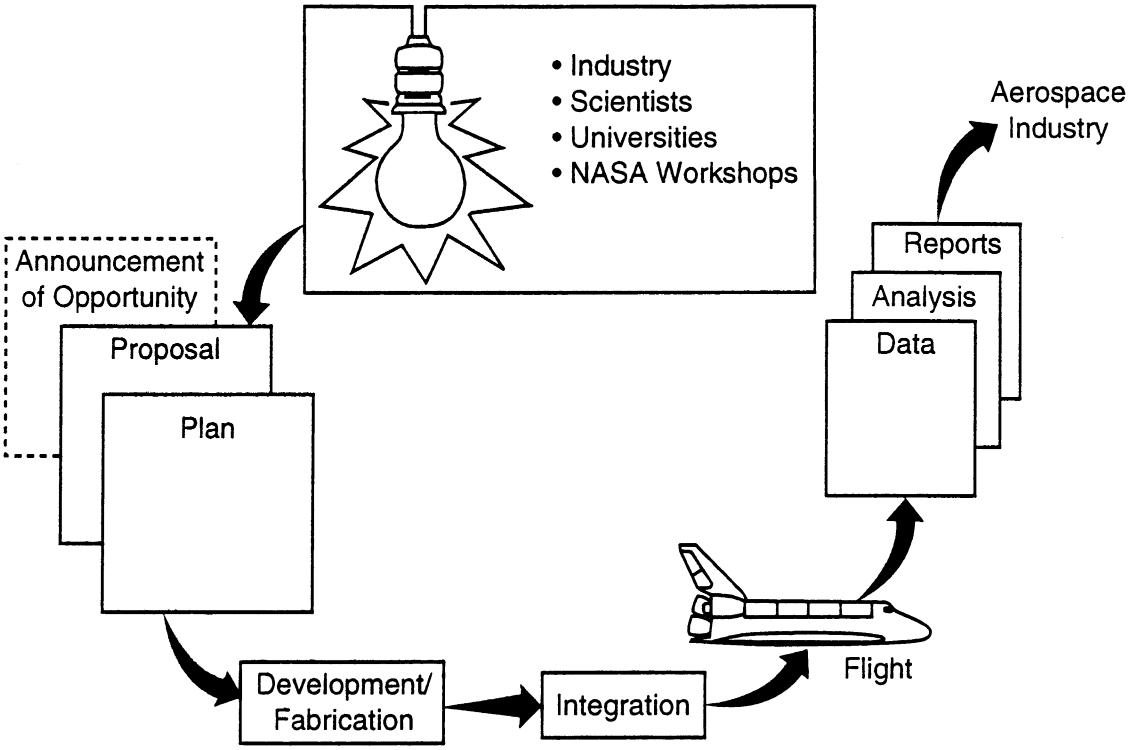

OEX Approach

- Experiments "born" through NASA Office of Aeronautics and Space Technology (OAST)
- Sponsored by Principal Technologists at NASA Centers
- Designated OEX because of appropriate Orbiter test bed
- Program managed out of OAST
- Project integrated through Office of Space Transportation Systems (OSTS)
- Integration project management at JSC (systems integration, mission integration plans-schedules, budget)
- Rockwell International integration contractor
- Project integration support - Lockheed Engineering & Sciences Co.

Implementation

- Experiment components developed at the Research Centers or at JSC, and delivered as GFE for vehicle integration
- Experiment components developed at the Contractor as Mission Kits or Mod Kits
- Experiments manifested through Orbiter Level-III/NSTS Level-II change process
- Experiment integration engineering and installation by Orbiter contractor at Palmdale or at KSC
- Experiments design and certified to Orbiter requirements and specifications (e.g., vs. payload)
- Principal Technologists responsible for experiment definition, requirements, performance, data reduction, experiment results, data base development and science aspects
- JSC responsible for installation, integration, flight data systems, maintenance, and post-flight data processing

OEX Program Functional Organization

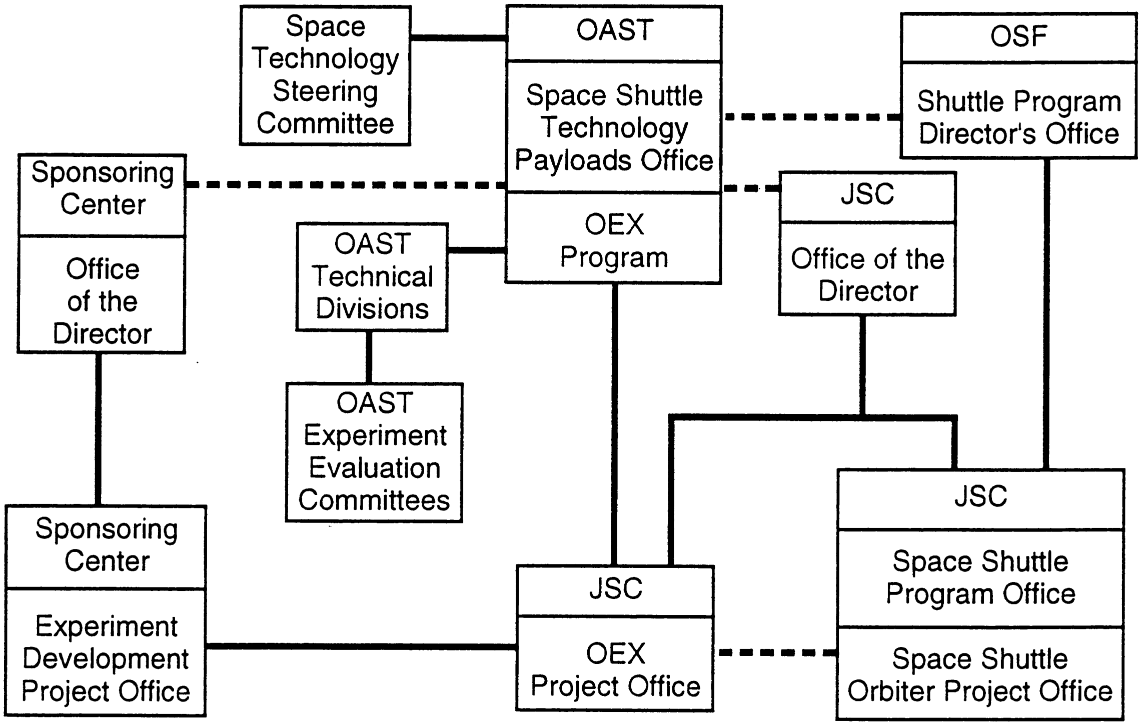
Space Technology Steering Committee
OAST
Space Shuttle Technology Payloads Office
OEX Program
OSF
Shuttle Program Director's Office
Sponsoring Center
Office of the Director
OAST Technical Divisions
JSC
Office of the Director
OAST Experiment Evaluation Committees
Sponsoring Center
Experiment Development Project Office
JSC
OEX Project Office
JSC
Space Shuttle Program Office
Space Shuttle Orbiter Project Office

Program Hierarchy

Management Level	Management Authority
Level I	NASA Headquarters Program Manager
Level II	Johnson Space Center Project Manager
Level III	Johnson Space Center Experiment Project Manager
Level IV	Johnson Space Center Sponsoring Centers Experiment Development Manager OEX Data Manager

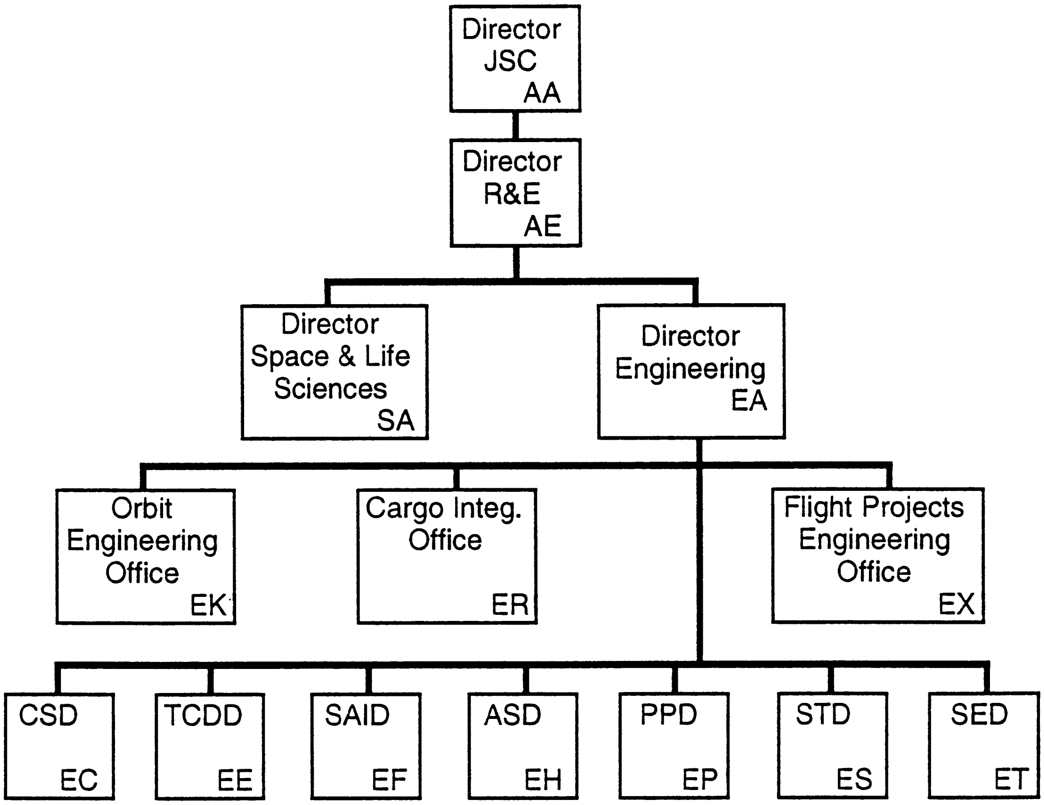

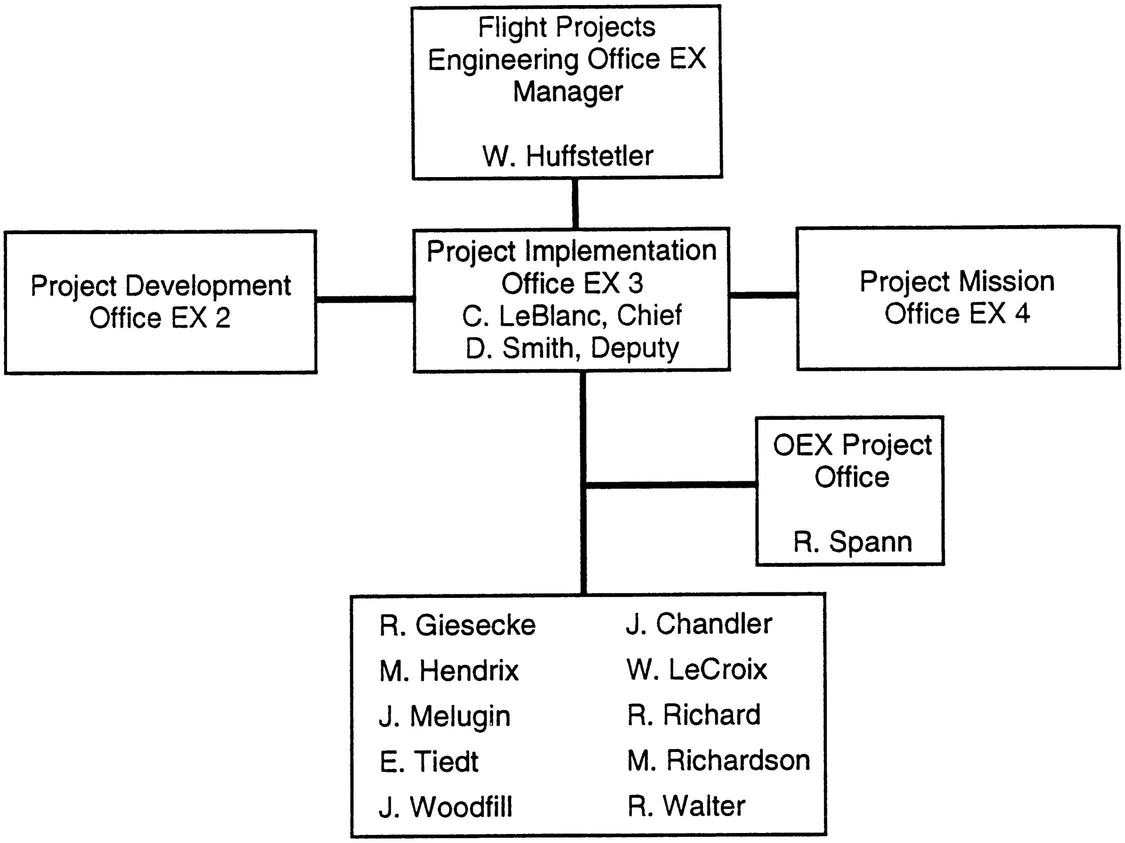
Flight Projects
Engineering Office EX
Manager
W. Huffstetler
Project Development
Office EX 2
Project Implementation
Office EX 3
C. LeBlanc, Chief
D. Smith, Deputy
Project Mission
Office EX 4
OEX Project
Office
R. Spann
R. Giesecke
J. Chandler
M. Hendrix
W. LeCroix
J. Melugin
R. Richard
E. Tiedt
M. Richardson
J. Woodfill
R. Walter

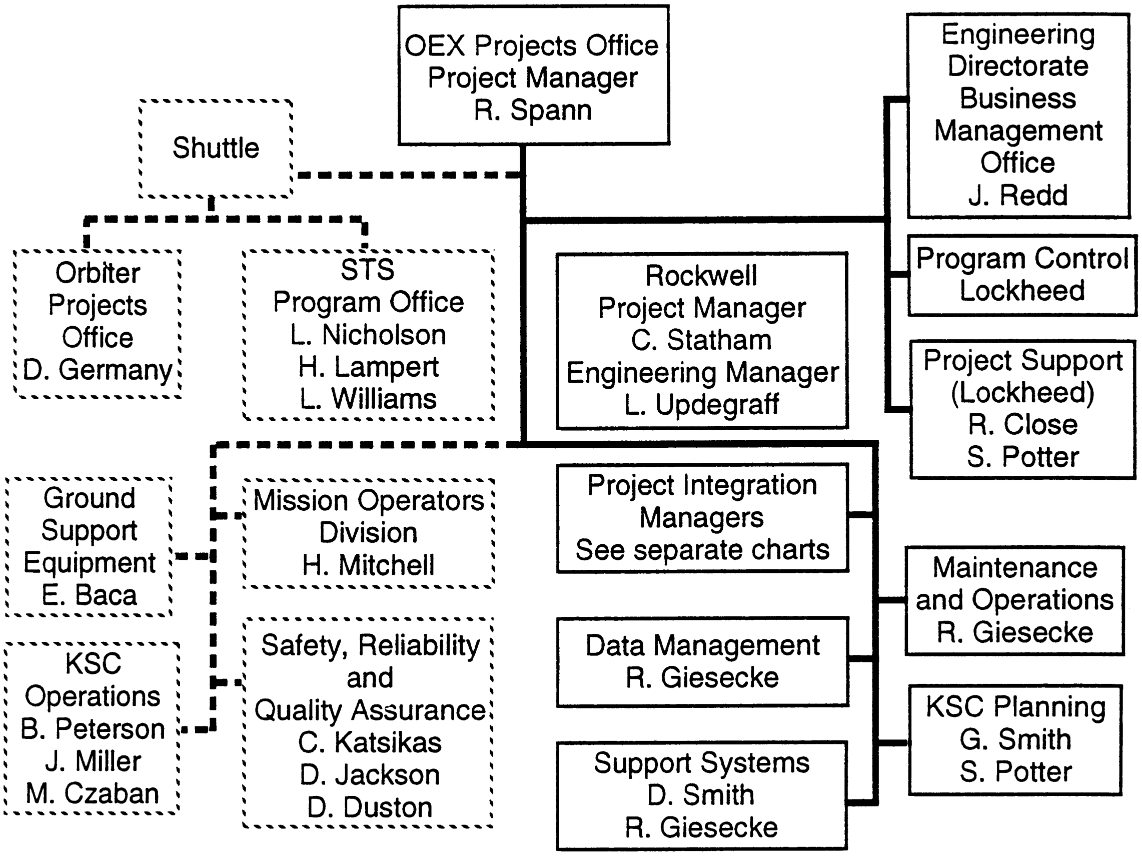
OEX Projects Office
Project Manager
R. Spann
Shuttle
Engineering
Directorate
Business
Management
Office
J. Redd
Orbiter
Projects
Office
D. Germany
STS
Program Office
L. Nicholson
H. Lampert
L. Williams
Rockwell
Project Manager
C. Statham
Engineering Manager
L. Updegraff
Program Control
Lockheed
Project Support
(Lockheed)
R. Close
S. Potter
Ground
Support
Equipment
E. Baca
Mission Operators
Division
H. Mitchell
Project Integration
Managers
See separate charts
Maintenance
and Operations
R. Giesecke
KSC
Operations
B. Peterson
J. Miller
M. Czaban
Safety, Reliability
and
Quality Assurance
C. Katsikas
D. Jackson
D. Duston
Data Management
R. Giesecke
KSC Planning
G. Smith
S. Potter
Support Systems
D. Smith
R. Giesecke

OEX Experiments

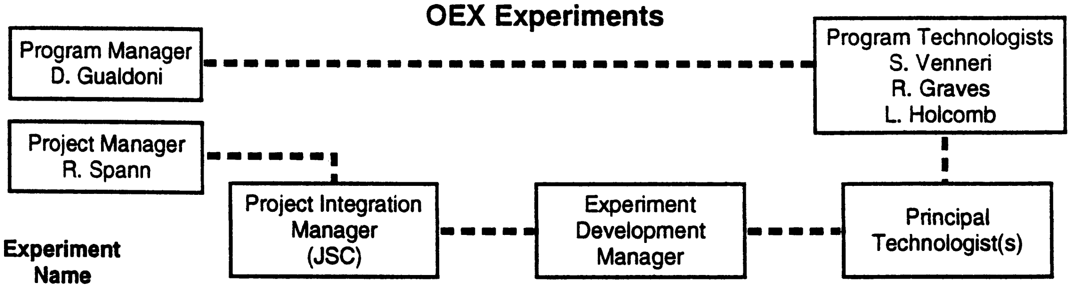

Experiment Name	Project Integration Manager (JSC)	Experiment Development Manager	Principal Technologist(s)
CSE	R. Richard	A. Covington (ARC)	D. Stewart (ARC)
TGHE	R. Richard	A. Covington (ARC)	W. Pitts (ARC)
ACIP/HiRAP	R. Giesecke	R. Giesecke (JSC)	R. Barton (ACIP) (JSC) R. Blanchard (HiRAP) (LaRC)
SILTS	R. Richard	W. Watson (LaRC) R. Dail (LaRC)	E. Zoby (LaRC) D. Throckmorton (LaRC)
SEADS	R. Spann	P. Siemers (LaRC)	P. Siemers (LaRC)
SUMS	R. Richard	R. Duckett (LaRC)	R. Blanchard (LaRC) R. Duckett (LaRC)
SSO/SCM	R. Giesecke	R. Giesecke (JSC)	N/A
AIP	R. Giesecke	R. Giesecke (JSC)	D. Throckmorton (LaRC)
AAPE	J. Woodfill	E. Chevers (JSC)	E. Kubiak (JSC)
OARE	M. Hendrix	M. Hendrix (JSC)	R. Blanchard (LaRC)
ACTPS	R. Richard	A. Covington (ARC)	D. Leiser (ARC)
OASIS	E. Tiedt	E. Tiedt (JSC)	J. Knight (USAF)

OEX Management Points-of-Contract

• NASA Hqs.	Dick Gualdoni (RX)
• JSC	Bob Spann (EX3)
• LaRC	Dave Throckmorton (366)
• KSC	Lynn Barnett (SO-MSO-B) (OFF-LINE)
• ARC	Al Covington (234-1)
• GSFC	Bill Bangs (302.0)
• RI	Walt Bunge (AE83)
• DFRC	Jack Kolf (OS)
• KSC	Bob Petersen (SE-PEO) (ON-LINE)

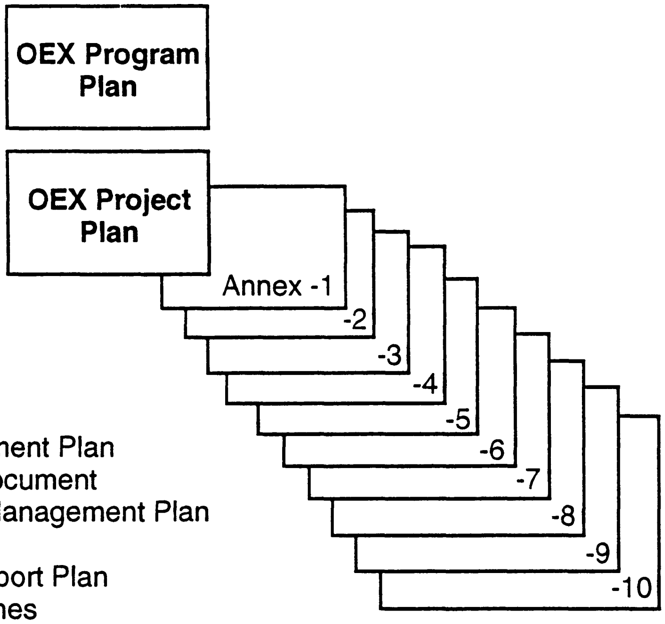

Annex - 1 - OEX CCP Management Plan
2 - OEX Procedures Document
3 - OEX Project Data Management Plan
4 - QA Plan
5 - OEX Reliability Support Plan
6 - OEX Safety Guidelines
7 - OEX M&O Plan
8 - OEX Launch Site Support Plan
9 - OEX Documentation Formats
10 - OEX Acronyms & Abbreviations

Orbiter Project Office/OEX Integration Plan

OEX Project Support Functions

- Provide overall management of the OEX Project integration tasks
- Provide individual project and technical management
- Provide program control functions
- Provide overall project integration and support activities
- Provide project documentation as required
- Provide proposal evaluation feasibility/compatibility assessments and make recommendations
- Develop hardware necessary for integration
- Provide data management services
- Develop data management and experiment support systems
- Provide maintenance and operations support
- Control cost and schedule within program constraints
- Define tasks, analyses, studies, etc., required to assure orbiter integrity and experiment success
- Design, develop and fabricate unique experiment components (tail pod, nose cone, electronics, etc.)

OEX Experiments and Support Equipment
Project Support Scope

Phase I

• ACIP	(Aerodynamic Coefficient Identification Package)	JSC
• HiRAP	(High Resolution Accelerometer Package)	LaRC
• CSE	(Catalytic Surface Effects)	ARC
• TGHE	(Tile Gap Heating Effects)	ARC
• AAPE	(Advanced Auto Pilot)	JSC
• SILTS	(Shuttle Infrared Leeside Temperature Sensing)	LaRC
• SUMS	(Shuttle Upper Atmosphere Mass Spectrometer)	LARC
• SEADS	(Shuttle Entry Data System)	LaRC
• SSO	(Support System for OEX)	JSC
• FFSSO	(Forward Fuselage Support System for OEX)	JSC
• GSO	(Ground Support Station for OEX)	JSC
• OASIS	(OEX Autonomous Supporting Instrumentation System)	JSC

Phase II

• AIP	(Aerothermal Instrumentation Package)	LaRC
• ACTPS	(Advanced Ceramic Thermal Protection System)	ARC
• AFRSI Inspection Program		ARC
• Plume Survey Experiment (Study)		LaRC
• OARE	(Orbital Acceleration Research Experiment)	LaRC
• Laser Photodiagnostics (Study)		ARC

OV-102 OEX Configuration

Definitions:

CSE - Catalytic Surface Effects Experiment
FFSSO - Forward Fuselage Support System for OEX
RMDU - Remote Multiplexer/ Demultiplexer Unit
SEADS - Shuttle Entry Air Data System
SSO - Support System for OEX
TGHE - Tile Gap Heating Experiment

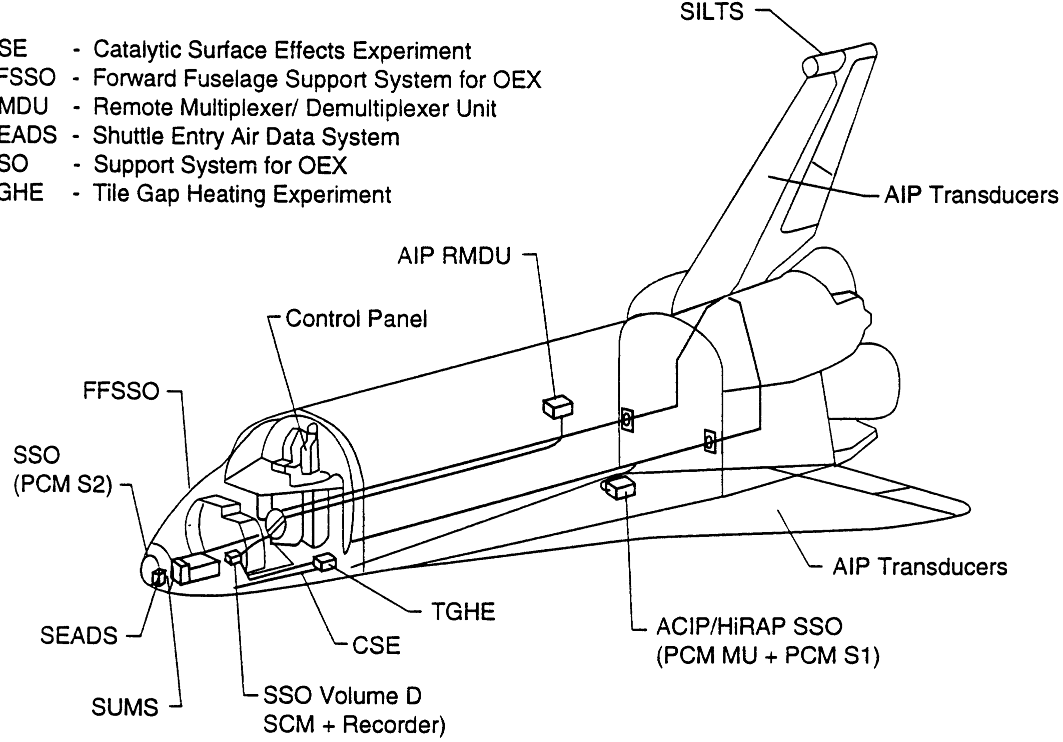

M&O (Maintenance And Operations)

- Objective
  - To provide engineering support to complete development, test, modification, repair, calibration and data analysis as required for the Orbiter Experiments

- Purpose
  - To establish and maintain flight readiness of Orbiter Experiments

- Approach
  - Establish engineering group at JSC to provide required training, expertise and facility support. The Systems Engineering Branch under the Experiments and Operations Support Division is responsible for this support.

Data Management

- Objective
  - To provide the Principal Technologists and the rest of the scientific community with raw and processed OEX experiment data and to provide a data bank to the users for future reference

- Purpose
  - To provide the PT'S and the scientific community with usable and efficient data to support evaluation of the OEX Program experiments

- Approach
  - All OEX experiment specific data and data products are generated within EOSD as specified in the OEX Data Requirements Documents and the OEX Project Data Management Plan. EOSD will be the conduit for providing other supporting data (OI/DFI/TFI/ETC) to the OEX program supporters within the latitudes provided in the Shuttle Data Plan.

Data Management

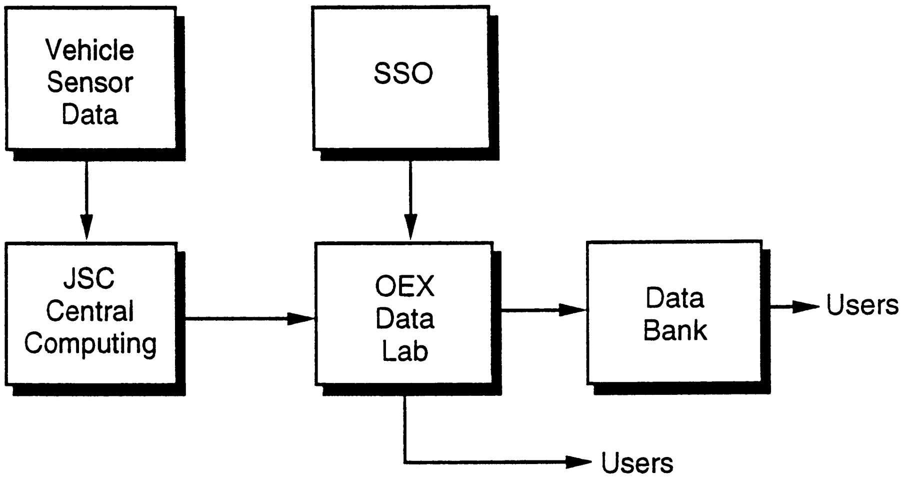

OEX Return-To-Flight Activities

- Heavy concentrated effort by core personnel
  - Recertify all OEX hardware to requirements resulting from STS 51-L
  - Complete corrective actions to OEX anomalies from STS 61-C
  - Refurbish, upgrade, and test flight hardware, software, GSE, and facilities after long standby period
  - Revise, correct, and create critical documentation (e.g., FMEA, CIL, SAR, HR, CR, CAR, OMRSD, OMI, Design Requirements Review Document, DRR waivers, SPEC requirements, etc.)
  - Prepare presentations and documents for submittal to various stages of review and approval at Level III and II Pre-Boards and Change Boards at the Safety Review Panel

OEX Return-To-Flight

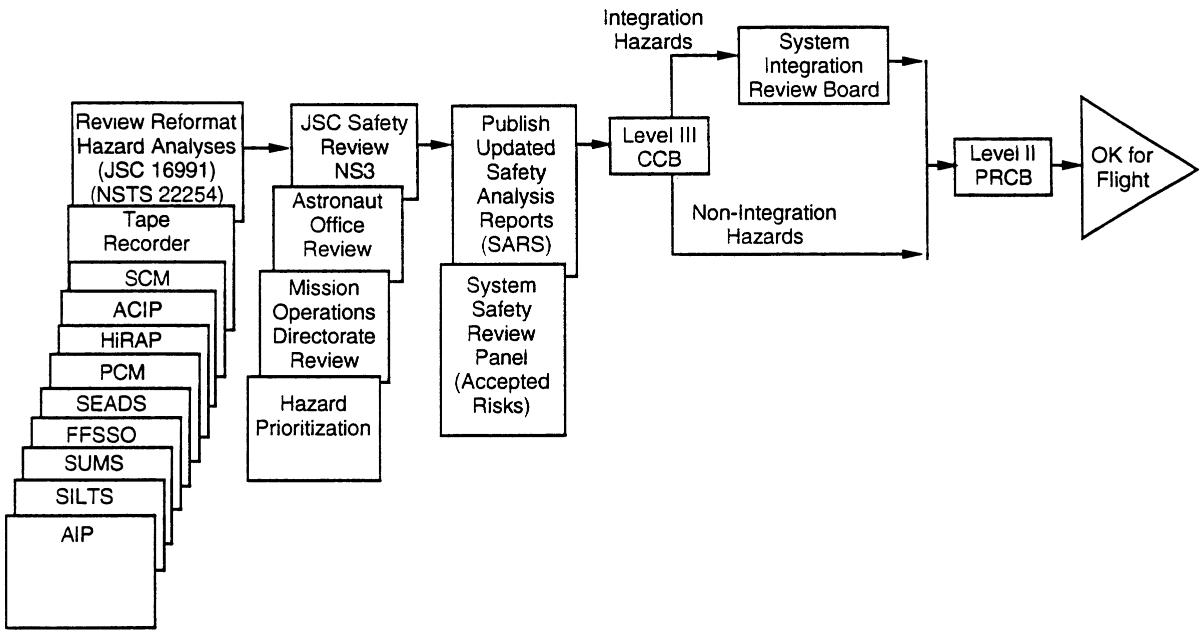
Review Reformat Hazard Analyses (JSC 16991) (NSTS 22254)
Tape Recorder
SCM
ACIP
HiRAP
PCM
SEADS
FFSSO
SUMS
SILTS
AIP
JSC Safety Review NS3
Astronaut Office Review
Mission Operations Directorate Review
Hazard Prioritization
Publish Updated Safety Analysis Reports (SARS)
System Safety Review Panel (Accepted Risks)
Level III CCB
Integration Hazards
System Integration Review Board
Non-Integration Hazards
Level II PRCB
OK for Flight

OEX Return-To-Flight

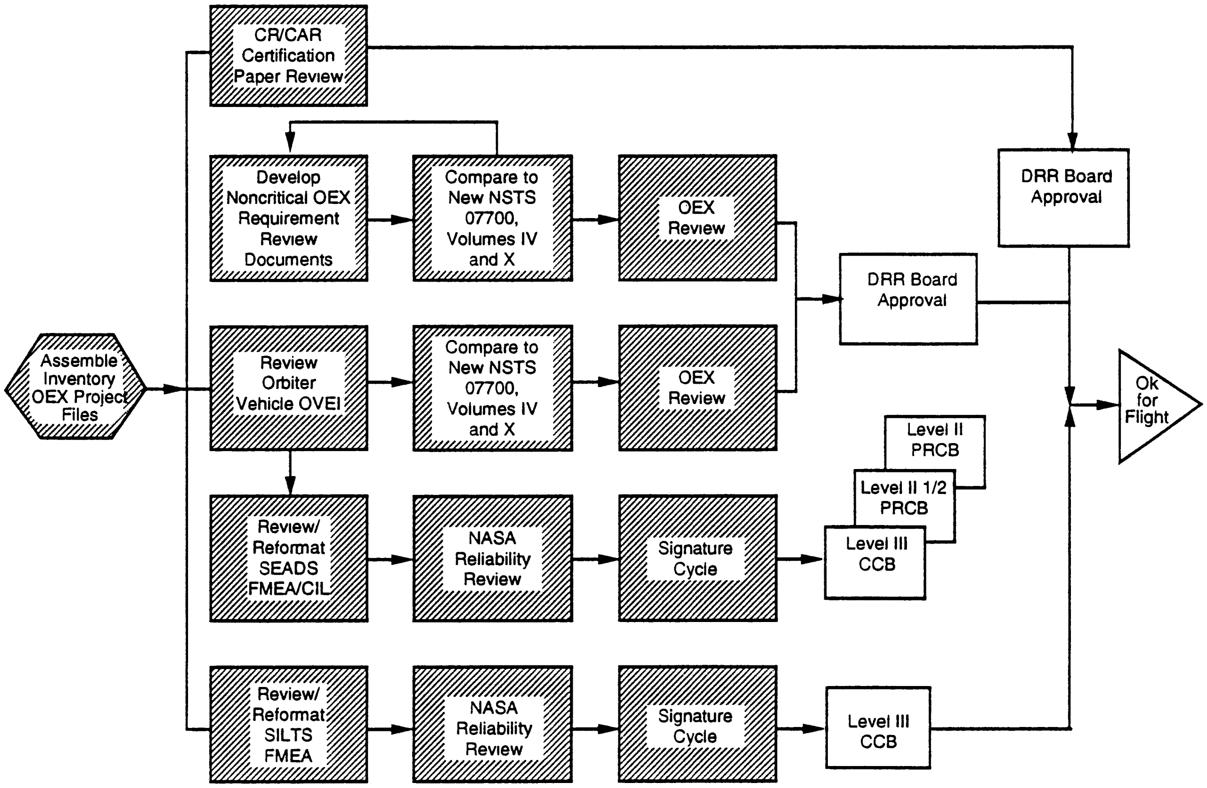
CR/CAR Certification Paper Review
Develop Noncritical OEX Requirement Review Documents
Compare to New NSTS 07700, Volumes IV and X
OEX Review
DRR Board Approval
DRR Board Approval
Assemble Inventory OEX Project Files
Review Orbiter Vehicle OVEI
Compare to New NSTS 07700, Volumes IV and X
OEX Review
Ok for Flight
Level II PRCB
Level II 1/2 PRCB
Level III CCB
Review/ Reformat SEADS FMEA/CIL
NASA Reliability Review
Signature Cycle
Review/ Reformat SILTS FMEA
NASA Reliability Review
Signature Cycle
Level III CCB

OEX Experience

1. Initial assumptions:

   - Initially the OEX concept provided an unprecedented opportunity for the highest order of aeronautical research
     - Utilize "ready-made" orbiter testbed that was going to fly anyway
     - Unlimited access to space
     - Use unique orbiter flight regime to obtain benchmark data not duplicated on the ground
     - Data applications for improved future reusable winged reentry vehicles
     - Future benefits of pure aeroscience data to be generated

   - Caveat – during long term programs, times do change

2. Manifesting OEX as a part of Orbiter was judged to be an advantage vs manifesting as a payload

   - Common documentation and requirements – better understood by the technical infrastructure

   - Better control over development and integration of experiments

   - Much help and economics provided by the Orbiter Projects organization

   - Mutual benefits and more common objectives

   - OEX equipment subject to the same standards and certification rigor as Orbiter

3. Extreme importance was attached to establishing and maintaining a strong and close relationship with the Orbiter Projects Office, the Space Shuttle Program Office, KSC Operations, and the JSC technical and engineering community to assure common goals

OEX Experience (Continued)

4. It was important to secure a common contractor for integration engineering with the Orbiter
    - Space Shuttle Program is documentation intensive
    - Language must be common
    - Reanalysis and recertification to a common baseline required for many flights

5. In addition to a unique OEX contract with R.I., OEX also utilized the Orbiter Projects contract with R.I. (NAS 9-14000, Schedules A, B, & E)

    Great economies of scale were realized in the relations with Orbiter and the Space Shuttle Program
    - The tools and systems for management, manufacturing, engineering and control were already in place
    - Lower overhead – much OEX work was often included in on-going Orbiter work
    - Very efficient and astute OEX contractor management at R.I.
    - Mutual benefits between Orbiter and OEX
    - Space Shuttle Program covered costs of integration at KSC

- A disciplined vertical organizational structure was chosen for the OEX Project
    - Matched rigid requirements and standards demanded by the manned spaceflight program
    - Experiments became part of the Orbiter structure and aerodynamic surfaces
    - Could impose criticality one failure modes and hazards to the crew and vehicle

OEX Experience (Continued)

6. It was very important that the basic OEX complement of experiments be flown very early in the program – planned first 6 flights of the Shuttle Program

   - The value of the data was more vital then – but current events overtook some of the original objectives

   - Extended/delayed programs become very expensive

   - The priorities and interests within the funding, supporting, and participating organizations can change radically over the years

   - Times change, the political climate changes, priorities change

   - Extreme turnover of personnel (especially management) can cause a loss of continuity – thus a strong, well thought out management plan and organization are needed

7. Agreements within NASA for flight manifesting OEX hardware tended to dissolve over time

   - Lack of a hard agency agreement (no Form 100, etc.) with Code M or Space Shuttle Program for flights

   - Decisions based on personal beliefs and personality of current top program management

   - Priorities of the time were very volatile

   - Success was hard to be had – only by the extreme persistence of the project at the PRCB, time after time

8. There was substantial "growth" over the life cycle of the OEX program that in today's political environment may be unacceptable

   - Extreme stretch-out due to unexpected Space Shuttle Program programmatic changes that OEX could not control

   - Aging instruments required more and more care

   - Escalating contractor "rates" in out years due to inflation and loss of work base

OEX Experience (Continued)

- Deferred installation and checkout of new installations at KSC, in a climate where *flight rates became a top priority* – shorter turnaround times than earlier in program
- The 2½ year delay due to the Challenger accident and waiting for a major modification window

9. OEX suffered priority lapses for earlier installation windows
    - The experiments were classified as a set of DTO's (Development Test Objectives)
    - OEX not perceived as a customer (as opposed to payload customers)
    - OEX work had a lower priority than the work of turning a vehicle around during a mission flow at KSC
    - OEX could be literally planned out of the KSC flow (serial time syndrome was a killer)
    - Changing top management – different strokes for different folks

10. The advent of OV-102 becoming a dedicated Spacelab vehicle was a setback to OEX
    - Conflicts for: adequate power, manifesting flow time, operational time on orbit
    - Conflicts with: timelines, crew activity, Orbiter performance

11. The choice of JSC to function as central Level II Project Office was appropriate
    - Drew on considerable internal resources and Orbiter discipline experts
    - Credibility in dealing with the "system" and near the system for manifesting
    - Provided a non-biased customer oriented (NASA HQ & P.I.'s) project manifesting
    - Strong will to succeed

OEX Experience (Continued)

12. Using a matrix of technical disciplines at JSC worked relatively well
    - Good communication
    - Good enthusiastic support from engineering and administrative sectors
    - Good support from technical counterparts at the contractors
13. The level of cooperation between the participating NASA centers, other organizations, and contractor organizations was excellent
    - Fully participative management style
    - Good communications
    - High level of camaraderie experienced
    - Employment of many TQM principles (whether we knew it or not)
14. The relationship with NASA Headquarters was excellent
    - Professional
    - Reliable and good support during times of trouble
15. A good bottom line here is that a widely dispersed single project infrastructure among several centers, even with diverse backgrounds, can work well
16. In the future, use a systems approach and process to development
17. A more centralized and systems-oriented management approach adopted in the mid-course of OEX development
    - Improved communications and control
    - Improved consistency
    - Lessened competition for the same resources – promoted cooperation

OEX Experience (Continued)

18. Have good project support and program/project control capability resident within the project

19. Keep good records and files. Recommend a good information management system these days

    - Good tools available now

    - Traceability of what you have done, especially in requirements, is mandatory to recertify for future flights
        - Return to flight activity after Challenger
        - Installation and certification of new experiments

20. Create a good strong advocacy within NASA, with the science community at the centers, with the contractors, and with your own organization for long term programs, if you want to complete them

    - Our political system has a short term memory about commitments

    - Otherwise you may find yourself standing alone, naked in the wind, and at the wrong end of a shooting gallery in hard times

21. Don't ever give up. OEX was dead many times in the minds of many of those we had to deal with, but with extreme perseverance, overcame

SHUTTLE ENTRY AIR DATA SYSTEM (SEADS) - ADVANCED AIR DATA SYSTEM RESULTS: AIR DATA ACROSS THE ENTRY SPEED RANGE

Paul M. Siemers III*
NASA Langley Research Center
Hampton, VA

Martin W. Henry**
Analytical Mechanics Associates, Inc.
Hampton, VA

and

James B. Eades, Jr.***
Analytical Mechanics Associates, Inc.
Hampton, VA

ABSTRACT

The Shuttle Entry Air Data System (SEADS) has successfully completed its flight test program. SEADS is the implementation of a flush orifice air data system concept, a new concept in air data systems developed at the Langley Research Center. The flush orifice concept, which has application to a variety of flight vehicles, incorporates an array of flush-mounted pressure orifices located in the nose and forward fuselage of the vehicle and makes use of flowfield modeling for the analysis of flight measurements to determine the desired air data parameters. Although the concept is fundamentally simple, its implementation into the Space Shuttle Orbiter as an across-the-speed-range air data system required the development of new technologies in both the system's hardware and in data analysis techniques.

The development and certification of the SEADS were accomplished through an extensive series of essential wind tunnel and arc jet tests, computer simulations, and aircraft flight tests. However, the concept's full performance capability could not be assessed until after flight data could be evaluated. Consequently, analyses of the SEADS flight data, obtained on Shuttle Orbiter Columbia flights STS-61C, 28, 32, 35, and 40, were used to show that the experiment met, and exceeded, all of its performance requirements, and that the concept is capable of furnishing real-time air data over a broad spectrum of flight regimes.

---

*Aerospace Engineer, Special Assistant, Space Systems Division.
**Senior Programmer/Analyst.
***Senior Scientist.

NOMENCLATURE

C1, C2, C3	flow field correction coefficients
Cp	Coefficient of Pressure
F	Degrees Fahrenheit
h	altitude
M	Mach number
P	pressure, static
P_{t_2}	total pressure behind a normal shock
q	dynamic pressure
R	pressure ratio $[Pi/P_{t_2}]$
X,Y,Z	orbiter geometric coordinates
$\underline{X}$	aerodynamic state vector
α	angle of attack
β	angle of sideslip
γ	ratio of specific heats
ζ	orifice clock angle
η	orifice cone angle
θ	orifice normal flow incidence angle

Subscripts

E	estimated value
∞	freestream value
i	Referenced to orifice i
t	total condition
f	flight condition

Acronyms

BET	Best Estimate of Trajectory
CRES	Corrosion Resistant Steel
DFI	Development Flight Instrumentation
HRSI	High Density Reusable Surface Insulation
IMU	Inertial Measurement Unit
MSC	Master Sequencer and Controller
OADS	Operational Air Data System
OML	Outer Mold Line
OV	Orbiter Vehicle
psia	pounds/square inch absolute
RCC	Reinforced Carbon-Carbon
RCS	Reaction Control System
SEADS	Shuttle Entry Air Data System
STS	Space Transportation System
SUMS	Shuttle Upper-Atmosphere Mass Spectrometer

INTRODUCTION

Analyses of the air data derived from multiple flights of the Shuttle Entry Air Data System (SEADS) have demonstrated that the SEADS experimental air data system provided research quality data. In addition, they verified the across-the-speed-range capabilities of the flush orifice air data system concept. Previously, conventional air data systems, based on the pitot-static tube concept, have been used--almost universally--on flight vehicles operating in a continuum atmosphere. Also, when flow direction angles were required in addition to air speed, Mach number, and pressure altitude, these angles were typically obtained from either flow direction vanes or differential pressure sensors. These conventional systems have been adapted for use on a wide variety of flight vehicles operating in low speed flight. However, such conventional air data concepts cannot be adapted to entry and hypersonic flight vehicles due to the associated harsh thermal environment. This environment, which characteristically forces flight vehicles to have blunt body contours, with large radii of curvature, to minimize the stagnation-point heat-transfer rate, also prohibits the use of conventional air data sensing vanes or probes having small radii of curvature or exposed sharp edges.

This thermal constraint on air data system design was encountered early in the X-15 program, and resolved through the development of the "ball nose" air data sensor, (Refs. 1-4). For flight tests at Mach numbers less than 3, the X-15 utilized a conventional pitot-static tube, mounted on a boom and augmented by angle-of-attack (α) and angle-of-sideslip (β) flow sensing vanes. For flight tests at Mach numbers in excess of three, the conventional nose boom was replaced by the "ball nose" sensor. This sensor was spherical in shape and partially housed in a truncated cone at the forward fuselage station. A hydraulic servo-mechanism rotated the sphere to maintain a zero pressure differential between pairs of symmetrically situated (vertical and lateral) flush orifices. Thus, the sphere was positioned, in flight, in such a manner that the center orifice sensed total pressure and the orthogonal rotation angles of the "ball nose" corresponded to the aerodynamic flow or attitude angles. The flow field's static pressure was derived from pressure measurements obtained at fuselage "static" orifices which, in turn, were used in conjunction with the orifices in the "ball nose."

The reentry flight envelope for the Space Shuttle Orbiter had a range in Mach number from 0.3 to 27, a range of angle of attack from 6° to 45°, and maximum nose stagnation temperatures of approximately 2,660F. These conditions posed air data system sensing problems which were unique and challenging.

Existing air data systems, being unable to meet such rigorous operational requirements, forced a compromise solution for the Space Shuttle Orbiter. In the supersonic and subsonic flight regimes, during the final minutes of descent, the orbiter relied on air data provided by two conventional, fuselage-mounted, differential pressure probes which were deployed at a Mach number of 3.5. During the approximate 25 minutes of hypersonic flight, prior to probe deployment, air data parameters are estimated from the inertially derived navigation state. This situation is less than ideal, however, since the navigation-derived air data parameters are contaminated. Errors are introduced as a result of a dependency on imprecisely known aerodynamic coefficients, the necessary assumption of zero winds, and the ever present inherent navigation state errors. It is worth noting that even a temporary failure of the navigation solution could jeopardize the vehicle's controllability. Hence, special measures had to be taken to avoid any "violent maneuvers" during the transition of passing from one sensing system to another.

The Shuttle Entry Air Data System (SEADS), developed at the NASA Langley Research Center, was an experimental system designed to provide research quality air data, across the speed range encountered by the orbiter, at altitudes below 280,000 ft. The system also demonstrated the utility of this concept to provide operational air data. The first of these objectives supported the National Aeronautics and Space Administration's Orbiter Experiments (OEX) Program (Refs. 5-8), especially in the accomplishment of entry technology related flight research. The latter was to provide a demonstration of the advanced flight system technology needed for future flight air data systems.

SEADS is based on the idea that the forward section of the fuselage, even though it is asymmetrical, can be instrumented to function both as a pitot-static probe, and as a differential-pressure flow direction sensor (Refs. 9,10). Like the X-15 "ball nose" scheme, SEADS is a flush mounted pressure orifice sensing system. Unlike the X-15 ball nose, SEADS requires no electro-mechanical devices for its operation.

As a hardware system SEADS consists of 20 flush orifices, each connected to a pair of absolute pressure transducers. Of these 20 there were 14 primary orifices arranged to form a cruciform array (8 in the orbiter's vertical plane of symmetry and 3 symmetrically located lateral pairs) located in the orbiter's nose cap. In addition, there were six supplementary orifices, located in the orbiter's forward fuselage section aft of the nose cap (Fig. 1). Even though the SEADS concept is basically a simple sensor system, its implementation in the Space Shuttle Orbiter required the development of new technologies both in system hardware and in data analysis techniques.

The SEADS experiment successfully flew on Orbiter OV-102/Columbia during missions STS-61C, 28, 32, 35, and 40 and provided research-quality, entry-air-data at speeds ranging from Mach 27 (at an altitude of 280,000-ft.) to near zero speed at landing.

It should be mentioned that the OEX/SEADS experiment was also operational during lift-off and ascent, and that pressure data were obtained during this phase of the flights. Even though it was not done as part of the SEADS experiment, it is believed that accurate air data could be derived following the development of properly calibrated pressure models for the various launch/ascent configurations. (Preliminary work has been done by Woeste, Ref. 11.) The present authors believe that more analysis and testing will be required before an acceptable pressure model can be developed and air data can be obtained.

PURPOSE

The purpose of this paper is to provide an overview of the SEADS concept and configuration, to verify the performance of the flight hardware, and to assess the quality of the in-situ measurements and the derived air data. The data assessment has been made by comparing the SEADS flight results with those obtained from other sources, such as the data developed through the pre-flight wind tunnel test program, Refs. 12-18, and the post-flight Best Estimate Trajectory (BET) (Refs. 19-21). Also presented is a brief evaluation of the implications which these results would have on the concept's application to advanced vehicle configurations, as a source of real time air data.

EXPERIMENT DESCRIPTION

The SEADS experiment objectives, its flight hardware definition and development, the data reduction and analysis techniques, and results from early flight data analyses are described in specific detail in a series of earlier reports (Refs. 22-33). SEADS was developed within the OEX Program, a program which was defined to accomplish a broad spectrum of entry research on the Shuttle during ascent and descent. The measured pressure data and the derived air data from SEADS support the technology based aerodynamic and aerothermodynamic research conducted by OEX. Also, these data demonstrate the utility of the flush orifice air data system concept.

SEADS FLIGHT CONFIGURATION

The SEADS experiment, which is shown schematically in Fig. 1, consists of 20 flush-mounted pressure orifices. The 14 primary orifices are located in the SEADS baseline Orbiter geometry reinforced carbon-carbon (RCC) nosecap. Eight of the orifices are in the plane of symmetry; the remaining six are arranged as three symmetrical lateral pairs. Lastly, there are six supplementary orifices located on the orbiter's forward fuselage.

The above description defines the nominal configuration which flew on flights STS-61C, 35, and 40. On the remaining missions (STS-28 and 35) orifice 18 was not available due to the installation of an uninstrumented RCC chin panel. On STS-40 orifice 18 was available; however, the SEADS transducers were disconnected and the replacement low pressure transducer located within the Shuttle Upper-Atmosphere Mass Spectrometer (SUMS) experiment failed to perform. The consequences due to the loss of orifice 18 will be discussed in a later section: **Flight Results; Air Data**. The location of each of the SEADS orifices is presented in Table I, expressed in orbiter X,Y,Z.

The SEADS nose cap assembly, as installed on the Orbiter Columbia, is shown in Fig. 2. An aft view and a cross-sectional schematic of the nose cap assembly, showing the 28 bulkhead mounted transducers and connecting corrosion resistant steel (CRES) tubing and the other interior components door are presented in Fig. 3 and Fig. 4, respectively.

Each of the 14 nose cap orifice penetration assemblies (Fig. 5) is connected, via a structurally tuned silicide coated columbium tube and 1 of 2 drilled and insulated aluminum support structures and CRES tubing, to a pair of absolute pressure transducers (one 0-1 psia and one 0-20 psia in range) mounted on the aft side of the nose cap bulkhead. This installation, which is described in detail in Ref. 23, is shown schematically in Fig. 4.

The forward fuselage orifices penetrate the orbiter's thermal protection system (TPS) tiles, via a quartz tube connected to a heat sink, and transmit pressures through CRES tubing to similar pairs of transducers. This instrumentation was developed as a part of the orbiter's development flight instrumentation (DFI) package and incorporated into the SEADS experiment.

The hardware design of SEADS was predicated on the anticipated harsh entry flight environment and on the requirement that SEADS would not compromise the multimission performance capabilities of the nose cap, nor adversely affect crew safety. Further design restraints were imposed by the coated RCC nose cap material itself and its thermal and mechanical properties, as well as vehicle step and gap criteria.

Thermally, a nominal entry trajectory can produce nose cap stagnation region temperatures up to 2,660F, with internal nose cap temperatures reaching 2,450F. In order to ensure a multimission capability at these temperatures the carbon-carbon material was coated with silicon carbide to minimize oxidation. Since the nose cap's manufacturing and coating processes do not allow for the drilling of small holes as required for the pressure orifices, it was necessary to develop a nose cap orifice penetration assembly. The resulting design is shown schematically in Fig. 5. This silicide coated columbium assembly was designed to accommodate a pressure orifice. The assemblies were developed to be thermally and mechanically compatible with the RCC nose cap material as well as the expected entry environment and to provide the needed interface between the aerodynamic surface and the remaining system's hardware. The development and flight certification of this assembly were the most critical elements in the SEADS hardware design, development, and test activities. The details of this development can be found in Refs. 22-25.

For completeness, it should be mentioned that the SEADS included six radiometers mounted on the nose cap's access hatch door. These radiometers were intended to provide a thermal distribution map for the nose cap's inner surface. They did not, however, provide useful data. Finally, due to the temperature and applied voltage sensitivities of the pressure transducers, diagnostic engineering instrumentation was used to monitor the transducer and support structure temperatures, and the voltage applied to the transducers. The data from these sensors are required as part of the transducer calibration and data reduction procedures, as indicated in Ref. 26.

SEADS PRESSURE MODEL/DATA ANALYSIS TECHNIQUE

The SEADS air data determination analysis technique is based on a modified form of Newton's impact pressure model (Ref. 27) and symbolically represented by the equation:

$$Cp_i = Cp_2 \mathrm{Cos}^2\theta_i. \tag{1}$$

This expression shows the pressure coefficient for any with orifice, CP_i, on a blunt body to be a function of the stagnation pressure coefficient, Capstan, and the cosine of the local flow incidence angle, θ. For the SEADS application (Refs. 9, 10) this expression is rewritten, to model the pressure at any ith orifice, as:

$$P_i = (P_{t_2} - P_\infty)\mathrm{Cos}^2\theta_i + P_\infty. \tag{2}$$

The data analysis technique (Refs. 9, 10, 28, and 29) incorporates this Modified Newtonian pressure prediction model with solver algorithms to mathematically model the pressure field over the vehicle's forebody as a function of an "aerodynamic state vector." This "aerodynamic state vector" is composed of independent air data parameters and orifice position variables. The solver algorithms are based on an adaption of filter theory. Air data are iteratively obtained through the minimization of the sum of the squares of the weighted residuals of the "aerodynamic state vector" parameters. Other desired air data quantities, such as free stream dynamic pressure, q_∞, are subsequently derived from the "aerodynamic state vector." For SEADS applications, the "aerodynamic state vector," $\underline{X}$, consists of four independent air data parameters, i.e.,

$$\underline{X} = \begin{bmatrix} P_t \\ P_\infty \\ \alpha \\ \beta \end{bmatrix} \tag{3}$$

thus, the predicted pressure at any orifice "i" can be symbolically expressed as:

$$P_i = F\,(\underline{X}\,;\, \eta_i,\, \zeta_i\,) \tag{4}$$

where $\underline{X}$ is the state vector and η_i and ζ_i are orifice location variables.

The use of Newtonian theory, as the basis for an across-the-speed-range pressure model, was recognized to have inherent limitations, particularly at low speeds. However, the simplicity of this theory and the derived pressure model provided the most economical and convenient technique for local pressure estimations. To extend the model's range of applicability and to increase its accuracy it was modified empirically through the development of *"flow field correction coefficients"* C1, C2, and C3. The C1 coefficient corrects for the observed bias between predicted results and the experimentally determined angles-of-attack, α. The C2 and C3 coefficients correct for the observed non-linearities in measured and predicted attitude angles, α and β, and the pressure ratio, $R = Pi/Pt2$, respectively. Initially, these coefficients were obtained by comparing wind tunnel test data (Refs. 14-18, 28) to the Newtonian predictions. Subsequently, these quantities were modified by means of similar comparisons with flight data (Refs. 29 and 30). The initial and the final *"flow field correction coefficients"* are presented as a function of $\sqrt{R}$ in Fig. 6. Also shown are the individual wind tunnel data points incorporated. Each data point represents the results of a linear regression analysis of all of the wind tunnel data for the specific Mach number. The derivation of the final coefficients is discussed in **Flight Results: Air Data**.

FLIGHT RESULTS

The success of the SEADS experiment required that the system (hardware and software) provide consistent research quality air data and that the hardware demonstrate a multimission capability. The primary data used to verify the accomplishment of the first objective are found in the consistent comparisons between flight and wind tunnel pressure measurements (Refs. 31, 32, 33, 35). The verification of the first objective, per se, is found in the agreement between the air data derived by the SEADS algorithm and that developed in the Best Estimated Trajectory (BET).

To verify the hardware's multimission capability, detailed post mission inspections of the RCC, the primary columbium components, and the deposited material were conducted. Additionally, comparisons were made between the findings from these inspections and the results from preflight thermal tests and evaluations. Also pre- and post-flight pressure tests of the pressure measurement assemblies were conducted to ascertain the system's integrity.

Hardware

The major concern in the design and development of SEADS and therefore the evaluation of the hardware's performance was the columbium pressure port assembly, its connecting tubing, and the effects that pressure ports had on the nose cap and its multimission capability. The results of the hardware performance verification process demonstrated that the nose cap and the SEADS hardware were in excellent postflight condition, and that the SEADS particular hardware had: (1) performed per design specifications; (2) demonstrated a multimission capability; and (3) had no adverse effect on the RCC nose cap. The SEADS nose cap assembly is shown pre- and post-mission (after all five flights) in Fig. 7. A high resolution closeup of the surface of pressure port number 7, pre- and post mission, is shown in Fig. 8. Port 7 is nominally at the stagnation point during high altitude hypersonic flight and experiences the most severe heating. An interior view of the nose cap, providing an aft-view of several of the penetration assemblies, tubing, and some of the nose cap internal insulation, pre- and post-mission, is presented in Fig. 9.

The general RCC nose cap discoloration and/or glazing, seen on both the external and internal surfaces, is typical of the conditions seen on the nose caps of other orbiters and/or on RCC components during thermal tests. These effects are a consequence of the high-temperature external flows, the associated normal "thermal curing" of the RCC coatings and the Type A sealant, and the outgassing from the interior insulation. The dark streaks associated with the nose cap penetrations, which provide an unexpected visualization of the flow patterns, are a result of the flow disturbance caused by the penetration and the resulting effects on the RCC curing process. The appearance of the nose cap's components represents no cause for concern and shows no adverse effects on mission life capability (Ref. 36).

The discoloration and appearance of the penetration assemblies (pressure ports) is typical of that experienced during the SEADS development and certification arc jet test programs (Refs. 22-25). The white deposits emanating from several of the ports, especially port 5, are the result of the induced high temperature flowing of excess Type A sealant--a sealant applied to the RCC/silicon carbide coating to reduce oxidation and sub-surface mass loss. This material was also used, in the case of SEADS, to meet a prescribed OML smoothness criterion between the penetration assembles and the nose cap. A closer examination of ports 5 and 11 (Fig. 10) showed deposits with a yellow hue, indicating the presence of columbium pentoxide and a possible failure of the penetration assembly's silicide coating. Further examination of these ports and the associated deposits, employing photomicrographic techniques and chemical analyses, showed that while there was coating failure and some columbium mass loss, the structural integrity of the ports had not been compromised and further mission life could be expected (Ref. 36).

Although some minor thermal scorching was noted on the nose cap's interior insulation, due to internal cross flows notably on the starboard support post, all components operated within the thermal design margins. (This was determined by the diagnostic engineering thermal measurements discussed previously.) A detailed mission by mission assessment of the hardware performance is presented in Refs. 41-45.

Pressure Data

The pressure data used to evaluate the performance of the pressure measurement system concerned all 20 SEADS pressure ports, and their associated 40 transduces, from all 5 flights. These data were obtained at a data rate of 28 Hz and digitized by a 12-bit system for recording purposes. Postflight analyses of these data indicate that measurements were obtained from all of the SEADS transducers. However, because of the orbiter's flight attitude and suspected flow separations, and due to pressure model-geometry constraints, some leeward (ports 1 and 15) and aft (ports 19 and 20) fuselage-mounted orifices did not provide useful data for the air data analyses. In addition, the 0-20 psia transducer at orifice 7 malfunctioned, hence data from this transducer was not incorporated into the analyses.

A significant factor important to the evaluation of any transducer's performance was the reference ("zero" pressure) measurement obtained just prior to entry into the atmosphere. The on-orbit "zero" bias, which was incorporated into all postflight analyses, provided a final verification of the performance and repeatability of the SEADS transducers. Table 2 presents the pressure "zero" bias data for representative transducers. The repeatability of these measurements is excellent and indicates a high degree of instrument reliability. In addition, as part of the postflight analyses, at the "transition" from the 1-psia to the 20-psia transducer, the 20-psia transducer was "zeroed" relative to the 1-psia transducer, to provide the final "in-flight calibration."

A typical calibrated pressure time-history (from port 5) is shown in overlay for each flight in Fig. 11. This is intended to illustrate the repeatability of the measurements. Fig. 12 presents an overlay of calibrated pressures measured during STS-35 at several port locations, and is presented to indicate the variation in pressures as a function of geometric location.

Low density inlet effects:

The pressure and air data results obtained from the initial flight of SEADS, on STS-61C, showed that pressures were sensed at altitudes up to 310,000 ft. Even though accurate attitude, α/β, data could be determined starting at that altitude an accurate freestream dynamic pressure, q_∞, could not be obtained. An analysis of the data showed that while the determination of vehicle attitude is dependent on an accurately determined pressure distribution, and not on accurate absolute values of pressure, free stream dynamic pressure, and thence density, are dependent on absolute measurement values. It was therefore concluded, based on the stated accuracy requirements and the existing pressure model and data reduction methodology, that the applicability of the

SEADS for these air data (q_∞, ρ) determinations would be limited to altitudes below 265,000 ft.

Subsequently, a review of work conducted by Potter (Refs. 37 and 38) and by Moss (Ref. 39) showed that, in the transition and free molecule flow regimes, low-density effects in a pressure orifice must be taken into consideration if one is to extract accurate pressure measurements. This low-density inlet flow phenomenon, which is a function of the degree of rarefaction, causes the pressure inside an orifice to be much different than the pressure at the surface outside of the orifice.

Therefore, to extend the operating envelope of SEADS to include the full operating range of the transducer's capabilities, data from flight STS-61C were analyzed incorporating the semiempirical methods developed by Potter (Ref. 40) and direct simulation Monte Carlo (DSMC) results from Moss. This led to the development of "corrections" which were subsequently applied to account for the "orifice effect" and adjust the measured data. A comparison of the corrected and uncorrected densities for flights STS-61C and STS-35 is shown in Figs. 13(a) and (b), respectively. These results indicate that appropriate pre-flight corrections can be developed, based on estimates of the degree of rarefaction present, temperature differences, gas properties, and tube diameter.

Air Data

The principal objectives of the SEADS experiment were to acquire research quality air data in support of the OEX Program, and to demonstrate the technologies required to use the flush orifice air data system concept. These objectives were interpreted as requiring that SEADS should be capable of providing, as a "stand-alone" system, the air data parameters: angle of attack, α, angle of sideslip, β, and freestream dynamic pressure, q_∞. These specific parameters were to be determined to an accuracy of 0.5°, 0.5°, and 5 percent, respectively, in the hypersonic/supersonic speed regime starting at an altitude of 280,000-ft., and to determine these parameters to an accuracy of 1°, 1°, and 5 percent in the transonic and subsonic regimes.

The results from all five flights contributed to the full verification of the SEADS concept. However, the air data performance assessment has focused on the results obtained from flights STS-61C and 35 due to the loss of the chin panel orifice (orifice 18) data on flights STS-28, 32, and 40. The loss of this data compromised the accuracy of the derived angle of attack. As should be recalled, the air data assessment was accomplished through a comparison of SEADS and the best estimate trajectory (BET) derived air data. Experience with the BET, over the many prior flights of the Space Shuttle Orbiter, has provided a high level of confidence with regard to the accuracy of its output. This is especially true insofar as attitude and state data are concerned.

Therefore, for the purposes of analysis the BET has been considered as the provider of "benchmark" air data.

Comparisons of the SEADS "corrected" air data parameters (α, β, and q_∞) with the BET results from STS-61C (Ref. 20) and 35 (Ref. 21) are presented in Fig. 14. The significance of the wind tunnel derived *"flow field correction coefficients,"* insofar as they apply to the Newtonian pressure model, is obvious from the comparison shown for α in this figure. The figure also shows the excellent agreement which exists between the "corrected" SEADS and BET results.

As previously stated, the loss of the chin panel orifice (orifice 18) data (on flights STS-28, 32, and 40) compromised the accuracy of the derived angle of attack. The decrease in accuracy is due to the lack of sufficient pressure measurements to the windward of stagnation from which a definitive pressure distribution can be produced at high angle of attack. The inclusion of orifice 18 data provides the required distribution. This conclusion was verified by comparable results obtained from an analysis of the STS-61C and 35 when data from orifice 18 was excluded (Ref. 30). These results demonstrate the importance of orifice location in relation to operating envelope.

Based on these data comparisons, an error analysis was performed (Ref. 29) and demonstrated that the SEADS results met or exceeded the previously stated preflight requirements and, therefore, provided the performance verification required for the SEADS flush orifice concept. However, a set of final "flow *field correction coefficients"* based on flight data were derived in order to optimize the air data algorithm. These final flight derived *"flow field correction coefficients"* are presented in comparison to the pre-flight values in Fig. 6. The details of the derivation process are presented in Refs. 29 and 30 and summarized herein.

In an attempt to identify the source(s) of the differences between the pre- and initial post-flight coefficients (i.e. the differences between wind-tunnel and flight determined values), a thorough review of both sets of data was undertaken (Ref. 30). It was determined that during the final determination of the pre-flight coefficients the data from Refs. 17 and 18 was weighted more heavily due to the fidelity of the test model and the test program. The application of an equal weighting to all acceptable high speed data and the incorporation of data not originally included in the pre-flight data base, namely those data obtained from the 4.0 percent model in the UPWT (ref. 17) and the 2.0 percent model in M=6 air (Ref. 15) and M=10 air (Ref. 16), have resulted in a resolution of the differences between the pre- and post-flight *"flow field correction coefficients."*

Of particular note in the assessment of the experimental data was an evaluation of the effect of including wind tunnel data typically not within the operational attitude range of the SEADS -- at the associated Mach number -- in the determination of the *"flow field correction coefficients."* The results from this assessment showed that the use of limited (operational) range attitude data only provided more "accurate" wind tunnel based *"flow field correction coefficients"* as long as the zero angle-of-attack data were also included. The incorporation of other non-operational range data did not significantly influence the correction coefficients, Ref. 30. As a result, these data could be deleted from the algorithm calibration process, thereby reducing testing requirements in support of future system designs.

The assessment of the low speed ($M<1.5$) results, specifically, verified that the use of a Newtonian-pressure model does not produce the same degree of predictability, as does the high speed evaluations, insofar as "accurate" air data are concerned. It must be remembered that Newtonian theory is based on an assumption of a high velocity impact flow, and such is certainly not the case at low speeds. This fact is borne out by the results of this research. However, the application of an empirically derived pressure model, based on Newtonian theory corrected initially by wind tunnel data and finally by flight data, is certainly capable of determining low speed air data. This, too, has been demonstrated by the current research results. As for the high speed data, a semi-empirical algorithm was developed, based on modified-Newtonian theory and corrected using wind tunnel data. The significant difference, as noted in Fig. 6, between the high and low speed coefficients is that the low speed C1 varies with $\sqrt{R}$ as opposed to being a constant value as it is for high speeds.

A review of the final calibrated and corrected data from all 5 flights reveals that, even though the SEADS design requirement was for accurate air data below 280,000 ft, useful/accurate pressure data were obtained at altitudes up to 300,000 ft. This is attributed to the rigorous system calibration procedure imposed on the SEADS experiment. A complete compilation of the pressures and derived air data from all 5 flights is available in Refs. 41-45.

OPERATIONAL CONSIDERATIONS

Results from the SEADS experiment have provided verification of the technologies associated with the flush orifice air data system concept. In addition to being capable of providing across-the-speed-range air data, the flush orifice concept also has demonstrated a significant advantage over conventional (pitot static probe) air data systems. Specifically, it does not rely on calibrations based on specific pressure ratios or differences. Rather, it is based on fitting an overall pressure model to *all* measured pressure data. The SEADS methodology is therefore fault tolerant and less susceptible to the errors introduced by unavoidable differences between the wind-tunnel calibration models and those ascertained from flight.

Specific air data requirements related to the Space Shuttle Orbiter during reentry are an accurate knowledge of angle of attack, dynamic pressure, and Mach number. Such air data information is invaluable in supporting and safe-guarding a variety of critical events during reentry. It is worth mentioning that the orbiter's master sequencer and controller (MSC) uses q_∞ to model reaction control system (RCS) jet activities, and that M_∞ is employed to activate aerodynamic surfaces and control vent door sequencing.

Also, the flight control system requires attitude information to maintain vehicle stability during flight, while q_∞ and M_∞ are needed for control gain and control surface deflection scheduling. Obviously, a sizable error in the computation of these air data quantities would preclude the use of any automatic flight control system. In addition, it is important to note that control gain scheduling errors could prevent even direct pilot "stick inputs" from controlling and maintaining vehicle stability.

The capability to compute highly accurate air data parameters can have major impact on nominal flight performance also. For example, that portion of the RCS fuel budget which has been allocated to navigation derived air data parameter errors would be reduced.

In the current orbiter configuration air data parameters are computed in modules which reside within the navigation software prior to the time when the Operational Air Data System (OADS) probes are deployed at about Mach 2.5 ($h \approx 85K$ ft). In addition to being totally dependent on a viable navigation system, these computed air data quantities suffer from several unavoidable error sources, such as a lack of knowledge of winds, state vector errors, inertial measurement unit (IMU) platform attitude errors, and aerodynamic coefficient uncertainties. Furthermore, special provisions must be made to accommodate the switch from navigation-derived to OADS-obtained values.

The SEADS concept, with its system of flush pressure orifices distributed about the nose cap and forebody of the vehicle, measures surface pressure distributions directly, and can determine dynamic pressure and vehicle attitude in a straightforward manner throughout the entire atmospheric portion of entry. In this air data system, there are no pressure discontinuities in any of the flight regimes, and there is no deployment mechanism(s) and only minimal pneumatic lag. With a multiple of pressure-sensing orifices, the system is capable of delivering accurate air data parameters even in the presence of (several) sensor failures.

The SEADS concept, therefore, has the capability of making flight control more independent of navigation, and allows for direct crew control, in such case as a catastrophic navigation failure. Also, the use of SEADS flush orifice technology would enhance the flight capability of the Shuttle Orbiter or any other vehicle to which the concept is adapted.

CONCLUSIONS

A system capable of obtaining research quality air data has been designed, flown and successfully demonstrated. This demonstration was accomplished through the incorporation of a flush orifice air data system, one specifically designed and developed for the Space Shuttle Orbiter. This system, the Shuttle Entry Air Data System (SEADS), was developed to demonstrate that the flush orifice air data system concept's capability as (first) an across-the-speed range (subsonic through hypersonic) air data system and (second) to provide the air data required in the development of other flight technologies.

The flight tests of the SEADS and the postflight data analyses have demonstrated that a relatively simple flush orifice air data system concept could be physically incorporated into a complex flight vehicle and could obtain the data necessary to accurately determine the vehicle's attitude, as well as the state data required for guidance, navigation, and flight control.

REFERENCES

1. Fischel, J. and Webb, L. D., "Flight-informational Sensors Display, and Space Control of the X-15 Airplane for Atmospheric and Near Space Flight Missions," NASA TN D-2407, August 1964.

2. Larson, T. J. and Webb, L. D., "Calibration and Comparison of Pressure-Type Airspeed-Altitude Systems of X-15 Airplane From Subsonic to High Supersonic Speeds," NASA TN D-1724, February 1963.

3. Cary, J. P. and Keener, E. R., "Flight Evaluation of the X-15 Ball Nose Flow Direction Sensor as an Air-Data System," NASA TN D-2923, July 1965.

4. Webb, L. D., "Characteristics and use of X-15 Air-data Sensors," NASA TN D-4597, June 1968.

5. Siemers, P. M. III, "Shuttle Entry Technology Payloads," AAS Paper 75-251, August 1975.

6. Siemers, P. M. III, and Larson, T. J., "Space Shuttle Orbiter and Aerodynamic Testing," *Journal of Spacecraft and Rockets*, Vol. 16, No. 4, July/August 1979, p. 227.

7. Jones, J. J., "OEX - Use of the Shuttle Orbiter as a Research Vehicle," AIAA Paper 81 - 2512, November 1981.

8. Throckmorton, D. A., "Shuttle Entry Aerothermodynamic Flight Research: The Orbiter Experiments (OEX) Program," AIAA Paper 92-3987 (Invited), July 1992.

9. Pruett, C. D., Wolf, H., Heck, M. L., and Siemers, P. M. III, "An Innovative Air Data System for the Space Shuttle Orbiter: Data Analysis Techniques," AIAA Paper 81-2455, November 1981.

10. Pruett, C. D., Wolf, H., Heck, M. L., and Siemers, P. M. III, "Innovative Air-Data System for the Space Shuttle Orbiter," *Journal of Spacecraft and Rockets*, Vol. 20, No. 1, January-February 1983, pp. 61-69.

11. Woeste, T. J., "Shuttle Entry Air Data System - An Experimental Investigation of Calibration for Ascent Flight," AAIA 92-0133, March 1991.

12. Larson, T. J., Flechner, S. G., and Siemers, P. M. III, "Wind Tunnel Investigation of an All Flush Orifice Air Data System for a Large Subsonic Aircraft," NASA TP 1642, May 1980.

13. Larson, T. J. and Siemers, P. M. III, "Use of Nose Cap and Fuselage Pressure Orifices for Determination of Air Data for Space Shuttle Orbiter Below Supersonic Speeds," NASA TP 1643, July 1980.

14. Bradley, P. F., Siemers, P. M. III, Flanagan, P. F., and Henry, M. W., "Pressure Distributions on a 0.04-Scale Model of the Space Shuttle Orbiter's Forward Fuselage in the Langley Unitary Plan Wind Tunnel," NASA TM-84628, March 1983.

15. Bradley, P. F., Siemers, P. M. III, Flanagan, P. F., and Henry, M. W., "Pressure Distribution Obtained on a 0.04-Scale and 0.02-Scale Model of the Space Shuttle Orbiter's Forward Fuselage in the Langley 20-Inch Mach 6 Tunnel," NASA TM-84629, March 1983.

16. Bradley, P. F., Siemers, P. M. III, Flanagan, P. F., and Henry, M. W., "Pressure Distributions on a 0.04-Scale and 0.02-Scale Model of the Space Shuttle Orbiter's Forward Fuselage in the Langley Continuous Flow Hypersonic Tunnel," NASA TM-84630, March 1983.

17. Siemers, P. M. III and Henry, M. W., "Pressure Distribution Obtained on a 0.10-Scale Model of the Space Shuttle Orbiter's Forebody in the Ames Unitary Plan Wind Tunnel," NASA TM-87654, January 1986.

18. Siemers, P. M. III and Henry, M. W. "Pressure Distributions Obtained on a 0.10-Scale Model of the Space Shuttle Orbiter's Forebody in the AEDC Propulsion Wind Tunnel," NASA TM 87653, January 1986.

19. Compton, H. R., Findlay, J. T., Kelly, G. M., Heck, M. L., "Shuttle (STS-1) Entry Trajectory Reconstruction," AIAA Paper 81-2459, November 1981.

20. Findlay, J.T., Kelly, G.M., "61-C Columbia Entry BET Products and Summary Results," NASA CR-178262, June 1987.

21. Oakes, K. F., Findlay, J. T., Jasinski, R. A., Wood, J. S., " Final STS-35. Descent BET Products and Results for LaRC OEX Investigations," NASA CR-189569.

22. While, D. M., "Shuttle Entry Air Data Systems (SEADS) Hardware Development," NASA CR-166044, Contract NAS1-16000, January 1983.

23. Hamilton, R. M., "Shuttle Entry Air Data System (SEADS) Development History," Contract NAS9-17244, July 1987.

24. Cunningham, J. A., Rochelle, W. C., Norman, I., Ting, P. C., and Gallegos, "Shuttle Entry Air Data System (SEADS) Columbium Pressure Port Pre-Flight Testing and Analysis," AIAA Paper 85-1021, June 1985.

25. Cunningham, J. A., Rochelle, W. C., Norman, I., Ting, P. C., and Gallegos, J. J. "Shuttle Entry Air Data System Preflight Testing and Analysis," *Journal of Spacecraft and Rockets*, Vol. 24, No. 1, January-February 1987, pp. 33-39.

26. Siemers, P. M. III, Bradley, P. F., Wolf, H., Flanagan, P. F., Weilmuenster, K., and Kern, F. A., "Shuttle Flight Pressure Instrumentation: Experience and Lessons For the Future," NASA CP-2293, March 1983.

27. Lees, L., "Hypersonic Flow," IAS-RAeS: Proceedings of the 5th International Aerodynamics Conference, Los Angeles, CA., 1955, pp. 241-273.

28. Siemers, P. M., Wolf, H., Henry, M. W., "Shuttle Entry Air Data System (SEADS)- Flight Verification of an Advanced Air Data System Concept," AIAA Paper 88-2104, May 1988.

29. Wolf, H., Henry, M. W., and Siemers, P. M. III, "Shuttle Entry Air Data System (SEADS): Optimization of Preflight Algorithms Based on Flight Results," AIAA Paper 88-2053, May 1988.

30. Gibson, F.A., Henry, M.A., and Eades, J. B., Jr., "Shuttle Entry Air Data System (SEADS) Data Analysis: A Historical Perspective," Analytical Mechanics Associates, Inc. Report No. 92-7, December 1992.

31. Bradley, P. F., Siemers, P. M. III, "Comparison of Forward Fuselage Space Shuttle Orbiter Flight Pressure Data to Wind-Tunnel and Analytical Results in the Hypersonic Mach Number Range, AIAA Paper 81-2477, November 1981.

32. Siemers, P. M. III, Wolf, H., and Flanagan, P. F., "Shuttle Entry Air Data System Concepts Applied to Space Shuttle Orbiter Flight Pressure Data to Determine Air Data - STS 1-4," AIAA Paper 83-1003, January 1983.

33. Larson, T. J., Whitemore, S. A., Ehernberger, L. J., Johnson, J. B., and Siemers, P. M. III, "Qualitative Evaluation of a Flush Air Data System at Transonic Speeds and High Angles of Attack," NASA TP 2716, April 1987.

34. Henry, M. W., Siemers, P. M. III, and Wolf, H., "An Evaluation of Shuttle Entry Air Data System (SEADS) Flight Pressure: Comparison With Wind Tunnel and Theoretical Predictions," AIAA Paper 88-2052, May 1988.

35. Larson, T. J. and Siemers, P. M. III, "Subsonic Tests of an All Flush Pressure Orifice Air Data System," NASA TP 1871, June 1981.

36. Leifeste, M. R., and Brownfield, C. D., " Metallurgical Evaluation of Flown SEADS Ports," M&P Engineering Report 1262-2040, Rockwell International Space Transportation Systems Division, September 1992.

37. Kinslow, M., and Potter, J. L., "Reevaluation of Parameters Relative to the Orifice Effect," 7th International Symposium on Rarefied Gas Dynamics, Vol. 1, edited by Dino Dini, Editrice Tecnico Scientifica, Pisa, Italy, 1971, pp. 399-408.

38. Hurlbut, F. C., and Potter, J. L., " Tethered Aerothermodynamic Research Needs," *AIAA Journal of Spacecraft and Rockets*, Vol. 28, No.1, February 1991.

39. Moss, J. N., Bird, G. A., "Monte Carlo Simulations in Support of the Shuttle Upper Atmospheric Mass Spectrometer Experiment," *AIAA Journal of Thermophysics and Heat Transfer,* Vol. 2, No. 2, April 1988.

40. Potter, J. L., "Correction of Measured Pressures to Account for Thermolecular Flow in Orifices and Tubes: User Guide and Program," Analytical Mechanics Association, Inc. Report No. 90-02, October 1991.

41. Siemers, P. M. III, Henry, M. W., Schutte, P. C., Gibson, F. A., Eades, J. B. Jr., "Shuttle Entry Air Data System (SEADS) STS-61C Mission Report," NASA TM 107716. (Unpublished)

42. Siemers, P. M. III, Henry, M. W., Gibson, L. S., Gibson, F. A., Eades, J. B. Jr., "Shuttle Entry Air Data System (SEADS) STS-28 Mission Report," NASA TM 107717. (Unpublished)

43. Siemers, P. M. III, Henry, M. W., Gibson, L. S., Gibson, F. A., Eades, J. B. Jr., "Shuttle Entry Air Data System (SEADS) STS-32 Mission Report," NASA TM 107718. (Unpublished)

44. Siemers, P. M. III, Henry, M. W., Gibson, L. S., Gibson, F. A., Eades, J. B. Jr., "Shuttle Entry Air Data System (SEADS) STS-35 Mission Report," NASA TM 107719. (Unpublished).

45. Siemers, P. M. III, Henry, M. W., Gibson, L. S., Gibson, F. A., and Eades, J. B. Jr., "Shuttle Entry Air Data System (SEADS) STS-40 Mission Report, " NASA TM 107720.

Table 1 SEADS orifice coordinates.

SEADS Orifice Number	X (in.)	Y (in.)	Z (in.)
1	238.160	0.00	347.729
2	236.569	0.00	343.217
3	236.000	0.00	338.500
4	236.498	0.00	333.852
5	238.021	0.00	329.302
6	240.396	0.00	325.168
7	243.466	0.00	321.416
8	247.005	0.00	318.086
9	240.466	-13.50	334.422
10	238.281	-9.25	334.108
11	236.920	-4.75	333.913
12	236.920	4.75	333.913
13	238.281	9.25	334.108
14	240.466	13.50	334.422
15	269.600	-3.00	376.000
16	269.600	34.20	327.800
17	269.600	-34.20	327.800
18	269.300	-4.70	305.500

Table 2 SEADS transducer "zero" bias*, typical.

Transducer	Flight				
	61C	28	32	35	40
8370	-1.059	-1.396	-1.394	-1.505	-1.221
8075	-0.596	-0.838	-0.842	-0.479	-0.579
7707	3.793	2.777	2.948	3.255	3.644
8069	1.419	1.278	1.303	1.462	1.454
8070	-0.637	-0.925	-0.902	-0.793	-0.757
8071	1.981	3.124	3.072	3.195	3.296
8073	-0.343	-0.576	-0.510	-0.337	-0.018

* Bias is given in psf

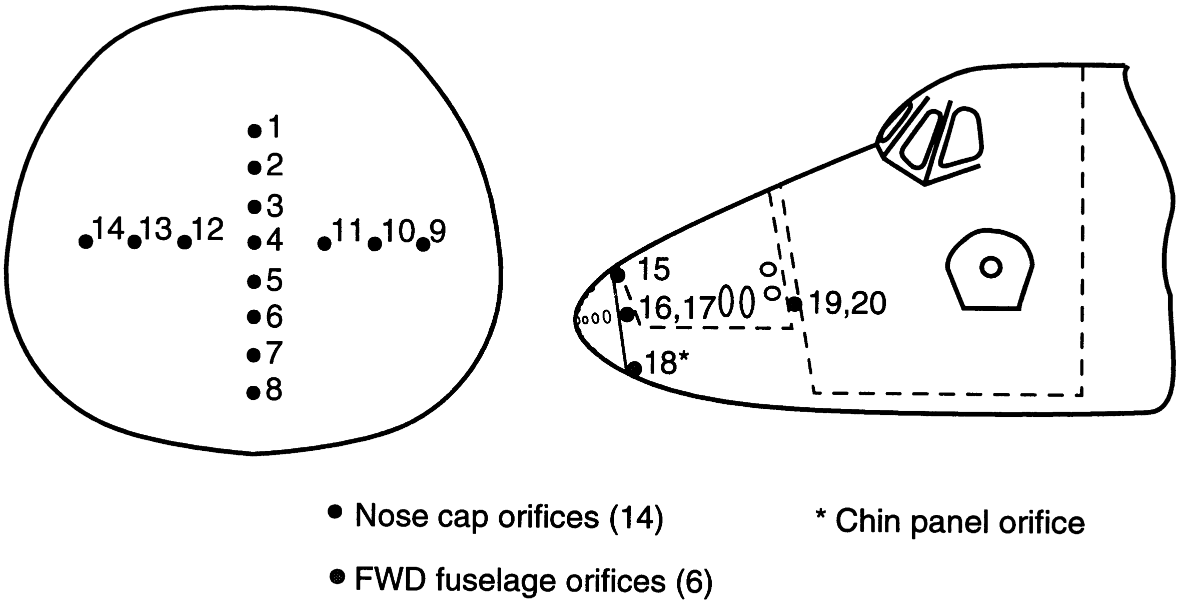

Figure 1. SEADS orifice arrangement - schematic.

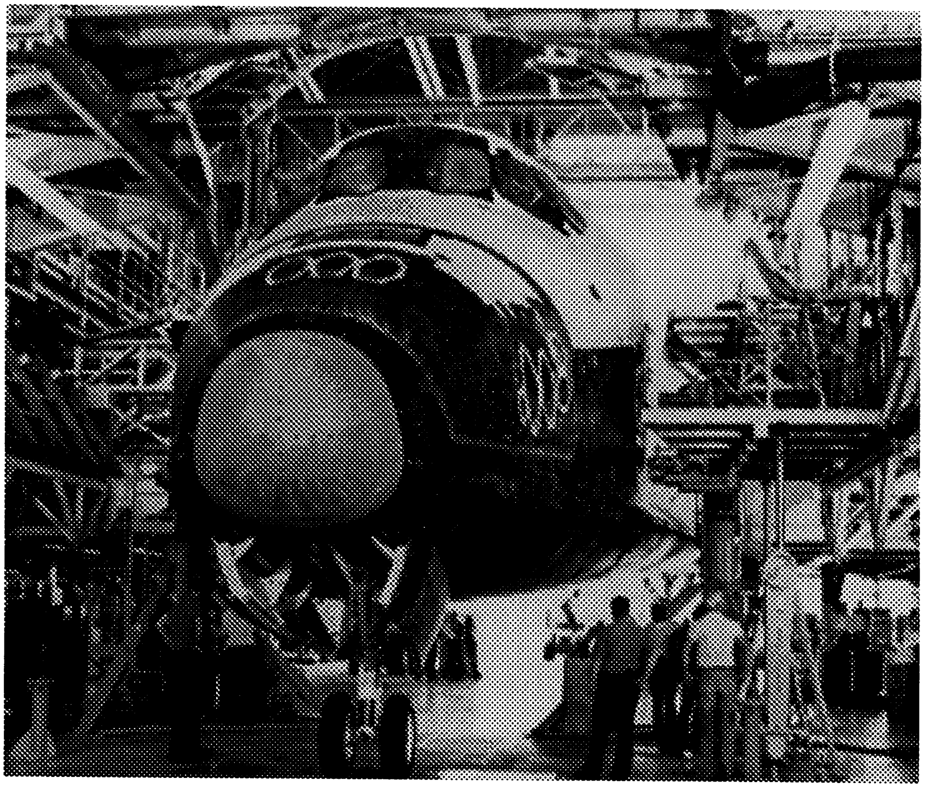

Figure 2. SEADS nose cap assembly as installed on the Orbiter Columbia.

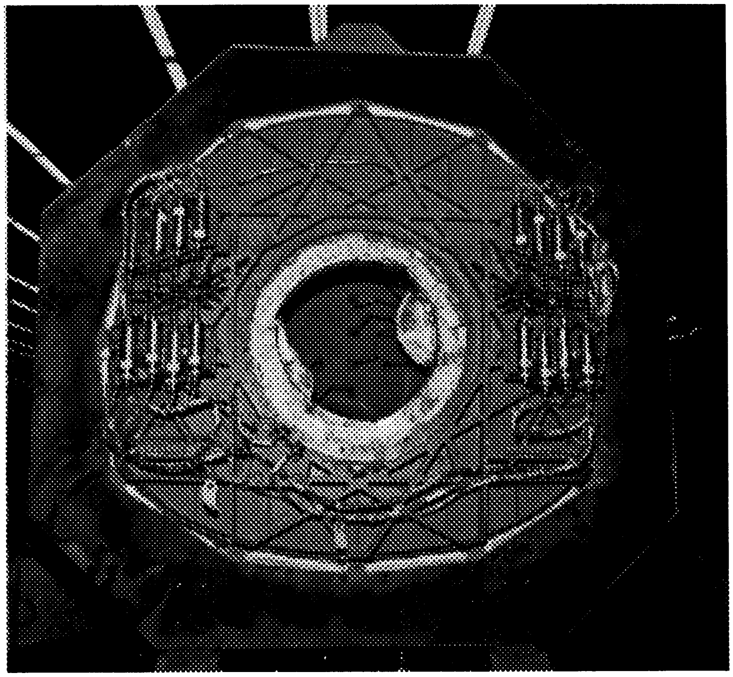

Figure 3. SEADS nose cap assembly - AFT view.

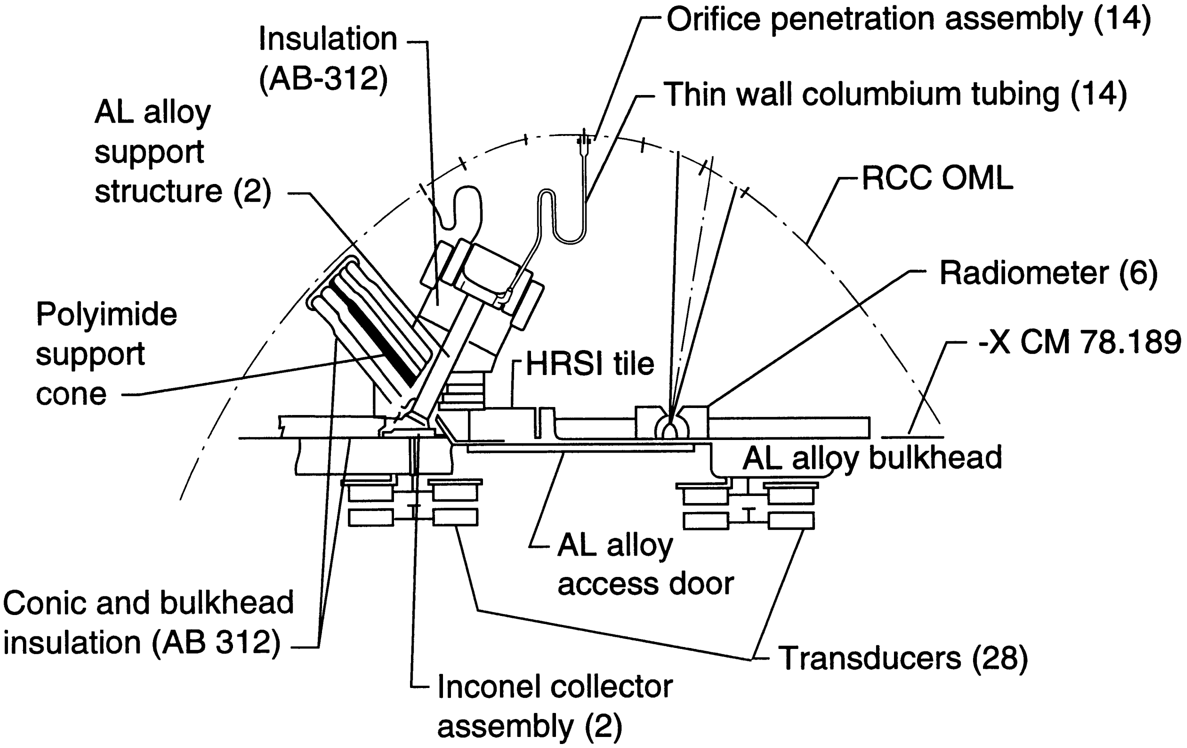
Orifice penetration assembly (14)
Insulation (AB-312)
Thin wall columbium tubing (14)
AL alloy support structure (2)
RCC OML
Radiometer (6)
Polyimide support cone
HRSI tile
-X CM 78.189
AL alloy bulkhead
AL alloy access door
Conic and bulkhead insulation (AB 312)
Transducers (28)
Inconel collector assembly (2)

Figure 4. SEADS internal configuration schematic.

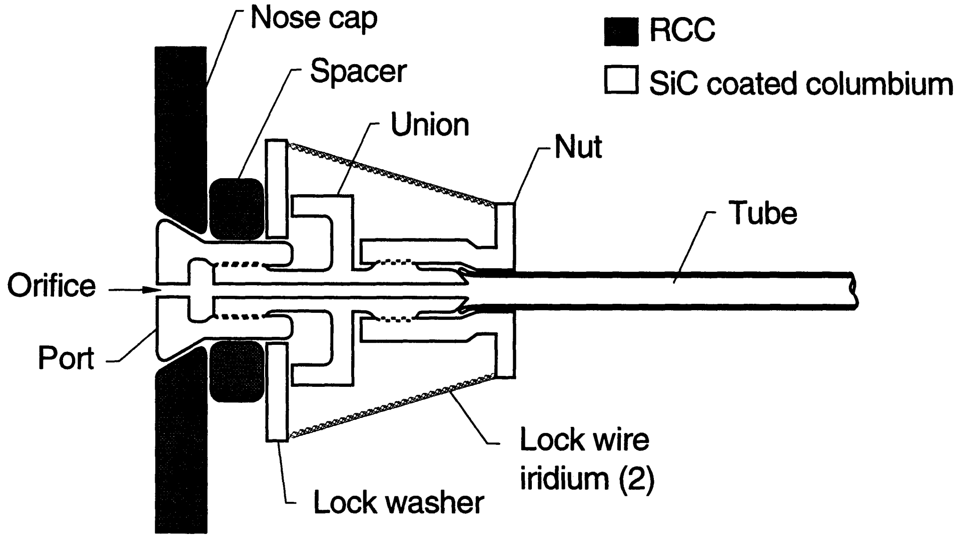

Figure 5. SEADS penetration assembly.

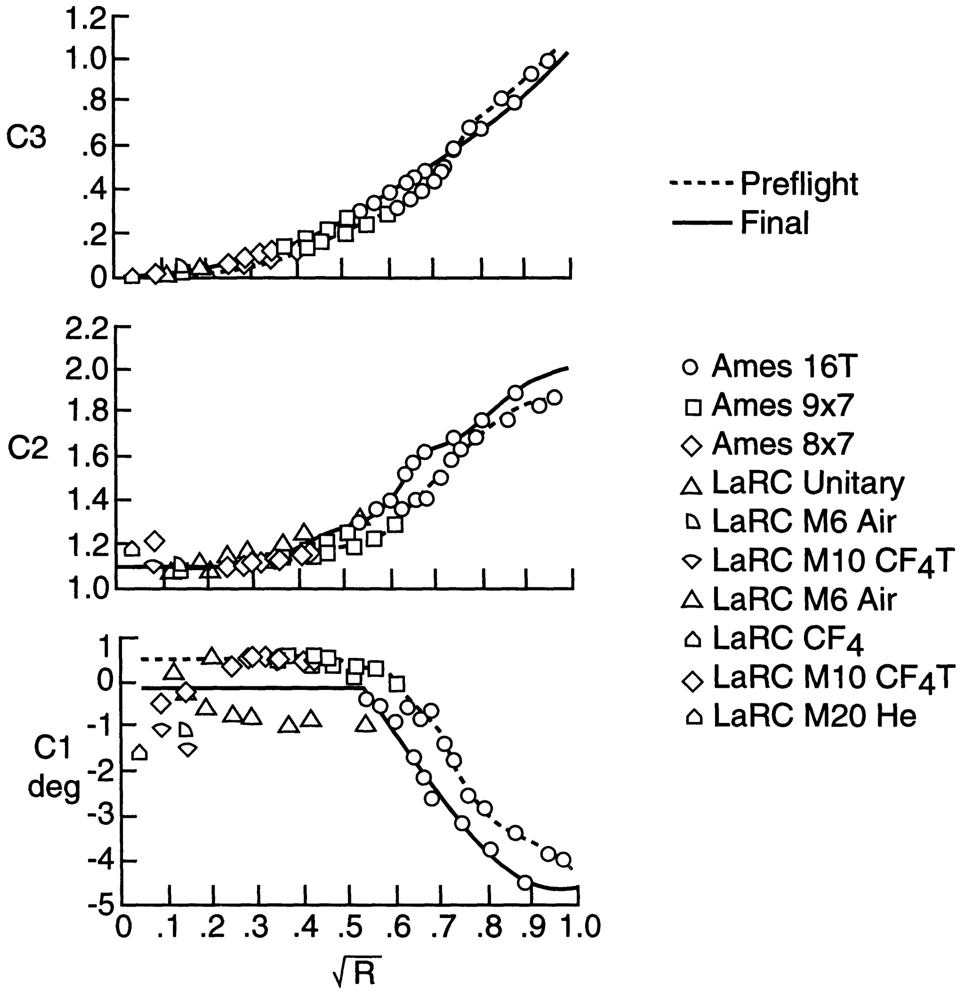

Figure 6. SEADS flow field correction coefficients.

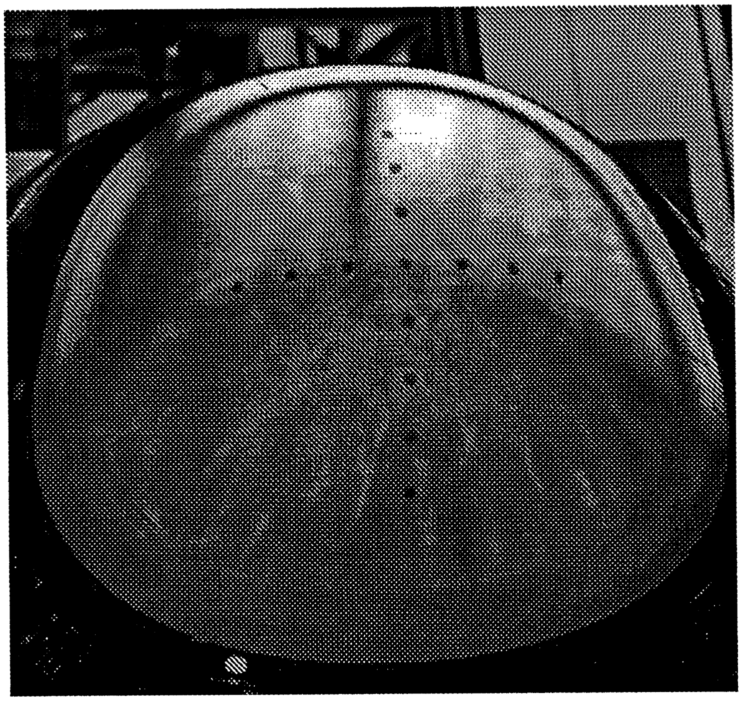

(7a) Pre-flight

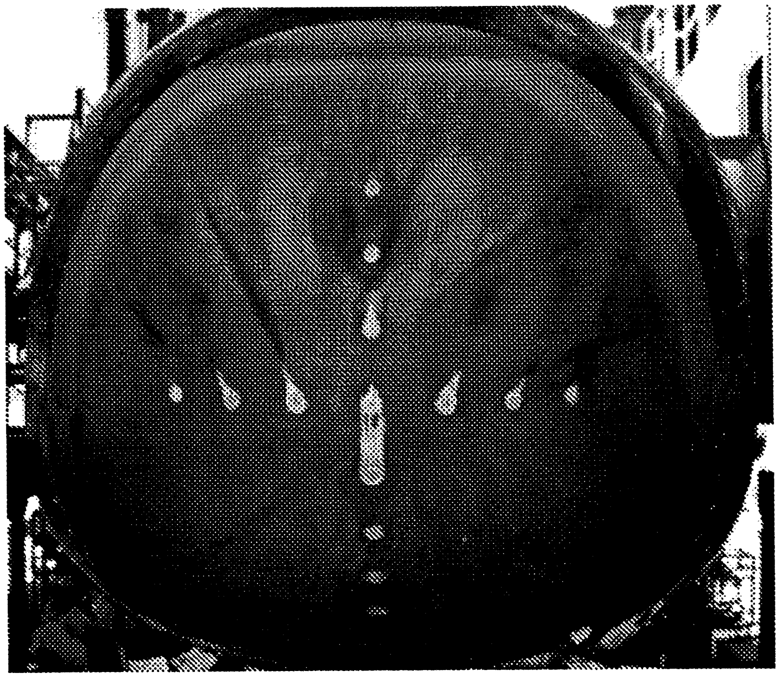

(7b) Post-flight

Figure 7. SEADS nose cap assembly pre- and post flight.

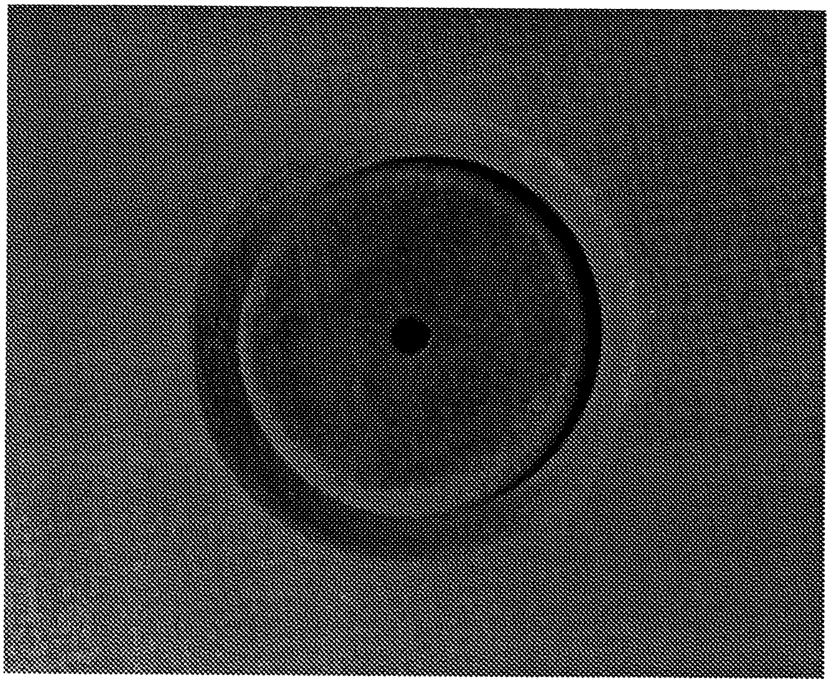

Port 7 pre-flight

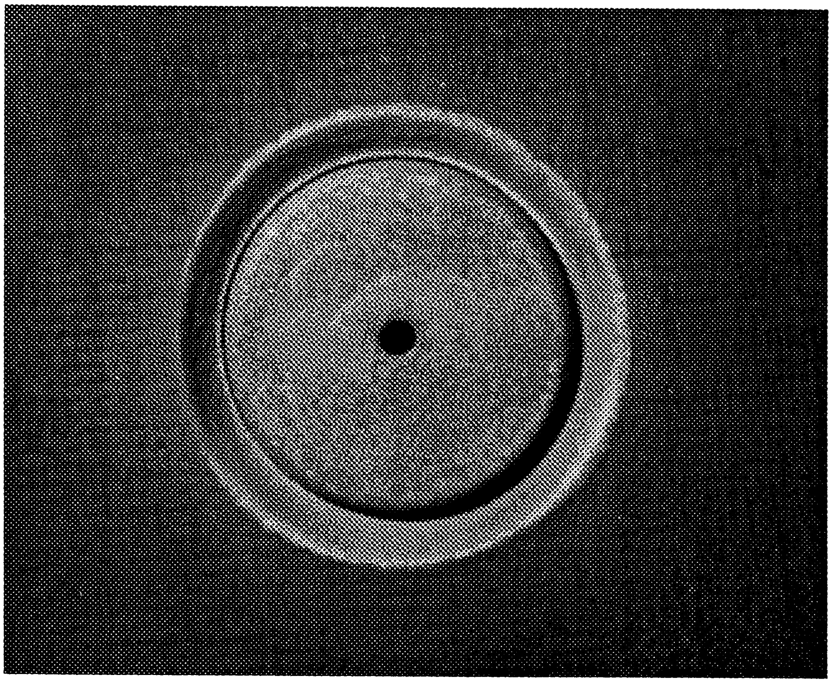

Port 7 post STS 40

Figure 8. SEADS pressure port 7 pre- and post flight.

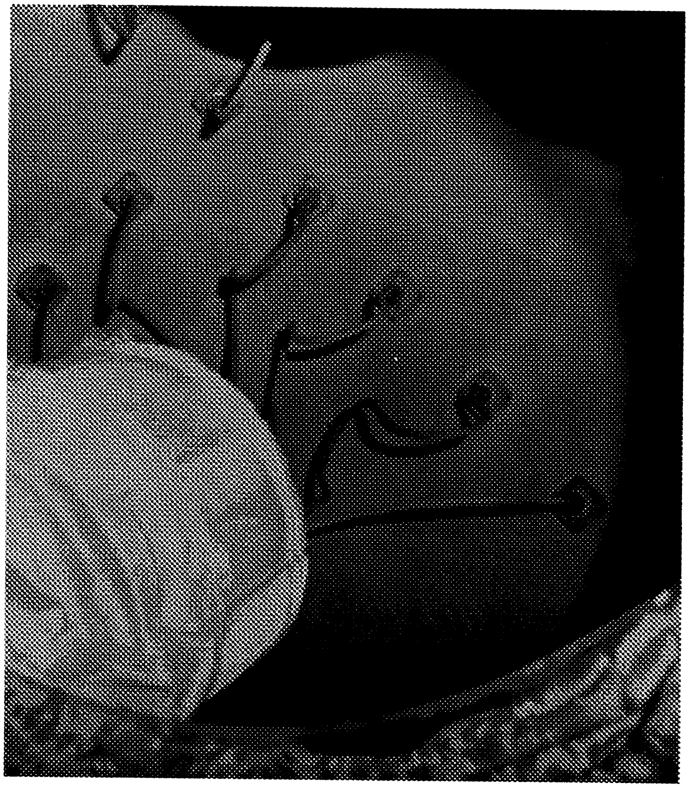

(9a) Pre-flight

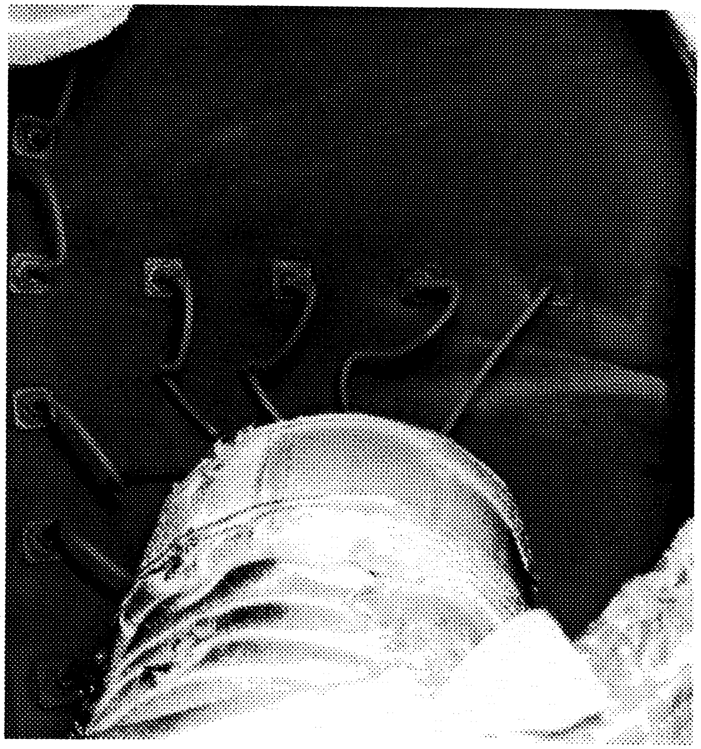

(9b) Post-flight

Figure 9. SEADS nose cap interior pre- and post flight.

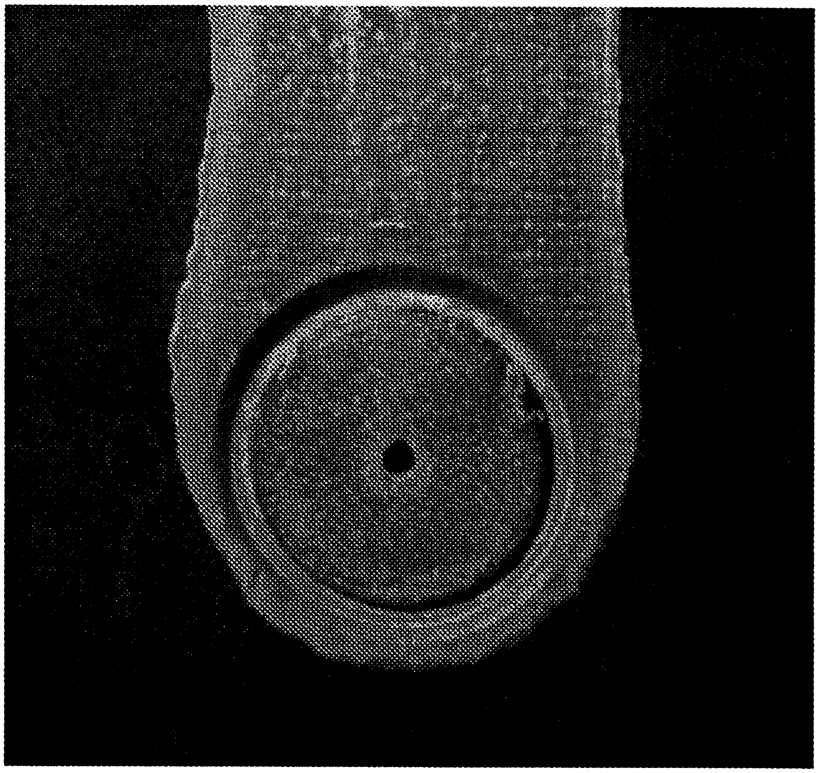

(10a) Port 5

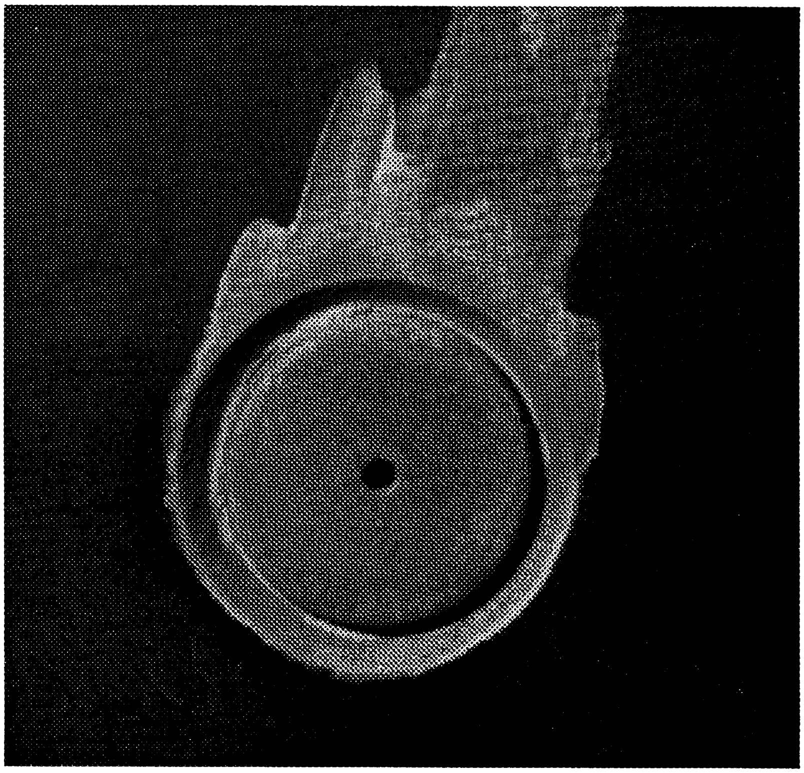

(10b) Port 11

Figure 10. SEADS ports showing effect of five flights.

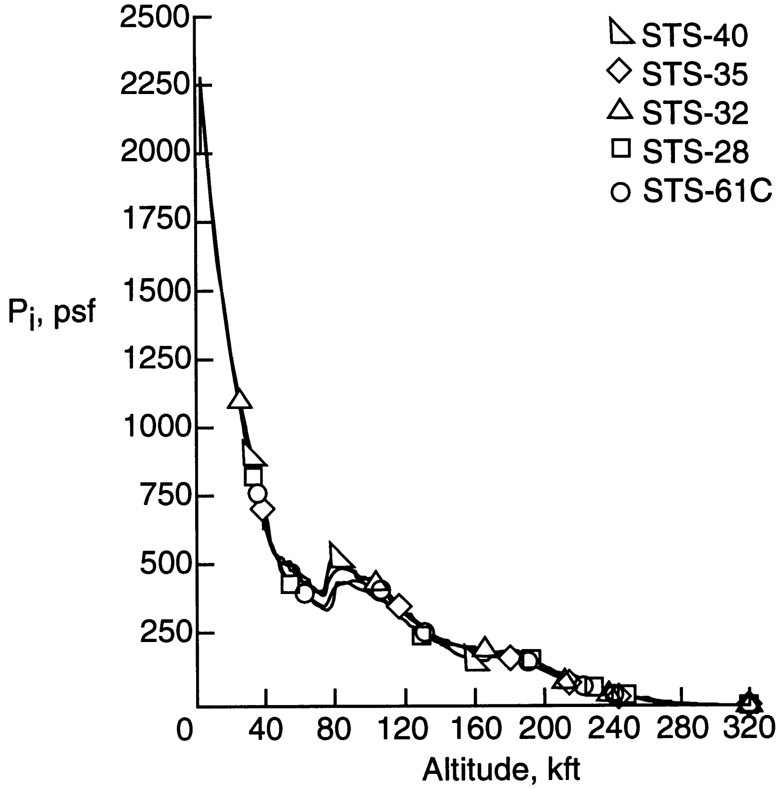

Figure 11. Typical SEADS calibrated pressure time-history port 5.

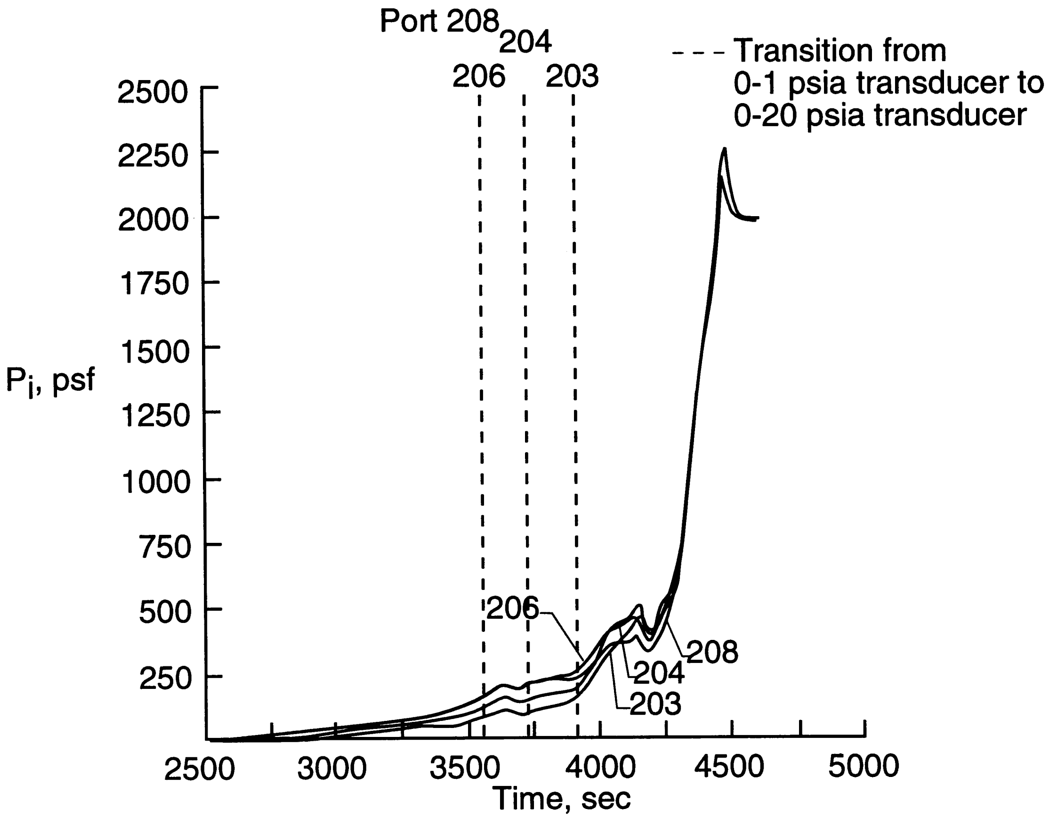

Figure 12. SEADS typical geometric variation of pressure STS-35.

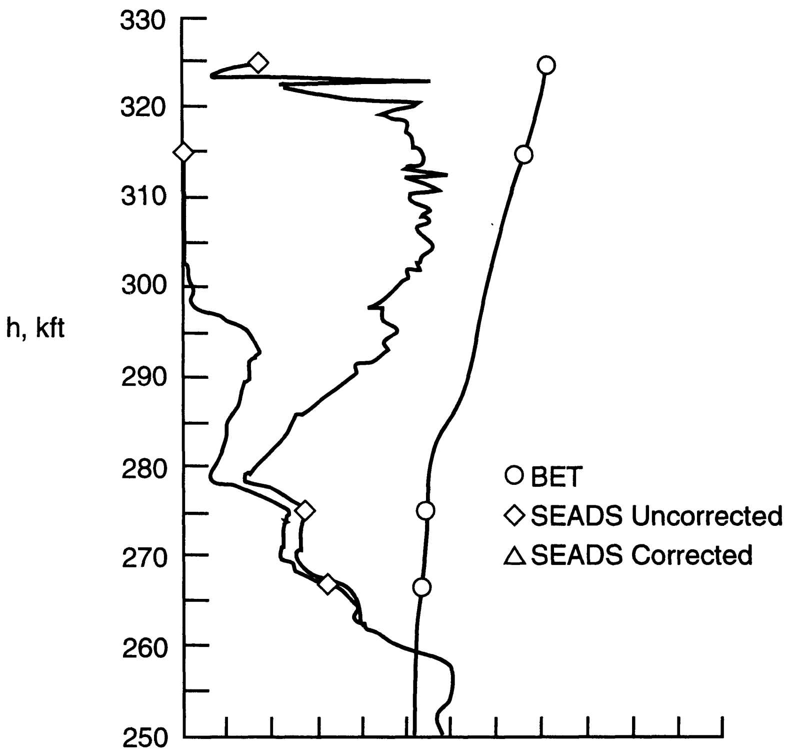

(13a) STS-61C

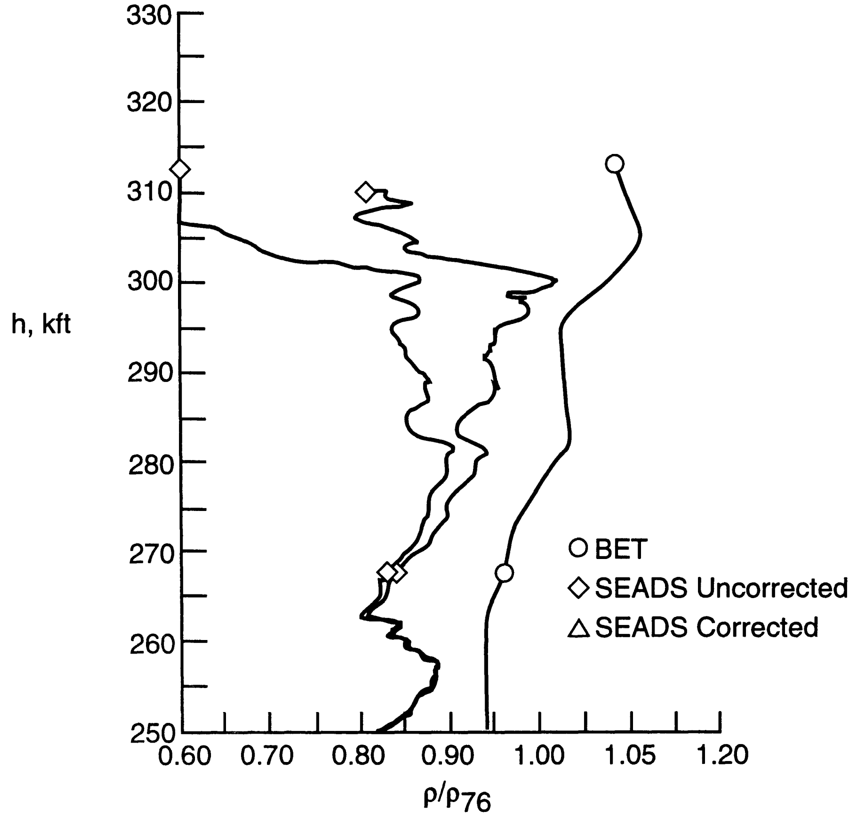

(13b) STS-35

Figure 13. Effect of low density inlet correction on SEADS derived density and comparison with BET.

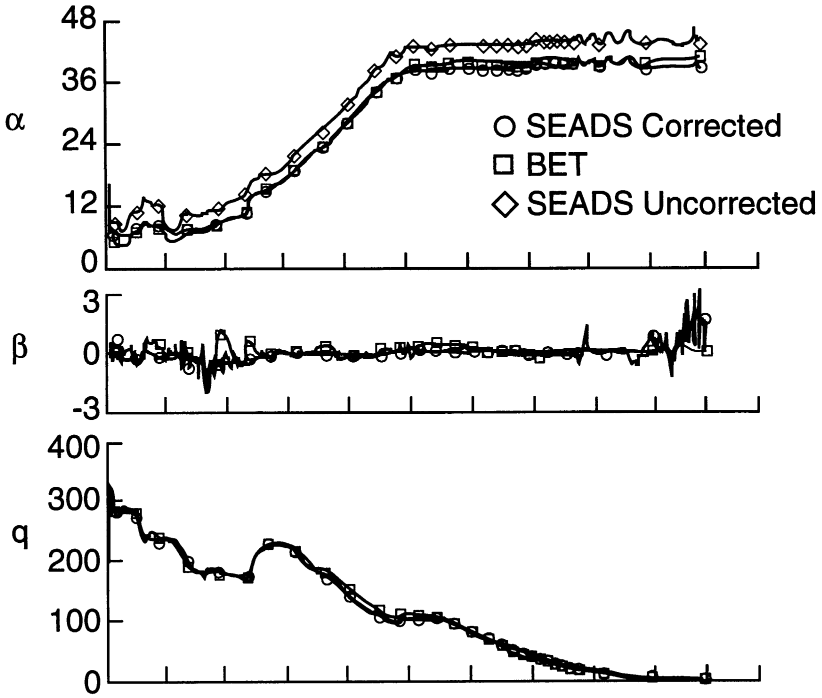

(14a) STS-61C

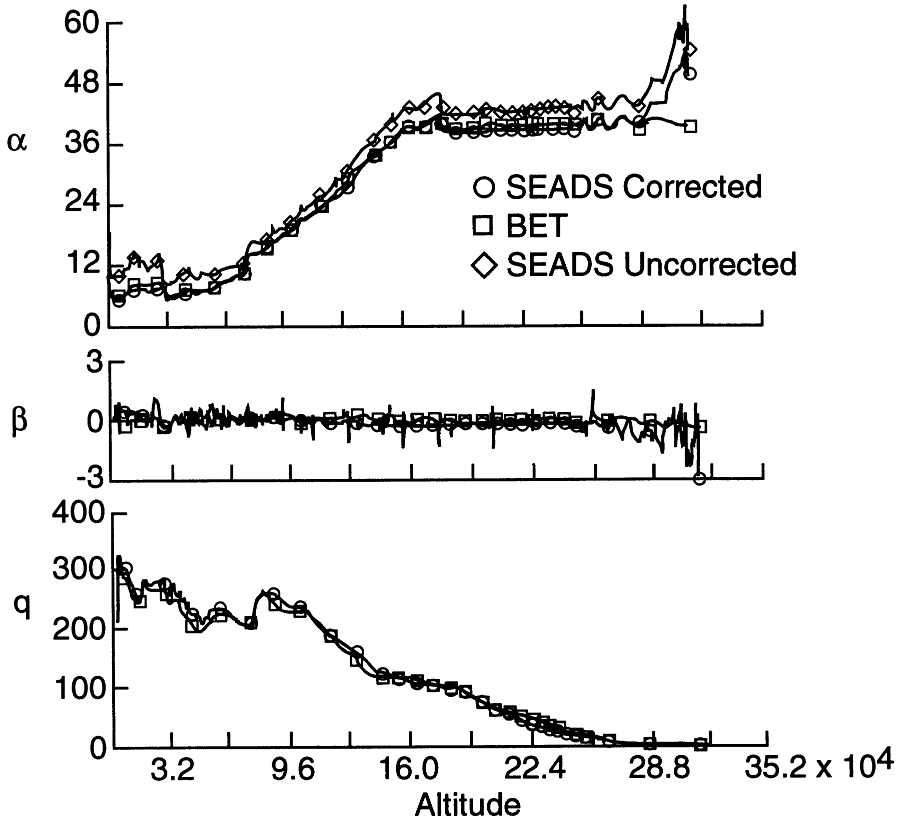

(14b) STS-35

Figure14. SEADS derived air data parameters with comparison to BET values

SHUTTLE UPPER ATMOSPHERE MASS SPECTROMETER (SUMS) EXPERIMENT FLIGHT RESULTS ON STS-35

Robert C. Blanchard

NASA Langley Research Center
Hampton, Virginia 23681-0001

Thomas A. Ozoroski
and
John Y. Nicholson

ViGYAN, Inc.
Hampton, Virginia 23666-1325

Abstract

Calibrated pressure measurements for species with mass to charge ratios up to 50 amu/e^- were obtained from the Shuttle Upper Atmosphere Mass Spectrometer (SUMS) experiment during reentry on the STS-35 mission. Data were collected from 180 km, when the signal rose above the background, to about 87 km, when the SUMS system automatically closed the gas inlet valve. However, data above 115 km were contaminated from a source of gas emanating from pressure transducers connected in parallel to the mass spectrometer. At lower altitudes, the pressure transducer data are compared to the mass spectrometer total pressure with excellent agreement. The free-stream density in the rarefied flow flight regime is calculated using an orifice pressure coefficient model based upon direct simulation Monte Carlo results. This density, when compared with the 1976 U.S. standard atmosphere model, exhibits the wave-like nature seen on previous flights using accelerometry. In addition, selected spectra are presented at higher altitudes (320 km) showing the effects of the ingestion of gases from a forward fuselage fuel dump. An analysis of the spectra data from this event is presented to show that no significant permanent changes occurred which affected the data interpretation at lower altitudes. Further, the localized chemistry from the individual species during the onset of aerodynamic heating is examined to the extent possible for a closed source system, such as SUMS. Near the orifice entrance, a significant amount of CO_2 was generated from chemical reactions with the carbon panels of the Orbiter and adsorbed oxygen on the system tubing.

Nomenclature

amu/e^- =atomic mass unit per unit charge
$(C_p)_e$ =equilibrated pressure coefficient
C1,C2 =inlet system flow restrictors (i.e., leaks)
F_i =mole fraction of species i
I_i =ion current of species i
k_o =sensitivity coefficient constant ; 140.0 for range valve closed or 1.0 for range valve open
P_i =pressure of species i
P_e =equilibrated pressure
P_s =surface pressure
P_t =total pressure due to all species
q_∞ =free-stream dynamic pressure (i.e., $\frac{1}{2}\rho V^2$)
psia =pounds per square inch absolute
S_i =sensitivity coefficient of species i
x,y,z =body axes
V =velocity
V1,V2,V3 =inlet valve, dynamic range valve, and protection valve, respectively
α =angle of attack
β =sideslip angle
ρ =density
τ_i =change in pressure of species i due to chemistry

Acronyms

DSMC =direct simulation Monte Carlo
GSE =ground support equipment
HiRAP =High Resolution Accelerometer Package
OEX =Orbiter Experiments
PCM =pulse code modulator
SEADS =Shuttle Air Data System
SIP =strain isolation pads
STS =Space Transportation System
TPS =thermal protection system
UAMS =Upper Atmosphere Mass Spectrometer

Introduction

The main objective of the Shuttle Upper Atmosphere Mass Spectrometer (SUMS) experiment is to obtain measurements related to free stream density in the hypersonic, rarefied flow regime during the Shuttle atmospheric reentry.

These measurements, when combined with acceleration measurements, allow the determination of Orbiter aerodynamic coefficients in a flow regime previously inaccessible to experimental techniques. This report presents the results of analysis of flight data from the SUMS experiment taken during the Orbiter's reentry on the STS-35 mission. A complete description of the SUMS experiment is given in Ref. 1; however, a brief review is given here for continuity.

Experiment Description

The main elements of the SUMS flight equipment consist of a 0.1 psia pressure transducer, an inlet system, and a flight mass spectrometer. As depicted in Fig. 1, the pressure transducer is in parallel with the inlet system and it provides backup protection to the mass spectrometer in the event of valve closure failures as well as a source of independent pressure data to compare with the mass spectrometer data. It is important to note that two additional pressure transducers from a different experiment were connected to the same orifice for a total of three transducers connected in parallel with the mass spectrometer.

The inlet system includes stainless steel tubing connecting a filter, an inlet valve, large and small calibrated pinched tube leaks in parallel (see C1 and C2 in Fig. 1), and a dynamic range valve. When the dynamic range valve closes, the gas flows exclusively through leak C2 thereby expanding the measurement range. The mass spectrometer is located remotely from the inlet system within a pressure housing which is filled with sulfur hexafluoride at 1.0 atm pressure. A protection valve is placed in the gas line to the mass spectrometer as a backup to an inlet valve failure. The physical arrangement of the SUMS components on the Orbiter is shown schematically in Fig. 2. Inlet tubing penetrates the Orbiter chin panel just aft of the nose cap and connects to the inlet system after passing through the nose wheel-well bulkhead. The inlet system is connected with another tube to the mass spectrometer which is mounted on the nose wheel-well bulkhead as shown in Fig. 2. The actual installation of the SUMS flight equipment on OV-102 is shown in Fig. 3. The view is looking toward the nose while standing inside the wheel-well. The device on the upper right of the bulkhead is the PCM slave which routes the data to the tape recorder for remote recording on the OEX data system during the Shuttle flight.

The SUMS mass spectrometer is a flight spare from the Viking (Mars Mission) Project Upper Atmosphere Mass Spectrometer (UAMS) experiment that has been modified to provide mechanical, electrical, and data compatibility with the Shuttle. SUMS experiment operation during flight is controlled by commands stored in the Shuttle computer and by internal "firmware" logic. The application of power for vacuum maintenance and for normal equipment operation is controlled by stored Shuttle commands while internal operation, such as opening and closing valves, is performed by the SUMS control electronics which depend upon atmospheric conditions as measured by the SUMS pressure transducer and/or mass spectrometer.

The mass spectrometer has a mass range of 1 to 50 amu/e^- in increments of 0.25 amu/e^- and can measure gases hydrogen (H_2) through carbon dioxide (CO_2) at a rate of 1 scan every 5 seconds. One typical 5 second SUMS measurement scan obtained near 90 km altitude during STS-35 is shown in Fig. 4. SUMS is powered on shortly before the initiation of deorbit burn and then samples the inlet gases with the range valve open until an altitude of about 108 km is reached. At that point, the range valve closes leaving only the small leak to transmit gas to the mass spectrometer until about 87 km. Below 87 km, the inlet valve closes, but the mass spectrometer continues to operate until landing to observe the system decay characteristics as it is pumped down. The complete reentry data set on STS-35 consists of approximately 760 scans representing about a 4000 second measurement time interval. The free-stream gas flow relative to the orifice is at an angle of -29^0 when the Orbiter is at the nominal reentry angle-of-attack of 40^0.

SUMS System Calibration

Laboratory Tests

Calibration of the instrument was accomplished in the laboratory using a setup of specially designed ground support equipment (GSE) connected to the flight hardware. Calibration includes introducing a test gas to the GSE and varying pressure statically (i.e., set a pressure and hold) as well as dynamically (i.e., vary pressure with time). The dynamic test setup provides a method to simulate pressure changes expected during flight. Inlet pressures are then measured (using a sensitive Baretron pressure gauge) and compared to the resulting ion peak currents measured by the mass spectrometer itself. The ion current when divided by inlet pressure provides the sensitivity coefficients (amps/torr) of individual gases (e.g., N_2, CO, O_2, and CO_2) connected to the inlet test setup. This procedure allows the partial inlet pressure of each species to be determined from a measured ion current in the mass spectrometer during flight. Currents were also recorded for peaks which resulted from the double ionization or "cracking" of a molecule. Examples of these measurements include the ion current peak measured at 14 from doubly ionized N_2 and the ion current peak measured at 28 and 16 as CO_2 splits into $CO^+$and O^+. Knowledge of the doubly ionized to singly ionized ratios and the cracking patterns allows the determination of the amount that each species contributes to a particular peak. This amount is necessary for calculating the correct composition of the gas as it enters the mass spectrometer. These ratios are specific to the SUMS instrument and the important ones are listed in Table 1.

System Response Function

A change in gas pressure at the inlet is not sensed immediately by the mass spectrometer because a time lag response exists due to the enclosed volumes and tube lengths. During some time interval when the descent rate of the Orbiter is fairly constant, the time lag can also be expressed as an altitude shift. Consideration of the shift is most important when SUMS data must be combined with, or compared to other data. For example, to compare the SUMS ambient density predictions to the 1976 U.S. standard atmosphere, it would be necessary to account for the system response time.

An electrical network analog was developed to predict the sensor lag or response function of the SUMS system. The conductances of the inlet tubing and the UAMS terminator were modeled as resistive elements; the volumes of the system were modeled as capacitive elements, and the time dependent input pressure was modeled as an applied voltage. The coefficients of the solutions to the differential equations describing the electrical network model were obtained from a series of static and dynamic calibration laboratory tests of the flight equipment.[2] A volume which represents the tubing forward of the inlet system was used during the tests. However, this laboratory setup did not physically include the two flight pressure transducers which are connected in parallel to the inlet line. Attempts to apply the electrical analog model results for the system as flown were unsuccessful because air, which was trapped behind the filter of each pressure transducer, slowly leaked into the system. This effect could not be satisfactorily adapted to the pre-flight system response model results due to the lack of knowledge of the characteristics of the phenomena. Therefore, the electrical analog model proved to be of little practical use for post-flight estimates of the time lags. However, pressure transducer flight data did allow an experimental determination of the pressure lag for the range valve closed condition.

Estimate of the System Response

SUMS Time Lag

The SUMS measurement time lag can be determined from the pressure transducer output for the range valve closed condition. The correlation with the pressure measurements requires the calculation of total pressure using the mass spectrometer data. SUMS total pressure can be calculated by summing the individual species measurements as follows:

$$P_t = k_o \sum_i \frac{I_i}{S_i}, \tag{1}$$

where k_o is a constant dependent upon the state of the range valve; I_i is the measured ion current of species i, and S_i is its sensitivity coefficient. Figure 5(a) shows the results of the calculations from the data taken on STS-35 for the range valve closed condition using species N_2, O_2, CO_2, Ar, and NO. Range valve closure occurs at 108 km and the tubing system evacuation process is clearly observed in Fig. 5(a). Included in Fig. 5(a) are the pressure transducer data over the same altitude interval. At these lower altitudes, pressure changes are rapidly transmitted through the tubing, but compositional changes are delayed. It would be expected, therefore, that the pressure transducer measurements are nearly instantaneous and that the lag between the mass spectrometer measurements and pressure transducer measurements represents the total lag of the mass spectrometer system. An apparent 0.2 km lag (1.5 seconds) is seen in Fig. 5(a) at the lower altitudes. Figure 5(b) shows the improved results, particularly below 95 km, after a 0.2 km upward altitude shift is applied to the SUMS data. This shift is based on the measured total pressure referenced to the start of the scan time. The individual ion currents have been interpolated to this common time.

Leak Switch Transient

The comparison between the pressure data and the mass spectrometer data at altitudes beyond the data transmission gap (above 97 km) does not compare well in Fig. 5(b). The main difference is due to the remnants of gas trapped in the tubing after the leak switch. Removing this transient requires an application of the pump-down characteristics of the system.

After the range valve closes, gas remains in the tubing and requires some time before it is pumped from the system. SUMS measures this gas in addition to the fresh gas which is sampled from the atmosphere. As a result, the data obtained after the range valve closes contains a decaying pressure transient as shown in Fig. 6 for the Nitrogen component. This transient pressure drop can be estimated by observing the system pump down characteristics after the inlet valve closes and no more external gas enters the system. By subtracting the percent drop per measurement time interval in the pump down region, the transient can be removed from each of the species and a corrected data set can be obtained. This correction can be applied to the data shown in Fig. 5(b) to obtain an improved measurement, particularly for altitudes above 95 km. When this effect is removed, excellent agreement is noted with the pressure transducer data as shown in Fig. 7.

Free Stream Density Determination

Equilibrated Pressure Coefficient

In flight, the total surface pressure measured at the SUMS inlet tube is higher than the free stream dynamic pressure.[3,4] Inside the tube, the gas pressure quickly drops as it equilibrates to the wall temperature of the inlet tube. To obtain information about the ambient atmospheric conditions from the SUMS instrument, it is necessary to determine the relationship between the free stream pressure and the inlet tube equilibrated pressure which is subsequently measured by the mass spectrometer. The approach involves a model of the flow field and a model of the gas behavior in the tube near the entrance of the inlet orifice.[5] Results from a theoretical model using direct simulation Monte Carlo (DSMC) calculations were developed specifically for the SUMS instrument[6] so that the equilibrated pressure, P_e, could be related to the free stream dynamic pressure, $\frac{1}{2}\rho V^2$, by the equilibrated pressure coefficient, $(C_p)_e$, which is defined as:

$$(C_p)_e = \frac{P_e}{\frac{1}{2}\rho V^2} = \frac{P_e}{q_\infty} \tag{2}$$

The $(C_p)_e$ values used in this analysis are shown as a function of P_e in Fig. 8. Shown on the figure are the data from Ref. 6 along with a curve which is derived from a combination of pressure and accelerometer flight data. The higher altitude $(C_p)_e$ data developed for the SUMS instrument did not extend to the lowest measurement altitudes. For this reason, an experimental pressure coefficient was developed based on pressures measured by the pressure transducers, accelerations measured by the HiRAP accelerometer, and aerodynamic coefficients inferred from previous HiRAP flights.[7] The experimental pressure coefficient is the product of a flow-field coefficient ratio which relates the surface pressure to the free-stream dynamic pressure and an inlet coefficient ratio which relates the equilibrated internal pressure to the surface pressure. That is,

$$(C_p)_e = \frac{P_s}{q_\infty}\frac{P_e}{P_s} \tag{3}$$

As continuum conditions are approached during reentry, the flow-field coefficient ratio decreases while the inlet coefficient ratio rapidly increases. Results of a 7th order curve fit to the flight data are shown for $(C_p)_e$ on Fig. 8. This curve is used for pressures greater than about 10 N/m^2. At lower pressures, a curve fit (not shown) to the Moss and Bird[6] data is used. In this figure the coefficient increases steadily with pressure until reaching a value of about 1.5 where it levels and gradually declines to about 1.41, the modified Newtonian limit. The experimental pressure coefficient extends the DSMC analytic model to higher pressures, but for pressures above 100 N/m^2, the experimental coefficient exceeds the theoretical limit of 1.41 which is calculated using the modified Newtonian approach for continuum hypersonic conditions. An explanation for this result is that when using any common criteria for continuum conditions, such as the ratio of molecular mean-free-path to characteristic length, the inlet coefficient reaches a continuum state before the flow-field coefficient.

A rearrangement of Eq. (2) can be applied to the SUMS equilibrated pressure measurements to allow the calculation of the dynamic pressure and, subsequently, the free stream density. That is, given P_e as measured by the SUMS (or a pressure transducer), and the $(C_p)_e$ model (Fig. 8), the dynamic pressure is simply the ratio of these quantities. With dynamic pressure, the atmospheric density, ρ can be calculated since velocity, V, is known from the trajectory reconstruction process.[8]

Density Results

SUMS data were gathered from orbital altitudes (~346 km) down to approximately 87 km where the inlet valve closed. Fig. 9 shows the altitude profile as flown during a portion of the STS-35 reentry mission. SUMS spectra scans are transmitted continuously from deorbit altitude, but, for this flight, the SUMS signal came out of the background at about 180 km (labeled "Measurable Signal"). The delay in the signal emerging from the background signal was unexpected and later investigations identified the cause to be trapped gas behind the filters of the pressure transducers. The details of the background signal will be discussed later. Thus, during reentry, SUMS data covered an interval of about 18 minutes from approximately 180 km to 87 km. During this time interval, the Orbiter was at an angle-of-attack of about 40^o traveling at a speed of about 7500 m/s. Figure 9 also shows the altitude location of the range valve closure which switches leaks (labeled "Range Valve Closed") and allows measurements deeper into the atmosphere.

The density has been calculated from the mass spectrometer spectra using the method outlined in the previous section, and is shown in Fig. 10. Included in the figure, for comparison, is the density from the 1976 U.S. standard atmosphere model.[9] At altitudes less than 115 km, the SUMS data compare well with the model and show traces of the characteristic wavy density pattern that appear in other separate flight experimentation.[10] At higher altitudes (> 115 km), however, the data obviously are being influenced by the background gas.

System Background

The background levels of the spectra taken at orbital altitudes were extraordinarily high. An extensive investigation of the equipment after the flight revealed that ground composition air was trapped behind the filter within each pressure transducer connected in parallel to the mass spectrometer. Most of the trapped air escaped quickly as the Shuttle attained orbit. However, once in orbit, the pressure dropped, and free molecule flow conditions were reached causing the effective conductivity of the filters to drop to only a fraction of that at higher pressures. Under these conditions, the remaining air leaked continuously into the inlet tubing producing a small background pressure source while on orbit. The pressure was nearly constant at about .08 N/m^2, and the composition (N_2, O_2, Ar, and CO_2) matched sea level air.

Figure 10 shows the effect of the trapped air background source on the density calculations. Above about 120 km, an exponential-like free-stream density decrease is expected, but the density is unreasonably high at a near constant level. Indeed, the density measurements eventually exceed a standard atmosphere by a factor of more than 10. A similar unreasonable density result occurs when the measurements are corrected by simply subtracting a constant background. Only by subtracting a semi-empirical variable background pressure can a reasonable behavior of density variation be obtained. Based on these results, it is concluded that the background pressure during the high altitude measurements varies in a manner which requires further study of the conductances of the pressure filters before a reliable background model can be established. For this reason, the high altitude data are not reliable. Below about 120 km, the external pressure of the gas rises high enough so that the background source is no longer a contributing factor and reliable results can be obtained.

Fuel Dump Analysis

During a period of about 120 seconds, as the Orbiter descended through 320 km, pulses were observed in the SUMS spectra data for some of the species. Upon a closer examination of the HiRAP[6] accelerometer data on STS-35, it was clear that the spectra were affected by the ingestion of gas from the forward fuselage fuel dump of methyl-hydrazine ($CH_3HN_2H_2$). Figure 11(a) shows the Orbiter x body axis accelerometer data taken during reentry. At about 18,300 seconds GMT, the HiRAP sensor detected a large (600 ug) x-axis disturbance which was traced to the forward fuselage fuel dump prior to the entry interface. An examination of the spectra data was made in order to determine if the fuel gas contaminants altered the interpretation of the data at lower altitudes. Figure 11(b) shows the corresponding ion currents measured by SUMS for some selected species during the fuel dump time period. Most noticeable is the large peak at 15 amu/e$^-$ which is assumed to be the methyl radical, CH_3. Both the methyl-hydrazine at 46 amu/e$^-$ and HN_2H_2 (i.e., a free radical resulting from CH_3 splitting from methyl-hydrazine) at 31 amu/e$^-$ show no appreciable increases and are not shown in Fig. 11(b). Similarly, both the water at 18 amu/e$^-$ and the OH at 17 amu/e$^-$ show no peak.

The remaining species (N_2,O_2,CO_2, Ar, and O) all show increases in varying amounts. Nitrogen (28 amu/e$^-$) shows a peak which could possibly be due to a decomposition product of methyl-hydrazine, or could be swept from the system walls. Ion peaks appear at both 32 and 16, but the 16 peak, relative to its pre-dump background readings, is much larger than the 32 peak compared to its background. If we examine the ratio I_{16}/I_{32} , shown on Fig. 12(a), then this difference becomes evident. Since the ratio persists at a level larger than the pre-dump background and seems to decay toward it, this result suggests that CH_4 has been generated and is adhering to the walls. Below about 180 km, the ratio decreases abruptly as the O_2 concentration increases.

The 16 ion peak can be predicted using the ionization and cracking ratios in Table 1, assuming that the 16 ion peak was produced totally from O_2 (32) and CO_2 (44). When I_{16} observed is divided by I_{16} predicted using this assumption, a huge peak appears at the time of the dump as seen in Fig. 12(b). The fact that this ratio is much larger than unity demonstrates that the 16 peak is not coming solely from O_2 and CO_2.

Figure 13 shows the ratio of I_{14} measured to I_{14} predicted, assuming I_{14} predicted comes from doubly ionized N_2 and from doubly ionized CO, which comes from CO_2. The ratio is near unity throughout except for a small drop at the time of the fuel dump, as can be seen in Fig. 13. This suggests that CO rises in the system slightly after the fuel dump over that produced from CO_2 fractionation, but is pumped from the system readily.

Based upon the preceding analysis, the spectra after the fuel dump showed no significant permanent changes occurred due to the ingestion of the fuel gas into the system.

Chemistry Considerations

It is well known[11] that high temperature flow phenomena at lower altitudes cause chemical reactions which change the local undisturbed atmospheric composition. Thus, it is expected that the composition measured by SUMS differs from the composition near the orifice entrance, and is different from the ambient atmosphere. It is possible to gain some insights into the behavior of the gas composition near the Orbiter surface at the onset of aerodynamic heating. Mass spectrometer species data provide more information than a simple pressure transducer, but the information is not complete since the behavior of atomic oxygen (and other highly reactive species) is totally masked by a closed source system, such as SUMS.

The mole fraction, F_i, for species i in a gas mixture containing n species can be calculated using the equation,

$$F_i = \sum_j \frac{P_i}{Pj} , \qquad j=1, 2,\cdots n \tag{4}$$

where Pi is the partial pressure of species i and the P_j's are the partial pressures of the n gases measured by the mass spectrometer. The mole fractions for CO_2, O_2, and N_2 are shown as a function of altitude in Figure 14(a). Together with Ar, which remains constant at approximately 1 percent, the partial pressures of these species combine to account for almost all of the pressure measured by the mass spectrometer on STS-35. For reference, Fig. 14(b) is a graph of the mole fractions of the ambient atmosphere based upon the 1976 U.S. standard atmosphere model.[9] For these calculations, atomic oxygen is combined with O_2 to represent the total number of oxygen molecules available to the mass spectrometer before flow-field chemistry. That is, all of the atomic oxygen which does not react with other elements, or is not adsorbed by the walls, combines to form O_2 before it is measured by the mass spectrometer. As seen in Fig. 14(a), the mole fractions remain fairly constant to about 100 km, similar to expectations without flow-field chemistry. It is not until below about 100 km that the mole fractions begin to change. At that altitude, both the O_2 and N_2 mole fractions begin to decrease as the mole fraction of CO_2 begins to increase. Since CO_2 concentration rapidly increases, chemistry caused by aerodynamic heating has begun.[12] There are at least two sources of carbon; one is the carbon in the steel tubing, and the other is the Orbiter's surface chin panel and nose cap which are made of coated carbon-carbon materials. The exact method for the production of CO_2 is not known, but a possible mechanism is that the heated carbon-carbon chin panels near the Orbiter's nose region interact with oxygen to produce a mixture of C, CO, and CO_2. This mixture then reacts with atomic oxygen adsorbed to the walls of the inlet tubing, and produces almost exclusively CO_2 before being measured by the mass spectrometer.

The change in partial pressure of species i, τ_i, due to chemistry sources or sinks can be estimated using the above equation by letting

$$P'_i = P_i + \tau_i \ , \qquad (5)$$

where P_i is the partial pressure of species i if there were no aerodynamic heating and P'_i is the altered partial pressure of species i due to aerodynamic heating (P'_i is measured by the mass spectrometer). The values of τ_i can be solved by combining Eq. (5) with Eq. (4) and considering the mole fractions prior to aerodynamic heating as constants, i.e., similar to Fig. 14(b). Assuming that N_2 undergoes no chemical changes due to heating results in 4 independent equations and 4 unknowns for a gas consisting of CO_2, O_2, and N_2. The 4 unknowns are the pressures P_{CO_2} and P_{O_2} (both without chemistry changes), and the pressure changes τ_{CO_2} , and τ_{O_2} at any altitude. The results from the solution of these equations , as a function of altitude, are shown in Fig. 15. The results, expressed as a percentage, show that the production of CO_2 is significant; over 20 percent of the gas measured at lower altitudes is CO_2. Concurrently, at this altitude, oxygen is being depleted by about 7 percent of the total gas sampled, which represents nearly half of the oxygen measured.

It is worth reiterating that the actual chemical composition at the orifice entrance is probably different due to the presence of atomic oxygen. At altitudes near 100 km, the standard atmosphere model predicts an ambient composition containing about 10 percent atomic oxygen, O. Any molecular oxygen, O_2, dissociation in the shock/boundary layer would produce additional atomic oxygen, but as expected, atomic oxygen was not measured at any altitude during the SUMS experiment. This result suggests that O readily combined with carbon and other molecules before it was measured.

Conclusions

The SUMS experiment has provided partial pressure measurements in the altitude range from 180 km to 87 km during STS-35 reentry. However, above about 115 km altitude, the measurements are contaminated with sea level composition air. The source of this contamination was identified as a slow release of gas trapped behind pressure transducer filters which were connected in parallel to the mass spectrometer. Below about 115 km, as the Orbiter surface pressure rises to values much larger than the trapped gas source, the sum of the SUMS partial pressure measurements correlates well with available local pressure transducer measurements. The free-stream density in the rarefied-flow regime has also been calculated from the SUMS measurements. The procedure involved using an analytical/empirical model for the pressure coefficient at the SUMS orifice. The SUMS density measurements corroborate earlier accelerometer measurements which indicate that large scale density waves exist in the upper atmosphere relative to standard atmosphere models. At 320 km, the SUMS registered the effects of the gas resulting from the Orbiter forward fuselage fuel dump. Examination of the spectra in this altitude region showed a large 15 ion current peak transient, probably CH_3, along with other species, but no significant permanent changes occurred due to the ingestion of the fuel gas into the system. The initial effects on gas composition due to aerodynamic heating were observed beginning at about 100 km. The production of CO_2 and the corresponding depletion of O_2 are clearly seen as the reactive gases from the flowfield, near the surface, react with the abundant carbon from the carbon-carbon nose and chin panels and subsequently with some of the atomic oxygen adhering to the tubing walls. It is estimated that at the lowest measurement altitude of SUMS (87 km), about 20% of the total pressure comes from CO_2.

Acknowledgments

The authors wish to express their appreciation to Ed Hinson of STX Corp. and Roy Duckett of NASA Langley Research Center without whose participation this experiment would not have materialized. Ed Hinson, now retired, developed the codes and generated solutions for the original SUMS system response function. He was responsible for the development of all of the initial data reduction processes at Langley Research Center. Roy Duckett, now retired, performed the many laboratory tests on the flight equipment, participated in the installation and removal of the flight equipment from the Orbiter, performed the post-flight instrument functional analysis immediately after the flights and assisted with the data interpretation.

References

[1]Blanchard, R. C., Duckett, R. J., and Hinson, E. W.: The Shuttle Upper Atmosphere Mass Spectrometer Experiment. Journal of Spacecraft and Rockets, vol. 21, no. 2, March-April 1984, pp. 202-208.

[2]Wright, W., "Support Activities to Maintain SUMS Flight Readiness," Volumes 1-9, University of Texas at Dallas, CR-189656, June 1992.

[3]Bird, G. A., "Low Density Aerothermodynamics," AIAA Paper No. 85-0994, June 1985.

[4]Bird, G. A., Molecular Gas Dynamics, Clarendon Press, Oxford, 1976.

[5]Bienkowski, G. K., "Inference of Free Stream Properties from Shuttle Upper Atmosphere Mass Spectrometer (SUMS) Experiment," Rarefied Gas Dynamics, Vol. 1, Proceedings of the 14th International Symposium, edited by Hakuro Oguchi, 1984, pp. 295-302.

[6]Moss, J. N. and Bird, G. A., "Monte Carlo Simulations in Support of the Shuttle Upper Atmospheric Mass Spectrometer Experiment," Journal of Thermophysics and Heat Transfer, vol. 2, no. 2, April 1988, pp. 138-144.

[7]Blanchard, R. C., Larman, K. T., Barrett, M., "The High Resolution Accelerometer Package (HiRAP) Flight Experiment Summary for the First 10 Flights," NASA RP-1267, April, 1992.

[8]Oakes, K. F., Findlay, J. T., Jasinski, R. A., and Wood, J. S., "Final STS-35 'Columbia' Descent BET Products and Results for LaRC OEX Investigations," NASA CR-189569, Nov. 1991.

[9] U.S. Standard Atmosphere, 1976, NOAA, NASA, USAF, Oct. 1976.

[10]Blanchard, R. C., Hinson, E. W., and Nicholson, J. Y., "Shuttle High Resolution Acceleration Package Experiment Results: Atmospheric Density Measurements Between 60-160 km," Journal of Spacecraft and Rockets, Vol. 26, No. 3, May-June 1989, pp. 173-180.

[11]Cuda, V. Jr., Moss, J. N., "Direct Simulation of Hypersonic Flows Over Blunt Slender Bodies," AIAA Paper No. 86-1348, June 1986.

[12]Hartung, L.C., and Throckmorton, D. A.: "Space Shuttle Entry Heating Data Book, Volume 1-STS-2, Parts 1 and 2," NASA RP-1191, May 1988.

Table 1. SUMS Ionization and Cracking Ratios for CO, N_2, O_2, Ar, and CO_2

GAS	MASS (amu)	ION CURRENT RATIOS	
Carbon monoxide, CO	28	I_{12}/I_{28}	.024
		I_{14}/I_{28}	.012
		I_{16}/I_{28}	.0056
Nitrogen, N_2	28	I_{14}/I_{28}	.068
Oxygen, O_2	32	I_{16}/I_{32}	.075
Argon, Ar	40	I_{20}/I_{40}	.27
Carbon Dioxide, CO_2	44	I_{14}/I_{44}	.0007
		I_{16}/I_{44}	.12
		I_{22}/I_{44}	.033
		I_{28}/I_{44}	.06

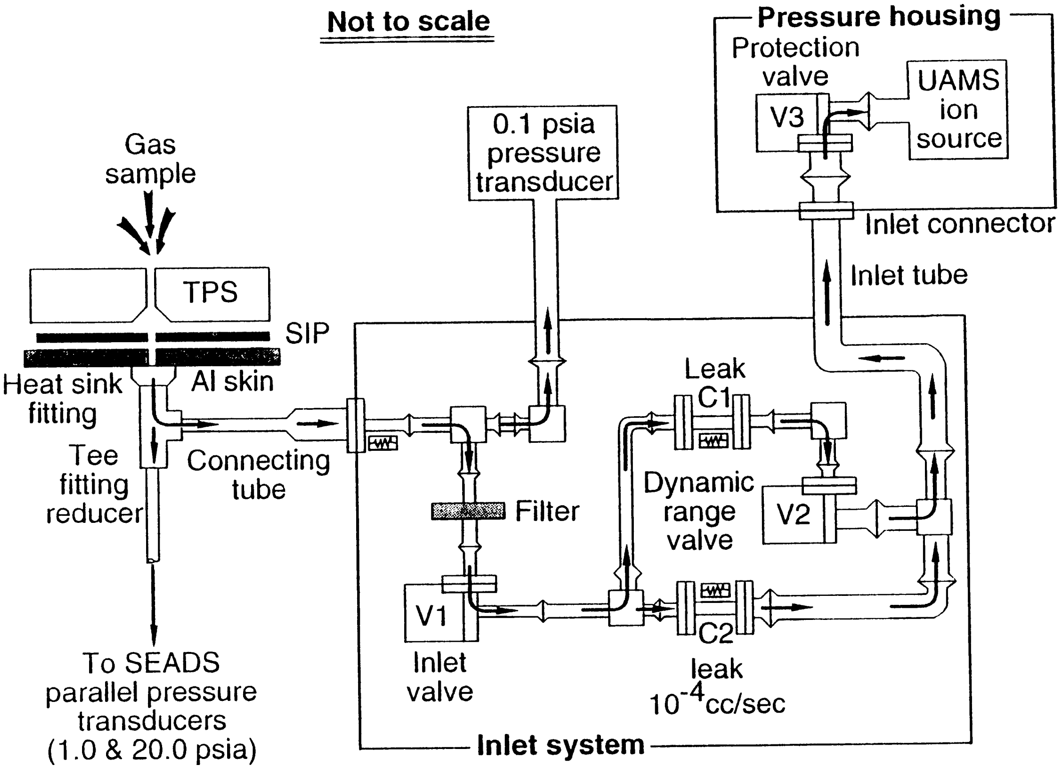

Fig. 1 SUMS system planar flow diagram.

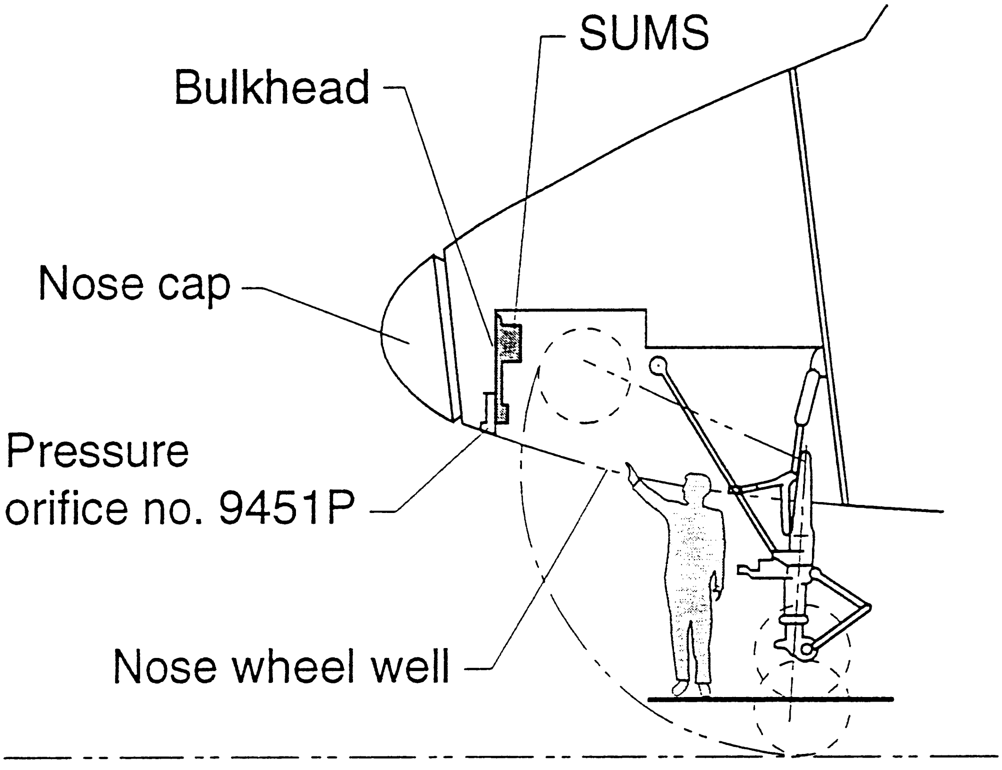

Fig. 2. SUMS instrument location in the Shuttle nose wheel well.

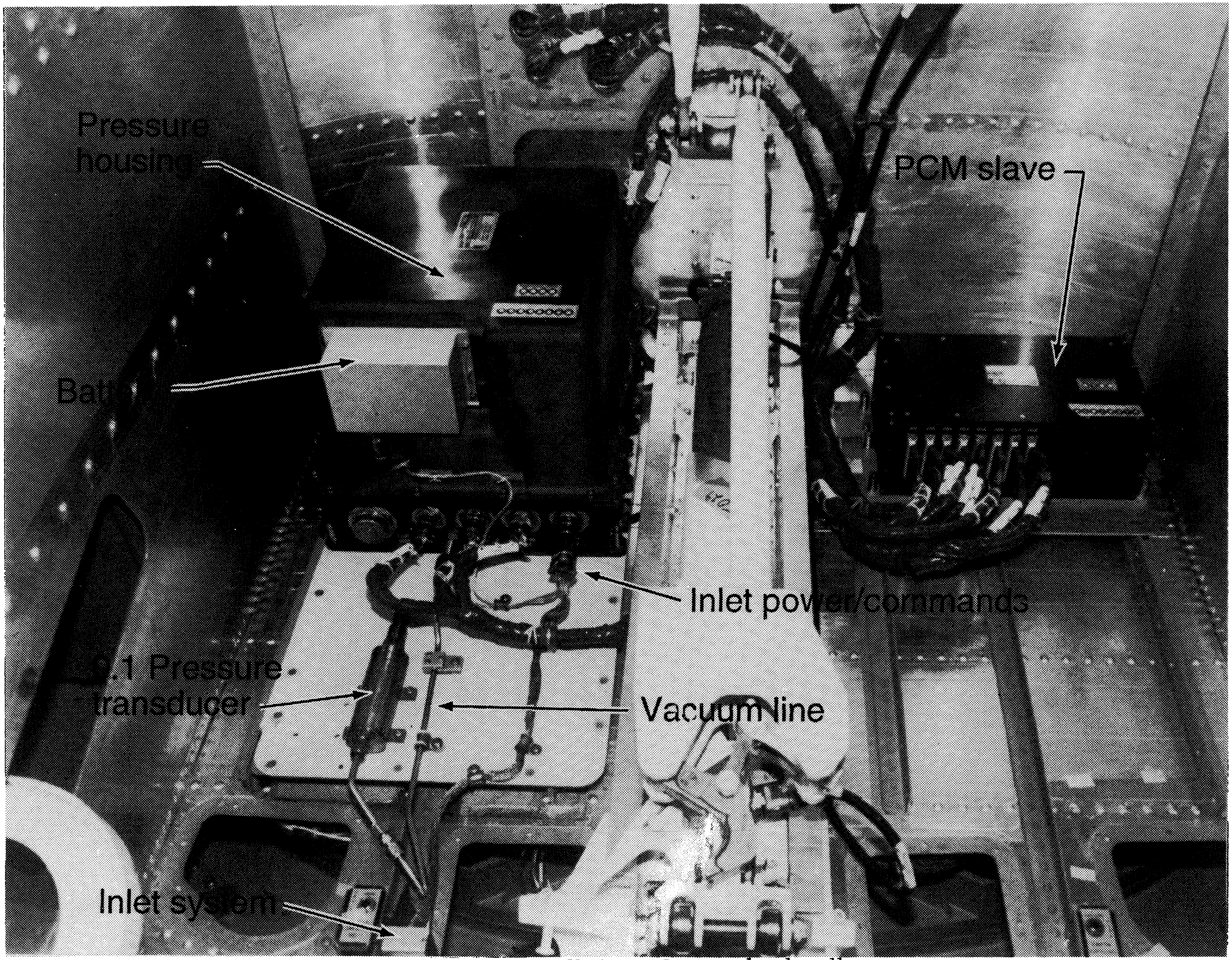

Fig. 3 SUMS installed in STS-35 wheel well.

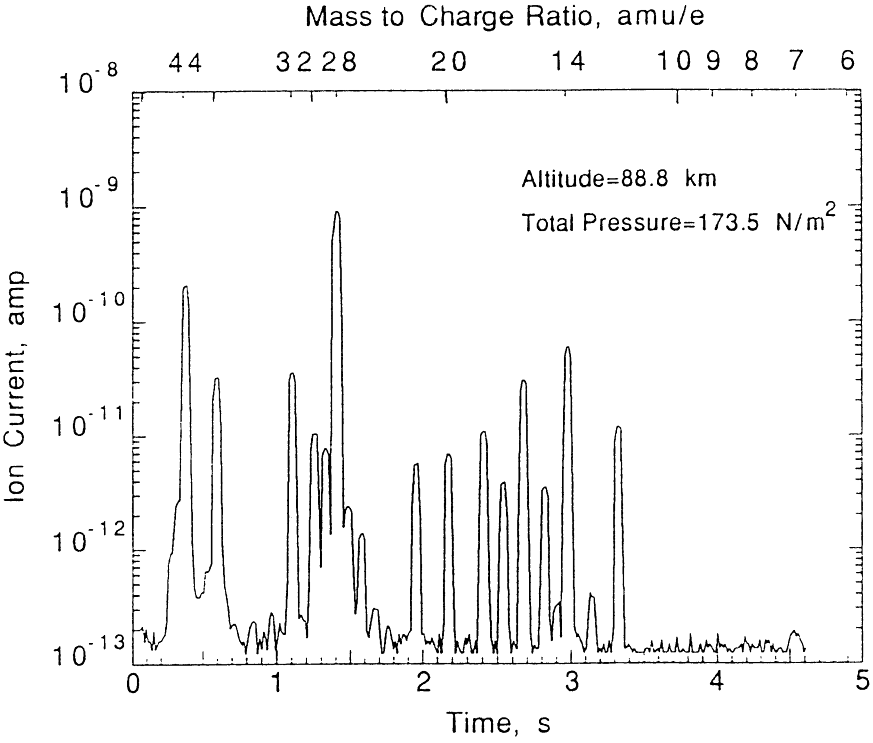

Fig. 4. Typical SUMS spectra taken on STS-35.

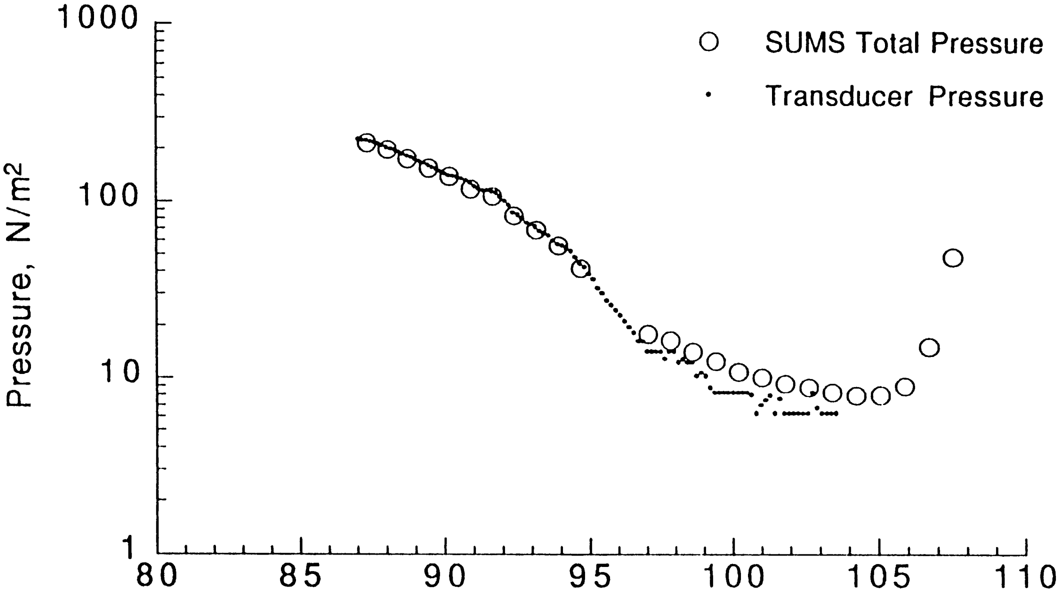

(a) no corrections

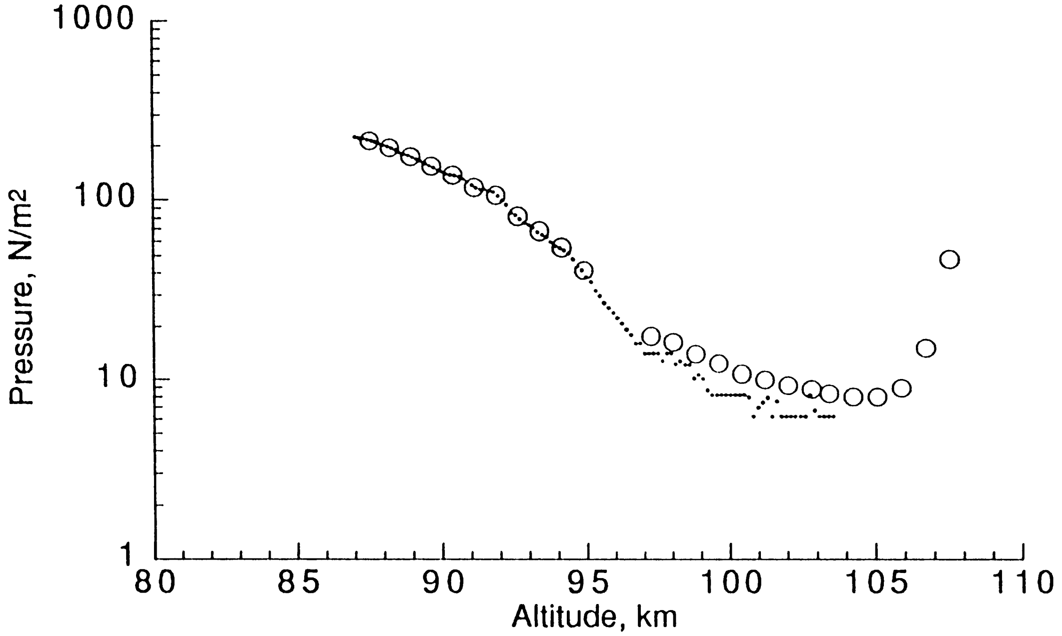

(b) corrected for time lag

Fig. 5. SUMS total pressure and transducer measurements

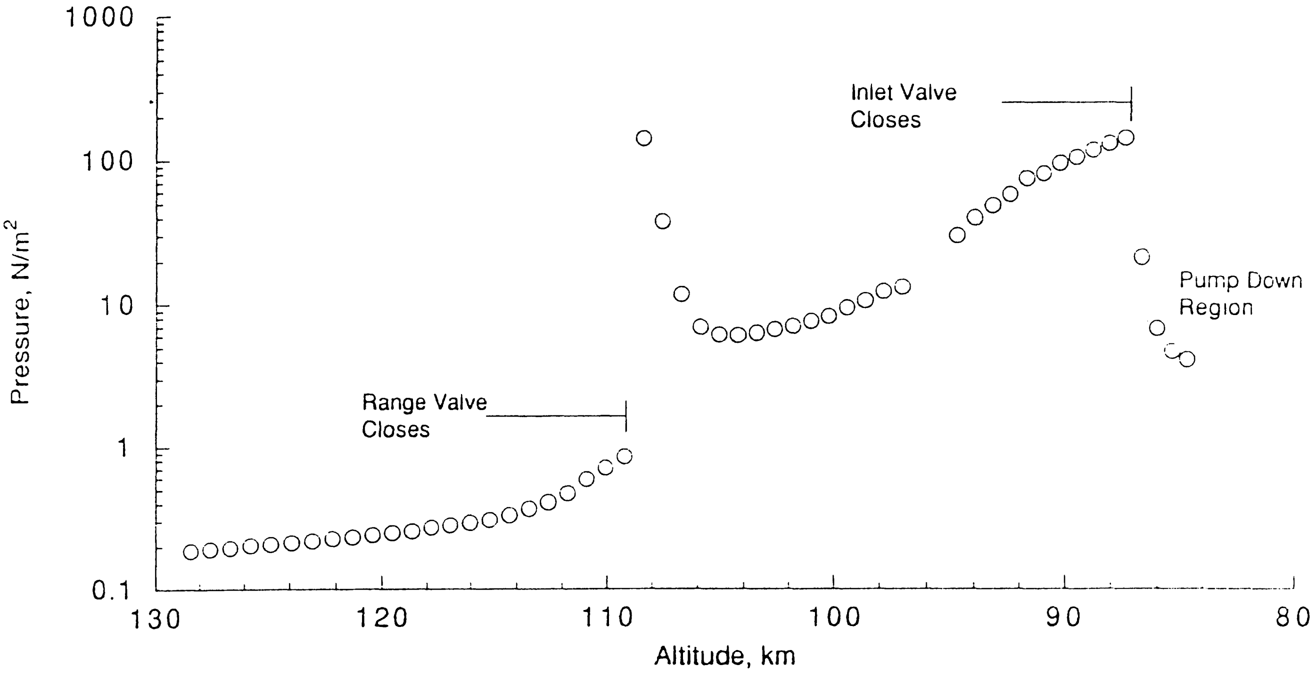

Fig. 6. SUMS Nitrogen pressure measurements

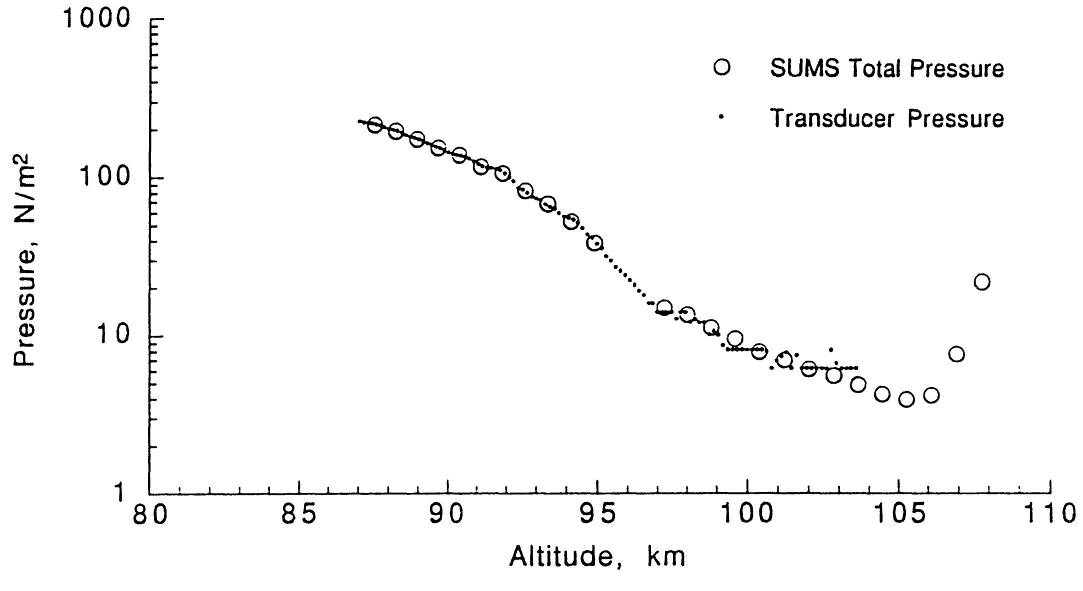

Fig. 7. Comparison of transducer data with SUMS total pressure measurements corrected for valve closure transient and time lag.

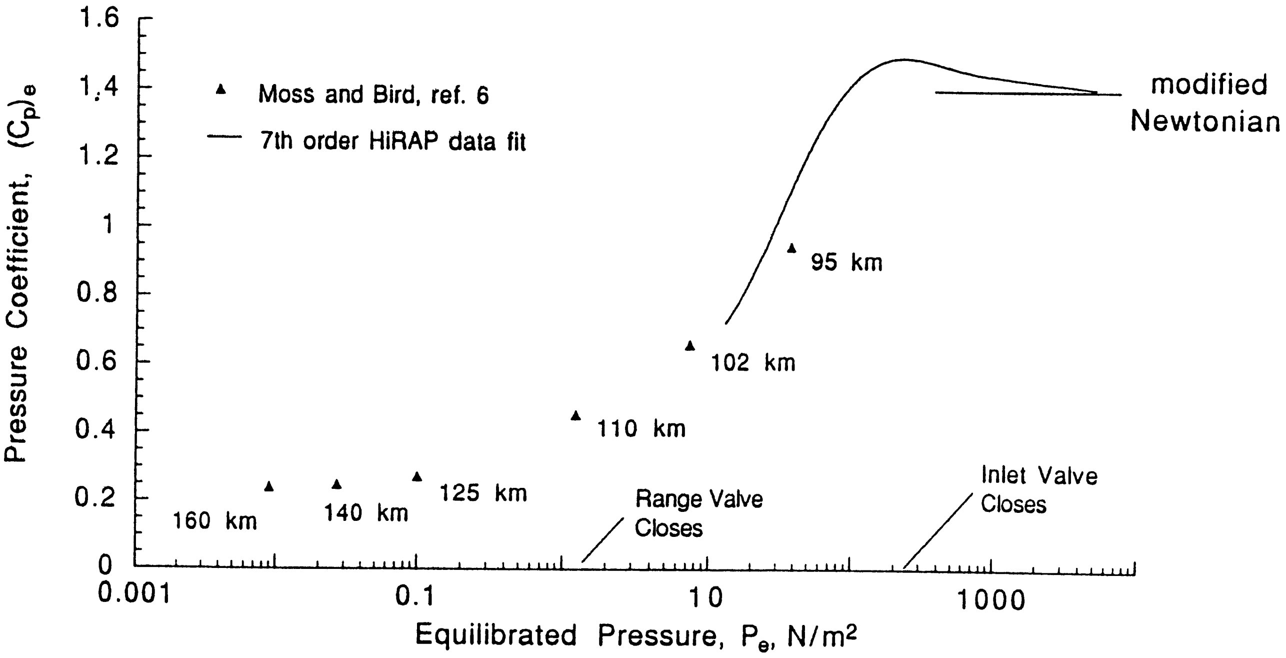

Fig. 8. SUMS orifice pressure coefficient as a function of equilibrated pressure.

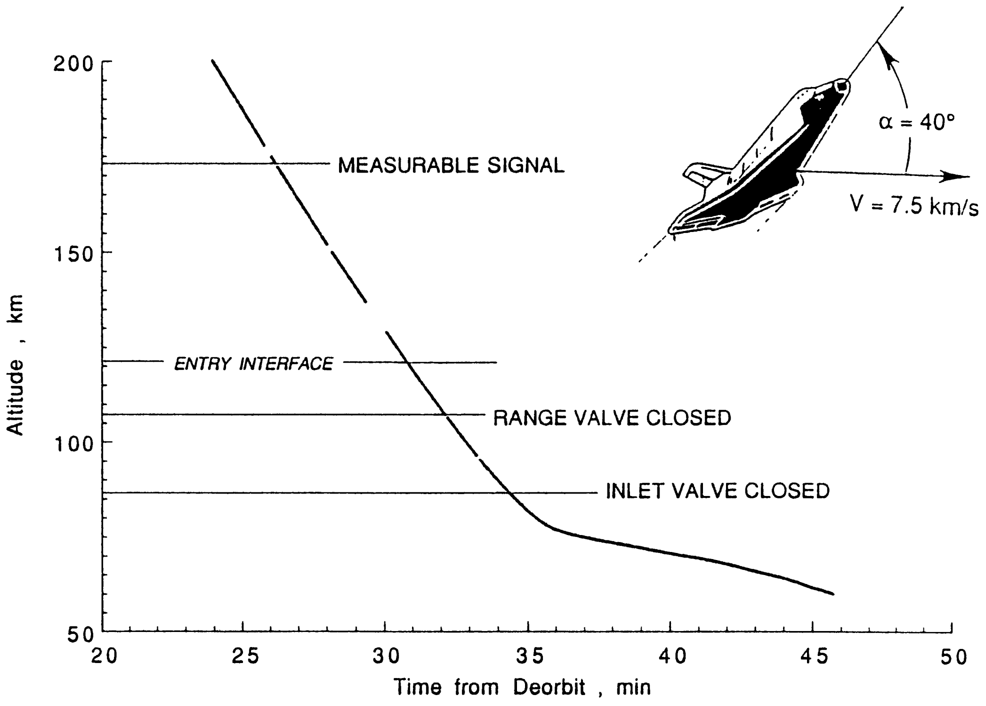

Fig. 9. SUMS altitude measurement domain during STS-35 reentry.

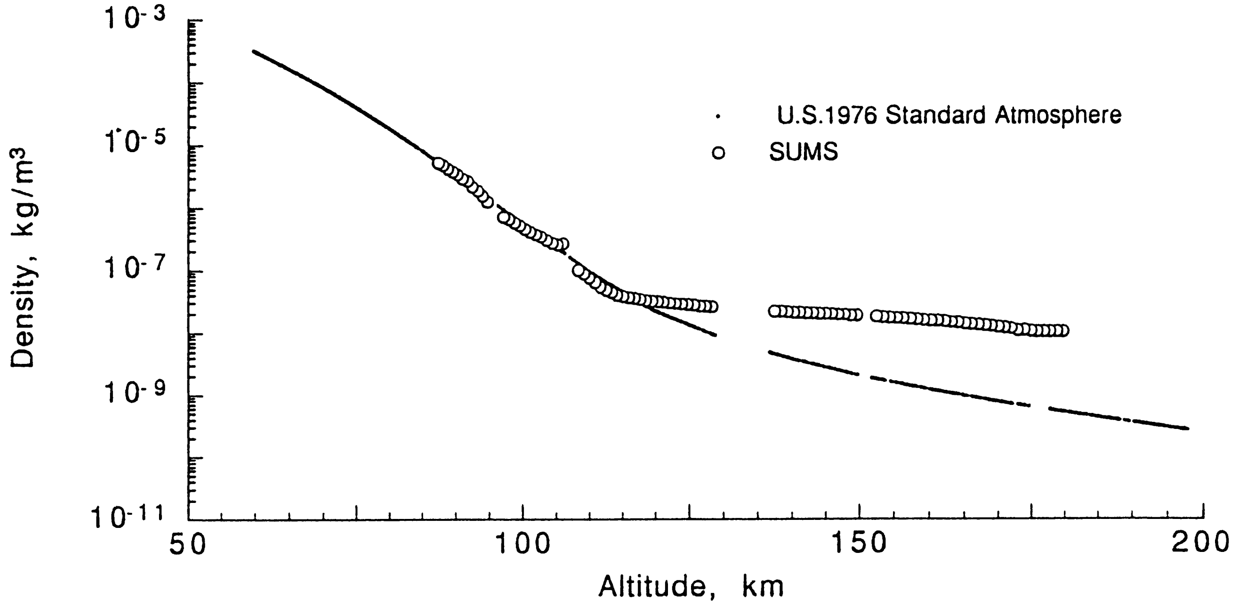

Fig. 10. Comparison of the SUMS measured atmospheric density to the U.S. 1976 Standard atmosphere model.

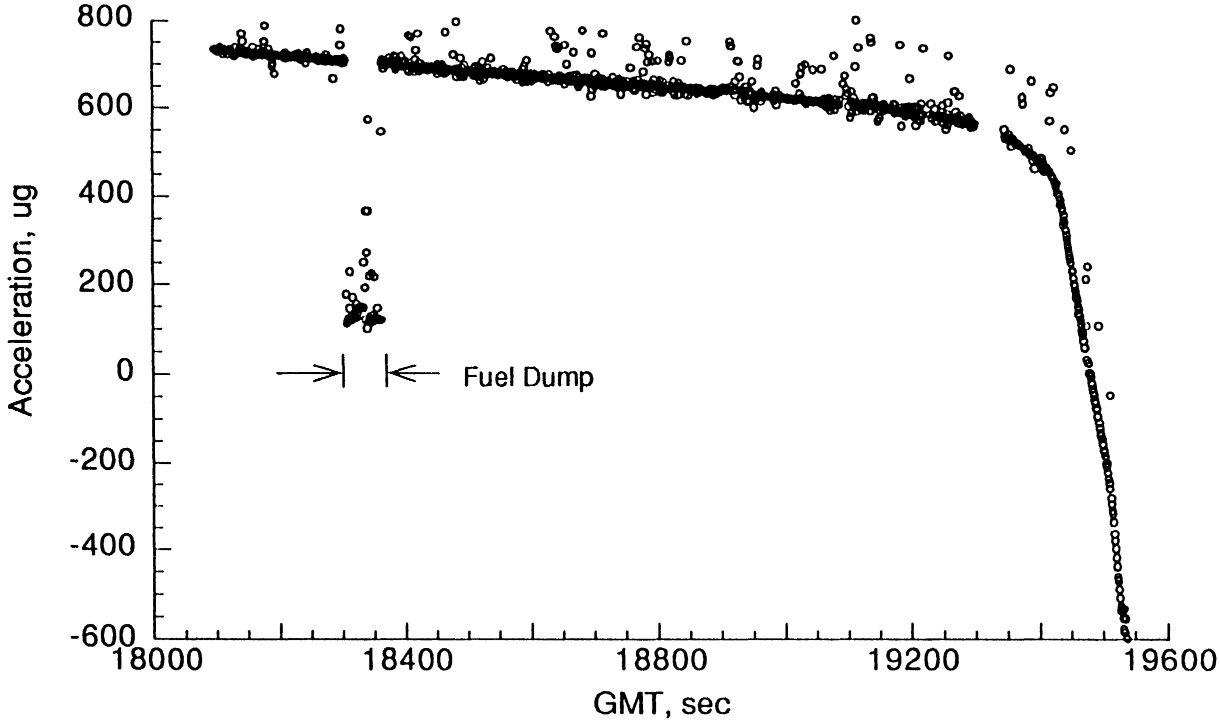

(a) HiRAP x-axis accelerometer data

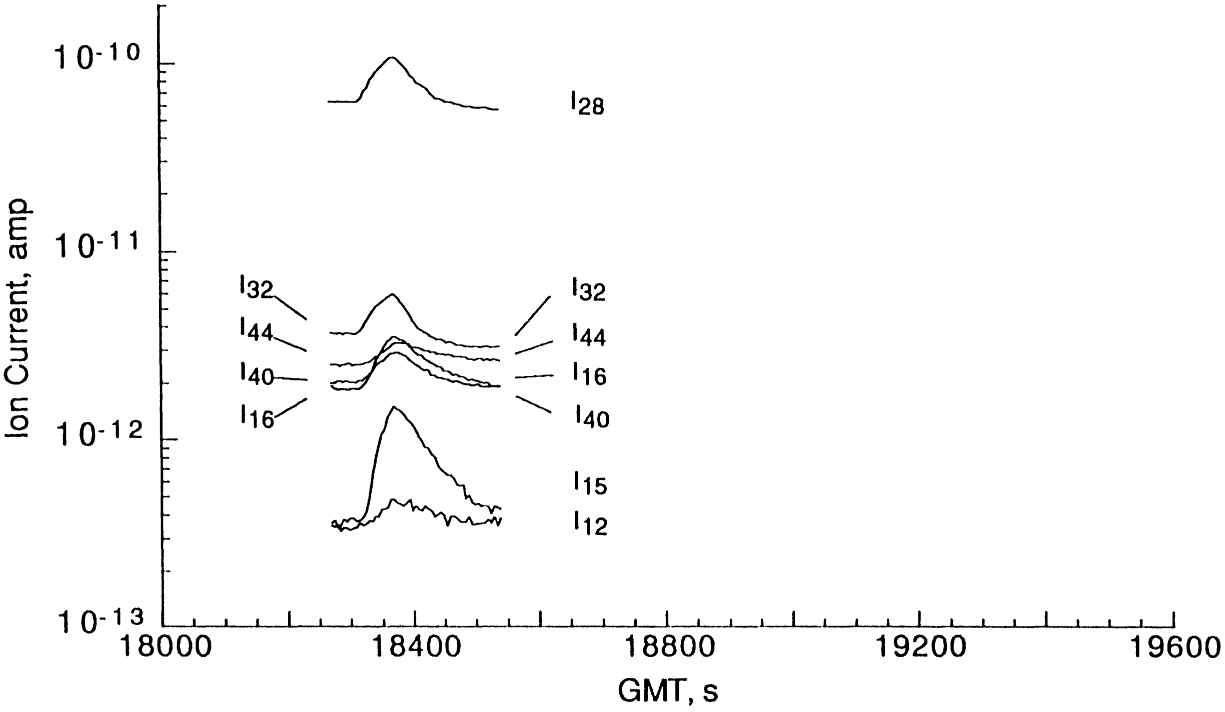

(b) SUMS ion current data

Fig. 11. Comparison of fuel dump induced spectra data.

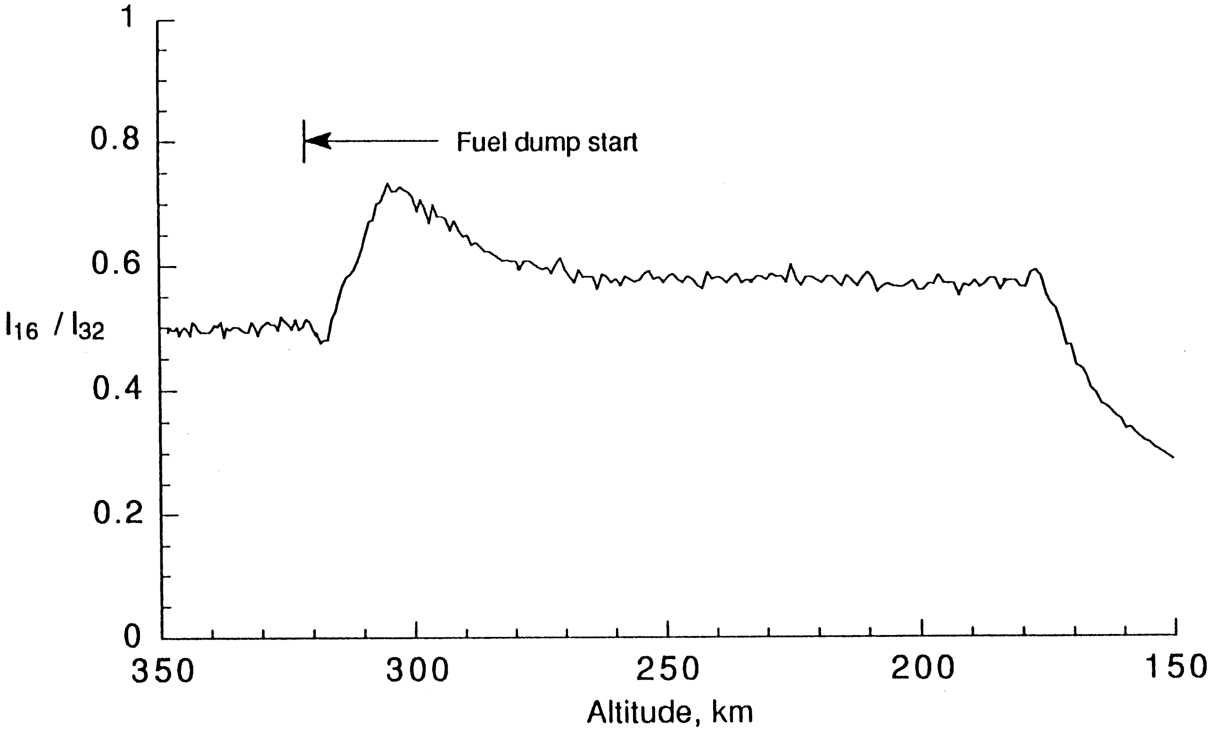

(a) Ratio of measured 16 to 32 ion current

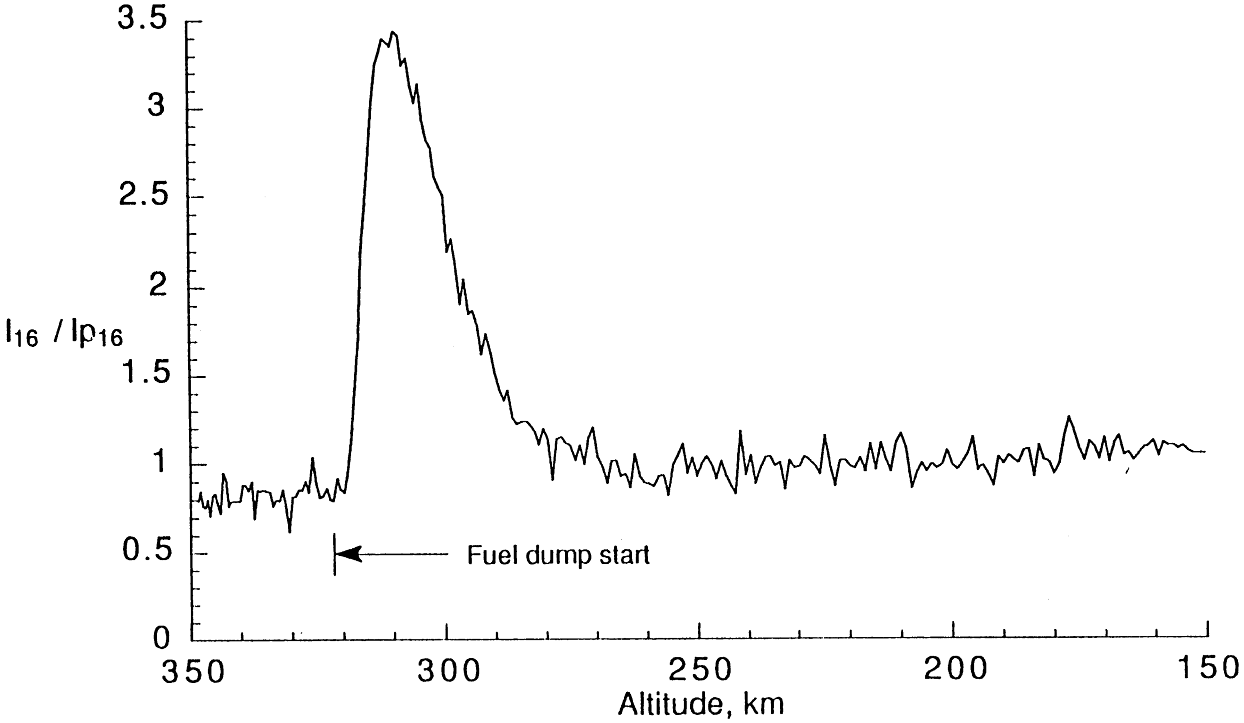

(b) Ratio of measured to predicted 16 ion current

Fig. 12. Ratios of ion currents of peak 16.

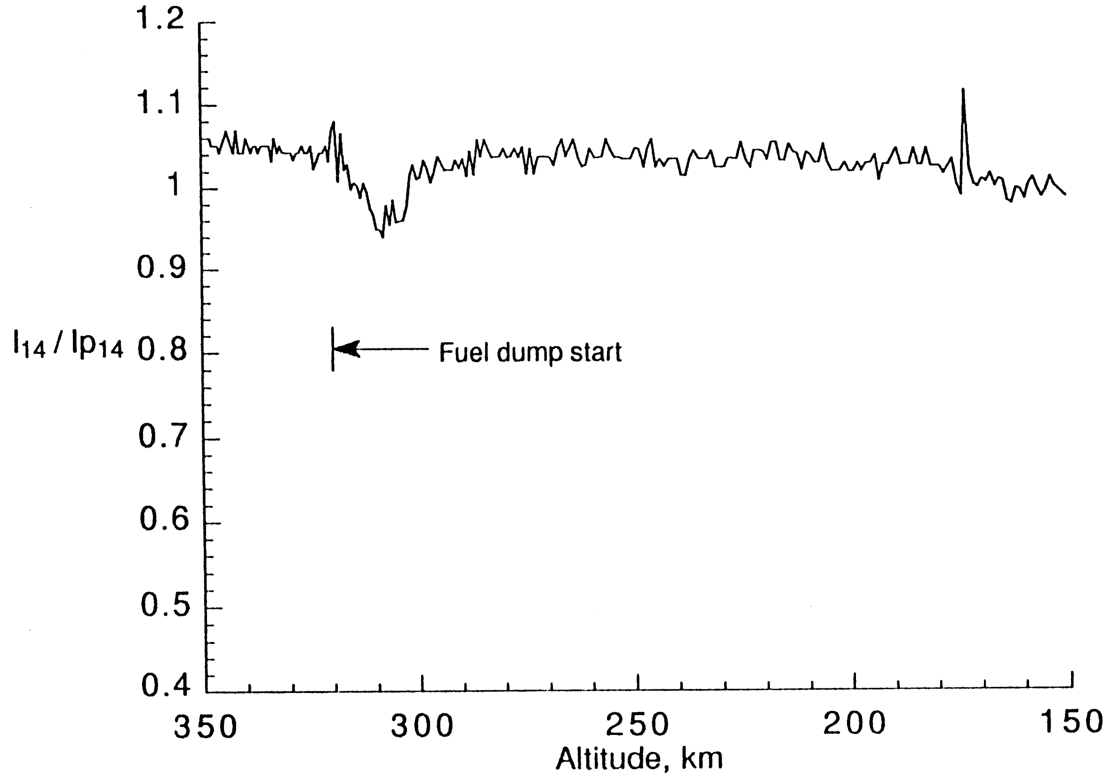

Fig. 13. Ratio of the measured to the predicted 14 peak ion current.

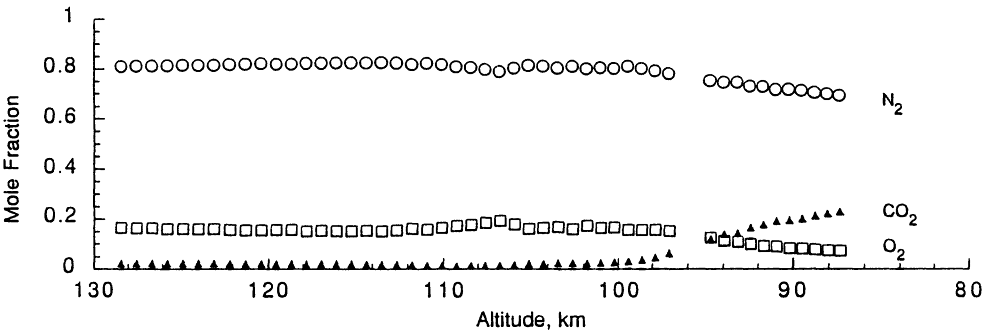

(a) SUMS measurements

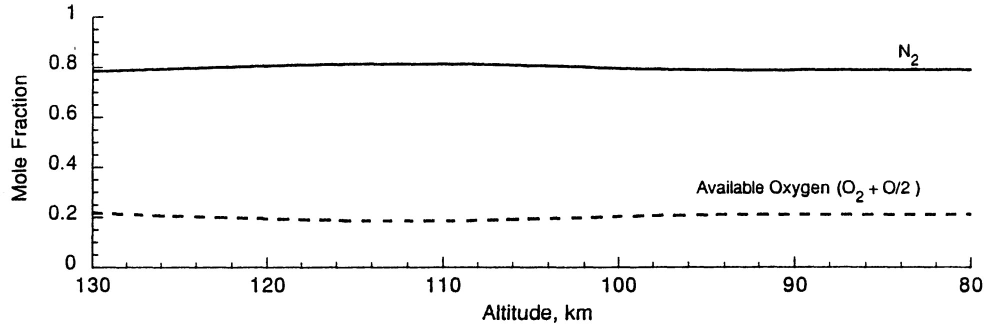

(b) 1976 U.S. standard atmosphere model (free-stream)

Fig. 14. Comparison of the SUMS measurements to the 1976 U.S. standard atmosphere model.

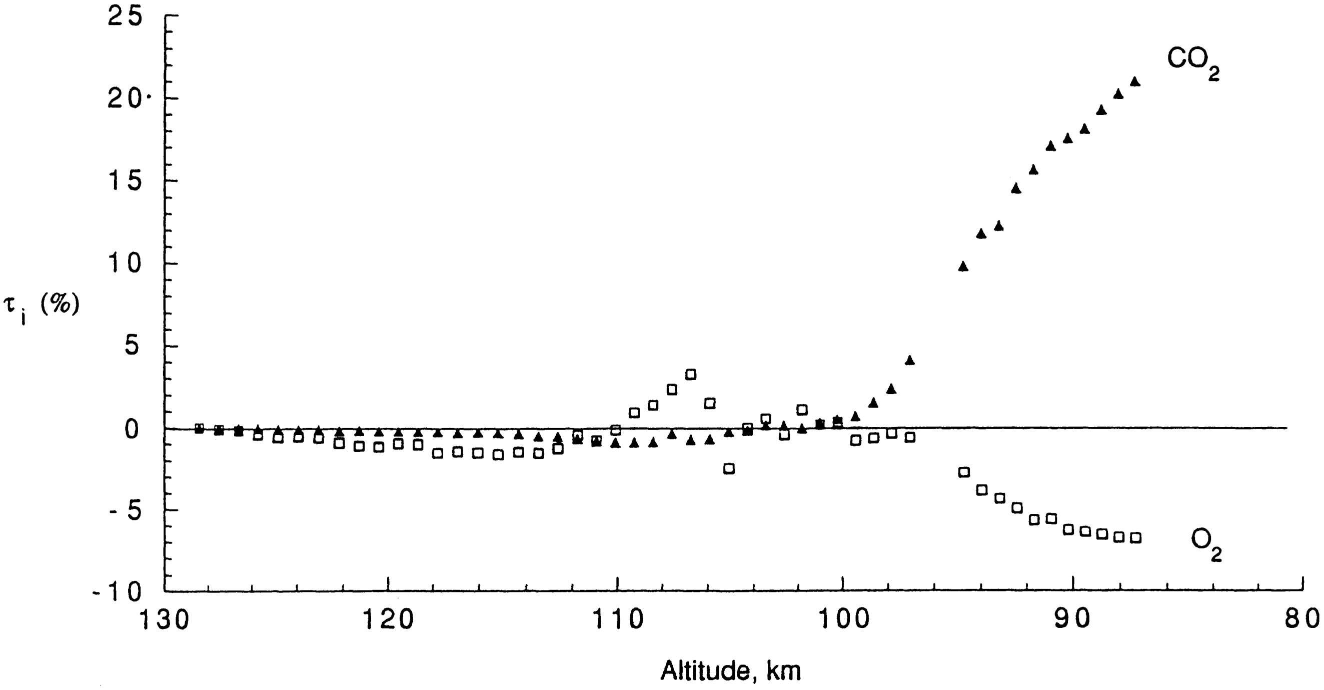

Fig. 15. Change in pressure due to chemistry associated with initial aerodynamic heating during STS-35 reentry.

AERODYNAMIC COEFFICIENT IDENTIFICATION PACKAGE (ACIP)

Robert L. Giesecke and Paul O. Romere
NASA Johnson Space Center
Houston, TX

A written version of this paper was not provided by the authors.

Copies of presentation materials used at the Symposium are presented herein.

Overview

- Objectives
- Implementation
- Description
- Sensor Ranges and Resolution
- System Integration
- Flight History
- Future Usage

Experiment Objectives

- Acquire Space Shuttle Orbiter aerodynamic data in hypersonic, supersonic, and transonic flight regimes
- Establish an extensive data base for verification of and correlation with ground-based test data

Hardware Objective

- Design, develop, and implement an instrument package that
- Provides vehicle dynamics data (accelerations and rates) with performance characteristics not available from baseline Orbiter flight data systems
  - Axial acceleration
  - Higher data sampling rates
  - Increased resolution
  - Precise time correlation

Implementation

- ACIP hardware developed by Bendix Aerospace Systems Division
- Vehicle integration design and implementation by Rockwell International
- Hardware development and integration managed by Johnson Space Center
- Two ACIP systems fabricated and installed
  - OV-099 *Challenger*
  - OV-102 *Columbia*
- Data processing and distribution by JSC OEX Data Lab

Hardware Description

- Major subassemblies
  - Triaxial Accelerometer/Gyro Instrument Package (TAGIP)
  - Triaxial Angular Accelerometer (TAA)
  - Data Handling Electronics (DHE)
- TAGIP contains three orthogonally-mounted linear accelerometers and three orthogonally-mounted rate gyros
- Linear accelerometers employ the force-rebalance, pivot and jewel, suspended pendulous-mass design
- Rate gyros are single-degree-of-freedom units, employing liquid hydrostatic suspension for reduced friction, and use a torque-rebalance servo system for rate sensing

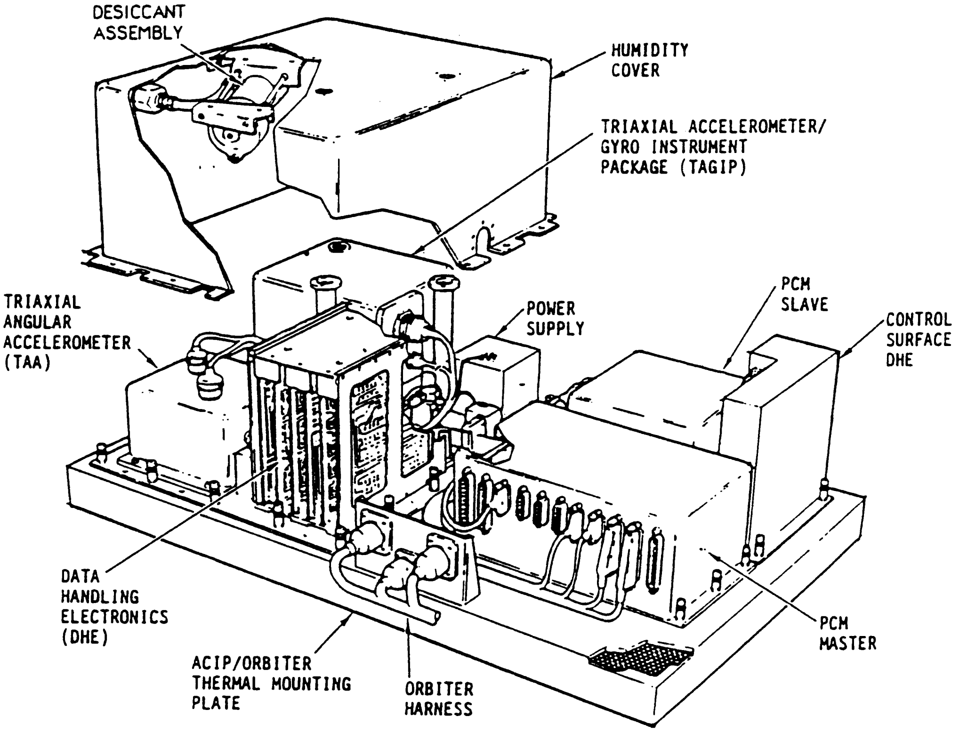
DESICCANT ASSEMBLY
HUMIDITY COVER
TRIAXIAL ACCELEROMETER/ GYRO INSTRUMENT PACKAGE (TAGIP)
TRIAXIAL ANGULAR ACCELEROMETER (TAA)
POWER SUPPLY
PCM SLAVE
CONTROL SURFACE DHE
DATA HANDLING ELECTRONICS (DHE)
ACIP/ORBITER THERMAL MOUNTING PLATE
ORBITER HARNESS
PCM MASTER

ACIP Component Layout

Hardware Description (Cont'd)

- TAA contains three orthogonally mounted single-axis fluid rotor angular accelerometers
    - Fluid enclosed in an angular tube serves as the main inertia element
    - Angular acceleration about the input axis results in fluid motion which tends to deflect the vane
    - Servo system current that restores vane to null position is a direct measure of angular acceleration magnitude
- DHE conditions each sensor output and provides housekeeping data
    - Sensor outputs are pre-sample filtered, multiplexed, digitized to 14-bit resolution, and formatted into a serial digital data stream
    - Presample filters (in conjunction with high sampling rate-213 S/S) eliminate data aliasing, but limit sensor frequency response to 20 HZ
    - Housekeeping data include ACIP temperatures, voltages, and currents
- Serial digital data are routed to a PCM Master in the Support System for OEX (SSO)
- Housekeeping data are routed to a PCM Slave for multiplexing and digitizing to 8-bit resolution
- PCM Master tags the data with Greenwich Mean Time (GMT) obtained from the Orbiter
- ACIP test mode, when commanded, results in each sensor servo system being offset by a fixed amount, thereby providing an indication that the servo loop is functioning properly
- Each sensor subassembly is accurately aligned to the ACIP baseplate by combinations of precisely machined pins and dowels

Hardware Description (Cont'd)

- ACIP baseplate is aligned to the orbiter structure via precision pins
- ACIP cover provides
  - A degree of passive thermal control
  - Humidity control through use of a flow-through desiccant assembly
- "Mini" DHE acquires selected instrumentation outputs from the orbiter Operational Instrumentation system
  - Four elevon position measurements
  - Rudder position measurement
  - One Reaction Control System jet chamber pressure measurement
  - Like the DHE, the Mini DHE provides similar presample filtering, multiplexing, and digitization
- Mini DHE serial data output is sent to PCM Master
- Control surface position data are thereby melded with ACIP data
  - Same sampling rate as ACIP sensor data
  - High resolution
  - Precise time correlation with sensor data

Sensor	Axis (Orbiter Reference)	Range	Resolution
Linear Accelerometer	X-Axis (Longitudinal)	±1.5g ±3.0g*	183µg 366µg* *STS-9 effectivity
Linear Accelerometer	Y-Axis (Lateral)	±0.5g	61µg
Linear Accelerometer	Z-Axis (Normal)	+3.0g	366µg
Rate Gyro	X-Axis (Roll, p)	±30°/S	.0036°/S
Rate Gyro	Y-Axis (Pitch, q)	±10°/S	.0012°/S
Rate Gyro	Z-Axis (Yaw, r)	±10°/S	.0012°/S
Angular Accelerometer	X-Axis (Roll, $\dot{p}$)	±2.0 rad/sec^2	244 µrad/sec^2
Angular Accelerometer	Y-Axis (Pitch, $\dot{q}$)	±1.0 rad/sec^2	122 µrad/sec^2
Angular Accelerometer	Z-Axis (Yaw, $\dot{r}$)	±1.0 rad/sec^2	122 µrad/sec^2

Integration

- ACIP located beneath payload bay in wing box
- Mounted on shelf assembly which provides
  - Rigid attachment to orbiter centerline rib
  - ± 10 arc minute alignment of sensor axes with orbiter axes
  - Thermal isolation
- PCM system and Mini DHE share ACIP shelf
- All ACIP PCM data stored on tape during mission and dumped to ground recorders after landing
- Multilayer insulation blanket over ACIP/PCM/Shelf assembly provides passive thermal control
- Active thermal control via thermostatically-controlled strip heater bonded to ACIP baseplate

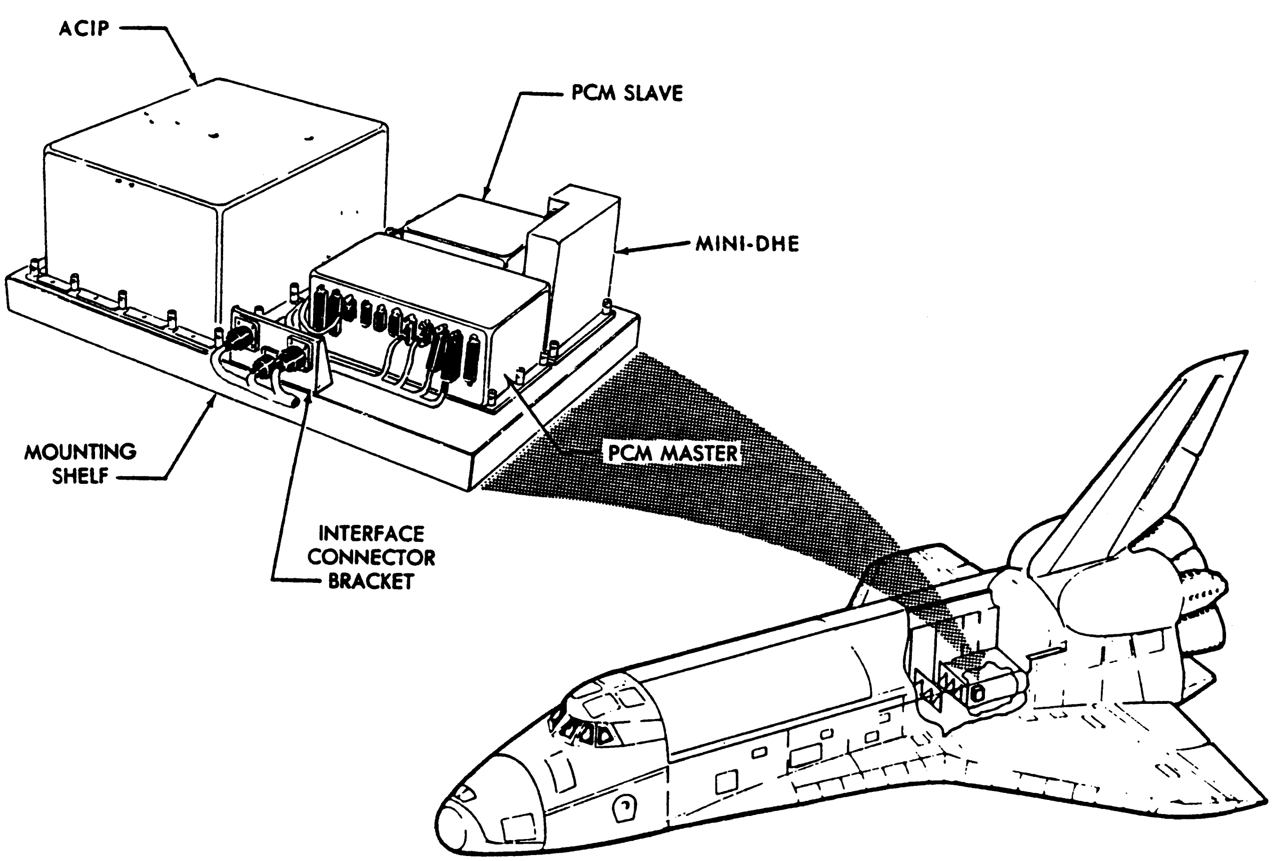

ACIP/PCM Location On Orbiter

Flight History

- Two ACIP units (S/N 1 and S/N 2) were built
- S/N 1 has flown 6 times on OV-099 and 7 times on OV-102
- S/N 2 flew 4 times on OV-099 and 5 times on OV-102. It was lost with Challenger on STS-51L
- Due to tape recorder failure, no entry data were obtained on STS-2
- Z-axis rate gyro failed during entry phase of STS-41B
- Due to failure of the ACIP +5 VDC power supply a few minutes before launch, no data were obtained during STS-41G

Flight History (Cont'd)

- Because of a component failure in the DHE, X-axis rate gyro data were not obtained during STS-61C
- Angular accelerometers performed normally during the earlier flights, but began to evidence serious performance degradation, which continued to worsen
- Angular accelerometers were not replaced and data are not used
  - Satisfactory acceleration can be obtained by differentiating the rate gyro data
  - Replacement costs would have been excessive
- In summary many complete sets of linear accelerometer and rate gyro data have been acquired
  - Ascent - 16 sets
  - Entry - 17 sets
  - On-orbit -- varying amounts from most of the flights
- Partial sets from two other flights
- Several flights of acceptable angular accelerometer data were obtained
- Using the most current recalibrations, the OEX Data Lab processed, distributed, and archived the data

The Future

- ACIP is to acquire aero data on STS-55 and STS-58, with STS-62 as a contingency
- ACIP will provide supporting data to OARE on STS-58 and STS-62
- ACIP not planned for removal until after STS-67, so barring hardware problems, data will be recorded during STS-65 and STS-67
- ACIP may be refurbished and flown on first shuttle flights that utilize the Advanced Solid Rocket Motor

High Resolution Accelerometer Package (HiRAP)

Robert C. Blanchard
NASA Langley Research Center
Hampton, Virginia 23681-0001

Kevin T. Larman
and
Robert P. Borchardt, Jr.
Lockheed Engineering & Sciences Company
Hampton, Virginia 23666-1339

ABSTRACT

A flight accelerometer experiment, the High Resolution Accelerometer Package (HiRAP), has been designed and used to measure the reentry rarefied flow aerodynamic acceleration characteristics of the Space Shuttle Orbiter. The HiRAP experiment is a component of the Orbiter Experiments (OEX) flight research program. The HiRAP equipment includes a tri-axial, orthogonal set of linear, pendulous, gas-damped accelerometers with a 1×10^{-6} g resolution. To date, low-frequency, low-acceleration (e.g. aerodynamic) measurements have been made on 14 missions beginning in April, 1983. The process of reducing the flight measurements to calibrated aerodynamic acceleration data sets is discussed. A two step process is presented which involves first removing the non-aerodynamic signals and then calibrating the subsequent aerodynamic acceleration signal. The final aerodynamic acceleration data sets are calibrated using a post-flight procedure specifically developed for the HiRAP data. An example of this process using flight data from mission STS-35 is discussed. Selected characteristics from the twelve currently analyzed missions are presented.

Nomenclature

A =acceleration
C =count acceleration data
C_N/C_A =normal to axial coefficient
g =acceleration due to gravity, 9.81 m/s^2
p,q,r =angular rates about the body axes
$\dot{p},\dot{q},\dot{r}$ =angular accelerations about the body axis
SF =scale factor
$\overline{X},\overline{Y},\overline{Z}$ =distance along each respective axis from HiRAP to Orbiter Center of Gravity
ΔA =induced acceleration due to rotation
Ω =rotational matrix
μg =$1x10^{-6}$ g

Acronyms

ACIP =Aerodynamic Coefficient Identification Package
APU =Auxilliary Power Unit
CFD =Computational Fluid Dynamics
HiRAP =High Resolution Accelerometer Package
OEX =Orbiter Experiments
OV =Orbiter Vehicle
STS =Space Transportation System

Subscripts
x,y,z =body axes

Introduction

Aerodynamic performance of a winged reentry vehicle traversing the rarefied flow regime from free-molecule to hypersonic continuum was not well understood at the beginning of the Orbiter Experiments (OEX) Program. Winged-vehicle reentry aerodynamic performance in this flight regime had not been adequately measured, analytically modeled or simulated in a wind tunnel. A flight research effort was undertaken by NASA to create a data base of the aerothermodynamic characteristics which describe the behavior of the Orbiter in this regime. The program included the High Resolution Accelerometer Package (HiRAP)[1] experiment which was developed to make in situ rarefied flow aerodynamic measurements during reentry. In parallel, computational fluid dynamics (CFD) techniques were initiated[2] to support the development of the data base. The existing wind tunnel testing program contained some rarefied-flow performance data[3], but further testing was not specifically planned since the combination of flight data and CFD could provide the needed information.

Instrument Description

HiRAP is specifically designed to investigate the aerodynamic performance characteristics of the Orbiter during descent through the rarefied flow flight regime (e.g. C_N/C_A). The HiRAP equipment is an orthogonal, tri-axial set of linear, pendulous, gas-damped accelerometers each with a resolution of 1×10^{-6} g (1 μg) and a range of ±8000 μg. The package is 3.5 in x 4 in x 5 in and weighs about 2.5 lb. The experiment is mounted in the wing box of the Orbiter with the accelerometer input axes aligned with the Orbiter body axes. The HiRAP instrument is co-located with the Aerodynamic Coefficient Identification Package (ACIP) and shares some electronic components, such as filters, power conditioning, analog to digital conversion and other data handling functions. The operation of the HiRAP is controlled by the ACIP in that HiRAP is powered on whenever power is applied to the ACIP. HiRAP flight data is routed through ACIP and recorded on the OEX payload recorder. The post-flight analyses of HiRAP data produce a calibrated measurement of low frequency, low level (e.g. aerodynamic) accelerations exerted on the Orbiter during reentry. To date, two HiRAP instruments have completed 14 OV missions [4,5,6,7]. Figure 1 illustrates the reentry ground tracks for the 12 currently analyzed HiRAP missions.

The HiRAP design[6] uses three identical filtering stages as shown in figure 2. The output from each accelerometer is first integrated using a low pass filter with a 1.0 Hertz corner frequency and a roll-off of 80 dB/decade. The second signal integration is performed by a filter with a 20 Hz frequency cutoff. The filter output is converted to a binary representation using a 14- bit analog to digital converter. After each flight, the recorded HiRAP flight data is transformed into a computer compatible output, referred to as 'count' data, having a range from 0 to 16383 counts. During flight, the raw accelerometer count data is recorded at either 173.9 or 112.6 samples/s. The HiRAP instrument is sensitive to temperature changes. These temperature changes introduce a bias to the output count value. As a result of this thermal sensitivity, each HiRAP accelerometer has a temperature transducer output which is also sampled and recorded at 2.7 or 1.8 samples/s. Post flight data processing uses this temperature data to correct the thermal instrument bias.[8]

Instrument Location

The HiRAP instrument sketch is illustrated in figure 3. The input axes of the accelerometers are illustrated to indicate their position within the instrument. The HiRAP instrument is placed behind, below and left of the OV center of gravity [7]. Figure 4 illustrates the position of the HiRAP instrument. The HiRAP instrument position away from the OV center of gravity causes induced acceleration whenever rotation of the vehicle occurs. The rotations about the body axes are measured by the OV navigational gyro systems or the Aerodynamic Coefficient Identification Package (ACIP) rate gyroscopes. The level of acceleration at each of the HiRAP accelerometers produced by rotation about the OV center of gravity is given by:

$$\begin{vmatrix} \Delta A_x \\ \Delta A_y \\ \Delta A_z \end{vmatrix} = \Omega \begin{vmatrix} \bar{X} \\ \bar{Y} \\ \bar{Z} \end{vmatrix} \qquad (1)$$

where:

$$\Omega = \begin{vmatrix} -(q^2+r^2) & (pq-\dot{r}) & (pr+\dot{q}) \\ (pq+\dot{r}) & -(p^2+r^2) & (qr-\dot{p}) \\ (pr-\dot{q}) & (qr+\dot{p}) & -(p^2+q^2) \end{vmatrix}$$

These values are added algebraically to the recorded flight data to offset rotational effects [9].

Data Interpretation

The interpretation of the data is a two phase process which requires first removing non-aerodynamic accelerations and then applying calibration factors. The removal of non-aerodynamic signals involves either adjusting or removing the data from the data stream. The flight derived calibration technique uses both pre-flight laboratory calibration factors and post-flight analyses.

Aerodynamic Signal Isolation

Time tagged HiRAP flight acceleration and sensor temperature data are recorded on the OEX tape recorder. Aerodynamic acceleration data are subsequently extracted through ground processing[5,6,9,10]. Figure 5 illustrates the modules of the analysis process. The first module in the process is to examine the count data time tags to verify the mission time line, locate time reversals and data drop-outs. This is followed by a conversion of acceleration and sensor temperature count data into engineering units. Laboratory determined scale factors are used to complete this second module. The third analysis module accounts for the linear accelerations induced by Orbiter angular motions. The thrust acceleration signals are removed in the fourth module. The final two modules involve calibration of the aerodynamic acceleration and making the APU adjustment to the Z-axis data.

Instrument Calibration

Calibration of HiRAP is accomplished by pre-flight instrument testing and post flight analysis to account for the offset bias in the recorded flight data. A flight calibration using post-flight analyses is required to determine thermal biases since they cannot be currently corrected using only ground testing. However, pre-flight ground calibrations can be obtained for scale factor conversions (converting counts to μg) and sensor output linearity. The laboratory method uses a laser interferometer device at temperatures ranging from 30°F to 150°F [6] for precision measurement of the angle between the HiRAP axes and the Earth gravity vector. The calibration involves using an aerodynamics model[7] ,the aerodynamic flight data, and the sensor temperature data. The calibration technique is described in detail in reference 10. These final, calibrated accelerations are then available for a variety of subsequent analyses, including aerodynamics[11,12,13,14].

Illustration

An example of the HiRAP flight data analysis process is presented using selected reentry data from the STS-35 mission. The objective of the post-flight data analysis procedure is to produce the aerodynamic acceleration measurements in the X and Z directions. The Y-axis signal, although measured, is not analyzed or presented here. A 200 second segment of unprocessed count data from the X and Z accelerometers is presented in figures 6(a) and 6(b).

The count data is converted to engineering units using the following linear relationship[6]:

$$A = \frac{20\frac{C}{16383} - 10}{SF} \quad ,\mu g \qquad (2)$$

where C is the HiRAP count data in any given axis and SF (in volts/ μg) is the appropriate scale factor for that axis. The resulting application of this equation to the STS-35 data, in units of μg's, is presented in figures 7(a) and 7(b). Figures 7(a) and 7(b) contain a variety of non-aerodynamic signals.

These include the influence of OV center of gravity offset, thruster signals, thermal biases and the APU shift. Thruster firings induce predominant impulses on the X and Z axis data as shown in figures 7(a) and 7(b).

Auxiliary power units (APU) on the OV are used to provide hydraulic power during reentry and the exhaust ports for these gas turbines are located on the top rear of the Orbiter, just in front of the vertical tail. There are three APU exhaust ports which act as thrusters and produce a net acceleration on the Orbiter of about 300 μg[6]. The accelerations induced by the APU's act only in the Z direction and are visible in figure 7(b) among the thruster acceleration spikes.

The accelerations induced by the sensor not being at the center of gravity are calculated using the above equation (1). These calculations depend upon angular rates and accelerations which come from gyro data. These induced accelerations are removed from the total signal. The thrust signals are removed from the data by deletion, thus, leaving data gaps.

An average of the data for each one second time interval is then made. Linear regressions of sensor temperature to this average sensor output are performed to remove the biases and correct the shift in the Z-axis due to the APU. A detailed analysis report is provided in the literature[10] as to the process and the results of removing the biases. It is estimated that the absolute acceleration error after post-flight processing is within ± 5.7 μg.

Figures 8(a) and 8(b) illustrate the final re-entry HiRAP aerodynamic data for STS-35 on the X and Z axis. These data are the reentry aerodynamic acceleration data set which is the product supplied to users for further analyses. The gaps in the plot illustrate the areas where non-aerodynamic data were removed.

Data Application

Figure 9 illustrates the extent of the currently available acceleration data during ascent, orbit and reentry. Table 1 illustrates the currently existing HiRAP data library and includes LaRC tape reference numbers grouped by flight number[6]. Most of the orbital flight data have been categorized, but not yet analyzed. All of the reentry data has been completely analyzed, except for 2 flights, STS-32 and STS-50. STS-32 has not been analyzed because the X-axis sensor malfunctioned. The STS-50 analysis is near completion awaiting only the ancillary control surface information.

Calibrations performed on the HiRAP orbital data set could have many potential applications. Orbital accelerations can be used to analyze OV mass properties, structure, crew motion, thruster behavior, satellite deployment, etc. Some examples of investigations completed to date are an OV mass properties determination of the center of gravity in orbit[15] and the determination of pitching moment coefficient in the rarefied-flow regime[16].

The majority of the analyses of HiRAP data have been done on the reentry data set, in particular, the inference of atmospheric density. The reentry trajectory of the Orbiter provides a nearly horizontal slice of the lower thermosphere region of the atmosphere. This horizontal snapshot of this region of the sky is unique. This atmosphere region is not readily accessible by any other flight vehicle. In addition, the longevity of the HiRAP has permitted the creation of a data base which includes spatial and temporal phenomena. A variety of atmospheric density analyses have been performed and reported using HiRAP[4,5,6,10,12,13].

Summary

The Space Transportation System provides a unique opportunity to make repeated in-situ measurements of the aerodynamic characteristics of a winged flight vehicle in the rarefied flow flight regime. Aerodynamic forces are determined with knowledge of the accelerations acting on the Orbiter and the Orbiter's mass. In order to make reentry rarefied flow aerodynamic acceleration measurements, equipment which resolves low frequency (< 1Hz), low acceleration ($\sim 1\text{x}10^{-6}$ g) signals is required. The High Resolution Accelerometer Package (HiRAP) experiment is designed for and is making these measurements. HiRAP is an experiment in the Orbiter Experiments (OEX) program.

HiRAP equipment includes a sensitive, tri-axial, linear accelerometer which has been in use since 1983. Each sensor has a resolution of $1\text{x}10^{-6}$g and a range of $\pm 8000\text{x}10^{-6}$g. The measurement cut-off frequency is 1.0 Hz. The equipment is located in the wing box of the Orbiter and shares some of the data handling electronics with the Aerodynamic Coefficient Identification Package (ACIP). To date, 14 sets of HiRAP flight data have been recorded. This flight data base includes measurements made during ascent, orbit and reentry. Twelve of the reentry data sets have been analyzed, one is near completion (STS-50) and one was not analyzed due to an X-axis sensor failure (STS-32). The results of the 12 analyzed missions have been published.

Key to the success of HiRAP were the development of the equipment and a calibration technique which resolves the rarefied flow aerodynamic acceleration signal. The HiRAP instrument was developed and thoroughly tested for stability and repeatability. Flight experience with the HiRAP indicates that equipment calibration to the ug levels in a 1g field is unreliable for producing an absolute acceleration flight measurement. A flight derived calibration procedure for HiRAP data processing has been developed. This procedure includes an Orbiter aerodynamics model, selected reentry data segments, and selected laboratory calibration factors. An analysis of the procedure provides an estimate of the accuracy of the absolute acceleration measurements to within $\pm 5.7\text{x}10^{-6}$ g.

To date, significant achievements from results of the HiRAP experiment include, extensive characterization of a micro-g resolution instrument through both laboratory testing and multiple flight experiences, the development of a flight calibration technique, an Orbiter reentry rarefied-flow aerodynamics model, inference of upper-atmospheric density, a determination of Orbiter center of gravity on orbit, and a measurement of Orbiter pitching moment coefficients during reentry in the rarefied-flow regime. A large data base currently exists which includes orbital and some ascent information.

References

1. Compton, H.R.; Blanchard, R.C.; and Walberg, G.D.: An Experiment for Shuttle Aerodynamic Force Coefficient Determination from In-flight Dynamical and Atmospheric Measurements. AIAA Paper 78-795, April 1978.

2. Moss, J.N. and Bird, G.A., "Direct Simulation of Transitional Flow for Hypersonic Reentry Conditions," AIAA Paper 84-0406, January 1984.

3. "Aerodynamics Design Substantiation Report-Vol. I: Orbiter Vehicle", Rockwell International, Space Division, Downy, CA SD74-SH0206-1H, January 1986

4. Blanchard, R.C.; and Rutherford, J.F.: The Shuttle Orbiter High Resolution Accelerometer Package Experiment: Preliminary Flight Results. AIAA Paper 84-0490.

5. Blanchard, R.C., and Buck, G.M.: Determination of Rarefied-flow Aerodynamics of the Shuttle Orbiter from Flight Measurements on STS-6 and STS-7. AIAA Paper 85-0347, January 1985.

6. Blanchard, R. C., Larman, K. T. and Barret, M., "The High Resolution Accelerometer Package Flight Experiment Summary for the first 10 flights," NASA Reference Publication 1267, April 1992.

7. Blanchard, R.C., Larman, K.T., Moats, C.D.; Rarefied-Flow Shuttle Aerodynamics Model, NASA TM 107698, February, 1993.

8. Thompson, J. M. and Russell, J. W., Blanchard, R. C., "Methods for Extracting Aerodynamic Accelerations from Orbiter High Resolution Accelerometer Package Flight Data," AIAA Paper 87-2365, August 1987.

9. Blanchard, R. C., Larman, K. T., Moats C. D., "Flight Calibration Assessment of HiRAP Accelerometer Data," AIAA Paper 93-0836, January 1993.

10. Moats,C.D., Blanchard, R.C., Larman, K.T.; Improved HiRAP Flight Calibration Technique, NASA TM-107656, July 1992.

11. Blanchard, R.C.: Rarefied Flow Lift-to-Drag Measurements of the Shuttle Orbiter. ICAS Paper 86-2.10.2, London, United Kingdom, September 1986.

12. Blanchard, R.C.; and Buck, G.M.: Rarefied Flow Aerodynamics and Thermosphere Structure from Shuttle Flight Measurements. Journal of Spacecraft and Rockets, vol 24, no 6, November-December 1987.

13. Blanchard, R.C.; and Hinson, E.W.: Hypersonic Rarefied-Flow Aerodynamics Inferred from Shuttle Orbiter Acceleration Measurements. Paper No. 7 presented at the International Congress on Hypersonic Aerodynamics, Manchester, England, September 4-6 1989.

14. Rogers, M.J.B.; Baugher, C.R.; Blanchard, R.C.; DeLombard, R.;Durgin, W.W.; Matthheisen, D.H.; Neupert,W.; and Roussel, P: Low Gravity Environment On-board Columbia During STS-40. AIAA 93-0833, January 1993.

15. Hinson, E.W.; Nickolson, J.Y.; Blanchard, R.C.: Determination of Shuttle Orbiter of Center of Gravity from Flight Measurements. NASA TM 102627, Jan., 1991.

16. Blanchard, R.C.; and Hinson, E.W.: Flight Measurements of Shuttle Orbiter Pitching Moment Coefficient and Elevon Effectiveness in the Rarefied-flow Regime. NASA TP 2889, March 1989.

Table 1 HiRAP Summary Characteristics

HIRAP MISSION	SERIAL#	ORBITER	DATE	ANGLE OF ATTACK*	FLAP* (DEG)	ELEVON* (DEG)	VELOCITY (m/s)	Kn**
STS-06	1	Challenger	04/09/83	38.8 - 41.5	7.0	5.6	7389 - 4841	5.2 - 1.9E-5
STS-07	1	Challenger	01/24/83	38.9 - 41.4	6.7	-0.6	7392 - 4846	2.5 - 1.7E-5
STS-08	1	Challenger	09/05/83	37.3 - 41.4	6.9	3.6	7355 - 4993	3.1 - 2.0E-5
STS-09	2	Columbia	12/08/83	37.5 - 42.2	6.8	4.5	7527 - 5387	11.1 - 2.6E-5
STS-41B	1	Challenger	02/11/84	38.1 - 41.8	7.2	3.5	7386 - 5151	5.2 - 2.3E-5
STS-41C	1	Challenger	04/13/84	38.6 - 41.5	6.9	7.7	7464 - 5011	2.0 - 2.1E-5
STS-51B	1	Challenger	05/06/85	38.5 - 42.0	7.1	1.4	7589 - 5119	5.6 - 2.1E-5
STS-51F	2	Challenger	08/06/85	38.9 - 41.8	4.3	-2.7	7517 - 5147	3.4 - 2.2E-5
STS-61A	2	Challenger	11/06/85	39.0 - 41.8	-4.7	-2.7	7583 - 5200	3.0 - 2.2E-5
STS-61C	1	Columbia	01/18/86	38.8 - 41.4	-4.7	-2.7	7406 - 5123	4.5 - 2.4E-5
STS-35	1	Columbia	12/11/90	33.8 - 43.0	-4.5	-2.8	7503 - 5347	4.3 - 2.5E-5
STS-40	1	Columbia	06/14/91	29.5 - 42.1	-4.7	-2.7	7512 - 5074	1.0 - 1.9E-5

* Control surface position above ~ 95 km.

** Reference Length is the Orbiter Mean Aerodynamic Chord(MAC = 12.06m)

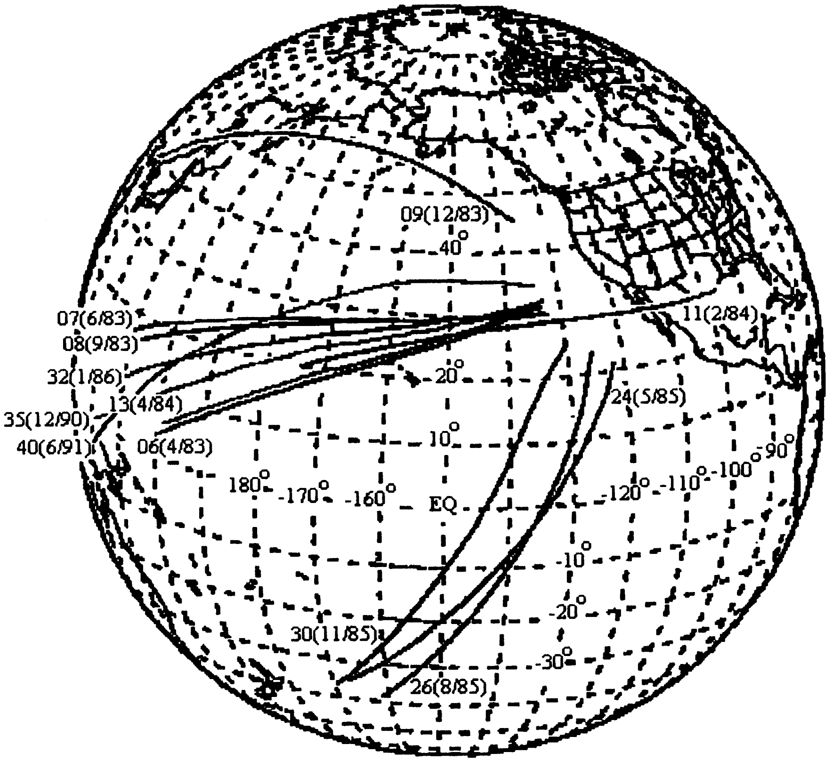

Fig. 1. HiRAP Reentry Ground Tracks

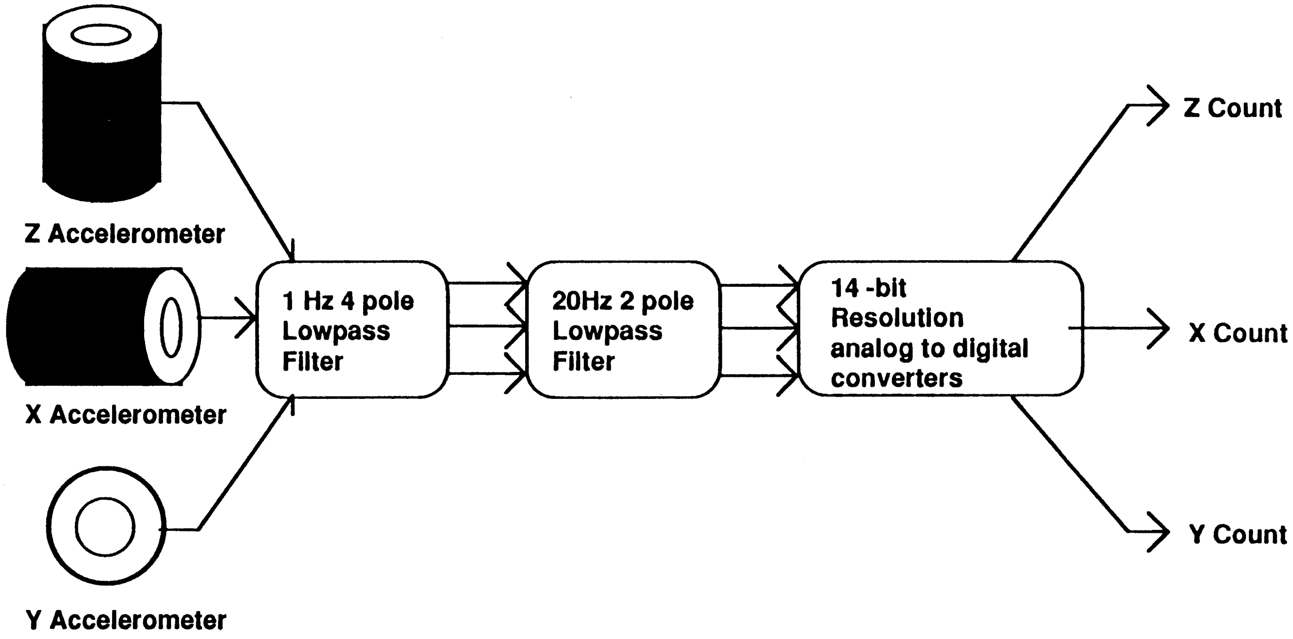
Z Accelerometer
X Accelerometer
Y Accelerometer
1 Hz 4 pole Lowpass Filter
20Hz 2 pole Lowpass Filter
14 -bit Resolution analog to digital converters
Z Count
X Count
Y Count

Fig. 2. Signal Filter Stages in the HiRAP Equipment

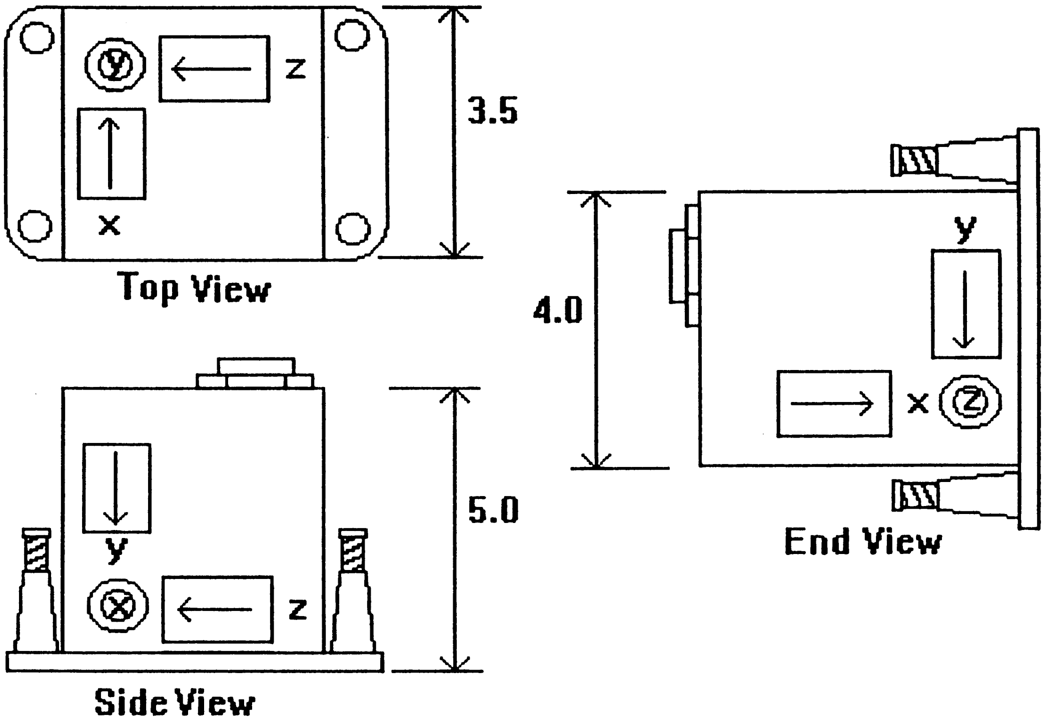

Fig. 3. HiRAP 3-View Drawing

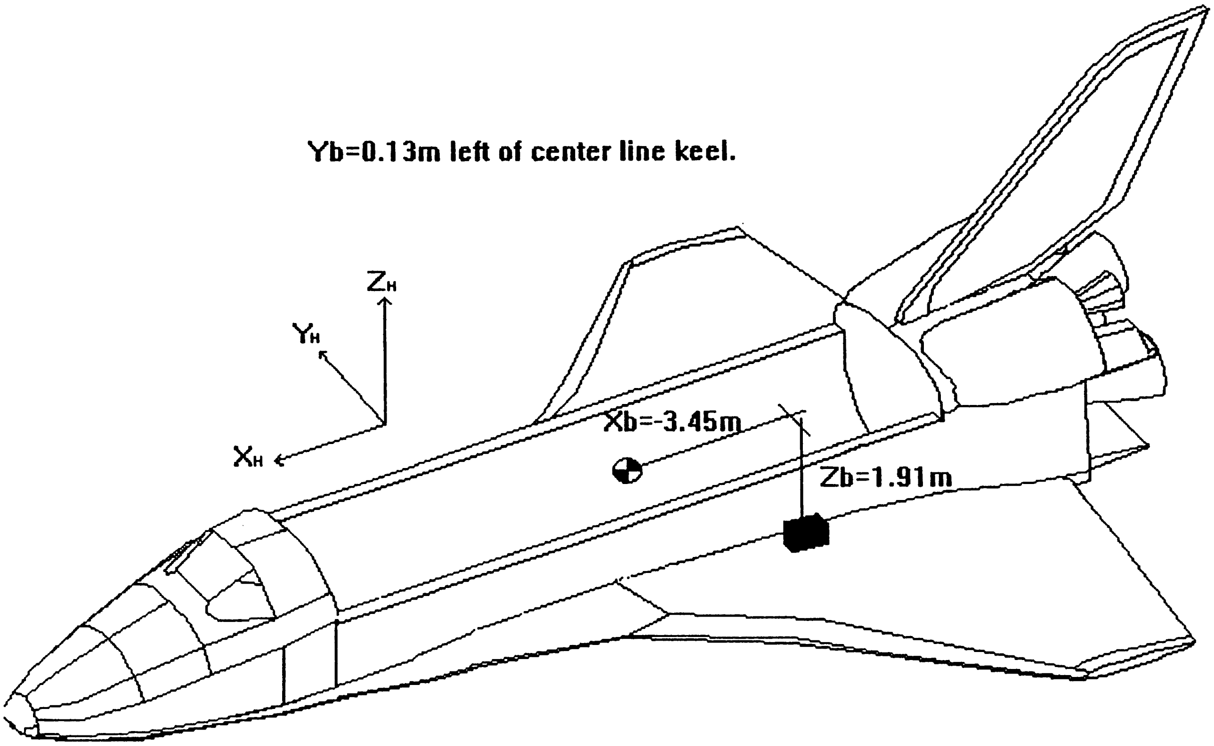

Fig. 4. Location of HiRAP on the Orbiter

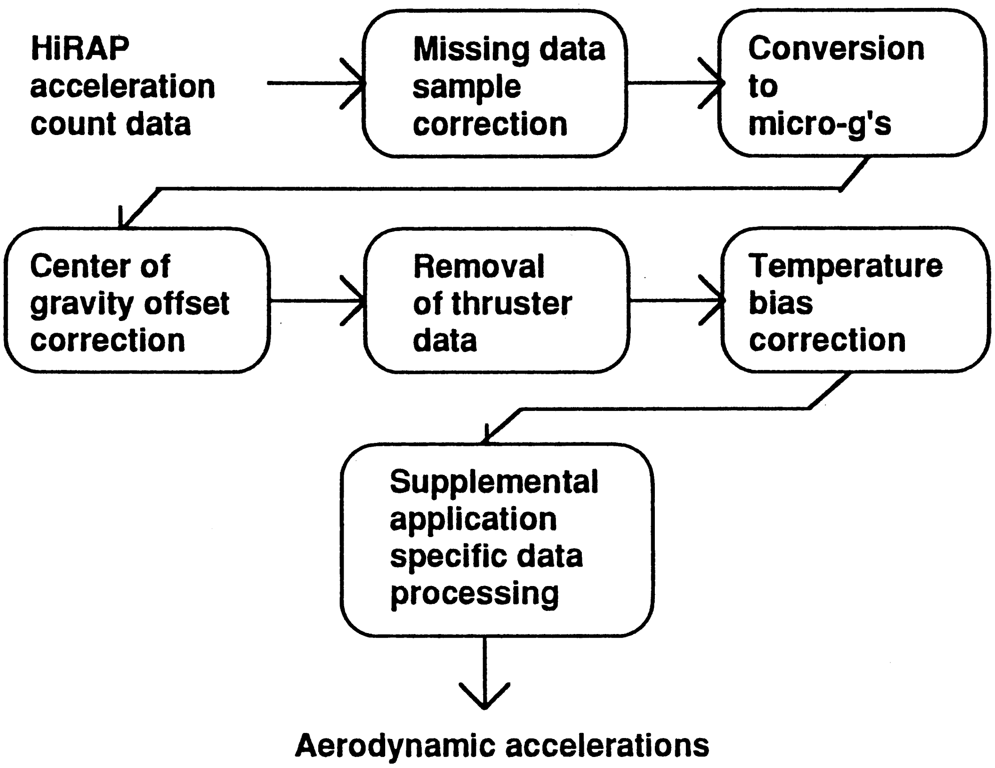
HiRAP acceleration count data
Missing data sample correction
Conversion to micro-g's
Center of gravity offset correction
Removal of thruster data
Temperature bias correction
Supplemental application specific data processing
Aerodynamic accelerations

Fig. 5. HiRAP Analysis Procedure

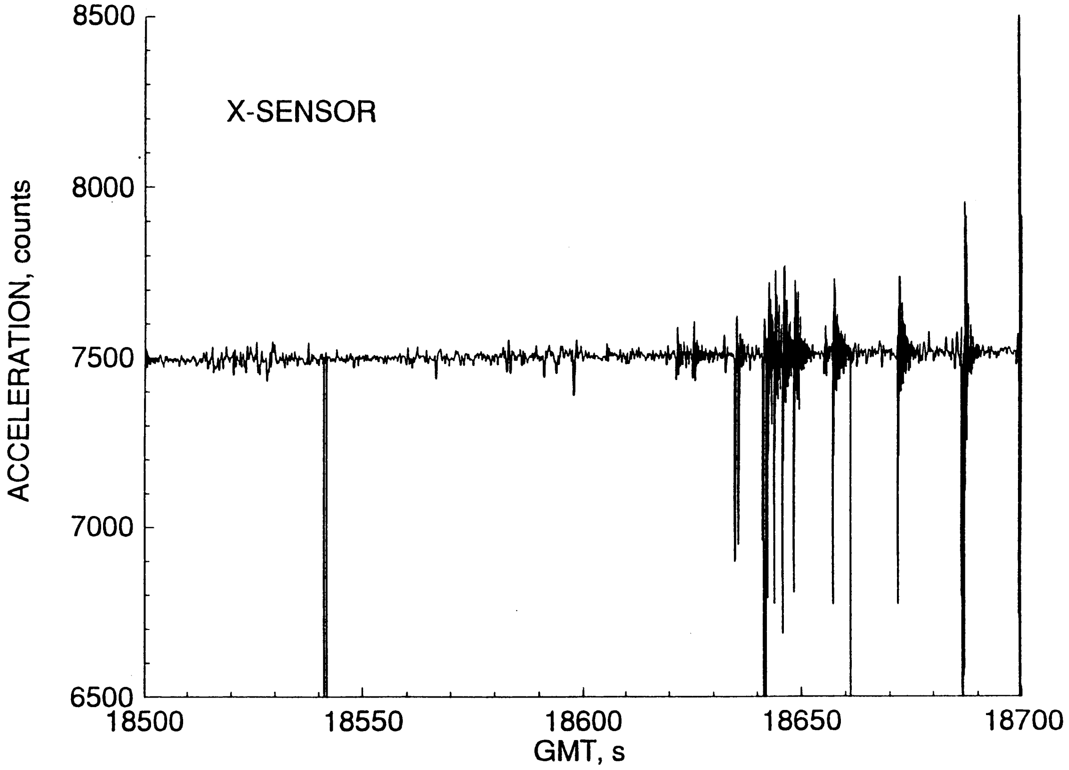

Fig. 6a. STS-35 Descent Data Segment

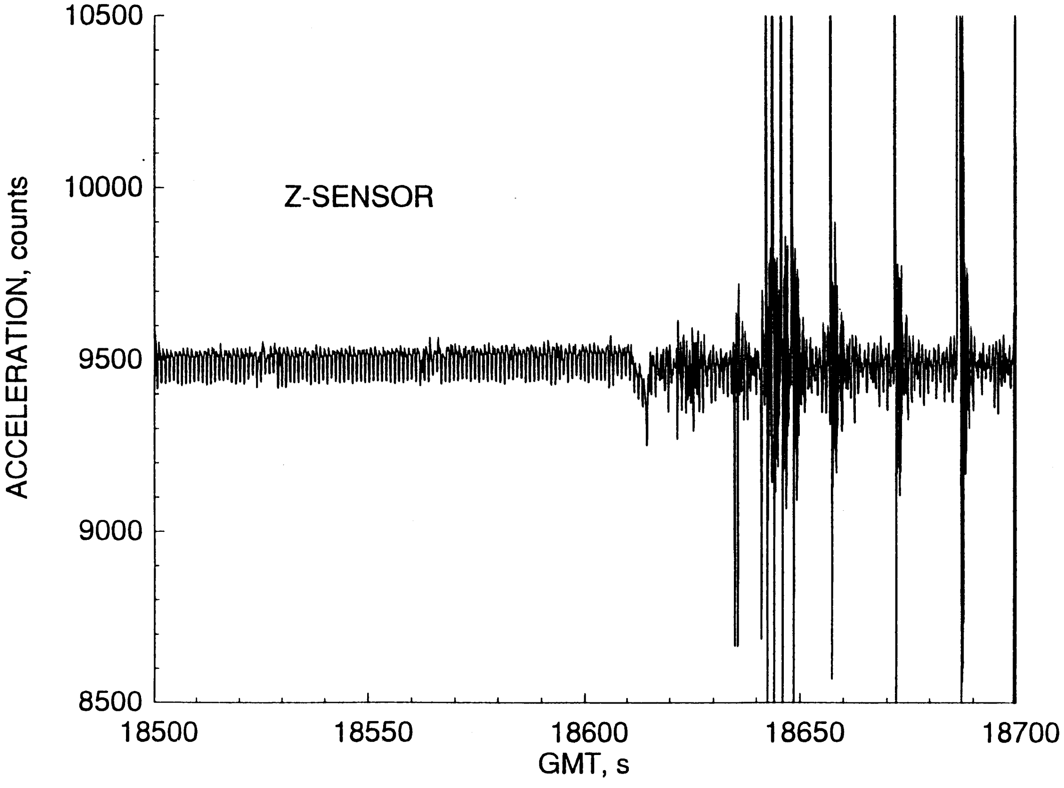

Fig. 6b. STS-35 Descent Data Segment

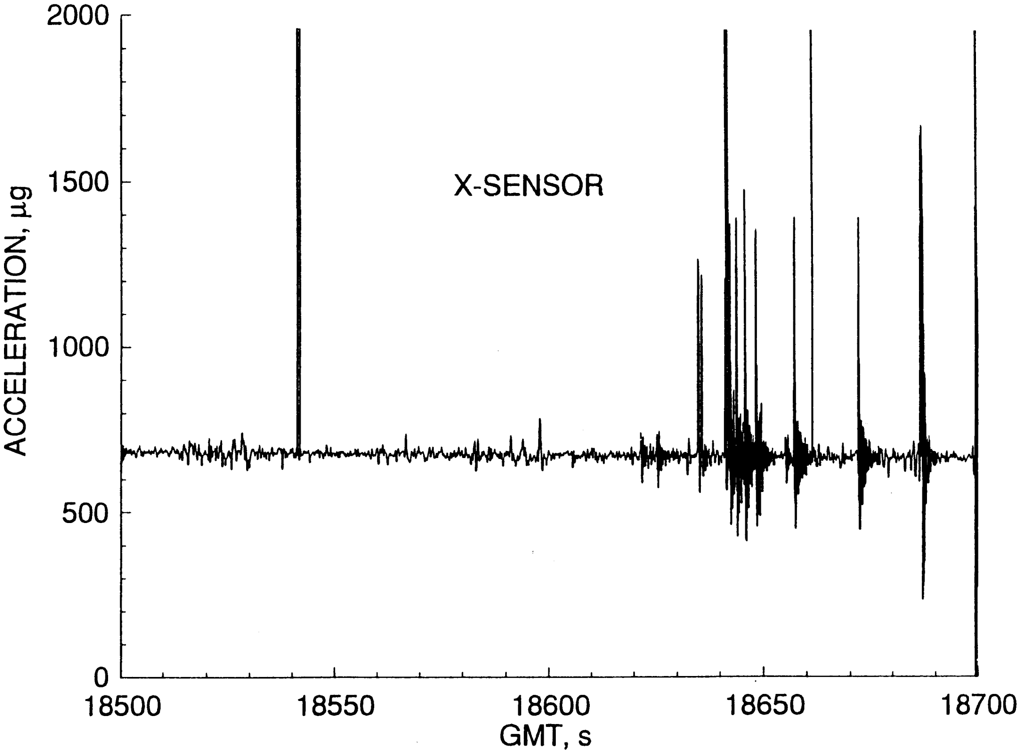

Fig. 7a. STS-35 Uncalibrated Data

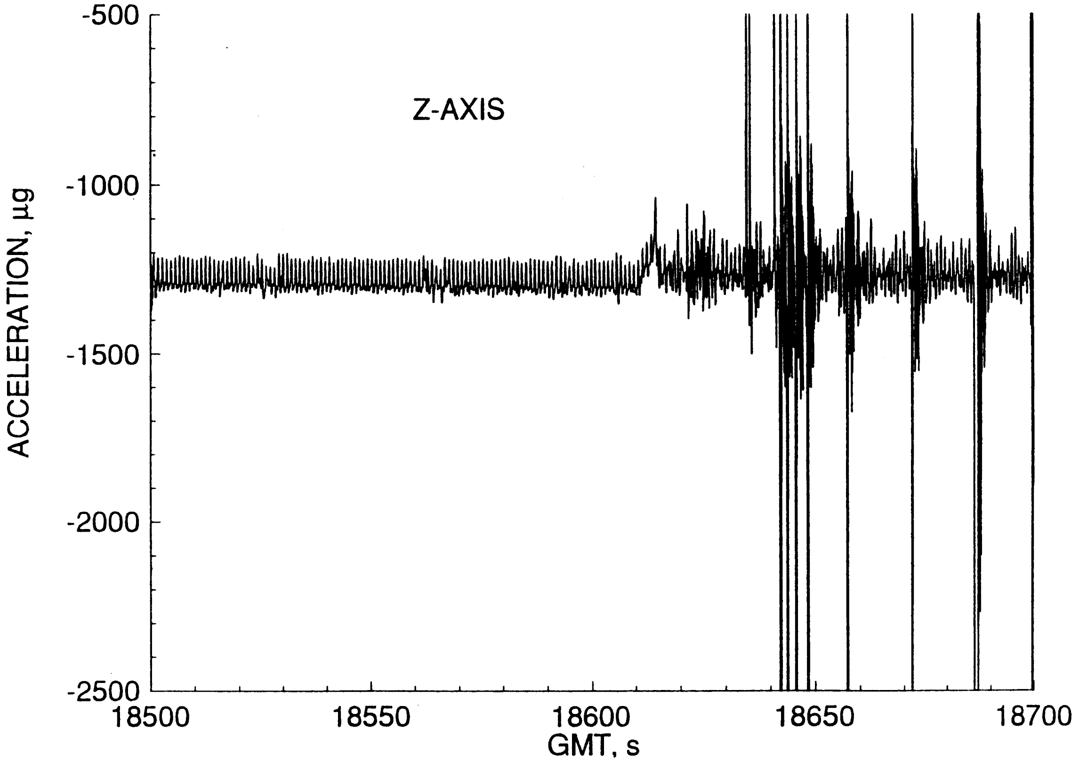

Fig. 7b. STS-35 Uncalibrated Data

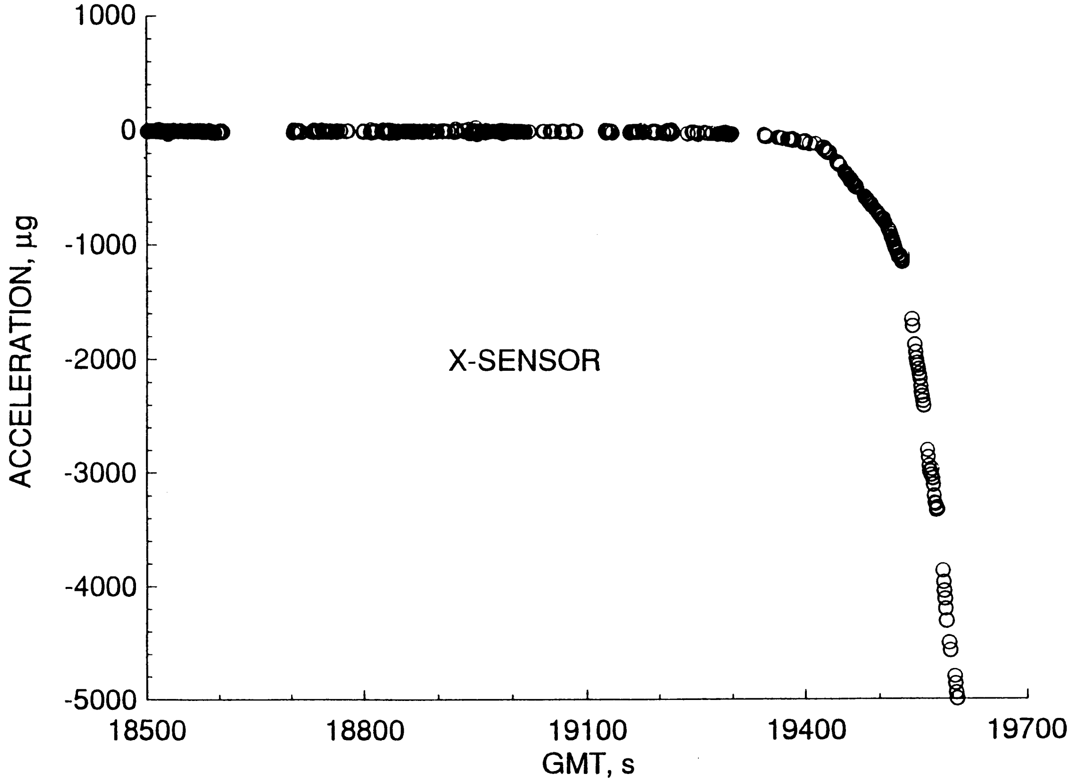

Fig. 8a. STS-35 Calibrated Descent Data

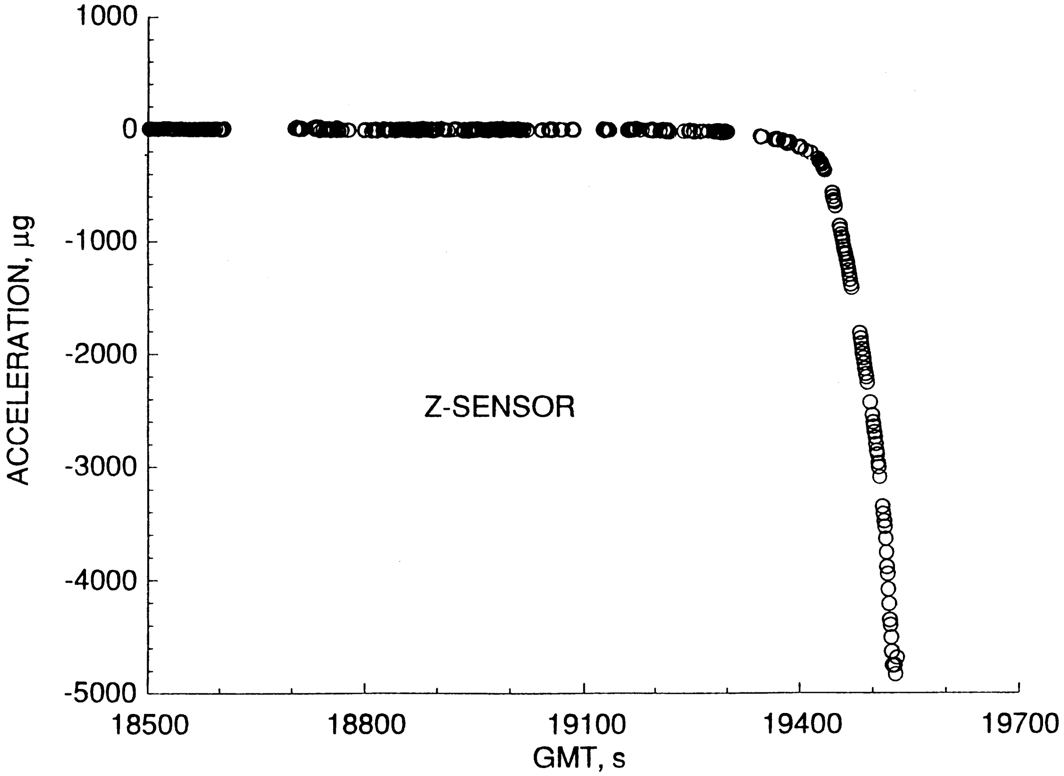

Fig. 8b. STS-35 Calibrated Descent Data

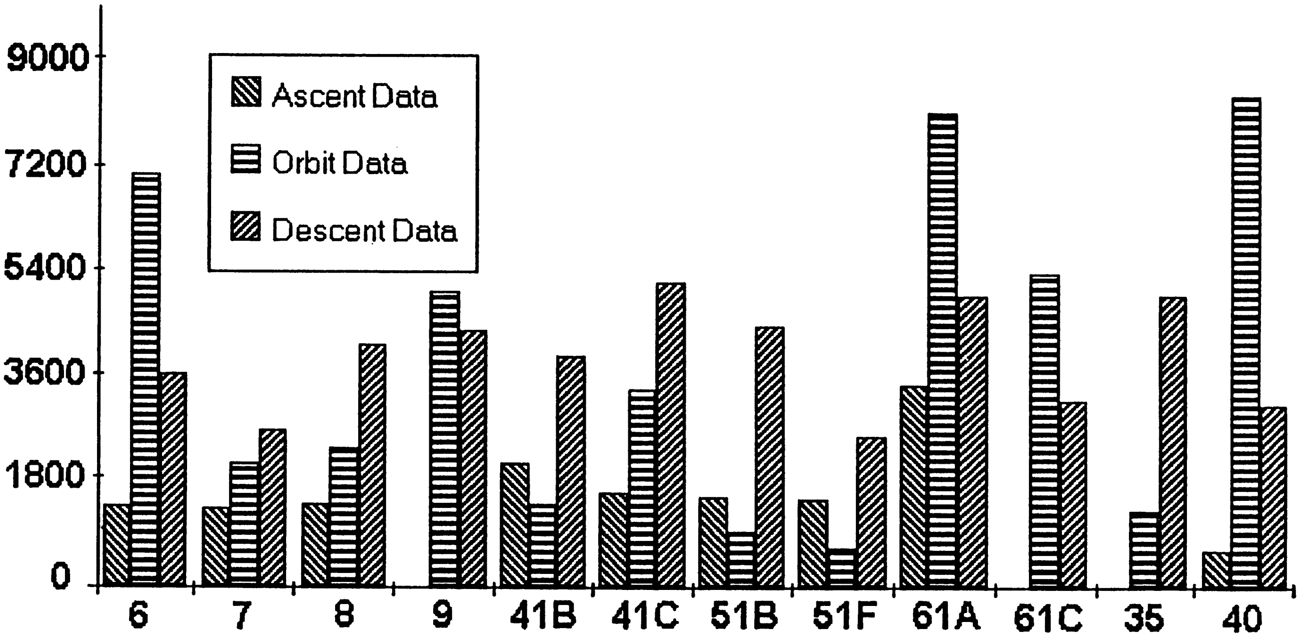

Fig. 9. Current HiRAP Data Base

ORBITAL ACCELERATION RESEARCH EXPERIMENT (OARE)

Robert C. Blanchard
NASA Langley Research Center
Hampton, Virginia 23681-0001

John Y. Nicholson
ViGYAN, Inc.
Hampton, Virginia 23666-1325

James R. Ritter
Lockheed Engineering & Sciences Company
Hampton, Virginia 23666-1339

Abstract

The Orbital Acceleration Research Experiment (OARE), which has flown on STS-40 and STS-50, contains an accelerometer with a non-pendulous, electrostatically suspended proofmass which can resolve accelerations to the nano-g (1×10^{-9} g) level. The experiment contains on-orbit bias and scale factor calibration capabilities, thereby eliminating the uncertainty of ground based calibrations encountered with accelerometers flown in the past. OARE can therefore measure absolute acceleration levels to an accuracy heretofore unachieveable on the Orbiter. It has been designed to measure and record a wide range of accelerations which enables it to measure signals on-orbit (e.g. aerodynamic drag up to about 350 km) and during re-entry (down to about 60 km). Results from OARE flights on STS-40 and STS-50 are presented. Measurements taken during the first flight of OARE, STS-40, have been analyzed and illustrate OARE's ability to obtain useful information on making orbital drag measurements, despite a sensor malfunction. Results of an analysis from a portion of the second flight, STS-50, show the full potential of the sensor and its calibration facility to provide absolute acceleration measurements at orbital altitudes. Subsequent to STS-50, OARE was removed and minor revisions were made in preparation for the next flight, STS-58.

Nomenclature

a_c	centripetal acceleration
a_{sensor}	sensor acceleration
A_{Xb}	acceleration in orbiter X body axis direction
A_{Yb}	acceleration in orbiter Y body axis direction
A_{Zb}	acceleration in orbiter Z body axis direction
B_X	bias in the X direction
c.g.	center of gravity
C_A	axial coefficient
C_D	drag coefficient
C_N	normal coefficient
C_Y	side force coefficient
g	gravitational acceleration (9.81 m/s^2)
L/D	lift to drag ratio
m	mass
q	dynamic pressure
r	length
S	aerodynamic reference area
S_X	bias free signal in X direction
V	velocity
α	angle of attack
β	side-slip angle
ρ	atmospheric density
ω	rotation rate
μg	micro-g

Acronyms

ACIP	Aerodynamic Coefficient Identification Package
CAS	Calibrated Ancillary System
CEF	Customer Extended Facility
CGF	Crystal Growth Facility
EEPROM	Electrostatically Erasable Programmable Read Only Memory
GSE	Ground Support Equipment
HiRAP	High Resolution Accelerometer Package
IMU	Internal Measurement Unit
JSC	Johnson Space Center
MCC	Mission Control Center
MET	Mission Elapsed Time
MSFC	Marshall Space Flight Center
OARE	Orbital Acceleration Research Experiment

OEX	Orbiter Experiment
OIS	OARE Interface Subsystem
OSS	OARE Sensor Subsystem
PCM	Pulse Code Modulation
PCS	Power Control System
RCS	Reaction Control System
RSS	Root Sum Squared
RTA	Rotary Table Assembly
SCS	Servo Control Subsystem
SLS	Space Life Sciences
SPCS	Signal Processor and Control Subsystem
STA	Sensor Table Assembly
STS	Shuttle Transportation System
SSF	Space Station Freedom
SUMS	Shuttle Upper-Atmosphere Mass Spectrometer
TDRSS	Tracking and Data Relay Satellite System
USML	United States Microgravity Lab

Introduction

The Orbital Acceleration Research Experiment[1] (OARE) is a triaxial accelerometer package which uses a free-floating (non-pendulous) electrostatically suspended cylindrical proofmass. The sensor assembly is mounted to a microprocessor-controlled, dual-gimbal platform in order to perform in-flight bias and scale factor calibrations. Flight data is processed and stored in the OARE flight computer reserved memory. The OARE is the third-generation Orbiter Experiment (OEX) Program accelerometer package. Its capabilities exceed both the Aerodynamic Coefficient Identification Package[2] (ACIP)* and the High Resolution Accelerometer Package[3] (HiRAP)** in sensitivity and performance. Drag measurements at typical Orbiter altitudes of 300 km become less than one micro-g, as shown in Figure 1. OARE, however, has capability to provide aerodynamic drag measurements up to altitudes of about 350 km.

---

* ACIP has flown on all OV-099 and OV-102 flights (Challenger and Columbia respectively). The ACIP sensor best resolution is 61 ugs on the lateral axis channel (Y-body).

** The High Resolution Accelerometer Package (HiRAP) is a more sensitive triaxial accelerometer package interfaced to the ACIP system. HiRAP has flown on all OV-099 and OV-102 flights subsequent to STS-5. The HiRAP accelerometers have a resolution of 1 ug, with ± 5 ug accuracy.

It should be noted that the OARE is unique in that it has the capability to perform both bias and scale factor calibrations on orbit and the sensor is a non-pendulous type accelerometer. Pendulous accelerometers, such as HiRAP, do not readily lend themselves to calibration on orbit because they are highly temperature sensitive in the micro-g range. In the past, pendulous accelerometers have depended upon ground calibrations. Experience has shown[4] ground calibration to be unreliable in predicting absolute bias on orbit. Consequently, these accelerometers are unable to measure absolute acceleration signals with accuracy and reliability. Therefore, OARE stands alone in its ability to establish exact absolute accelerations on orbit. Such measurements are crucial to interpreting many experiments on the Orbiter, such as those involving crystal growth.

The first flight of the OARE was in June, 1991 on Shuttle mission STS-40. Data was collected from launch to orbit insertion and for a period of about 3.5^d beginning approximately 5.5^d after launch. The instrument was programmed to perform a calibration sequence approximately every hour while in orbit. Some equipment problems affected the acceleration measurements; however, acceleration measurements could still be interpreted during an astronaut sleep period period (MET: 7^d). This flight provided valuable insights into the nature of determining nano-g, low-frequency acceleration drag measurements with in-flight calibrations. After STS-40, the equipment was removed and the sensor problems were isolated and repaired.

The second flight of the OARE, STS-50, was flown in July and August of 1992. The duration of the flight was more than 13 days and included 60 full calibration sequences which provided both bias and scale factor measurements for 3 axes and 3 ranges. The problems present during STS-40 had been resolved and reliable data were gathered throughout the entire orbital time period. A time interval between MET 1^d to 3^d was studied in detail in order to provide low frequency, low acceleration information for the spacelab furnace application, the Crystal Growth Facility (CGF). In addition, this relatively quiet period provided a good opportunity to evaluate the OARE measurements during a nearly circular orbit (316-325 km).

Two unexpected occurrences took place during this flight: (1) The OARE shut down earlier than expected and only 18 minutes of reentry data were taken and (2) scale factor measurements for the Y- and Z-axes in the C (most sensitive) range were unusable. The Y/Z "C" range scale factor anomaly was circumvented by using data collected during the OARE orbiter flight maneuvers. The anomalies uncovered during the STS-50 development flight have been addressed and corrected. The OARE will be flown a third time in August, 1993 on Shuttle mission STS-58.

This paper discusses the OARE instrument and its capabilities, and provides sample results from the two missions flown.

Instrument Description

Figure 2 is a schematic of OARE, showing the various instrument components. OARE is a multi-range instrument which completely covers HiRAP's re-entry measurement domain and provides a smooth measurement transition from orbit throughout re-entry. As shown in Figure 3, the acceleration range of OARE exceeds that of HiRAP. In its most sensitive range, OARE measurement resolution is less than 5 nano-g's. In this chart the frequency limits reflect the 3 db roll-off of the low-pass anti-aliasing filters. Both instruments have been designed with low band pass filters in order to make the required, low-frequency aerodynamic measurements. HiRAP has a higher data collection rate and a less steep low-pass filter roll-off, so it is able to respond to slightly higher frequencies. In fact, most of the environmental stimuli shown in this chart are theoretically observable with HiRAP. However, the ability to make absolute acceleration measurements with only ground based calibrations is highly questionable. In addition, HiRAP, a pendulous accelerometer, has a large temperature dependent bias.

In-flight Calibration

OARE bias and scale factor calibration data are acquired in flight using a dual-gimbal rotary table. A sketch of the OARE Rotating Table Assembly is shown in Figure 4.

Calibration involves measuring and applying instrument biases and scale factors. The bias and scale factor measurements are made on the basis of in-flight operations of the calibration table assembly. Together, the bias and scale factor are used to obtain an absolute reference for the measured signal. Bias determination is handled through scheduled reorientations of the sensor, and scale factor calibrations are handled through controlled rate rotations. The bias measurement accounts for instrument offset measured when little or no signal is present; the scale factor provides a means to scale the output signal across the useful range of the instrument.

The bias process for the X-axis is shown schematically in Figure 5. The sensor is shown mounted on the table, offset from the inner gimbal axis. The bias is measured by rotating the sensor 180° and comparing the measurements at 0° and 180°. The algebraic sum and difference of the two signals taken from opposite orientations equal twice the bias and bias-free signal, S_X, respectively. Specifically, the X-axis bias calibration involves rotating the inner gimbal, while the Y- and Z-axis calibrations involve rotating the outer gimbal. The total bias calibration takes 8 to 10 minutes (3 axes, 3 ranges) and is performed periodically throughout the mission. The bias measurements are processed and stored in the OARE flight computer.

Figure 6 is a schematic drawing of the sensor and table viewed along the outer gimbal axis. The sensor is offset from the rotation centers of the table such that a steady table rotation (ω) produces a measurable centripetal acceleration on the sensor. The scale factor is a function of these gimbal rotation rates, which are carefully controlled. The centripetal acceleration sensed during rotation is easily calculated, because the rotational rates and the distances from the sensor proof mass to the axes of rotation are precisely known. For a perfectly linear instrument, the scale factor is the slope defined by the ratio of centripetal measurement to sensor measurement. By rotating the table at two different rates per range, the linearity of the scale factor can be established.

Accelerometer instruments are affected by variances in physical environment including temperature, inherent electronic drift, and degradation of electronic components over time. These all impose a slowly changing bias to the measured signal. Because of these and other instrument output variations during flight, periodic bias and scale factor determinations are required to assure instrument accuracy. Slight correlations between instrument temperatures and biases have been observed in the data from STS-50.

Flight Maneuvers and Attitudes

Orbiter flight maneuvers and attitudes are scheduled during the mission in order to evaluate aerodynamic coefficients throughout different wind angles, to ascertain OARE alignment, and to establish center of mass location. The maneuvers may also be used to determine vehicle mass and moments of inertia.

The top half of Figure 7 shows prescribed aerodynamic maneuvers. These maneuvers produce centripetal accelerations which stimulate the OARE sensors. Using accurate rotational rate data from the ACIP gyros, or the orbiter IMU gryos, the OARE instrument alignment can be verified. With absolute bias and scale factor corrected data, the OARE signals can be used to establish the actual location of the Orbiter center of mass.

The lower half of Figure 7 shows other typical Orbiter flight orientations for OARE. The full drag, 'belly into the wind' attitude produces the largest, and hence most accurate, aerodynamic signal. It simultaneously produces a near zero aerodynamic acceleration signal on the X and Y axes. The calibration 'wing into the wind' attitude produces a near zero aerodynamic acceleration signal on the X- and Z-axis, isolating other low frequency acceleration components, such as gravity gradient terms. Because the instrument sensors are not located on the center of mass, a gravity gradient signal is present. The gravity gradient term has an "out-of-plane" component when the c.g. to OARE vector possesses a horizontal component. The vertical component is about 7 nano-g/inch and the horizontal component is about 3.5 nano-g/inch. The center of gravity location relative to the OARE sensor is typically about 60 inches in the X direction, 1 inch in Y, and 55 inches in Z.

Allowing the Orbiter to rotate slowly in orbit due to gravity gradient effects provides free-molecule flow conditions at different attitudes.

Data Specifications

Table 1 shows that the dynamic range of OARE is 3.2 nano-g's (C range, X instrument axis) to 25,000 micro-g's (A range, Y/Z instrument axes). This wide span is accomplished by auto-ranging. The criteria for auto-ranging is established using predetermined adaptation parameters which are instrument program variables. The bandwidth high-frequency limit is 1.0 Hz. A 6-pole Bessel filter prevents aliasing while maintaining a frequency-invariant time delay. The instrument is linear throughout its complete range, within approximately 0.1%.

Data is stored in Electrostatically Erasable Programmable Read Only Memory (EEPROM) within the OARE system itself. Data is also buffered for transmission via the Shuttle tape system which is downloaded during flight through the Tracking and Data Relay Satellite System (TDRSS). Most of the data which is stored on OARE is filtered using a trimmed-mean filter, which reduces the quantity of data and permits onboard storage of large time segments of data. This filter sorts the data, calculates a "quality index" based upon the outlier content, and eliminates a fraction of the low and high values based upon the quality index. The remaining data are then averaged. The filter parameters are input to the flight program as adaptation parameters and are chosen to provide quality low-frequency data which can be used in extracting aerodynamic quantities.

The right side of Table 1 shows table rotation durations for the scale factor measurements. During the scale factor calibration process, the table rates are such that the centripetal acceleration levels shown on the righthand side of Table 1 are registered by the sensor. The first flight calibration data indicated that the starting and stopping table angular accelerations were too high during the "A" range scale factor calibrations. Table rates for the "A" range were subsequently slowed to match "B" range rates.

End-to-End System Errors

The total end-to-end system errors have been divided and evaluated in several categories. The categories considered uncertainties in the Orbiter center of gravity, Orbiter orientation and rotation rates, and alignment of the sensor with respect to the Orbiter body axes, and a collection of effects which are grouped into a marginal category. The marginal category includes effects which, by themselves, contribute errors less than the resolution of the instrument, such as Orbiter interactions with the Earth's magnetic field, cabin air leakage and outgassing, solar radiation pressure, and the gravitational attraction of the various components of the Orbiter on the OARE proofmass. For all these sources, the best RSS error, during a quiet period in the C range, is estimated to be about 15 nano-g. Recent estimates[5] indicate that a more realistic value for total error is about 45-50 nano-g's, the increase being due to noise which is still present during quiet times.

OARE Flight Data Analysis

OARE has flown on two flights to date, for 7 days on Columbia STS-40 in the summer of 1991 in conjunction with the SLS-1 and for 13 days on Columbia STS-50 in the summer of 1992, in conjunction with the USML-1. Data analysis from these flights is accomplished in the manner shown on the flowchart of Figure 8.

The OARE instrument produces continuous analog data. The data is filtered using a 6-pole Bessel filter, and then digitized to produce a data rate of 10 samples per second. This data is telemetered from the Orbiter during flight via Pulse Code Modulation (PCM). The PCM data stream is subsequently transcribed into a digital format, which is the data source for the processing shown on this flowchart.

Orbiter attitude (from which gravity gradient effects can be calculated) and rotational motion (centripetal acceleration) contribute to the OARE measured signals. Once the Orbiter c.g. has been established, these signal components can be accurately determined and removed using orbiter state vectors which are available from Calibrated Ancillary System (CAS) data support groups or from the Customer Extended Facility (CEF) of the JSC Mission Control Center (MCC). The remaining absolute acceleration is the starting point for aerodynamic analysis. Aerodynamic coefficients can be calculated using the orbiter mass, reference area, and dynamic pressure as illustrated in Fig. 8. Density can be determined from an experiment such as the Shuttle Upper-Atmosphere Mass Spectrometer (SUMS) experiment[6], or atmospheric models[7,8] based on theory and previous flight data. The ratio of aerodynamic forces or coefficients (e.g. C_N/C_A) depends only on the acceleration signals, and hence is a direct OARE measurement.

STS-40 Results

The primary payload for STS-40 was Space Life Sciences Lab, SLS-1. This laboratory filled much of the payload bay and shielded the OARE instrument from the sun, minimizing temperature variations.

During STS-40, the sensor exhibited unanticipated random bias shifts, and the absolute signal level could not always be derived[9]. Post-flight analysis revealed that some degradation of the sensor had occurred over the five year interval between the instrument construction and flight. The causes of degradation were identified and corrected prior to the STS-50 mission. Nevertheless, some important aerodynamic results were observed on orbit during STS-40. Figure 9 shows flight-stored and trim filtered data for a two-hour section of flight during a prescribed quiet period (astronauts asleep). The signals closely match the aerodynamic model (using the

Hedin MSIS-83 model atmosphere[7]). Linear adjustments have been made to account for the bias jumps in the case of the OARE Z-axis.

A second chart, Figure 10, shows the OARE aero maneuvers, pitch, yaw, and roll. The X and Z sensors (spacecraft coordinates) are seen to be stimulated during pitch, as is the Z sensor during roll. The Y sensor shows little activity because of its small Y-axis displacement relative to the orbiter center of mass. The on-board, flight processed data is superimposed on the full data rate telemetry signal, confirming that the on-board trim-mean digital filter is working properly.

Figure 11 is a pictorial summary of the activities which occur during an OARE mission. The Ground Support Equipment (GSE) is connected to the OARE before flight in order to install adaptation parameters and permit instrument checks. The GSE is installed after the flight in order to download all data files created during flight. The chart in the figure is an OARE data set from the STS-40 flight showing the periapsis and apoapsis changes in aerodynamic drag during four orbits.

After the flight, the electrostatic sensor was examined and found to contain beryllium oxide crystal growth on the beryllium proof mass. This growth was traced to shipping material problems prior to initial installation. There were burn marks on both the suspension electrodes and the proofmass which were attributed to electrical arcing. The radium sulfate proofmass discharge chip was found to be improperly grounded due to degradation of the epoxy used to mount the chip to the sensor housing. These problems were corrected prior to mission STS-50.

STS-50 Results

On STS-50[5], the problems associated with STS-40 were found to be resolved; the instrument did not exhibit any of the random bias shifts seen previously. An examination of the onboard processed data showed that the sensor performed very well. The sensor exhibited very little change of bias with temperature. Futhermore, the OARE "trimmed-mean" filter, which produces the processed data, operated even better than expected in reducing the noisy signal to useable accelerations. During this flight, there were two crews which worked in 12 hour shifts, so there were no strictly quiet periods available. Figure 12 shows digitally filtered data between 38 and 84 hours mission elapsed time (MET). This data was analyzed in support of the CGF and shows the acceleration levels at the Orbiter center of gravity. The data in Figure 12 was processed from telemetered data in the same manner as occurred during flight, i.e., using a trimmed-mean filter, but with different filtering parameters (i.e. 200 second window compared to 50 seconds). The accelerations at the OARE were corrected to those at the orbiter c.g. Note that the X and Z (spacecraft body coordinate) signals are not zero and appear to oscillate slightly with about the same frequency and out of phase. Great care has been taken to assure that all known possible gravitational and electromagnetic forces have been reexamined and none produces the observed effect. It is tentatively concluded that the orbiter is creating the environment observed. The phenomenon is under continued investigation.

The primary mission of STS-50 was the first flight of the U. S. Microgravity Laboratory, USML-1. As in STS-40, the primary experiment equipment was mounted in the shuttle payload bay in such a manner that the OARE instrument was shielded from the sun. It is not known at this time whether there were activities within the USML-1 experiment which may have contributed to the oscillating signal seen in Figure 12.

During data analysis, it was observed that the Y and Z channels gave erroneous readings in the C range during the constant rate scale factor table rotations. This problem was traced to table motor jitter. Subsequent to STS-50, the OARE was examined and it was discovered that the table jitter was actually saturating the A/D signal conditioner during Y and Z axis scale factor rotations in the C range. The problem has been corrected by the addition of a larger capacitor in the C range signal filter circuit.

As stated earlier, scale factor calibrations for OARE in the C range were successfully performed on this flight using the data taken during the OARE maneuvers. The calibrated HiRAP data was used with the attitude and rotation rate data to establish the location of the orbiter center of mass by a method similar to that done previously on STS 61-C[10].

STS-58 Preparations

The next scheduled flight of OARE is in August of 1993. The primary Shuttle mission will be the second flight of the Space Life Science Lab, SLS-2. It is anticipated that the aerodynamic signal will be similar to the previous flights, and the instrument temperature conditions and flight attitudes will be similar to STS-40. No problems are anticipated with data collection and no special consideration is required for post-flight processing. However, because of knowledge gained on STS-50, some changes have been made in the operation of the instrument for this flight. One significant change is that the scale factor measurements will be obtained only once during active crew periods and twice during the sleep period. This is desirable since it was difficult to assure that the instrument remained in the most sensitive range for scale factor calibration during active crew periods. The bias calibration will be performed approximately once every four hours, as on STS-50.

Summary

OARE is an accelerometer with nano-g sensitivity which is capable of in-flight calibrations and is used to examine and evaluate Space Shuttle Orbiter aerodynamics during Earth orbit and during reentry. There have been two flights to date, STS-40 with SLS-1, and STS-50 with USML-1. The next flight will be aboard STS-58, with SLS-2.

During the STS-40 flight, the instrument exhibited some erratic behavior in which the sensor changed its bias randomly along all three axes. However, some useful data was still collected during this flight. Portions of this data have been analyzed and correspond to expected density variations theoretically predicted for the Shuttle's orbit. The data demonstrated the potential of OARE to measure atmospheric drag at orbital altitudes. The sensor was dismantled after the flight and proved to be faulty; necessary repairs were made.

Data gathered during the next flight, STS-50, showed a vast improvement in the operation of the sensor. All nine bias calibrations worked exceptionally well and exhibited very little change with temperature. These calibrations, along with the "trimmed-mean" averaging technique proved to be the key in establishing reliable absolute acceleration measurements on orbit. Two of the six scale factor calibrations were not acceptable, namely the Y and Z axes in the sensor's most sensitive range. However, reliable estimates of these scale factors were made from OARE data taken during pitch, yaw and roll maneuvers. After corrections for the scale factors, filtered data (averaged over 200 seconds) was used to characterize the absolute acceleration environment at the Orbiter's center of gravity and at the USML crystal growth experiment during part of this flight. Analysis of the remainder of the data from this flight is in progress. Subsequent to the STS-50 landing, OARE was removed from the Orbiter, and the scale factor problem was isolated and corrected. No problems are anticipated in OARE's upcoming flight, STS-58.

References

[1] Blanchard, R.C., Hendrix, M.K., Fox, J.C., Thomas, D.J., and Nicholson, J.Y., "The Orbital Acceleration Research Experiment," Journal of Spacecraft and Rockets, Vol. 24, No. 6, Nov.-Dec. 1987, pp. 504-511.

[2] "ACIP/HiRAP End Item Specification," Drawing No. 3291583, Bendix Corp., Aerospace Systems Div., Ann Arbor, MI, May, 1982.

[3] Blanchard, R.C.; and Rutherford, J.F.: The Shuttle Orbiter High Resolution Accelerometer Package Experiment: Preliminary Flight Results. Journal of Spacecraft and Rockets, vol. 22, No. 4 July-August 1985, p 474.

[4] Blanchard, R. C., Larman, K. T., Moats C. D., "Flight Calibration Assessment of HiRAP Accelerometer Data," AIAA Paper 93-0836, January 1993.

[5] Blanchard, R.C., Nicholson, J.Y., and Ritter, J.R., "Preliminary OARE Absolute Acceleration Measurements on STS-50," NASA TM-107724, Feb., 1993.

[6] Blanchard, R.C.; Duckett, R.J.; and Hinson, E.W.:The Shuttle Upper Atmosphere Mass Spectrometer Experiment. Journal of Spacecraft and Rockets, vol 21, no.2 March-April 1984, pp. 202-208.

[7] Hedin, A. E., "A Revised Thermospheric Model Based on Mass Spectrometer and Incoherent Scatter Data: MSIS-83," Journal of Geophysical Research, Vol. 88, December 1983, pp. 10170-10188.

[8] U.S. Standard Atmosphere, 1976. NOAA, NASA USAF, 1976

[9] Blanchard, R.C., Nicholson, J.Y., and Ritter, J.R., "STS-40 Orbital Acceleration Research Experiment Flight Results During a Typical Sleep Period," Microgravity Science and Technology, Vol. 2, 1992, pp. 86-93.

[10] Blanchard, R.C., Hinson, E.W., Rarefied Flow Pitching Moment Coefficient Measurements of the Shuttle Orbiter, ICAS-88-1.5R1, Jerusalem, Israel, August 1988.

Table 1 OARE sensor and calibration table specifications

WEIGHT (lbs) : 117
SIZE (in) : 16.8 x 41.5 x 13.4
POWER (watts) : 110

SENSOR			SCALE FACTOR CALIBRATION			
Range	Full Scale X Axis ($10^{-6}g$)	Full Scale Y, Z Axis ($10^{-6}g$)		Range	Angular Velocity (rad / sec)	Travel Time (sec)
			X Axis			
A	10000	25000		A	2.0	2.9
B	1000	1770		A	1.0	6.0
C	100	150		B	0.6325	8.2
				B	0.4472	11.7
				C	0.1455	21.5
				C	0.0970	32.3
Range	Resolution X Axis ($10^{-9}g$)	Resolution Y, Z Axis ($10^{-9}g$)	Y,Z Axis			
A	320.0	800.0		A	2.0	2.9
B	32.0	57.0		A	1.0	6.0
C	3.2	4.8		B	0.5891	8.8
				B	0.3905	13.4
				C	0.1390	22.6
				C	0.1193	26.3

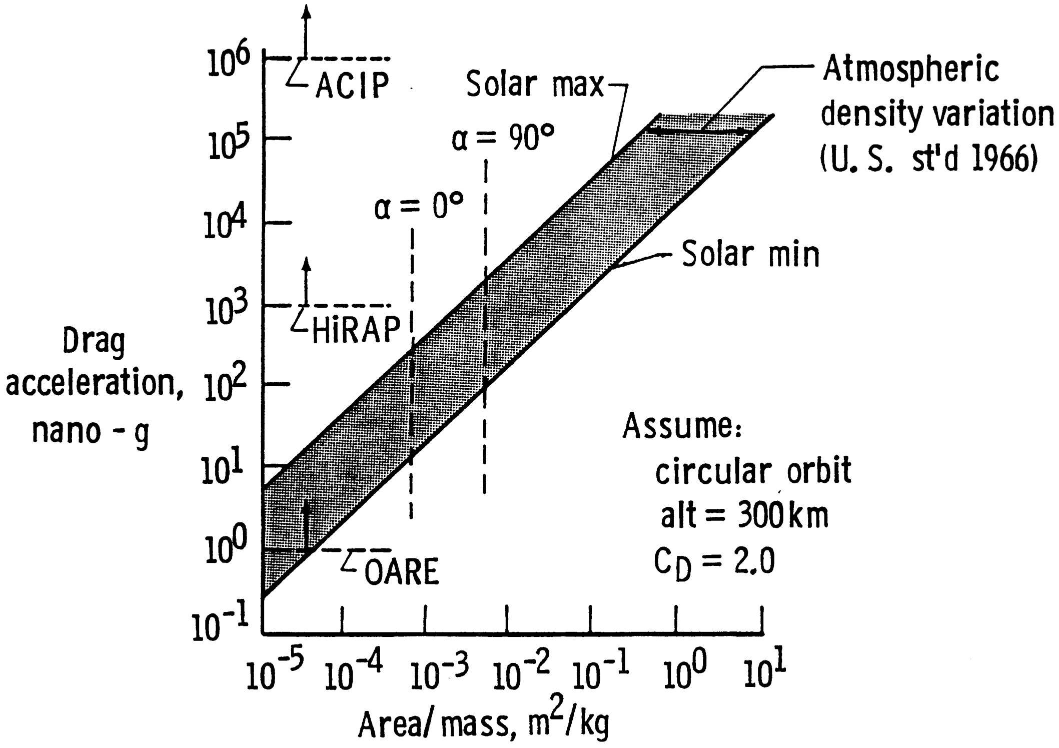

Fig. 1 Predicted Shuttle orbital drag acceleration at 300 km altitude.

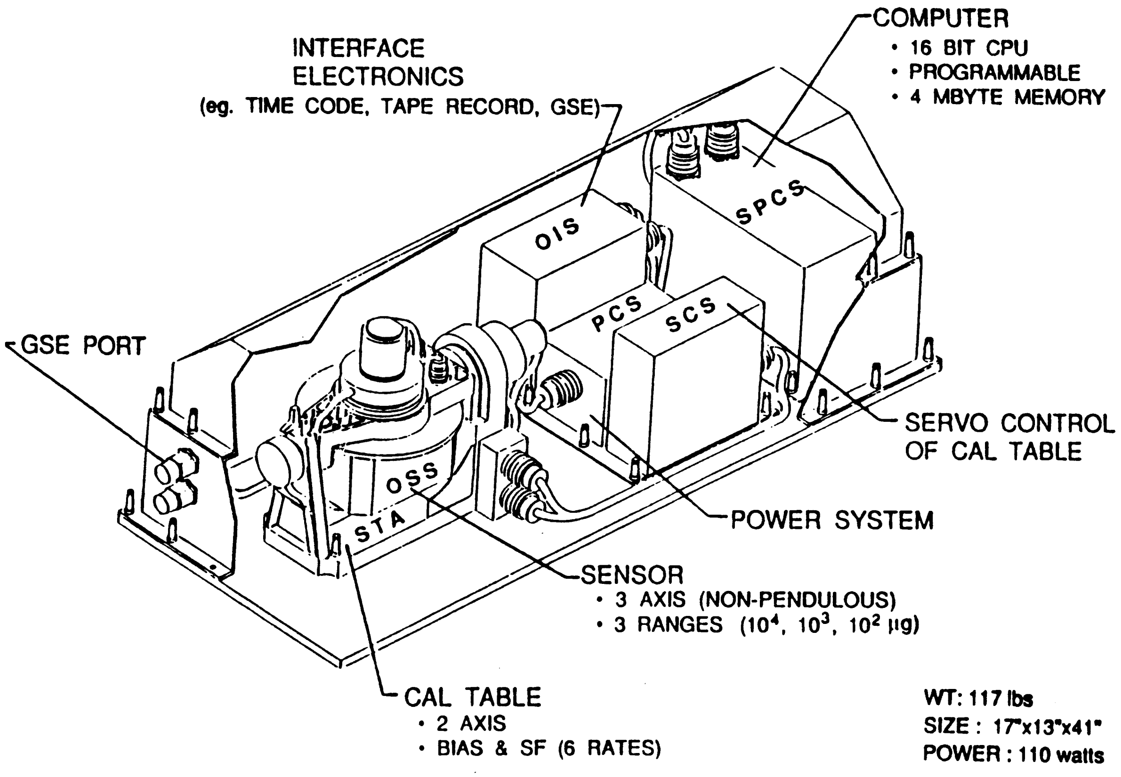

Fig. 2 OARE packing layout schematic.

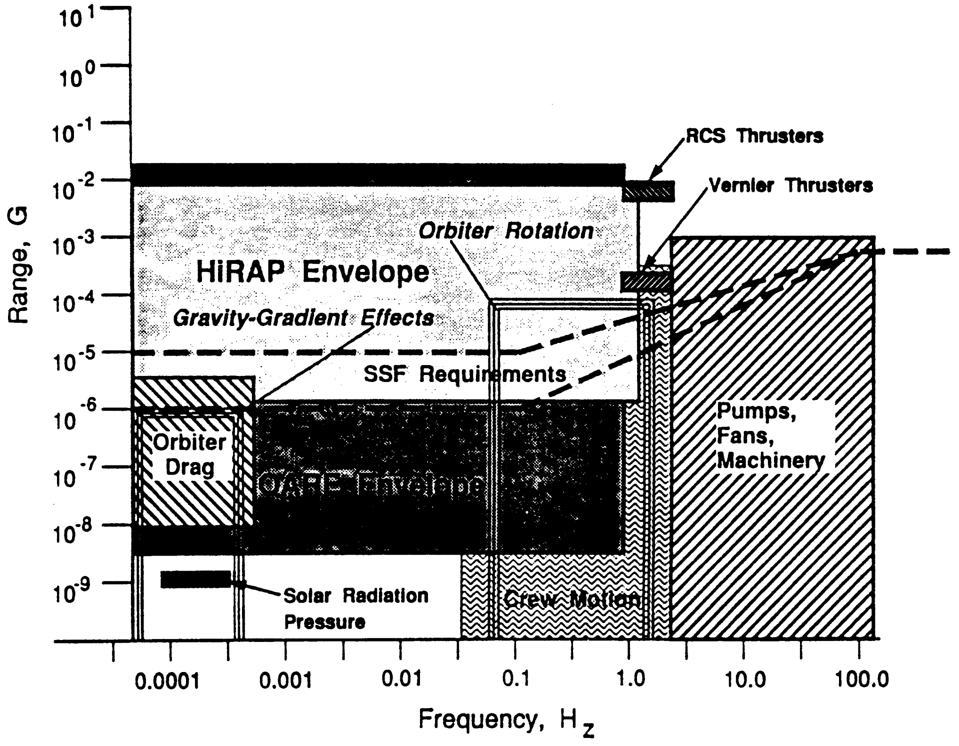

Fig. 3 HiRAP and OARE operating envelopes with Orbiter environments and SSF requirements.

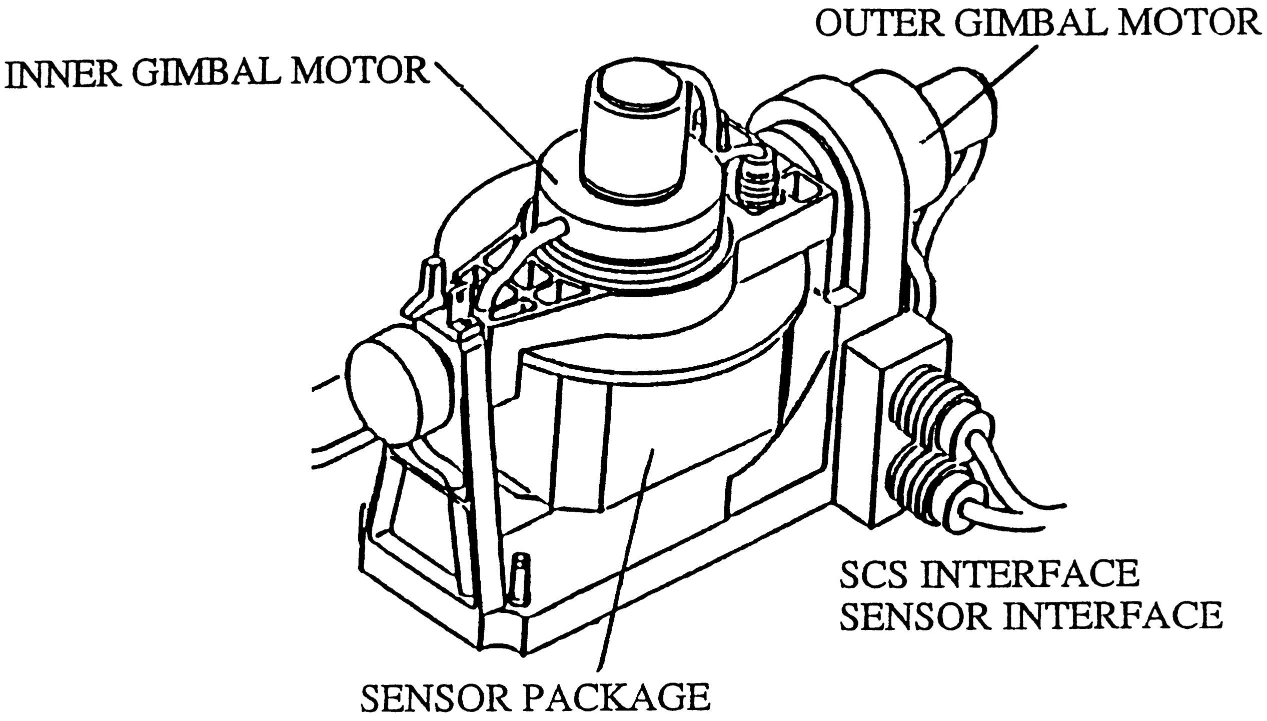

Fig. 4 Rotating table assembly sketch.

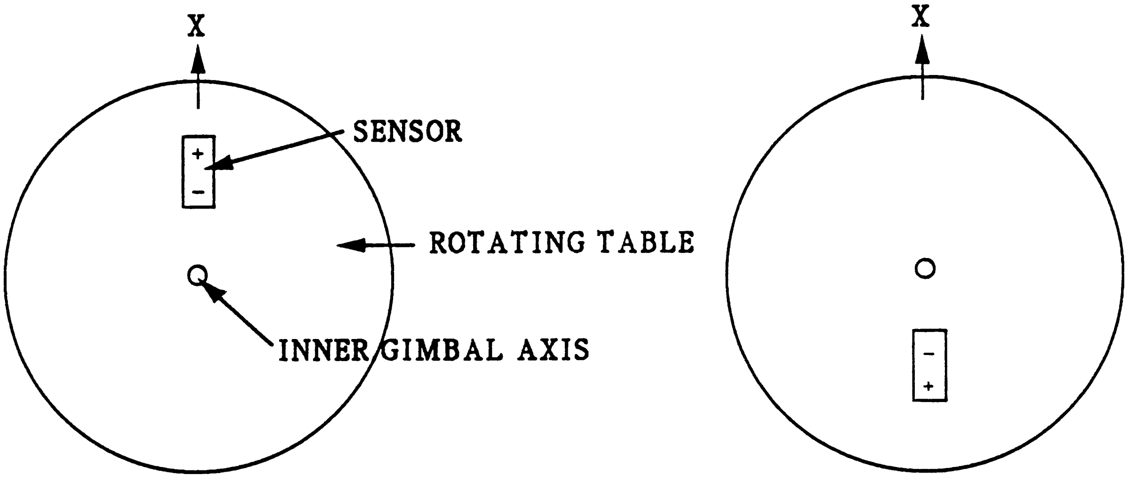

TABLE AT 0 DEGREES

$A_{X_0} = S_X + B_X$

TABLE AT 180 DEGREES

$A_{X_{180}} = -S_X + B_X$

ADD: $A_{X_0} + A_{X_{180}} = 2B_X$

SUBT: $A_{X_0} - A_{X_{180}} = 2S_X$

Fig. 5 Bias calibration illustration.

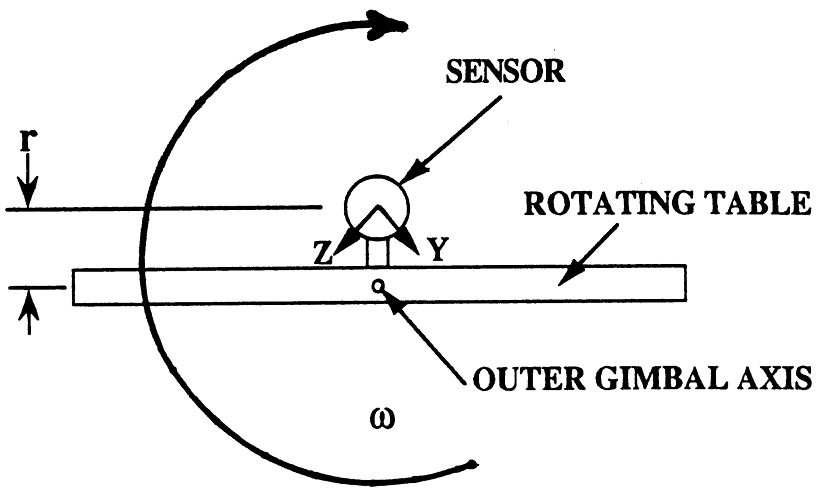

$$\mathbf{SCALE\ FACTOR} = \omega^2 r \,/\, a_{\mathrm{sensor}}$$

Fig. 6 Scale factor calibration illustration.

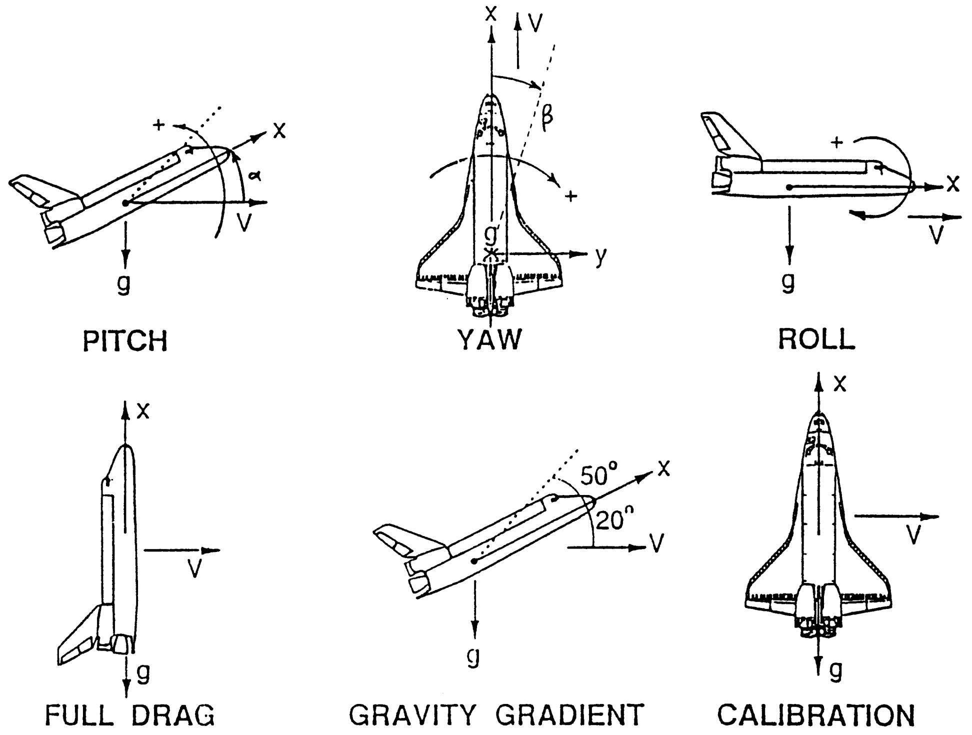

Fig. 7 OARE maneuvering orientations and flight attitudes.

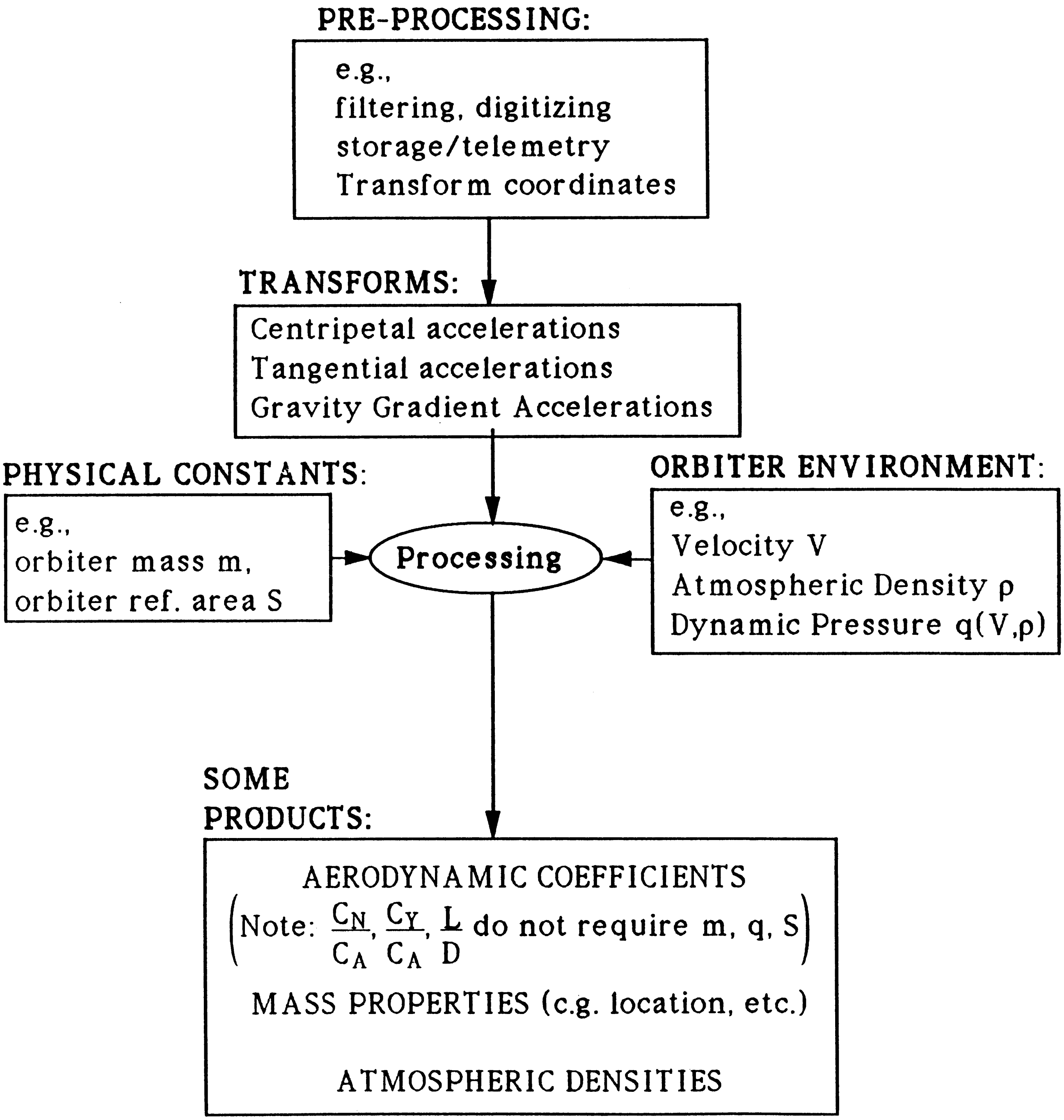

Fig. 8 OARE data processing flowchart.

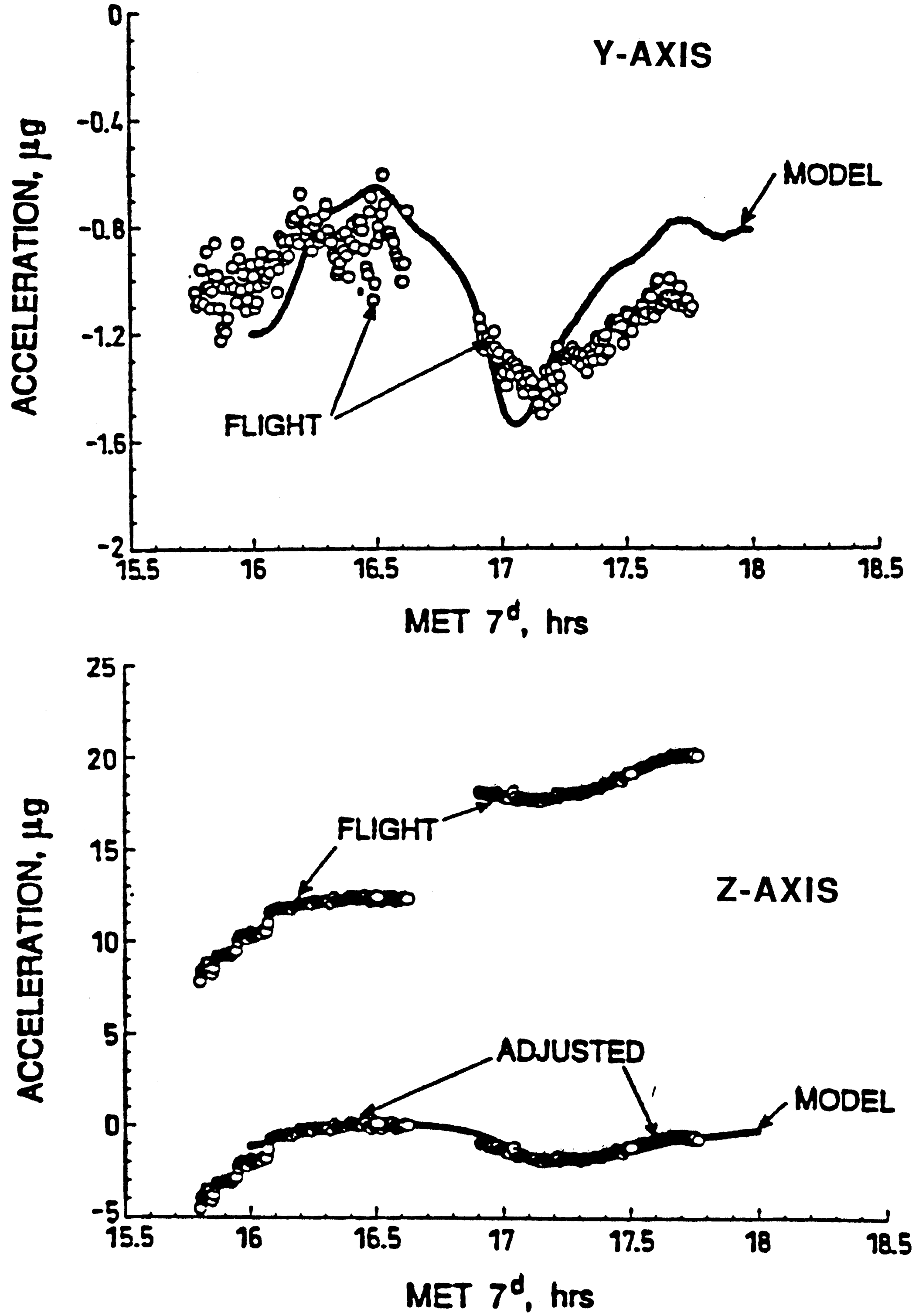

Fig. 9 OARE flight data comparison with Hedin atmosphere model, STS-40.

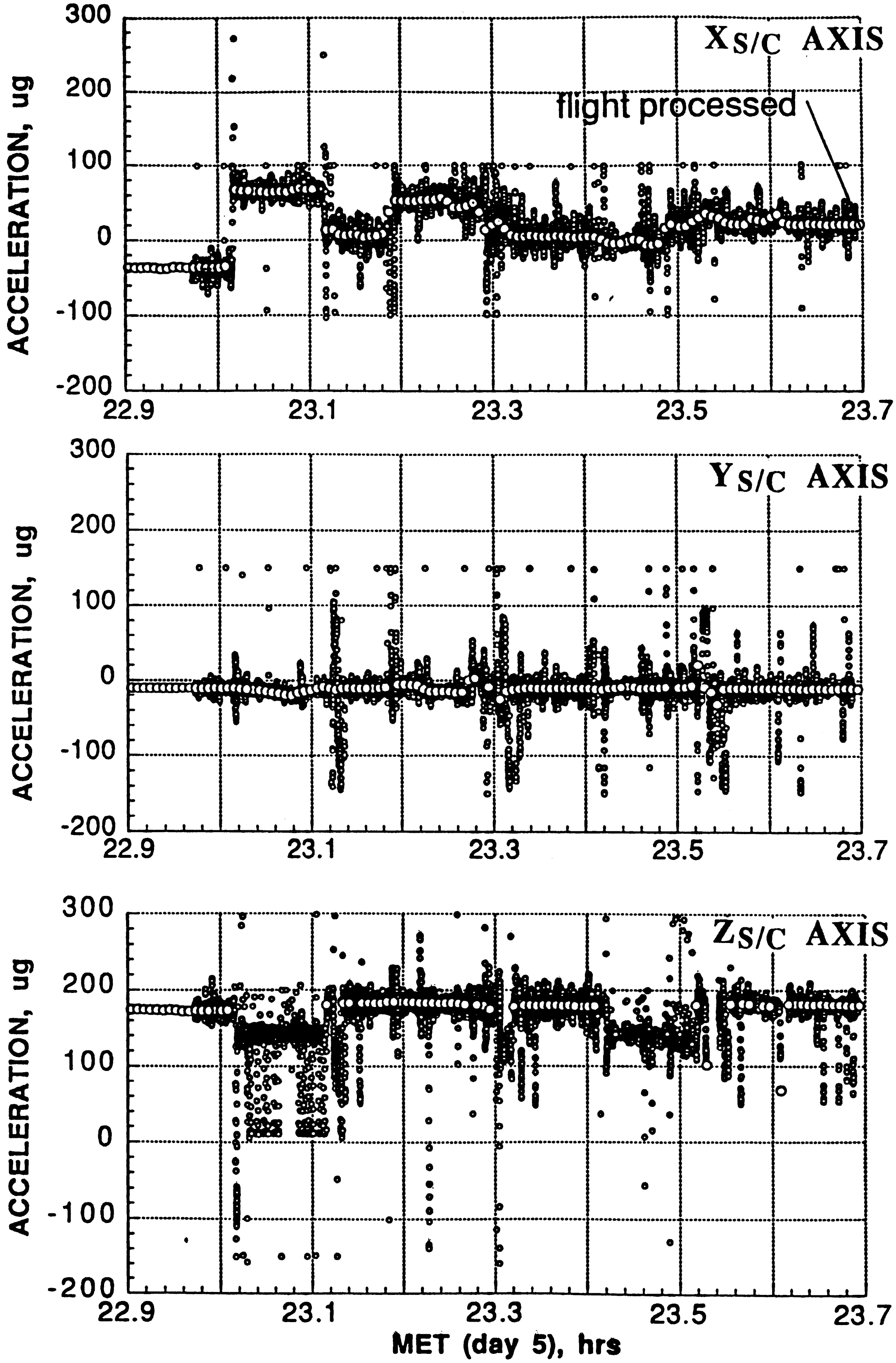

Fig. 10 OARE flight data during pitch, yaw, and roll maneuvers, STS-40.

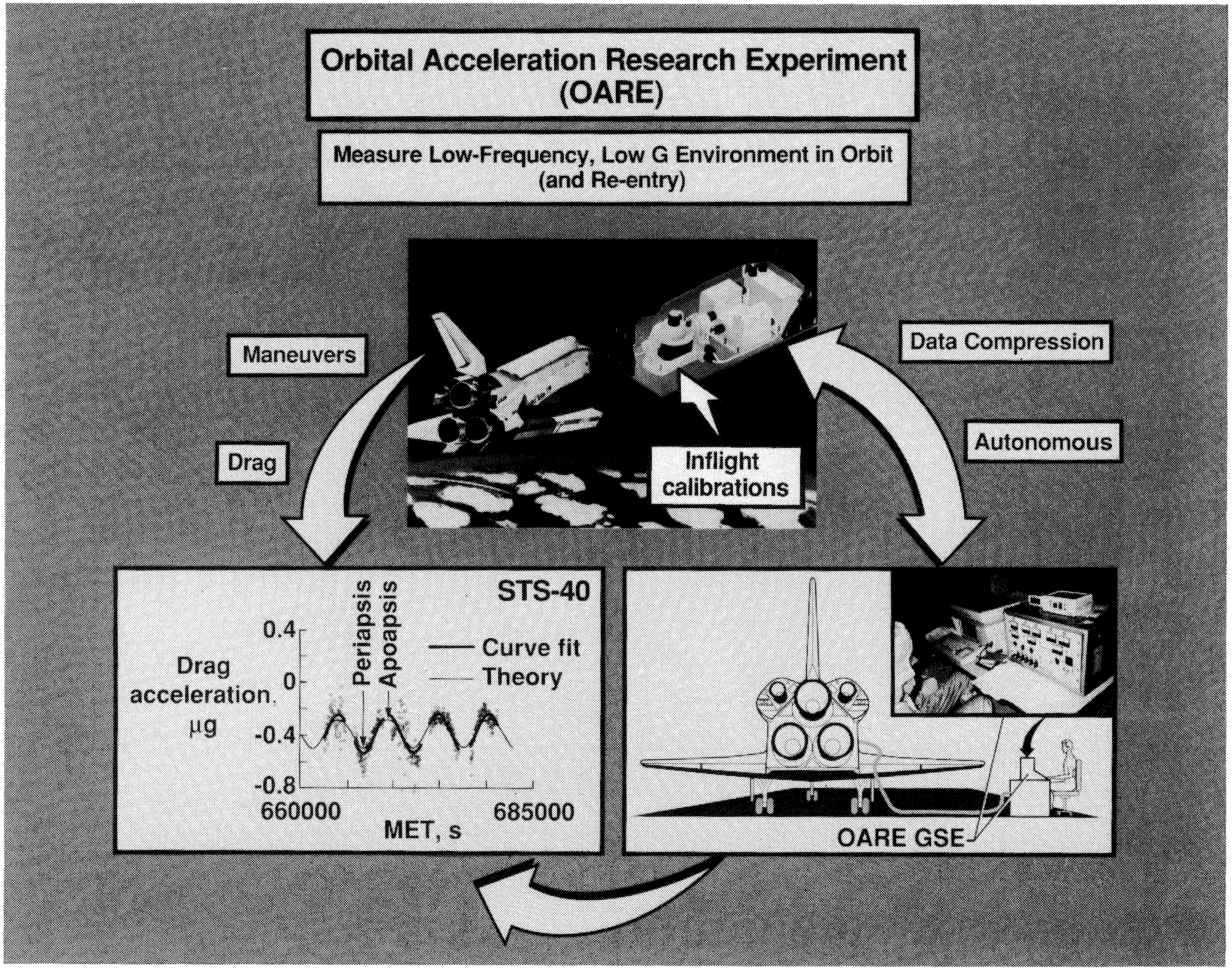

Orbital Acceleration Research Experiment (OARE)

Measure Low-Frequency, Low G Environment in Orbit (and Re-entry)

Maneuvers

Drag

Inflight calibrations

Data Compression

Autonomous

Fig. 11 OARE mission overview (objectives, capabilities, and results).

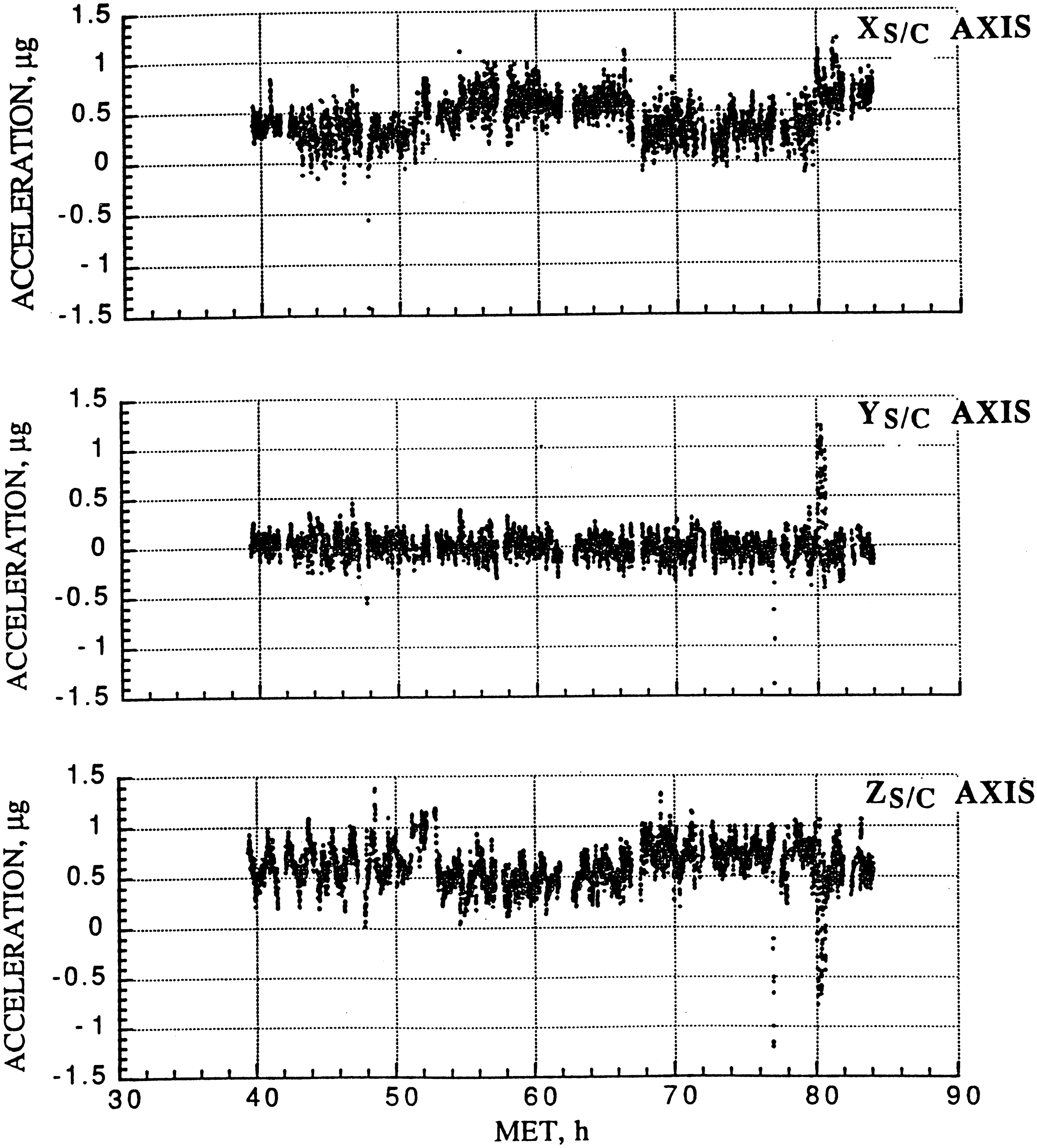

Fig. 12 OARE acceleration measurements at the orbiter center of gravity, STS-50.

DEVELOPMENT FLIGHT INSTRUMENTATION (DFI) AND THE AEROTHERMAL INSTRUMENTATION PACKAGE (AIP)

David A. Throckmorton
NASA Langley Research Center
Hampton, VA

SUMMARY

The Development Flight Instrumentation (DFI) and the Aerothermal Instrumentation Package (AIP) provided for measurements of aerodynamic-surface temperature and pressure at discrete locations distributed about the external surfaces of the orbiter *Columbia*. The DFI system provided for collection of these data, over the complete configuration (both windward and leeward surfaces), during the Orbital Flight Test Missions of *Columbia*. The AIP system, which measurement complement comprised a subset of the DFI (limited to leeside surfaces), was operated on flights in conjunction with the Shuttle Infrared Leeside Temperature Sensing and Shuttle Entry Air Data System experiments.

INTRODUCTION

During the Shuttle Orbital Flight Test (OFT) missions, STS-1 thru -5, the Orbiter *Columbia* was equipped with a large complement of diagnostic instrumentation referred to as the Development Flight Instrumentation (DFI). DFI measurements were implemented to provide the requisite data for post-flight certification of space-shuttle subsystems designs, prior to the start of operational missions. Included among the DFI measurement complement, and of particular interest to aerothermodynamic researchers, were measurements of both static pressure and surface temperature at the orbiter's aerodynamic surface, at multiple locations distributed about the vehicle.

A subset of the aerothermodynamic-related DFI instrumentation was reactivated for missions STS-28, -32, -35, and -40, through implementation of an Orbiter Experiments (OEX) system referred to as the Aerothermal Instrumentation Package (AIP). The AIP-selected measurements were intended to provide corollary data on flights of the OEX Shuttle Infrared Leeside Temperature Sensing (SILTS) and Shuttle Entry Air Data System (SEADS) experiments.

NOMENCLATURE

AFRSI	advanced flexible reusable surface insulation
AIP	Aerothermal Instrumentation Package
ANSI	American National Standards Institute
DFI	Development Flight Instrumentation
FM	frequency modulation
FRSI	flexible reusable surface insulation

HRSI	high-temperature reusable surface insulation
LRSI	low-temperature reusable surface insulation
OEX	Orbiter Experiments
PCM	pulse code modulation
RCS	reaction control system
SEADS	Shuttle Entry Air Data System
SILTS	Shuttle Infrared Leeside Temperature Sensing
SIP	strain isolator pad
TPS	thermal protection system

DEVELOPMENT FLIGHT INSTRUMENTATION

The Development Flight Instrumentation (DFI) system flew aboard the Orbiter *Columbia* during the vehicle's five Orbital Flight Test (OFT) missions, STS-1 thru STS-5. DFI measurements were implemented to provide vehicle designers with the requisite flight data for postflight certification of space-shuttle element subsystems designs, prior to the start of operational shuttle missions. The DFI system was comprised of sensors, wire harnessing, data-handling electronics, and flight data recorder.

DFI measurements provided data relative to the performance of a multitude of flight system components, not only on the orbiter, but also on the external tank, the solid rocket motors, and the Space Shuttle Main Engines. Data types included temperatures, pressures, accelerations and vibrations, currents and voltages, and forces, stresses and strains, etc. In flight, these data were sampled at varying frequencies depending on the data type and required time-resolution. Some measurements provided PCM-encoded digital data recorded at data rates as low as 1 hz, while other measurements provided data which was recorded as continuous, FM-encoded analog data.

While the DFI sensors were, by and large, located integrally with subsystems hardware, the performance of which they were intended to document, much of the supporting data-handling electronics was mounted on a large cruciform-shaped "pallet" mounted in the orbiter's payload bay (Fig. 1). The DFI pallet structure and the data-handling electronic components it carried occupied a significant portion of the aft payload-bay volume, and weighed some 10,000 lbs. Wire harnesses which "snaked" throughout the orbiter structure connected sensors to the data-handling electronic components located on the DFI pallet.

Included among the orbiter's DFI sensors, and of particular interest to aerothermodynamic researchers, were measurements of static pressure and surface temperature at the orbiter's aerodynamic surface, each at multiple discrete surface locations distributed about the orbiter. While these measurements were initially intended simply to provide information for confirmation of the adequacy of orbiter aerodynamic and aerothermal design predictions, it was clear to the Orbiter Experiments community that these data had a value far greater than their use as simple design "checkpoints." Like other data to be gathered by OEX-unique instrumentation, the DFI data, too, represented heretofore unavailable, benchmark flight information for a lifting vehicle operating in the hypersonic flight environment.

Temperature Measurements

Thermocouples

Development Flight Instrumentation measurements of the orbiter's aerodynamic-surface temperature were obtained at some 252 surface locations (Fig. 2). These measurements were obtained using thermocouples installed at the aerodynamic surface of the thermal protection system (TPS) materials, in thermal contact with the TPS surface coating, at its interface with the underlying thermal protection material (Ref. 1). Orbiter thermal protection materials in which thermocouples were installed included flexible reusable surface insulation (FRSI), and both the high- and low-temperature reusable surface insulations (HRSI and LRSI, respectively).

FRSI was used in areas where the maximum surface temperature was anticipated to be less than 1160 °R (Ref. 2). The FRSI material is a Nomex[1] felt sheeting which is directly bonded to the vehicle structure (Fig. 3). The Nomex felt is coated with a silicon rubber film with a nominal thickness of 5 to 8 mils. Thermocouple installation in this material was achieved by cutting a slit in the silicon coating and laying the thermocouple bead into place within this slit, with the lead wires extending through the backside of the material. After placement of the thermocouple, a patch of the silicon coating material was applied to protect the thermocouple wires.

LRSI (white tile) was used in areas where the maximum surface temperature was anticipated to remain below 1660 °R; and HRSI (black tile) was used for areas of anticipated maximum temperature up to 2760 °R (Ref. 2). The LRSI and HRSI silica tiles are bonded to a strain isolator pad (SIP) of uncoated FRSI material, which is in turn bonded to the vehicle structure (Fig. 3). Thermocouples were installed at the aerodynamic surface of these tiles by placement in a shallow trench, of width and depth approximately equal to the thermocouple wire diameter (0.010 in.), which was cut in the silica tile material prior to the application of the surface coating. The uninsulated thermocouple wires lie along the surface for approximately 0.75 in. on either side of the bead, to minimize heat conduction along the wire, before entering the tile through holes drilled normal to the tile surface. The reaction cured glass (RCG) coating, nominally 0.015 in. thick, was then applied to the aerodynamic surface of the tile. Because the coating is thin and its thermal conductivity is high, compared with the underlying silica material, it is essentially isothermal at high surface temperatures. Therefore, thermal contact between this coating and the thermocouple bead ensured that the actual surface temperature was measured.

Two types of premium-grade thermocouples were used for orbiter TPS temperature measurements: chromel-alumel (ANSI type K), and platinum-platinum/13-percent rhodium (ANSI type R). The selection of thermocouple type used at each measurement location was based upon the maximum temperature level anticipated to occur at that location during entry.

The DFI also included temperature measurements in-depth, within the TPS materials, at some 19 locations, and along TPS tile sidewalls within the gaps between tiles at 16 locations.

Radiometers

Installation of thermocouples was incompatible with the reinforced carbon-carbon (RCC) material of the orbiter's nosecap and wing leading edges. Consequently, where temperature measurements were

---

[1] Nomex is a registered trademark of E. I. duPont de Nemours & Co., Inc.

to be made of these structures, radiometers viewing the backface of the RCC material were used to obtain temperature measurements during entry.

Heat-Flux Measurements

The STS-1 and -2 DFI-complement of instrumentation included surface calorimeters, for direct determination of heat flux, at some 30 locations on the upper surface of the fuselage and wing, and an additional 16 locations on the fuselage side and orbital maneuvering system pod (see Fig. 2). An inability to accurately interpret the STS-1 and -2 data obtained by these calorimeters, coupled with the good quality of data which had been obtained with the thermocouples, resulted in a decision to replace the calorimeters with surface thermocouples for STS-3 and subsequent flights.

Pressure Measurements

Aerodynamic surface-pressure measurements were obtained at some 200 locations distributed about the orbiter vehicle in a manner similar to the surface-temperature measurements. Each pressure transducer was capable of sensing the pressure level within one of eight distinct measurement ranges. The selection of measurement range, and thus transducer implemented, at any specific measurement location was dependent on the flight phase (ascent or entry) during which the primary data were to be obtained, as well as the anticipated magnitude of the pressure to be measured at that location.

Fifty-six (56) of the DFI surface-pressure measurements were made in the 0-15 psia measurement range, and were primarily intended to provide vehicle ascent aerodynamic pressure data. The remaining 144 measurements were primarily intended to provide aerodynamic surface pressure data during entry. The transducers utilized to obtain the entry pressure data were sensitive to pressures within measurement ranges which varied from a high-range of 0-0.2 psia to a low-range of 0-0.01 psia.

All DFI pressure transducers were physically mounted on the orbiter's internal structure, as close as practicably possible to the surface orifice through which the static pressure was to be sensed. Thus, influences of both tube losses and aerodynamic pressure transients on the sensed pressures were minimized.

Data Handling System

Analog-to-Digital Conversion

The pulse-code-modulation (PCM) units of the DFI provided digitization of sensor output data, both temperature and pressure, at a resolution of 8 binary bits. Of the resulting 256 (2^8) discrete measurement levels available, the DFI data system was set-up to provide for 250 levels to span the selected full-scale range of each data channel, with the remaining levels available for over-ranging (Ref. 1).

Pressure Transducer Ranging

The DFI data-handling system's assignment of full-scale ranges to pressure transducers presumed an identically-zero output voltage at a zero-pressure (or hard-vacuum) condition. Having been configured in this manner, the DFI data-handling system was **incapable** of recording negative transducer-output voltages. Unfortunately, many of the DFI pressure transducers exhibited a negative output voltage (bias) at the zero-pressure condition. Since the DFI data system could not record these negative outputs, the magnitudes of these zero-pressure biases were not determinable.

Data Rates

Temperatures. All aerodynamic-surface-temperature measurements were recorded at a data rate of 1 hz.

Pressures. All surface-pressure measurements intended primarily to provide ascent data were recorded at a data rate of 10 hz. These included all of the 0-15 psia transducers, plus a group of 7 lower-range transducers which were intended to sense orbiter base pressure. All other aerodynamic-surface-pressure measurements were recorded at a data rate of 1 hz.

Data Recording

DFI data were recorded on a DFI-dedicated flight data recorder. DFI data were also telemetered to the ground during entry.

Sensor Calibration

Thermocouples

DFI thermocouples were **not** individually calibrated. Raw thermocouple output data were processed to engineering units postflight using standard thermocouple calibration tables.

Pressure Transducers

DFI pressure transducers were **not** individually calibrated. As an "Acceptance" test, the outputs of each pressure transducer provided by the vendor were checked against a "standard," linear calibration curve established in the specification for transducer procurement (different for each transducer type, i.e., full-scale range). Transducers having outputs which fell within a band of ±2-percent of transducer full-scale output about the "standard" calibration curve were "accepted" for use in the DFI system. No further calibrations were performed on individual transducers. Postflight processing of raw transducer output data to engineering units was performed using the "standard" calibration curve for **all** transducers for each measurement range.

Since none of the DFI pressure transducers had been individually calibrated, researchers attempted postflight to improve the accuracy of the measured pressure data by empirically determining the zero-pressure output bias (intercept of the calibration curve) of individual pressure transducers. This was accomplished by observing on-orbit (hard vacuum) sensor output data to document the zero-pressure bias. As previously indicated (see above, *Pressure Transducer Ranging*), many transducers exhibited a negative output bias at this condition, which was not determinable by the DFI data system. Consequently, the accuracy of the flight data obtained by these transducers could not be empirically improved, and cannot be adequately assessed.

Flight History and Data Availability

The Development Flight Instrumentation system was aboard *Columbia* on missions STS-1 thru-5. However, mission unique circumstances limited the amount of hypersonic entry temperature and pressure data collected on these flights.

On missions STS-1 and -4, failures of the onboard flight data recorder precluded collection of data when the orbiter was not in communications contact with a ground telemetry station. Consequently, data from these flights, either temperature or pressure, are available only for flight conditions of approximately Mach 12 and below.

On STS-2, the pressure instrumentation were not "powered-up" during entry. This was the result of a constrained orbiter-power budget during entry on this mission, due to an in-flight failure of one of the orbiter's three fuel cells.

Pressure data were obtained over the complete entry trajectory only on missions STS-3 and -5.

Temperature data were obtained over the complete entry trajectory only on missions STS-2, -3, and -5. The DFI-derived surface-temperature data from STS-2, -3, and -5 have been processed to infer aerodynamic heat-transfer rates, using the methodology described in reference 3. The resulting orbiter flight heat-transfer data are contained in references 4-6.

AEROTHERMAL INSTRUMENTATION PACKAGE (AIP)

Following the STS-5 mission, the Orbiter *Columbia* was removed from flight status and ferried to the orbiter fabrication plant at Palmdale, California, for the purpose of modification to enable *Columbia* to carry Spacelab payloads. As part of what was known as the "Spacelab-Only Mod," the Development Flight Instrumentation pallet and associated hardware were removed from the orbiter's payload bay. Much of the wiring which had connected DFI sensors to the data-handling electronics located on the pallet was also stripped from the vehicle. Wire harnesses which connected the sensors to the data-handling electronics were removed to points as close to the sensors as were practicably possible. Selections of where wire harnesses would be terminated were based primarily upon trade-offs between residual wire-harness weight to remain in the orbiter structure, versus the required labor hours and costs associated with removal. Many of the DFI wire harnesses were simply removed back to the first existing interface junction outside of the payload-bay envelope. Termination of wire harnesses in this manner required only disconnection of the harnesses on one side of the interface. Where no such convenient interface/termination point was available, wires were simply cut, then "coiled and stowed." In the DFI hardware removal process, all aerodynamic-surface temperature and pressure sensors were left in place; no effort was made to remove these sensors, as they were located integrally with the vehicle's structure and thermal protection materials.

Implementation of the Aerothermal Instrumentation Package (AIP) constituted a "reactivation" of a subset of the existing DFI sensors on the Orbiter *Columbia*. The AIP included some 125 measurements of aerodynamic-surface temperature and pressure at locations on the leeside of the orbiter's left wing, side and upper fuselage, and vertical tail. AIP wire harnesses were fabricated to connect these sensors with a new, AIP-unique data handling system.

The Aerothermal Instrumentation Package was implemented prior to the STS-28 mission of *Columbia*. The objective of the AIP system was to enable collection of in-situ aerodynamic-surface temperature and pressure data on the same flights that the OEX Shuttle Infrared Leeside Temperature Sensing (SILTS) and Shuttle Entry Air Data System (SEADS) experiments would be active. AIP temperature sensors provided in-situ measurements which comprised both "ground-truth" and corollary information for the SILTS experiment. The AIP pressure sensors were intended to provide data to support investigations of reaction control system jet interactions with the aerodynamic flowfield. The SEADS experiment flight data would provide corollary flight environmental information to support such investigations.

Surface Temperature Measurements

The AIP complement of 66 surface-temperature measurements is shown in Figure 4. These measurements, with two exceptions, were all obtained using reactivated DFI thermocouples. The two non-DFI temperature measurements included in the AIP were new thermocouple installations on the forward-facing dome of the SILTS pod, atop the Orbiter's vertical tail.

In the same time-frame that development and implementation of the AIP system was on-going, an upgrade to *Columbia's* thermal protection system was also being designed and implemented. This TPS upgrade resulted in replacement of white LRSI tiles on the fuselage sides and vertical tail with advanced flexible reusable surface insulation (AFRSI) blankets. This upgrade not only provided for replacement of fragile LRSI tiles, but also brought the thermal protection system configuration of *Columbia* into closer alignment with that of the other orbiters.

AIP temperature measurements were to be made in some areas where the TPS upgrade process would replace existing, instrumented TPS material with AFRSI. However, the AFRSI material cannot accommodate thermocouple installations in the manner of the original TPS materials. In order to preserve the AIP temperature measurements to be made in these areas, the upgraded TPS configuration was designed with "islands" of LRSI tile material, with surface thermocouples installed, in lieu of the AFRSI at each surface-temperature measurement location.

Surface Pressure Measurements

The AIP complement aerodynamic-surface-pressure measurements numbered 55, and all were obtained with reactivated DFI pressure transducers. As with the surface-temperature measurements, at locations where AIP surface-pressure measurements were to be made within the area of the AFRSI TPS upgrade, "islands" of LRSI material were incorporated. These tile surfaces provided a rigid structure for pressure orifice installation.

Reaction Control System (RCS) Jet Chamber-Pressure Measurements

The AIP measurement complement also included 10 measurements of chamber pressure for orbiter aft reaction-control-system jets. RCS-jet chamber-pressure data provide jet operation and duty-cycle information during entry. The sensors which provide these data are part of the orbiter's Operational Instrumentation. Incorporation of these measurements as part of the AIP implementation was accomplished by "splicing" into the operational instrumentation system wiring to create a parallel path for data from these sensors to be processed by the AIP data system. The RCS-jet data were incorporated in the AIP data stream in order to ensure accurate time-correlation between the RCS-jet operation data and the aerodynamic response data obtained by the OEX Aerodynamic Coefficient Identification Package (ACIP).

Data Handling System

Analog-to-Digital Conversion

The AIP pulse-code-modulation (PCM) unit provided analog-to-digital conversion of raw sensor analog output signals at a resolution of 12 binary bits, resulting in the availability of 4096 (2^{12}) discrete measurement levels. Both sensor-output full-scale ranges and data sampling rates were channel selectable.

Pressure Transducer Ranging

The selected full-scale measurement ranges for all channels processing pressure-transducer outputs were configured to be **capable** of recording negative transducer-output voltages. Consequently, postflight empirical determination of transducer zero-pressure output biases is possible for AIP surface-pressure measurements.

Data Rates

Temperatures. AIP temperature measurements were recorded at a data rate of 5.3 hz.

Surface Pressures. AIP aerodynamic-surface-pressure measurements were recorded at a data rate of 21.3 hz.

RCS-Jet Chamber Pressures. AIP measurements of RCS-jet chamber pressures were recorded at a data rate of 53.3 hz.

Data Recording

All AIP data were recorded on the OEX flight data recorder. There was no telemetry of AIP data.

Sensor Calibration

No new sensor calibration activity was performed as part of the AIP implementation. AIP postflight data processing was performed in the same manner as previously described for the Development Flight Instrumentation.

Flight History and Data Availability

The Aerothermal Instrumentation Package flew aboard *Columbia* on missions STS-28, -32, -35, and -40. The AIP obtained complete sets of data during the hypersonic portion of atmospheric entry on missions STS-28, -32, and -40.

Early in the entry of *Columbia* on STS-35, a computer failure at a ground-telemetry station resulted in a temporary loss of the ground-to-orbiter telemetry link. This failure precluded timely transmission of the command sequence which would have initiated AIP operation. AIP operation was initiated after the telemetry link was reestablished. However, as a result of the late start of AIP operation, only limited data were obtained on that flight. STS-35 AIP data were obtained only at flight conditions below approximately 238 kft altitude and Mach 24.

As with the DFI results, the AIP-derived surface temperature data from STS-28, -32, and -40 have been processed to infer aerodynamic heat-transfer rates, using the methodology described in reference 3. The resulting orbiter flight heat-transfer data are contained in references 7-9.

CONCLUDING REMARKS

The Development Flight Instrumentation (DFI) and the Aerothermal Instrumentation Package (AIP) systems provided for measurements of aerodynamic-surface temperature and pressure at discrete locations distributed about the external surfaces of the orbiter *Columbia*. The DFI system provided for collection of these data, over the complete configuration (both windward and leeward surfaces), during the Orbital Flight Test Missions of *Columbia*. The AIP system, which measurement complement comprised a subset of the DFI (limited to leeside surfaces), was operated on flights in conjunction with the Shuttle Infrared Leeside Temperature Sensing and Shuttle Entry Air Data System experiments.

REFERENCES

1. Stoddard, L. W., and Draper, H. L.: Development and Testing of Development Flight Instrumentation for the Space Shuttle Orbiter Thermal Protection System. *Proceedings of the 24th International Symposium,* Instrument Society of America, 1978.

2. Anon.: *National Space Transportation System Reference.* NASA TM-101,877, June 1988.

3. Throckmorton, D. A.: Benchmark Determination of Shuttle Orbiter Entry Aerodynamic Heat-Transfer Data. *Journal of Spacecraft and Rockets,* Vol. 20, No. 3, May-June 1983, pp. 219-224.

4. Hartung, L. C., and Throckmorton, D. A.: *Space Shuttle Entry Heating Data Book, Volume 1 - STS-2, Parts 1 and 2*, NASA RP-1191, May 1988 (ITAR Restricted Distribution).

5. Hartung, L. C., and Throckmorton, D. A.: *Space Shuttle Entry Heating Data Book, Volume 2 - STS-3, Parts 1 and 2*, NASA RP-1192, May 1988 (ITAR Restricted Distribution).

6. Hartung, L. C., and Throckmorton, D. A.: *Space Shuttle Entry Heating Data Book, Volume 3 - STS-5, Parts 1 and 2*, NASA RP-1193, May 1988 (ITAR Restricted Distribution).

7. Throckmorton, D. A., and Hartung, L. C.: *Space Shuttle Orbiter Entry Lee-Side Heat-Transfer Data -- STS-28*, NASA RP-1306, September 1993 (ITAR Restricted Distribution).

8. Throckmorton, D. A., and Hartung, L. C.: *Space Shuttle Orbiter Entry Lee-Side Heat-Transfer Data -- STS-32*, NASA RP-1307, September 1993 (ITAR Restricted Distribution).

9. Throckmorton, D. A., and Hartung, L. C.: *Space Shuttle Orbiter Entry Lee-Side Heat-Transfer Data -- STS-40*, NASA RP-1308, September 1993 (ITAR Restricted Distribution).

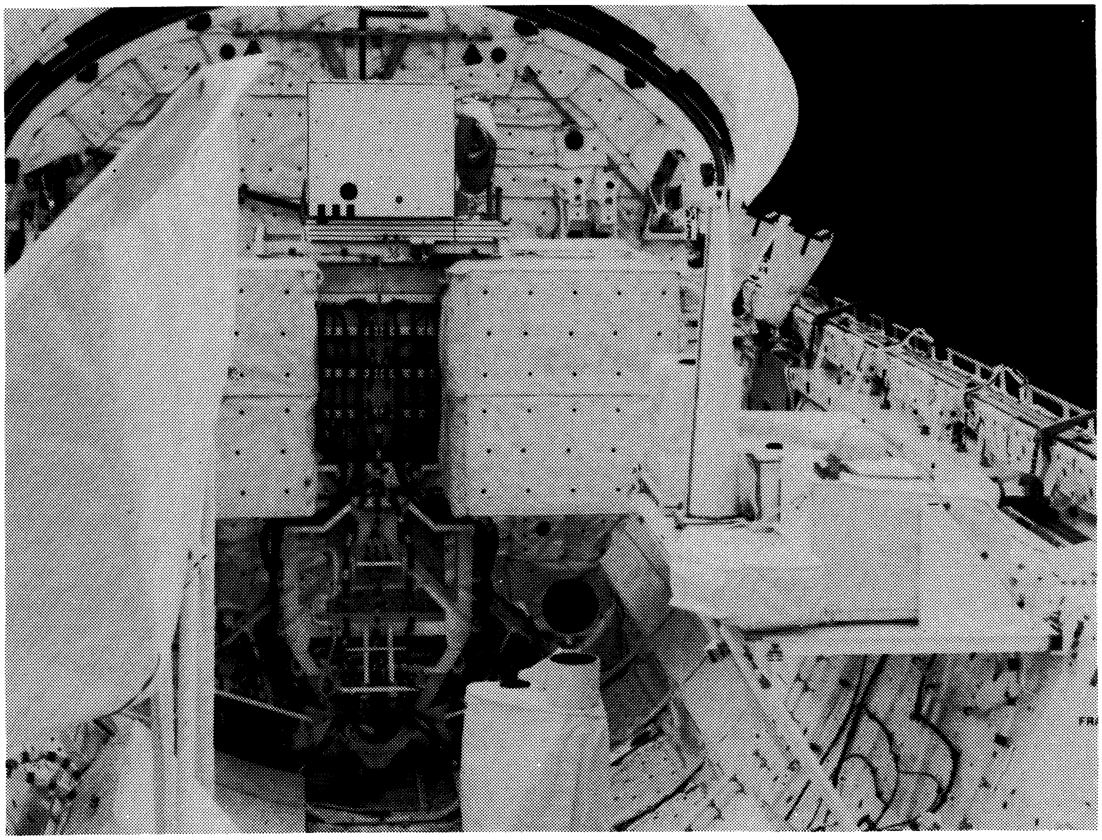

Figure 1 -- DFI system pallet in *Columbia's* payload bay during STS-2.

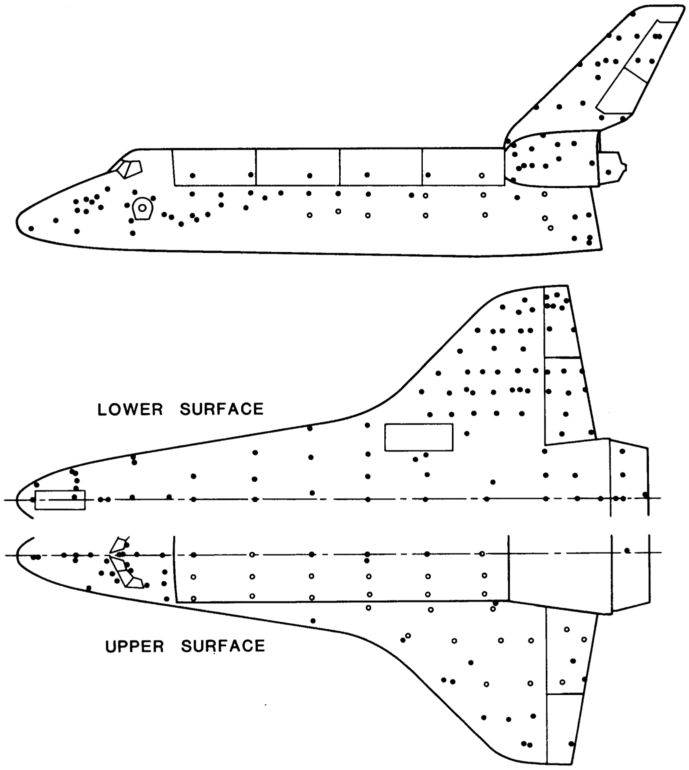

Open Symbols Denote Calorimeter Locations for STS-1 and STS-2

Figure 2 -- DFI aerodynamic-surface-temperature measurement locations.

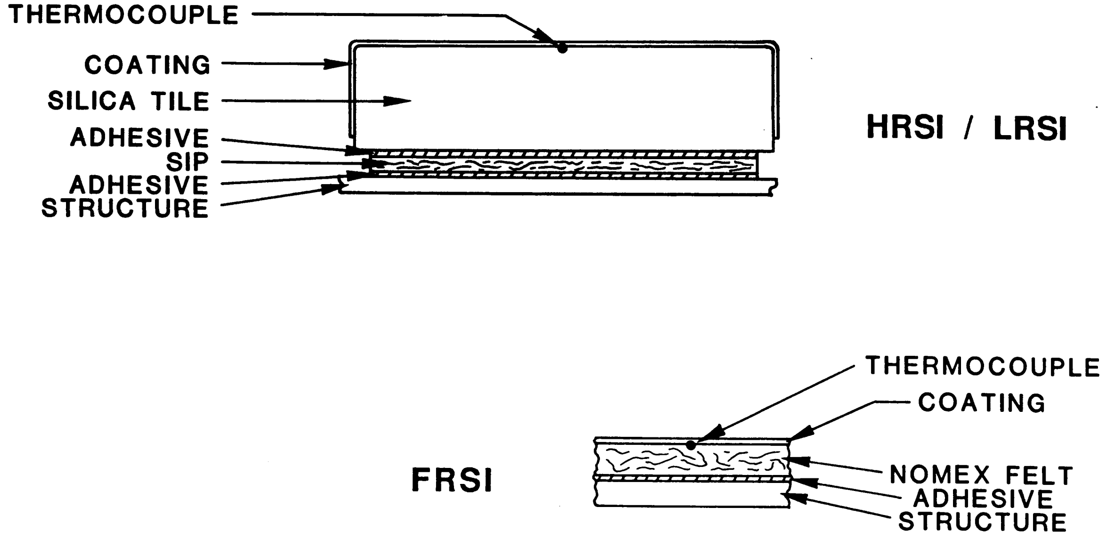

Figure 3 -- Orbiter thermal protection system and DFI thermocouple installation schematic.

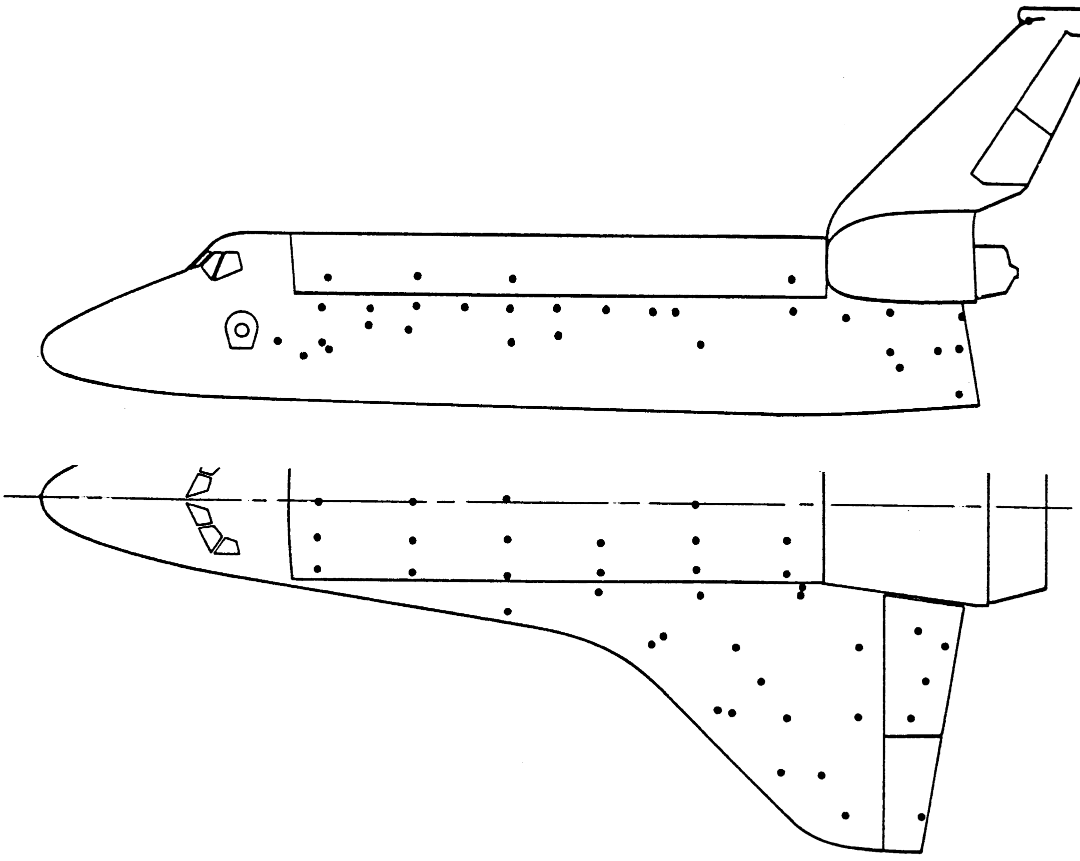

Figure 4 -- AIP aerodynamic-surface-temperature measurement locations.

CATALYTIC SURFACE EFFECTS (CSE) EXPERIMENT FOR SPACE SHUTTLE

David A. Stewart
NASA Ames Research Center
Moffett Field, CA

SUMMARY

This paper describes pre-flight data that were obtained for the Catalytic Surface Effects Experiment (CSE). The CSE experiment was flown as part of the OEX experiments on the Space Shuttle Orbiter. Selection, application and aerothermal response data taken from a high efficiency catalytic overcoat, developed to measure the effect of surface catalysis on the heating rate to the Orbiter heat shield during its high-speed earth entry, are discussed. Surface catalytic efficiency and performance characteristics of the Orbiters' baseline heat shield and the overcoat were determined using arc-jet aerothermodynamic heating environments. These data were used in BLIMPK solutions to make pre-flight predictions of the effect of surface catalysis on the heating rate distribution over the mid-fuselage of the Orbiter for the CSE flight experiment.

NOMENCLATURE

H = Total enthalpy, MJ/kg
h_D = dissociation energy, MJ/kg
k = Boltzmann constant
k_W = reaction rate constant
L = Orbiter length (32.7 m)
L_e = Lewis number
m_o = mass of atom or molecule
p = pressure, atm.
q = heat-transfer rate, W/cm^2
R = radius, cm
Re = Reynolds number
S = arc-length from stagnation point
St_h = local stanton number
T = temperature, K
t = nominal structure thickness
U = velocity, Km/s
X = axial distance, m
α = angle-of-attack, deg
α_e = fraction of molecules dissociated
γ = atom recombination coefficient
λ = wavelength, cm
μ = viscosity, m^2/s
ρ = mass density of mixture, g/cc

Subscripts:

b = body
cw = cold wall
e = boundary-layer edge
eff = effective radius
fc = fully catalytic
hw = hot-wall
i = species
max = maximum
min = minimum
N = nitrogen
n = nose
O = oxygen
T = total
w = wall
∞ = free stream

INTRODUCTION

The possibility of reduced heating to a space vehicle due to a reduction in surface catalytic activity on its heat shield during a high-speed entry into the earth's atmosphere has been recognized and discussed (refs. 1-2). Catalytic efficiency of various coated materials has been studied for many years in ground test facilities, using dissociated nitrogen or air streams (refs. 3 -5) However, whether this phenomenon occurs on a space vehicle during atmospheric entry had not been demonstrated by a flight experiment before the Space Shuttle flights. Therefore, the designers did not allow for the possible substantial decrease in heating to the Space Shuttle Orbiter thermal protection system (TPS) due to low catalytic efficiency surfaces.

The Orbiters' thermal protection system (TPS) uses coated reinforced carbon-carbon composite (RCC) for the nose cap, wing and vertical stabilizer leading edges (ref. 6) Reusable surface insulation (RSI) is used over most of the lower and upper surfaces of the fuselage and wing. The RSI on the upper surfaces of the vehicle consists of both coated rigid fibrous insulation and coated woven blanket materials. Over the lower surfaces of the vehicle, high temperature reusable surface insulation (HRSI) tiles (roughly 15.24 cm by 15.24 cm wide that range from 2.54 cm to over 10 cm in thickness), are used for most of the TPS. These tiles are coated with a reaction cured glass (RCG).

This paper describes a pre-flight study to select a catalytic overcoat that would survive the launch environment and clearly demonstrate the effect of surface catalysis on the heat transfer rate to a vehicle's TPS. Included in the study are predictions to insure that the catalytic overcoat would not have an adverse effect on the thermal performance of the vehicle structure during atmospheric entry.

FLIGHT EXPERIMENT

In high-velocity dissociated flow, characteristic of Earth entry, it is predicted, from a reacting boundary-layer computation, (ref. 7) that the heat flux to a TPS with a fully noncatalytic surface would be between 30% to 50% below the value of one where total atom recombination occurs, Fig. 1.

The catalytic surface effects (CSE) Orbiter experiment used the baseline TPS and flight instrumentation without any effect on the Space Shuttle Orbiter operations. A catalytic overcoat was sprayed onto selected tiles located along the mid fuselage and lower wing area of the Orbiter, Fig. 2. The proposed CSE experiment was to be conducted in two phases.

1) Selected tiles along the mid-fuselage and lower wing area would be coated with a high catalytic efficiency overcoat to determine the relative effect of surface catalysis on the heat transfer rate to the Orbiter's TPS during Earth entry. Direct side-by-side measurements of surface temperature from tiles with the catalytic overcoat and tiles having just the RCG coating would be compared. The first phase of the experiment was conducted during STS-2 through STS-5.

2) Apply a catalytic overcoat to a tile that would be located within a panel containing an inline array of thermocouples. The panel would be positioned along the centerline of the mid-fuselage at $x/L = 0.27$. The thermocouple array would provide a temperature profile history of a TPS surface which had variable surface catalyticity. These data, collected through several flight regions, would provide a set of baseline flight data for validation of advanced codes.

The phase 1 and 2 studies required flight data between onset of measurable aerodynamic heating (altitude of 91 km) and landing. Change in surface temperature alone cannot firmly establish the effect of surface catalysis on surface heat transfer rate to a TPS. Properties of the TPS surface such as chemical stability and emittance must also be well understood.

Ground test facilities were used to obtain information that was used to aide in the selection of the catalytic overcoat, evaluate its performance in an aerothermodynamic heating environment, and provide data for prediction of its flight performance.

GROUND TEST FACILITIES

Ground tests used to select and evaluate the catalytic overcoat included a microwave cavity and two arc-plasma facilities, Fig. 3. The arc-jet facilities were the Ames Aerothermodynamic Heating Facility and 20 MW Pilot Test Facility (ref. 8). Both facilities use a constricted arc-heater to produce high-energy dissociated flow.

Microwave Cavity

A sketch of the microwave cavity test equipment is shown in Fig. 3a. The equipment consisted of a glass tube, 2.54 cm diam by 56 cm long, with a bleed valve and gas regulator at one end and vacuum pump and model support at the other. The microwave cavity was located approximately halfway along the test tube. Test models were positioned just downstream of the cavity.

High-purity nitrogen gas (99.99% pure) was dissociated as it passed through the microwave cavity resonating at 24.5 MHz. During each test, a constant flow rate was maintained by monitoring the static pressure with a thermocouple vacuum gage. Also, during each test, the microwave power was maintained at a constant value.

Aerothermodynamic Heating Facility (AHF)

This facility provides high-energy hypersonic flow (total enthalpies from 7.0 - 23. MJ/kg) by passing the test gas between concentric toroidal electrodes and expanding it through a 16° total angle conical nozzle, Fig. 3b. Surface conditions on the test model were varied by changing the area ratio of the nozzle exit to the inlet, heater pressure, or electrical power dissipation in the arc-heater. During this investigation, the geometric area ratio of the nozzle exit to throat were varied from 144 to 900. Free-stream properties were determined from a computer code which uses a freeze Mach number concept to define the chemical state of the gas (ref. 9). Stagnation point conditions on the models were then determined using heat transfer rate and pressure measurements taken from a 10.2 cm diam copper hemisphere.

20 MW Pilot Test Facility

High-energy 20 MW Pilot Test Facility uses a constricted arc-heater similar to the one used in the AHF; however, the flow in this facility is expanded through a semi-elliptical nozzle (with a throat aspect ratio of 1/4) and across a 48.3 cm x 50.8 cm flat-plate configuration containing multiple HRSI tiles, Fig. 3c. Part of the nozzle wall ahead of the flat-plate consists of silica, 25.4 cm long and 40 cm wide, to insure a smooth hot-wall flow transition between the nozzle and test article surface. Boundary-layer flow over the test article is in the transition region (Reynolds number > 500,000 1/ft). Total enthalpy of the stream was determined from measured total pressure, mass flow, and electrical power dissipation.

Test Models

Test models used in the various environments to select and evaluate the catalytic overcoat are shown in Fig. 4. The model used for the microwave cavity tests was a disk (1.91 cm in diam and 1.27 cm thick) cut from HRSI and coated with the RCG, Fig. 4a. The disk was bonded to a glass tube 0.98 cm in diam and 36 cm long. The tube was sealed at both ends with RTV 560. A thermocouple was installed at the center of the disk and the thermocouple wires extended 25 cm beyond the tube to a voltmeter.

The three configurations used for the tests conducted in the Aerothermodynamic Heating Facility are shown in Fig. 4b. They include two flat-faced cylinders and a truncated 40° blunt cone. The larger of the two cylinders was made from copper and water-cooled. The outside diameter of this holder was 20 cm. The holder was used to test RCG coated silica specimens (10 cm diam by 5 cm thick) which were inserted into a cavity located at its center. A pressure port and calorimeter were located 90° apart and at a radius of 6.3 cm on the face of the holder. The smaller of the two holders, a silicon carbide coated carbon disk (10 cm in diam) was used to test samples of reinforced carbon carbon composite (RCC). These samples were 7.11 cm diam by 0.66 cm thick. The truncated cone was made from a silica HRSI (density of 0.352 g/cm^3) which also contained 2.5% silicon carbide particles and was coated with RCG. Thermocouples were installed at the stagnation point of all three test configurations. In addition, five thermocouples were installed along the surface of the conical portion of the truncated 40° blunt cone at locations $S/R_n > 1.15$.

Finally, a flat-plate (48 cm by 50 cm) made up of multiple RCG coated HRSI tiles was tested in the 20 MW Pilot Test Facility, Fig. 4c. A surface thermocouple was installed at the center of the two tiles located symmetrically about the centerline of the model. The 3.8 cm thick tiles were bonded to a baseline strain isolation pad (SIP) which in turn was bonded to a 0.081 cm thick aluminum plate. The tiles were positioned so that their leading edge was swept 45° to the flow; there was a gap of about 0.15 cm between the tiles. High density silica strips were placed around the outer edge of the tile array to prevent damage to the edge tile by the effect of the flow in the gaps.

Platinum-platinum/13% rhodium thermocouples were used in all samples made from HRSI and coated with RCG. The thermocouples were installed so that they were partly encased within the RCG coating. Tungsten-5% rhenium / tungsten-26% rhenium thermocouples were installed in the RCC samples. These thermocouples were installed through the back surface of the RCC sample. However, they are in contact with the front surface after installation.

EXPERIMENT

Candidate Overcoats

The RCG glass was used as a reference material for determining the relative surface catalytic efficiency of each candidate overcoat. The manufacture of the RCG glass includes the mixing of a reactive high-silica borosilicate glass frit with 2.5% by weight tetra boron silicide, B_4Si, (ref. 10). The mixture was then sprayed onto a silica tile and glazed at 1473 K. Upon cooling the coating rapidly to room temperature, a thin borosilicate glass layer similar to vycor (6-7% B_2O_3) and less than 0.002 cm thick is formed on its surface.

Several candidate catalytic overcoats were applied to RCG coated tiles using vapor deposition and spraying techniques. Copper, nickel, gold, and aluminum were applied by vapor deposition and platinum black and a C-742 spinel by spraying. A combustible turpentine carrier was required for spraying the platinum black overcoat onto the tile. The C-742 overcoat used a water carrier and consisted of a black iron cobalt chrome spinal in a polyvinyl acetate binder.

Overcoat Selection

Screening tests to select a catalytic overcoat were conducted using the microwave test cavity and one-inch diameter disks (Fig. 4). During these tests, 80 KW of power was used and the cavity was resonated at 24.5 MHz. The model was positioned just downstream of the microwave cavity and exposed for 6 min to dissociated nitrogen gas flowing at a constant flow rate and a static pressure of $P_W = 0.002\ N/cm^2$. Surface temperature of each candidate coating was measured. Before each test, the glass tube was purged several times with the test gas. The surface temperature of each candidate coating was measured and compared with the temperature from a RCG coated sample. Total hemispherical emittance was calculated for each candidate coating using room temperature spectral hemispherical reflectance data and integrating between appropriate limits.

Overcoat Evaluation

High temperature performance and characterization data for the selected overcoat were obtained using models shown in Figs. 4b through 4d. These tests were conducted in the convectively heated environments of the Aerothermodynamic Heating and 20 MW Pilot Test Facilities.

Flat-faced models were used to obtain stagnation point temperature data from baseline HRSI and RCC materials in the Aerothermodynamic Heating Facility. A typical stagnation point test using the flat-faced cylinder is shown in Fig. 5. The high-energy gas (dissociated oxygen and nitrogen atoms) flowing over the front surface of the model is apparent from the photograph. Dual samples were used in these tests, one with the overcoat and one without the overcoat. The sample without the overcoat was used to establish a baseline surface temperature for the test. The sample with the overcoat was then tested relative to the baseline (same test condition). The truncated 40° blunt cone was used to measure the effect of a surface catalysis on the heat flux to a surface with variable catalytic efficiency. These tests were also conducted in the Aerothermodynamic Heating Facility with test times up to 180 sec.

Finally, the multiple tile flat-plate configuration (Fig. 4c) was used to evaluate the catalytic overcoat on a full-scale tile and at a Reynolds number closer to the flight conditions for the CSE experiment. The flat-plate was mounted in the 20 MW Pilot Test Facility at zero angle of attack and flush with the nozzle exit. The catalytic overcoat was applied to the tile with the thermocouple located downstream from the center of the model. The model was exposed to the hypersonic air stream for 7 min.

RESULTS AND DISCUSSION

Results from the microwave cavity screening tests are summarized in Table 1. Material, application, temperature ratio (sample/RCG), emittance and reaction rate constant are listed for each candidate overcoat. The total hemispherical emittance was calculated for a surface temperature of 1366 K using measured room temperature spectral hemispherical reflectance data, assuming $\alpha = \varepsilon$, and integrating between appropriate limits. Typical temperature histories from a RCG coated sample with and without a C-742 overcoat tested in the microwave facility are shown in Fig. 6. Steady-state conditions were reached within 3 min after the nitrogen gas was introduced. In general, the surface temperature of all samples with the candidate overcoats was 50% -60% higher than the values obtained from a RCG coated sample.

A relative catalytic efficiency (reaction rate constant) for each candidate overcoat was calculated using eq. 1.

$$k_W = \gamma_i \, (k \cdot T_W / 2 \cdot \pi \cdot m_o)^{1/2} \quad \text{cm/sec} \tag{1}$$

Recombination coefficients (g_i) used in eq. 1 were obtained from side-arm reactor experiments conducted on materials similar to the candidate overcoats (refs. 11,12). All candidate overcoats appeared to have high atom recombination efficiency.

For the flight experiment, the first four overcoats listed in table 1 would require that the tile be replaced after each flight, because these materials have to be vapor deposited onto the RCG coating. Copper and nickel overcoats fail to meet the Space Shuttle design requirements for total hemispherical emittance ($e_{TH} > 0.8$) and oxidize very quickly in air at high temperature. The next two overcoats were sprayed onto the test samples. However, platinum black was eliminated due to the combustible turpentine carrier required for spraying. The C-742 overcoat was chosen as the only satisfactory candidate for the CSE experiment because of its spray-on application, water carrier and similar total hemispherical emittance to the RCG coating, Fig. 7.

The chemical stability of the C-742 overcoat was first evaluated relative to the launch pad environment using tests in an environmental chamber. These tests showed the C-742 overcoat was chemically unaffected after exposure to humidity greater than 95% for 72 h. Thermogravimeter analysis (TGA),determined, at atmospheric pressure, most of the binder would burn out at 622 K. These test results suggest that this overcoat is environmentally stable while the Orbiter is on the ground, burns out during the ascent trajectory, and provides a high catalytic surface during Earth entry.

High temperature data for the overcoat, such as relative catalytic efficiency and thermochemical stability, were obtained using coated RCC samples. The C-742 coating was applied over both single and two layered oxidation control coatings already on the RCC, Fig. 8. The single layer coating consisted of tetraethylorthosilicate (TEOS) and the two layer coating consisted of TEOS covered with a sodium silicate based glass (Type "A"). These data show that the application of the C-742 overcoat to the RCC samples increased the surface temperature by 200 K during an arc-jet exposure. However, the stability of the C-742 at 1800 K varied depending on which coating system was sprayed onto it. C-742 remained stable for a longer period of time (600 s) on the RCC sample with the Type "A" glass than on the sample with the single coating(300 s). It is believed that the lower viscosity Type "A" glass allowed the C-742 overcoat to be absorbed into it, therefore slowing down the decomposition of the Cr_2O_3 and CoO compounds within the spinal.

Surface catalytic efficiency of the coatings used on these RCC samples is compared with baseline RCG in Fig. 9. The stagnation point heat transfer rate to a flat-faced cylinder (Fig. 4b) is plotted against the heat flux to a hemisphere which was used to represent the relative stream condition for each test. These data show that the surface catalytic efficiency of the coated RCC samples is similar to the RCG and that both of them are much lower than the C-742 overcoat. In order to estimate the surface temperature of the tiles with the C-742 overcoat on them for the Space Shuttle flight experiment, the recombination coefficients for atomic oxygen and nitrogen were calculated using BLIMPK and Goulard's theory (eqs. 2 and 3) below (refs. 13-15). Maximum heat flux to the model was estimated using eqs. 4 and 5 (ref. 16).

$$k_w=(r_\infty \cdot U_\infty \cdot St_h)/\rho_w . Le^{2/3} \cdot (q_o-q_{min})/(q_{max}-q_o) \qquad (2)$$

$$q_{min}/q_{max} = 1 - Le^{2/3} \cdot \alpha_e \cdot h_D/H_{eo} / 1-(Le^{2/3}-1)\alpha_e \cdot h_D/H_{eo} \cdot (1-\phi) \qquad (3)$$

where $\phi = 0$.

$$q_{max} = C \cdot (P_o/R_{eff})^{1/2} \cdot (U_\infty/10{,}000)^{1.99} \cdot (1-h_w/H_{eo}) \qquad (4)$$

The hot-wall heat-transfer rate was calculated from the well known expression,

$$q_{HW} = q_{CW} \cdot [1-(h_w/H_{eo})] \qquad (5)$$

The nose radius used in Goulard's theory was determined from stagnation point heat-transfer rate measurements taken from a water-cooled 10 cm diam copper hemisphere and an equivalent diameter flat-faced cylinder, Fig. 10.

$$R_{eff}=1.38 \cdot R_n \qquad (6)$$

Comparative rate constants were obtained from BLIMPK. BLIMPK is a reacting boundary layer code known as "Boundary-Layer Integral Matrix Procedure with Kinetics" (Ref. 7). BLIMPK solutions require inputs of total enthalpy, nose radius or surface pressure distribution, and gas and surface kinetics expressions. Early, BLIMPK solutions for the flat-faced cylinder used an effective radius; however, current solutions use a surface pressure distribution obtained from the Ames Method of Integral Relation, AMIR, (ref. 17). Also, in earlier solutions, the heat flux to the TPS surface was calculated assuming a constant wall temperature rather than the current practice of satisfying an energy balance with surface reactions. Both solutions assumed a Rideal reaction mechanism. They also assume only the recombination of oxygen and nitrogen atoms at the surface of the TPS, include Park's five species model of 20 reactions (ref. 18) as the gas model, and that the surface temperature is related to the heat flux by the following expression.

$$T_w = (q_w/\varepsilon_{th} \cdot \sigma)^{1/4} \qquad (7)$$

where σ is the Stefan-Boltzmann constant and ε_{th} is the total hemispherical emittance.

Surface kinetic expressions (recombination coefficients) for both the RCG and the catalytic overcoat are plotted as a function of surface temperature in Fig. 11. These expressions are curve fits to calculated values of the recombination coefficients for RCG and the C-742 overcoat obtained from BLIMPK (refs. 19, 20). Low temperature coefficients (<1000 K) on the figure were obtained using side-arm reactor data and kinetic theory (ref. 21).

Included on the figures are the earlier estimates of the recombination coefficients (dash line) for the coatings calculated using Goulard's theory. The dash line also includes low temperature coefficients obtained from side-arm-reactor data for Quartz (refs. 22, 23). These earlier coefficients from the literature for quartz are much lower than the current values calculated by Kim for RCG (ref. 21).

Both thermodynamic and transport properties used in the above equations were for air in conditions of complete thermal equilibrium (ref. 24). Coefficients for oxygen atoms were set equal to the air value. Coefficients for the nitrogen atoms were then determined using Tong's analysis of arc-jet data obtained from a material similar in high catalytic efficiency to the C-742 overcoat (ref. 7).

Fig. 11 displays two notable characteristics of the recombination coefficients for the RCG coating: 1) a rapid raise in the coefficient between the annealing point temperature (1183 K) and softening point temperatures (1650 K) of the glass, and 2) a rapid decrease in the coefficient above the softening point temperature. The rapid rise in the coefficients corresponds to a typical first order reaction and the rapid decrease above 1650 K might be attributed to second order or secondary reactions at the surface of the low viscosity RCG. These secondary reactions are possibly the result of the inability of the O_2 and N_2 molecules formed at the surface to reach an equilibrium state before they leave again through the volatilization process occurring at the surface of the RCG glass (ref. 22, 23).

Typical S-shaped curves that relate surface heat flux to the energy transfer, due to atom recombination at the stagnation point on the flat-faced cylinder tested in the arc-jet air stream, were calculated using Goulard's theory and BLIMPK, Fig. 12. The solutions show good agreement for values $k_w > 10{,}000$ cm/s, but poor agreement for values $k_w < 500$. Comparison of measured stagnation point heat-transfer rates to the flat-faced model with the predictions, at this arc-jet test condition, showed a value of $k_w = 3000$ cm/s for the C-742 overcoat and values of either $k_w = 100$ cm/s or $k_w = 350$ cm/s for the RCG coating depending upon which solution is used.

BLIMPK predictions of the heating distribution over a blunt 40° cone and a flat-plate , with multiple HRSI tiles, are compared with data taken during their exposure to arc-plasma air streams. Boundary layer flows over the respective models were laminar and near turbulent.

Also, BLIMPK predictions of the heating distribution over a blunt 40° cone and a flat-plate, with multiple HRSI tiles, were made using the earlier determined recombination coefficients, Fig. 11. These predictions were compared with data taken during their exposure to arc-plasma air streams. During these tests the boundary layer flow over the models was laminar (40° cone) and near turbulent (flat-plate).

Photographs of the truncated 40° blunt cone are shown in Fig. 13. These photographs show top views of the cone partially and fully coated with the C-742 overcoat. Fig. 13a shows the cone in the arc-jet air stream without the overcoat applied to the RCG. Location of the C-742 overcoat on the cone is indicated by the brighter areas in the photographs, Figs. 13b and 13c. Not shown is a cone where the overcoat was applied to areas covering the stagnation point and the surface near the trailing edge of the model. The heating distribution data taken from these cones are plotted in Fig. 14.

The heat flux (normalized by a calculated fully catalytic wall stagnation point value obtained using BLIMPK, ($k_w = 10^5$ cm/s) is plotted as a function of the ratio of arc-length to nose radius. The data shows that the stagnation point heat-transfer rate to the cone with RCG was approximately 40% lower than the cone with the C-742 overcoat, Fig. 14a. Also, the data shows that a sudden change in catalytic efficiency results in a sudden change in the heat-transfer rate to the cone surface, Fig. 14c. Heat-transfer rate to the areas on the cones, where the C-742 overcoat was applied, was over 50% higher than those areas which were covered with the RCG coating. Calculated heating rate distributions over the cones were made using a constant value of the reaction rate constant and wall temperature in BLIMPK.

Data taken from the multiple tile flat-plate model are shown in Fig. 15. Included on the figure is a sketch of the test arrangement used in the 20 MW Pilot Test Facility. Post test inspection of the model showed that the C-742 overcoat remained stable during the arc-jet exposure. The heat flux to both tiles was calculated using measured temperature data. Application of the C-742 overcoat resulted in an 18% increase in the heat transfer rate to the tile during its exposure to the near turbulent boundary layer flow. These data were compared to a BLIMPK prediction of the heating distribution across the model.

The prediction was made assuming that all tile surfaces, except the tile covered with the C-742 overcoat were almost fully noncatalytic (k_W = 13 cm/s). Again, the reaction rate constant for C-742 overcoat was obtained from the dashed line in Fig. 9. The surface heat flux distribution was calculated by starting with the total stream conditions at the nozzle throat and moving downstream across the model. Heat loss to the cold walls of the nozzle is included in the total enthalpy calculation (ref. 25). Assuming laminar flow, the predicted heating transfer rates across the model are about half the measured values. Assuming fully turbulent flow, the heat-transfer rates across the model are about 20% higher than the values found from the experimental data. Therefore, the measured heating rates and BLIMPK solutions support the assumption that transitional flow did exist across the model. The surface catalysis effect between RCG and the C-742 overcoat was shown to be appreciably less during transitional flow over the flat-plate than during laminar flow over the cone.

CATALYTIC OVERCOAT FOR THE ORBITER

Finally, to insure that the catalytic overcoat would not affect the thermal performance of the Orbiter's structure, the heating distribution along the mid fuselage was calculated using BLIMPK and surface properties determined from the arc-jet tests for RCG and the catalytic overcoat. Laminar flow exists over the windward centerline of the Orbiter during most of the time that the data will be recorded for the CSE experiment. The effect of surface catalysis on the heating distribution over the mid fuselage of the Orbiter was estimated for a 14414 design trajectory, Fig. 16. The BLIMPK solution was for the flight where the C-742 overcoat was applied to the five selected locations for the CSE experiment. The trajectory point selected for the solution was at an altitude near where maximum heating to the vehicle will occur (alt. = 75 km). The peak surface temperature was higher than values calculated assuming equilibrium flow over the vehicle. Figures 16b and 16c show the unique characteristic shapes of the surface heating profiles relative to a sudden change in surface catalytic efficiency for two altitudes during the trajectory. These predicted heating profiles were calculated at locations on the Orbiter of X/L = 0.15 and X/L = 0.3 and at altitudes of 75 km and 91 km respectively. Comparison of flight data with these types of predictions will lead to a better understanding of the thermodynamic and transport properties as well as surface catalytic efficiencies currently being used in advanced codes for TPS design.

An important concern in adding a catalytic overcoat to the selected tiles was whether the aluminum skin of the vehicle would overheat during Earth entry. Using an average surface heating rate, from the calculated pulse at various times during the 14414 design trajectory, the aluminum skin temperature rise was estimated using one- and three dimensional thermal models (ref. 26). The one-dimensional solution showed that the peak temperature of the structure would remain well within the Rockwell design limit with the C-742 overcoat applied to the selected tiles. When lateral conduction into the structure is included in the computation (three-dimensional solution) the increase in peak temperature of the aluminum skin caused by the catalytic overcoat is only a few degrees more.

CONCLUSIONS

A spray-on high catalytic overcoat (C-742) was developed for the CSE experiment. Goulard's theory, BLIMPK solutions and arc-plasma data were used to predict the catalytic efficiency of the C-742 overcoat and baseline TPS (RCC and HRSI) used on the Orbiter. The following observations were made, based on the test data and computations:

1) Selected catalytic overcoat (C-742) exceeded launch and Earth entry performance requirements for the CSE experiment.

2) Atom recombination coefficients for the catalytic overcoat were approximately an order-of-magnitude greater than the RCG baseline coating over the temperature range of interest.

3) Current data show that for the C-742 overcoat, the coefficient for atom recombination of nitrogen was much greater than for oxygen.

4) Catalytic efficiency of the coated RCC materials was similar to the baseline RCG coating.

5) Effect of surface catalysis on the heating rate to a ceramic TPS was much greater in laminar flow than in transitional flow (35%-40% relative to 15%-18%). The difference is attributed to lower total enthalpy and mixing in the boundary layer of the transitional flow.

6) Predicted heating distribution over the mid fuselage showed that the application of the catalytic overcoat would not result in an increase in bond-line temperature above its design limit during Earth entry.

Acknowledgments: The author would like to thank J.V. Rakich and Y. K. Chen for their support in the BLIMPK solutions used in the paper.

REFERENCES

1. Goulard, R., "On Catalytic Recombination Rates in Hypersonic Stagnation Heat Transfer," Jet Propulsion, Vol. 28, Nov. 1958.

2. Rosner, D. E., "Boundary Conditions for the Flow of a Multicomponent Gas," Jet Propulsion, Vol. 28, Aug. 1958, pp. 555-556.

3. Chung, P. M., "Shielding Stagnation Surfaces of Finite Catalytic Activity by Air Injection Hypersonic Flight," NASA TN-D-27, Aug.. 1959.

4. Sheldahl, R. E., and Winkler, E. L., "Effect of Discontinuities in Surface Catalytic Activity on Laminar Heat Transfer in Arc-Heated Nitrogen Streams," NASA TN-3615, 1966.

5. Stewart, D. A., "Cyclic Arc Plasma Tests of RSI Materials Using a Preheater," NASA TM-2720, 1973.

6. Space Shuttle Orbiter Entry Aerothermodynamic Heating Data Book, Rockwell International Space Division Document No. SD 73-SH-0814, Rev. C, Books 1 and 2, Oct. 1978.

7. Tong, H., Buckingham, A. C., and Curry, D. M., "Computational Procedures for Evaluations of Space Shuttle TPS Requirements," AIAA Paper 74-518, 1974.

8. Ames Research Facilities Summary, 1974

9. Yoshikawa, K. K. and Katzen, E. D., "Charts for Air-Flow Properties in Equilibrium and Frozen Flows in Hypervelocity Nozzles," NASA TND-693, 1961.

10. Goldstein, H.E., Leiser, D.B. and Katvala, V., "Reaction Cured Borosilicate Glass Coating for Low-Density Fibrous Silica Insulation, Borate Glasses, Plenum Corp., New York, 1978, pp. 623-634.

11. Marshall, T. C., "Surface Recombination of Nitrogen Atoms Upon Quartz," Journal of Chemical Physics, Vol. 37, 1962, pp. 2501-2502.

12. Wood, B. J. and Wise, H., "The Interaction of Atoms with Solid Surfaces," Stanford Research Institute Project Squid, Office of Naval Research, 1960.

13. Rosner, D. E., "Analysis of Air Arc-Tunnel Heat Transfer Data," AIAA Journal, Vol. 2, May 1965, pp. 945-948.

14. Rosner, D.E., "Analysis of Air Arc-Tunnel Heat Transfer Data," AIAA Journal, Vol. 11, May 1973, pp. 649-656.

15. Pope, R. B., "Stagnation Point Convective Heat Transfer in Frozen Boundary Layers," AIAA Journal, Vol. 5, Apr. 1968, pp. 619-626.

16. Marvin, J. G. and Deiwert, G. S., "Convective Heat Transfer in Planetary Gases," NASA TR-224,1965.

17. Inouye, M. and Marvin, J.G., "Comparison of Experimental and Theoretical Shock Shapes and Pressure Distributions on Flat-Faced Cylinders at Mach 10.5," NASA TN D-4397, Feb. 1968.

18. Park, C., "A Review of Reaction Rates in High Temperature Air," AIAA Paper 89-1740, Buffalo, NY, 1989.

19. Stewart, D. A. Chen, Y. K., and Henline, W. D., "Effect of Non-Equilibrium Flow Chemistry and Surface Catalysis on Surface Heating to AFE," AIAA Paper 91-1373, 1991.

20. Stewart, D.A., Rakich, J.V., and Lanfranco, M.J., "Catalytic Surface Effects Experiment on the Space Shuttle," Thermophysics of Atmospheric Entry, Vol. 82, 1982, pp. 248 - 272.

21. Kim, Y.C., "Study of the Recombination of Nitrogen and Oxygen Atoms on Surfaces of Materials Used in Space Vehicles," Final Report, NCA2-158, Stanford University, Stanford, CA, Sept. 1988.

22. Harrison, D. E. and Moratis, C. J., "Ceramics, Glasses, and Micas," "Handbook of Materials and Processes for Electronics, McGraw-Hill Book Co., New York, 1970, pp. 6-43.

23. Van Vlack, J. L., "Thermal Properties and High Temperature Behavior," Physical Ceramics for Engineers, Addison-Wesley, Reading Mass., 1964, pp. 156.

24. Hansen, F. C., "Approximations for the Thermodynamic and Transport Properties of High-Temperature Air," NASA TR -50, 1959.

25. Winovich, W., "On the Equilibrium Sonic-Flow Method for Evaluating Electric Arc Heater Performance," NASA TND-2132, 1964.

26. Derry, S. M., Personal communication, 1981.

Table 1. Summary of microwave cavity test results

COATING MATERIAL	APPLICATION	EMITTANCE ϵ_{TH} $T_w = 1366°K$	$\frac{T_{w_i}}{T_{w(RCG)}}$	γ_N	k_w cm/sec
Cu	VAPOR DEPOSIT	0.22	1.58	$7 * 10^{-2}$	964
Ni	VAPOR DEPOSIT	0.32	1.52	10^{-1}	1352
Au-BLACK	VAPOR DEPOSIT	0.92	1.57	10^{-1}	1375
Al-BLACK	VAPOR DEPOSIT	0.95	1.48	10^{-1}	1390
Pt-BLACK	SPRAY PAINT	0.90	1.61	$6 * 10^{-2}$	801
C742	SPRAY PAINT	0.88	1.54	10^{-1}	1360
RCG GLASS	BASELINE	0.82	1.0	$8 * 10^{-4}$	10.0

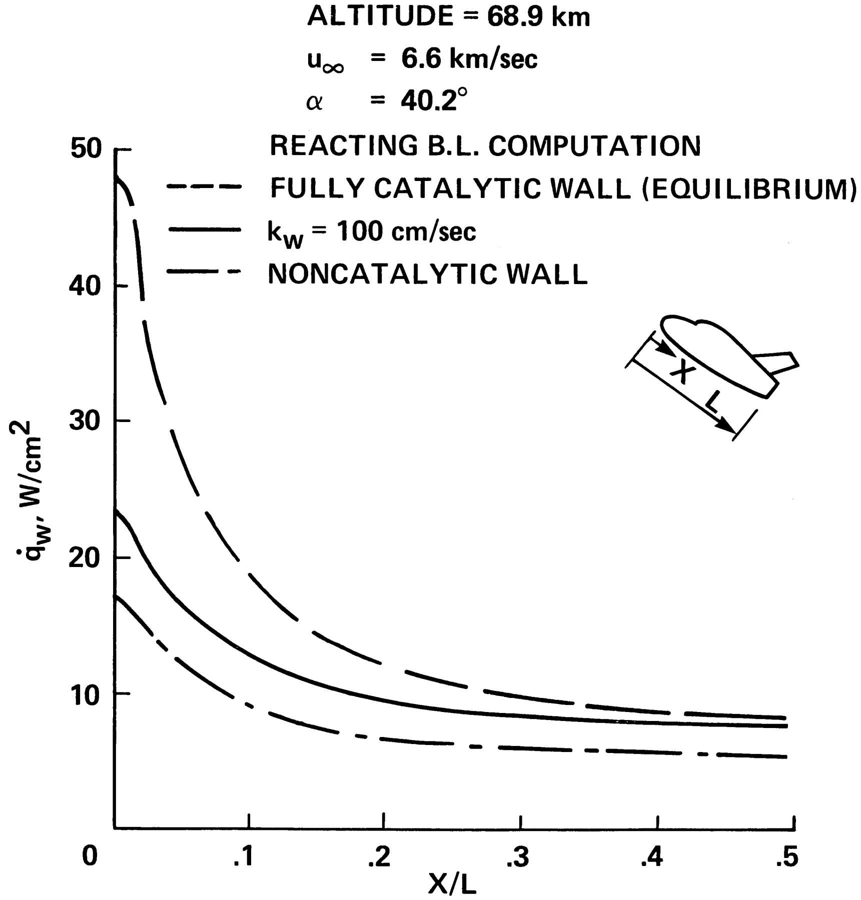

Fig. 1. Reduced Orbiter centerline heating, assuming a fully noncatalytic TPS surface during Earth entry.

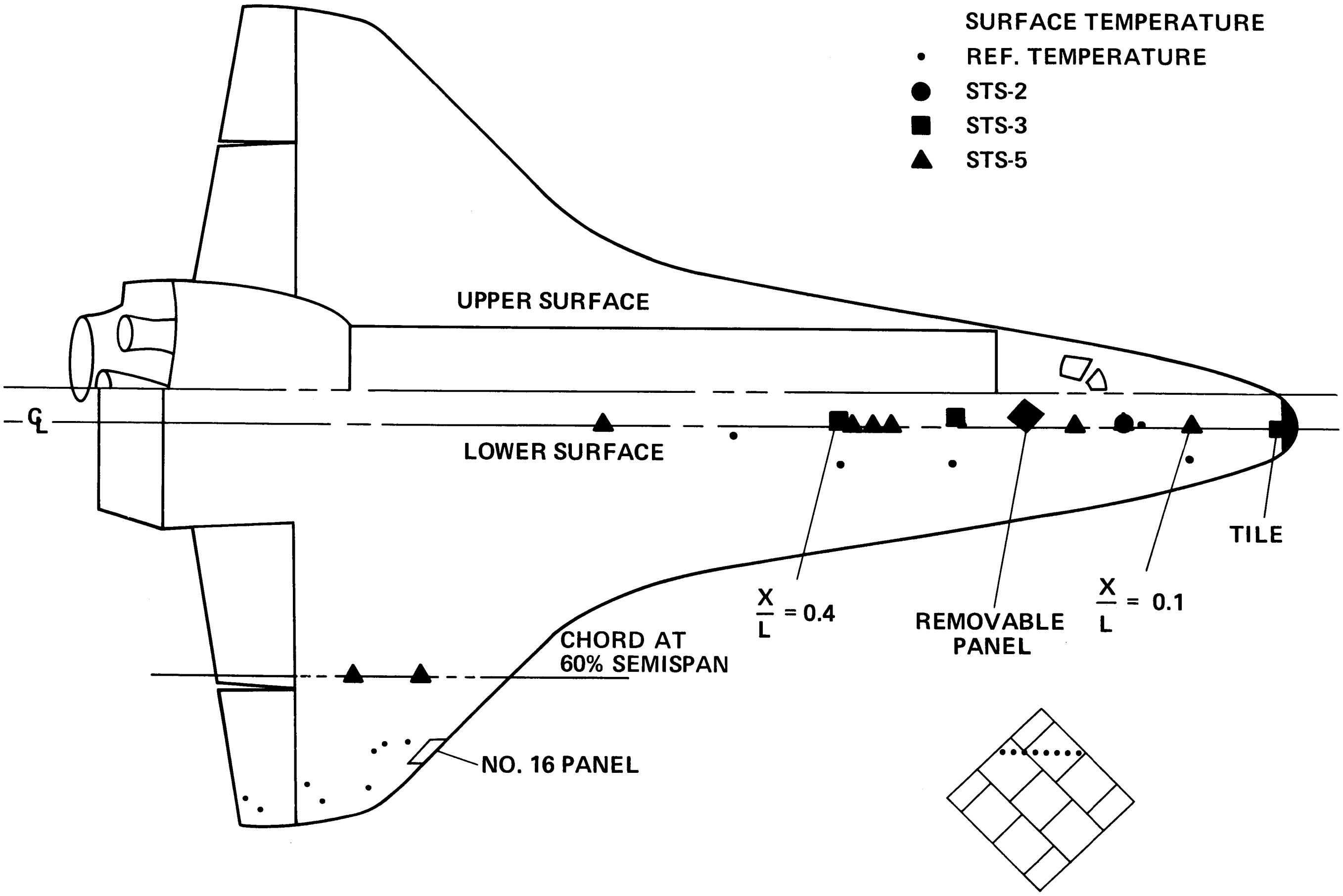

Fig. 2. Catalytic surface effects OEX experiment locations on Space Shuttle.

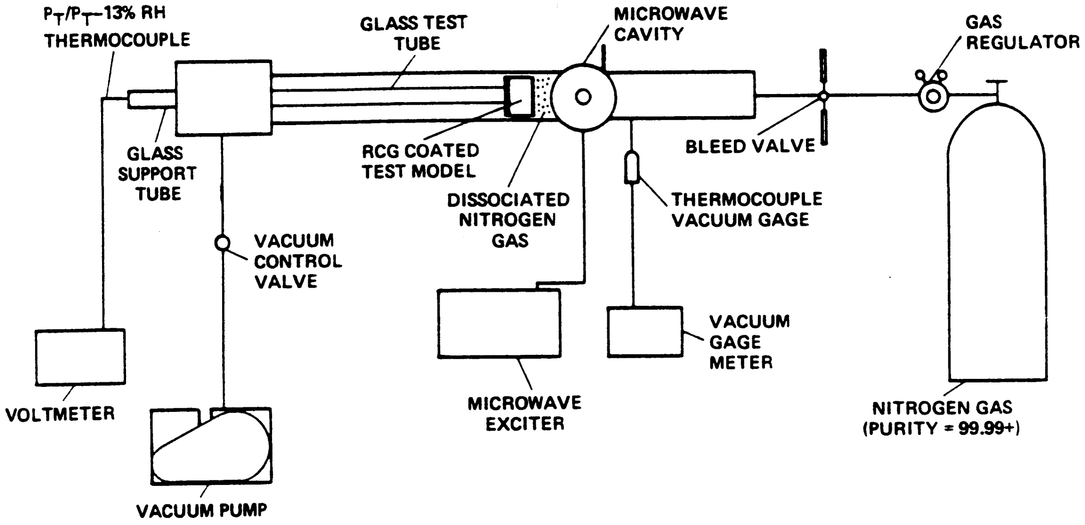

a) Microwave Cavity

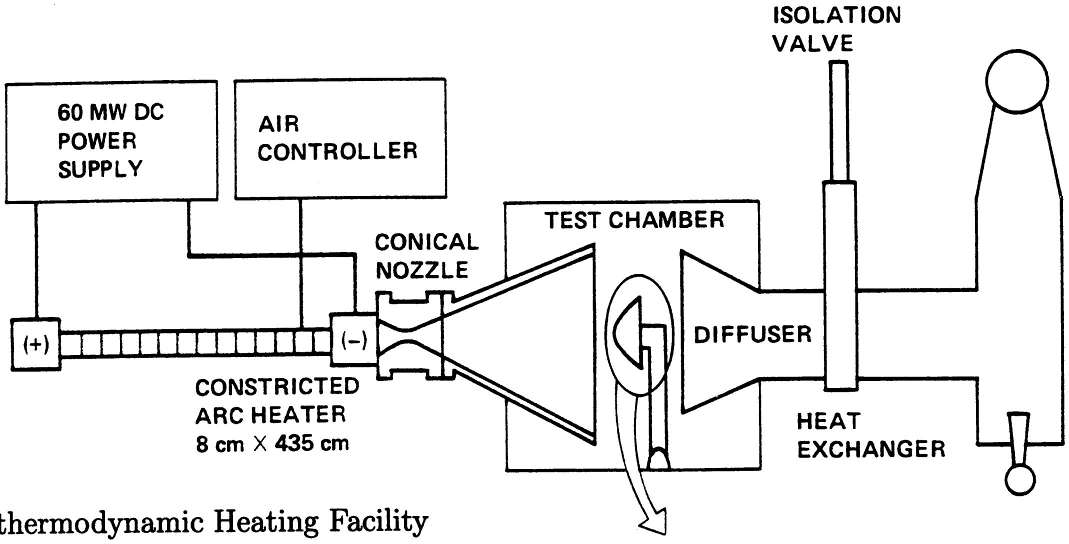

b) Aerothermodynamic Heating Facility

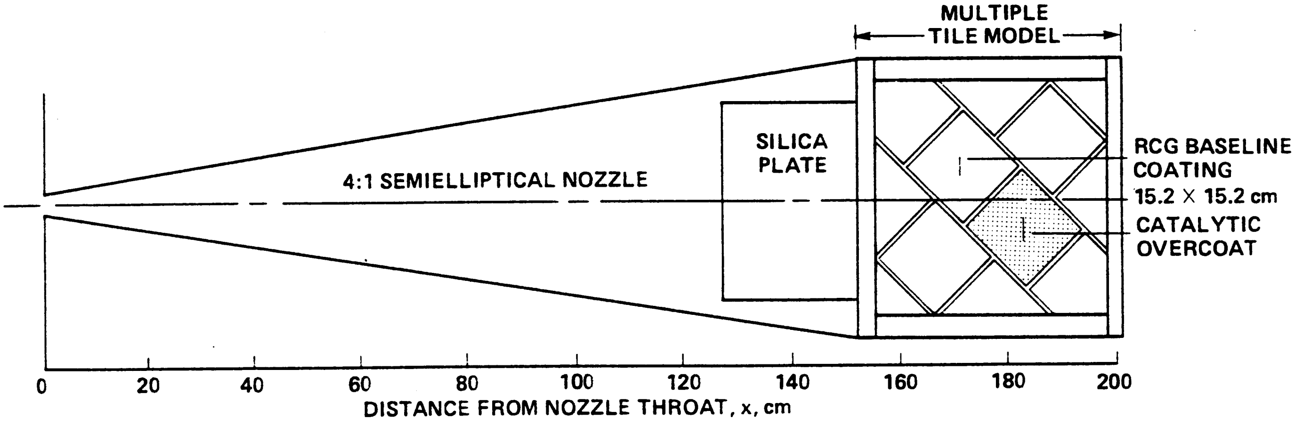

c) 20 MW Pilot Test Facility

Fig. 3. Test facilities.

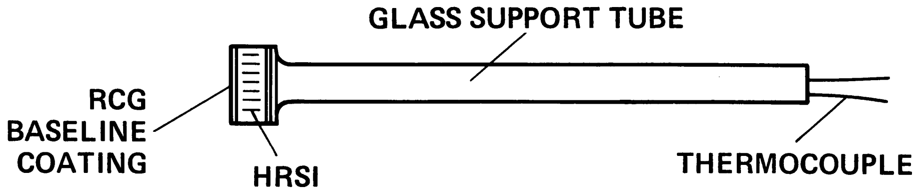

a) Microwave Cavity

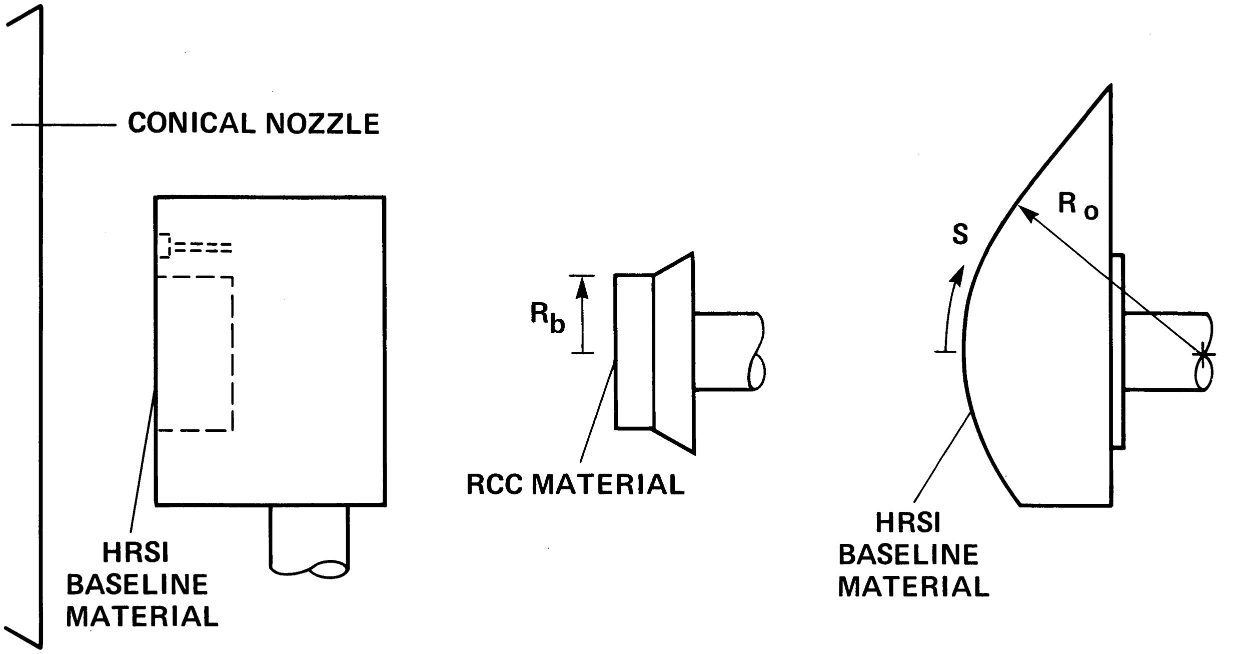

b) Aerothermodynamic Heating Facility

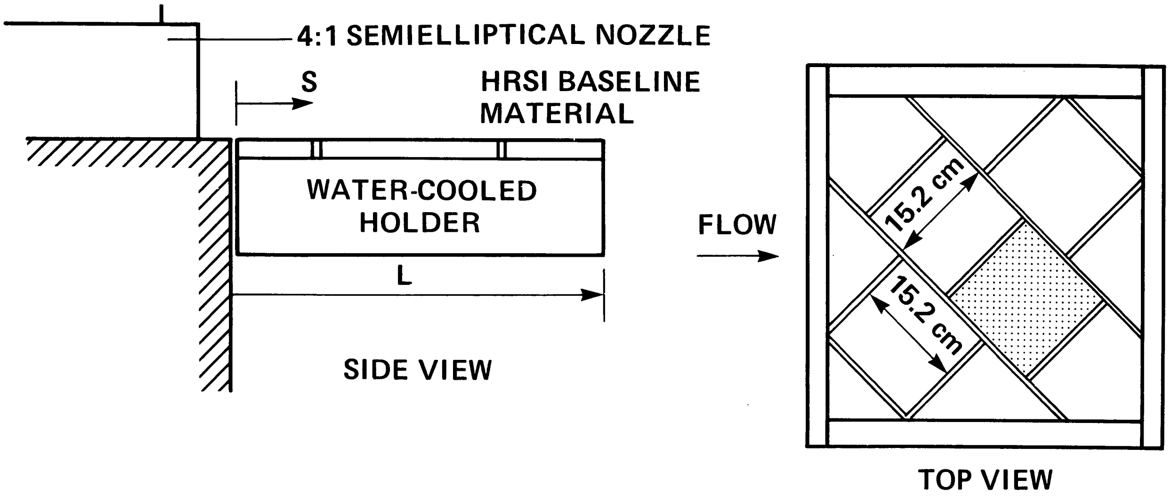

c) 20 MW Pilot Test Facility

Fig. 4. Test models.

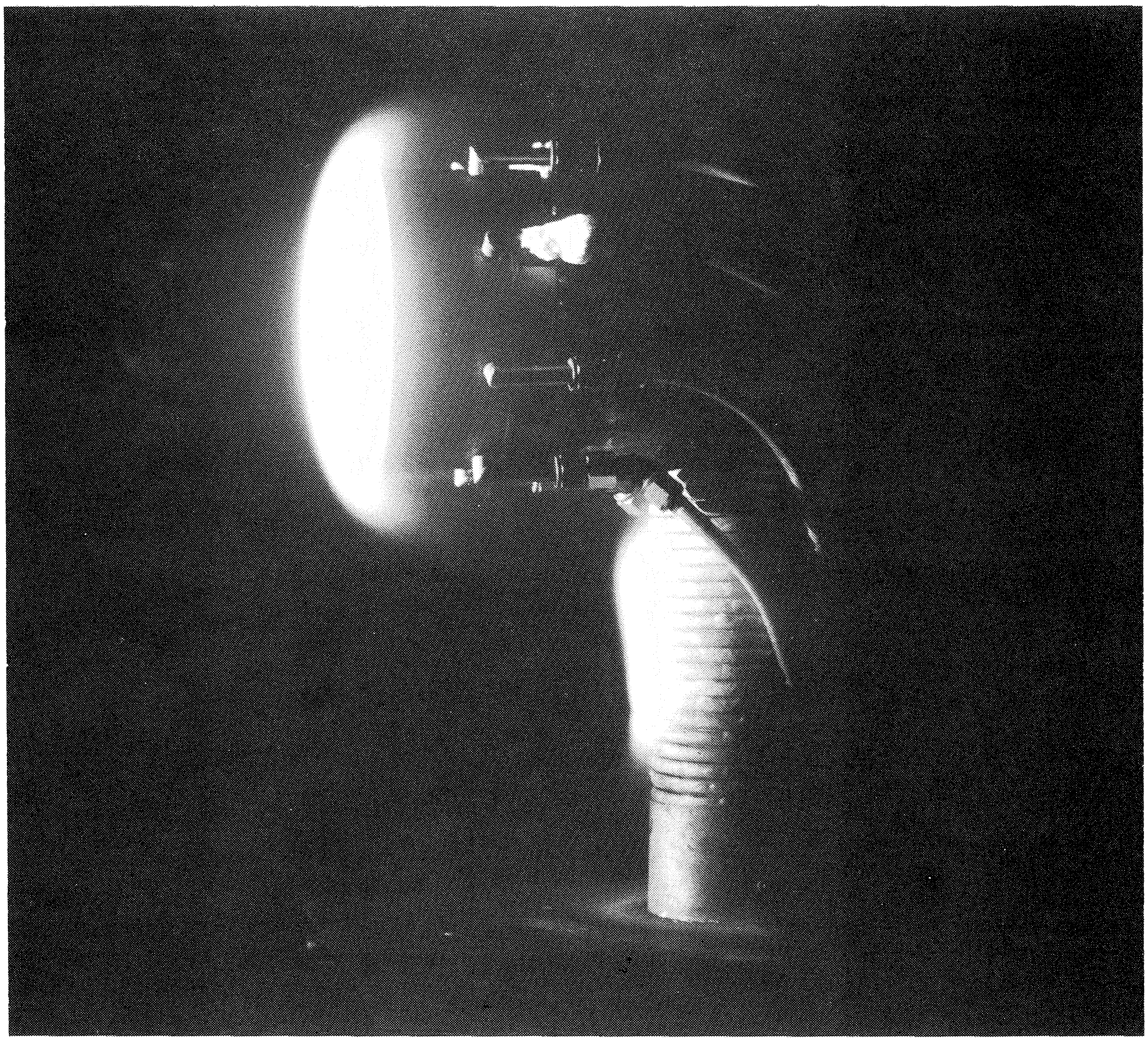

Fig. 5. Exposure of test model to hypersonic arc-jet air stream in the Aerothermodynamic Heating Facility.

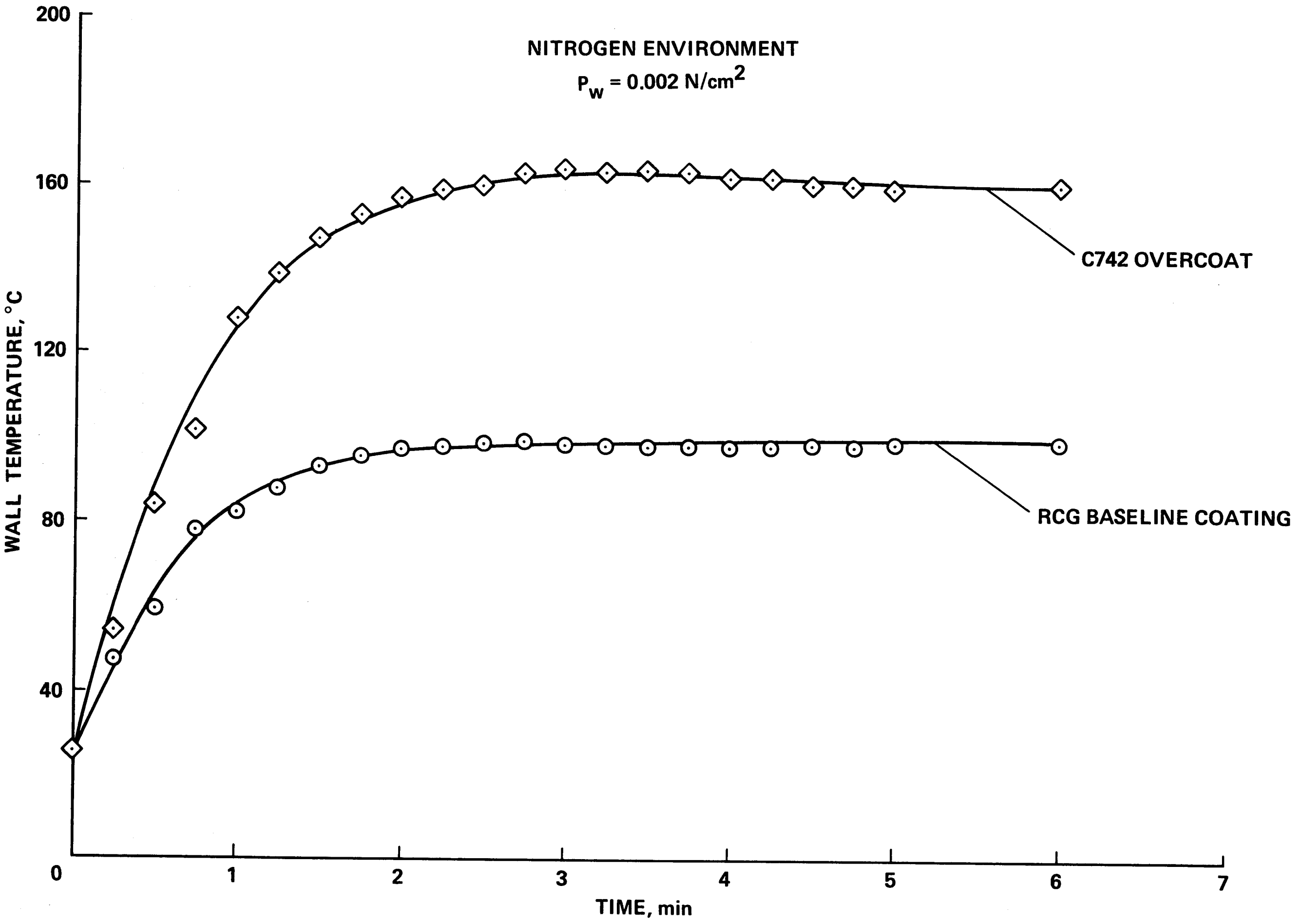

Fig. 6. Temperature response of HRSI surface with and without a high catalytic efficiency overcoat.

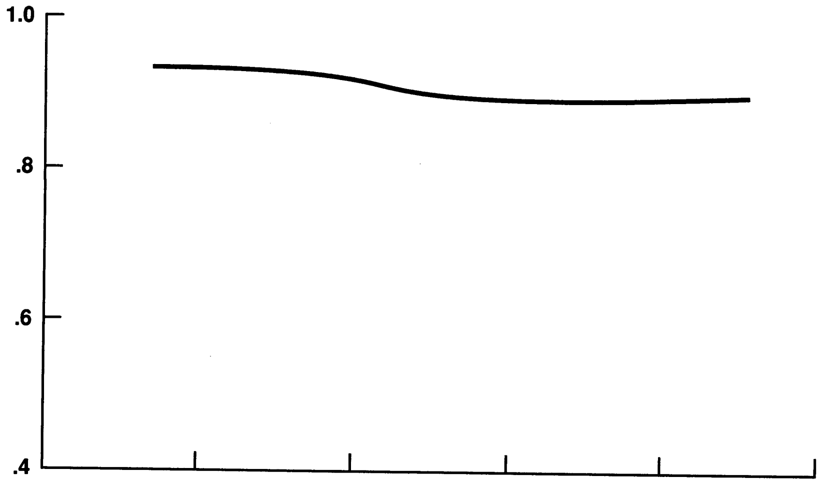

a) RCG baseline coating

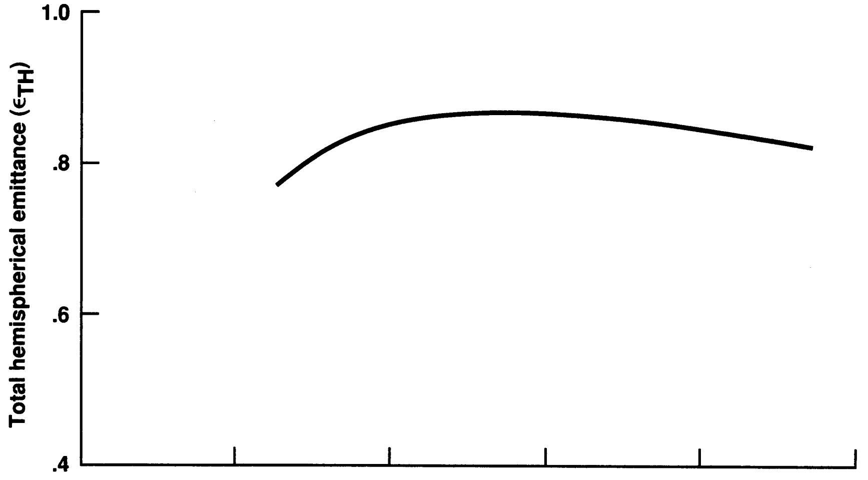

b) TEOS coated RCC

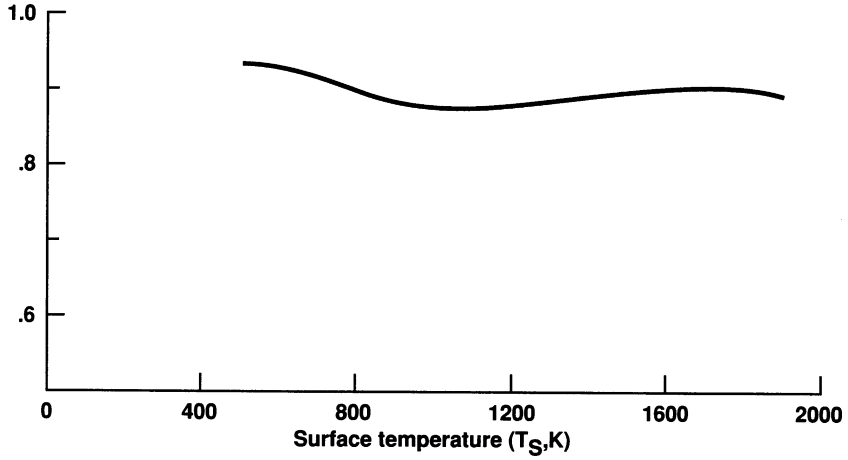

c) C-742 catalytic overcoat

Fig. 7. Total hemispherical emittance.

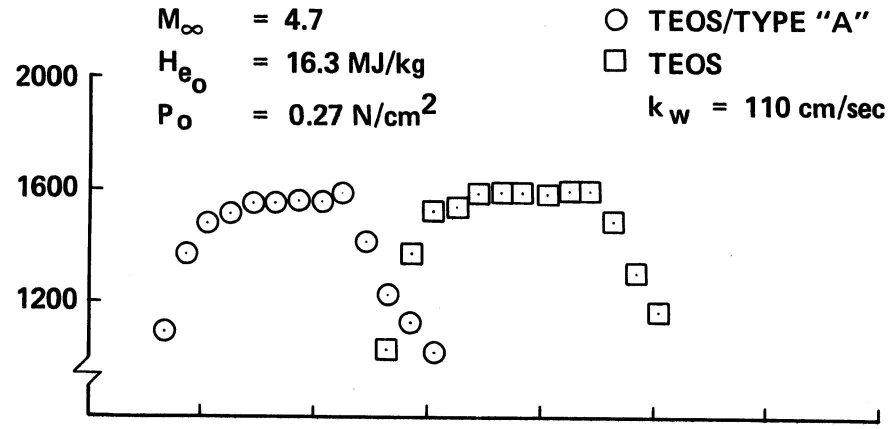

a) RCC

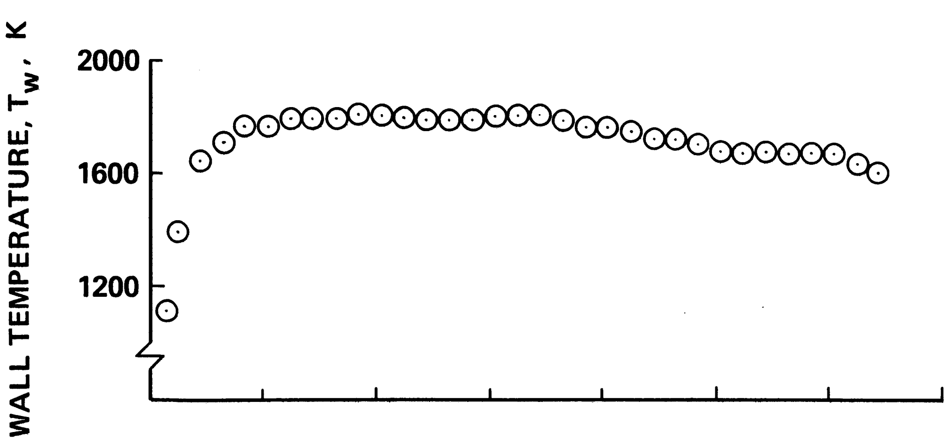

b) Type "A" coated RCC with C-742 overcoat

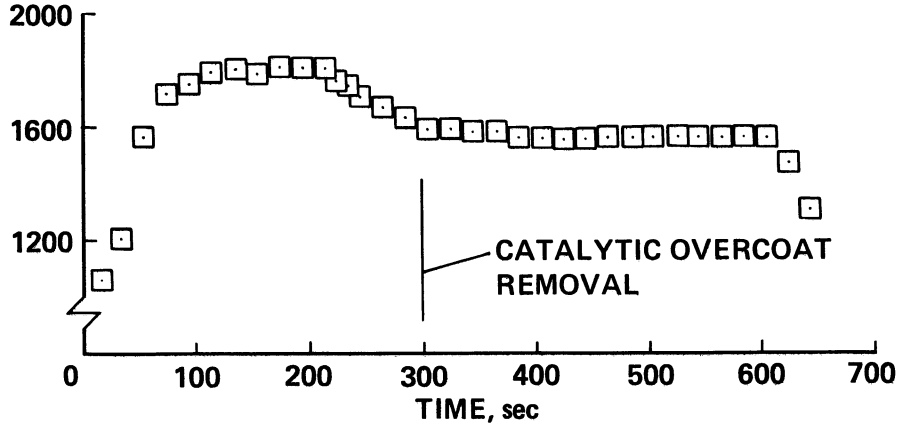

c) TEOS coated RCC with C-742 overcoat

Fig. 8. High temperature performance of C-742 overcoat in arc-jet air stream.

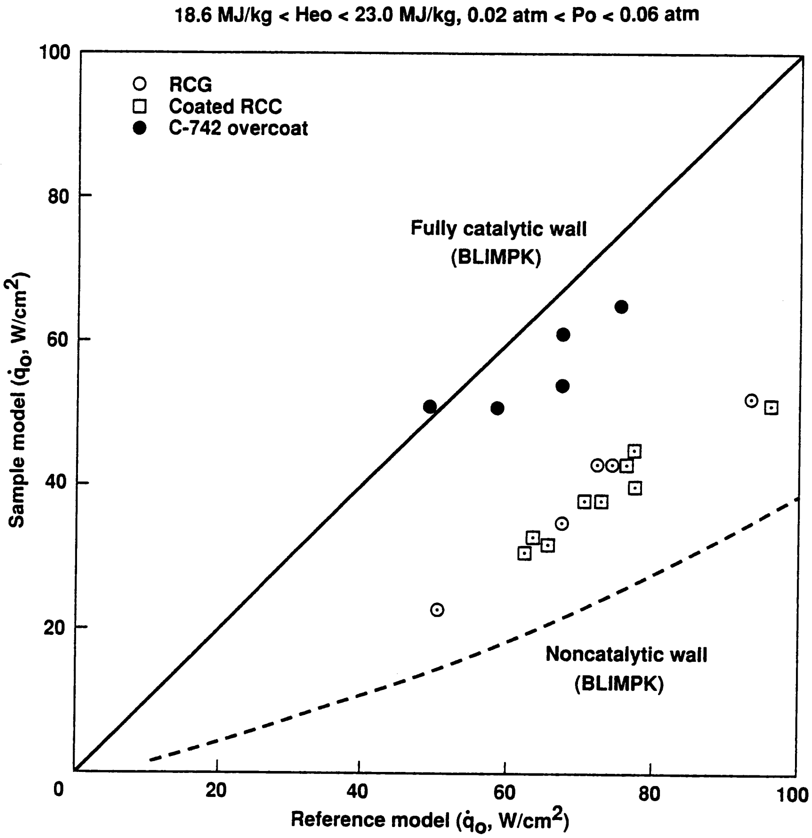

Fig. 9. Relative catalytic efficiency of baseline Orbiter TPS and C-742 overcoat.

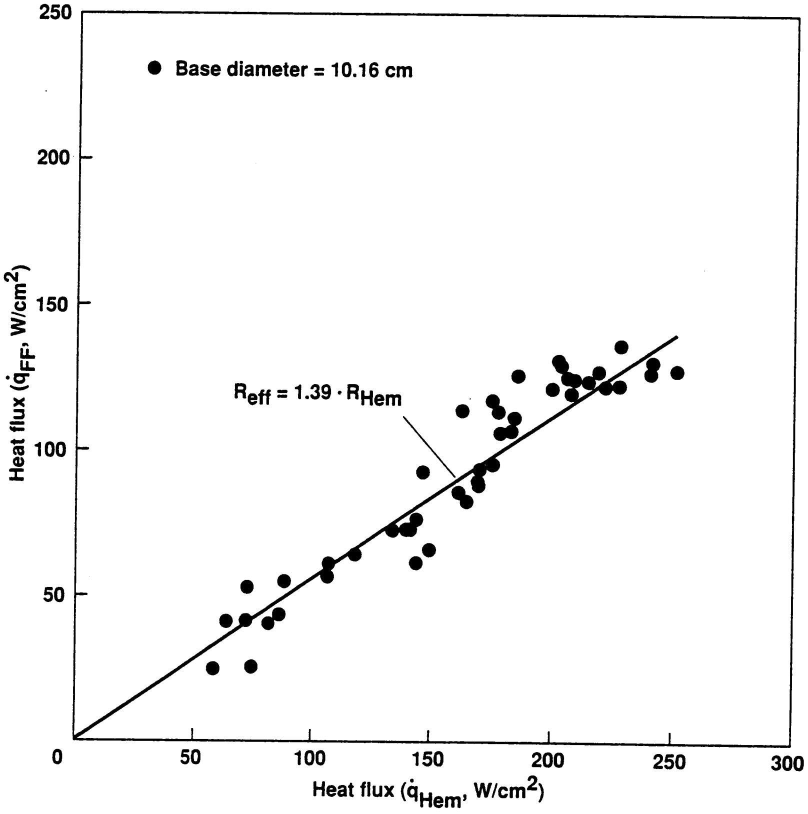

Fig. 10. Effective nose radius of flat-faced cylinder (Eq. 4).

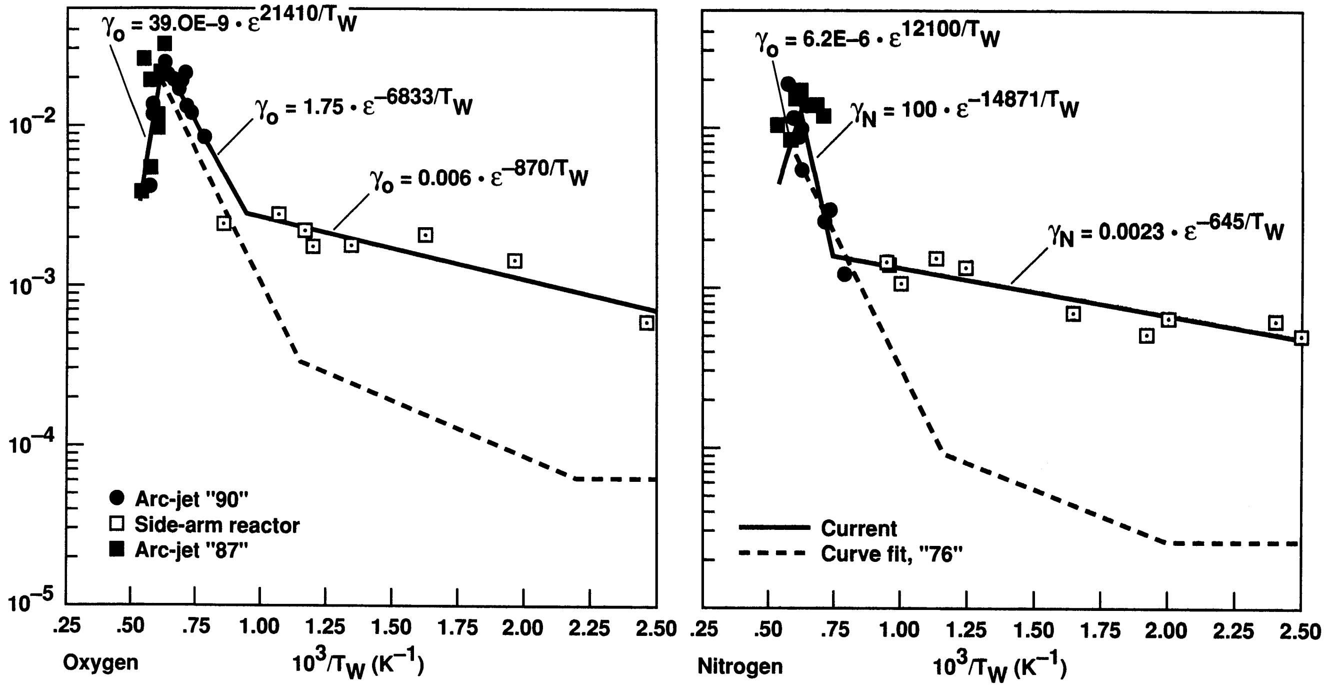

a) RCG

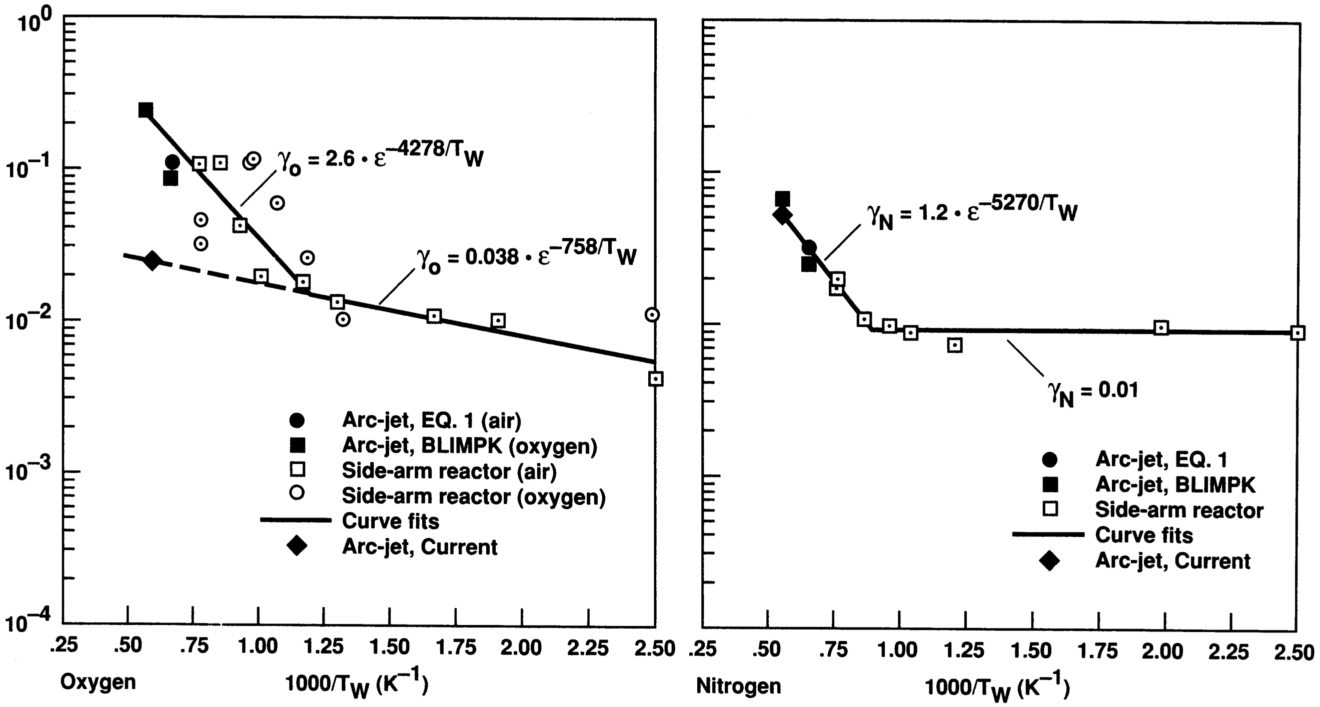

b) C-742 (spinel)

Fig. 11. Recombination coefficients.

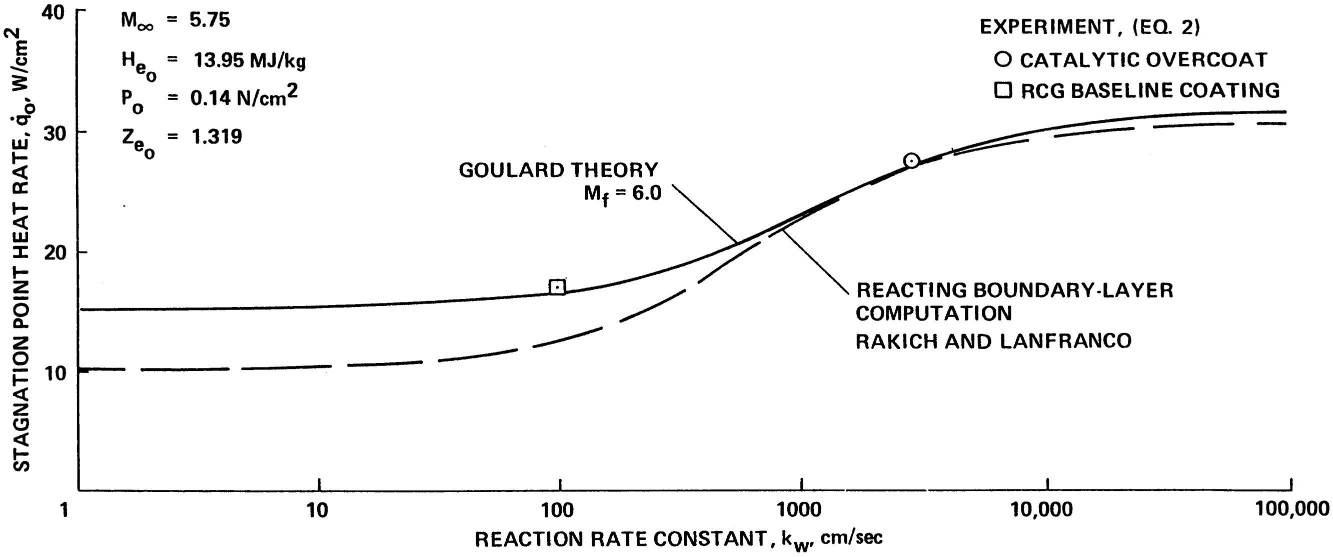

Fig. 12. Comparison of measured and predicted heat transfer rate to flat-faced cylinder during arc-jet exposure.

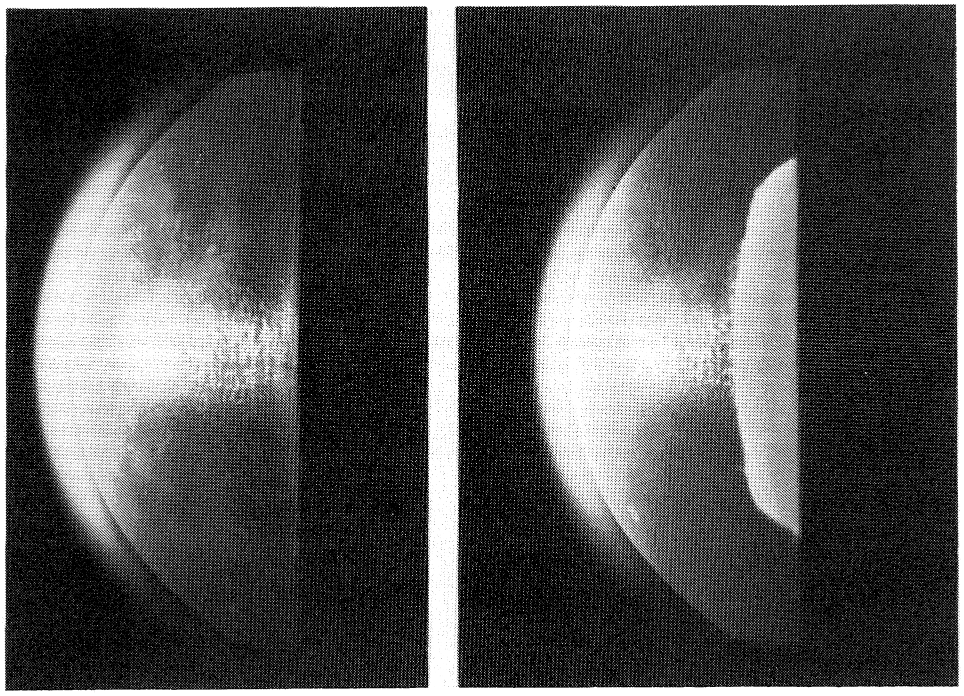

a) RCG baseline

b) catalytic overcoat on trailing edge

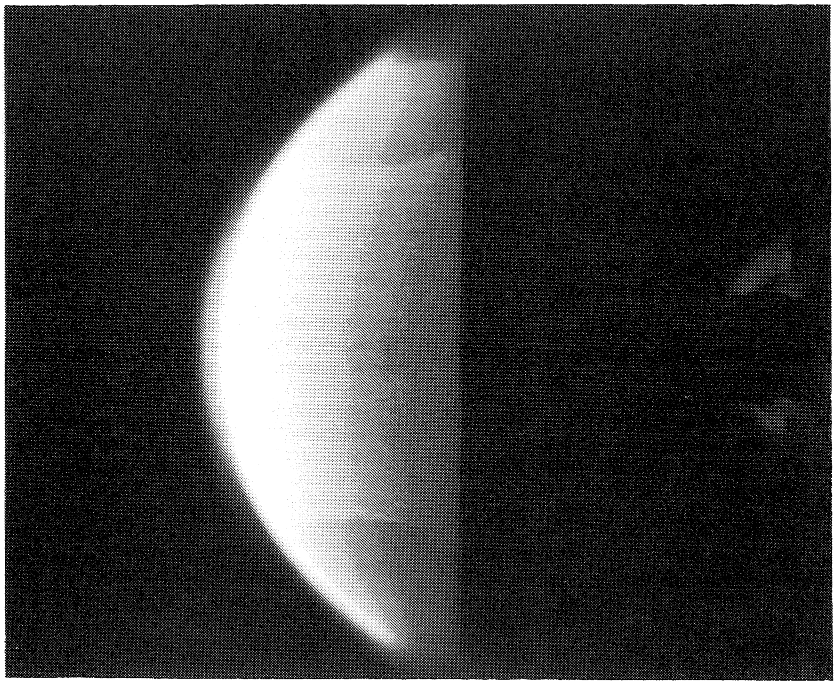

c) catalytic overcoat strip

Fig. 13. Photographs of forty-degree blunt cone in arc-jet air stream.

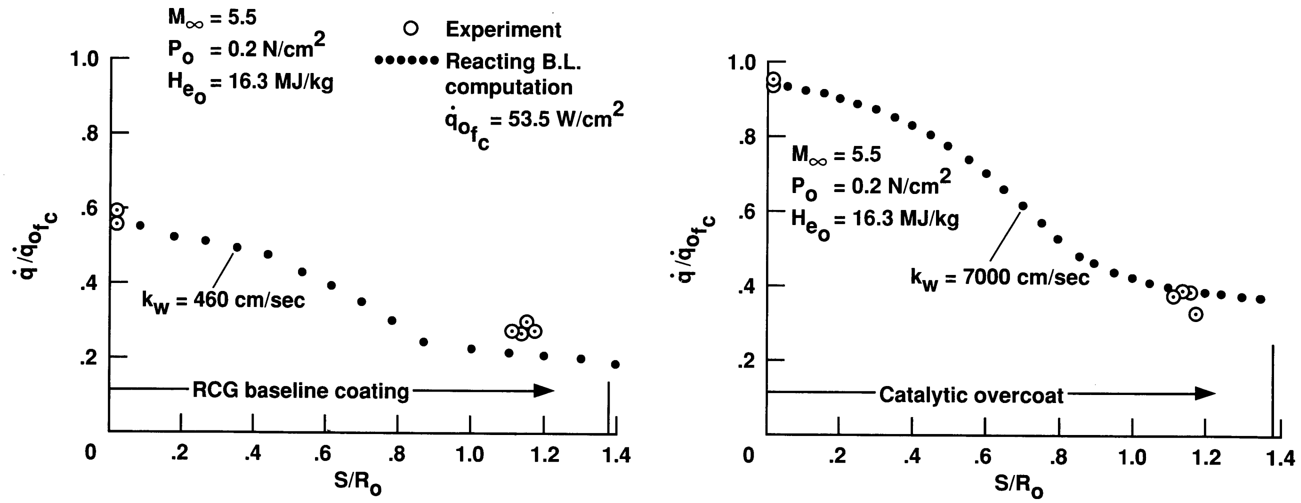

a) Noncatalytic and fully-catalytic surfaces

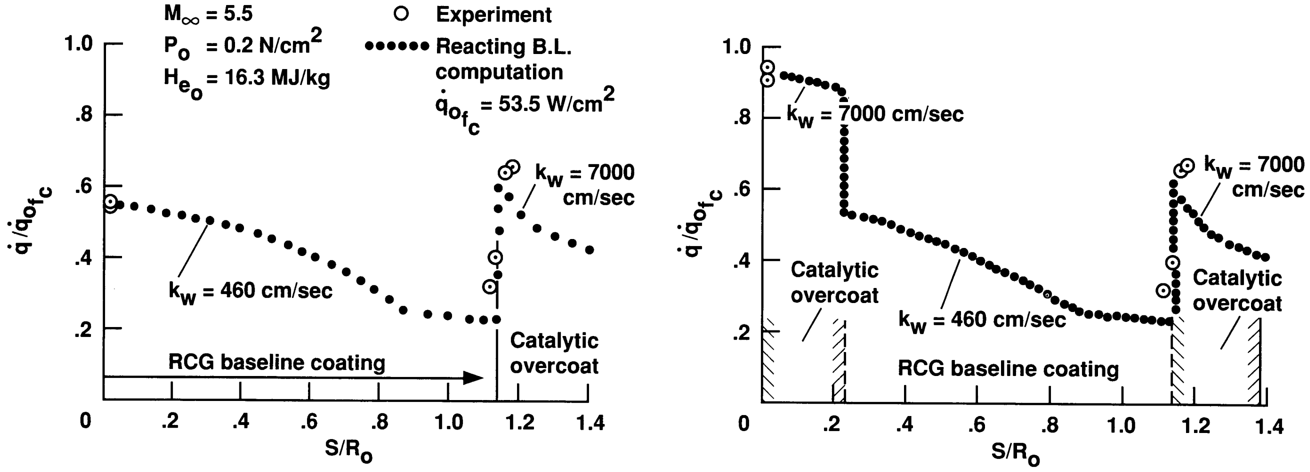

b) Partial catalytic surface

Fig. 14. Heating disrtribution over 40° blunt cone during exposure in laminar flow during arc-jet tests.

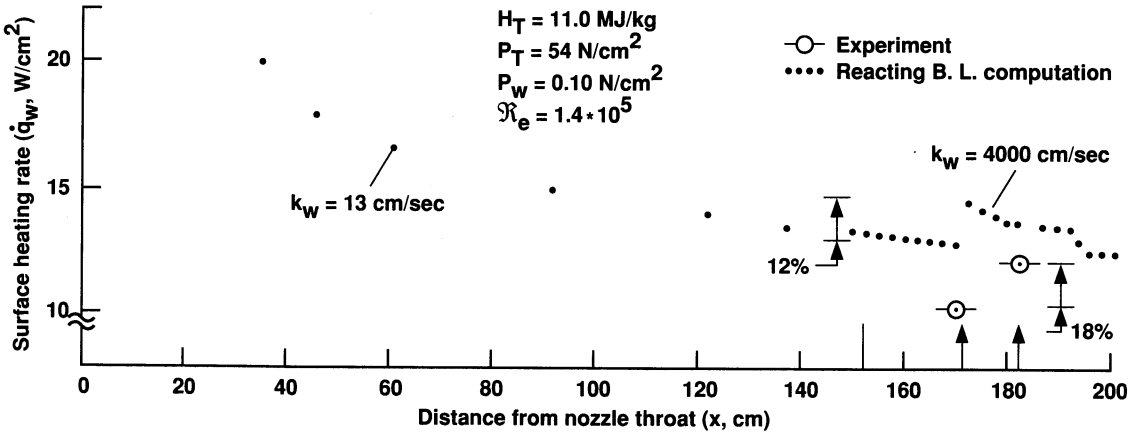

a) Heating distribution along nozzle wall and test model

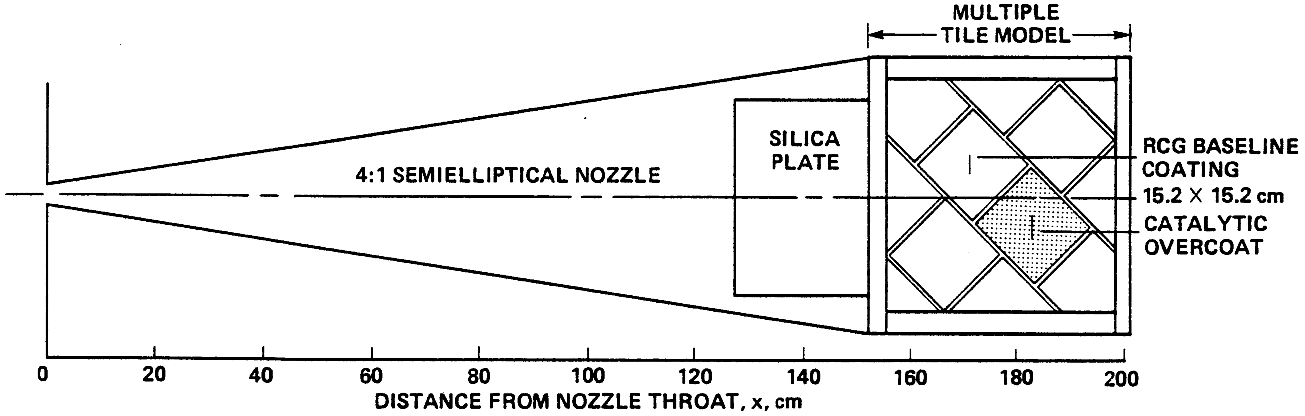

b) Test configuration

Fig. 15. Heating distribution over flat-plate in transitional flow during arc-jet tests.

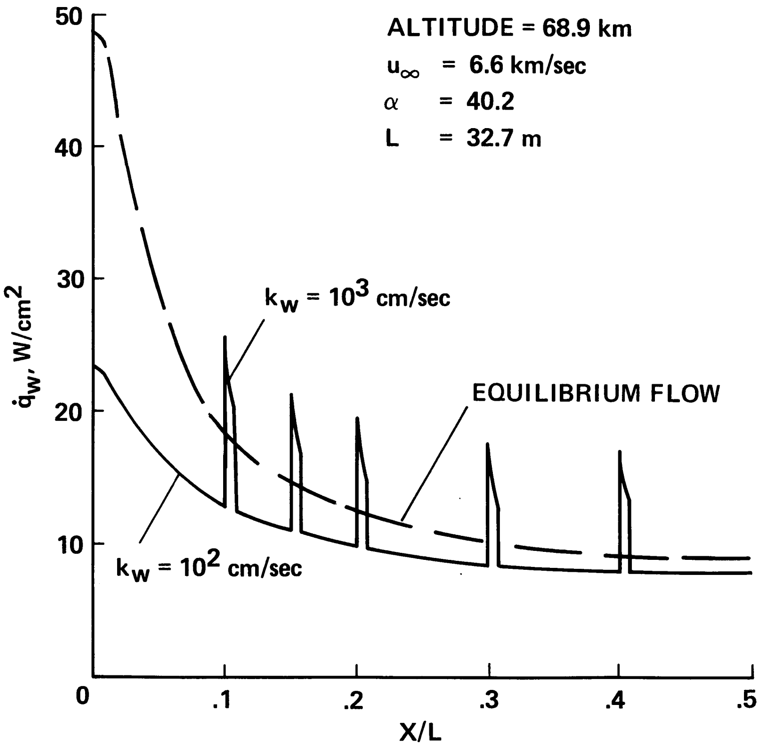

a) Heating distribution along centerline of the Orbiter

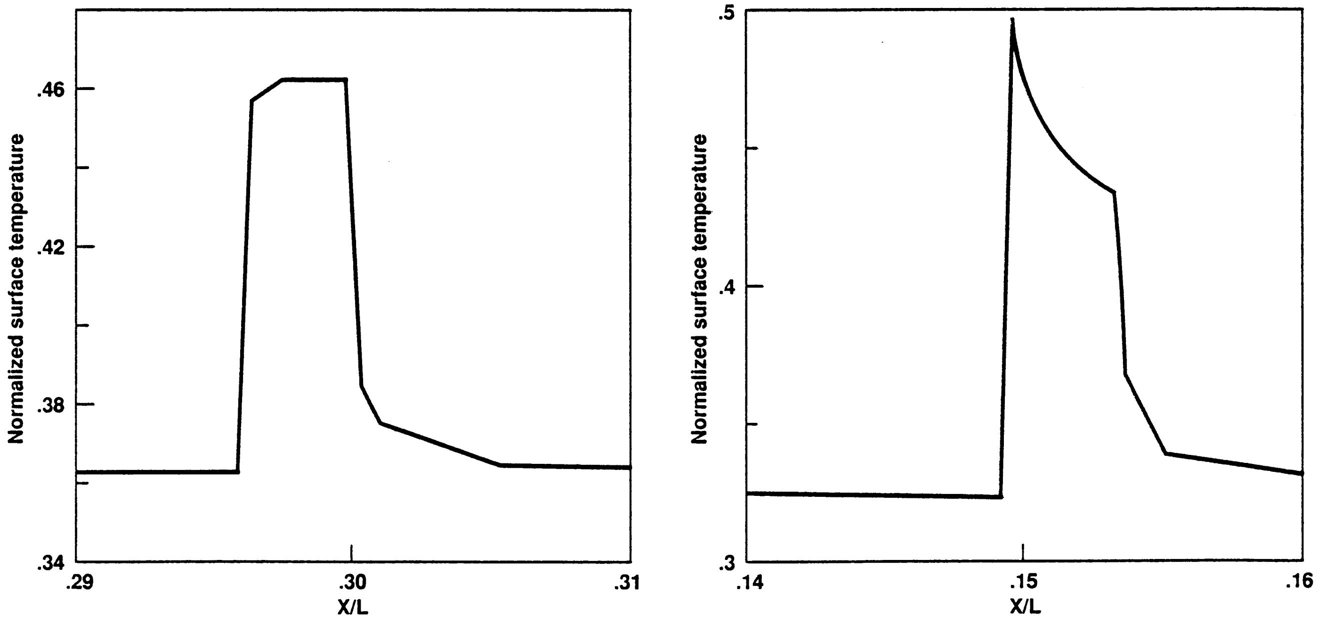

b) Temperature Profile (alt. =91 km) c) Temperature Profile (alt. = 75 km)

Fig. 16. Predicted effect of the C-742 overcoat on the heating distributions for selected areas on the Orbiter.

TILE GAP HEATING (TGH) EXPERIMENT

W. C. Pitts
Eloret Institute
Sunnyvale, CA

M. S. Murbach
NASA Ames Research Center
Moffett Field, CA

SUMMARY

Data are presented from Space Shuttle (STS-2) flight measurements of the temperature distribution within the gaps of the reusable surface insulation tiles. This was the first of a planned series of flight measurements in which the gap width and tile edge radii were to be systematically varied. The data show in depth temperature responses to variations in surface heating, including the variation due to the passage of the flow transition boundary over the test panel. The local heating rates along the gap wall surfaces were calculated from the measured temperature distribution. Unfortunately, the gaps partially closed during launch or reentry so that these gap wall heating rates were found to be only slightly larger than the surface heating rates. Modifications are described to alleviate the gap closure problem for later flights. The TGH panel was loaned to Rockwell for a Scorched Filler Bar test for the STS-4 and STS-5 flights. Some results of this test are also presented.

INTRODUCTION

The under surface of the Space Shuttle Orbiter is thermally protected from reentry heating by a High Temperature Reusable Surface Insulation (HRSI). The HRSI is made in nominally 6-inch by 6-inch tiles which are bonded to the aluminum structure through an intermediary strain isolation pad (SIP). Because of thermal expansion of the structure during entry, it was necessary to leave gaps between the individual tiles. The challenge was to make the gaps wide enough to avoid mutual crushing due to thermal expansion, but not to allow excess heating down the gap. The ease of fabrication was also a significant factor. A great deal of development work went into the determination of the optimum gap width and edge radius for the tiles. The flow in the gaps is very complex because, among other things, the local transition to turbulence passes over the panel during reentry, the gaps are at angle to the local flow, and they are short and intersecting.

Therefore, most of the development work was experimental. It was not possible to simulate exactly the reentry flight environment. Nevertheless, hundreds of heat flux measurements were made by many investigators. These were assembled and correlated to produce empirical equations for estimating heat fluxes to the gap walls for a variety of gap configurations (Ref. 1). Although valuable, these equations and test data from tile models in arc-jet facilities could not be relied upon to assure the adequacy of the thermal protection system. Therefore, margins of safety had to be added to the tile thickness and the tolerance on the tile gap width was made smaller than actually required. This made the thermal protection system heavier and more costly to fabricate than actually necessary.

To minimize the HRSI mass and fabrication cost for future, advanced space transportation vehicles, it is necessary to understand the heat flow within the tile gaps of a reentering vehicle. For this reason a Tile Gap Heating (TGH) Experiment was developed to be flown on the early Space Shuttle missions. This experiment was designed to provide temperatures within the gaps during reentry. These data were to be used to assess the adequacy of analytical and empirical methods, and of ground test data (Refs. 2 and 3) to simulate flight conditions, and ultimately to improve the confidence in tile gap design for future reentry spacecraft. In this paper the data from the TGH panel on the STS-2 flight are presented and discussed.

SYMBOLS

A	Visible area of opposite gap wall
F	View factor
k	Thermal conductivity
l	Orbiter body length
n	Normal to local surface
q_c	Convective heat flux
t	Time
T	Temperature
T_S	Local surface temperature
T_W	Surface temperature of opposite wall
x	Axial distance from Orbiter nose
ε	Emissivity
λ	Coating thickness
σ	Stefan-Boltzmann constant

THE TGH EXPERIMENT

The basic purpose of the TGH experiment was to provide information on how to safely optimize the tile gap configuration so that future advanced space transportation vehicles could be designed with smaller margins of safety on tile thickness and larger gap widths . The basic features of the gap configuration were its width and the tile edge radius at the top of the gap. The plan of the experiment was to measure temperatures within the gaps during successive reentries for a matrix of gap widths and edge radii. This matrix is shown in Table 1. For the STS-2 flight, the design gap width was 0.11 cm (45 mils) and the tile edge radius was .08 cm (30 mils). Preflight measurements verified that all gaps on the tile panel were 0.11 $^{+.05}/_{-0.0}$ cm (45 $^{+20}/_{-0}$ mils). The first three geometry options were fixed for fabrication prior to the first flight. The fourth gap design was tentative and subject to change if so dictated by the early flight data. The intention was that the gap design for the final flights should approach an optimum configuration. Flights STS-4 and STS-5 do not appear because the panel was loaned to Rockwell for a Scorched Filler Bar Test which will be discussed later.

Table 1. Parameter Matrix for TGH

STS Flight #	2	3	6	7	8
Gap Width					
cm	0.114	0.114	0.114	0.165	TBD
(in)	(0.045)	(0.045)	(0.045)	(0.065)	
Radius					
cm	0.076	0.152	0.229	0.152	TBD
(in)	(0.030)	(0.060)	(0.090)	(0.060)	

The instrumented tiles are mounted on a panel under the fuselage (Fig. 1). The center of the panel is located 27% of the body length aft of the nose (x/l = 0.27) and is 20 cm off the centerline. The panel consists of 11 tiles (Fig. 2) which were cemented to an aluminum carrier plate via a strain isolation pad (SIP) as indicated in Fig. 3. The SIP was required because of the difference in thermal expansion between the tiles and the aluminum structure. This plate was bolted to the Shuttle structure and was replaced after each flight with another assembly from the test matrix. Just before mounting the panel, measurements were made of all gap widths and step heights between adjacent tiles. These measurements were repeated after the flight. For all of the test panels, the top surface was kept as flat as possible.

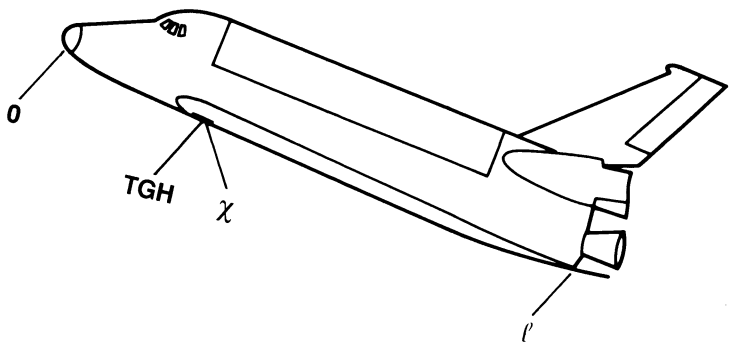

Fig. 1 Location of Tile Gap Heating Experiment on Orbiter.

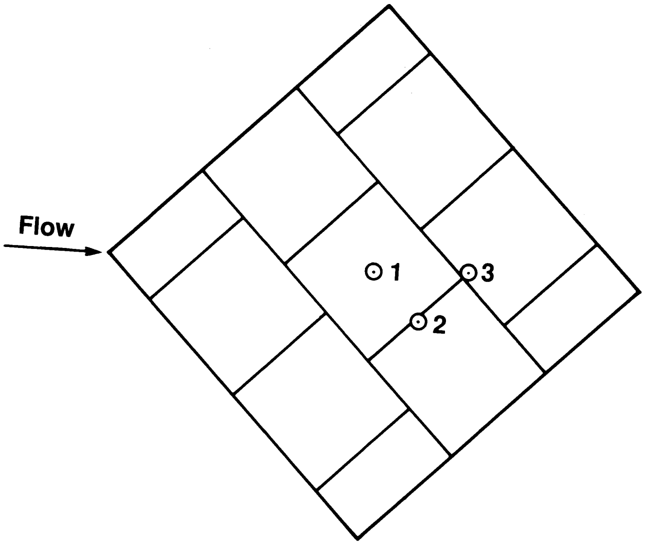

Fig. 2 Thermocouple locations and stack designations for flight test panel.

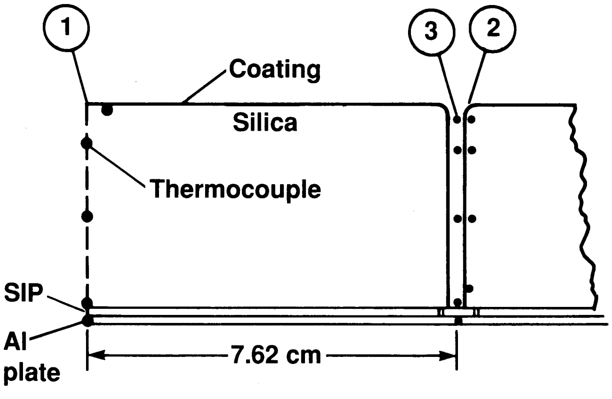

Thermocouple depth, cm

①	③	②
.005	–	–
–	0.23	0.23
0.64	0.64	0.64
1.90	1.90	1.90
–	–	3.81
4.16	4.16	–
Aℓ	Aℓ	–

Fig. 3 Thermocouple locations in cross section through stacks #1 and #2, looking down gap to stack #3.

Three of the tiles were instrumented with thermocouples mounted in three stacks down the tile, as shown in Fig. 3. Stack #1 consists of 5 thermocouples. The middle thermocouples in the stack were mounted in a plug made of the same high-purity silica fiber as the tile. The bottom thermocouple was mounted on the aluminum carrier plate. The upper thermocouple was left exposed at the top of the tile. The plug was press fit into the center tile so that the surfaces were flush. The thermocouples in the other two stacks were positioned as indicated, and left exposed on the side surface of the tiles. This assembly was then sprayed with a thin layer of reaction cured glass containing a black pigment for high emissivity. Although the surface thermocouples were not actually on the surface, they sensed a temperature very close to the surface temperature because the coating is very thin, and the thermal conductivity of the coating is an order of magnitude larger than that of the silica fiber.

Temperatures measured from stack #1 served as a reference for the temperatures from other stacks. Because of its position, its in depth thermocouples should approximate one-dimensional heat conduction. Stacks #2 and #3 should exhibit progressively more complex gas flow.

FLIGHT DATA

Flight data for TGH and other OEX experiments were recorded on magnetic tape using the Development Flight Instrumentation (DFI) described in Ref. 4. Temperature data were recorded once each second throughout the entry phase of the mission. Figure 4 shows the STS-2 temperature histories for all thermocouples of the TGH experiment from initiation of entry to about 15 minutes after touchdown. The surface temperatures for the top thermocouple of stack #1 show a rapid rise, a plateau, and then a step. The surface temperature then remained relatively constant for about 500 seconds until the peak entry heating phase was completed and cooling began. At about 1250 seconds there was a sudden temperature rise as the transition flow front passed over the TGH panel.

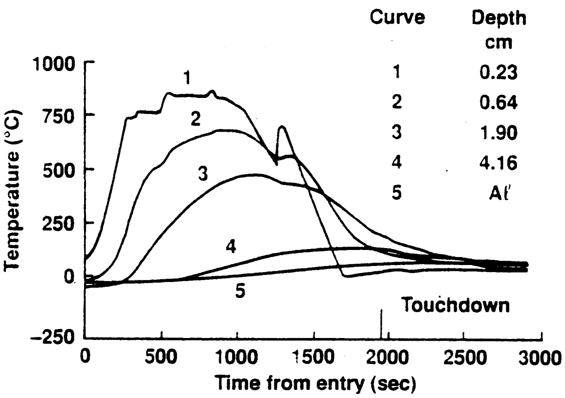

Fig. 4a STS-2 flight data temperature profiles, Stack # 1.

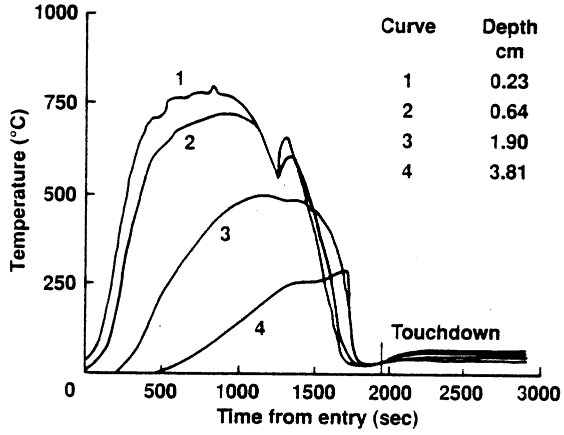

Fig. 4b STS-2 flight data temperature profiles, stack #2.

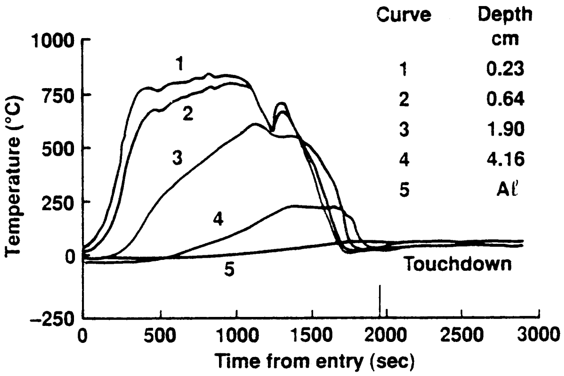

Fig. 4c STS-2 flight data temperature profiles, stack #3.

The in-depth temperature variations within stack #1 are shown in Fig. 5 for several times. The temperatures exhibit the familiar one-dimensional transient profile (time = 500 seconds) during the first part of the entry. During the period of constant surface temperature it assumes the linear, steady-state shape (1000 seconds). The remaining curves show how the center core of the tile cools down. By touchdown the bottom of the tile has started to cool (compare 1600 and 1950 seconds).

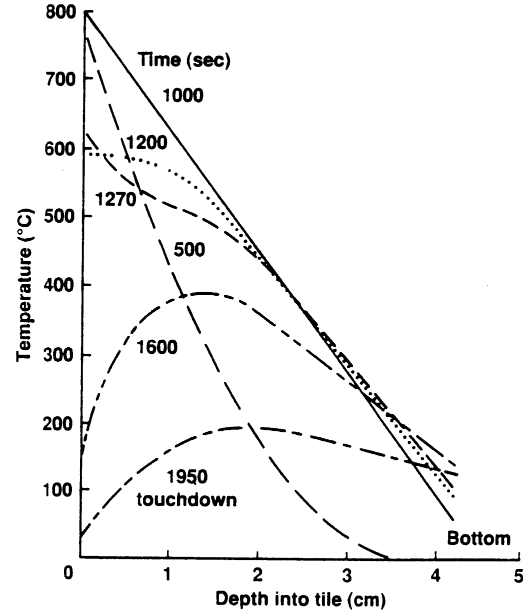

Fig. 5 Time dependent temperature profiles for stack #1; flight data.

The gap temperatures are related to the center of tile data in Fig. 6. This figure is intended to show qualitative trends only. The temperature rises are relative to an approximate average tile temperature at the start of entry, - 43 C. The gap temperatures were no more than 20 percent larger than those at the same depth in stack #1, except near the bottom of the gap where the magnitude of the temperature rise was small. The reason for the small effect is that the instrumented gap widths had been compressed during flight. Pre launch measurements verified that all gaps on the panel were the nominal $0.114\ {}^{+0.05}/_{-0.00}$ cm ($0.045\ {}^{+0.02}/_{-0.00}$ in). Post flight measurements showed the instrumented gaps to be about 0.013 cm (.005 in). Not all of the other panel gaps were compressed. More will be said of this compression later.

Corresponding temperatures in stacks #2 and #3 are quite close. The one interesting observation is that the temperatures in stack #3 were always slightly higher than those in stack #2 while the tiles were heating, and slightly cooler while the tiles were cooling. This substantiates the speculation, made earlier, that flow within the gap at stack #3 should be better developed than that at stack #2 because of the longer, continuous gap.

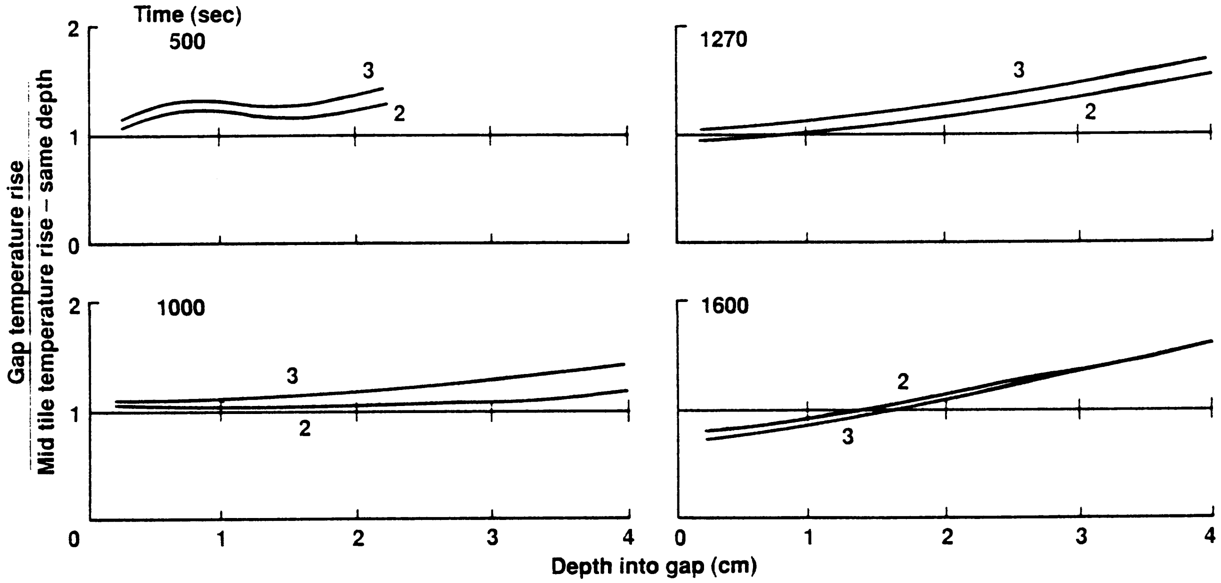

Fig. 6 Comparison of internal temperatures at stacks #1, #2 and #3.

Fig. 7 shows that the aluminum structure temperature below stack #3 differed very little from that near the center of the panel. At touchdown the structure was starting to cool.

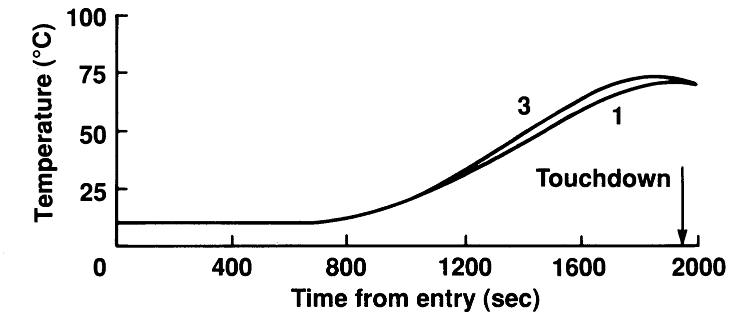

Fig. 7 Temperature of aluminum carrier plate.

After the STS-2 flight, design modifications were implemented to minimize the gap compression problem, but fabrication could not be completed in time for the next flight. The STS-3 flight panel was, therefore, flown as originally designed. Again the instrumented gaps were compressed during the mission, so no significant data were obtained.

DATA ANALYSIS

The basic plan of the TGH experiment was to determine from data, from a series of Orbiter flights, the effects of tile gap widths and edge radii on the convective heat transfer within the gap. The fulfillment of this purpose, therefore, required the completion of several Orbiter flights. For this reason, and because the data from the STS-2 flight showed such small gap effects, no detailed analysis of the gap flow was undertaken after the STS-2 flight. Instead the analysis was limited to backing out the heat fluxes to the surface at the thermocouple locations. This was done using the NASTRAN thermal analyzer code.

NASTRAN is a finite element code that was originally implemented to perform stress analysis of large structural systems. It was adapted to the solution of thermal conduction problems by taking advantage of analogies between elasticity and heat conduction equations. Both steady state and transient problems can be worked. It was intended that temperature dependent thermal properties could be utilized, but difficulties inherent to the code were encountered. Therefore, the calculated results presented were obtained using average values for thermal conductivity, heat capacity, and emissivity.

For the analysis of the TGH data, the time varying, measured temperatures were applied as boundary conditions to a computer model that simulated the tile. The output was a detailed, time dependent temperature distribution within the volume of the tile. The convective heat flux to the surface was then determined from the basic energy balance equation for the tile coating:

$$q_C = -k\,(\partial T/\partial n) + \rho\, C_p\, \lambda\, (\partial T/\partial t) + \varepsilon\sigma\left(T^4_S - \int F T^4_W\, dA/A\right)$$

All of the terms on the right are either known tile material properties or temperature variations provided by the NASTRAN output. The first term is the heat flux conducting into the surface. The second term is the transient heat storage term. The last term is the net radiation emitted locally from the tile surface and absorbed by the tile surface from the visible portion of the opposite wall of the gap.

Two NASTRAN models were constructed for this analysis. A one dimensional model for stack #1 and a two-dimensional model (shown in figure 8) for stack #2. The one-dimensional model consists, essentially, of one of the columns at the right of the model in Fig. 8, but with adiabatic side walls and expanded to 73 elements. All models assumed the bottom of the aluminum plate to be adiabatic. A three-dimensional model, constructed for stack #3, proved to be too large to run on the computer system available at the time. For the two dimensional model, flight temperatures were available at only four locations down the gap, so it was necessary to interpolate for intermediate points in the model. Symmetry was assumed across the gap.

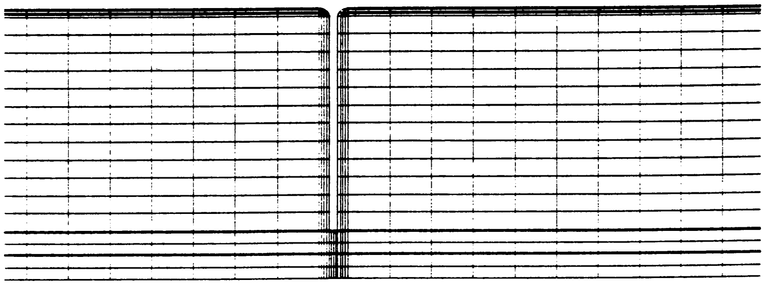

Fig. 8 NASTRAN two-dimensional model.

Some results of the one-dimensional analysis are shown in Fig. 9. The solid curve in the upper part of the figure shows the STS-2 flight temperatures for the top surface of stack #1, with the small spikes in the raw data smoothed out. The TGH panel was not flown on STS-1, but surface temperatures are presented (dashed curve) for a point 0.03 body length forward of the panel center location. Due to recorder problems, flight temperature data were not obtained for this flight prior to 1150 seconds.

The solid curve in the bottom part of the Fig. 9 shows the convective heat fluxes backed out from the STS-2 flight temperature data using the above technique using a surface emissivity of 0.8. The upper, dashed, curve was obtained the same way, except for an emissivity of 0.9. Together, they show the sensitivity of the calculated heat flux to emissivity. The short, dotted, curve shows the corresponding heat fluxes for STS-1, as calculated by Throckmorton (Ref. 5), using an emissivity that varied with temperature from 0.77 to 0.86.

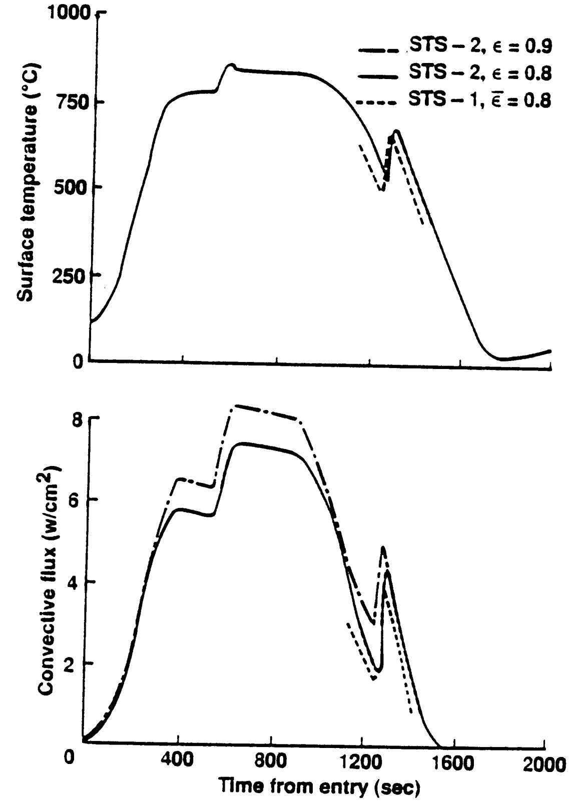

Fig. 9 Comparison of surface temperatures and heat fluxes for STS-1 and STS-2 flights.

In depth temperatures for stack #1 were calculated using the one-dimensional model, and are compared with the flight data in Fig. 10. For this calculation, the surface temperature was constrained to the measured values for the full entry time, so there is no calculated value corresponding to curve #1. The good agreement between the measured and calculated interior temperatures shows that the computer model properly simulated the tile heating process.

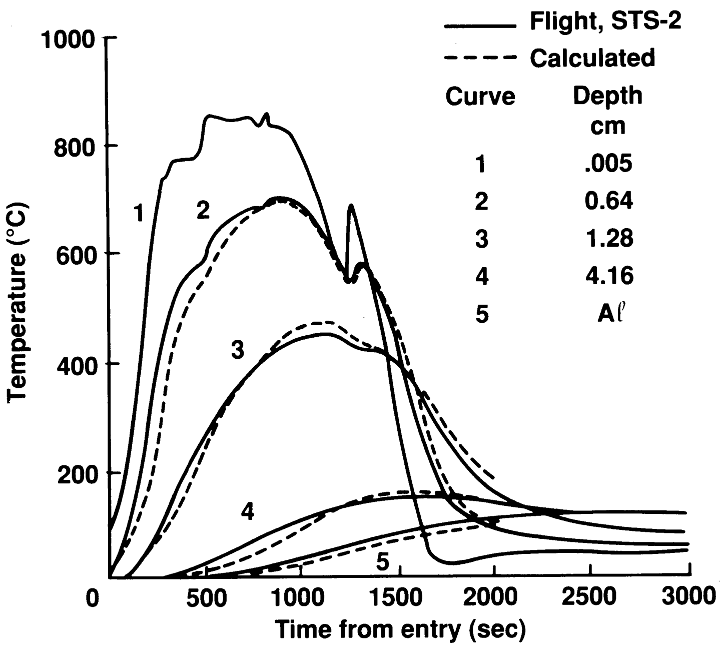

Fig. 10 Comparison of calculated one-dimensional temperature profiles with flight data from Stack #1.

Figure 11 shows the net convective heat flux to the side wall of stack #2 at 0.57 cm (0.22 in) depth. The maximum flux to the wall is only about 1 % of the top surface heat flux. This low heat flux further indicates that the gap width was much less than the preflight measured value, and perhaps even smaller than the post flight measured value.

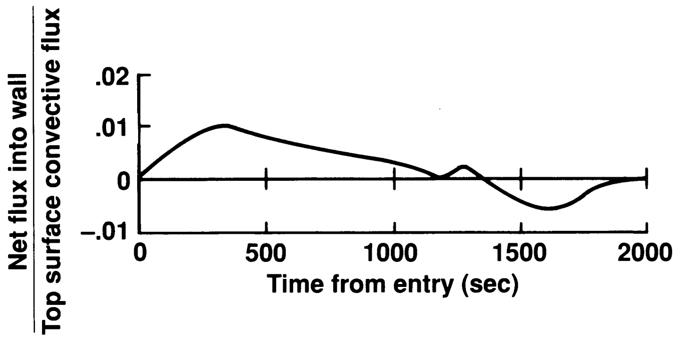

Fig. 11 Net heat flux to gap surface, 0.57 cm (0.22 in) deep at Stack #2.

Figures 12a through 12d also show that the convective heating down the gap was very small near stack #2 during the heating phase. The figures show calculated isotherms in the tile cross section through stacks #1 and #2 for four times. During the heating phase, the flight temperatures in the two stacks differ very little. Thus, the isotherms are constrained to be virtually parallel to the top surface. This means that the major mechanism for heat transfer near the gap is conduction through the tile material. However, just before touchdown, the isotherms show that the gap walls are just as effective in cooling as the top surface. This is due, at least in part, to the higher pressure in the gap, but it may also be due to the gap partially reopening as the tiles cool.

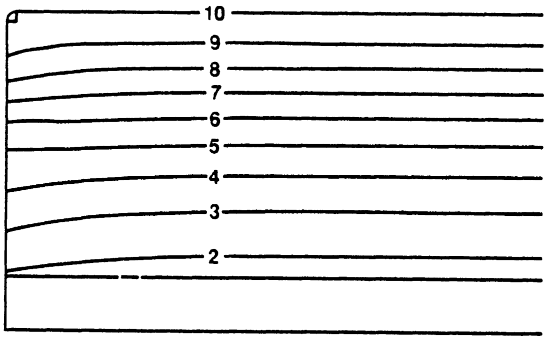

a) Time = 800 sec, max. temperature = 823 °C (isotherm #10).

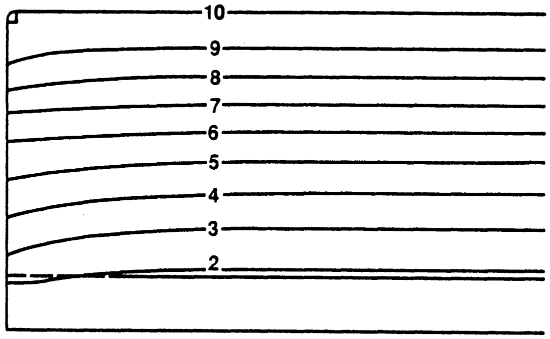

(b) Time = 1000 sec, max. temperature = 793 °C (isotherm #10).

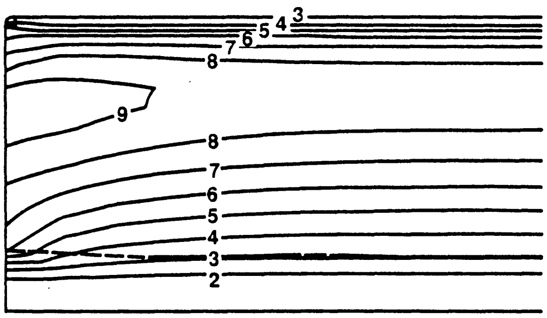

(c) Time = 1600 sec, max. temperature = 414 °C (isotherm #10).

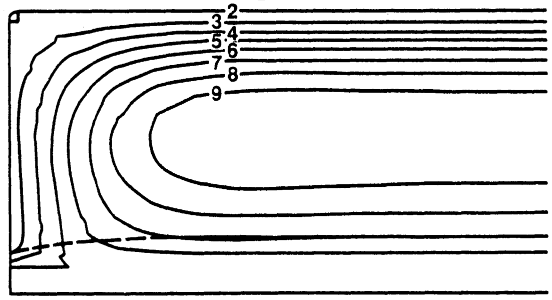

(d) Time = 1900 sec, max. temperature = 200 °C (isotherm #10).

Fig. 12 Isotherms within tile calculated from NASTRAN two-dimensional model with data from Stacks #1 and #2 imposed as surface boundary conditions.

FIXES TO PANEL FOR FUTURE FLIGHTS

There were several causes for the tile gap closure. The basic problem was that the tiles were bonded to the structure through the SIP. This, by design, allows lateral flexing of the tiles. Because of the SIP flexibility, there was no guarantee that the gap width was either the preflight or post flight value while the measurements were being taken. A compounding problem was that the gaps around the edge of the TGH panel contained a gap filler. This filler material is known to expand when heated. So, during the heat pulse, there was probably an inward pressure all around the panel. A third problem was that, for conservatism, the smallest of the test plan gap widths was chosen for the first flight.

To minimize these problems, the panel assembly was redesigned. First the gap filler around the panel was removed. Second the gap width was increased to the maximum allowed. Finally, small rigid spacers were placed at the bottom of the gaps. A modified panel was fabricated, but was not flown.

SCORCHED FILLER BAR TEST

Post flight examination of the tiles after the STS-1 flight revealed that the SIPs at the bottom of some of the gaps were scorched. Because of the high priority to understand the conditions that led to scorching, the TGH panel was loaned to W. Neuenschwander of Rockwell International, Downey, California, to run a Scorched Filler Bar Test on the STS-4 flight. The tiles were purposely installed on the panel so that there were height differences between adjacent tiles. Also the thermocouples were rearranged. Because of these modifications, the temperature data from the test could not contribute significantly to the TGH program. Because of data acquisition problems on the STS-4 flight, the panel was again flown on STS-5 as a Scorched Filler Bar Test.

The results of these tests were published in Ref. 6. The panel characteristics as observed after the STS-5 flight are summarized in Fig. 13. The circled numbers are the measured gap widths in thousandths of an inch (.004 mm). The squared numbers are the measured height differences between adjacent tiles. The sites of SIP scorching are indicated. Note that several of these gaps also closed to 0.02 mm (5 mils) during this flight. From post flight observations and measurements for several flights, a correlation equation was developed that relates the gap geometry characteristics to the probability of filler bar scorching. This is shown in Fig. 14 with application to the STS-5 flight observations. The conclusion was that when the correlation parameter, Φ, exceeds 0.4, scorching is to be expected.

Scorched filler-bar experiment: STS-5

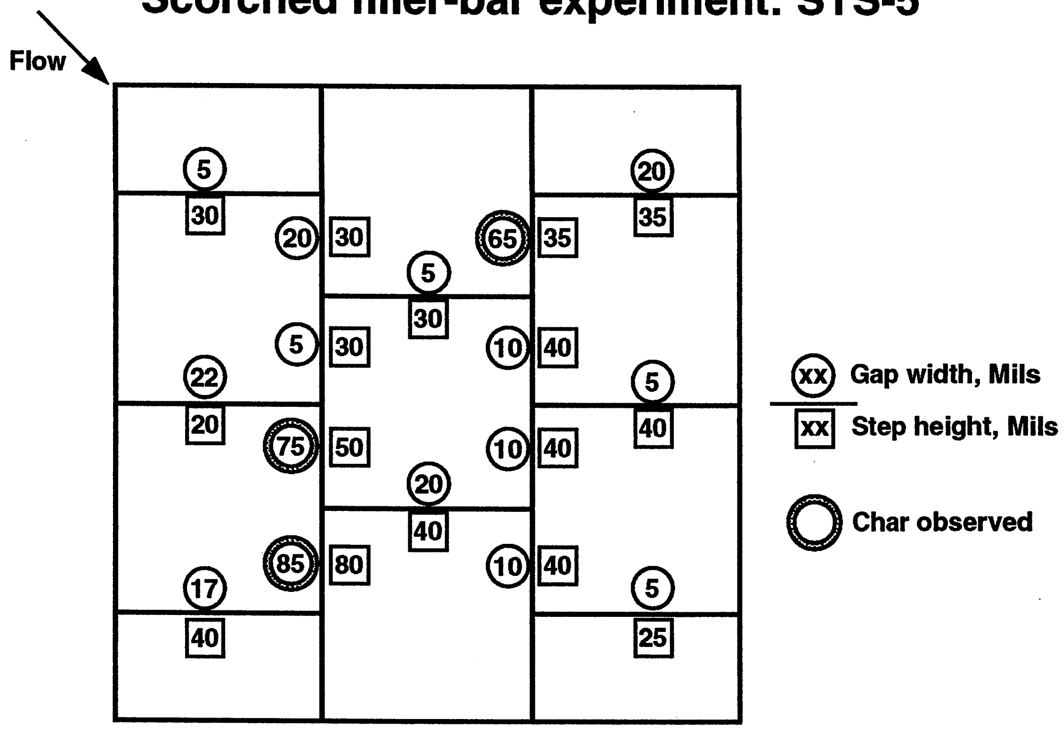

Fig. 13 Post flight measurements and observations of Scorched Filler Bar panel.

Correlation of STS-5 OEX panel data

Correlation parameter

$\Phi = (T/1000)^{0.5} (\Delta^{0.5} + W^{0.83})/(\Delta^{0.12} D^{0.5})$

T Peak surface temperature, R

Δ Step height at scorch, in

W Gap width at scorch, in

D Depth of gap, in

Post flight observations

Φ	W (MILS)	D (MILS)	Appearance
.56	85	80	Scorched
.50	75	50	Scorched
.43	65	35	Dull
.36	20	40	Normal
.36	17	40	"
.35	20	35	"
.34	10	40	"
.34	10	40	"
.34	10	40	"
.33	20	30	"
.31	5	40	"
.30	22	20	"
.29	5	30	"
.29	5	30	"
.28	5	30	"
.27	5	25	"

Fig. 14 Correlation relating tile gap geometry to filler bar scorching probability.

CONCLUDING REMARKS

Two of the proposed series of TGH test panels were flown. In depth temperature data were obtained within two typical gap locations in the Orbiter HRSI. These locations represented an approximately two-dimensional flow region, and a complex three-dimensional flow region. These data were compared with in-depth data in the center of a tile where it was demonstrated that the heat conduction was essentially one-dimensional. The gap temperatures were only slightly higher than those within the center of the tile at corresponding depths. The data from the near two-dimensional flow region were analyzed to estimate the surface heat flux that would produce the measured temperatures. It was found that the maximum heat flux to a point 0.57 cm down the gap wall was about 1% of the surface heat flux. The probable reason for this low heat flux was the compression of the instrumented gaps revealed by comparison of preflight and post flight gap width measurements. A TGH panel, modified to minimize gap compression, was fabricated but not flown.

The TGH panel was loaned to a Scorched Filler Bar Test program conducted by Rockwell International for the STS-4 and STS-5 flights. This program developed a correlation that relates tile gap geometry to the probability of scorching of the filler bar at the bottom of the tile during reentry.

REFERENCES

1. Christensen, H. E. and Kipp, H. W.: Data Correlation Analysis of Arc Tunnel and Wind Tunnel Tests of RSI Joints and Gaps, Final Report, McDonnell Douglas Corp., MDC E1003, Jan. 1974.

2. Scott, C. D. and Maria, R. J.,: Gap Heating With Pressure Gradients, AIAA 79-1043, June 1979.

3. Rochelle, W. Hale, M. and Kimbrough, B.: Prediction of Orbiter RSI Tile Gap Heating Ratios From NASA Ames Double Wedge Model Test Data, NASA CR-160147, April 1978.

4. Throckmorton, D. A.: Development Flight Instrumentation (DFI) and the Aerothermal Instrumentation Package (AIP), NASA CP-3248, 1995.

5. Throckmorton, D. A.: Benchmark Aerodynamic Heat Transfer Data from the First Flight of the Space Shuttle Orbiter, AIAA 82-003, Jan. 1982.

6. Neuenschwander, W. E., McBride, D. U., and Armour, G. A.: Shuttle TPS Thermal Performance and Analysis Methodology, In NASA, Langley Research Center Shuttle Performance: Lessons Learned, Pt. 2, October 1983.

A REVIEW OF THE INFRARED IMAGERY OF SHUTTLE (IRIS) EXPERIMENT

William C. Davy (Retired)

and

Michael J. Green

NASA Ames Research Center
Moffett Field, CA

INTRODUCTION

As NASA was preparing to enter the new era of space shuttle flight, we at the Ames Research Center (ARC) were giving considerable thought to techniques for measuring the performance of the Thermal Protection System (TPS). Several members of the then Entry Technology Branch had been very active in the development of the tile system that constituted a major part of the TPS system. Three onboard OEX experiments -- the Aerothermal Instrumentation Package, the Tile Gap Heating Experiment, and the Catalytic Surface Effects Experiment -- were designed to measure tile temperatures with thermocouples embedded near tile surfaces and in-depth near tile gaps. However, only Orbiter 102 was to be instrumented; thus, if a remote temperature sensing technique could be developed, it would allow the possibility for obtaining tile temperatures on STS missions using orbiters other than 102. Also it would provide spacially resolved information over the entire windward surface, including leading edges where onboard measurements would be extremely difficult. This information was not available from even the Orbiter 102, because Development Flight Instrumentation (DFI) data was limited. To provide such a measurement, Howard Goldstein advanced the idea of obtaining a remote absolute intensity image in the infrared during Shuttle entry, either from the Earth's surface or using an airborne platform. These intensity data could be directly reduced to temperatures if the surface emissivity of the tile were known. Such data were well in hand, since tile processing included a coating to increase its emissivity, and the optical properties of the coating had been extensively documented from laboratory experiments.

In addition, an independent intensity measurement would have an important synergistic value to the thermocouple measurements mentioned above. Surface and gap heating rates were to be inferred from local temperatures through a first-law energy balance. But because the primary function of the TPS tiles was to reject incoming energy through reradiation from their hot surfaces, the radiation term in such an energy balance would be necessarily large. Moreover, because of the powerful dependence of surface emission on temperature, relatively small errors in temperature measurements could introduce disproportionately larger errors in estimates of emission and hence heating rates. Thus, an independent and direct measurement of tile surface emission would be a valuable adjunct to the heating rate determination mentioned above, as well as giving another independent measure of TPS performance. A radiant intensity measurement experiment to obtain temperatures would now exploit the strong sensitivity of emission on temperature.

As a result of Goldstein's suggestion, an inhouse study was performed (Ref. 1) that indicated the concept had potential application, and an airborne encounter was probably the more optimum approach, since it placed much less constraint on the entry trajectories from which images could be reasonably acquired. A feasibility study contract was then awarded to Martin Marietta Corp. (MMC) (Ref. 2) that concluded that indeed an airborne platform could produce a shuttle image with good probability. The platform proposed for this experiment, which came to be known as the IRIS (Infrared Imagery of Shuttle) experiment, was the Kuiper Astronomical Observatory (KAO). An artist's rendition is shown in Fig. 1. The KAO is a modified C-141 aircraft that is operated by ARC using a 0.91 m (36 in) Cassegrian telescope on a stabilized platform to obtain principally astronomical data. MMC was subsequently awarded the construction phase contract and was responsible for the hardware and experiment-specific software for the IRIS experiment.

This paper describes the IRIS experiment, including an overview of hardware design, its rationale, and its operational impact. In addition, we briefly discuss the IRIS image obtained during the entry of STS-3 and its analysis.

HARDWARE DESIGN

Hardware design challenges were principally in two areas: 1) devising a scheme to overcome the limited mobility and inertia of the telescope platform system, and 2) designing a detector and its ancillary circuitry. We consider herein only the system-critical or innovative aspects of that design; further detail may be found in Ref. 2.

Target Acquisition System

The KAO telescope platform is a rather massive structure and consequently has a relatively slow slew acceleration. In addition, the maximum slew velocity is limited by the servo control system to less than 1 degree per sec. Contrast that rate to that of an orbiter, which at 75 km, could be expected to overtake the KAO at an angular rate of about 6 degrees per second. Another complication, apparent in Fig. 1, is that major excursions of the telescope platform are limited to a plane normal to the KAO longitudinal axis. Clearly, the KAO platform had to be considered essentially stationary during the image acquisition, and so some method of vectoring the telescope line-of-sight (e.g., a mirror or prism) had to employed. Or alternately, the telescope had to be prealigned to the shuttle trajectory such that the orbiter would be captured within the telescope's field-of-view. The solution proposed by MMC was the latter option and was subsequently implemented by augmenting the main platform control system with a small telescope of rather large angular aperture. This device, known as the tracker, was two dimensionally gimballed (about 45 degrees maximum) to move in a plane normal to motion of the main telescope. It was mounted on the head-ring of the main telescope, shown schematically in Fig. 2. Mounted in the tracker focal plane was a position sensitive detector that produced a two-component signal proportional to the vector displacement of an image from an arbitrary origin, which was to be the boresight of the main telescope. The tracker system loop included a software analysis component that computed error corrections and, in turn, motion directives to the tracker and main telescope platforms such that their motion would move the acquired signal closer to tracker origin. Hence, the overall servo system moved the main telescope to such an attitude so as to view the shuttle trajectory, using error corrections based on data from the tracker position detector. The tracker telescope was designed with a 9 degree view field, giving a 12 km surveillance field at 75 km altitude.

The operational strategy using this acquisition system follows. Prior to an orbiter entry, the KAO attained operating altitude (approximately 13 km) and flew a ground track parallel to that expected for the shuttle. The flight crew, using the latest estimate of the shuttle entry trajectory available for Ground Control (at NASA Dryden), iteratively updated the shuttle position with respect to the KAO. The tracker and main telescope elevation angles were then vectored manually (open loop) for acquisition, based on trajectory data. Once a signal was acquired and locked-in by the tracker system, a switch into closed loop mode was activated via software. At that time the array data transfer subsystem was also activated, and data from the 600 array detectors were transferred to tape until such time as the tracker system lost lock.

The tracker acquisition system, while straightforward in concept, proved to be somewhat complex in execution, both in terms of hardware/software configuration and in operation by the flight crew. Several behavioral anomalies were identified and resolved through rigorous system analysis and several test flights with a target aircraft (an SR-71). Also, it became very clear from the experience gained on the STS-1 and STS-2 missions, in which images were not successfully acquired, that very close data communication between Ground Control and the KAO was vital. Resolution of these problems was successful, and affirmation of the tracker system viability is offered in the form of the STS-3 image to be discussed below.

Detector Array

The ARC study (Ref. 1) had pointed out early on that, for conditions of interest (e.g., peak heating), the vast speed differential between the shuttle and the observation platform would permit only a very limited viewing time, on the order of 10 msec. Moreover, during such a short interval, it was very unlikely that flow conditions over the shuttle would change significantly enough to warrant the effort to acquire more than one image. Consequently, the idea was advanced in support of a "streak" camera concept using a linear detector array as opposed to a matrix array. A one-dimensional, or linear array could be situated normal to the shuttle image motion. Then, by virtue of that motion, repeated sampling of a given detector would produce a series, or streak of emission measurements along that portion of the image that traversed it. Clearly a two-dimensional emission image could then be constructed from a montage of such strips.

Mean tile surface temperatures were anticipated to be on the order of 1000 K (1300 F) at peak heating during an entry, so that the maximum spectral emission from the tile surfaces, using *Wien's Law,* could be expected to occur in the 2 to 3 μm range. But more importantly, the derivative of emission with respect to temperature (this is the point of greatest temperature resolution) reaches its maximum at about 2 μm. Both of these factors militated for a detector having good responsivity in that wavelength range. In addition, the use of a streak camera design indicated the need for a relative fast detector, since requirements were to achieve a one meter spatial resolution. Thus for a 33 meter shuttle length, at least 30 to 40 samplings would be required during the image transit time.

These requirements taken together made the choice of liquid nitrogen-cooled Indium Antimonide (InSb) photodiode devices a fairly straightforward selection. The detector system was further customized to shuttle emission by the use of a cooled optical filter having a bandpass of 2.12 to 2.62 μm. This band captures most of the shuttle emission while rejecting background noise in the range of the InSb response band. In addition, it blocked shuttle emission in the infrared water absorption bands, thereby removing some ambiguity from the data in as much as the extent of water absorption could only be estimated.

Several considerations entered into the selection of detector size. These included the diffraction limit spot size of the telescope and, of course, the spatial resolution. Also, the array should cover enough of the focal plane diameter, using a tractable number of detectors, to ensure a high probably of an image capture. Suffice it to say that the resulting detection system consisted of 400 detectors, 63.5 by 63.5 μm, arranged in two rows as shown in Fig. 3. Between rows there was a one detector offset in the array direction so that a contiguous spanwise coverage could be achieved. Note from Fig. 3 that the 400 element array, known as the primary array, was backed up by another linear array of 200 detectors centered laterally on the primary. This secondary array was intended as redundancy to the primary.

Both of these arrays were rather uniquely coupled to the readout circuitry. The primary array was divided in half, with corresponding elements in each half (e.g., detectors nos. 1 and 201), as well as the analogous position in the secondary array (e.g., detector no. 401) connected in parallel to the input of a single channel of the readout electronics. Thus the output from any channel at a given time was the result of the combined signals from three detectors. The resolution of this seemingly ambiguous situation ensued from the physical size and location of the detector arrays. For the design conditions of the encounter, the telescope magnification was such that a shuttle image could be incident on only one of the three connected detectors at a given time, i.e., only one of any detector triad could produce a signal attributable to the shuttle image, while the other two would be reading background. Thus, a three-fold economy in readout circuitry was affected at the expense of tripling the radiometric background noise. This noise constituted only a fraction of the total system noise due in part to the spectral filter mentioned above and was considered acceptable for the accuracy requirements.

The raw data as transferred to storage contained two spatial distortions. The first was due to the array-normal offset between the odd and even detector half-rows evident in Fig. 3. In sampling detectors sequentially, a spatial jitter was introduced that was equivalent to different longitudinal stations on the shuttle. This effect could amount to perhaps as much as two meters, depending on the attitude at encounter. The other distortion arose from the finite time required to sample the complete array. The readout circuitry consisted of five channels that were commutated electronically among the 200 detector triads. The cycle time required to complete one read and data handoff cycle was 1.25 μsec. Thus, a complete sweep of the array (i.e., 40 read cycles) required 50 μsec. Due to this finite time, the resulting data were slightly skewed in time, or equivalently in TPS location, since the shuttle image moved slightly during the sweep cycle. For a nominal acquisition range (60 to 75 km) and for shuttle velocities of about 6 km/sec, the shuttle image required about 6 msec to transit the array. Thus, the image moved less than 1 percent of its total length during an array sweep.

Because data were being recorded continuously at a constant rate, a straightforward linear interpolation in time of the raw data was used to obtain a continuous montage construct of data with both distortions removed. This was accomplished by post processing using onboard hardware and software (Ref. 3).

The absolute responsivity of the diode array was determined through a two-step process described in Ref. 3. A laboratory standard black body was used as a calibration source, but because of small aperture size, its focal plane image covered only a few detectors. To obviate this difficulty, a reference detector was chosen and its absolute responsivity was calibrated from 600 K to 1450 K in 50 K increments. The remaining detectors in the array were then calibrated at two temperatures, 1100 K and 1300 K, and their relative responsivity was obtained by ratioing their outputs to that of the reference detector at the same temperatures. The responsivity of a given detector was then obtained as the product of the reference detector responsivity and the above ratio. With detector responsivities in hand, it became a straightforward procedure to obtain temperatures, providing, of course, an emissivity could be assigned to the radiating surface (Ref. 4).

IRIS IMAGE OF STS-3

On the morning of 30 March 1982, during the entry of STS-3, the IRIS tracker achieved lock that held for approximately 14 seconds. At 7:43:44 (PST), an IRIS image of STS-3 was recorded. The flight conditions for the Shuttle at encounter are given in Table 1, and those for the KAO conditions, in Table 2. The encounter occurred approximately 150 miles south of Los Angeles, CA. The geometry of the encounter is shown in Fig. 4. The line-of-sight separation was 51.7 km, somewhat closer than the design distance. As a consequence, the tracker detector signal was about 4 times design nominal; however, based on extrapolation of STS-2 data, the tracker signal was within about 20 percent of that expected (Ref. 5).

Shown in Fig. 5 and obtained at encounter is the computer generated focal plane image, so termed because no attempt has been made to rectify the image for geometric projective skewing. This effect was present because, at the moment of the encounter, the shuttle windward surface was nonparallel to the telescope field-of-view plane, and hence an nonorthogonal projection resulted. The image incompleteness was traced to a misalignment between the tracker telescope and the main telescope line-of-sight of about three arc minutes. This caused the image to traverse off the focal plane centerline so that only 71 detectors received a signal, corresponding to about 60 percent of the shuttle span. The secondary array was missed completely. The image is composed of 147 sampling sweeps of the detector array. The two dark wing strips are due to nonfunctional detectors. Detector signals have been reduced to absolute temperatures using the calibration responsivities described above. In generating this thermograph, we have assigned colors from blue to violet to correspond to the temperature range from 800 K to 1150 K, which is the nominal range of temperatures that was observed. The side bar in this figure gives an indication of the correlation between color and temperature

IMAGE ANALYSIS

The image analysis proceeded in several phases. The first effort was to remove geometric effects due to a nonorthogonal projection. A three-dimensional graphics work station was first used to rotate the shuttle planform to obtain a fit to the IRIS image that would indicate the relative attitude between the shuttle TPS plane and telescope field-of-view plane. However, no combination of rotational angles could be found that produced what we felt was a satisfactory fit between shuttle projection and image. So an alternate approach was developed that relied on known attitudes of both vehicles at the time of encounter. These data, given in Tables 1 and 2, were known to fair precision (uncertainties of less than 1 degree), and by using a series of coordinate transformations, it was possible to develop a rigorous expression relating image coordinates to shuttle coordinates (Ref. 5). However, after generating this projection, the image appeared to be somewhat elongated compared to its analytical projection. Our attention then turned to an investigation of electro-optical and mechanical vibration effects. These phenomena give rise to blurring or defocusing of the image.

One way to obtain a qualitative estimate of these effects is to consider a sharply defined prominence of the source, characterized by large signal gradients such as produced by a leading edge. An example, shown in Fig. 6, is the signal history from channel 3, which responded to radiation from a strip of TPS located approximately on the shuttle symmetry plane. The first maximum occurred as the nose cap came into view, and the second corresponds to the body flap, which was deflected about 10 degrees at the time of encounter. The apparent rise time of the nose cap signal is about 1 msec (20 scans at 50 μsec per scan). We assumed that this rise time could be attributed essentially to three causes: 1) the electronic rise time, 2) the geometric, or ideal, optical rise time, and 3) the blurring due to mechanical vibrations or physical (i.e., nonideal) optics. These latter effects tended to produce a diffuse image of a sharp edge and cause large gradient signals to be distributed or averaged over a larger image area. An observed signal rise time is thus longer than would otherwise be the case.

Electronic rise time is due to a combination of the preamplifier analog circuits, the A to D converters, and the digital processor. All of these devices, however, were tailored by design to allow a 1.25 μsec sample time, so that the electronic rise time had to be an order of magnitude less than this time, which we considered negligible. The geometric rise time derives from over sampling of the image. This condition occurs when the sampling cycle time is shorter than the time required for a given image point to traverse a detector width. Numerically, this rise time is simply the ratio of detector width to image velocity. From the encounter geometry and the focal length of the optical system, the image focal plane velocity was calculated to be approximately 1.1×10^6 μm/sec, and using a detector active width of 63 μm, this rise time is found to be on the order of 60 μsec. This is much larger than the electronic rise time, but still significantly smaller than the observed quantity. Hence, we hypothesized that the apparent rise time was due primarily to image degradation by blurring.

This hypothesis was further reinforced by comparison of the IRIS data with onboard DFI measurements. Examples of such comparisons are shown in Figs. 7a and 7b, for the shuttle centerline and for the 60 percent semispan wing location, respectively. Note from Fig. 7a that agreement between IRIS and DFI data is remarkably good for the midfuselage region. This area is characterized by relatively low temperature gradients, as indicated by the uniform color of that region in Fig. 5. However, in regions of higher gradients, such as the nose cap and body flap, the disagreement becomes substantial. This characteristic is even more pronounced in the wing region comparison, where the only agreement between the data sets is in a small portion of the midcord region. One explanation for this type of behavior is that large gradients were being averaged out due to image blurring.

Mechanical vibration sources were diagnosed through extensive accelerometer monitoring of telescope components. Both airframe feedthrough and cavity acoustical sources were investigated by ground and inflight testing. Because most of the telescope elements were rather massive, with commensurately low resonance frequencies, no vibrations were found that could contribute significantly to the observed signal rise time.

Physical optical effects cause blurring by diffraction or refraction of a light beam. One source of diffraction is due to secondary wave systems that are generated by passage of a wave front through the telescope primary aperture. Bench tests of the KAO telescope had shown that about 85 percent of a point source image was captured by a focal plane aperture of 50 μm (Ref. 6). This blurring would induce rise times of the same order as the geometric optical rise, so that it was concluded that most of the image degradation was due to refraction phenomena.

Refraction causes blurring when the medium through which a light beam propagates contains density variations with slightly different refractive indices. These variations, which are usually time variable, cause parts of the beam to be refracted or bent along slightly different paths. Differences in path length can also result in diffractive degradation. Aero-optical diagnostic devices such as schlieren and shadowgraph systems exploit this phenomenon for flow field visualization. To effectively cause observable image degradation, the scale of the density variations must be of the same order or smaller than the propagating beam. Several sources were considered, including refraction by the shock envelope, free air turbulence, shear layer effects, and flow within the telescope cavity.

Because of the large density jump across the shock envelope surrounding the shuttle, there was undoubtedly some refraction of the beam to the telescope. However, with the exception of shock-on-shock interaction zones, the shock envelope is locally very smooth so that the image might be displaced somewhat, or perhaps slightly distorted, i.e., elongated or foreshortened, but would not be uniformly blurred. We therefore concluded that this effect was not a major source of image blurring. Similarly, because the scale of the free air turbulence cells (usually tens to hundreds of meters) with relatively long motion time constants, this source was discounted as a probable source of image blurring.

Through elimination, our attention was narrowed to near-field effects, i.e., the flow field around the C-141 and in the telescope cavity. Blurring sources here were thought to be:
1) turbulent structures in the shear layer over the cavity, and/or 2) convection cells within the telescope cavity. We did have an indication from Ref. 6 that there was serious degradation of a point source image taken while airborne. However these data were taken over a much longer time

period (essentially steady state) than for the STS-3 image, and so it was not clear that our data would be subject to the same degradation. Beyond this information, we had very little quantitative information regarding telescope image degradation, usually referred to the point spread function (PSF).

However, there was at Ames a Branch engaged in the processing of images obtained from satellite and high altitude aircraft. The Technology Applications Branch had expertise, hardware, and software to process data such as the IRIS image, and arrangements were made to apply this technology to try to improve the STS-3 image. The work, performed by D. N. Hein and reported in Ref. 7, consisted of several phases, one of which was edge, or gradient enhancement.

As the name implies, edge enhancement tends to highlight regions of large gradients and suppress low gradient areas. The method used here was an averaging scheme in which the data were processed in 5 by 5 pixel squares. The average of the 25 pixels was computed and subtracted from the center pixel. In regions where signal gradients were small, i.e., each pixel signal was of about the same value, the average was about the same magnitude as the center pixel and the resulting difference would be very small. In contrast, large gradient regions produced differences of substantial size. These data were then plotted as function of the center pixel location, as shown in Fig. 8.

Upon inspection of this figure, it is immediately apparent that the raw image is actually a composite of several subimages, each displaced by varying amounts in both longitudinal and lateral directions. Moreover, since the gray scale of this figure is proportional to the difference in magnitudes, it is probable that various subimages received varying amounts of the total beam energy.

Another technique, known as deconvolution, was to determine a PSF by an inverse Fourier transform method (Ref. 7). The PSF functions were determined for various portions of the raw image. The inverse PSF was then applied to the complete image to remove the blurring effects of the PSF. Unfortunately, none of these efforts substantially improved the raw image quality, judged primarily on the appearance of leading and trailing edges. We also tried a discrete PSF approach which assumed that each subimage was composed of a fraction of the total beam energy with a constant pixel offset. After estimating these parameters, deconvolution was achieved by finding that portion of the raw image that contained only one subimage, subtracting its contribution from the remaining data. This process would then expose a portion of the second subimage that would contain unique data, i.e., no data from any other subimages, which could then in turn be subtracted from the remaining data. This cycle was repeated until all subimages had been processed. The deconvolved image was generated by aligning all the subimages and summing. This effort produced results that were different from the continuous PFS efforts but were qualitatively judged to be no better. The reason for these failed efforts is thought to be that the PSF is not constant over the image. This would imply that the flow structures responsible for causing image degradation were changing on a time scale comparable to the image acquisition time.

The foregoing discussion essentially synopsizes the state of our understanding of the STS-3 image to date. In the interim since the IRIS experiment, there has continued to be interest in airborne optical performance. This has stimulated several computational fluid dynamic (CFD) and coupled optical studies of cavity flow fields effects on optical resolution, see, for instance, Refs. 8-11. One general consensus from these studies is that there are large scale flow structures in the shear layer over the cavity and in the cavity itself. Further, these structures significantly affect the optical beam propagation, and indeed, they are dynamically unsteady with characteristic time constants that are on the order of the STS-3 image acquisition time. During the analysis process described above, the flight of STS-4 occurred, and the KAO deployed to try for another image. However, due to equipment failure the encounter was missed. At that point, it was the decision of Ames Management to discontinue the IRIS experiment.

CONCLUDING REMARKS

The IRIS experiment represents an interesting and instructive attempt to utilize an airborne optical platform for acquisition of a short duration image, an entering shuttle in this case. The Kuiper Astronomical Observatory was designed and primarily used for astronomical studies involving relatively long observation times which required its telescope to remain inertially fixed. To adapt this relatively massive hardware to the IRIS mission required considerable innovation and some development. The experiment succeeded in obtaining one partial image during the STS-3 mission. The image quality, judged by such characteristics as leading edge crispness, was lower than expected. Processing the image for edge enhancement revealed that this degradation was probably due to the presence of several subimages. These subimages are thought to be caused by refraction effects induced by flow structures in the shear layer over the telescope cavity as well as within the cavity itself. Several attempts to deconvolve the image, i.e., put the subimages back together, were unsuccessful.

There are two principal lessons to be drawn from the IRIS experiment. The first is that tracker method of solving the telescope inertia problem is feasible. Its success depended strongly on rigorous understanding of the servo system controlling the tracker and telescope. In addition, very close communication between ground control and the aircraft was needed to insure that the tracker could be properly positioned to successfully acquire its target. Secondly, one has to be very cognizant of the powerful influence of flow field properties on optical performance. Since the advent of the STS-3 image, the community's understanding of near-body flow fields has improved dramatically. Particularly with recent advances in CFD methods, one can understand the flow dynamics over and in the telescope cavity. We estimate that an IRIS experiment of today, employing the most current technologies, would undoubtedly provide improved resolution capability well in excess of an order of magnitude over the STS-3 image. Thus we conclude that while the IRIS experiment achieved only a limited success in the STS-3 image, it does provide a valuable experience base should the Agency decide to build another airborne platform for this type of remote experiment.

REFERENCES

1. Swenson, B. L. and Edsinger, L. E.: Preliminary Analysis of Remote Infrared Imagery of Shuttle During Entry, an Aerodynamic Flight Experiment, NASA TM73-251, Ames Research Center, Moffett Field, CA, 1973.

2. Chocol, C. J.: Infrared Imagery of Shuttle (IRIS), Final Report, MCR 76-564, Martin Marietta Corp., Denver, CO, 1977.

3. Strange, D. A.: IRIS Software User's Manual, Vol. 1, Drw. no. 849ARC08000, Martin Marietta Corp., Denver, CO, 1979.

4. Stewart, D. A., Rakich, J. V., and Lanfranco, M. J.: Catalytic Surface Effects on Space Shuttle Thermal Protection System During Earth Entry of Flights STS-2 through STS-5, Shuttle Performance: Lessons Learned, NASA CP-2283, part 2, 1983.

5. Green, M. J., et. al.: Supporting Flight-Data Analysis for Space-Shuttle Orbiter Experiments at NASA Ames Research Center, NASA TM 84345, Ames Research Center, Moffett Field, CA, 1983.

6. Erickson, E. F. and Strecker, D. W.: Engineering Tests of the C-141 Telescope, NASA TM 78467, Ames Research Center, Moffett Field, CA, 1978.

7. Hein, D. N.: Processing of the IRIS STS-3 Image, private communication, NASA Ames Research Center, Moffett Field, CA, Sept. 5, 1982.

8. Venkatapathy, E., Lombard, C. K., and Nagaraj, N.: Numerical Simulation of Compressible Flow Around Complex Two-Dimensional Cavities, AIAA-87-0116, AIAA 25th Aerospace Sciences Meeting, Reno, NV, Jan. 12-15, 1987.

9. Clark, R. L. and Farris, R. C.: A Numerical Method to Predict Aero-Optical Performance in Hypersonic Flight, AIAA 87-1396, June 1987.

10. Farris, R. C. and Clark, R. L.: An Integrated Navier-Stokes and Wave Optics Numerical Simulation Technique for Predicting the Aero-Optical Performance about Subsonic Surveillance Aircraft, AIAA 88-0753, Jan. 1988.

11. Atwood, C. A.: Unsteady Fluid and Optical Simulation of Transonic Aero-Windows, AIAA-93-3017, July 1993.

Table 1. Shuttle Flight Conditions at Encounter Time

Shuttle trajectory data	
Time	988 sec after EI
Altitude	55.8 km
Velocity	4.30 km/sec
Mach number	13.0
Reynolds number	4 x 10^6
Angle of attack	39.66 deg
Sideslip	-0.13 deg
Bank	-44.5 deg
Elevon deflection	3 deg
Body flap deflection	7.7 deg
Euler angles*	
Yaw	51.1 deg
Pitch	26.8 deg
Roll	-51.3 deg
Shuttle free-stream conditions	
Density	5.092 x 10^{-4} kg/m^3
Pressure	39.70 Pa
Temperature	271.6 K

* Geodetic coordinate system

Table 2. Kuiper Astromonical Observatory Flight Conditions at Encounter Time

KAO flight data	
Altitude	12.5 km
Velocity	0.24 km/sec
Euler angles*	
Yaw	80.40 deg
Pitch	1.95 deg
Roll	0.25 deg
Telescope orientation	
Elevation angle	54.43 deg
Azimuth angle	2.90 deg

* Geocentric coordinate system

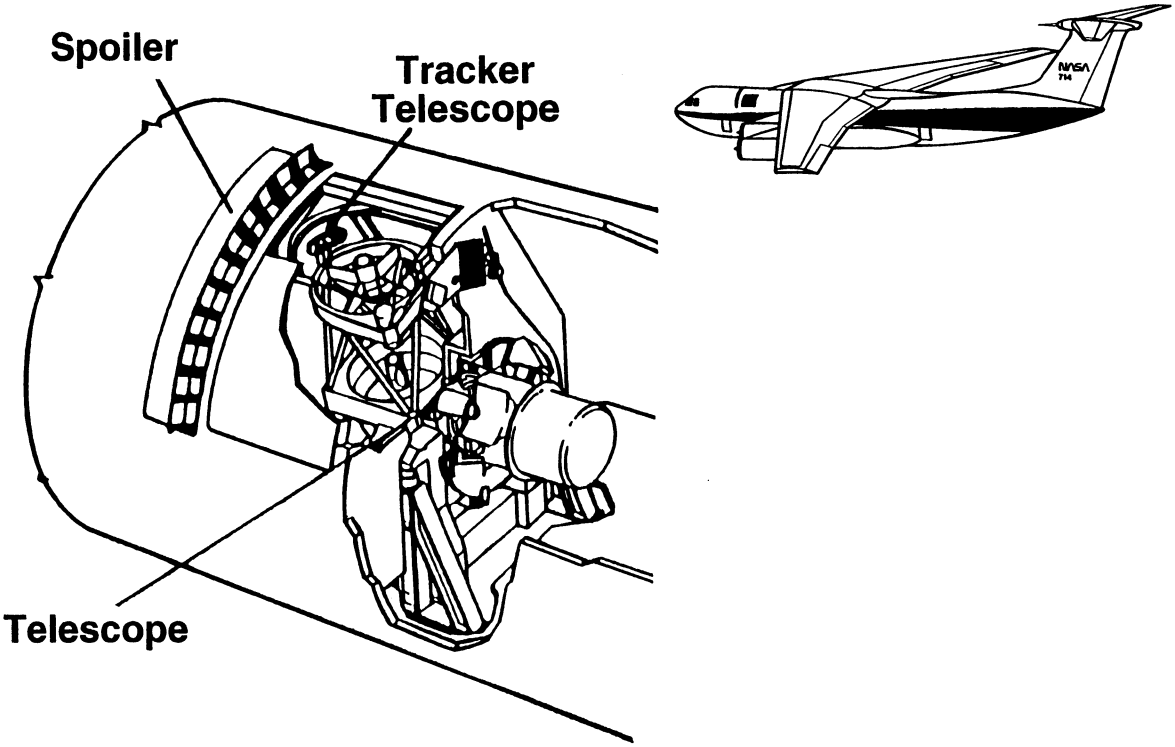

Figure 1. Kuiper Astronomical Observatory (KAO).

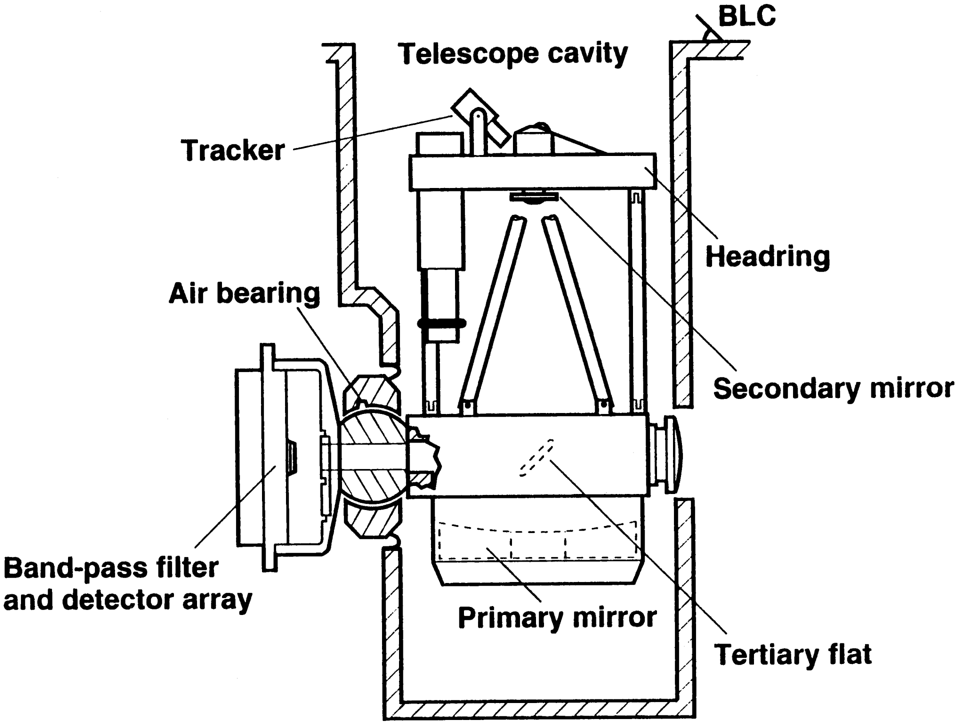

Figure 2. Tracker and main telescope configuration.

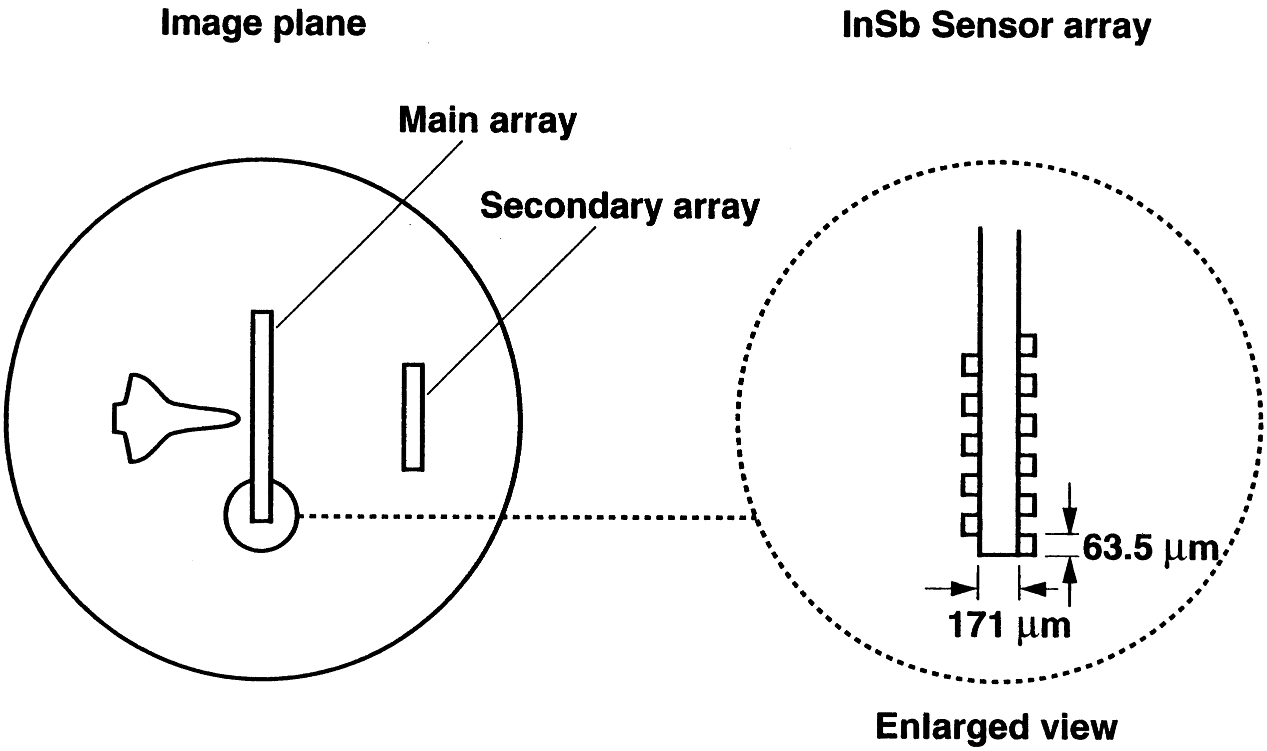

Figure 3. Focal plane detector arrangement.

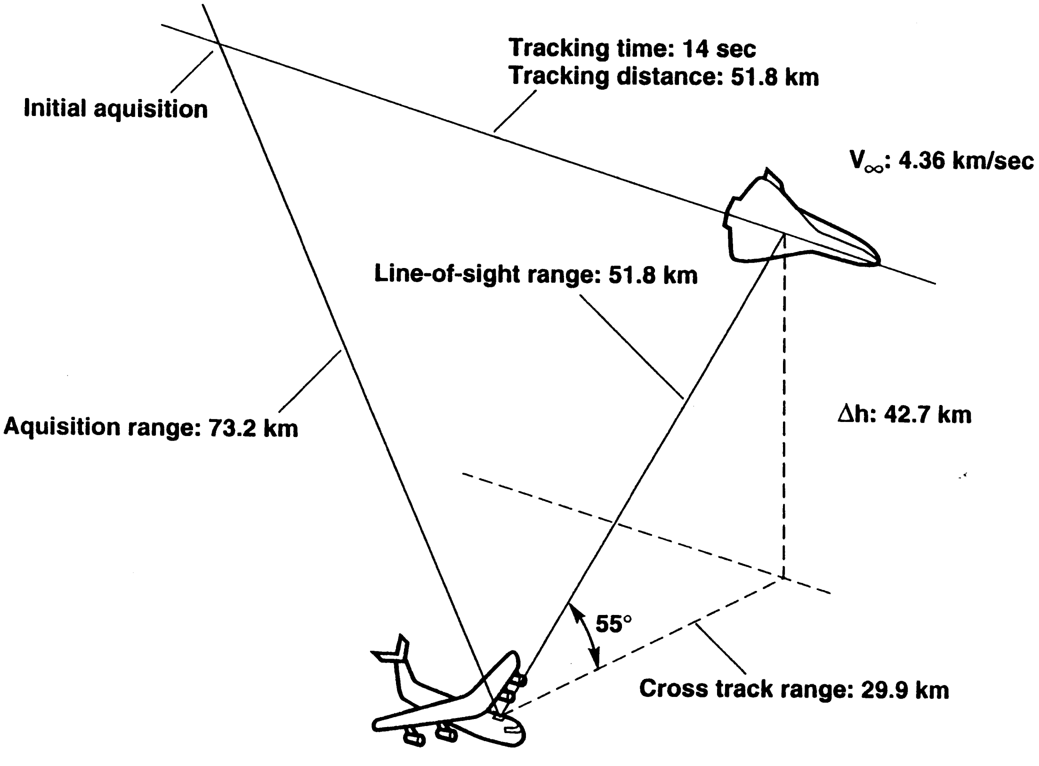
Tracking time: 14 sec
Tracking distance: 51.8 km
Initial aquisition
V∞: 4.36 km/sec
Line-of-sight range: 51.8 km
Aquisition range: 73.2 km
Δh: 42.7 km
55°
Cross track range: 29.9 km

Figure 4. Encounter geometry for STS-3.

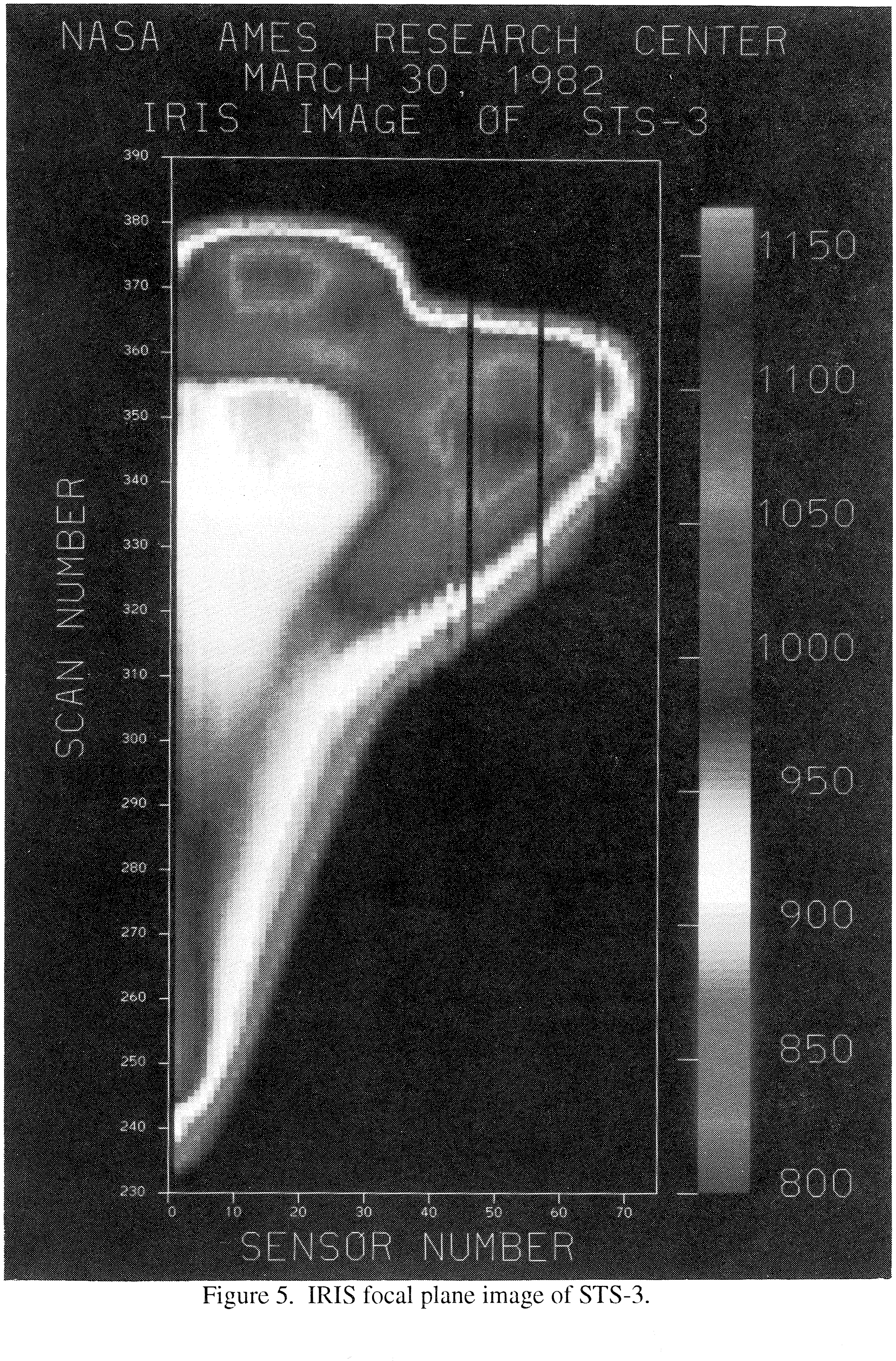

Figure 5. IRIS focal plane image of STS-3.

(A color version of figure 5 is shown on page 495.)

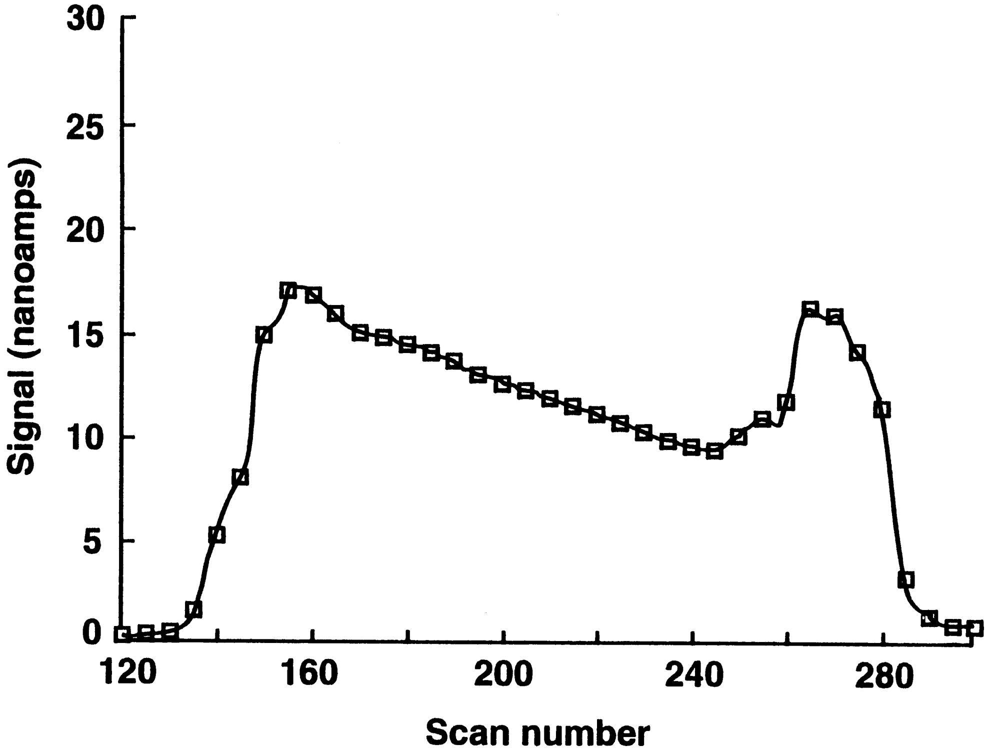

Figure 6. Channel 3 signal history.

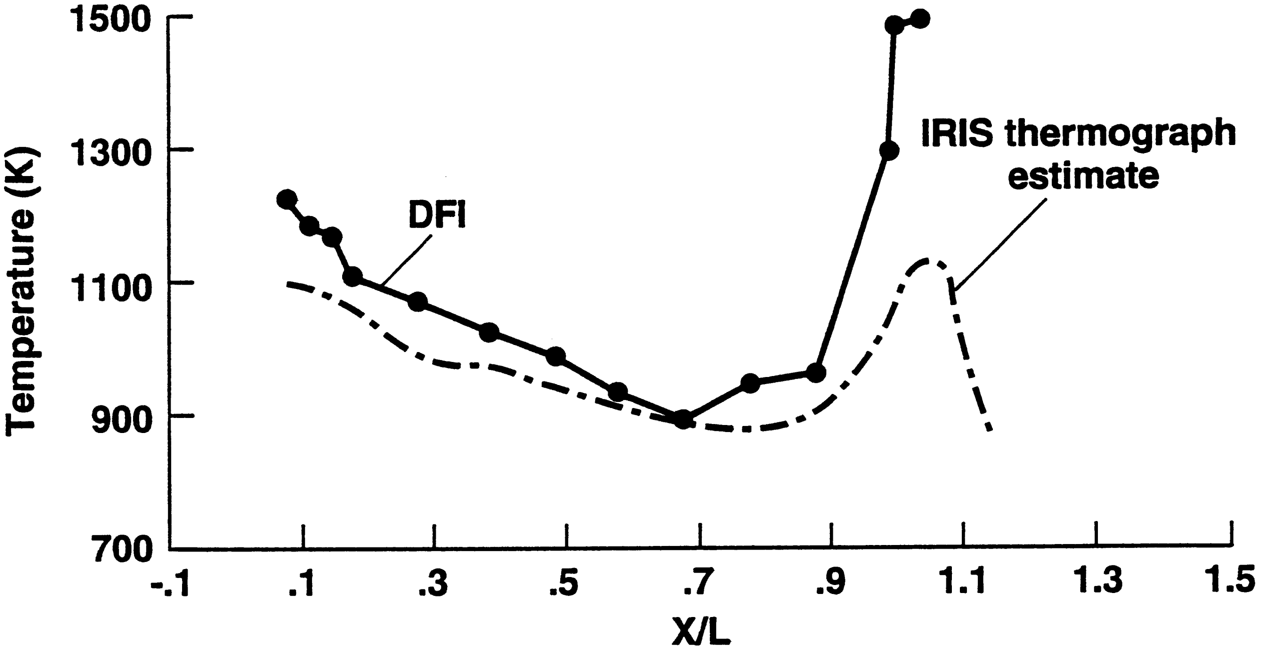

a. Centerline

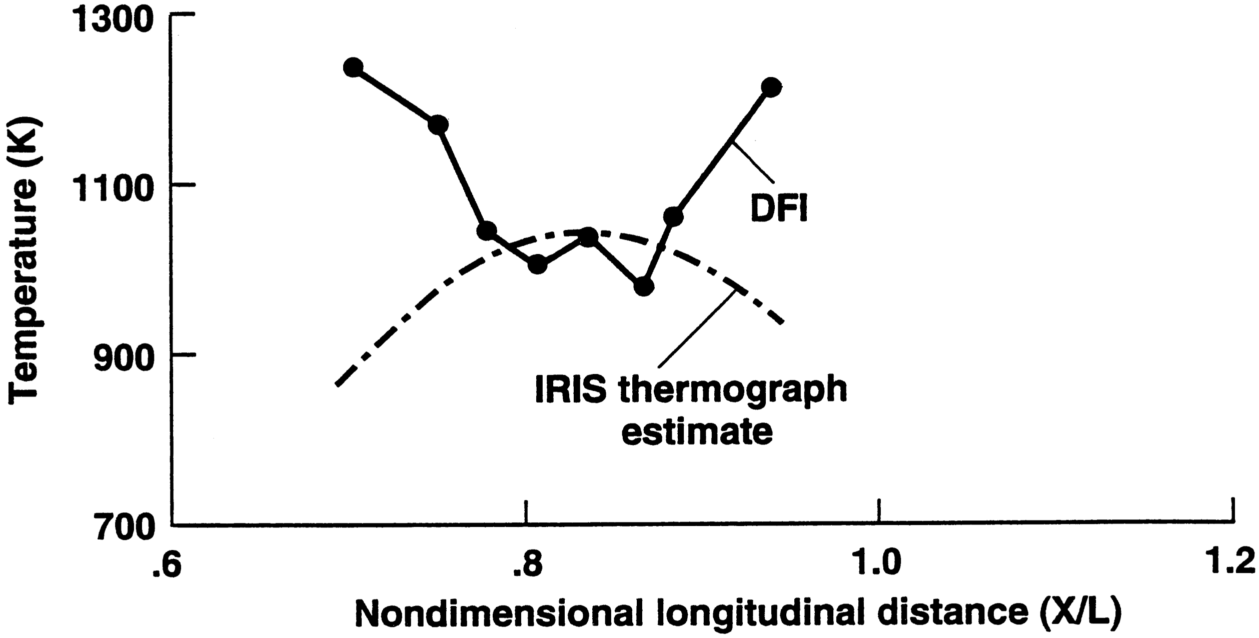

b. Wing at 60% semispan

Figure 7. Comparison of IRIS and DFI temperatures.

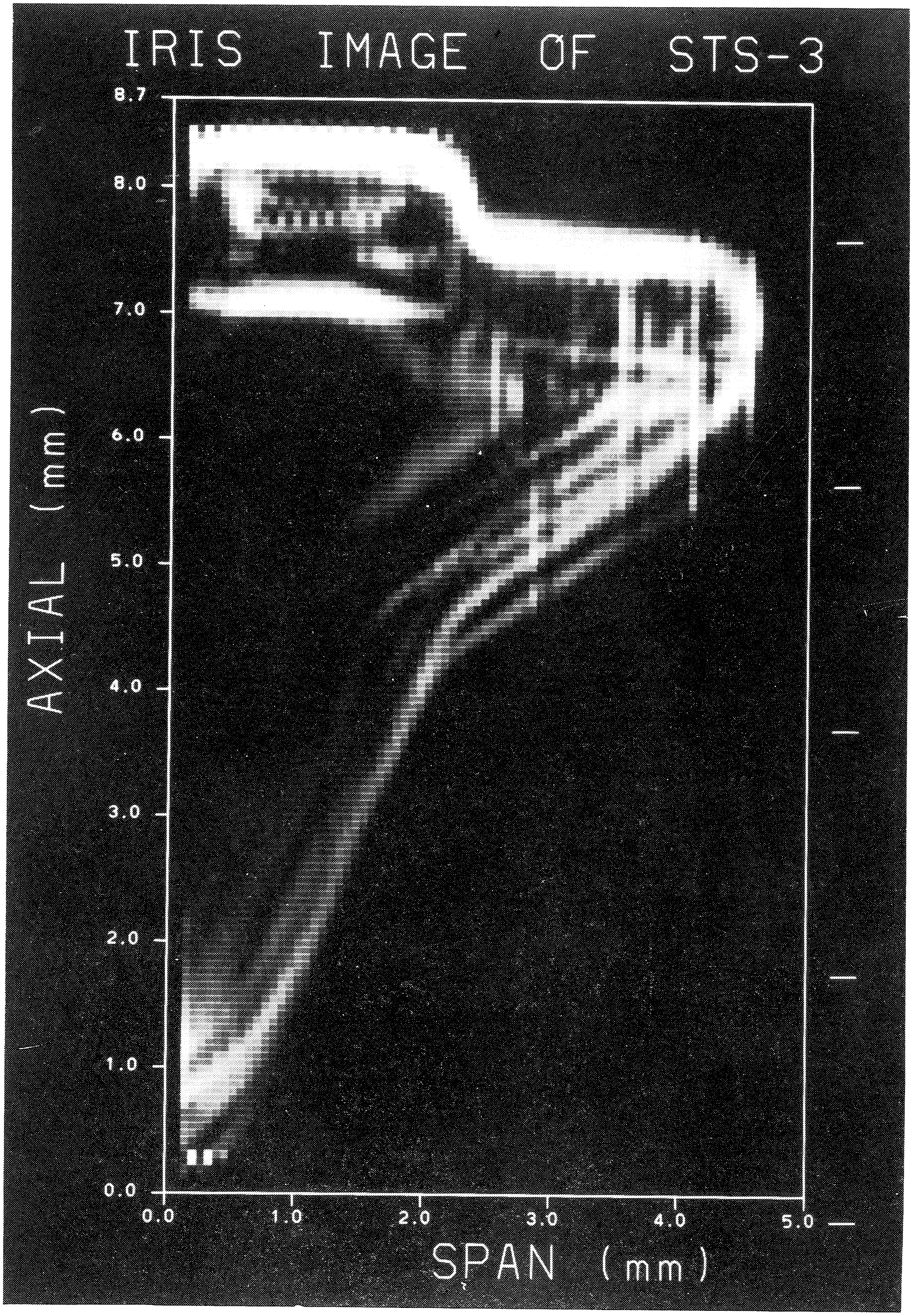

Figure 8. Edge enhanced IRIS STS-3 image.

SHUTTLE INFRARED LEESIDE TEMPERATURE SENSING (SILTS) EXPERIMENT

David A. Throckmorton and E. Vincent Zoby
NASA Langley Research Center
Hampton, VA

SUMMARY

The Shuttle Infrared Leeside Temperature Sensing (SILTS) experiment was designed to obtain high spatial-resolution measurements of the temperature of orbiter leeside (fuselage and wing) surfaces during the hypersonic portion of atmospheric entry. These measurements were obtained by means of an imaging, infrared radiometer (camera) located in a unique experiment pod atop the vertical tail of the orbiter *Columbia*. The SILTS experiment was installed on the orbiter *Columbia* during the vehicle's 1984-85 modification period. Subsequently, the SILTS experiment was flown on five missions: STS-61C, -28, -32, -35, and -40.

INTRODUCTION

The flowfield over the leeside of an entry vehicle, such as the shuttle orbiter, during the high-angle-of-attack portion of atmospheric entry when aerodynamic heating is significant, may be characterized as a three-dimensional, vortical, and separated flow regime. In the time frame of the shuttle orbiter's aerothermodynamic design, such a complex flowfield could not be analyzed by available computational methods, and major questions existed about the adequacy of leeside-flowfield simulations obtained in hypersonic wind-tunnel tests. Consequently, there was substantial uncertainty associated with extrapolating ground-test aerodynamic-heating results to the prediction of flight leeside aeroheating environments. Such uncertainty would naturally result in the inclusion of substantial conservatism in the design of leeside thermal protection systems. This design conservatism was applied not only to the shuttle orbiter, but in the absence of reduced predictive uncertainties would also apply to future entry vehicles. Consequently, one of the initial and more significant objectives of the Orbiter Experiments (OEX) Program was to gather flight-measured aerodynamic heat-transfer data on orbiter leeside surfaces for comparison with the results obtained in hypersonic wind-tunnel facilities.

NOMENCLATURE

CFD	computational fluid dynamics
EI	entry interface
FRSI	flexible reusable surface insulation
HRSI	high-temperature reusable surface insulation
LRSI	low-temperature reusable surface insulation
OEX	Orbiter Experiments
SCM	System Control Module
SILTS	Shuttle Infrared Leeside Temperature Sensing
TPS	Thermal Protection System

EXPERIMENT OBJECTIVE AND CONCEPT

Although the Development Flight Instrumentation (DFI) system was to obtain measurements of orbiter leeside surface temperatures during the Orbital Flight Test (OFT) missions, these measurements were to be made with thermocouples at only about 50 discrete locations distributed about *Columbia*'s upper fuselage and left wing (Ref. 1). The spatial resolution of these measurements was not sufficient to enable any sort of detailed mapping of the heat-transfer distributions over these surfaces. Thus, the SILTS experiment objective was to obtain high-spatial-resolution measurements of orbiter leeside surface temperatures throughout the hypersonic portion of atmospheric entry.

The SILTS concept for measurement of leeside surface-temperature data at high spatial-resolution was to mount an infrared camera atop the orbiter's vertical tail, to view both the upper fuselage and left wing during entry, and measure the amount of infrared radiation emanating from those surfaces. The infrared image data would be recorded onboard the orbiter, and processed postflight to produce detailed "maps" of leeside surface temperatures. These data could then be used to infer the magnitude and distribution of aerodynamic heating experienced by the leeside surfaces in flight.

Reference 2 contains detailed descriptions of the SILTS experiment system, its implementation aboard the Orbiter *Columbia*, and the concept of SILTS flight operation.

HARDWARE IMPLEMENTATION

The major elements of the SILTS experiment flight hardware included a scanning infrared radiometer (camera), a data and control electronics module, and a pressurized nitrogen system. These components were contained in a cylindrical experiment housing ("pod") which replaced the baseline fintip atop the vertical tail of the Orbiter *Columbia.* (A schematic of the entire SILTS experiment system is presented in Figure 1.) The SILTS pod was capped at the leading edge by a hemispherical "dome." The infrared camera, mounted within this dome, was able to "view" the orbiter's leeside surfaces through either of two infrared-transparent viewport windows located on the dome: one of which enabled viewing of the left wing, the other enabling viewing of the fuselage (Fig. 2). The data and control electronics module controlled experiment component operation, and provided power distribution and data signal conditioning. The pressurized nitrogen system provided gaseous nitrogen to a cryostat within the camera for cooling of the infrared detector, to the external window cavities for window transpiration cooling, and to pin-pullers which initiated the ejection of window protection plugs at experiment initiation. The OEX System (or Interface) Control Module (SCM), which provided an experiment initiation signal in response to an onboard computer command, and the OEX Tape Recorder were located within the pressurized crew compartment. Appropriate electrical wire harnesses tied all of these experiment components together.

Orbiter Configuration Modification

SILTS experiment implementation required replacement of the baseline fintip of the vertical tail of the Orbiter *Columbia* with the SILTS-unique experiment pod. Modifications to *Columbia* to incorporate SILTS were performed during the Orbiter's major modification period in 1984-85. The SILTS fintip assembly replaced the top 24.9 inches of the baseline vertical tail; the original tail height was unchanged. The underlying aluminum structures of the hemispherical dome and cylindrical sections had a diameter of 15.3 inches. The cylindrical portion retained its circular cross-section from its interface with the dome to a point approximately 50 inches aft, where the structure began to taper in order to fair with the baseline vertical tail airfoil section. Thermal protection system (TPS) material installation on the SILTS-pod assembly resulted in an external, aerodynamic surface moldline which was somewhat elliptic in cross-section. TPS tile thickness varied from 1.97 inches on the top centerline to 2.90 inches at the forward-looking-window location. The replacement fintip was identical to the baseline aft of the 60-percent chord line.

Additional modifications to the vertical tail TPS were incorporated as part of the implementation of the SILTS fintip. For the SILTS installation, baseline 9-lb/ft^3-density LRSI (white) tiles on the upper portion of the sides of the vertical tail were replaced by 22-lb/ft^3-density HRSI (black) tiles. This additional thermal protection allowed for increased entry heat loads anticipated to occur over these areas as a result of the presence of the SILTS-dome structure at the tip of the vertical tail.

See Reference 2 for a detailed description of the Orbiter configuration modification required to implement the SILTS experiment.

SILTS Experiment Components

Six primary components comprised the SILTS experiment system: the infrared camera, infrared-transparent windows, a temperature reference surface, the data-and-control electronics module, the pressurized nitrogen module, and window protection plugs.

The infrared camera was a commercially-available unit (circa 1975) extensively modified to meet the requirements of the SILTS experiment. The camera contained a single infrared detector, and dual rotating, scanning prisms (one horizontal and one vertical) which enabled the camera to produce two-dimensional imagery. The camera's indium-antimonide detector was cooled to cryogenic temperatures by liquid nitrogen generated by an internal Joule-Thompson cryostat.

The infrared transparent viewport windows were double-pane silicon, supported by carbon phenolic window mounts. The windows and window mounts were designed to withstand (fail-safe) the entry thermal environment to which they might be subjected, without the need for active cooling. However, the windows were transpiration-cooled with gaseous nitrogen during experiment operation in order to ensure the window panes would not reach temperatures at which they would become significant radiators in the infrared.

A thermostatically-controlled temperature-reference surface was located inside the dome structure, between the two window assemblies. This surface provided an in-flight temperature-reference source for the infrared camera.

The data-and-control electronics module controlled experiment component operation. It provided power conditioning and distribution to all experiment components, and also provided experiment data signal conditioning and encoding prior to data recording.

The pressurized nitrogen module was comprised of two 3000-psi gaseous-nitrogen bottles and all associated valves and plumbing. This system provided gaseous nitrogen to the camera cryostat for detector cooling, to the external window cavities for window transpiration cooling, and to pin-pullers which initiated the ejection of the window protection plugs.

The window protection plugs, which filled the conical viewport window cavities during ground operations and launch, were fabricated of multiple layers of flexible reusable surface insulation (FRSI). Spring-loaded separation plungers provided the required force to eject these plugs at experiment initiation.

A detailed description of the windows, window mounts, pin-pullers, and window protection plugs can be found in Reference 3.

Experiment Integration

Figure 1 schematically depicts the entire SILTS end-to-end experiment system. Wire harnesses electrically connected the SILTS experiment components atop the orbiter's vertical tail with the OEX System (or Interface) Control Module (SCM), the OEX tape recorder, and the aft flight deck control panel, all located within the orbiter's pressurized crew module.

The SILTS experiment was manually "enabled" by astronaut switches located on the aft flight deck. Manual switches controlled the availability of power to thermostatically-controlled heaters which maintained SILTS experiment components at "room" temperature during the on-orbit phase of a mission, and the availability of power to the experiment for operation during orbiter entry.

Actual initiation of experiment operation on entry was commanded by the OEX Systems Control Module, which controlled the ascent, on-orbit, and entry phase operations of a number of experiment systems, including SILTS. The SCM was programmable, and received updated instruction sets via telemetry at various times during a mission.

EXPERIMENT NOMINAL OPERATION AND TIMELINE

The SILTS operational concept envisioned the experiment to obtain infrared images of both the leeside fuselage and left wing, over a period of some 20 minutes during entry. The data period would begin when the orbiter reached the entry-interface (EI) altitude of 400 kft and terminate when the orbiter began the Terminal Area Energy Management (TAEM) phase of flight, at approximately 85 kft altitude. During this data period, the orbiter would have decelerated from orbital entry velocity to less than Mach 3, and the SILTS experiment would have collected data over the entire hypersonic portion of entry.

The nominal timeline for experiment operation is illustrated graphically in Figure 3. Just prior to the de-orbit burn, the SILTS experiment was manually "enabled" by proper setting of the switches on the aft flight deck. When the orbiter reached the entry-interface altitude, SILTS operation was initiated by command from the OEX SCM which resulted in power being applied to the SILTS experiment system. With power applied to the experiment, the infrared camera began to operate and solenoid valves opened to allow the flow of nitrogen gas. The flow of nitrogen gas precipitated ejection of the window protection plugs from the window cavities, window transpiration cooling, and cooling of the infrared detector. Following experiment initiation, approximately two minutes were required for camera electronics to "warm-up" and the infrared detector to "cool-down." Substantially more than these two minutes would pass before leeside TPS surface temperatures began to increase above the ambient.

At experiment "turn-on," a motor on the camera mount began to rotate the infrared camera so that it would alternately view the fuselage (through the centerline viewport window), the temperature reference surface, and the left wing (through the side-looking viewport window), and then return to the fuselage view. This sequence required approximately 10.9 seconds to complete, with 2.3 seconds spent viewing each of the three scenes and 4.0 seconds spent rotating from scene to scene. This rotation sequence would be continually repeated during experiment operation. Thus, during a nominal 20-minute data period, approximately 100 pairs of infrared images would be obtained.

FLIGHT EXPERIENCE

The SILTS experiment was operated, with mixed success, on five flights of *Columbia*. The following sections describe, flight-by-flight, the history of SILTS-experiment flight performance.

Mission STS-61C

The initial flight of the SILTS experiment occurred on STS-61C in January 1986. The SILTS experiment operational timeline for this initial flight was nominal. The SILTS hardware functioned throughout the entry, and a data record was obtained. However, two distinct, and unrelated, anomalies occurred on STS-61C which limited the quantity of data obtained and severely compromised its quality. The first anomaly was a lower than nominal and erratic rotation rate of the vertical scanning prism within the SILTS camera. This resulted in severe over-sampling of the image field and random distortion of the resultant images in the vertical direction (Refs. 4 and 5). Because of the image distortion, it was not possible to relate orbiter geometric surface locations with corresponding image pixels, thus precluding determination of surface temperature.

The second anomaly experienced on STS-61C was failure of the window coolant system to maintain window temperatures below the level at which the windows themselves become significant radiators in the infrared. On STS-61C, the gaseous nitrogen coolant was effective in protecting the windows during that portion of the entry when the leeside flowfield was laminar. However, upon reaching the flight condition (approximately Mach 16) at which the leeside flowfield experiences a laminar-to-turbulent transition (Ref. 6), the coolant was suddenly rendered ineffective at maintaining window temperatures at the low levels required to prevent them from becoming significant radiators (Refs. 4 and 5). No data were obtained subsequent to this flow transition as window temperatures increased rapidly and the images were obscured by radiation from the hot window panes.

STS-61C was the last shuttle mission prior to the *Challenger* accident. Consequently, the SILTS experiment was not flown again for a period of over three years.

Missions STS-28 and STS-32

Prior to STS-28, elements of the SILTS experiment system were modified to prevent a reoccurrence of the STS-61C anomalies on subsequent flights. Within the camera, modifications were made to both the vertical scanning mechanism and its electronic control circuitry. The window-coolant system was also redesigned to provide significantly increased rates of coolant mass flow to the windows during that portion of entry when the leeside flow is turbulent. This was accomplished by scheduling the window-coolant flow rate in two distinct stages: a low flow-rate stage for the early portion of entry when the leeside flowfield is laminar, and a high flow-rate stage for that portion of entry when the leeside flowfield is turbulent. The second-stage coolant flow rate was an order-of-magnitude greater than that of the first-stage. The resultant total coolant-mass requirement was so large that there was insufficient capacity in the coolant supply bottles to provide coolant to both viewport windows simultaneously throughout entry. Consequently, the redesigned SILTS experiment system allowed viewing through only one window per flight. On missions STS-28 and STS-32, the experiment was configured for observation of the left wing only. The fuselage, or forward-looking, window cavity was plugged with an HRSI thermal protection tile (Fig. 4).

STS-28

On the STS-28 mission, which took place in August 1989, the SILTS experiment was commanded ON when the orbiter reached the entry interface altitude of 400 kft. All elements of the experiment system operated normally for the entire entry data period. During experiment operation, an image was recorded approximately every 8.6 seconds. The experiment was commanded OFF after 22 minutes of operation, during which more than 150 images were recorded. Altitude at "turn-off" was 133 kft and the Mach number was less than 6.

As occurred on STS-61C, the viewport window temperature increased significantly as a result of the onset of turbulence in the leeside flowfield. However, the increased coolant mass flow applied to the window during this portion of entry was successful in providing sufficient window protection to prevent complete obscuration of the images by window radiation, as had been the case on STS-61C, and enabled data collection throughout the entire entry. Preliminary results from the STS-28 mission are summarized in Reference 7.

STS-32

On this mission, the experiment was again commanded ON at the entry interface altitude, and commanded OFF after 22 minutes of operation. Altitude at "turn-off" was 129 kft and Mach number was less than 6. All elements of the experiment system operated normally for the entire entry data period. Over 150 images were acquired on this mission.

Missions STS-35 and STS-40

Following the successful collection of wing data on flights STS-28 and STS-32, the SILTS experiment was configured, for STS-35 and STS-40, to view the leeside fuselage. In this configuration, the wing viewport window cavity was plugged with an HRSI thermal protection tile (Fig. 5). Valuable fuselage temperature data were acquired on each of these missions. However, unique operational anomalies which occurred on these flights (different for each flight) severely limited the amount of useful data obtained.

Preliminary results from the STS-35 and STS-40 missions are summarized in Reference 8.

STS-35

On STS-35, the entry phase instruction set which the OEX System Control Module (SCM) executes during entry, and which includes the SILTS initiation command, was not telemetered to the SCM at the proper time prior to entry. The untimely failure of a ground-based computer which was controlling antenna pointing on the Tracking and Data Relay Satellite (TDRS) resulted in a temporary loss of the ground-to-orbiter communication link, thus precluding telemetry of the entry phase instruction set. Once the telemetry link was reestablished, the entry phase instruction set was sent to the SCM, and the appropriate command sequences initiated. However, the SILTS command sequence was initiated almost 13 minutes late.

SILTS "turn-on" occurred 766 seconds *after* the entry interface (EI) time. Approximately 140 seconds later (EI+906 seconds), the orbiter reached the flight condition at which the leeside shock layer experienced the laminar-to-turbulent flow transition. At that time, the window-coolant flow rate was still at the very-low, first-phase level, and therefore the viewport window temperature began to rapidly increase. Radiation from the window completely "fogged" the images within an additional 40 seconds (EI+946 seconds). Since the infrared detector required about 110 seconds of operation, after experiment "turn-on," to reach its operating temperature and thus begin to obtain useful data, only about one minute of useful data were obtained on this flight.

STS-35 data were obtained over a Mach number range of approximately 17.6 to 16.0, with the vehicle operating at 40-degrees angle-of-attack. This range of flight conditions provided a small amount of data for both the laminar and turbulent states of the leeside flowfield. Figure 6 graphically identifies the flight conditions at which these data were obtained.

STS-40

STS-40 was the last planned flight of the SILTS experiment. The research objective of this flight was collection of the most accurate data possible during the early portion of entry, when the leeside shock-layer flow was laminar. In order to ensure minimal window radiation on this flight, the coolant flow-rate schedule was modified to provide a significantly increased level of coolant mass flow to the window very early in the entry.

On STS-40, the SILTS experiment was properly initiated at the entry interface (EI) altitude. However, the window protection plug failed to eject from the viewport window cavity at experiment "turn-on." Consequently, the SILTS camera could not "see" the orbiter surfaces. The coolant mass-flow rate was increased at the proper time, but the coolant was merely being injected behind the window protection plug which remained in the window cavity. At EI+1178 seconds, well after the peak turbulent heating pulse to the window, the window protection plug inexplicably cleared the window cavity, and the SILTS camera began to obtain image data. By approximately EI+1310 seconds, window temperature had increased to a level at which window radiation completely obscured the fuselage images. (By this point in the entry, the coolant mass-flow rate was extremely low, a result of the commitment to high coolant flow-rates early in the entry.) Consequently, only about 2 minutes of useful data were obtained on the STS-40 mission.

The STS-40 data were obtained over a Mach number range of approximately 8.5 to 5.9, and angles-of-attack from 36 to 28 degrees (Fig. 6). Turbulent leeside flowfield conditions existed throughout this data period. Although not a part of the STS-40 experiment objective, the serendipitous collection of these data represents a significant addition to the SILTS database. Collection of data this late in the entry trajectory was not previously thought possible because of concern that the window protection plug could not be ejected at flight conditions with such high freestream dynamic pressure.

DATA PROCESSING

Image Generation

SILTS infrared detector output data were recorded on the OEX tape recorder as a continuous analog signal. Horizontal and vertical synchronization signals, which indicated scanning prism rotational position, were recorded concurrently. Postflight data processing began with conversion of the detector output data to digital form. The vertical and horizontal synchronization data provided "beginning of frame" and "beginning of line" information, respectively, enabling construction of two-dimensional imagery from the continuous data record. The products of this initial data processing step were matrices of image data composed of 401 lines of information, digitized at 200 pixels per line, indicating the voltage output from the infrared detector. A two-dimensional (3x3) median filter was applied to the data at each pixel in order to suppress any random electronic noise which may have been inherent in the raw data. The resultant data are used to generate false-color images which denote the detector output voltage levels. Detector output is directly proportional to the level of infrared radiation emanating from the viewed surfaces, which is in turn directly proportional to surface temperature.

Figure 7 presents a typical wing data image obtained on STS-28. Features evident in the image include the wing leading-edge, the gap between the inboard and outboard elevons, the orbital maneuvering system (OMS) pod at the base of the vertical tail , the OMS engine nozzle, and the sidewalls of the conical window cavity through which the camera "looks." Along the wing leading-edge, the temperature variations across individual reinforced carbon-carbon (RCC) panels are apparent. The coolest temperatures are indicated by the color black with the colors blue-green-yellow-red-pink-white indicating progressively increasing temperature.

Figure 8 presents a typical fuselage data image obtained on STS-35. Clearly visible in this image are the leading edge of the vertical tail, the orbital maneuvering system (OMS) pods at the base of the tail, both wing leading edges, the upper fuselage, and the sidewalls of the conical cavity which surrounds the viewport window. Surfaces at the coolest temperature are indicated by the color black, with the colors blue-green-yellow-red-pink indicating progressively increasing temperatures. The color scale used for presentation of data in Figures 7 and 8 are *not* comparable; consequently, no valid comparisons can be made with respect to relative temperatures in these two images.

Window Radiation Correction

As has been observed, the transpiration cooling of the viewport windows was not fully effective in preventing window temperatures from rising to levels where the windows themselves became infrared radiators. Consequently, the raw image data were influenced by both the infrared radiation from the orbiter surfaces and radiation emanating from the viewport window; and these data must be corrected to account for the influence of the window radiation.

The window radiation signature has been shown to have a somewhat annular character about the center of the viewport window (Ref. 8). The magnitude of the window radiation was at a minimum at the window center and increased radially. This characteristic distribution of radiation from the window resulted from the specific implementation approach incorporated for the transpiration cooling of the window surface. Transpiration coolant was injected onto the window surface as six discrete, radial "jets" distributed at equal angular increments around the circular window (Ref. 3). The coolant gas was injected at the circumference of the window and directed toward the window center, resulting in more effective protection at the window center and less effective protection with increasing radial distance from the center. Consequently, aerodynamic heating of the window resulted in window temperatures which varied radially from the window center, thus the annular character of the window radiation signature.

The magnitude of the window radiation correction is determined by consideration of the levels of radiation indicated in the raw image data for areas which are "off" of the orbiter surface (i.e., "looking" into space). Camera output data for "off-orbiter" image areas are extracted from the data matrices. These data are then curve fit, using the method of least-squares, with a second-order polynomial (camera response as a function of radial position from the window center) which is constrained to have its minimum value at radius equal zero (i.e., the window center). This polynomial, which defines the radial distribution of window radiation, is then rotated about the window center in order to infer the level of window radiation at all points in the camera field of view. The result is a "target-like" window-radiation correction "mask." (See Ref. 8) The window-radiation contribution to the total radiation measured by the infrared detector is then simply subtracted from the raw image data, pixel by pixel, to produce a corrected data image. This process is performed independently for each data image.

Determination of Temperature

Conversion of the window-radiation-corrected camera output data to accurate surface temperature information requires an experiment system calibration, knowledge of the geometric relationship between the focal-plane image and the orbiter surfaces being viewed, and knowledge of the emissivity of the viewed surfaces.

Prior to each flight, a complete, end-to-end experiment system calibration was performed. This calibration was performed at multiple, distinct temperature levels, which spanned the full dynamic range of the experiment system, using a reference blackbody radiation source.

A complex geometric relationship existed between the camera focal-plane image and the actual orbiter surfaces being viewed. The mechanical-scanning optics of the SILTS camera produced an image which appears as though it were taken through a "fish-eye" lens (Ref. 7). Empirical image-distortion data were generated in the laboratory by imaging an orthogonal grid of heated wires spaced approximately 10 cm apart. This information was used to model the distortion inherent in the raw data imagery. Combining this image distortion information with the geometric information of camera focal-plane position and orientation relative to the orbiter coordinate system enabled a one-to-one correspondence to be established between each image pixel and its associated X, Y, Z location on the orbiter surface.

With the image pixel and associated X, Y, Z location relationship established, the type of thermal protection material being viewed at each image pixel was determined. Consequently, the surface emissivity for each image pixel was known. Emittance characteristics of orbiter thermal protection materials were determined from room-temperature measurements of surface spectral reflectance over the spectral band of interest for the SILTS infrared detector.

Orthogonal Data Projection

The coordinate transformation which related image-plane pixels to orbiter surface locations also enables orthogonal projection of the SILTS image onto an orbiter planview. This capability is illustrated in Figure 9. In this presentation, image pixels which do not represent orbiter surface locations have been eliminated from the projection. The result is a detailed, orthogonal mapping of the temperature distribution over the leeside surface for the specific flight condition at which the data were obtained. Since the coordinate location of each pixel is known in three dimensions, these data may also be used on a modern graphic workstation to produce three-dimensional perspective representations of the temperature distribution over the orbiter's leeside.

SUMMARY

The Shuttle Infrared Leeside Temperature Sensing (SILTS) experiment was designed to obtain high-spatial-resolution measurements of the temperature of orbiter leeside (fuselage and wing) surfaces during the hypersonic portion of atmospheric entry. These measurements were obtained by means of an imaging, infrared radiometer (camera) located in a unique experiment pod atop the vertical tail of the orbiter *Columbia*. The SILTS experiment was installed on the orbiter *Columbia* during the vehicle's 1984-85 modification period. Subsequently, the experiment was flown on five missions: STS-61C, -28, -32, -35, and -40.

Unique data processing software were developed to enable determination, from the SILTS imagery, of quantitative temperature data as a function of geometric surface location.

ACKNOWLEDGMENTS

While it is not possible to acknowledge the efforts of all those persons who made significant contributions to the design, development, implementation, and flight operations of the SILTS experiment, the authors wish to specifically recognize several individuals whose personal involvement was critical to the successful maturation of the SILTS experiment from concept to flight-ready spaceflight hardware, and subsequently, for the successful flight operations of the experiment.

James C. Dunavant conceived the SILTS experiment in the early 1970's, and was the SILTS Principal Investigator and guiding influence until his retirement from NASA Langley Research Center in 1981.

The following individuals were key members of the Langley Research Center team which designed, developed, fabricated, tested, and initially implemented the SILTS experiment system hardware: Nathan D. Watson, William I. Watson, B. B. Brown, Jr., Rufus K. Dail, and Hugh C. Halliday.

Subsequent to STS-61C, the efforts of Frederick L. Staggs and Frederick J. Rosensteel led directly to the SILTS Team's understanding of the hardware anomalies experienced on that flight. Reginald M. Holloway, Rufus K. Dail, James B. Miller, Thomas H. Leffel, Jr., and Obie H. Bradley, Jr., were instrumental in recreating the flight anomalies on the ground.

The following individuals designed and implemented the experiment mechanical and electrical modifications required to preclude reoccurrence of the anomalies experienced on STS-61C, and comprised the SILTS flight operations team for the remainder of the SILTS flight test program: Rufus K. Dail, Michael S. Grant, Thomas H. Leffel, Jr., and Frederick J. Rosensteel.

David L. Myrick was responsible for the mathematical formulations, and algorithm design and development, for all SILTS data processing software. He has performed all of the data processing and image generation for the SILTS program, including all ground calibration and system characterization test-data processing, as well as processing of the data which emanated from the five flights of the SILTS experiment.

The authors also gratefully acknowledge those personnel of the OEX Project Offices at both the NASA Johnson Space Center and Rockwell International who were responsible, within their organizations, for SILTS experiment implementation and operation. Their efforts were vital to the successful implementation and flight operation of the SILTS experiment.

REFERENCES

1. Throckmorton, D. A.: Development Flight Instrumentation (DFI) and the Aerothermal Instrumentation Package (AIP). *Orbiter Experiments (OEX) Aerothermodynamics Symposium,* NASA CP-3248, 1995.

2. Throckmorton, D. A., Zoby, E. V., and Kantsios, A. G.: The Shuttle Infrared Leeside Temperature Sensing (SILTS) Experiment. AIAA Paper 85-0328, January 1985.

3. Bradley, O. H., Jr.: Development of a Window Protection Assembly for a Shuttle Experiment. *15th Aerospace Mechanisms Symposium,* NASA CP-2181, May 1981, pp. 303-329.

4. Throckmorton, D. A., Dunavant, J. C., and Myrick, D. L.: Shuttle Infrared Leeside Temperature Sensing (SILTS) Experiment -- STS 61-C Results. AIAA Paper 88-2668, June 1988.

5. Dunavant, J. C., Myrick, D. L., Zoby, E. V., and Throckmorton, D. A.: *Shuttle Infrared Leeside Temperature Sensing (SILTS) Experiment -- STS 61-C Final Results,* NASA TP-2958, March 1990.

6. Throckmorton, D. A., and Zoby, E. V.: Orbiter Entry Leeside Heat-Transfer Data Analysis. *Journal of Spacecraft and Rockets,* Vol. 20, No. 6, November-December 1983, pp. 524-530.

7. Throckmorton, D. A., Zoby, E. V., Dunavant, J. C., and Myrick, D. L.: Shuttle Infrared Leeside Temperature Sensing (SILTS) Experiment -- STS-28 Preliminary Results. AIAA Paper 90-1741, June 1990.

8. Throckmorton, D. A., Zoby, E. V., Dunavant, J. C., and Myrick, D. L.: Shuttle Infrared Leeside Temperature Sensing (SILTS) Experiment -- STS-35 and STS-40 Preliminary Results. AIAA Paper 92-0126, January 1992.

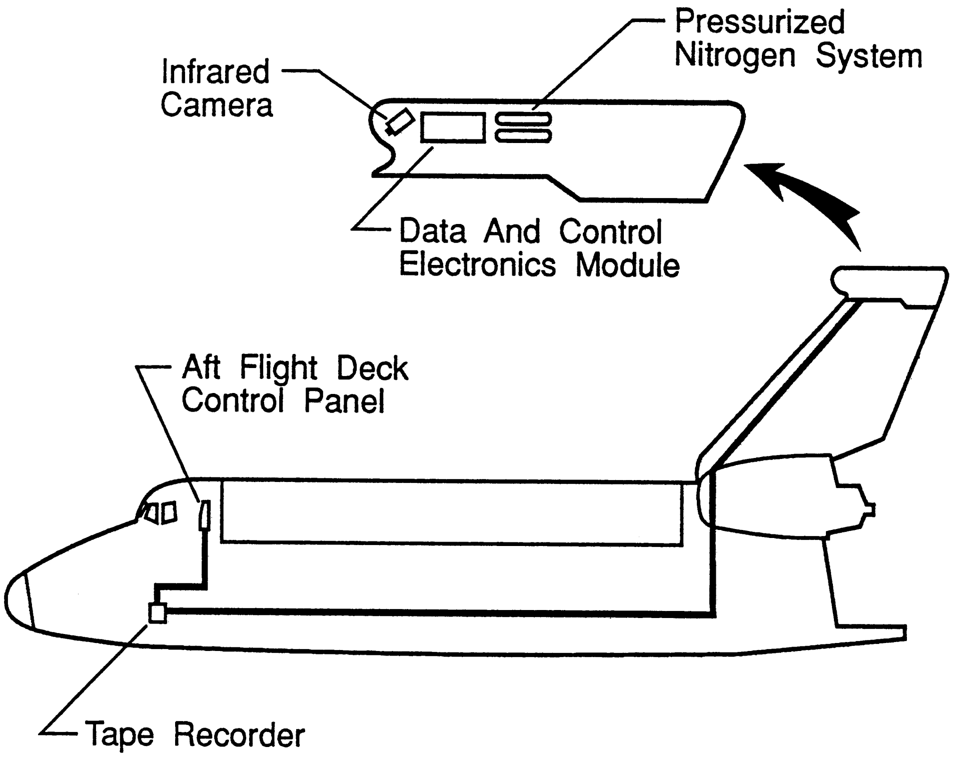
Pressurized Nitrogen System
Infrared Camera
Data And Control Electronics Module
Aft Flight Deck Control Panel
Tape Recorder

Figure 1 -- SILTS experiment system schematic.

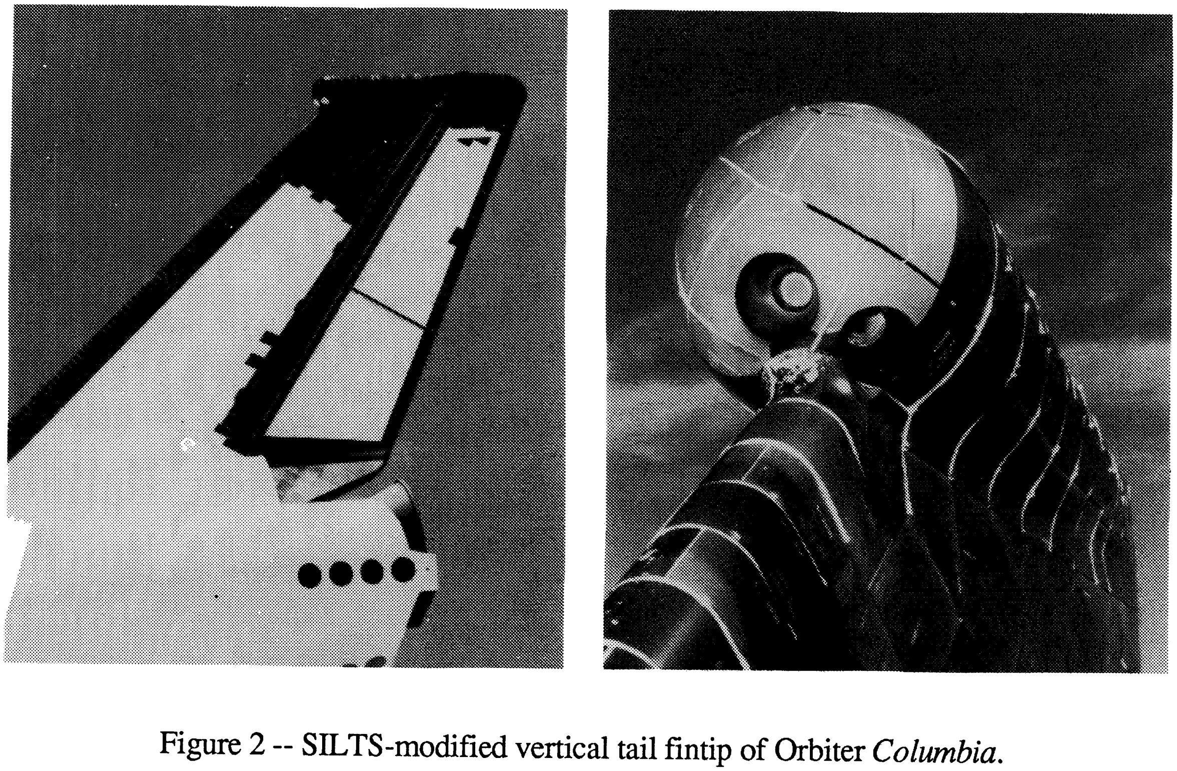

Figure 2 -- SILTS-modified vertical tail fintip of Orbiter *Columbia*.

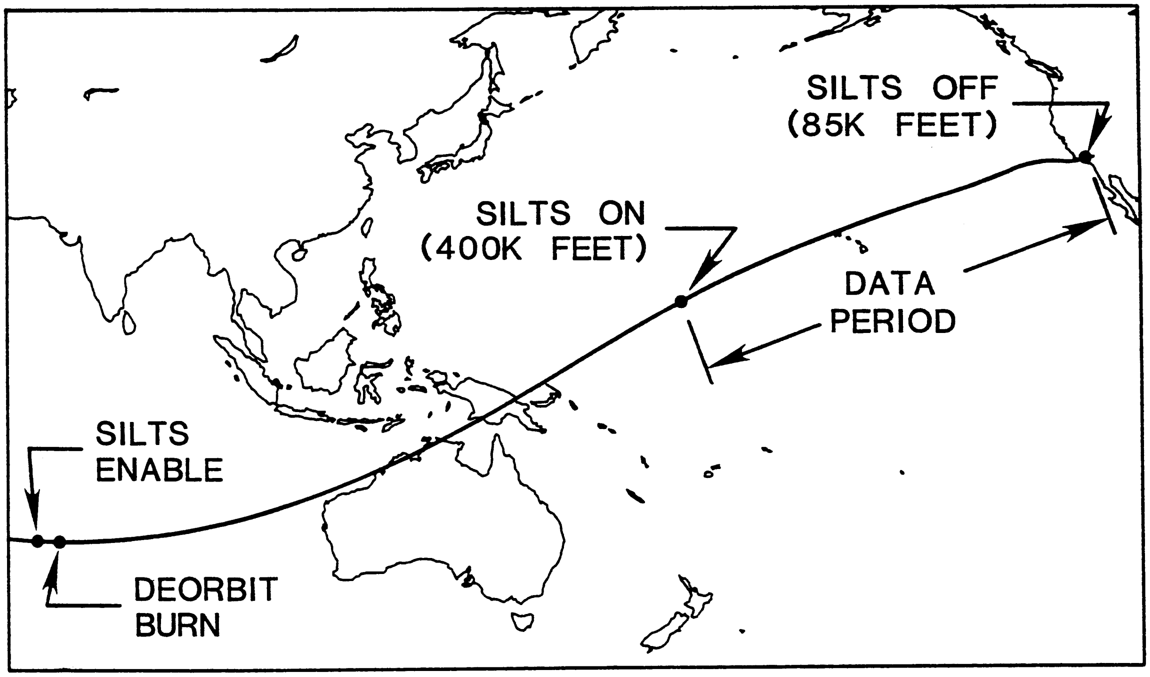

Figure 3 -- SILTS experiment nominal operational timeline.

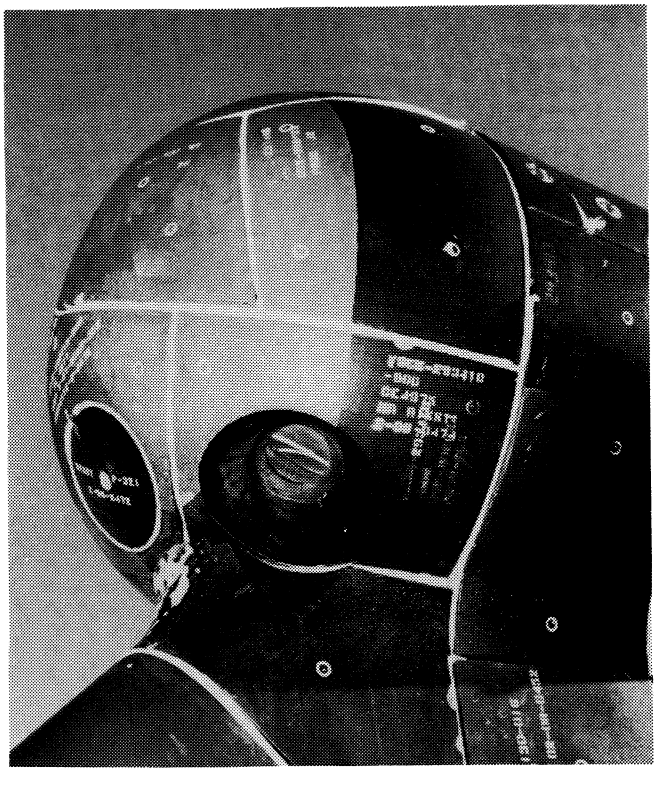

Figure 4 -- STS-28 and STS-32 SILTS-pod configuration (STS-28 post-flight photograph).

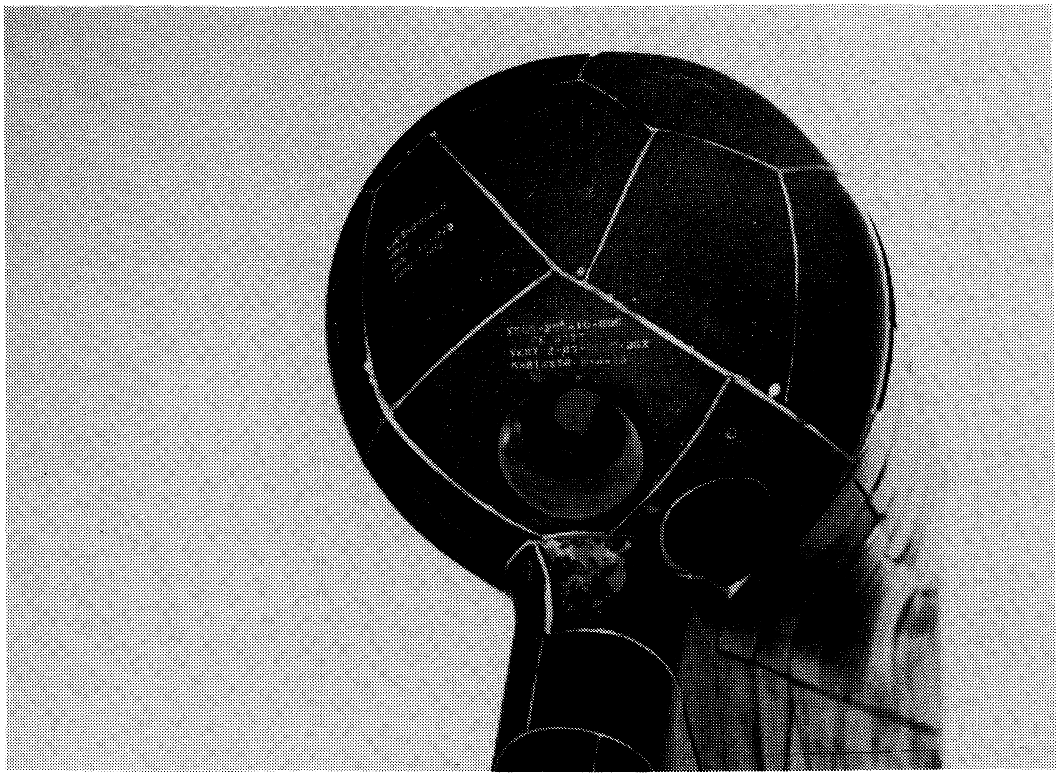

Figure 5 -- STS-35 and STS-40 SILTS-pod configuration (STS-40 post-flight photograph).

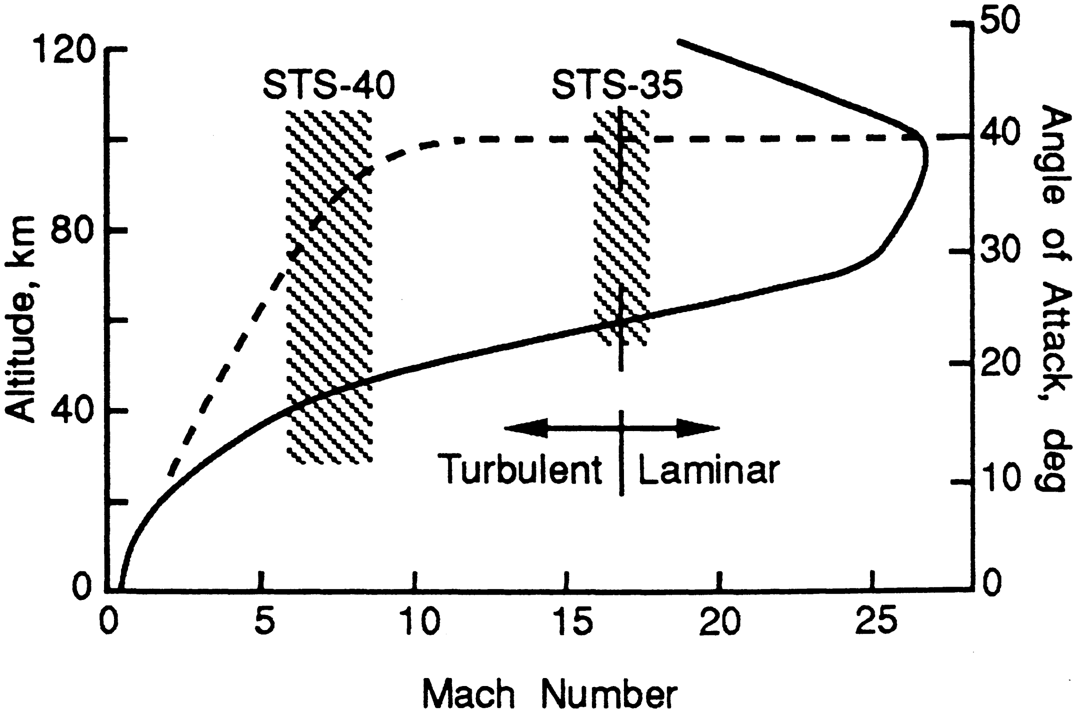

Figure 6 -- SILTS fuselage-data availability.

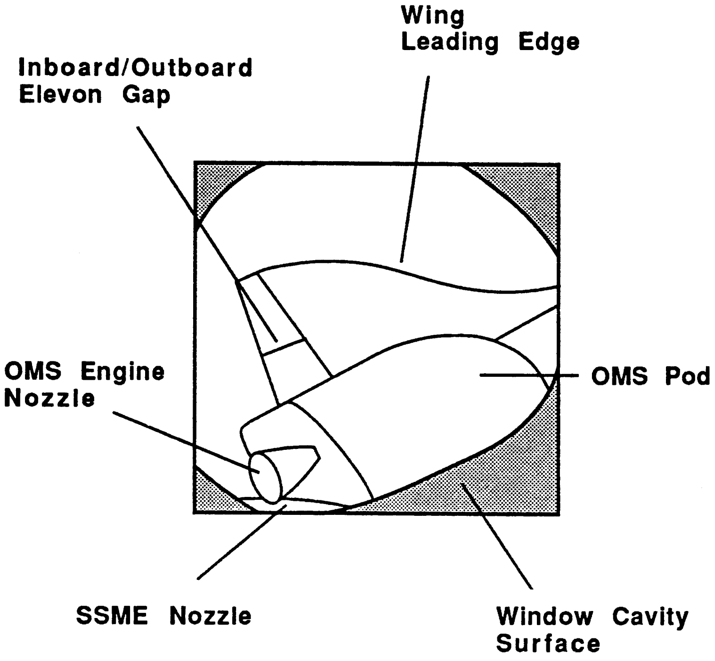

Figure 7 -- Typical SILTS wing-data image (from STS-28).

(See page 496 for color versions of figures 7 and 8.)

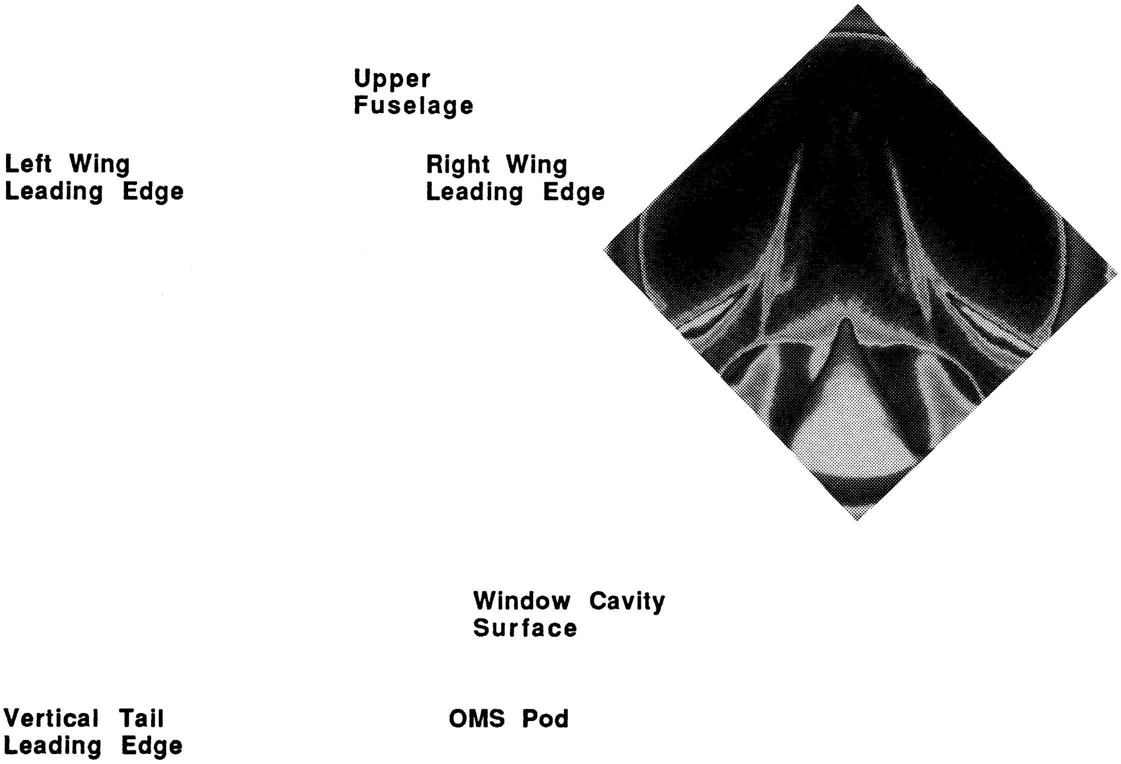

Figure 8 -- Typical SILTS fuselage-data image (from STS-35).

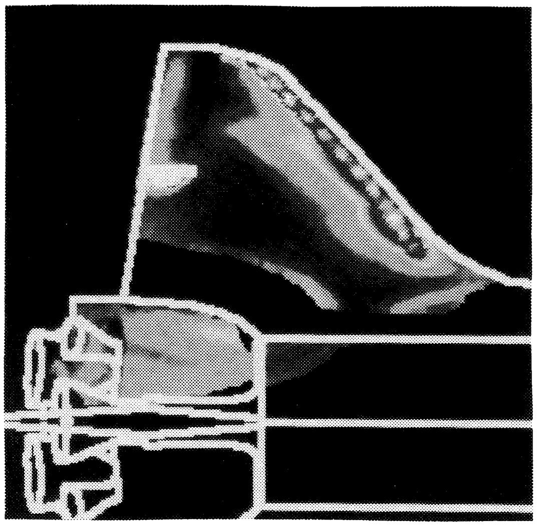

Camera View **Projection to Planview**

Figure 9 -- Typical data projection to orbiter planview.

(See color version of figure 9 on page 497.)

ORBITER (Pre STS-1) AERODYNAMIC DESIGN DATA BOOK DEVELOPMENT AND METHODOLOGY

Paul O. Romere*
NASA Johnson Space Center
Houston, Texas 77058

ABSTRACT

The major aerodynamic design challenge of the United States Space Shuttle Transportation System (STS) research and development phase was to design a vehicle that would fly as a spacecraft during early entry and as an aircraft during the final phase of entry. The design was further complicated because the envisioned vehicle was statically unstable during a portion of the aircraft mode of operation. The second challenge was the development of preflight aerodynamic predictions with an accuracy consistent with conducting a manned flight on the initial orbital flight.

A brief history of the early contractual studies, highlighting the technical results and management decisions influencing the aerodynamic challenges, provides an insight into the configuration development background. Following the baselining of the OV-102 outer mold lines definition, the development of the preflight aerodynamic data base to be utilized for the first Space Shuttle Orbiter flight, STS-1, was initiated. The wind tunnel test program of approximately 27,000 hours of testing is discussed, with particular emphasis on the STS-1 preflight data base development. The methodology of progressing from wind tunnel test data to the preflight data base is discussed along with the requirement for uncertainties definition to facilitate the parallel development of the vehicle flight control and the preflight aerodynamic design data base.

---

* Shuttle Manager, Aeroscience Branch
Associate Fellow, AIAA

INTRODUCTION

A traditional phased approach was used in the programmatic design evolution of the Space Shuttle Orbiter. The concept evaluation phase (Phase A) contractual studies were conducted in 1969. The Phase B concept definition phase extended over approximately 2 years beginning in mid 1970. The research and development phase (Phase C) and the production and flight test phase (Phase D) began in August 1972, with the selection of Rockwell International as prime contractor and their being given the Authority To Proceed (ATP).

This paper addresses the STS-1 preflight data base development and methodology, including the wind tunnel test program and the approach and landing test program. Of particular significance was the requirement for the definition of "design-to" uncertainties to facilitate the flight control system design.

NOMENCLATURE

Acronyms

ADDB	Aerodynamic Design Data Book
AFFTC	Air Force Flight Test Center
AEDC	Arnold Engineering Development Center
ALT	Approach and Landing Test
ARC	NASA Ames Research Center
ATP	Authority To Proceed
CDR	Critical Design Review
DFRF	Dryden Flight Research Facility
ET	External Tank
FCS	Flight Control System
FMOF	First Manned Orbital Flight
GN&C	Guidance, Navigation, and Control
JSC	NASA Johnson Space Center

LaRC	NASA Langley Research Center
LTV	Ling-Temco-Vought Corporation
NASA	National Aeronautics and Space Administration
NSWC	Naval Surface Weapons Center
OFT	Orbital Flight Test
OMS	Orbital Maneuvering System
OV	Orbital Vehicle
PDR	Preliminary Design Review
RCS	Reaction Control System
SRB	Solid Rocket Booster
SRR	Systems Requirements Review
SSME	Space Shuttle Main Engine
STS	Space Transportation System
TPS	Thermal Protection System
UPWT	Unitary Plan Wind Tunnel

SYMBOLS

A_{REF}	Jet reference area, 1.0 ft ^{2}
b	Reference wing span, ft (meters)
C_m	Pitching moment coefficient
C'	Factor of proportionality in linear viscosity-temperature relation
CG	Center of gravity
D	Drag
deg	Degrees
ft	Feet, foot
h	Altitude
K	Signifies unit of 1,000
L	Lift
L/D	Lift to drag ratio
lbs	Pounds
lbm	Pounds mass
L_B	Reference body length, 107.525 ft (32.7736 m)

M	Free-stream Mach number
$\dot{m}$	Mass flow rate, lbm/sec
m	Meters
$\frac{\dot{m}_j}{\dot{m}_\infty}$	RCS jet mass flow rate ratio
N	Newtons
n_j	Number of RCS jets firing
psf	Pounds per square foot
q	Dynamic pressure, lb/ft^2
Re	Reynolds number
S	Reference area, 2,690 ft^2 (249.9092 m^2)
sec	Second
V	Velocity, ft/sec
$\bar{V}_\infty$	Viscous interaction parameter (Lees and Probstein)
$\bar{V}'_\infty$	Viscous interaction parameter (Whitfield and Griffith)
X	Orbiter longitudinal axis body coordinate
$\lvert \ \rvert$	Signifies absolute value
α	Angle of attack, deg.
δ_{BF}	Body flap deflection, deg.
δ_e	Elevon deflection, deg.
δ_{SB}	Speed brake deflection, deg.
Δ	Signifies increment
ϕ	Roll Euler angle, deg
$\frac{\phi_j}{\phi_\infty}$	RCS jet stream momentum ratio
θ	Nozzle half angle at exit, deg.

SUBSCRIPTS

j	Jet exit conditions
∞	Free-stream conditions
REF	Reference

CONFIGURATION DEVELOPMENT

The Space Transportation System (STS) was initiated with the Phase A conceptual design contracts in 1969. These contracts studied various methods of producing a completely reusable spacecraft system capable of a runway landing. The results of the Phase A studies led to the selection of a two-stage, completely reusable vehicle as the focus for Phase B contractual studies. The majority of the studies addressed a first stage manned "flyback" booster in combination with an Orbiter second stage. Subsequent to staging, the flyback booster utilized air breathing engines to return to the launch site for a runway landing. The Orbiter would continue the launch phase until low earth orbit was achieved. Following a typical on-orbit mission of 5 to 7 days, the Orbiter would enter the Earth's atmosphere at a high angle of attack (up to 60 deg.), ultimately landing on a runway much like a conventional airplane. Midway through Phase B, estimates of system development costs indicated that the peak yearly funding requirements for the parallel development of the two manned, fully reusable vehicles would not be a viable programmatic approach. During this time, the second stage fuel tanks were removed from the Orbiter to minimize the impact of any Orbiter weight growth during program development.

During the final months of Phase B, a parallel-burn concept was selected. This concept consisted of the simultaneous burn of both the solid rocket boosters (SRB) and the three liquid-fueled Space Shuttle main engines (SSME). The two SRBs assisted lift-off and the initial ascent flight, The SSMEs, fed by an expendable external tank (ET), continued to burn until near orbital insertion. The orbital maneuvering system (OMS) engines provided the additional delta-velocity required for orbital insertion. With this configuration, Phases C & D were begun in August of 1972 with the selection of Rockwell International as the prime contractor. The result of Phase C & D efforts is the current Space Shuttle Orbiter illustrated in figure 1.

TYPICAL ORBITER MISSION

At an altitude of approximately 400,000 ft, the Orbiter is designed to perform an unpowered gliding re-entry at an angle of attack of approximately 40 degrees. The angle of attack is modulated depending upon the crossrange requirements. Downrange modulation is achieved by periodically performing bank reversals across the prescribed ground track. Figure 2 presents a typical entry trajectory.

Although entry interface is defined as 400,000 ft altitude, a sensible atmosphere is not reached until Mach 27 at an altitude of approximately 300,000 ft, with a dynamic pressure of 2 psf. Early entry stability and control is provided primarily by the aft-mounted reaction control system (RCS) jets, figure 3. The roll and pitch jets are reserved for on-orbit attitude control and ascent aborts. The roll and pitch jets are active until dynamic pressures of 10 and 20 psf, respectively, are obtained, at which point the elevons are sufficiently effective to provide pitch and roll control. The yaw jets provide stability augmentation until the vehicle has decelerated to Mach 1.

A gradual pitch down is initiated between Mach 14 and 12. By Mach 2 the vehicle is flying at more conventional angles of attack from 3 degrees to 10 degrees. Equilibrium subsonic gliding flight is achieved at an altitude of approximately 40,000 ft. The approach and landing interface occurs at 10,000 ft, and the vehicle subsequently reaches a glide slope of approximately -19 degrees. Nominal touchdown velocity is 195 knots with a rollout of 7,000 to 9,000 ft.

ORBITER FUNCTIONAL CHARACTERISTICS

The basic design ground rules, illustrated in Table 1, were established early in the configuration development phase. The configuration geometry was designed to meet those guidelines. The resultant orbiter configuration and its functional characteristics of the Orbiter are presented in figure 4. The thick, double-delta wing is configured with full span elevons, comprised of two panels per side. Each elevon panel is independently actuated. All four panels are deflected together as an elevator for pitch control and left and right elevons are deflected differentially as an aileron for roll control.

The bodyflap, originally designed as a heat shield for the SSMEs, is now also used as the primary longitudinal trim device. The elevons are programmed to follow a set schedule during entry to provide the optimum aileron effectiveness. The bodyflap maintains the desired trim angle of attack while also assuring the elevons stay within scheduled limits about the programmed elevon schedule.

The vertical tail consists of the fin and a split rudder. The rudder panels are deflected together for yaw control and are separated to act as a speedbrake to provide for subsonic energy modulation. The speedbrake, initially closed upon entry interface, opens fully just below Mach 10 and then follows a predetermined schedule until Mach 0.9 is reached. The rudder is not activated for yaw control until Mach 3.5.

Therefore, the prediction of the basic aerodynamic characteristics, aileron effectiveness, and elevon effectiveness are required from Mach 0.2 through 27, and at an angle of attack range from near 0 degrees to 40 degrees. Rudder effectiveness is required below Mach 3.5. The high dynamic pressure to be encountered forced consideration of structural deformation effects on aerodynamics. Also, the effectiveness of the Reaction Control System (RCS), as a function of jet thrust, plume impingement and the vehicle flowfield/plume interaction, would have to be determined from on-orbit conditions down to as low as 50,000 feet (Mach 1).

SELECTION OF SCALING PARAMETERS

In order to accurately simulate flight conditions in a wind tunnel, the appropriate similarity parameters must be matched. Traditionally, Mach number and Reynolds number are the key parameters. Problems in flow simulation occur when the geometric scaling of viscous flow is important, or when coupling between the viscous surface flow and the external flow field is strong. In the first case, the boundary layer can be considered separately from the inviscid flow field, and viscous effects can be scaled. This holds for Mach numbers up to approximately 10. It is well known, for example, that skin friction varies with Reynolds number in a predictable manner and can be scaled to flight conditions from suitable wind tunnel results.

For Mach numbers greater than approximately 10, a pressure interaction results from the outward streamline deflection induced by a thick boundary layer, and the viscous-inviscid interaction must be considered. For this case, there are two classical simulation parameters commonly considered:

(1) $\bar{V}_\infty$, the viscous interaction parameter introduced by Lees and Probstein (Reference 1)

$$\bar{V}_\infty = \sqrt{\frac{M^3 C'}{Re_{LB}}}$$

(2) $\bar{V}'_\infty$, the viscous parameter introduced by Whitfield and Griffith (Reference 2)

$$\bar{V}'_\infty = M_\infty \sqrt{\frac{C'}{Re_{LB}}}$$

where M is the free-stream Mach number, C' is the Chapman-Rubesin viscosity coefficient evaluated in the freestream based upon reference temperature conditions (Reference 3), and Re is the free-stream Reynolds number based on body reference length (L_B). The parameter $\bar{V}_\infty$ is the relevant parameter for the local effects (pressure coefficient, heat transfer, etc.) in both the strong and weak interaction cases; whereas $\bar{V}'_\infty$ is the relevant parameter in terms of overall integrated effect. For Shuttle, it has been observed that $\bar{V}'_\infty$ correlates total aerodynamic coefficients better than $\bar{V}_\infty$, and consequently, $\bar{V}'_\infty$ was selected as the hypersonic simulation parameter. A detailed discussion of the use of these scaling parameters for the Space Shuttle is presented in reference 4.

Figure 5 shows a comparison between flight Re_{LB} and $\bar{V}'_\infty$ and the simulation capability of typical wind tunnels used to develop the Orbiter aerodynamic data base. It can be seen that the tunnel capabilities reasonably match flight conditions above Mach 3. It should be noted that although flight Reynolds number and Mach number were not simulated above Mach 15, the assumption was made that if $\bar{V}'_\infty$ is the correct similarity parameter, the tunnel prediction of aerodynamic characteristics should be good. One inadequacy worth noting is that at the time of the Shuttle aerodynamic development (prior to STS-1) neither experimental facilities nor theory could accurately predict real gas effects.

SIMULATION OF REACTION CONTROL JET INTERACTION

Early entry aerodynamic characteristics are highly influenced by interactions between the RCS jet plumes and the local flow field over the Orbiter. The total jet effects are comprised of three factors: (1) jet thrust, (2) surface impingement, and (3) jet interaction with the flow field. Impingement and interaction effects are interrelated. Jet interaction was obtained from wind tunnel testing while surface impingement was estimated from vacuum chamber tests and theory. Coupling is present between the plume effects and aerodynamic surfaces, and between the jets themselves.

A series of scaled model RCS nozzles with different expansion ratios were employed during the wind tunnel test program. General Dynamics/Convair, under contract to the NASA (NAS9-14095) developed a method whereby the experimentally-measured induced plume effect (surface impingement plus flow field interaction) could be separated into two component parts and the impingement term extrapolated to flight conditions. To obtain a correct modeling of the RCS plume effects in the wind tunnel, it was necessary to observe certain scaling criteria. The primary factors for consideration, aside from dimensional scaling, are plume shape, jet-to-free-stream momentum ratio $\left(\frac{\phi_j}{\phi_\infty}\right)$ and mass flow rate ratio $\left(\frac{\dot{m}_j}{\dot{m}_\infty}\right)$. The RCS pitch jets (up and down firing jets) correlated better with momentum ratio whereas the yaw jets (side firing jets) correlated better with mass flow rate ratio. These scaling parameters are defined as:

$$\frac{\phi_j}{\phi_\circ} = \left(\frac{\dot{m}_j V_j}{q_\infty A_{REF}}\right)\left(\frac{A_{REF}}{2\,S_{REF}}\right) n_j = 0.1543\left(\frac{n_j}{q_\infty}\right)$$

where area = 1.0 ft^2, $S_{REF} = 2690\ \text{ft}^2$

and

$$\frac{\dot{m}_j}{\dot{m}_\infty} = \left(\frac{\phi_j}{\phi_\infty}\right)\left(\frac{V_\infty}{V_j}\right)\left(\frac{1}{n_j}\right)\left(\text{Sin}\,\theta_j\right)^{1/2} = 8.296 \times 10^{-6}\left(\frac{V_\infty}{q_\infty}\right)$$

A detailed discussion of the selection of these scaling parameters is presented in reference 5.

APPROACH AND LANDING TEST PROGRAM

The Preliminary Design Review (PDR) of the first Orbiter vehicle (OV-101) and subsystems for the Approach and Landing Test (ALT) program were completed in February 1974 with the PDR of the second Orbiter vehicle (OV-102) following in March 1975. Following the OV-101 rollout from final assembly in Palmdale, California, in September 1976, the ALT program was begun shortly afterwards with the mating of the Orbiter OV-101 to the Boeing 747 carrier vehicle. The first captive flight was completed in February 1977. The first ALT flight of the OV-101 from the Boeing 747 took place on August 12, 1977. The ALT program consisted of six flights from the Boeing 747, of which the first four flights were flown with the tailcone-on configuration and the remaining flights with the tailcone-off configuration. The tailcone was designed to reduce drag and buffet loads on the Boeing 747 vertical tail, which seriously limited the number of flights the Boeing 747 would be certified for carrying the OV-101 in the tailcone-off configuration. A detailed review of the ALT program is presented in reference 6. Flight test data from the ALT program was enhanced by the addition of specific flight test maneuvers designed to determine control surface effectiveness and basic vehicle stability and performance characteristics. Analysis of the data from the two tailcone-off flights contributed to the development of the low subsonic aerodynamic characteristics and uncertainties as reflected in the STS-1 Aerodynamic Design Data Book (Reference 7).

WIND TUNNEL TEST PROGRAM

The Shuttle Orbiter preflight entry aerodynamic data base was built on a foundation of approximately 27,000 hours of wind tunnel testing. Considerable effort was expended in assuring that the test program utilized state-of-the-art facilities. The wind tunnel test program was effectively divided into three phases, with the first addressing the configuration development. This phase covered the time period of ATP to Systems Requirements Review

(SRR) and addressed ATP configuration refinement, evaluation of the PDR configuration, and definition of the Critical Design Review (CDR) configuration. The prime contractor devoted the majority of the Phase II efforts to developing and verifying the aerodynamic characteristics for the ALT/carrier program, although initial development testing for the Orbital Flight Test (OFT) program was also performed. These latter development tests were directed toward establishing the basic stability and control characteristics across the Mach range; establishing control surface effectiveness and hinge moments; initial RCS testing; and viscous interaction testing. The Flight Control System (FCS) was converging on a detail design during the Phase II time period and concerns surfaced regarding the sensitivity of the FCS to nonlinear aerodynamics. In order to investigate potential nonlinearities, Johnson Space Center (JSC) management requested Langley Research Center (LaRC) to supplement the contractor's test program. These tests investigated the following areas: (1) non-linear aerodynamic characteristics of the basic vehicle and its control surfaces; (2) aerodynamic damping characteristics; (3) control surface interactions; and (4) high Mach/altitude simulations. In addition, the possibility of high altitude snap roll caused by asymmetric separation of the wing's leeside flow field was explored.

The final phase (Phase III) of the wind tunnel test program was initiated in early 1978 to verify the predicted aerodynamic characteristics of the final vehicle configuration prior to the first orbital flight (STS-1). The objectives of this phase were to (a) verify and/or update the aerodynamic characteristics of the final, "as built" configuration across the Mach range of 0.2 to 15, (b) test fine-cut (small increments) in Mach number, angle of attack, angle of sideslip, and control surface position along the nominal flight trajectory, and (c) minimize model-to-model and tunnel-to-tunnel discrepancies. The final, preflight Aerodynamic Design Data Book (ADDB) was primarily based on these verification tests (Table 2). The verification phase consisted of three parts: (1) initially planned verification tests; (2) anomaly resolution tests; and (3) supersonic/hypersonic lateral-directional nonlinearity tests.

Two high-fidelity wind tunnel models, of 2% and 5% scale, were designed and constructed based upon the March 1976 OV-102 configuration drawings to ensure accurate modeling of all aerodynamic surfaces and simulation of all relevant cavities and protuberances. Although some minor changes to the Thermal Protection System (TPS) thicknesses were made after March 1976, these changes were closely monitored to ensure that there were no aerodynamically significant differences between the wind tunnel models and the actual OV-102 flight vehicle.

Part 1 of the verification phase consisted of the wind tunnel tests required for verification as it was originally conceived. These tests covered the Mach range of 0.2 to 15 using the two high-fidelity models without planned duplication of test conditions with different combinations of models and facilities. Several additional tests and considerable analyses were required to actually complete the preflight verification process. In order to acquire the highest quality data possible within time and fiscal constraints, a test team was established for each test consisting of the prime contractor, JSC, and facility engineers, co-chaired by the JSC and the prime contractor lead engineers. This team followed the test from initiation through model design and construction, test plan development, conduct of tests, and analysis of results.

The design of the verification tests drew heavily on experience and the results of a series of wind tunnel tests conducted by LaRC. The LaRC tests utilized a 1.5% scale model (OV-101/140C configuration) with remotely controlled elevons. They were conducted to investigate transonic and low supersonic lateral-directional nonlinearities and showed the importance of obtaining wind tunnel data in small increments and of utilizing remotely controlled aerodynamic surfaces. Two of the major benefits of testing with remotely controlled surfaces are: (1) permits efficient acquisition of small increments of the primary variable of interest, i.e., the control surface position; and (2) permits the acquisition of more accurate data by "sweeping" the control surface position while other test variables are held constant.

Although Part 1 of the verification tests was largely successful, initial analysis of the data from these tests indicated additional wind tunnel tests were required to resolve the following test anomalies:

a. Transonic - resolve blockage and shock reflection effects
b. Supersonic - verify relatively large facility (AEDC) flow tare corrections

A quick-look analysis of the verification test addressing the transonic blockage/shock reflection and supersonic tare correction problems still did not provide any clear-cut solutions to the original problems. Therefore, in July 1978, the Technical Panel for Orbiter Aerodynamics was formed at the request of the JSC Center Director to address these problems. The objective of the Panel was to expedite the analysis of the Orbiter aerodynamic design data to produce a mature data base that would support the launch of the first manned orbital flight planned for March 1980. This Panel was comprised of working-level aerodynamicists representing expertise from ARC, DFRF, LaRC, JSC, AFFTC, and the prime contractor. The major functions of the Panel were:

a. Recommend and conduct wind tunnel tests.
b. Evaluate and recommend the most valid test data for use in establishing the ADDB preflight predictions.
c. Perform an independent, detailed analysis of critical areas.
d. Perform a through review of the proposed ADDB prior to publication and make recommendations for acceptance or change.
e. Obtain Panel consensus that the ADDB is the "best" representation of the Orbiter aerodynamics.

The results of a wind tunnel test conducted by LaRC to assess the OV-102 configuration showed that there were no significant aerodynamic differences between OV-101 and OV-102. As a result, the large number of wind tunnel tests LaRC had conducted using the 1.5% model (OV-101 configuration) were used in developing the final fairings for the preflight ADDB. The high fidelity OV-102 model data was still considered prime and weighed the heaviest of all the data. The LaRC tests contributed significantly to filling in gaps of the OV-102 data base and to establishing model-to-model and tunnel-to-tunnel repeatability. The product of the Panel was the official Space Shuttle Orbiter ADDB published in October 1978 (Reference 8) and revised in April 1979 (Reference 9).

Prior to the formation of the Technical Panel, the technique of reviewing the "correctness" of the ADDB published by the prime contractor was to conduct a formal review after publication. Unless major discrepancies were identified and agreed to, no changes were usually made as a result of the formal review. Because the Panel worked closely with the prime contractor, making recommendations and changes during the development of the ADDB, a much more detailed review and refinement than by previous means of review was made possible. Almost all of the changes recommended by the Panel were accepted and implemented with minimum schedule impact. A significant amount of work by individual members was published directly in the ADDB.

After the Panel's work was complete, a minor update to the April '79 ADDB was made and the official aerodynamic data base was frozen in May 1980 to conduct final Guidance, Navigation and Control (GN&C) verification for STS-1. This data, the official preflight Orbiter aerodynamic data base, was published as a NASA Contractor Report in November 1980, and was designated as the "STS-1 ADDB" (Reference 7)

In January 1980, while conducting an in-house research test on high angle of attack aerodynamics, LaRC found a large difference in directional stability at Mach 6 from that predicted by the STS-1 ADDB. This gave rise to some potential FCS concerns about performing a bank reversal in flight near Mach 6. An investigation of this potential problem led to Part 3 of the verification test phase: Supersonic/hypersonic lateral-directional nonlinearity tests.

It turned out that the lateral-directional characteristics are highly nonlinear with sideslip angle at certain angles of attack. Further, this phenomena is not limited to Mach 6, but occurs over a Mach range of 2 to 8, at various angles of attack. Also, nonlinearities of the sideslip derivatives with Mach and speedbrake position were identified that had not been observed previously. The basic problem was that the sideslip derivatives are linear only over a range of 0.5 degrees of sideslip in some cases. The smallest increment tested previously was 1 degree and most data was at 2 degrees. The cause of these nonlinearities is thought to be a complex vortex interaction with the vertical tail/speedbrake.

Discovery of a problem of this magnitude so late in the Shuttle program development (projected launch date of STS-1 was just over 1 year from discovery of the problem) presented a schedule problem of how to acquire the necessary wind tunnel data, analyze the results, and put the data fairings in a format that was acceptable for input to the simulators so that a safety assessment could be performed prior to STS-1.

In order to resolve the aerodynamic/FCS anomaly in time to support STS-1, a team was formed consisting of JSC, the prime contractor, LaRC, and wind tunnel facility engineers. This included aerodynamicists, flight control engineers, and simulation engineers at JSC. As a result of this team's actions, a detailed analysis of the test data was performed on-site during each wind tunnel test such that by the end of the year, final fairings were complete and the data had been converted into a form ready for the flight simulators. The data was then evaluated on an engineering simulator at JSC. The results showed that the large nonlinearities with Beta could cause loss of control during a bank reversal when combined with certain FCS uncertainties such as winds and angle of sideslip errors. As a result, the trajectory of the first flight (STS-1) was changed to avoid a bank reversal near Mach 6.

These new wind tunnel data were then used to produce a major update in the STS-1 ADDB, published in April 1982 as the Pre-Operational ADDB. The Pre-Operational ADDB, although published after STS-1, contained no flight data (except for limited ALT results) and represents the true best estimate of preflight aerodynamics for the Space Shuttle Orbiter.

Simply collecting the wind tunnel data base was a major undertaking. The fruits of this undertaking would have been meaningless unless the results of those tests could be presented to the aerodynamic analysts in a digestible form. The Space Shuttle Program management turned to the computer to facilitate this analysis. Chrysler Corporation's Space Division devised and operated a system of computer programs called "DATAMAN" (Reference 11) to document and present test results to the aerodynamic analysts in a variety of plotted forms. The analyst could have at his disposal the data in the desired form allowing an efficient analysis to be performed. Chrysler received data tapes from the various facilities, transformed the various tapes to a common format, and used the computer program system to correlate, document, and produce data upon request to the aerodynamic analysts.

WIND TUNNEL DATA BASE ADJUSTMENTS

The traditional freestream Reynolds number was selected for the flowfield scaling parameter below Mach 15, while a viscous interaction parameter was used at higher Mach numbers. No adjustment was applied to the wind tunnel data to account for the real gas effect, which could not be adequately simulated. At the low Mach numbers, adjustments were applied to friction drag for Reynolds number and profile drag for the roughness of the thermal protection system tiles and minor protuberances which could not be simulated on the wind tunnel models.

In general, no attempt was made to obtain a wind tunnel measurement of the effects of structural deformation on the longitudinal aerodynamics through testing of conventional aeroelastic or deformed models. Since at higher q's these effects can be significant, some adjustment to the wind tunnel data must be made to provide adequate estimates of the flight aerodynamics. The approach used in the Shuttle Program to estimate the aeroelastic effects is thought to be unique.

First, a sensitivity analysis was performed with the aid of a structural/aerodynamic analysis computer program (References 12,13). This program was used to systematically stiffen various portions of the vehicle structure to analytically evaluate the effect of the stiffness changes on the aerodynamics. The results indicated that the major longitudinal aeroelastic effects were produced by deformation of the wing back-up structure where the elevon actuators are attached, resulting in a change of the elevon position not measured by the actuator mounted, control surface position sensors. The effect was modeled by combining a rotary spring constant, as determined from vehicle loading tests, with wind tunnel derived aerodynamic hinge moment characteristics to determine a correction (usually less than 1 degree) to the "rigid" elevon deflection angle. The "elastic" elevon angle is used to look-up the rigid aerodynamic characteristics in determining the vehicle longitudinal aeroelastic characteristics.

The computer program indicated the major aerodynamic effect in the directional axis was the deformation of the vertical tail and the aft fuselage. Of particular concern was the predicted 40% reduction in rudder power due to twisting of the vertical tail around its elastic axis. It was felt that this large effect could not be left to theoretical prediction techniques alone. After establishing the structural characteristics of the vertical tail and aft fuselage from the structural test article, an aeroelastically scaled vertical tail was constructed which simulated the root spring constant and tail stiffness distribution. It was then tested on a standard force model across the high q Mach range. The results from these wind tunnel tests were then analytically adjusted to "free" the Orbiter from the sting mounting constraint necessary in the wind tunnel. The adjusted wind tunnel data were compared with the computer predictions for a q_{∞} of 300psf (14,364 N/m2). The correction was significant. A detailed development of this unique approach for evaluating aeroelastic effects is presented in reference 14.

AERODYNAMIC UNCERTAINITES

Two program management decisions, to freeze the Orbiter systems configuration at ATP and to fly a manned Orbital flight on the initial mission, had a significant influence on the approach selected for the aerodynamic design and verification of the Orbiter, particularly with regard to aerodynamic uncertainties. These decisions led to the development of two types of aerodynamic uncertainties: (1) Wind tunnel uncertainties, and (2) Wind tunnel-to-flight uncertainties.

(1) Wind Tunnel Uncertainties

The first decision baselined both the FCS and the aerodynamic configuration (as well as other systems and subsystems) in August 1972 at the ATP milestone. Thereafter, the only aerodynamic and FCS changes that were permitted were those which were required to fix critical system design problems. As evaluations of the baseline systems were conducted, it became clear that some significant changes to both the FCS and the aerodynamic design would be required. This resulted in the final FCS and the aerodynamic design being conducted in parallel. This presented a problem of how to design a FCS "tuned" to the vehicle aerodynamics while the baseline aerodynamic data base was still evolving. Somehow, the FCS had to be designed to be insensitive to "reasonable" changes in the aerodynamic characteristics. This led to the requirement for a set of aerodynamic "design-to" uncertainties that would be used along with the baseline nominal aerodynamics in FCS design. These "design-to" uncertainties, designated "tolerances", were defined as the minimum error that is expected in the preflight aerodynamic predictions.

With the wind tunnel data base as the foundation for the preflight predictions, it was assumed that the minimum error that could be expected would be the ability to reproduce experimental results between various wind tunnel tests. Therefore, repeat tests were performed using various wind tunnel facilities, different models, and on occasion, different test organizations. Although the individual causes for any differences were not specifically identified, it is felt the total differences are representative of what may be expected for wind tunnel test repeatability.

As an illustration of the mechanics of this procedure, consider pitching moment coefficient. The 0.05 scale model (model 39-O) was tested in all three legs of the ARC UPWT facility (11x11-foot, 9x7-foot, 8x7-foot), and in the LaRC 16-foot transonic facility. Similarly, a 0.015 scale model (model 44-O) was tested by LaRC in three facilities: 1) the Ling-Temco-Vought High Speed Wind Tunnel (LTV 4x4 foot); 2) the LaRC 8-foot tunnel; and 3) the ARC 11x11 foot facility. In addition, the 0.02 scale model (model 105-O) was tested in the LaRC 16T tunnel. With all these potential sources of differences, a peak-to-peak repeatability in pitching moment coefficient (Cm) of approximately 0.006 was observed. This repeatability represents the combined error sources of the following: 1) the same model in several tunnels (tunnel-to-tunnel repeatability); 2) different models in the same tunnel (model-to-model repeatability); and 3) different test organizations (testing technique differences).

Based on this correlation, the differences between the wind tunnel results and the ADDB at various angles of attack were correlated with Mach number. Tolerances (wind tunnel uncertainties) were obtained by fairing a curve through these data points using engineering judgment. The nominal flight angle of attack was given a high weighting in the fairing process. A similar process was used to develop tolerances for lift and drag coefficients, the sideslip derivatives, aileron derivatives, and rudder derivatives. Reference 15 provides a more detailed report on the development of the Orbiter wind tunnel uncertainties.

(2) Wind Tunnel-to-Flight Uncertainties

The second program management decision, to fly a manned vehicle on the initial orbital flight test of the Space Shuttle, raised the question of how to maximize mission safety without the benefit of conducting a graduated flight test program as is traditionally done in most aircraft development programs. This decision led to the requirement to provide a reasonable estimate of the maximum possible errors in the preflight aerodynamic predictions that might occur on the first Space Shuttle flight. These aerodynamic uncertainties were designated "variations".

In order to certify that the Space Shuttle Orbiter system was ready for the first flight, a multitude of flight simulations were conducted using the aerodynamic variations, along with other system uncertainties, to "stress" test the FCS. Based on the results of these simulations, a center of gravity, elevon schedule, and the FCS gains were selected for STS-1 which maximized the stability and control margins, thereby maximizing mission safety.

However, these "worst case" uncertainties must not be so conservative as to completely invalidate the FCS design. Since the preflight predictions were primarily based on wind tunnel tests, variations would represent the possible errors between wind tunnel and flight aerodynamics. It was felt that the most reasonable approach for the development of variations would be to analyze the wind tunnel to flight test differences of previous aircraft programs. Unfortunately, the verification of preflight predicted aerodynamics was not a major objective of most of the earlier flight test programs. This severely limited the amount of data available for conducting flight test to wind tunnel comparisons. The flight data base was further limited by restricting the comparison to those vehicles which were geometrically similar to the Orbiter, as illustrated in Table 3.

Variations were established by fairing the differences between the flight and predicted aerodynamics as a function of Mach number. Because the selections of the configurations and the fairing process are very subjective in nature, a team of aerodynamics from DFRF, JSC, LaRC, AFFTC, and the prime contractor was formed to conduct the analysis and reach a consensus on variations.

The team's flight-to-predicted pitching moment correlation and their recommended variation fairings are presented as a function of Mach number in figure 6. As can be seen from this figure, the flight data is limited to below Mach 3. In Mach regimes where flight data was unavailable and the ideal gas assumption was justified, variations were obtained by multiplying the wind tunnel-derived tolerances by a safety factor, usually 1.5. A similar process was used to develop variations for the other aerodynamic parameters. A more detailed development of variations is given in reference 16.

A detailed investigation of the effect of real gas effects (Reference 4) was conducted in 1974 using state of the art theoretical techniques. Geometric limitations of the computer codes at that time did not lend sufficient confidence to use these results in adjusting the ideal gas wind tunnel data. Instead, a conservative estimate of the real gas effect was added to the pitching moment tolerances to estimate variation in the high altitude flight region. The predicted real gas effects gave a more nose up moment to the basic vehicle pitching moment tolerances, resulting in unsymmetrical variations. A procedure for statistically combining these uncertainties is delineated in reference 17.

AERODYNAMIC DESIGN DATA BOOK DEVELOPMENT

The challenge of the management of the aerodynamic data base fell into two areas: 1) creating and controlling a common data base for the multitude of users within NASA and the contractors across the nation; and 2) verifying that data base. Late in Phase B, a common Orbiter aerodynamic configuration was selected as a focus for all in-house and contractor efforts. The aerodynamics for this configuration were compiled into an ADDB to be used for all computer simulations. The use of a central controlled ADDB continued into the Phase C & D time period. (An ADDB of estimated aerodynamic characteristics for the ATP configuration was submitted with the Rockwell proposal.) As the configuration evolved, a data book consisting of the estimated aerodynamic characteristics for each configuration was produced and subsequently verified experimentally. To further standardize the data base, the process of centrally digitizing and producing computer tapes of each data book was initiated early in Phase C & D. Thus, the aerodynamic data base evolved into an ADDB and its corresponding digital computer tape, under configuration control of one of the major program panels. ADDB verification was accomplished by a detailed technical review by NASA experts prior to each programmatic milestone until approximately 1 year before the first manned orbital flight. (The procedure used in this time frame was addressed previously in Phase III of the Wind Tunnel Test portion of this paper.)

The entry aerodynamic data base was published in Rockwell International reports throughout the evolution of the Space Shuttle development. The OV-102 Aerodynamic Design Data Book (ADDB) (SD72-SH-0600-I-J) represented the results of the wind tunnel testing prior to 1978. The Approach and Landing Tests (ALT) required the release of the ALT ADDB (SD72-SH-0600-IV-J), which contained the tailcone-on data base and the tailcone-off differences between OV-101 and OV-102 to be used with the Mach 0.25 to 0.8 data from the OV-102 ADDB. Just prior to STS-1, the STS-1 ADDB (SD72-SH-0600-1M) (Reference 8) was released and contained the results of the high fidelity model verification testing done after 1978. That data base was the first to reflect the input of the Aero Expert Team.

CONCLUDING REMARKS

This paper has briefly reviewed the Space Shuttle configuration development and the methodology of the development of the preflight predicted aerodynamic data base. The aerodynamic data base was ultimately derived from the most extensive, complicated, aerodynamic development program ever accomplished, namely, the approximately 27,000 hour Shuttle wind tunnel test program. The inability of ground test facilities to accurately predict the real gas effects was largely overcome, with moderate success, through the use of analytical methods.

Of particular importance was the establishment of the rationale for the development of uncertainties on the aerodynamic data base coefficients. Those uncertainties defined the expected flight to predicted differences and facilitated the parallel development of the vehicle flight control system. This approach was driven by the program management decision to fly a manned vehicle on the initial orbital flight test of the Space Shuttle and solved the question of how to maximize mission safety without the benefit of conducting a traditional graduated flight test program.

REFERENCES

1. Lees, L. and Probstein, R. F.: "Hypersonic Viscous Flow Over A Flat Plate," Rept. No. 195, Dept. Aero. Eng., Princeton University, Princeton, N. J., 1952.
2. Whitfield, Jack D. and Griffith, B. J.: "Hypersonic Viscous Drag Effects on Blunt Slender Cones," AIAA Journal, Vol. 2, No. 10, October 1964, pp 1714-1722.
3. Bertram, Mitchell H.: "Hypersonic Laminar Viscous Interaction Effects on the Aerodynamics of Two-Dimensional Wedge and Triangular Planform Wings," NASA TN-D3523, August 1966.
4. Woods, W. C.; Arrington, J. P.; and Hamilton II, H. H.: "A Review of Pre-flight Estimates of Real-Gas Effects on Space Shuttle Aerodynamic Characteristics," NASA CP-2283, Part 1, March 1983, pp 309-346.
5. Rausch, J. R., General Dynamics Convair Division, "Space Shuttle Orbiter Rear Mounted Reaction Control Systems Jet Interaction Study," May 1977, Report No. CASD-NSC-77-003.
6. Hooks, I.; Homan, D.; Romere, P. O.: "Aerodynamic Challenges of ALT," Space Shuttle Technical Conference, NASA CP-2342, Part 1, pp 295-312.
7. Rockwell International Space Division: Aerodynamic Design Data Book, Orbiter Vehicle, STS-1, Final Report, NASA CR-160903, November 1980.
8. Rockwell International Space Division: Aerodynamic Design Data Book, Vol. 1, Orbiter Vehicle, SD72-SH-0060-1M, October 1978.
9. Rockwell International Space Division: Aerodynamic Design Data Book, Vol. 1, Orbiter Vehicle, SD72-SH-0060-1L-2, April 1979.
10. Rockwell International Space Division: Aerodynamic Design Data Book, Vol. 1, Orbiter Vehicle, SD72-SH-0060-1L-7, April 1982.
11. Kemp, N. D.: "Compiling the Space Shuttle Wind Tunnel Data Base: An Exercise in Technical and Managerial Innovations," NASA CP-2283, Part 2, March 1983, pp 1213-1254.
12. "Aerodynamic Preliminary Analysis System, Part I - Theory," NASA CR-145283, April 1978.
13. "Aerodynamic Preliminary Analysis System, Part II - User's Manual and Program Description," NASA CR-145300, April 1978.

14. Rockwell International Space Division: Aerodynamic Design Substantiation Report, Volume 1, Orbiter Vehicle, SD74-SH-0206-1K, February 1978.
15. Young, James C. and Underwood, Jimmy M.: "The Development of Aerodynamic Uncertainties for the Space Shuttle Orbiter," AIAA Paper 82-0563, March 1982.
16. Weil, Joseph and Powers, Bruce G.: "Correlation of Predicted and Flight Derived Stability and Control Derivatives - With Particular Application to Tailless Delta Wing Configurations," NASA TM-81361, July 1981.
17. Gamble, J. D. and Young, J. C.: "The Development and Application of Aerodynamic Uncertainties in the Design of the Entry Trajectory and Flight Systems of the Space Shuttle Orbiter," AIAA 9th Atmospheric Flight Mechanics Conference, AIAA-82-1335, August 1982.

Table 1 - Orbiter Design Ground Rules

PARAMETER	VALUE
ANGLE OF ATTACK	
Hypersonic	15° to 40°
Supersonic	0° to 25°
Transonic	0° to 15°
Subsonic	-5° to 20°
CENTER OF GRAVITY	
Maximum travel for payload	2% Body Length
Design capability	0.65 L_B - 0.675 L_B
LANDING PERFORMANCE	
Payload	32,000 pounds
Landing weight (with payload)	187,900 pounds
Minimum design touchdown speed, V_D	171 knots
LONGITUDINAL STABILITY	
Minimum hypersonic static margin	Positive
Minimum subsonic static margin (aft center of gravity)	-2% L_B

Table 2 - Shuttle Wind Tunnel Utilization Summary

Test Identification	Facility	Model Scale
Transonic		
OA145A	ARC 11x11 ft	0.05
OA270A	LaRC 16T	0.05
OA270B	LaRC 16T	0.02
LA70	Calspan 8 ft	0.015
LA76	LTV 4x4 ft HSWT	0.015
LA77	ARC 11x11 ft	0.015
LA111	LaRC 8 ft TWT	0.015
LA115	LaRC 8 ft TWT	0.015
Supersonic		
OA145B	ARC 9x7 ft	0.05
OA145C	ARC 8x7 ft	0.05
OA208	AEDC "B"	0.02
OA209	AEDC "A"	0.02
LA63A	LaRC UPWT-1	0.015
LA63B	LaRC UPWT-2	0.015
LA75	LaRC UPWT-2	0.015
LA76	LTV 4x4 ft HSWT	0.015
LA101	LaRC UPWT-1	0.015
LA110	LaRC UPWT-1	0.015
LA114	LaRC UPWT-2	0.02
LA125	LaRC UPWT-2	0.02
LA131	LaRC UPWT-2	0.02
LA144	LTV 4x4 ft HSWT	0.02
OA257	LaRC 20 in.	0.01
OA258	AEDC "B"	0.02
OA259	AEDC "B"	0.01
Hypersonic		
OA113	Calspan HST (48 in.)	0.01
OA171	NSWC Tunnel 9	0.02

Table 3 - Orbiter Correlation Applicability (Reference 16)

Aircraft *	Geometric Factors					Remarks
	Delta Wing Planform	Wing Flap Long. Control	Wing Elevon Lat. Control	Single Vertical Tail	Large Fus.	
XB-70	√	√	√			Good pred. base, M range canard, limited range
YF-12	√	√	√			Good M range, limited α range
X-15				√	√	Wide α range
$\text{TACT}_{\Delta = 58^\circ}$	√			√	√	Only limited data currently available
HP115	√	√	√	√		Low speed data only
B-58	√	√	√	√		Good predictive base, M range
YF-16 F-8SCW				√		Source of rudder control data

* See reference 16 for aircraft identification.

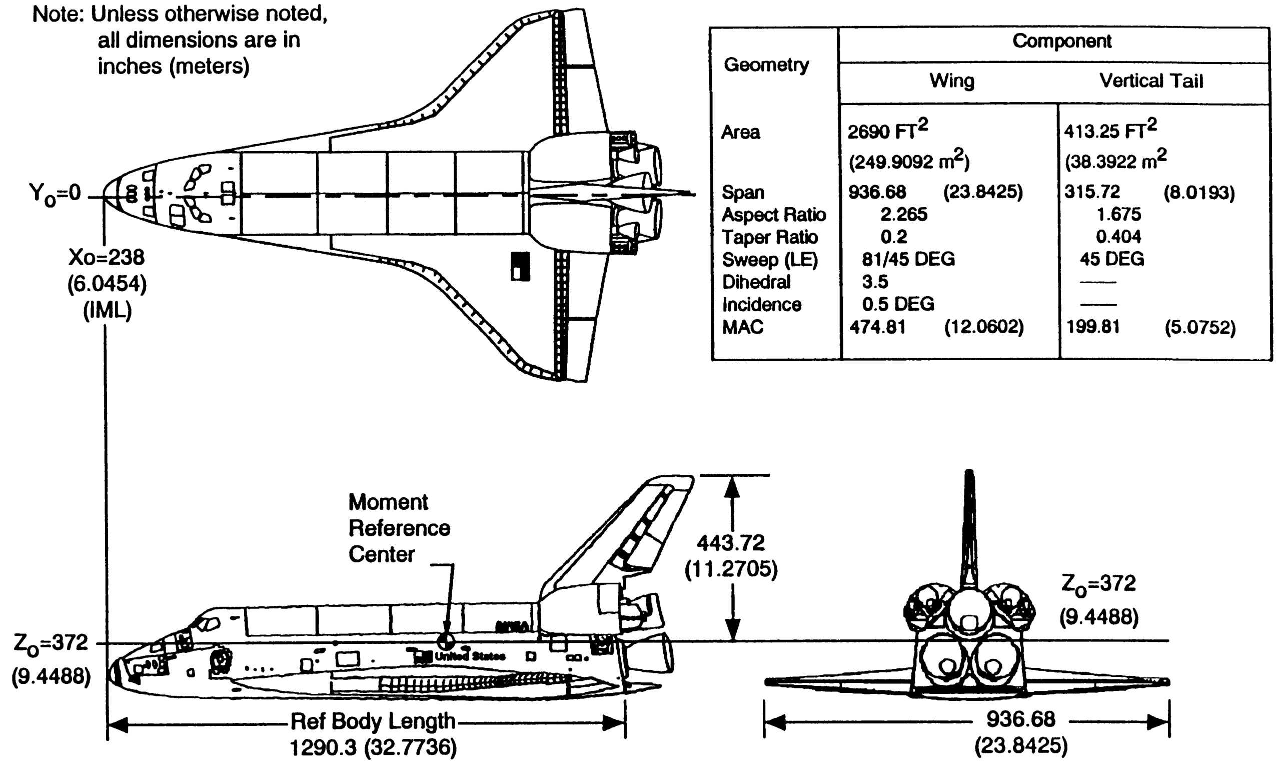

Geometry	Component	
	Wing	Vertical Tail
Area	2690 FT^2 (249.9092 m^2)	413.25 FT^2 (38.3922 m^2
Span	936.68 (23.8425)	315.72 (8.0193)
Aspect Ratio	2.265	1.675
Taper Ratio	0.2	0.404
Sweep (LE)	81/45 DEG	45 DEG
Dihedral	3.5	—
Incidence	0.5 DEG	—
MAC	474.81 (12.0602)	199.81 (5.0752)

Figure 1. Space Shuttle Orbiter configuration.

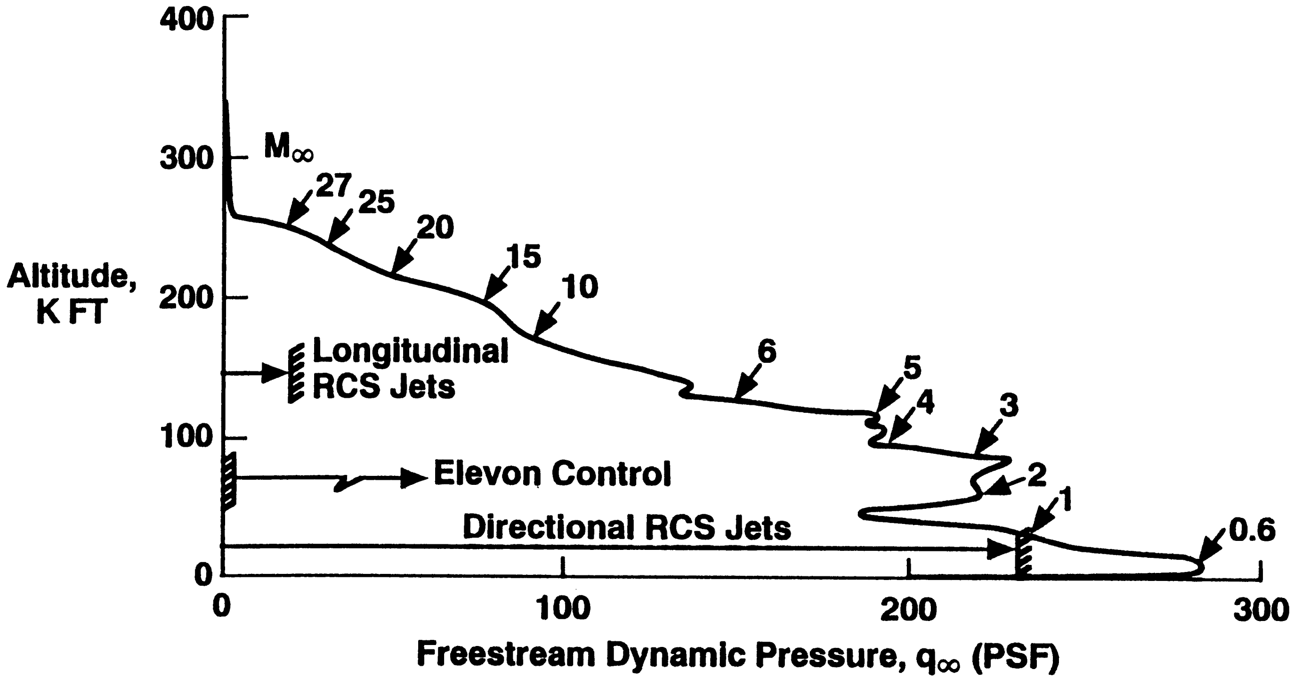

a) Nominal entry characteristics.

Figure 2. Typical Orbiter entry trajectory characteristics.

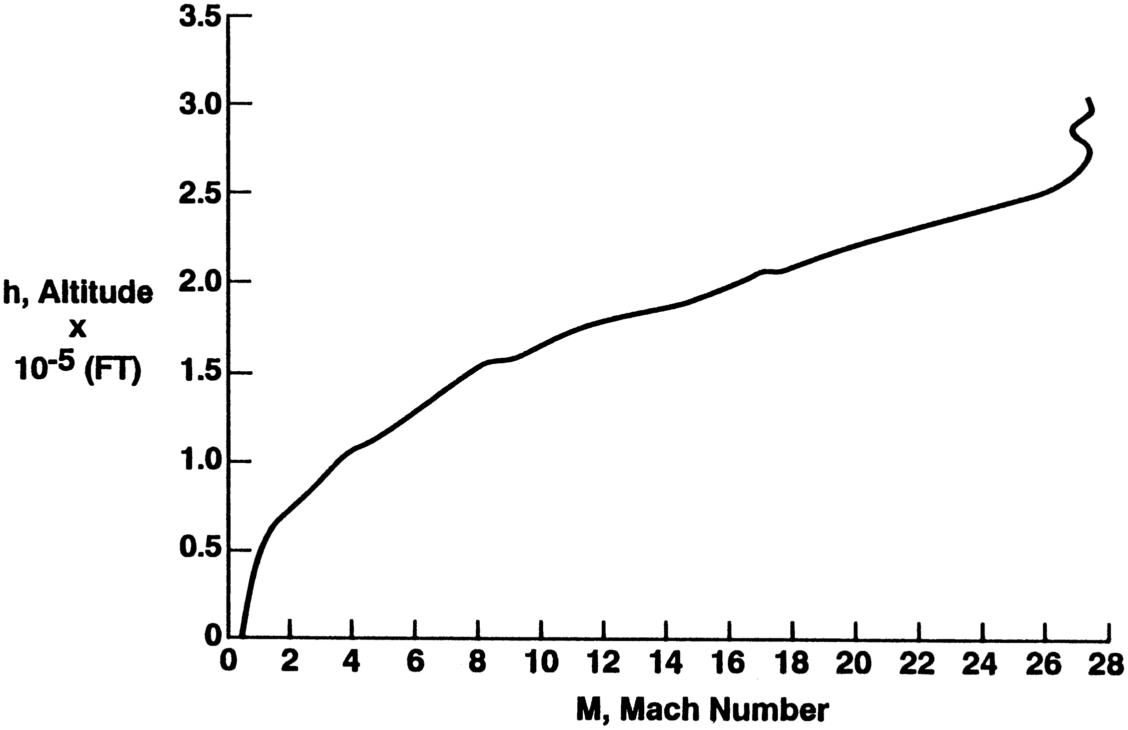

b) Altitude profile.

Figure 2. Continued.

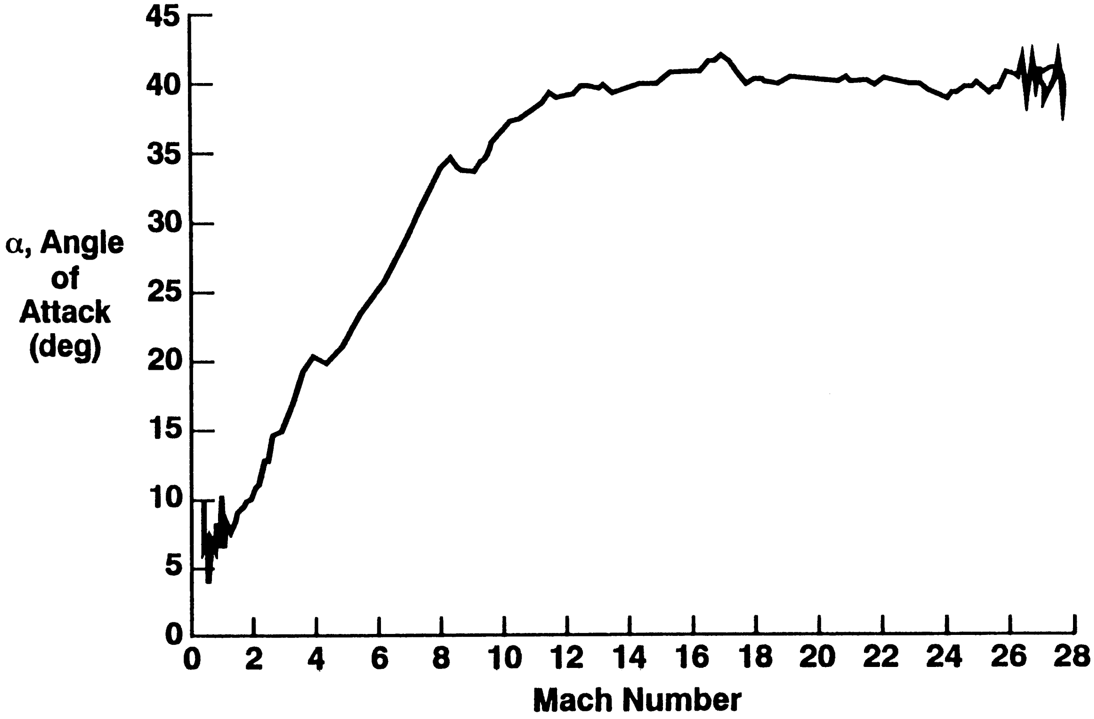

c) Angle of attack profile.

Figure 2. Continued.

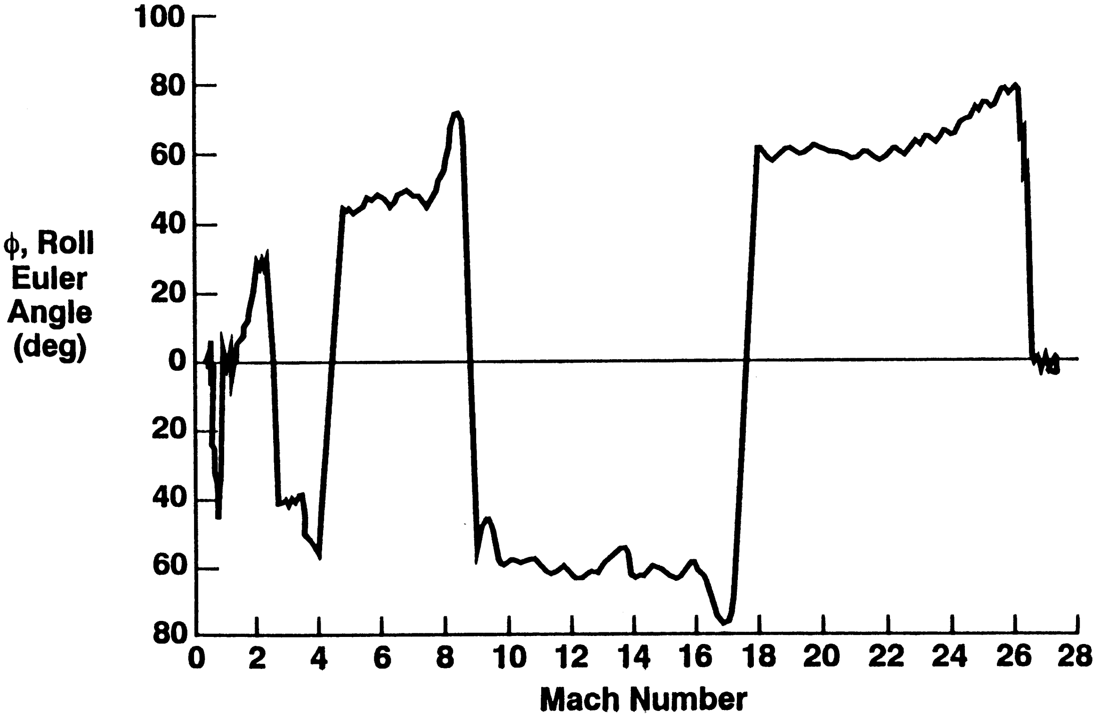

d) Roll angle profile.

Figure 2. Continued.

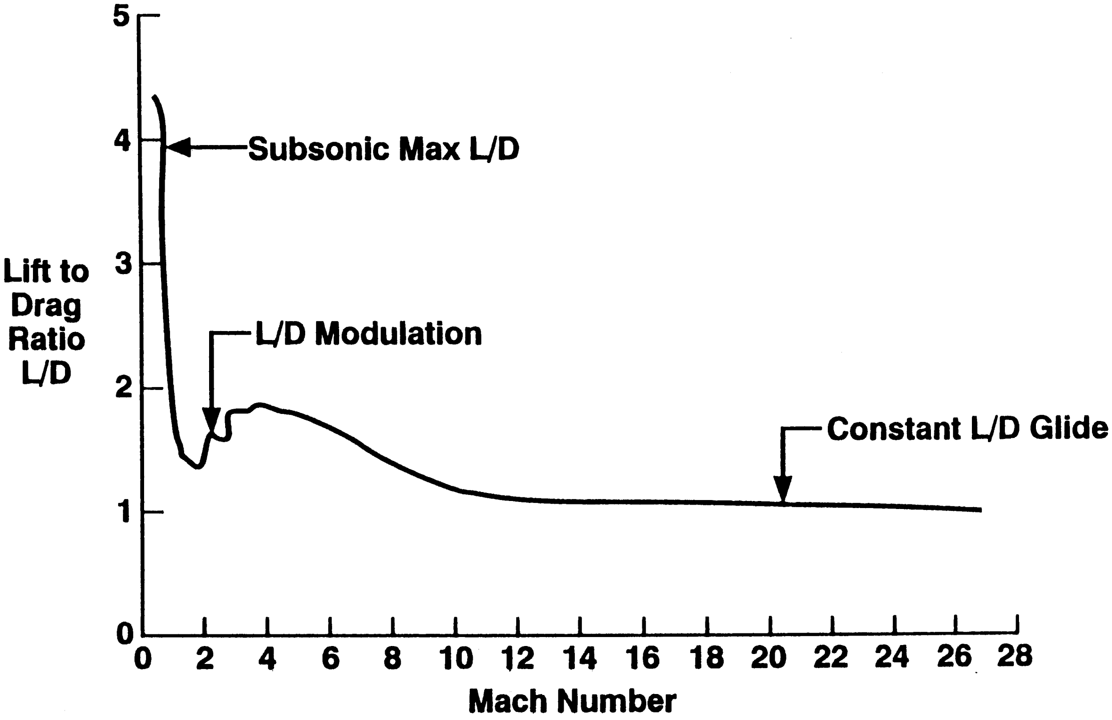

e) Lift to drag ratio profile.

Figure 2. Concluded.

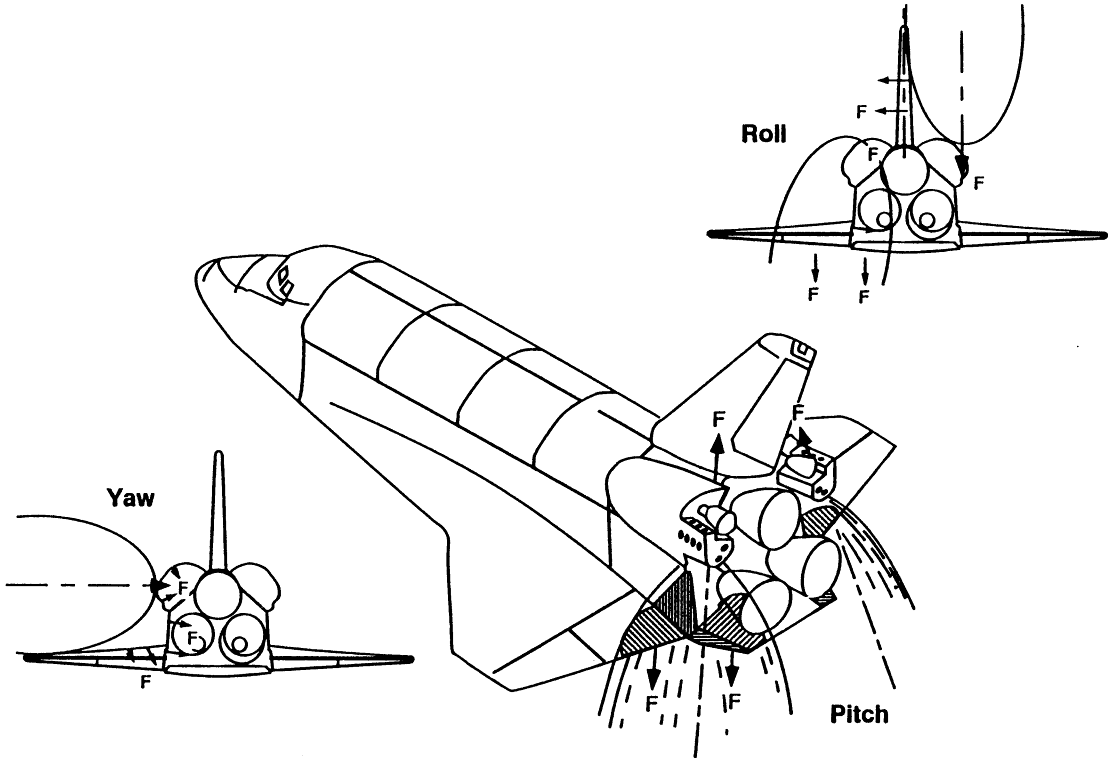

Figure 3. Aft-mounted reaction control system.

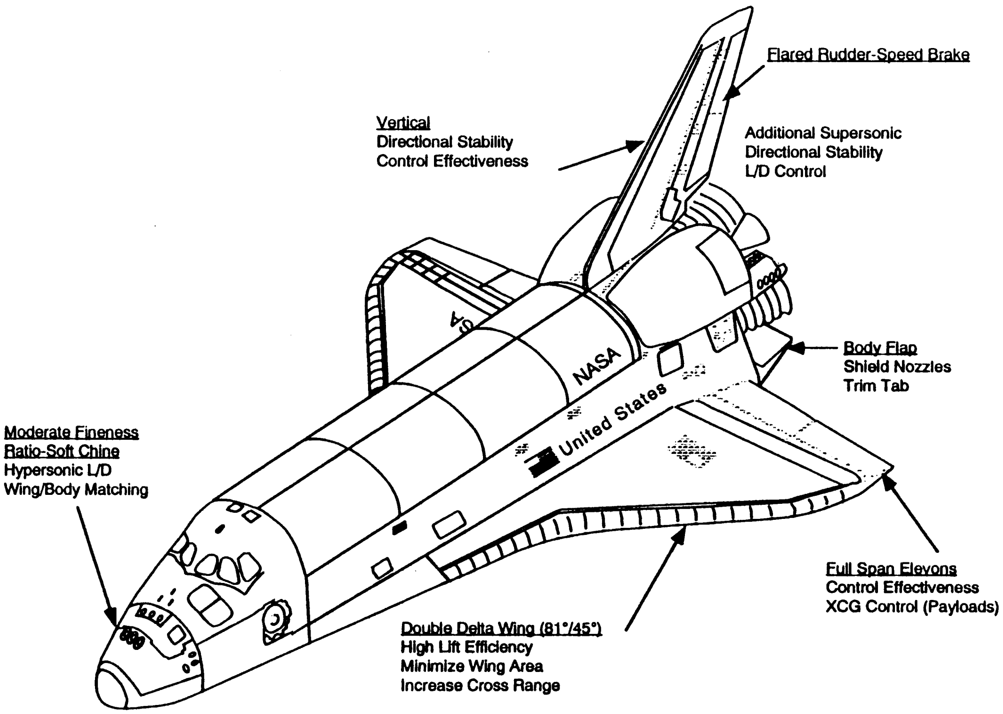

Figure 4. Orbiter vehicle functional characteristics.

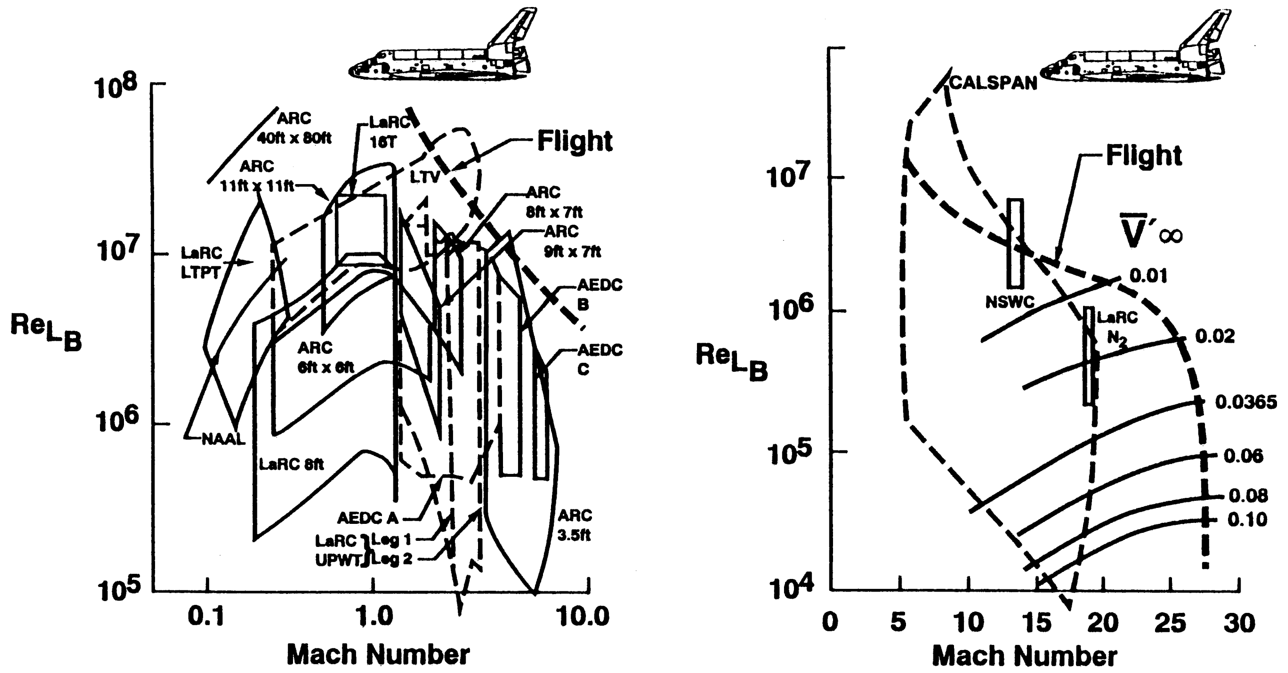

Figure 5. Comparison between flight RE_{L_B} and $V'\infty$ and the simulation capability of selected wind tunnel test facilities.

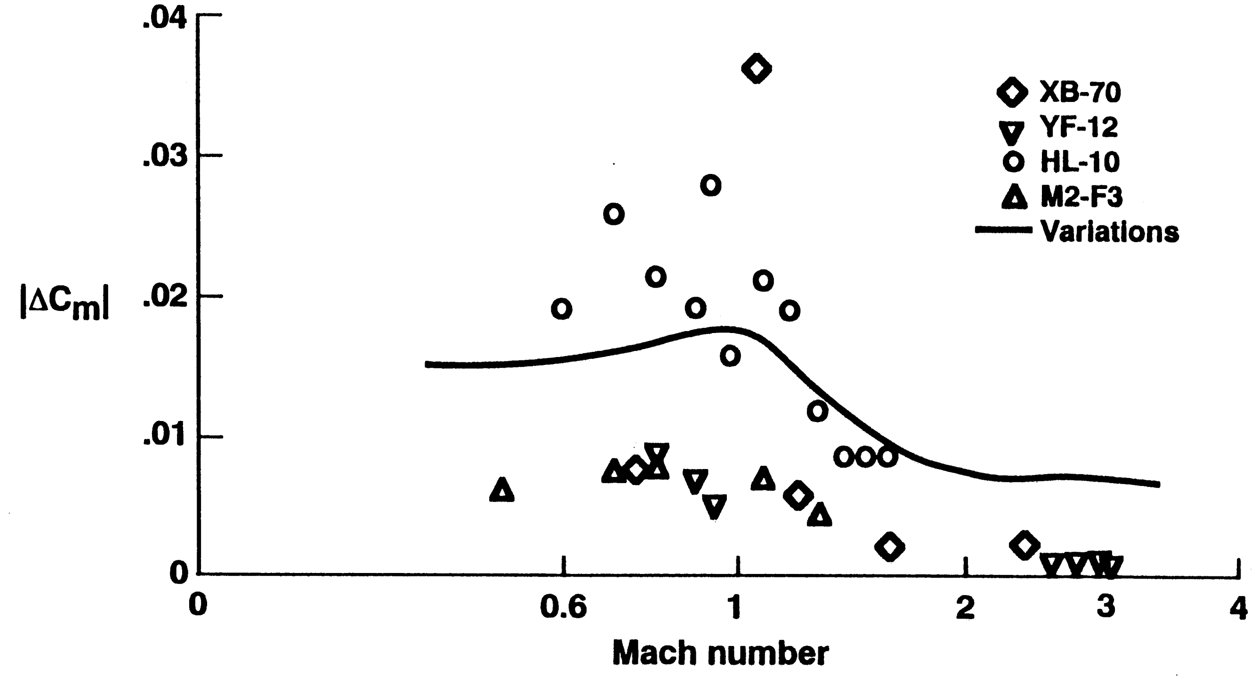

Figure 6. Correlation of flight and predicted pitching moment.

SPACE SHUTTLE ENTRY AERODYNAMICS FLIGHT TEST PROGRAM

Mary F. Allen
Lockheed Engineering & Sciences Company
Houston, Texas

Paul O. Romere
NASA Johnson Space Center
Houston, Texas

ABSTRACT

The Space Shuttle Orbiter Flight Test Program required the aerodynamicist to take a different approach in the determination of flight characteristics. Conventionally, a flight test program consists of slowly and cautiously approaching more severe test conditions. This was not possible with the Orbiter, which enters the atmosphere at about Mach 30 and then decelerates through the Mach range as an unpowered glide vehicle. A key part of this program has been the instrumentation of the vehicle, in particular, the ACIP (Aerodynamic Coefficient Identification Package) portion of the Orbiter Experiment (OEX) program. The high resolution and quality of this data has been instrumental in the progression of the entry flight test program.

NOMENCLATURE

ACIP =Aerodynamic Coefficient Identification Package
ADE =Aerodynamic data extraction
ASI =Aero Stick Input
BR =Bank Reversal
cg =center-of-gravity
CR =Cramer Rao
DFRF =Dryden Flight Research Facility
FAD =Flight assessment delta
FTR =Flight Test Requirement
M =Mach number
MMLE3 =Modified Maximum Likelihood Estimator program, Version 3
OADB =Operational Aerodynamic Data Book (1991)
OI =Orbiter Instrumentation
pEst =parameter Estimator program, Version 2.1
PTI =Programmed Test Input
PREOP =PreOperational Aerodynamic Design Data Book (April 1982)
q =dynamic pressure, psf
RCS =Reaction Control System
STS =Space Transportation System
xcg =x-axis center-of-gravity location
ycg =y-axis center-of-gravity location
Yj =aft side firing jets
α =Angle of attack, degrees
C_{l_β} =Derivative of rolling moment due to sideslip angle, per degree
$C_{l_{\delta a}}$ =Derivative of rolling moment due to aileron, per degree
$C_{l_{\delta r}}$ =Derivative of rolling moment due ro rudder, per degree
C_{n_β} =Derivative of yawing moment due to sideslip angle, per degree
$C_{n_{\delta a}}$ =Derivative of yawing moment due to aileron, per degree
$C_{n_{\delta r}}$ =Derivative of yawing moment due ro rudder, per degree
$C_{m_{\delta e}}$ =Derivative of pitching moment due to elevon, per degree
$C_{m_{\delta BF}}$ =Derivative of pitching moment due to body flap, per degree

δ_a =aileron deflection angle, deg
δ_{BF} =body flap deflection angle, deg
δ_e =elevon deflection angle, deg
δ_r =rudder deflection angle, deg
δ_{SB} =speed brake deflection angle, deg

INTRODUCTION

The space shuttle program was an eagerly anticipated challenge for the aerodynamics community. The shape of the vehicle and the dynamics of its entry gave flight to the imagination and enthusiasm of the space community. That the very concept of a reusable space plane was to become a reality brought a new excitement to the aero world. The shuttle vehicle, unpowered, in reality not much more than a glider, travelling at tremendous speed from orbit to a runway landing, gave the aero world an unparalleled opportunity to study the aerodynamic effects of the vehicle. Control of the vehicle, accomplished through the use of actuators and reaction control system jets, opened avenues of study that are still ongoing.

THE VEHICLE

The space shuttle vehicle was designed to be guided by a combination of control surfaces and RCS jets during entry. These allow the vehicle to be targeted to a runway landing. The orbiter control surface configuration is shown in figure 1. The thick double delta wings are configured with full span elevons comprised of two panels per side. Each of these panels is individually actuated. All four panels are deflected symmetrically as an elevator (δ_e) for pitch control. The left and right panels are deflected differentially as an aileron (δ_a) for roll control. The body flap, located on the back of the vehicle beneath the engine bells, was initially designed as a heat shield for the main engines but is now used as the primary trim device. The elevons are programmed to fly a specific schedule designed to provide the desired aileron effectiveness. The vertical tail consists of the fin and a split rudder. The rudder panels provide yaw control (δ_r) when deflected together and act as an energy modulating speed brake (δ_{SB}) when deflected separately. Deflection limits of these surfaces are shown in figure 2 along with a summary of the aero forces and moments affected by the surfaces. Figure 3 shows the RCS jet configuration[1]. The aft yaw (side firing) jets are active throughout most of the entry. They are not used below Mach=1. The aft pitch (up and down firing) jets are active only while $q \leq 40$ psf. This occurs at quite high altitudes. Roll couples, a combination of aft up and down jets on opposite sides firing simultaneously, are active only while $q \leq 4$ psf.

AERODYNAMICS

The aerodynamics of the space shuttle were initially investigated through one of the largest wind tunnel test programs ever undertaken. Over 25000 hours of wind tunnel tests[2] were executed prior to STS-1 in order to determine performance and stability and control characteristics. High fidelity wind tunnel models were constructed to accurately model aerodynamic surfaces and simulate aerodynamically relevant cavities and protuberances. The variety of tunnel facilities and models utilized helped to minimize the model-to-model and tunnel-to-tunnel differences and thus permitted more accurate preflight predictions. By the time the vehicle was ready for the first flight, aerodynamicists had derived an entry data book to cover those flight conditions which would be encountered during a nominal descent situation even though further tests would be necessary to validate the data book and resolve some unanswered questions. Today, this flight testing is ongoing.

FLIGHT TESTING

The Entry Flight Test program was set up and designed to allow analysts to explore the aerodynamic capabilities of the orbiter and ensure the safety of that vehicle during flight. Countless hours of simulation testing gave the aerodynamicists confidence in the preflight predicted data but still there was a need for real time, real world testing under actual flight conditions. The accomplishment of the program has required the use of Flight Test Requirements (FTRs)and Development Test Objectives (DTOs). While FTRs were used to resolve critical issues found prior to STS-1, a DTO is the current method by which the aerodynamics community can flight test selected regimes using controlled inputs at specified flight conditions.

The process of developing and submitting a DTO requires a lengthy lead time, sometimes as long as a year before it is approved, assigned to a flight (or flights) and actually flies. The process begins with the decision to flight test a selected regime or certain flight conditions by the Intercenter Aero Panel. This panel is composed of members of the NASA aerodynamics community and includes both civil service and contractor personnel from several space centers. This decision is based upon the evaluation of previous flight test results, programmatic requirements, and/or discussions with the flight control community regarding areas where a better understanding of the data book will be beneficial. Maneuvers are then designed and tested using the Shuttle Engineering Simulator at JSC.

A maneuver is a sequence of controlled inputs which are executed during a specified portion of the entry, usually identified by a Mach range. There are several types of maneuvers used. Programmed Test Inputs (PTIs) are the most common. These consist of elevon, aileron, rudder, and RCS pulses. Execution of a PTI is automated and implementation requires I-load changes. This requires scheduling several months prior to the flight. Figure 4 shows a sample PTI maneuver where a yaw jet pulse is followed by aileron, rudder, and elevon deflections. The yaw jet, aileron, and rudder pulses are evaluated lateral/directionally while the elevon pulse is analyzed longitudinally. A lateral analysis examines coefficients of side force, rolling moment, and yawing moment. Longitudinal analyses evaluate pitching moment, normal force, and axial force. Body flap pulses (figure 5) are also used frequently but are a manual maneuver. This means the control system is switched to a manual mode and the pilot executes the body flap pulse according to the specifications for duration and range identified in the DTO. This too necessitates a long lead time due to training requirements. Body flap maneuvers are also evaluated longitudinally. Two other maneuver types are Aero Stick Inputs (ASI) and a Push Over Pull Up (POPU), both of which are also manual. ASIs were used before complete implementation of the PTI software and POPUs (and PUPOs) were used on the early flights.

When the process of designing maneuvers has been completed, the actual DTO is written and submitted to the appropriate governing boards for evaluation and approval. Most entry DTOs are written with multiple parts which allow repetitive testing on several flights and with different vehicles. Because of the statistical nature of flight testing, this repetition is both necessary and desirable. Once approved, the DTO is assigned to a flight or flights which meet the criteria specified, for example, a requirement that the flights have an xcg of 1090.0 inches or less (a forward cg).

Prior to STS-1, placards in the flight envelope were identified where possible problems in the aerodynamics needed to be resolved by determination of the actual aerodynamic characteristics. These placards were established based on stability, control or performance problems at specific flight conditions assuming that the larger aero uncertainties (variations with wind tunnel to free flight worst case errors) occur at the design flight conditions. Eight Flight Test Requirements (FTRs) were designed to cover these selected flight conditions and resolve these unanswered questions. Each was designed to be flown on several flights. In order to minimize flight safety risks the first flight, STS-1, did not execute any specific maneuvers. However, with STS-2, the entry flight test program began in earnest.

Three of the placards concerned the vehicle center-of-gravity. The first four flights were constrained to a very narrow xcg range, only 6.5 inches. This meant that the xcg location had to be no more forward than 1094.7 inches and no more aft than 1101.2 inches. To achieve this, the orbiter must be balanced by the proper distribution of payload, forward and aft RCS fuel loading, and if necessary, ballast in the payload bay. This is a severe constraint in terms of payload weight restrictions and the excess weight which may be necessary as a ballast. As a result, expansion of the cg limits has been one of the primary goals of the Entry Flight Test Program.

Figure 6 summarizes the FTRs, and ranks them according to priority. With the stipulation that unforeseen circumstances might cause delays, the initial flight plan called for completion of the

FTRs within 11 flights. Despite the loss of the ACIP data on STS-2, the placards were removed on schedule. Figure 7 is a summary of the xcg expansion in both the forward and aft directions. Although not specified on the chart, the ycg limits were also extended as planned.

After the critical areas specified by the placards were resolved, additional areas remained where flight testing was desired. Heavier payloads increased the desire for a more forward xcg limit. More validation and verification of the predicted aerodynamic data was still necessary. Although the most pressing questions regarding key derivatives at specific flight conditions had been, to a certain extent, satisfactorily answered, there were still many regions where questions remained about the preflight data book predictions and where a reduction of their associated uncertainties was both desirable and necessary. A program of additional flight testing was set up, centering upon the reduction of uncertainties, particularly those of the aileron, rudder, sideslip, pitching moment, and RCS derivatives.

The two most recent DTOs have extended the range of flight experience by requiring the use of the forward and the alternate forward elevon schedules along with flights having a forward center of gravity. Simulator testing has shown that to move the xcg limit even more forward will require a more up elevon while still maintaining acceptable trim capabilities. The elevon schedules used for these DTOs are shown in figure 8. These schedules begin to ramp the elevon up from -3° at Mach 16. The forward schedule reaches a maximum -7° elevon between Machs 11 and 8.5. The alternate forward schedule achieves its maximum of -10° between Machs 12 and 8.5. These schedules then ramp back down to -2° at Mach 4. A sample of a schedule used for a flight with an aft xcg is also shown.

By widening the corridor of flight experience, the program benefits both from improved safety and a broadened flight envelope. Figures 9 and 10 show the PTI maneuvers flown during this program in a summary of the angle of attack and elevon ranges of flight experience. Each box represents a maneuver. The corners denote the minimum and maximum values for that parameter versus the Mach limits. To date, over 30 flights have flown maneuvers as part of the Entry Flight Test program, resulting in over 200 maneuvers. Gaps in the data represent areas where bank reversals occur. PTIs are preempted by bank reversals.

Continued flight testing has shown that the initial data book predictions were, on the whole, very good. While some parameters required adjustments, for the most part these changes were relatively small. One key parameter that required more significant changes was pitching moment. Flight testing showed a disparity between the predicted center of pressure and the actual flight center of pressure. After much analysis it was determined that real gas effects were acting upon the vehicle during flight but, since these could not be simulated in the wind tunnel tests, were not reflected in the predicted data. The addition of real gas derivatives and related changes to the equations used to calculate the predicted data solved this deficiency.

AERODYNAMIC DATA EXTRACTION

After a DTO has flown, the data recorded during the entry is analyzed to determine the aerodynamics that acted upon the vehicle during flight. The method decided upon for this analysis is a statistical approach using maximum likelihood estimation (figure 11). A controlled sequence of motion (in the form of a maneuver) is input into the shuttle control system. As the maneuver executes, noise and turbulence also have an impact on the system. Vehicle responses are recorded and input into the mathematical model of the vehicle. An estimated response and its associated error is computed. This error is fed through the maximum likelihood cost function, then the minimization algorithm. After an iterative solution is found (the error is reduced to within an acceptable boundary), the program is considered to have converged and the results are ready for further analysis. Two programs have been used for this purpose. The original version of the software, MMLE3 (Modified Maximum Likelihood Estimation program, version 3)[3] , was used successfully for several years. A more advanced program, pEst (parameter Estimation program, version 2.1)[4], is currently in use. Both programs are products of Ames-Dryden. MMLE3, an accepted industry standard for aircraft parameter estimation, is linear in nature and executes in a batch mode, and while it performs more than adequately, some problems are more complex and require more accurate and flexible nonlinear modelling. The program pEst is interactive and supports full nonlinear capability in the dynamic equations of motion yet has the option of using the linear equations.

Both programs required good, consistent flight data as input. The flight parameters determined to be necessary were, for a lateral/directional analysis, sideslip angle (b), yaw rate (r), roll rate (r), roll angle (f), and lateral acceleration (ay) and for a longitudinal analysis, angle of attack (a), pitch rate (q), pitch angle (q), normal acceleration (an), and axial acceleration (ax). Additionally, flight parameters such as control surface deflections (elevon (d_e), aileron (d_a), rudder, body flap, and speed brake), Mach, velocity, dynamic pressure,and RCS activity were also needed. The fidelity of the recording systems was tantamount to obtaining data of sufficient quality to allow good and accurate analysis of the flights. ACIP was decided upon as the preferred system for the recording of the linear and angular accelerations, rate gyros, and elevon and rudder control surfaces. The higher sample rate and larger word size of the ACIP recording system gave better resolution than the Operational Instrumentation (OI) data system. A comparison of two signals, one ACIP and one OI, is shown in figure 12. Note the flattened tops of the peaks on the OI signal and the flat spot just prior to the large motion. The smoother ACIP signal reflects the higher sample rate used to record it.

The evaluation of the DTO is currently performed by three different analysts: Ames-Dryden Flight Research Facility, Lockheed/Johnson Space Center, and Rockwell/Downey. A complete discussion of the intricacies of the data extraction process is discussed in the paper entitled "Stability and Control Aerodynamic Data Extraction" by Kenneth W. Iliff included in this publication.

After the analysis of a particular flight has been completed, further evaluation of the data is done by comparing the results with the predicted data from the current data book (OADB91[5]) and with the results from other flights. An example of this comparison is shown in figure 13. Each maneuver has been reduced to one data point plotted with the Cramer Rao (CR) bounds computed by the pEst (or MMLE3) program. A Cramer Rao is an indicator of the accuracy of the estimated parameters. For shuttle data extraction comparative purposes, the CRs are multiplied by a factor of 10. This factor was determined to be an acceptable representation of the orbiter flight uncertainties[4]. The best estimates are those with the smallest CRs. The solid line indicates the OADB91 predicted data with the dotted lines showing the uncertainty bounds associated with these predicted values. Trends are identified and regions where changes are suggested are isolated. Thus far, these changes have encompassed corrections and adjustments to the data book, reductions of uncertainties, and areas where knowledge has been expanded and increased.

To date, updates to the data book have been done several times. Most of these changes have been published in the form of Flight Assessment Deltas (FADs)[6]. These updates have expanded the center of gravity limit box from a preflight range of 6.5 inches (1094.7 - 1101.2) up to its current range of 32.3 inches (1076.7 - 1109.0) (figure 7). The current forward limit is equivalent to that of the unconstrained design limit of 65%[10]. This expansion was done in three steps: the first to 26 inches, the second to 30 inches and then finally to 32.3.

These three steps were accomplished through six groups of changes to the data book. These FADs were calculated as increments to the PreOperational Aerodynamic Data Book. The last update came with the publication of the Operational Aerodynamic Data Book which included all prior delta changes. Future changes are to be published as table replacements and not as deltas. The next update is scheduled for the fall of 1993.

CONCLUSIONS

The Entry Flight Test program has been very beneficial to the STS program. The verification and validation of the entry aerodynamic data book has improved flight safety, expanding the limits of the flight envelope to encompass a wider range of flight conditions and situations. The cg envelope has been greatly expanded and the next data book update should provide another significant forward expansion of this envelope. Future plans include exploring methods to verify ground effects derivatives in the data book. Among the possibilities are a combination of both wind tunnel and flight testing.

Although the OEX program has officially been terminated, the ACIP has been given continued life. Because of its importance to the Entry Flight Test program, the maintenance of the ACIP hardware has been continued by part of the Engineering Directorate (EK) at JSC. The reduction and processing of the ACIp flight data has been picked up by another part of that directorate, EG3. The DTO program has a current need for this data on STS-55, -58, and -62. A DTO to validate ground effects will add additional requirements. The ASRM program, although further down the road, has also expressed the need for ACIP data. In keeping with these plans, a recalibration of the package is scheduled during the next major mod for OV-102, after STS-67.

REFERENCES

1. "Pre-Operational Aerodynamic Design Data Book", SD-72-SH-0060, October 1978, Revision April 1982, Space Division, Rockwell International.

2. Whitnah, A. M., and Hillje, E. R., "Space Shuttle Wind Tunnel Test Program",AIAA 82-0562, presented as paper at AIAA 12th Aerodynamic Testing Conference at Williamsburg, Va., March 22-24, 1982.

3. Maine, R. E., and Iliff, K. W., "User's Manual for MMLE3, a General FORTRAN Program for Maximum Likelihood Parameter Estimation", NASA Technical Paper 1563, November 1980.

4. Murray, J. E. and Maine, R. E., "pEst Version 2.1 User's Manual", NASA Technical Memorandum 88280, September 1987.

5. "Operational Aerodynamic Data Book", STS85-0118, September 1985, Revision 3, Space Division, Rockwell International.

6. "Flight Assessment Package - Orbiter Aerodynamics", Flight Assessment Deltas (FADs) 4B, 9, 9B, 14, and 26, JSC Reports 18745, 19654, 20130, 20227, and 22078.

ORBITER CONTROL SURFACES

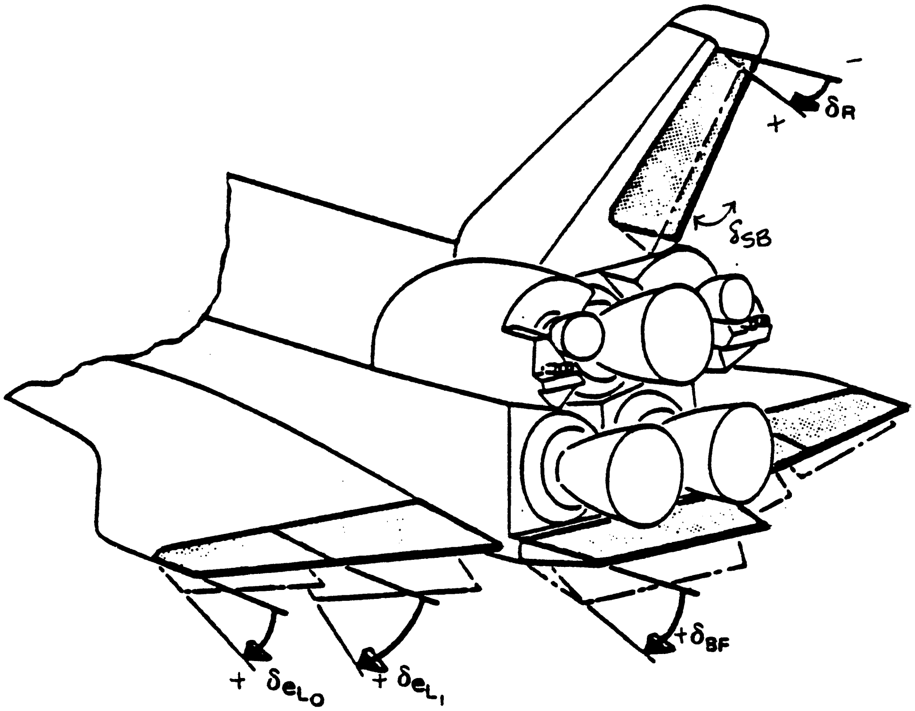

FIGURE 1

CONTROL SURFACE DEFECTION SUMMARY

Control Surface	Maximum Displacement (deg)	Rate (deg/sec)	Aero Forces and Moments
Elevator (δ_e)	-35 up, +20 down	20.	C_m
Aileron (δ_a)		20	C_l
Rudder (δ_r)	+ 22.8	10	C_Y, C_n
Speed Brake (δ_{SB})	0. to 87.2	5.	C_m
Body Flap (δ_{BF})	-11.7 up, +22.55 down	1.3	C_m

FIGURE 2

REACTION CONTROL SYSTEM CONFIGURATION

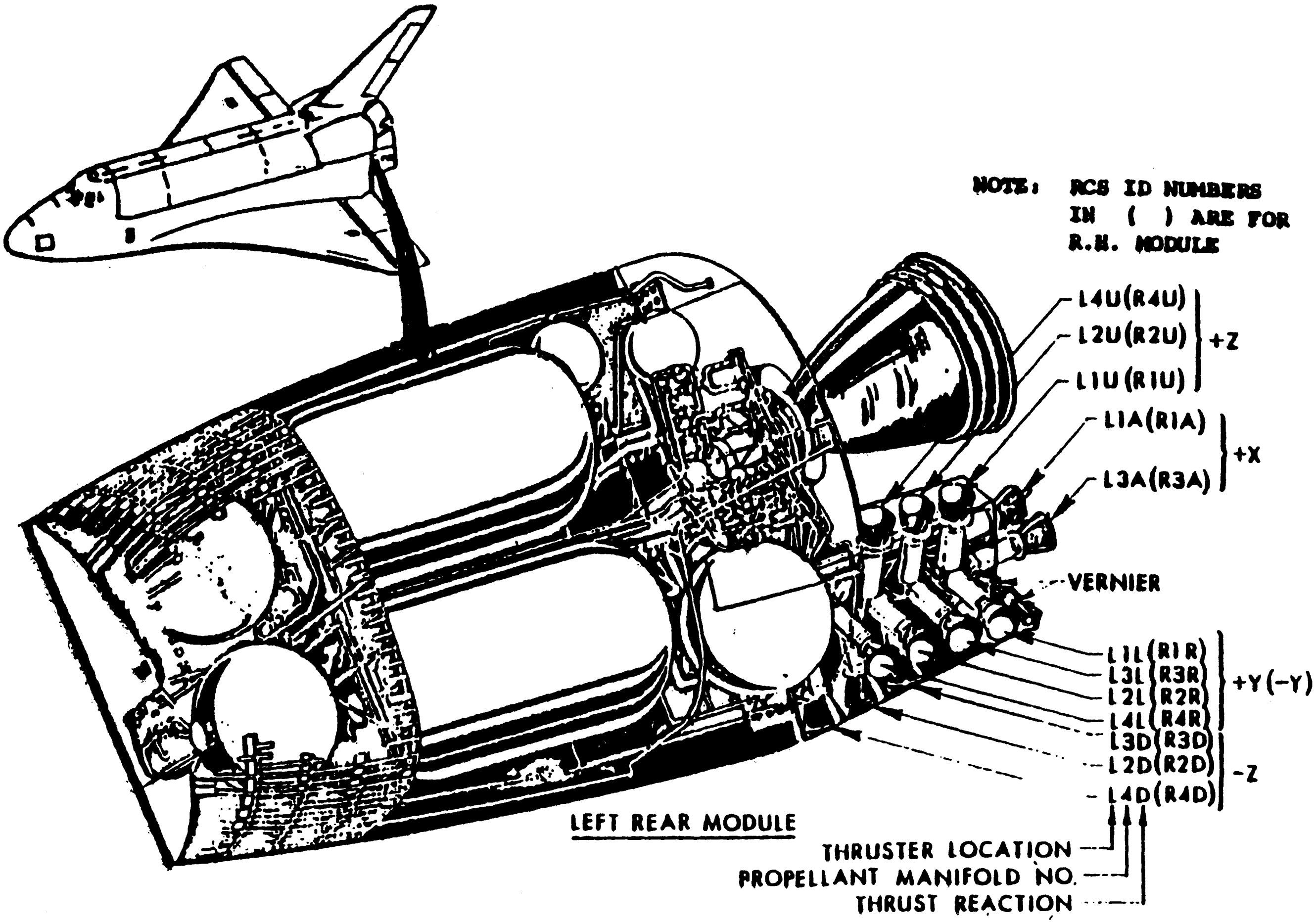

RCS THRUSTER IDENTIFICATION

FIGURE 3

SAMPLE PTI MANEUVER

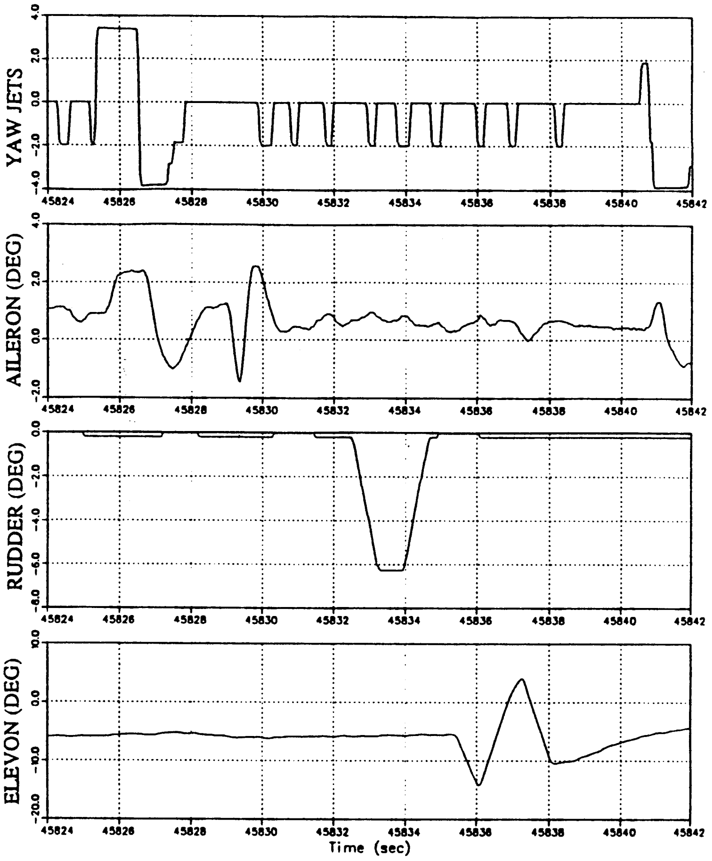

FIGURE 4

SAMPLE BODY FLAP PULSE

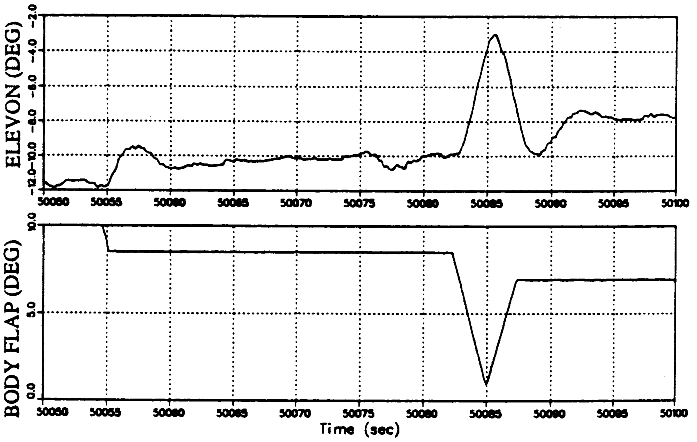

FIGURE 5

FLIGHT TEST REQUIREMENT SUMMARY

Priority	FTR No.	Region	Placard	Aero Derivatives in question	Problem Description
1	07VV013	$3.0<M<4.5$	Fwd cg Y cg	$C_{n_{\delta r}}$, $C_{l_{\delta r}}$ $C_{n_{\beta}}$, $C_{l_{\beta}}$	Lat/Dir trim and control authority; Uncertainty due to low Rudder, Aileron, and jet effectiveness
2	07VV007 $(2 \le q \le 20)$	$M>20$ Viscous	Fwd cg Aft cg	$C_{m_{\delta e}}$, Pitch jet effectiveness	Long. trim authority at cg extremes due to uncertainty in control effectors
3	07VV008	$1.7 \le M \le 2.5$	Fwd cg Aft cg	$C_{n_{\beta}}$, $C_{l_{\beta}}$, $C_{n_{\delta a}}$, $C_{l_{\delta a}}$, $C_{n_{\delta r}}$, $C_{l_{\delta r}}$,	Uncertainty in Lat/Dir control authority due to potential low Rudder effectiveness
4	07VV005	$4.8 \le M \le 7$	Fwd cg FCS Switch	$C_{n_{\delta a}}$, $C_{l_{\delta a}}$, $C_{n_{\beta}}$, $C_{l_{\beta}}$	Excessive RCS fuel usage due to Lat/Dir trim with adverse $C_{n_{da}}$
5	07VV011	$1.3 \le M \le 1.5$	Aft cg FCS Switch	$C_{n_{\beta}}$, $C_{l_{\beta}}$, $C_{n_{\delta a}}$, $C_{l_{\delta a}}$, $C_{n_{\delta r}}$, $C_{l_{\delta r}}$,	Uncertainty in Lat/Dir control authority due to potential low rudder and aileron effectiveness
6	07VV007 $(q<20)$	$M<20$ Viscous	Fwd cg Aft cg	$C_{m_{\delta e}}$	Potential Long. trim and control problems
7	07VV007 $(q<0.4)$	$M<20$ Viscous	Fwd cg	Pitch jet effectiveness	Excessive RCS pitch trim fuel at cg extremes due to uncertainty in control effectiveness
8	07VV014	$.75<M<.9$	Aft cg	$C_{n_{\delta r}}$, $C_{l_{\delta r}}$ $C_{n_{\beta}}$, $C_{l_{\beta}}$ $C_{n_{\delta a}}$, $C_{l_{\delta a}}$,	Loss of Rudder effectiveness and Lat. stability at low Speed Brake settings
9	07VV007 Body Flap	$M<20$ Viscous	Fwd cg Aft cg	$C_{m_{\delta BF}}$	Long. trim authority at cg extremes due to uncertainty in $C_{m_{BF}}$

FIGURE 6

FORWARD CG EXPANSION HISTORY

	Forward Limit	Aft Limit	Delta
Pre STS-1	1094.7	1101.2	6.5
Post FAD4	1083.0	1109.0	26.0
Post FAD9	1079.0	1109.0	30.0
Post FAD9B	1076.7	1109.0	32.3

FIGURE 7

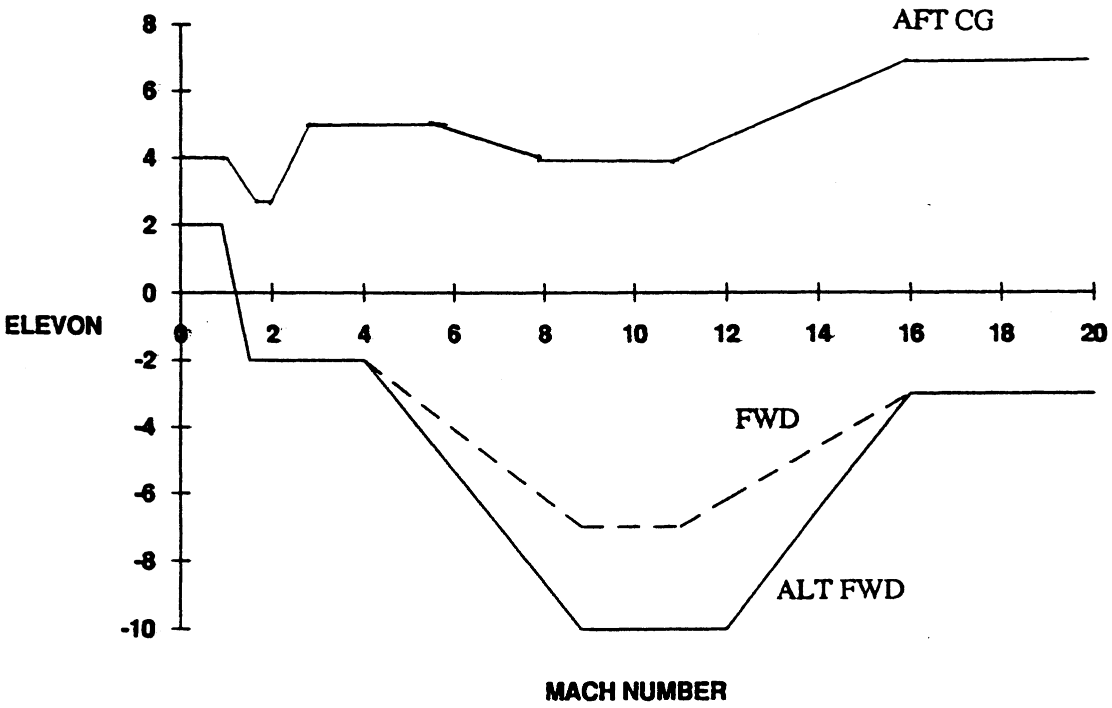
ELEVON SCHEDULES

FIGURE 8

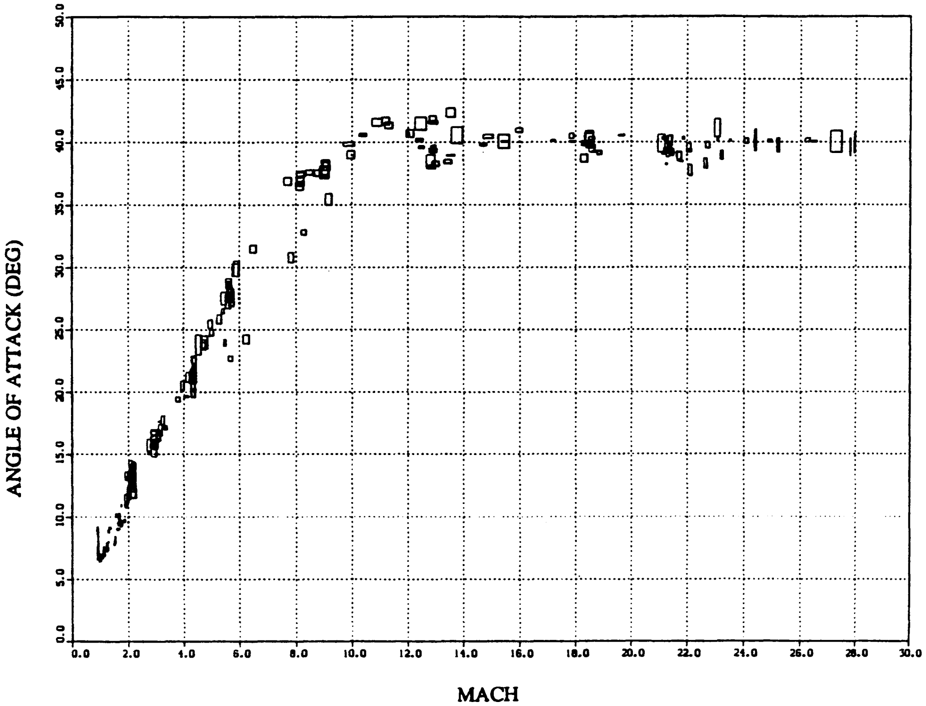
ANGLE OF ATTACK EXPERIENCE

FIGURE 9

ELEVON EXPERIENCE

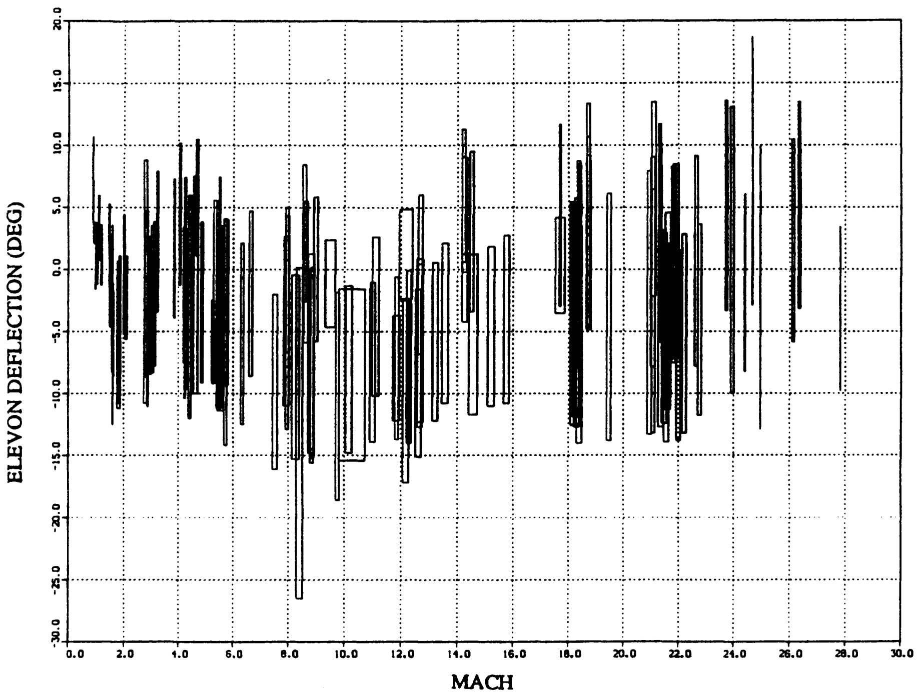

FIGURE 10

MAXIMUM LIKELIHOOD FLOWCHART

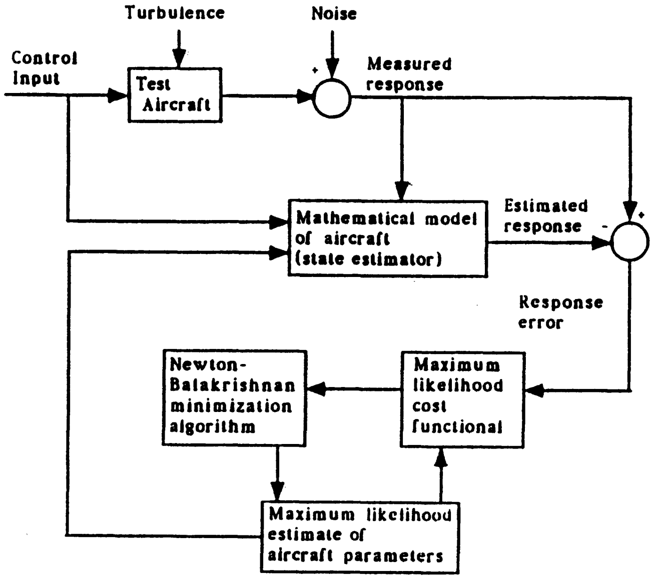
Turbulence
Noise
Control Input
Test Aircraft
+
Measured response
Mathematical model of aircraft (state estimator)
Estimated response
-
+
Response error
Newton-Balakrishnan minimization algorithm
Maximum likelihood cost functional
Maximum likelihood estimate of aircraft parameters

FIGURE 11

COMPARISON OF ACIP AND OI DATA SIGNAL

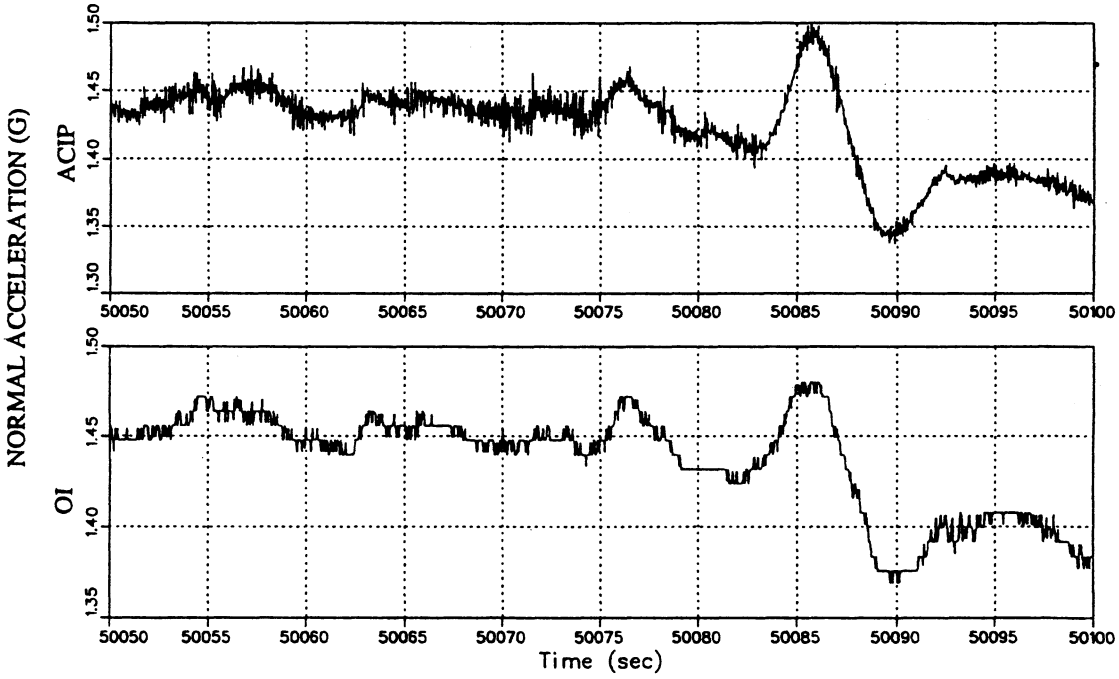

FIGURE 12

SAMPLE FLIGHT TEST RESULTS

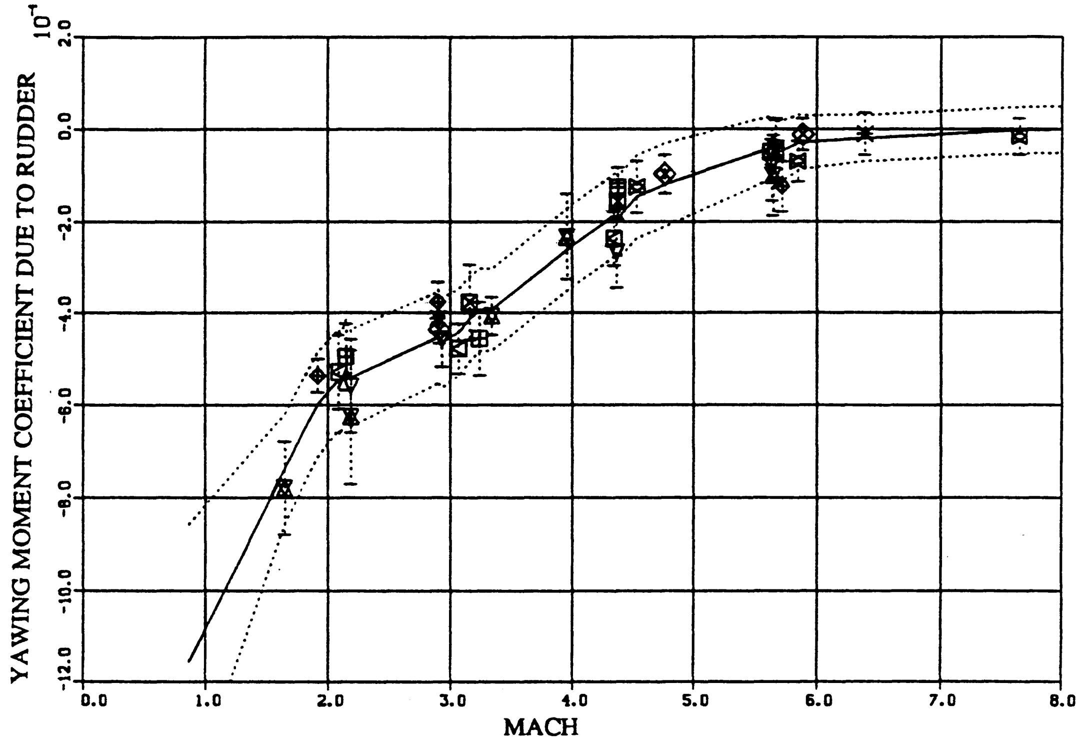

FIGURE 13

EXTRACTION OF STABILITY AND CONTROL DERIVATIVES FROM ORBITER FLIGHT DATA

Kenneth W. Iliff and Mary F. Shafer
NASA Dryden Flight Research Facility
Edwards, California

SUMMARY

The Space Shuttle Orbiter has provided unique and important information on aircraft flight dynamics. This information has provided the opportunity to assess the flight-derived stability and control derivatives for maneuvering flight in the hypersonic regime. In the case of the Space Shuttle Orbiter, these derivatives are required to determine if certain configuration placards (limitations on the flight envelope) can be modified. These placards were determined on the basis of preflight predictions and the associated uncertainties. As flight-determined derivatives are obtained, the placards are reassessed, and some of them are removed or modified. Extraction of the stability and control derivatives was justified by operational considerations and not by research considerations. Using flight results to update the predicted database of the orbiter is one of the most completely documented processes for a flight vehicle. This process followed from the requirement for analysis of flight data for control system updates and for expansion of the operational flight envelope. These results show significant changes in many important stability and control derivatives from the preflight database. This paper presents some of the stability and control derivative results obtained from Space Shuttle flights. Some of the limitations of this information are also examined.

INTRODUCTION

In the last 12 yr, the Space Shuttle Orbiter has provided unique and important information concerning aerothermodynamics and aircraft flight dynamics. Maneuvering manned flight over a wide range of hypersonic velocities was demonstrated for the first time. These data have provided the opportunity to assess flight characteristics in completely new flight regimes. Among the flight characteristics to be assessed are the stability and control derivatives.

Estimates of the stability and control derivatives can be used to expand the flight envelope, to update simulators, to enhance maneuvering capability and flying qualities, and to provide the information necessary to improve the flight control system. In the case of the Space Shuttle, these derivatives are required to determine if certain configuration placards (limitations on the flight envelope) can be modified. Many of these placards involve the longitudinal and lateral center-of-gravity (c.g.) limits. The placards were determined on the basis of preflight predictions and the associated uncertainties. As flight-determined derivatives are obtained, the placards are reassessed, and some are removed or modified.

The stability and control maneuvers performed by the Space Shuttle Orbiter were done so that the operational envelope could be safely expanded. Maneuvers were done specifically to update the aerodynamics and the associated uncertainties for Space Shuttle project support and were not done to provide aerodynamic research information. Lack of research emphasis limits the amount of general information that can be obtained. In spite of these limitations, much information of research value was obtained. At this time, the Space Shuttle has flown 54 flights. This paper presents some of the stability and control derivative results obtained from these Space Shuttle flights. In addition, some of the limitations of the information obtained are examined.

The authors greatly appreciate the conversations and information provided by Mr. Joe Baumbach at Rockwell International Space Division (Rockwell), Downey, California. The plots showing the results of research conducted by four groups of analysts were taken from Rockwell's Internal Letters SAS/AERO/86-062, June 26, 1986, by Mr. J.J. Baumbach and SAS/AERO/86-079, July 16, 1986, by Mr. Alan H. Weiner.

NOMENCLATURE

Abbreviations

ACIP	aerodynamic coefficient identification package
AFFTC	Air Force Flight Test Center, Edwards Air Force Base, California
c.g.	center of gravity
FAD	flight assessment deltas
GPC	general purpose computer
JSC	Johnson Space Center, Houston, Texas
MMLE	maximum likelihood estimation algorithm
NASA-Dryden	Dryden Flight Research Facility, Edwards, California
OI	operational instrumentation
PTI	programmed test input
RCS	reaction control system
STS	Space Transportation System (used with an assigned number to designate a mission)

Symbols

a_n	normal acceleration, g
a_x	longitudinal acceleration, g
a_y	lateral acceleration, g

$\mathbf{A}, \mathbf{B}, \mathbf{C},$ $\mathbf{D}, \mathbf{F}, \mathbf{G}$	system matrices
$C_{L_{\mathrm{BF}}}$	coefficient of lift due to body flap, deg^{-1}
$C_{l_{\mathrm{RJ}}}$	coefficient of rolling moment due to roll jet, per jet
$C_{l_{\mathrm{YJ}}}$	coefficient of rolling moment due to yaw jet, per jet
$C_{l_{\mathrm{YJ}_2}}$	coefficient of rolling moment due to two yaw jets, per jet
$C_{l_{\mathrm{YJ}_4}}$	coefficient of rolling moment due to four yaw jets, per jet
C_{l_β}	coefficient of rolling moment due to angle of sideslip (dihedral effect), deg^{-1}
$C_{l_{\delta_a}}$	coefficient of rolling moment due to differential aileron, deg^{-1}
$C_{l_{\delta_r}}$	coefficient of rolling moment due to rudder, deg^{-1}
$C_{m_{\mathrm{BF}}}$	coefficient of pitching moment due to body flap, deg^{-1}
$C_{m_{\mathrm{DJ}}}$	coefficient of pitching moment due to down-firing jet, per jet
$C_{m_{\mathrm{YJ}_2}}$	coefficient of pitching moment due to two yaw jets, per jet
C_{m_α}	coefficient of pitching moment due to angle of attack, deg^{-1}
$C_{m_{\delta_e}}$	coefficient of pitching moment due to elevon, deg^{-1}
$C_{m_{\delta_e^2}}$	coefficient of pitching moment due to elevon squared, deg^{-2}
$C_{m_{\delta_{e_0}}}$	coefficient of pitching moment due to elevon when quadratic terms are assumed, deg^{-1}
C_{m_0}	pitching moment bias
$C_{N_{\mathrm{DJ}}}$	coefficient of normal force due to down-firing jet, per jet
C_{n_β}	coefficient of yawing moment due to angle of sideslip (directional stability), deg^{-1}
$C_{n_{\delta_a}}$	coefficient of yawing moment due to differential elevon, deg^{-1}
$C_{n_{\delta_r}}$	coefficient of yawing moment due to rudder, deg^{-1}
$C_{Y_{\mathrm{YJ}}}$	coefficient of side force due to yaw jet, per jet
$C_{Y_{\mathrm{YJ}_2}}$	coefficient of side force due to two yaw jets, per jet
C_{Y_β}	coefficient of side force due to angle of sideslip, deg^{-1}
$C_{Y_{\delta_r}}$	coefficient of side force due to rudder, deg^{-1}

f	system state function
$\mathbf{GG}^*$	measurement noise covariance matrix
g	system observation functions
$\mathbf{H}$	approximation to the information matrix
J	cost function
L	iteration number
L_{YJ}	rolling moment due to yaw jet, ft-lbf/jet
M	Mach number
$\dot{M}_J/\dot{M}_\infty$	jet mass flow ratio
N	number of time points
$\mathbf{n}$	state noise vector
p	roll rate, deg/sec
$\dot{p}$	roll acceleration, $\mathrm{deg/sec^2}$
q	pitch rate, deg/sec
$\dot{q}$	pitch acceleration, $\mathrm{deg/sec^2}$
$\bar{q}$	dynamic pressure, $\mathrm{lb/ft^2}$
r	yaw rate, deg/sec
$\dot{r}$	yaw acceleration, $\mathrm{deg/sec^2}$
t	time, sec
$\mathbf{u}$	known control input vector
V	velocity, ft/sec
$\mathbf{x}$	state vector
$\dot{\mathbf{x}}$	time derivative of state vector
$\tilde{\mathbf{x}}$	predicted state estimate
$\mathbf{z}$	observation vector
$\tilde{\mathbf{z}}$	predicted Kalman filter estimate
α	angle of attack, deg

β	angle of sideslip, deg
Δ	increment of derivative added to preflight aerodynamic data book value to best represent flight
δ	difference between maneuver estimate and flight-derived derivative fairing
δ_a	differential elevon deflection, deg
δ_e	elevon deflection, deg
δ_r	rudder deflection, deg
$\boldsymbol{\eta}$	measurement noise vector
$\boldsymbol{\phi}$	transition matrix
ϕ_J/ϕ_∞	jet momentum ratio
$\boldsymbol{\psi}$	integral of the transition matrix
$\boldsymbol{\xi}$	unknown parameter vector
$\hat{\boldsymbol{\xi}}$	estimate of $\boldsymbol{\xi}$

VEHICLE DESCRIPTION

Figure 1 shows the Space Shuttle Orbiter, a large double-delta-winged vehicle designed to enter the atmosphere and land horizontally. This vehicle is 122-ft long with a wingspan of 78 ft. The entry control system consists of 12 vertical reaction control system (RCS) jets (6 down-firing and 6 up-firing), 8 horizontal RCS jets (4 to the left and 4 to the right), 4 elevon surfaces, a body flap, and a split rudder surface.

The vertical jets and the elevons control pitch and roll. These jets and elevons are used symmetrically to control pitch and asymmetrically to control roll. Used as a secondary pitch trim control, the body flap helps maintain the predetermined elevon schedule as a function of flight condition. The rudder and side-firing (yaw) jets provide directional control. The split rudder also functions as the speed brake. The vertical jets operate in roll (roll jets) only for dynamic pressures, $\bar{q}$, of less than 10 lb/ft^2 and in pitch (pitch jets) for dynamic pressures less than 40 lb/ft^2. The yaw jets are active when the Mach number, M, is greater than 1. The body flap and elevons activate at a dynamic pressure of 2 lb/ft^2. The rudders activate at Mach numbers below 5.

PREDICTIONS

The predicted stability and control derivatives are presented in the preflight aerodynamic data book (ref. 1). These predictions were based on more than 25,000 hr of wind-tunnel testing. In addition to the predicted values of the derivatives, the aerodynamic data book also contains estimates of the uncertainty in the predictions. These preflight uncertainties are called the variations. These variations are based on the evaluation of previous correlations between wind-tunnel and flight-determined derivatives for similar aircraft. The variations in reference 1 are based, in part, on the study of wind-tunnel and flight correlations presented in reference 2.

ORBITER STABILITY AND CONTROL EXAMPLE

The primary reasons for analyzing the Space Shuttle flight dynamic data are to support expansion of the operational envelope and to improve overall safety of this vehicle. This example shows how these analyses are used in conjunction with the flight program.

The Space Shuttle Orbiter trajectory during reentry and, therefore, its heating profile are controlled through a series of energy-management bank reversals. The vehicle is controlled by conventional aerodynamic surfaces and by the RCS jets. The first bank reversal on the first Space Shuttle flight, STS-1, resulted in a significantly larger response than had been predicted.

Figure 2 shows the response to the automated control inputs computed using the predicted stability and control derivatives. Note that the control inputs shown here (and for all the other simulation comparisons) are the closed-loop commands from the Orbiter control laws. The maneuver was to be made at a velocity, V, of 24,300 ft/sec and at $\bar{q} = 12\ \mathrm{lb/ft^2}$.

Figure 3 shows the STS-1 maneuver that occurred at this flight condition and depicts a more hazardous maneuver than was expected. At this flight condition, the excursions must be kept small. This flight maneuver resulted in twice the angle-of-sideslip, β, peaks than were predicted and in a somewhat higher than predicted roll rate. In addition, more yaw jet firing than was anticipated occurred, and the motion was more poorly damped than was predicted.

From comparing the predicted maneuver with the actual maneuver (fig. 4), obviously, the stability and control derivatives were significantly different from those that were predicted. It is fortunate that a conservative control system design philosophy had been used for the Space Shuttle. Although the flight maneuver resulted in excursions greater than planned, the control system did manage to damp out the oscillation in less than 1 min. With a less conservative design approach, the resulting entry maneuver could have been a great deal worse.

To assess the problem with the first bank maneuver, the flight-determined stability and control derivatives were extracted from the measured in-flight vehicle motions and compared with the predictions. Procedures for the stability and control derivative extraction are discussed in the Stability and Control Derivative Extraction section. Of the derivatives obtained from STS-1, the two important ones that differed most from the predictions for the bank maneuver were dihedral effect or coefficient of rolling moment due to angle of sideslip, C_{l_β}, and the rolling moment due to yaw jet firing, L_{YJ}. Because the entry tends to be monotonically decreasing in Mach number, the derivatives are portrayed here as a function of the Mach number derived from the general purpose computer (GPC), or GPC-derived Mach number; that is, $V/1000$.

Figure 5 shows C_{l_β} as a function of GPC-derived Mach number, and figure 6 shows L_{YJ} as a function of GPC-derived Mach number. Only the estimates from STS-1 are shown in these figures. The estimate for this maneuver is shown at Mach 24.

When only the change in C_{l_β} was entered in the simulation database, the maneuver looked very much like the original prediction. As expected, however, the frequency of the oscillations changed and more closely matched the actual flight frequencies.

Figure 7 shows the difference between the preflight simulation with only L_{YJ} changed and the flight response. These two time histories are very close, considering that all other differences between the flight-determined and -predicted derivatives have been ignored.

The primary problem with the initial bank maneuver was the poor prediction of L_{YJ}. The Space Shuttle control system software is very complex and cannot be changed and verified between missions. As a result, an interim approach was taken to keep this large excursion from occurring on future flights. First, the flight-determined derivatives were put into the simulation database. Next, Space Shuttle pilots practiced performing the maneuver manually, trying to attain a smaller response within more desirable limits. Then, the maneuver was performed manually on STS-2 through STS-4.

Figure 8 shows the manually flown maneuver from STS-2. For this maneuver, roll rate, yaw rate, and sideslip angle were within the desired limits. The maneuver does not look like the originally predicted response because the derivatives and input differed, and the basic control system remained unchanged. Because the response variables were kept low and the inputs were slower and smaller, flight responses on STS-2 through STS-4 did not show a tendency to oscillate. The software was updated for STS-5, and the resulting automated maneuver is essentially indistinguishable from that shown in figure 8. This maneuver has been used on all subsequent Space Shuttle flights.

STABILITY AND CONTROL DERIVATIVE EXTRACTION

The general parameter estimation or extraction problem is discussed in reference 3. The parameter estimation technique used for the Space Shuttle, as discussed in the Orbiter Stability and Control Example section, enabled the extraction of the stability and control derivatives from flight data. Although the parameter estimation technique described here was used to extract stability and control derivatives, the same technique applies to any process governed by differential equations, such as heat transfer or other thermal processes.

Key issues in extracting stability and control derivatives from flight data are best categorized into four areas. These areas include the mathematical model; the flight data measurements; the maneuvers or programmed test inputs (PTI's); and the maximum likelihood, or extraction, method. The Space Shuttle is modeled by a set of dynamic equations containing unknown stability and control derivatives. The equations used are those given in reference 4, except that dimensional derivatives are used for RCS jets. The other three areas are discussed in the next three subsections.

Flight Data Measurements

The Space Shuttle flight data used for stability and control derivative estimation were recorded on three onboard systems (ref. 5). The primary data were recorded on the aerodynamic coefficient identification package (ACIP). This package was specifically intended for providing high-quality data at a high sample rate to enhance the stability and control derivative estimates. A second system recorded data from the onboard GPC to provide the parameters defining the flight condition and the vehicle Euler angles. The third system was the operational instrumentation (OI) system. Time histories of the RCS jet chamber pressure were obtained from this system. These chamber pressures are used because they reflect the thrust buildup and decay. The RCS jet time histories presented in this paper are sums of the active chamber pressures divided by the nominal single chamber pressure, which gives the number of jets firing for nominal conditions. The following list of instrumentation properties gives the data source of the important signals used in the analysis as well as the individual sample rates and measurement resolutions:

Measurement	Sample rate, sample/sec	Source	Resolution	Bits
p	174	ACIP	0.004	14
q, r	174	ACIP	0.001	14
a_x	174	ACIP	0.0002	14
a_y	174	ACIP	0.00006	14
a_n	174	ACIP	0.0004	14
$\dot{p}$	174	ACIP	0.01	14
$\dot{q}$, $\dot{r}$	174	ACIP	0.007	14
Elevons	174	ACIP	0.004	14
Rudder	174	ACIP	0.003	14
Body flap	12.5[a]	GPC	0.04	10
RCS jets	25	OI	0.004	8
α	1	GPC	---	---
β	5	GPC	---	---
Euler angles	5	GPC	---	---
Flight condition	1	GPC	---	---

[a] Body flap sampled at 1 sample/sec on STS-1 and -2.

The resolution of the ACIP parameters allows the analysis of some very small maneuvers. These data from the three sources were corrected for time skew, converted to engineering units, and merged into a single file with constant sample rate.

Maneuvers or Programmed Test Inputs

Maneuvers for stability and control data have been carefully developed to provide the maximum amount of information. It is important in this testing to excite the motions that affect the derivatives in question to make them identifiable from the flight data. Because of the limited testing of the Space Shuttle and the characteristics of the flight control system, precise maneuver design and execution are very important.

The flight control system of the Space Shuttle Orbiter heavily modifies inputs through the stick and is designed to damp oscillations and transients. This design causes difficulty in pulsing a control surface. In pulsing the Orbiter, the control system modifies the stick input with filters, responds to rate and acceleration feedback values, and damps the response with further surface motion. In general when the vehicle is pulsed, all available controls are put into action to quickly damp the vehicle motion. Such control system implementation can cause difficulty in separating the effects of various control and response variables.

Programmed test inputs were developed to somewhat overcome this important problem and to provide exact designed inputs. This type of maneuver is input directly to the flight control system through onboard software. The amplitude and timing are governed by programmed variables to generate a specific input at a predesignated flight condition.

These programmed inputs are made through the flight control system, and they go to an integrator at the point where the surface deflection is commanded. The input is added to the command, a surface rate, which is then processed through a maximum rate-limit function. Signals can be sent to the elevon, aileron, and rudder as well as to the pitch, roll, and yaw jets. The input from the automatic PTI is not completely free of flight control system interference, but the design does allow for enhanced maneuvers.

All of the stability and control flight data discussed in the remainder of this paper were obtained from PTI maneuvers. Very small maneuvers, an order of magnitude smaller than those from the PTI, were successfully analyzed for the Orbiter, and those results are discussed in detail in references 6 and 7.

Maximum Likelihood, or Extraction, Method

The aircraft equations of motion can be written as a general system model in the continuous discrete form as follows:

$$\mathbf{x}(t_0) = \mathbf{x}_0 \tag{1}$$

$$\dot{\mathbf{x}}(t) = f[\mathbf{x}(t), \mathbf{u}(t), \boldsymbol{\xi}] + \mathbf{F}(\boldsymbol{\xi})\mathbf{n}(t) \tag{2}$$

$$\mathbf{z}(t_i) = g[\mathbf{x}(t_1), \mathbf{u}(t_1), \boldsymbol{\xi}] + \mathbf{G}(\boldsymbol{\xi})\boldsymbol{\eta}_i \tag{3}$$

where $\mathbf{x}$ is the state vector, $\mathbf{z}$ is the observation vector, f and g are system state and observation functions, $\mathbf{u}$ is the known control input vector, $\boldsymbol{\xi}$ is the vector of unknown parameters, $\mathbf{n}$ is the state noise vector, $\boldsymbol{\eta}$ is the measurement noise vector, $\mathbf{F}$ and $\mathbf{G}$ are system matrices, and t is time. The state noise vector, $\mathbf{n}$, is assumed to be zero-mean white Gaussian and stationary, and the measurement noise vector, $\boldsymbol{\eta}$, is assumed to be a sequence of independent Gaussian random variables with zero-mean and identity covariance. For each possible estimate of the unknown parameters, a probability that the aircraft response time histories will attain values near the observed values can then be defined. The maximum likelihood estimates are defined as those that maximize this probability. Maximum likelihood estimation has many desirable statistical characteristics; for example, it yields asymptotically unbiased, consistent, and efficient estimates (ref. 8).

If there is no state noise, then the maximum likelihood estimator minimizes the cost function

$$J(\boldsymbol{\xi}) = \frac{1}{2}\sum_{i=1}^{N}[\mathbf{z}(t_i) - \tilde{\mathbf{z}}_{\boldsymbol{\xi}}(t_i)]^*(\mathbf{G}\mathbf{G}^*)^{-1}[\mathbf{z}(t_i) - \tilde{\mathbf{z}}_{\boldsymbol{\xi}}(t_i)] + \frac{1}{2}N\ln|(\mathbf{G}\mathbf{G}^*)| \tag{4}$$

where $\mathbf{G}\mathbf{G}^*$ is the measurement noise covariance matrix, $\tilde{\mathbf{z}}_{\boldsymbol{\xi}}(t_i)$ is the predicted response estimate of $\mathbf{z}$ at t_i for a given value of the unknown parameter vector $\boldsymbol{\xi}$, and N is the number of time points. The cost function is a function of the differences between the measured and computed time histories.

If equations (2) and (3) are linearized (as is the case for the stability and control derivatives in the aircraft problem), then

$$\mathbf{x}(t_0) = \mathbf{x}_0 \tag{5}$$

$$\dot{\mathbf{x}}(t) = \mathbf{A}\mathbf{x}(t) + \mathbf{B}\mathbf{u}(t) + \mathbf{F}\mathbf{n}(t) \tag{6}$$

$$\mathbf{z}(t_i) = \mathbf{C}\mathbf{x}(t_i) + \mathbf{D}\mathbf{u}(t_i) + \mathbf{G}\boldsymbol{\eta}_i \tag{7}$$

where $\mathbf{A}$, $\mathbf{B}$, $\mathbf{C}$, and $\mathbf{D}$ are system matrices. For the no-state-noise case, the $\tilde{\mathbf{z}}_{\boldsymbol{\xi}}(t_i)$ term of equation (4) can be approximated by

$$\tilde{\mathbf{x}}_{\boldsymbol{\xi}}(t_0) = \mathbf{x}_0(\boldsymbol{\xi}) \tag{8}$$

$$\tilde{\mathbf{x}}_{\boldsymbol{\xi}}(t_{i+1}) = \boldsymbol{\phi}\tilde{\mathbf{x}}_{\boldsymbol{\xi}}(t_i) + \boldsymbol{\psi}[\mathbf{u}(t_i) - \mathbf{u}(t_{i+1})]/2 \tag{9}$$

$$\tilde{\mathbf{z}}_{\boldsymbol{\xi}}(t_i) = \mathbf{C}\tilde{\mathbf{x}}_{\boldsymbol{\xi}}(t_i) + \mathbf{D}\mathbf{u}(t_i) \tag{10}$$

where the transition matrix, $\boldsymbol{\phi}$, and the integral of the transition matrix, $\boldsymbol{\psi}$, are given by

$$\boldsymbol{\phi} = \exp[\mathbf{A}(t_{i+1} - t_i)] \tag{11}$$

$$\boldsymbol{\psi} = \int_{t_i}^{t_{i+1}} \exp(\mathbf{A}\tau)\, d\tau\, \mathbf{B} \tag{12}$$

The Newton-Raphson algorithm (or some other minimization technique) can be applied to minimize the cost function, $J(\boldsymbol{\xi})$. Such techniques choose successive estimates of the vector of unknown coefficients, $\hat{\boldsymbol{\xi}}$ ($\hat{\ }$ denoting estimate). If L is the iteration number, then the $L+1$ estimate of $\boldsymbol{\xi}$ is obtained from the L estimate as

$$\hat{\boldsymbol{\xi}}_{L+1} = \hat{\boldsymbol{\xi}}_L - [\nabla^2_{\boldsymbol{\xi}} J(\hat{\boldsymbol{\xi}}_L)]^{-1}[\nabla^*_{\boldsymbol{\xi}} J(\hat{\boldsymbol{\xi}}_L)] \tag{13}$$

If $(\mathbf{GG}^*)^{-1}$ is assumed fixed, then the first and second gradients are defined as follows:

$$\nabla_{\boldsymbol{\xi}} J(\boldsymbol{\xi}) = -\sum_{i=1}^{N} [\mathbf{z}(t_i) - \tilde{\mathbf{z}}_{\boldsymbol{\xi}}(t_i)]^* (\mathbf{GG}^*)^{-1} [\nabla_{\boldsymbol{\xi}} \tilde{\mathbf{z}}_{\boldsymbol{\xi}}(t_i)] \tag{14}$$

$$\nabla^2_{\boldsymbol{\xi}} J(\xi) = \sum_{i=1}^{N} [\nabla_{\boldsymbol{\xi}} \tilde{\mathbf{z}}_{\boldsymbol{\xi}}(t_i)]^* (\mathbf{GG}^*)^{-1} [\nabla_{\boldsymbol{\xi}} \tilde{\mathbf{z}}_{\boldsymbol{\xi}}(t_i)] - \sum_{i=1}^{N} [\mathbf{z}(t_i) - \tilde{\mathbf{z}}_{\boldsymbol{\xi}}(t_i)]^* (\mathbf{GG}^*)^{-1} [\nabla^2_{\boldsymbol{\xi}} \tilde{\mathbf{z}}_{\boldsymbol{\xi}}(t_i)] \tag{15}$$

The Gauss-Newton approximation to the second gradient is

$$\nabla^2_{\boldsymbol{\xi}} J(\boldsymbol{\xi}) \cong \sum_{i=1}^{N} [\nabla_{\boldsymbol{\xi}} \tilde{\mathbf{z}}_{\boldsymbol{\xi}}(t_i)]^* (\mathbf{GG}^*)^{-1} [\nabla_{\boldsymbol{\xi}} \tilde{\mathbf{z}}_{\boldsymbol{\xi}}(t_i)] \tag{16}$$

The Gauss-Newton approximation is computationally much easier than the Newton-Raphson method because the second gradient of the innovation never needs to be calculated. In addition, it can have the advantage of speeding the convergence of the algorithm (ref. 4).

Figure 9 illustrates the maximum likelihood estimation concept. The measured response is compared with the estimated response, and the difference between these responses is called the response error. The cost function of equation (4) includes this response error. The minimization algorithm is used to find the coefficient values which minimize the cost function. Each iteration of this algorithm provides a new estimate of the unknown coefficients on the basis of the response error. These new estimates are then used to update values of the coefficients of the mathematical model, providing a new estimated response and, therefore, a new response error. Updating of the mathematical model continues iteratively until a convergence criterion is satisfied. The estimates resulting from this procedure are the maximum likelihood estimates.

The maximum likelihood estimator also provides a measure of the reliability of each estimate based on the information obtained from each dynamic maneuver. This measure of the reliability, analogous to the standard deviation, is called the Cramér-Rao bound (refs. 9 and 10) or the uncertainty level. The Cramér-Rao bound, as computed by current programs, should generally be used as a measure of relative rather than absolute accuracy. The bound is obtained from the approximation to the information matrix, $\mathbf{H}$, which is based on equation (16); the actual information matrix is defined when evaluated at the correct values (not the maximum likelihood estimates) of all the coefficients. The bound for each unknown is the square root of the corresponding diagonal element of $\mathbf{H}^{-1}$; that is, for the ith unknown, the Cramér-Rao bound is $\sqrt{(\mathbf{H}^{-1})_{i,i}}$.

STABILITY AND CONTROL DERIVATIVE EXTRACTION JUSTIFICATION

There was a well-defined requirement for the extraction of stability and control derivatives from flight data for the Space Shuttle. This requirement had two sources: the need to improve the preflight predictions of the stability and control derivatives and the need to reduce the associated uncertainties of each derivative. These preflight predictions and their associated uncertainties (ref. 1) were used for control system design, for operational envelope definition, and for high-fidelity flight-training simulators. These flight data were required to update the coefficients of the mathematical model, so the flight control system could be improved, the operational envelope expanded, and the simulators would have increased fidelity.

Stability and control derivatives are usually determined in a flight program by performing repeated stability and control maneuvers throughout a matrix of conditions in the flight envelope of the aircraft. The coefficients and, sometimes, the form of the mathematical model originally based on preflight ground predictions are then updated with the new information. This procedure is usually followed whether the derivative extraction is done to improve the operational envelope or to obtain flight research data.

For a variety of reasons, the Space Shuttle Orbiter could not fly repeated maneuvers throughout its envelope. This limitation meant that there was not enough data to update the preflight aerodynamic data book in the traditional manner. The following discussion of the process used for the Orbiter was selectively excerpted from reference 11, which was written from the perspective of the Space Shuttle team in 1983, following the first four flights:

> Stability and control testing of the Space Shuttle is driven by conflicting program desires, while limited by unique problems. Space Shuttle flights are very costly when compared with test flights of other aircraft. There is an intense desire within the program to bring the Shuttle to an operational mode.... On the other hand, it is important to assure the safety of entry flight and to identify the real limitations of the Shuttle through flight testing. This conflict in goals has resulted in the need for a minimum amount of highly productive testing.
>
> Conventional flight test techniques and computer programs have formed the basis for the Shuttle flight test program. Modifications to these techniques have been necessary, however, due to the inherent constraints in Shuttle testing. Measures have been taken to ensure the quality of maneuvers and the data from them, so that the number of repeat maneuvers can be minimized.
>
> The flight test plan developed for the Shuttle contains very few test points when compared to test programs of military aircraft. Enough maneuvers are scheduled only to verify the safety of the Shuttle entry, not enough to build a flight test data base. Where significant differences exist between the flight data and the wind-tunnel data base, further test points are scheduled [ref. 1]....
>
> Derivative [flight assessment] deltas calculated between flight and values from the Shuttle Aerodynamic Design Data Book [ref. 1] are provided to Shuttle simulators to demonstrate the safety of further testing on upcoming flights and to assure the safety of flying c.g.'s associated with planned payloads [ref. 1]....
>
> Aerodynamic test requirements have arisen from two sources. The original source is the preflight wind tunnel and the associated uncertainties. The other source of requirements is the flight data from the initial flights, during which anomalies occurred. The types of problems identified involve either potentially excessive RCS fuel usage for longitudinal and lateral trim, or potential loss of control....
>
> Preflight wind-tunnel data for the orbiter is [sic] very extensive and provided sufficient confidence to fly the initial missions under benign conditions and within a limited range of [center of gravity positions]. From wind-tunnel test data, a preflight data base was developed for use in simulators and for design of the entry guidance and flight control systems. Uncertainties on these data were developed because of wind tunnel to flight differences noted

in previous flight test programs on other aircraft. Uncertainties were also assessed for high Mach number, low dynamic pressure flight regimes where wind tunnels were heretofore either unverified or not capable of reproducing flight conditions.

Design specifications require[d] that the orbiter be able to fly safely with a c.g. range of 65 to 67.5% of the reference body length. Extremes of this range result in the limits of trim capability necessary to operate the vehicle. At the c.g. extremes, analysis indicates combinations of the uncertainties in pitching moment and the stability and control derivatives result in potential control problems. The problem areas defined from preflight data were the drivers in setting entry flight placards....

Anomalies in the actual flight data have extended the test requirements as originally conceived. These anomalies have in some cases accentuated the need for certain data already planned for. Others have pointed to a need for more concentrated investigation of certain flight regimes....

These anomalies have not restricted the flight placards further. However, they have accentuated the need for data in certain flight regimes. They have also caused the planning of further testing in specific areas....

The Shuttle test program is the product of significant planning and integration with other program requirements. The flight test requirements from wind-tunnel uncertainties and flight anomalies dictated the flight conditions at which maneuvers would be done. Sufficient maneuvers were planned at nominal conditions to indicate repeatability of results. Additional maneuvers were planned over the ranges of elevon and angle of attack that will be seen operationally to check coefficient sensitivities to these parameters. The test plan has been modified to provide additional information in areas where anomalies have occurred. This is necessary to establish an understanding of the anomaly and to develop a database for simulators, in areas where the wind tunnel data is deficient....

The flight testing has been planned to meet program objectives. The first and most important is to open the c.g. placards as quickly as possible, to verify the safety of flying planned payloads. In addition, data resulting from tests is [sic] scheduled to support planned flight control system changes, which will improve control where in-flight aerodynamic anomalies have occurred....

An important product of the flight test program is the confidence that is gained from flight test results in assessing the safety of upcoming flights. Vehicle c.g.'s associated with specific payloads must be shown to be safe. In addition, further testing in the flight test program depends on values of derivatives obtained from previous tests. For instance, it is important to understand as much as possible about stability and control characteristics for down elevon positions, before it is safe to fly with elevons at more negative settings. To accomplish this, fairings are developed for the flight test results and are provided to the Shuttle flight control system community. These fairings of "assessment" values are incorporated into simulators which are used to verify the safety of upcoming flights. Exact maneuvers and trajectory profiles are simulated with correct c.g.'s. In addition, stability analyses are performed using the flight derived aerodynamic data to update c.g. placards for the vehicle....

The primary goal of the entire data extraction effort is to open c.g. placards for the Shuttle, so that the full payload carrying capability can be utilized. Through the planned maneuvers, and elevon and angle-of-attack schedules, sufficient data is [sic] to be obtained to verify the Shuttle operational safety during entry. The operational limits for c.g. have been specified to be from 65 to 67.5 percent of the reference body length.

STABILITY AND CONTROL DERIVATIVE ASSESSMENT PROCESS

This section discusses the first author's perception of the stability and control assessment process. This perception is based on experience gained while serving continuously on various Space Shuttle aerodynamics and flight test panels for the past 18 yr.

Most of the stability and controls maneuvers from the Space Shuttle flights were analyzed by four sets of analysts. These four sets were composed of groups at the Rockwell International Space Division (Rockwell), Downey, California, the NASA Johnson Space Center (JSC), Houston, Texas, the Air Force Flight Test Center (AFFTC), Edwards Air Force Base, California, and the NASA Dryden Flight Research Facility (NASA-Dryden), Edwards, California. All four sets of analysts used the maximum likelihood estimation algorithm (MMLE) derivative extraction computer program (ref. 12). This discussion is based on the MMLE analysis of the Space Shuttle Orbiter PTI maneuvers by these four sets of analysts. Some of this work was previously reported in references 11, 13, and 14. Many other Orbiter maneuvers, including bank angle reversals and incidental vehicle motions, were analyzed. Although not presented in this paper, results of these analyses were used to resolve ambiguous information obtained from the PTI maneuvers.

The flight data used to improve the original preflight aerodynamic data book predictions and the associated uncertainties (ref. 1) were originally viewed as providing incremental changes to the data book. These incremental changes were called flight assessment deltas (FAD's). The delta in this name refers to the incremental change. The FAD's were generated after STS-2, -4, -6, -9, -14, and -26.

The AFFTC stopped analyzing these data after the first 13 flights. An additional change in the aerodynamic data book is due after STS-57. The PTI's have been analyzed by the three remaining groups through the 54 Space Shuttle flights (through STS-56). At this time, the Space Shuttle has flown 54 flights: 13 by *Columbia*, 10 by *Challenger*, 16 by *Discovery*, 12 by *Atlantis*, and 3 by *Endeavour*. Dynamic maneuvers from 45 of these have been analyzed. Data from these flights have been analyzed, and the results are still being assessed for incorporation into the aerodynamic data book in the fall of 1993. The results of this latest assessment are not included in this paper.

As discussed in the Stability and Control Derivative Extraction Justification section, one of the primary reasons that the stability and control derivatives are determined is to expand the c.g. envelope. The current longitudinal c.g. envelope is from 1076.7 in. (65-percent reference body length) to 1109.0 in. (67.5-percent reference body length). Figure 10 shows the current longitudinal and lateral c.g. envelope, and all centers of gravity flown are shown.

The remainder of this paper concentrates on the results of the analyses that were incorporated into the preflight aerodynamic data book from STS-1 through STS-26. This set of incremental changes is known as FAD–26. Rockwell was charged with implementing the procedure for defining FAD's. Briefly, this implementation involved collecting the estimated stability and control derivatives from the four groups of analysts and presenting these estimated derivatives in various formats, so a consensus fairing for the derivatives and the associated uncertainties could be assessed by the four groups of analysts and by other aerodynamics experts.

The four primary sets of Space Shuttle Orbiter flight condition parameters are Mach number, angle of attack, elevon position, and body flap position. At high altitudes and low dynamic pressures (below 20 lb/ft^2), dynamic pressure was also used as a primary parameter. Mass flow ratio and momentum ratio for the RCS jets were also examined (ref. 13). Because Mach number decreases monotonically for the Orbiter during entry, most of the stability and control derivatives estimated from flight were assessed primarily as functions of true (not GPC-derived) Mach number.

Rockwell plotted the stability and control derivatives as functions of two flight condition parameters, using carpet plots to aid in assessing which were the primary variables that affected given derivatives. In addition, Rockwell provided data comparing the flight-derived estimates with the aerodynamic data book predictions. This effort included procedures and recommendations for merging the FAD's with the aerodynamic data book values for regions where no flight data were provided. The aerodynamic data book predictions used in these comparisons were obtained by interpolating all of the primary flight condition parameters (for example, Mach number, angle of attack, center of gravity location, altitude, and elevon and body flap positions) so that the flight-derived estimates were compared with the predictions at the same flight conditions.

DERIVATIVE RESULTS

In this section, the stability and control derivative estimates obtained from the flight are compared with predictions. Complicated functional dependence of the derivatives predicted in reference 1 cannot be validated by the data from a single flight. These predictions are a function of many parameters defining the flight conditions. Such parameters include Mach number, angle of attack, altitude, dynamic pressure, body flap position, and elevon deflection. Between entry interface (400,000 ft) and final approach, the true Mach number monotonically decreased from above 28 to below 1. Thus, for any particular Mach number in any given flight, these data are available only at a single value of angle of attack, dynamic pressure, altitude, body flap position, and other parameters.

Several of these parameters continually change; therefore, conclusively attributing any trends observed in the derivatives of specific flight condition parameters to a given factor is impossible. Most of the estimates presented here are plotted as a function of true Mach number. This form of presentation is adopted only for convenience and is not meant to imply that the trends observed are necessarily directly related to Mach number. For instance, the trends between Mach 12 and 2 may be more influenced by the angle of attack, which decreases from 40° to 10°, than by the Mach number. The predictions were determined at the particular flight condition which occurred at each Mach number of the flight. Thus, these predictions are comparable to the flight results.

Figure 11 shows elevon deflection, body flap deflection, and angle of attack as functions of Mach number for Space Shuttle Orbiter flights from STS-1 through STS-26. This figure shows why a large amount of scatter exists in the plots of the derivatives as functions of Mach number. Using the Mach number obscures the large changes in flight condition, and much of the scatter is attributable to these large changes in flight conditions. In reality, these derivatives were plotted against each other in a carpet plot fashion. To define the flight fairing, this approach was used to account, as much as possible, for variations in flight condition parameters. In a normal flight research program, a matrix of flight conditions (Mach number, angle of attack, elevon position, and body flap position) would be specified and maneuvers performed at each combination of conditions. In this manner, the effect of each flight condition parameter can be assessed independently of the other flight condition parameters. For the Orbiter, these maneuvers are included in the reentry to reduce the uncertainties of the estimates, rather than being used for research purposes to determine which parameters have given effects. Therefore, the matrix of flight conditions for the Orbiter is too sparse for full cross plotting. This inability to cross-plot because of sparseness results in a significant amount of scatter, as seen in the derivative plots.

The effects of the rotary derivatives are very small for the high-speed flight regimes. Primarily for this reason, all of the maneuvers were analyzed with the rotary derivatives set at the predicted nominal values from reference 1. Therefore at Mach numbers below 3, where the rotary derivatives begin to have some effect, any errors in the predicted rotary derivatives affect the estimates of other derivatives. The effect would appear primarily in the control derivative estimates because changes in these derivatives would best account for errors in the rotary derivatives. The effect would be unnoticeable above a Mach number of 3. The RCS yaw jet derivatives were determined throughout the entry, offering a significant set of flight data on RCS jet interference effects. The RCS pitch and roll jets were active only during the early portions of the entry. Again, note that dynamic pressure, altitude, velocity, and angles of attack and sideslip are GPC parameters from the inertial measurement unit. Errors in these parameters will result in errors in the estimated stability and control derivatives. Below Mach 2, buffet, which degrades the accuracy of the derivative estimates, was encountered.

The moments and forces due to yaw jets are so instantaneous and so large that they have a masking effect on the aerodynamic control derivatives. Better estimates of the aerodynamic control derivatives could be obtained if the RCS jets could be held to zero during the aerodynamic control surface pulse portion of the maneuver.

In addition to the potential causes of data scatter peculiar to the Space Shuttle Orbiter, reasons for error or scatter also occur in the analysis of flight data. These reasons include (1) accuracy of vehicle mass properties (mass, center-of-gravity location, and moments of inertia); (2) accuracy of instrumentation system (calibration, location, and orientation errors); (3) accuracy in data recording (data resolution, sample rate effects, and time skews); (4) accuracy of sensors (sensor error and noise); (5) size of maneuver; (6) excitation of state variables; (7) errors in mathematical models; and (8) independence of state and control variables. Some of these general errors are discussed in more detail in references 4 and 15.

A standard format is followed in figures 12 through 26. The derivatives are plotted as a function of true Mach number in the upper portion of the figures. The value of an estimate itself is represented by a symbol, and the uncertainty level (refs. 15 and 16) is represented by a vertical bar. (The larger the uncertainty level, the less reliable the estimate.) The uncertainty level is 10 times the calculated Cramér-Rao bound. A value of 10 was chosen because there was not a great deal of data, and the maneuvers were not ideal for derivative estimation. The dotted fairing on each plot represents the nominal predictions from the preflight aerodynamic data book. The solid line on each plot is the fairing of the flight-determined derivatives based on the estimates of all four groups of analysts. The lower part of the figure shows the delta values, which are the flight data value minus the flight-fairing value at that condition, plotted against true Mach number. The dashed lines (on the lower part) represent the current uncertainty bounds based on flight and prediction results.

Results of Analyses at NASA-Dryden

The stability and control derivative estimates from Space Shuttle flights STS-1 through STS-26 are presented in this subsection. For purposes of discussion, it is easiest to examine the results obtained from just one group of analysts. This approach eliminates the scatter which results from the differing estimates by various groups. In addition, use of fewer data points makes it easier to see the uncertainty level for each estimate. The flight fairing, solid line shown on figures 12 through 23, is the fairing based on the estimates of all four groups of analysts. The key NASA-Dryden results are discussed in the following sub-subsections. Then, some key results from the four groups of analysts are discussed in the Results of Analyses by All Groups subsection.

Lateral-Directional Stability and Control Derivative Estimates

Figure 12 shows the directional stability, C_{n_β}, estimated by NASA-Dryden for flights STS-1 through STS-26. In the upper part of figure 12(a), as in all figures discussed in this and the Longitudinal Results sub-subsection, the dotted line is the fairing from the preflight aerodynamic data book (ref. 1), and the solid line is the fairing based on the flight-derived estimates from all the analyst groups. Each symbol is the NASA-Dryden estimate for the PTI maneuver, and the vertical bar is the uncertainty level of the estimate for that maneuver. Estimates with small uncertainty levels are considered to be better estimates than those with large uncertainty levels. The differences between the fairing for the estimates from all groups (solid line) and the NASA-Dryden estimates are shown in the lower part of figure 12(a) as δC_{n_β}; that is, for δC_{n_β},

$$\delta C_{n_\beta} = C_{n_{\beta_{\text{flight estimate}}}} - (C_{n_{\beta_{\text{data book}}}} + C_{n_{\beta_{\text{FAD}}}}) \tag{17}$$

The dashed lines in the lower part of figure 12(a) show the flight-derived uncertainties of the derivatives. For these uncertainties to be meaningful, most of the data points should lie between the dashed lines. In particular, the data points with the small vertical bounds should be within the dashed lines.

Figure 12(b) shows only the results for Mach numbers less than 7. Showing just these estimates makes the individual estimates more clearly visible. Although the scatter in the estimates is fairly large (as discussed in the Derivative Results section), the trends indicated by the flight fairing can be clearly seen, and most of the estimates are between the flight-derived uncertainties.

Before discussing other derivatives, it may be useful to examine the reasons for some of the scatter in the estimates. The effect of the scatter for Mach number is shown in figure 12(b), for elevon position in figure 12(c), and for angle of attack in figure 12(d). Fourteen estimates for Mach numbers between 4 and 5 are plotted as a function of elevon position in figure 12(c) and as a function of angle of attack in figure 12(d). The individual points can now be located on figures 12(b), (c), and (d), and the effects of the three flight condition parameters can be examined. In addition, effects of the flight estimates and the corresponding predictions can be seen for each of these three parameters. Much of the scatter results from change in the flight condition parameter and not from randomness in the estimate.

The significant differences between flight and prediction occur between Mach 1 and 3, between Mach 5 and 6 (fig. 12(b)), and above Mach 20 (fig. 12(a)). Adjusting the flight simulator to match the flight-derived values resulted in improved harmony between the flight simulator and the vehicle, which was the primary purpose of analyzing the PTI maneuvers.

Figure 13 shows the dihedral effect, C_{l_β}, as a function of Mach number. As desired, most of the estimates of δC_{l_β} fall between the dashed lines in the lower part of figure 13. Cross-plotting C_{l_β} as a function of elevon position and angle of attack yields results similar to those for C_{n_β}. (These plots are not shown here.) The most significant difference between flight and prediction is that the flight values show a 40- to 50-percent reduction in the magnitude of C_{l_β} for Mach numbers above 15.

Figure 14 shows the comparison of flight and prediction for roll control power, $C_{l_{\delta_a}}$. Once again, the estimates of $\delta C_{l_{\delta_a}}$ fall between the dashed lines in the lower part of figure 14(a). A 10- to 20-percent reduction occurred for flight to prediction between Mach 5 and 13 and between Mach 18 and 22. The reduction in effectiveness between Mach 18 and 22 is actually an effect of elevon position, which can be seen in figure 14(b). The reduced effectiveness is a result of the effect of up elevon position between 2° and 4°.

Figure 15 shows the coefficient of side force due to two yaw jets, $C_{Y_{\mathrm{YJ}_2}}$, as a function of mass flow ratio, $\dot{M}_J/\dot{M}_\infty$. The importance of the yaw jets was discussed in the Orbiter Stability and Control Example section and is also discussed extensively in references 13 and 17. Good agreement exists between flight and prediction for this derivative. The importance of considering the uncertainty levels is illustrated by the large scatter of those estimates with large uncertainty levels. Most of the $\delta C_{Y_{\mathrm{YJ}_2}}$ points lying outside the dashed line in the lower part of the figure have large uncertainty levels.

Figure 16 shows the coefficient of rolling moment due to two yaw jets, $C_{l_{\mathrm{YJ}_2}}$, as a function of mass flow ratio, $\dot{M}_J/\dot{M}_\infty$. The large difference between flight and prediction at high mass flow ratios is the same effect shown for L_{YJ} at high Mach numbers in the Orbiter Stability and Control Example section in figure 6. After the flight fairing is subtracted from the estimates, all of the resulting $\delta C_{l_{\mathrm{YJ}_2}}$ values fall between the dashed uncertainty bounds on the lower part of the figure.

Figure 17 shows the effect of four yaw jets firing on the rolling moment, $C_{l_{\mathrm{YJ}_4}}$, plotted as a function of mass flow ratio, $\dot{M}_J/\dot{M}_\infty$. The discrepancy between flight and prediction at high mass flow ratios is significant but not as large as the discrepancy for two yaw jets firing (fig. 16). The resulting $\delta C_{l_{\mathrm{YJ}_4}}$ values lie well within the flight-derived uncertainties. The lower flight estimates of $C_{l_{\mathrm{YJ}_4}}$ at values of $\dot{M}_J/\dot{M}_\infty$ between 0.002 and 0.001 (corresponding to a Mach number between 5 and 10) were not seen for $C_{l_{\mathrm{YJ}_2}}$. The difference between the effect on rolling moment of two and four yaw jets ($C_{l_{\mathrm{YJ}_2}}$ and $C_{l_{\mathrm{YJ}_4}}$) was not predicted. As a result, this effect and a similar effect on C_Y and C_n for yaw jet firings had to be added to the Orbiter mathematical model. This new parameter can be defined in the same manner as the rest of the FAD, but this effect was one of several found in flight that was best implemented as changes in the form of the mathematical model of the Orbiter rather than as an incremental change in just the values of the stability and control derivatives.

Figure 18 shows the coefficient of rolling moment due to roll jets, $C_{l_{\mathrm{RJ}}}$, as a function of the jet momentum ratio, ϕ_J/ϕ_∞. The change in the values of the jet momentum ratio is small because the roll jets only operate at dynamic pressures below 10 lb/ft^2. The faired flight value of $C_{l_{\mathrm{RJ}}}$ is essentially double that of the prediction.

Longitudinal Results

This sub-subsection discusses the results of the NASA-Dryden analysis for the longitudinal PTI maneuvers. Figure 19 shows the longitudinal stability term, C_{m_α}, as a function of Mach number. The flight data confirm the prediction throughout most of the range. Most of the δC_{m_α} values with small uncertainties are between the dashed lines on the lower part of this figure. A disappointingly large amount of scatter exists for this important and usually easily extracted parameter. Some of the scatter was caused by the effects of the other flight condition parameters. However, still more scatter exists than would normally occur. A major cause of the unusually high scatter is the extremely low sample rate of 1 sample/sec for angle of attack. (See the list of instrumentation properties in the Flight Data Measurements subsection.) The effect of the low sample rate is compounded by the associated unknown sample lags and the rolling time skews. Until higher sample rate data are obtained, the estimates of C_{m_α} will not improve (ref. 7).

Figures 20 and 21 show the coefficients of pitching moment due to elevon position, δ_e, and elevon position squared, δ_e^2, respectively, or $C_{m_{\delta_{e_0}}}$ and $C_{m_{\delta_e^2}}$. The original model included only $C_{m_{\delta_e}}$ effects because $C_{m_{\delta_e^2}}$ effects were assumed to be negligible. These maneuvers could not be successfully analyzed with only the $C_{m_{\delta_e}}$ term, so $C_{m_{\delta_e^2}}$ was added. Then, the results of the analysis with the added $C_{m_{\delta_e^2}}$ term compared favorably with the original predictions (ref. 7). Figures 20 and 21 show the flight-derived values of $C_{m_{\delta_{e_0}}}$ and $C_{m_{\delta_e^2}}$; however, because of the original assumptions, there are no predictions for $C_{m_{\delta_e^2}}$ on figure 21(a). To check this effect on the predicted model, the nonlinear curve, $C_{m_{\delta_{e_0}}}\delta_e + C_{m_{\delta_e^2}}\delta_e^2$ (determined from flight), must be compared with the aerodynamic data book values. This comparison was made. The flight values were consistent with prediction; therefore, no FAD update was needed for C_m due to δ_e.

Figure 22 shows the pitching moment due to two yaw jets firing, $C_{m_{\mathrm{YJ}_2}}$, as a function of mass flow ratio, $\dot{M}_J/\dot{M}_\infty$. The flight value is lower than the prediction above $\dot{M}_J/\dot{M}_\infty$ of 0.0005. The flight values are essentially zero at mass flow ratios below 0.01.

Figure 23 shows the coefficient of pitching moment due to down-firing jets, $C_{m_{\mathrm{DJ}}}$, as a function of momentum ratio, ϕ_J/ϕ_∞. The values found throughout the range of momentum ratios tested were 50 percent more negative than those predicted. The down-firing jets operate only below a dynamic pressure of 40 lb/ft^2. All of the points with small uncertainty for two down-firing jets firing occur within the uncertainty bounds for $\delta C_{m_{\mathrm{DJ}}}$. This result shows, once again, the value of considering the uncertainty level when assessing the flight-derived values.

Results of Analyses by All Groups

This subsection describes the results of analyses by all four groups. Because results from all four groups of analysts were included, the number of points increased greatly, and the uncertainty levels (the vertical bars in figures 12 through 23) are not included on the figures. Some of the results presented here were also presented in the Results of Analyses at NASA-Dryden subsection.

Programmed Test Input Estimates

Only the three derivatives presented in figures 24, 25, and 26 are discussed in this sub-subsection. In the cases of the other derivatives discussed in the Results of Analyses at NASA-Dryden subsection, similar results were obtained by the four analyst groups.

Figure 24 shows C_{n_β} as a function of Mach number for all the PTI maneuvers as determined by the four sets of analysts. These flight and prediction fairings are the same as those used in figure 12(a). The same analysis and cross plotting were used to assess the contributions of Mach number, elevon position, angle of attack, and body flap position to the estimates of C_{n_β}. As can be seen in the lower part of figure 24, most points fall inside the uncertainty bounds. Flight-derived C_{n_β} estimates were used to formulate FAD–26. This use improved the fidelity between the flight data and the simulator. The reduction of uncertainty shown in FAD–26 allowed an expanded Space Shuttle Orbiter flight envelope.

Figure 25 shows the variation of $C_{l_{\delta_a}}$ with Mach number and elevon position, δ_e. The estimates from all groups of analysts cluster fairly well near those estimated by NASA-Dryden (fig. 14). This clustering shows how strongly this derivative is defined by the PTI maneuvers. The strong dependence of $C_{l_{\delta_a}}$ on elevon position is, once again, shown in figure 25(b). Few of the estimates fall outside the uncertainty bounds for this derivative, which reduced the overall uncertainty for this extremely important control derivative. This reduction in uncertainty improved the overall robustness of the Orbiter control system.

Figure 26 shows the results from all of the analyst groups for $C_{l_{\mathrm{YJ}_2}}$ as a function of mass flow ratio, $\dot{M}_J/\dot{M}_\infty$. The same strong trend is shown here, at high mass flow ratios, as was seen in the NASA-Dryden analysis (fig. 16). As shown in the lower half of the figure, virtually all of the data from all the analyst groups fall between the uncertainty bounds at the high mass flow ratios. These results indicate the preponderance of evidence that reduced the uncertainty in $C_{l_{\mathrm{YJ}_2}}$.

Flight Assessment Deltas-Only Results

Figure 27 presents the remainder of the flight assessment deltas which were changed between FAD–14 and FAD–26 and which have not been previously discussed. The differences (or deltas) discussed here, such as ΔC_{Y_β} (fig. 27(a)), are the increments added to the preflight aerodynamic data book values to get the current best representation of the flight-derived stability and control derivatives. These data are presented as a function of the Mach number, mass flow ratio, or momentum ratio. These data are taken from reference 18. These figures show that the flight analyses have resulted in significant changes from the original predictions for many of the derivatives and their associated uncertainties. In addition, these changes continued to be made well into the flight program, as more flight data were obtained after FAD–14, between STS-14 and STS-26. The changes most significant to the Space Shuttle Orbiter envelope expansion (and not discussed before) were the changes in $C_{n_{\delta_a}}$, $C_{n_{\delta_r}}$, $C_{l_{\delta_r}}$, and $C_{m_{\mathrm{BF}}}$. Results of the FAD for these parameters (and all parameters discussed previously) have resulted in improved harmony between the flight simulation and the flight vehicle.

To assess the effectiveness of the determination of the stability and control derivatives from the Orbiter flight data, it is instructive to examine the case of an important derivative, looking at the changes in the derivative as a function of the FAD number. Such a derivative is directional stability, C_{n_β}, for which ΔC_{n_β} from a number of FAD's is plotted against Mach number (fig. 28). The ΔC_{n_β} fairing for FAD–2 was positive from Mach 1 to Mach 3, negative from Mach 3 to Mach 7, positive from Mach 7 to Mach 13, and negative (and small) above Mach 13. Each succeeding FAD showed the same general pattern of positive and negative increments. However, the size of the increment and the Mach number "switch points" were modified in each succeeding FAD, as increased numbers of maneuvers were analyzed. As can be seen, the refinement in the FAD's is an iterative process with each successive FAD adding more smoothness to ΔC_{n_β}. In FAD–26, ΔC_{n_β} is a fairly smooth curve, with smaller changes in the positive and negative increments as compared with earlier versions. This refinement shows the value of having more PTI maneuvers at a wide variety of flight conditions.

Figure 29 is a final illustration of the value of the FAD for improving the estimated value of a derivative and reducing the overall uncertainty range of a derivative. The ΔC_{l_β} is shown with its associated flight-derived uncertainty for FAD–26. The original preflight aerodynamic data book variation for C_{l_β} is also shown. It can be seen that more maneuvers improve the estimates of the derivative and reduce the flight-derived uncertainty. Although the change in the derivative is quite substantial hypersonically, particularly above Mach 16, the uncertainty in that region is reduced to 40 percent of the original, preoperational variation. The combination of the estimate improvement and the uncertainty reduction has a substantial effect on the operational envelope of the vehicle. This fact, coupled with the associated improved robustness of the control system, adds markedly to the overall safety margin of the Space Shuttle Orbiter reentry. A further discussion of related Space Shuttle issues is found in reference 19.

CENTER-OF-PRESSURE LOCATION

The STS-1 showed that significantly more body flap deflection was required to trim the vehicle hypersonically at an angle of attack of 40° than was predicted, as shown in figure 30 (ref. 14). During entry, the Space Shuttle is preprogrammed to fly at a given angle of attack for each Mach number. Because the angle of attack is maintained by setting the elevon at a position scheduled by angle of attack and Mach number, the body flap is deflected to maintain that angle of attack. To maintain 40° angle of attack hypersonically on STS-1, the body flap was deflected to 16° instead of the predicted 7°. Because 9° more body flap deflection than predicted was required, the body flap experienced more heating than predicted. The misprediction also resulted in the body flap being deflected to within 5° of its maximum deflection to trim the vehicle. In addition, increases in deflection of the body flap increase drag. This increased drag reduces the cross-range capability.

To examine this misprediction of body flap trim position, the location of the center of pressure was investigated. Figure 31 shows a comparison between flight and predicted locations of the center of pressure plotted as a function of Mach number for STS-2 (ref. 20). Variations for the prediction are also shown. These flight data were well outside of the predicted variations. Above Mach 16, the misprediction is about 0.8 percent of the body length, or 10 in. The error must be due to a misprediction of pitching moment, a misprediction of normal force, or an error in the location of the flight center of gravity. Error in the flight center-of-gravity position was less than 1 in. Also, the normal force predictions and flight values agreed fairly well; therefore, almost all of this 10-in. error was caused by a misprediction in the pitching moment. For the Space Shuttle, the pitching moment is a function of coefficients of pitching moment due to angle of attack (C_{m_α}), pitching moment due to elevon deflection ($C_{m_{\delta_e}}$), pitching moment due to body flap deflection ($C_{m_{\text{BF}}}$), and pitching moment bias (C_{m_0}) at a given Mach number and angle of attack.

Figure 19 shows the flight-derived estimates of C_{m_α}, figure 20 shows $C_{m_{\delta_e}}$, and figure 27(q) shows $C_{m_{\text{BF}}}$ for the Space Shuttle flights through STS-26. Above Mach 16, the predictions and flight estimates agree well for these three derivatives. Thus, the error in body flap deflection required for trim is attributable to C_{m_0}. The error in C_{m_0} that would account for the discrepancy shown in figure 31 would be about 0.03 nose up. An error in C_{m_0} up to about 0.020 to 0.025 can be attributed to the real gas effects and Mach number effects. Neither effect was completely simulated in wind tunnels (refs. 21 and 22).

Between Mach 16 and 8, the center-of-pressure position misprediction went from 0.8 percent to less than 0.1 percent (fig. 31). Real gas effects become less important as the Mach number decreases. Some of the error in center-of-pressure location prediction between Mach 16 and 8 may be attributed to the misprediction in boundary-layer transition (refs. 23 and 24). Preflight predictions indicated that boundary-layer transition would start to occur at Mach 16, but the flight data indicated that the boundary layer transitions quickly at about Mach 8. This delayed transition may also affect some of the stability and control derivatives. The real gas effects, the delayed boundary-layer transition, and the rolling moment due to yaw jets ($C_{l_{\text{YJ}}}$) are the three phenomena observed in flight for the Space Shuttle Orbiter which are of most general research interest at this time.

CONCLUDING REMARKS

The goal of expanding the operational flight envelope of the Space Shuttle Orbiter was achieved, but the approach used to do so clouded some of the research value of the results. The extraction of the stability and control derivatives was justified by operational, not research, considerations. Still, the discussion in this paper shows that there have been some significant research results. However, using flight results to update the predicted database of the Orbiter is one of the most completely documented processes for any flight vehicle. Such thorough documentation processes followed from the requirement for analysis of flight data for control system updates and for expansion of the operational flight envelope.

The flight-derived stability and control derivative results described here document the outcome of this important process. These results show significant changes in many important stability and control derivatives from the preflight database. The process has also shown why the knowledge of the stability and control derivatives improves with the number of flights. The most interesting aerodynamic research results were the real gas effects which resulted in a 10-in. misprediction of the center-of-pressure location, the delay in boundary-layer transition from Mach 15 to 8, and the interference effects of the rolling moment due to the firing of the yaw jets.

REFERENCES

1. *Aerodynamic Design Data Book Orbiter Vehicle STS-1*, SD72-5H-0060 revision M, Rockwell International, Space Division, Nov. 1980.

2. Weil, Joseph and Bruce G. Powers, *Correlation of Predicted and Flight Derived Stability and Control Derivatives—With Particular Application to Tailless Delta Wing Configurations*, NASA TM-81361, July 1981.

3. Iliff, Kenneth W., "AIAA Dryden Research Lectureship—Aircraft Parameter Estimation," AIAA-87-0623, Jan. 1987.

4. Maine, Richard E. and Kenneth W. Iliff, *Application of Parameter Estimation to Aircraft Stability and Control—The Output-Error Approach*, NASA RP-1168, 1986.

5. Throckmorton, David A., "Shuttle Entry Aerothermodynamic Flight Research: The Orbiter Experiments (OEX) Program," AIAA 92-3987, July 1992.

6. Iliff, Kenneth W., Richard E. Maine, and Douglas R. Cooke, "Selected Stability and Control Derivatives From the First Space Shuttle Entry," AIAA 81-2451, Nov. 1981.

7. Maine, R.E. and K.W. Iliff, "Selected Stability and Control Derivatives From the First Three Space Shuttle Entries," AIAA 82-1318, Aug. 1982.

8. Balakrishnan, A.V., *Communication Theory*, McGraw-Hill, New York, 1968.

9. Maine, Richard E. and Kenneth W. Iliff, *Identification of Dynamic Systems*, NASA RP-1138, 1985.

10. Iliff, Kenneth W. and Richard E. Maine, "More Than You May Want To Know About Maximum Likelihood Estimation," AIAA 84-2070-CP, Aug. 1984. (See also NASA TM-85905, 1985.)

11. Cooke, Douglas R., "Minimum Testing of the Space Shuttle Orbiter for Stability and Control Derivatives," *Shuttle Performance: Lessons Learned*, NASA CP-2283, pt. 1, Mar. 1983, pp. 447–471.

12. Maine, Richard E. and Kenneth W. Iliff, *User's Manual for MMLE3, A General FORTRAN Program for Maximum Likelihood Parameter Estimation*, NASA TP-1563, 1980.

13. Stone, J.S., J.J. Baumbach, and B.B. Roberts, "Space Shuttle Orbiter Reaction Control Subsystem Flight Data Anomalies," *Shuttle Performance: Lessons Learned*, NASA CP-2283, pt. 1, Mar. 1983, pp. 381–395.

14. Kirsten, Paul W., David F. Richardson, and Charles M. Wilson, "Predicted and Flight Test Results of the Performance, Stability and Control of the Space Shuttle From Reentry to Landing," *Shuttle Performance: Lessons Learned*, NASA CP-2283, pt. 1, Mar. 1983, pp. 509–524.

15. Iliff, Kenneth W., Richard E. Maine, and T.D. Montgomery, *Important Factors in the Maximum Likelihood Analysis of Flight Test Maneuvers*, NASA TP-1459, 1979.

16. Iliff, Kenneth W., "Aircraft Identification Experience, *Parameter Identification*, AGARD-LS-104, paper 6, 29 Oct.–2 Nov. 1979.

17. Scallion, W.I. et al., "Space Shuttle Third Flight (STS-3) Entry RCS Analysis," AIAA 83-0116, Jan. 1983.

18. *Flight Assessment Package Orbiter Aerodynamics: FAD26*, NASA JSC-22078, Apr. 1986.

19. *Shuttle Performance: Lessons Learned*, NASA CP-2283, pts. 1 and 2, 1983.

20. Romere, Paul O. and A. Miles Whitnah, "Space Shuttle Entry Longitudinal Aerodynamic Comparisons of Flights 1–4 With Preflight Predictions," *Shuttle Performance: Lessons Learned*, NASA CP-2283, pt. 1, 1983, pp. 283–307.

21. Griffith, B.J., J.R. Maus, and J.T. Best, "Explanation of the Hypersonic Longitudinal Stability Problem—Lessons Learned," *Shuttle Performance: Lessons Learned*, NASA CP-2283, pt. 1, 1983, pp. 347–380.

22. Woods, W.C., J.P. Arrington, and H.H. Hamilton, II, "A Review of Preflight Estimates of Real-Gas Effects on Space Shuttle Aerodynamic Characterisitics," *Shuttle Performance: Lessons Learned*, NASA CP-2283, pt. 1, 1983, pp. 309–346.

23. Iliff, Kenneth W. and Mary F. Shafer, "Space Shuttle Hypersonic Flight Research and the Comparison to Ground Test Results (Invited)," AIAA-92-3988, July 1992.

24. Harthun, M.H., C.B. Blumer, and B.A. Miller, "Orbiter Windward Surface Entry Heating: Post-Orbital Flight Test Program Update," *Shuttle Performance: Lessons Learned*, NASA CP-2283, pt. 2, 1983, pp. 781–804.

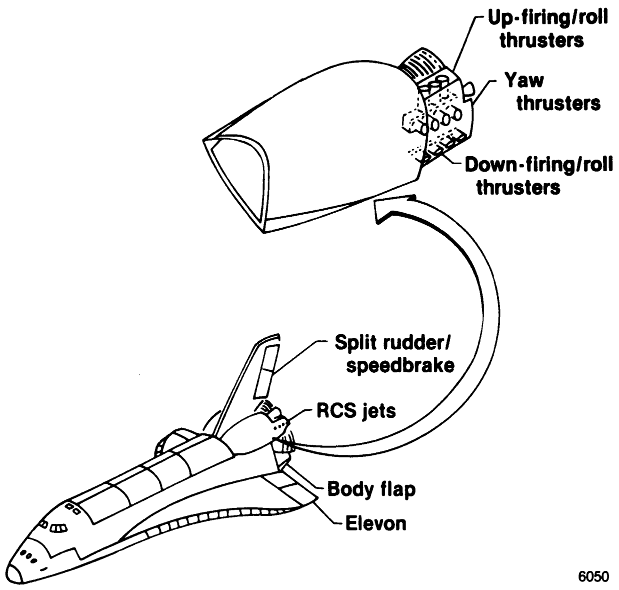

Figure 1. Space Shuttle Orbiter configuration.

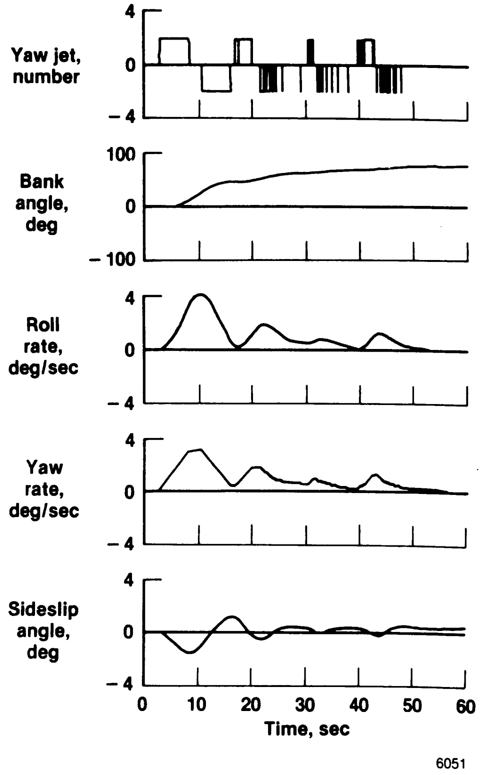

Figure 2. Predicted STS-1 bank maneuver at $V = 24,300$ ft/sec.

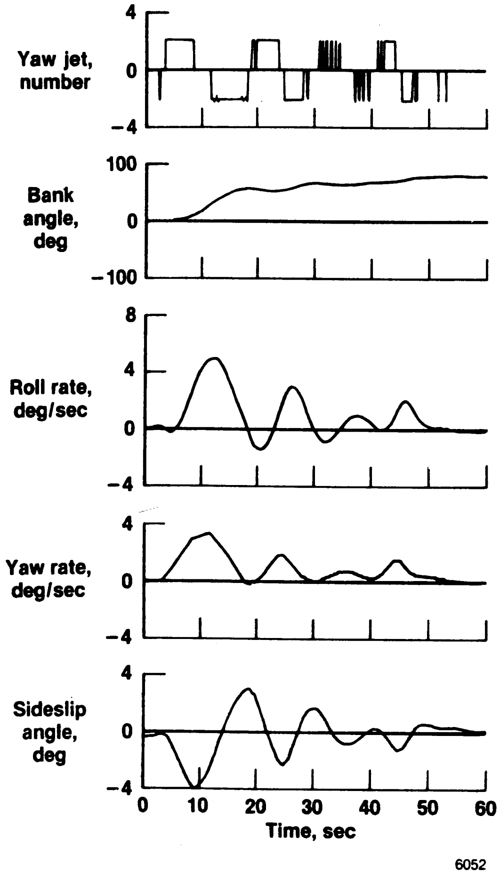

Figure 3. Actual STS-1 bank maneuver at $V = 24,300$ ft/sec.

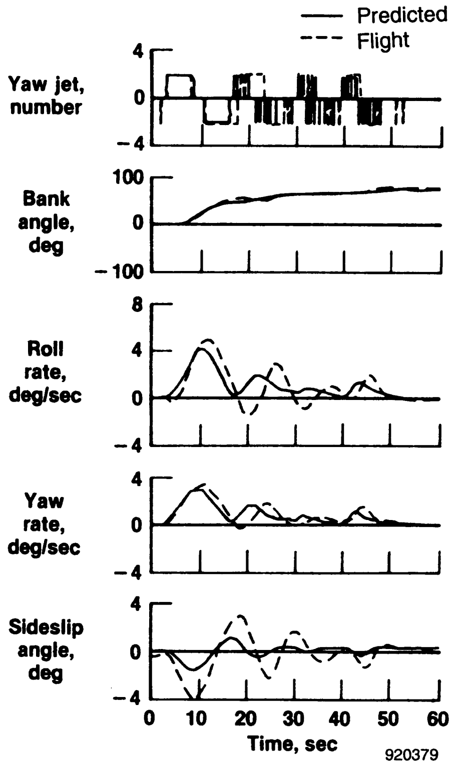

Figure 4. Comparison of actual and predicted STS-1 bank maneuver at $V = 24,300$ ft/sec.

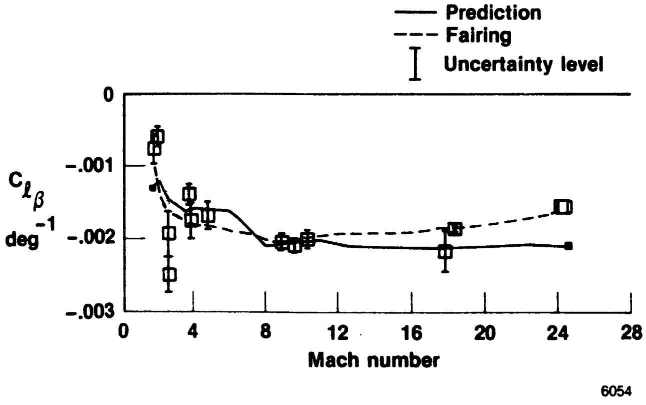

Figure 5. Estimates of C_{l_β} for the Space Shuttle Orbiter.

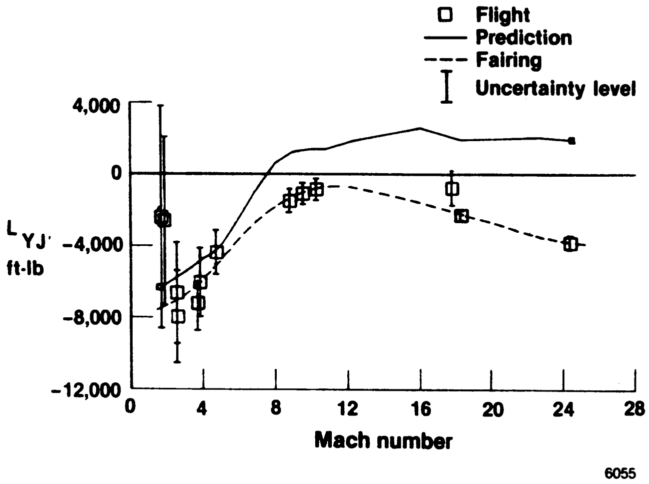

Figure 6. Estimates of L_{YJ} for the Space Shuttle Orbiter.

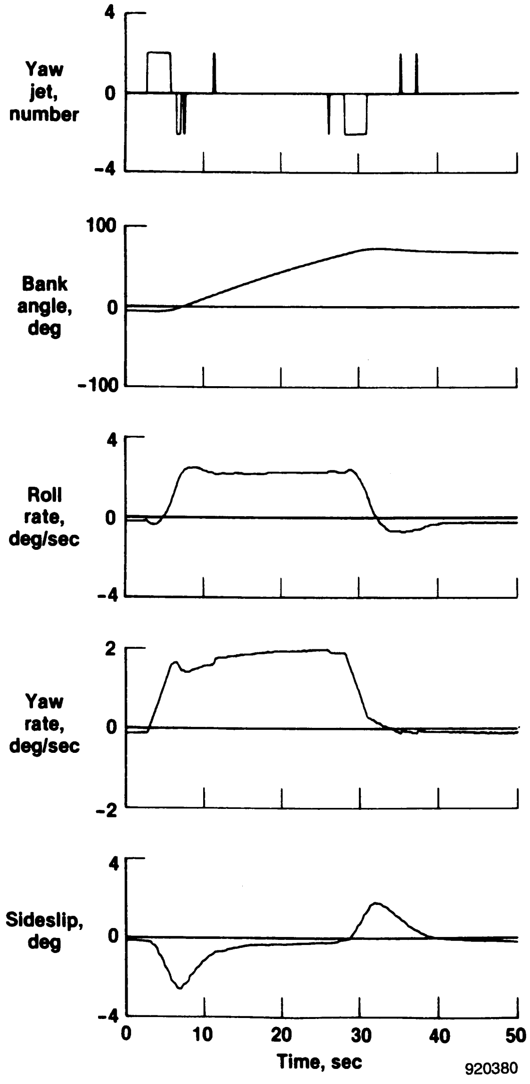

Figure 7. Comparison of simulated bank maneuver with L_{YJ} at a flight-estimated value with the actual STS-1 bank maneuver.

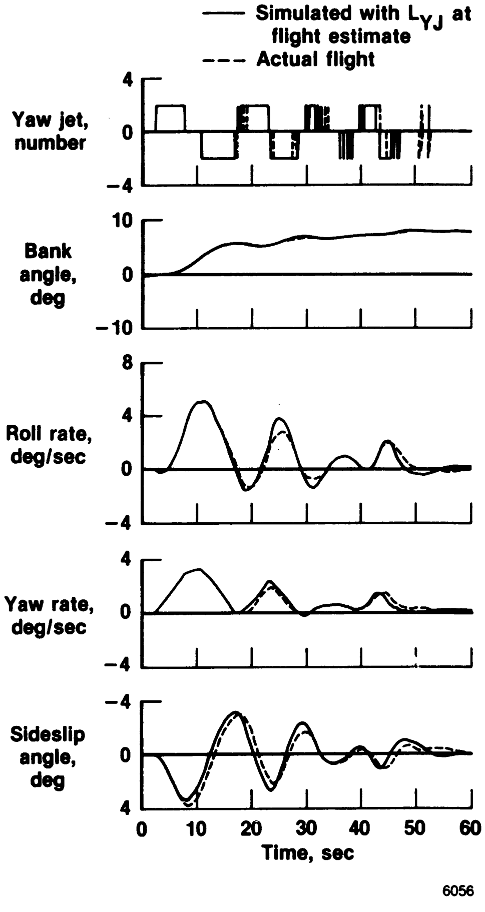

Figure 8. Manual bank maneuver at $V = 24,000$ ft/sec from STS-2.

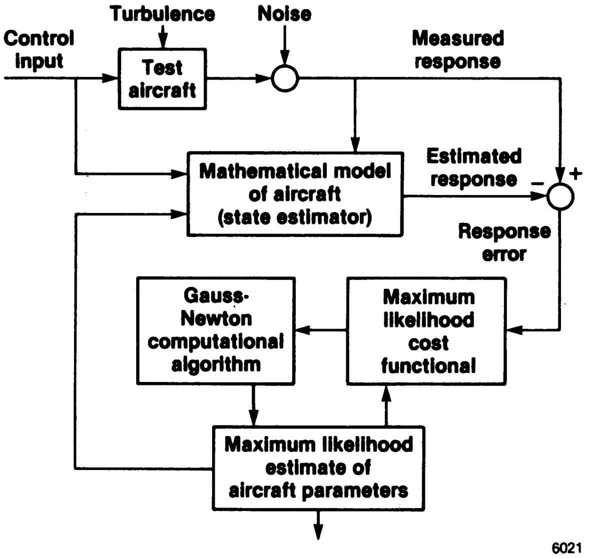
Turbulence
Noise
Control input
Test aircraft
Measured response
Mathematical model of aircraft (state estimator)
Estimated response
–
+
Response error
Gauss-Newton computational algorithm
Maximum likelihood cost functional
Maximum likelihood estimate of aircraft parameters
6021

Figure 9. Maximum likelihood estimation concept.

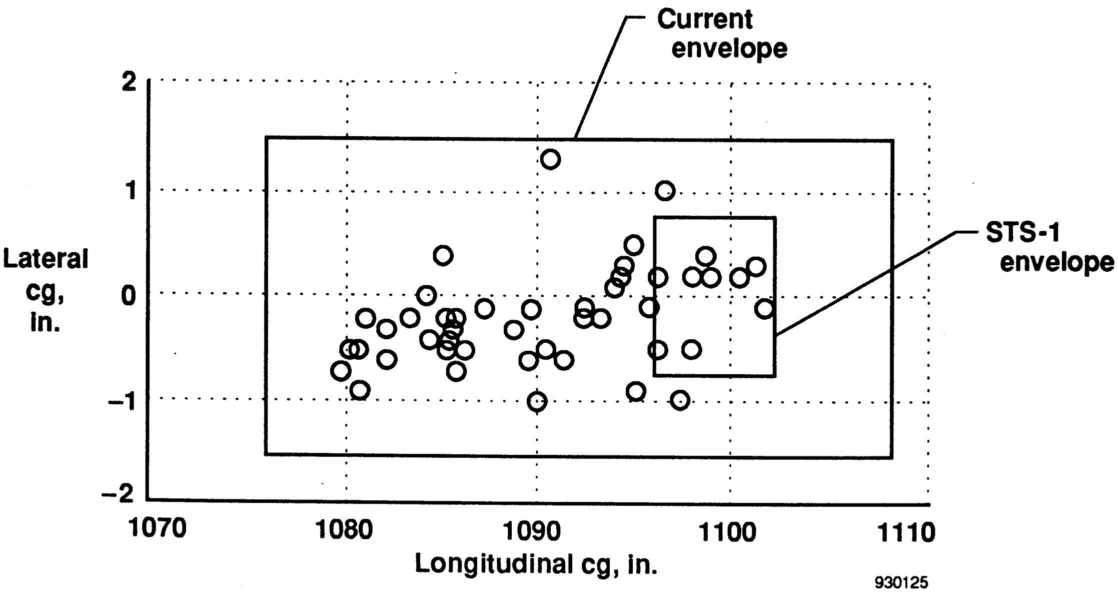

Figure 10. Orbiter center of gravity at entry interface (400,000 ft).

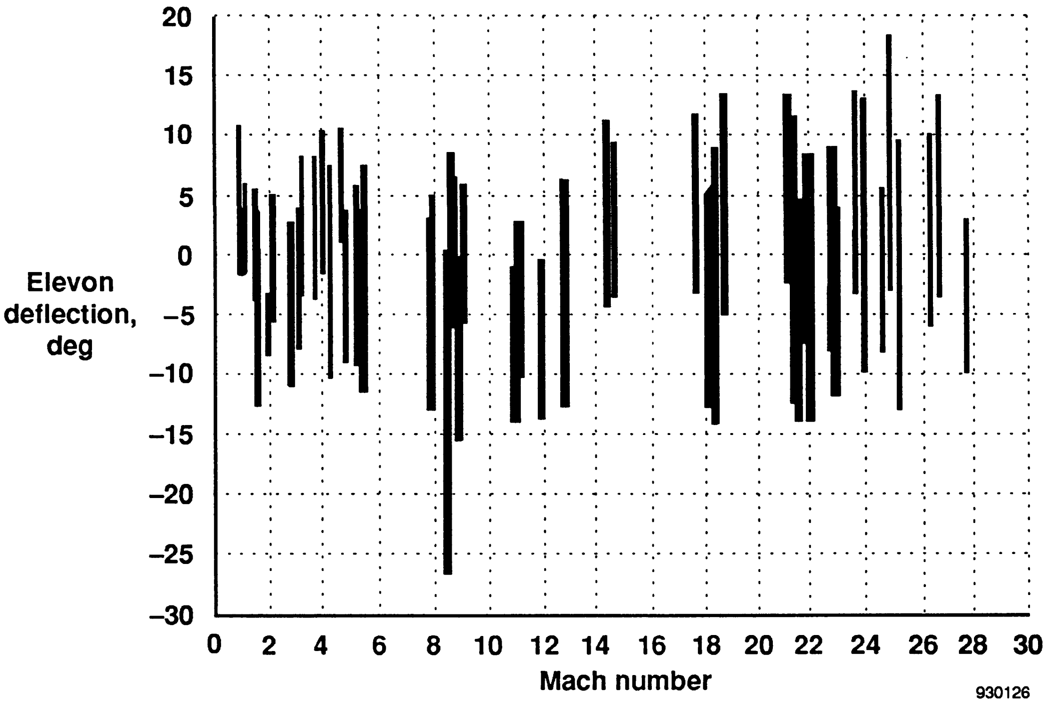

(a) Elevon deflection.

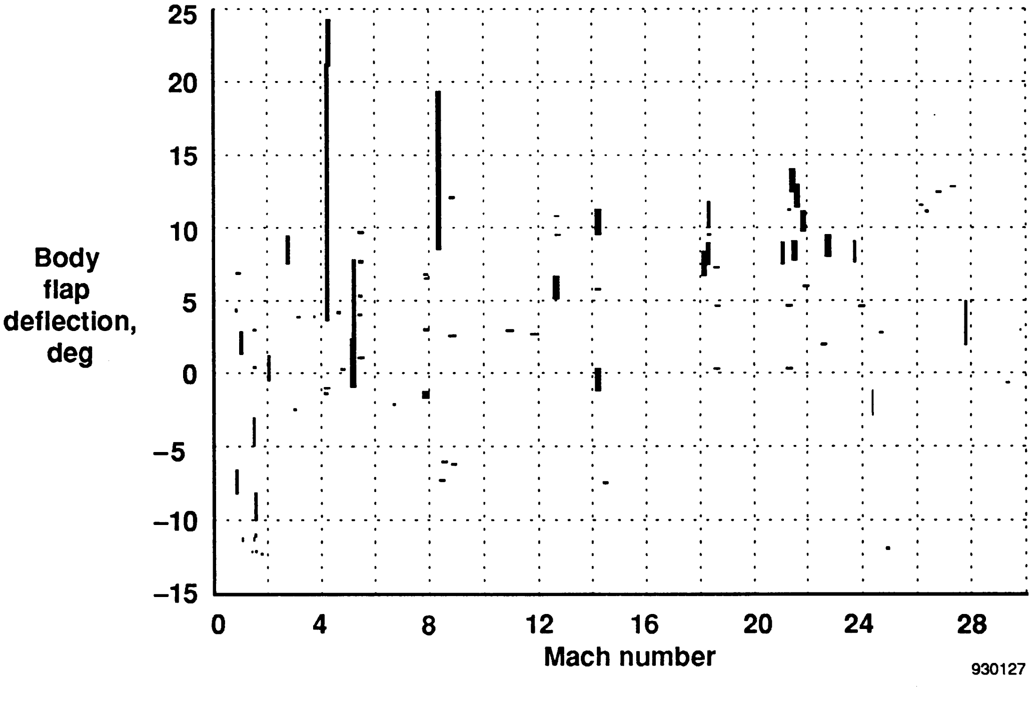

(b) Body flap deflection.

Figure 11. Variations of elevon deflection, body flap deflection, and angle of attack as a function of Mach number.

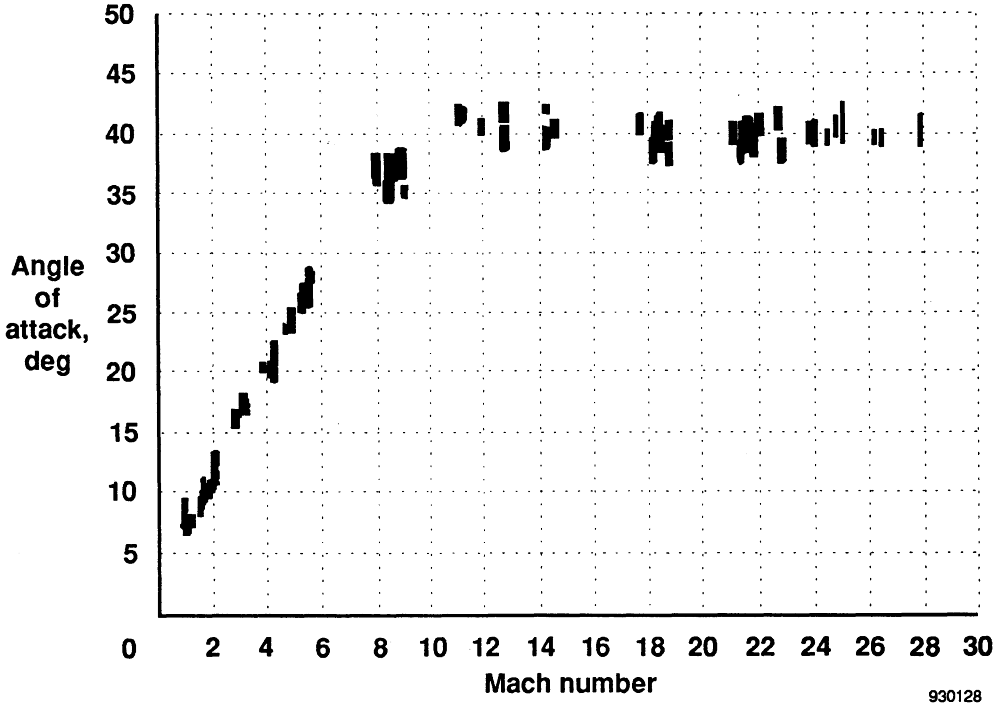

(c) Angle of attack.

Figure 11.Concluded.

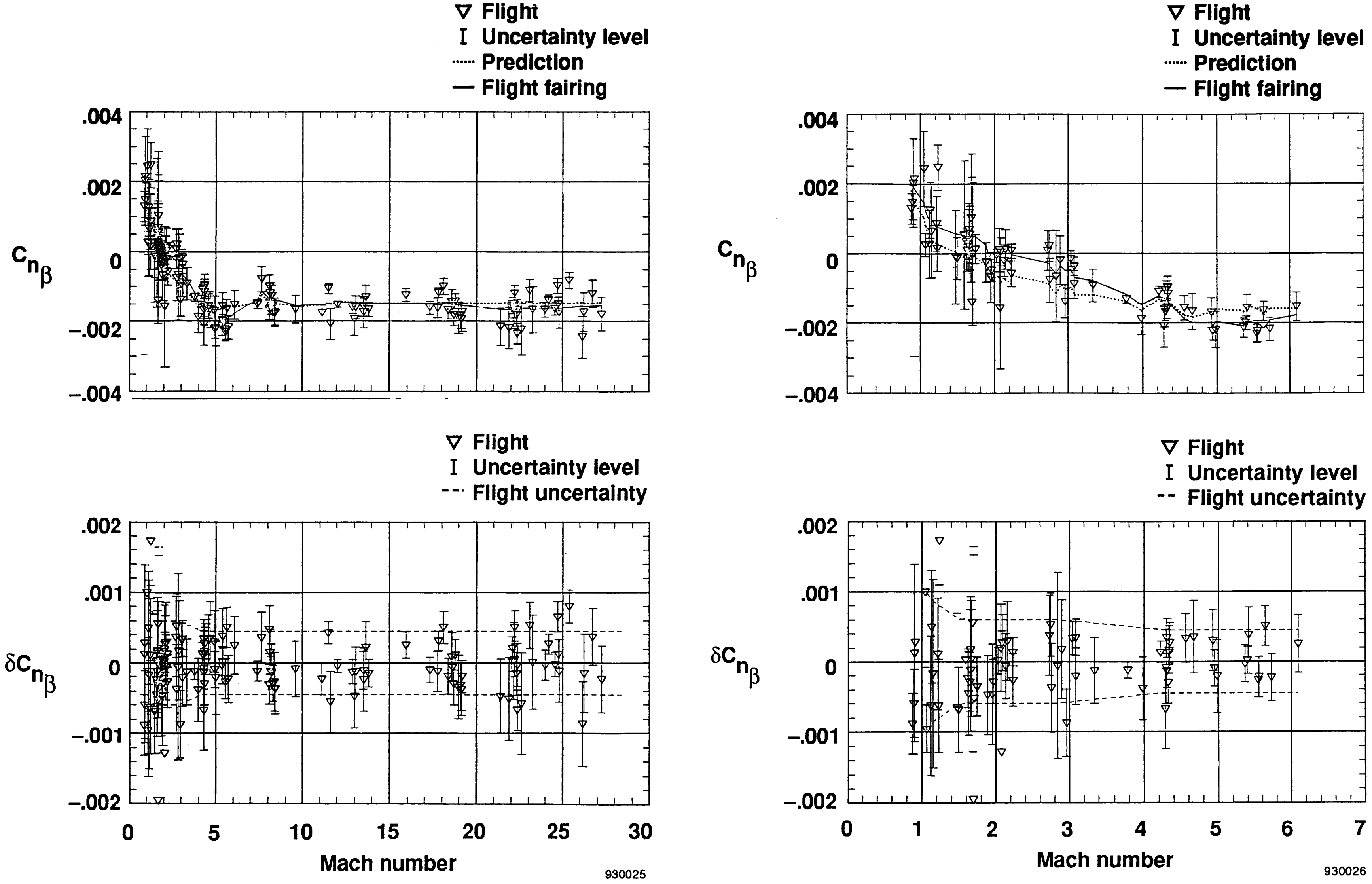

(a) The C_{n_β} and δC_{n_β} as a function of Mach number.

(b) The C_{n_β} and δC_{n_β} as a function of Mach number, $M \leq 7$.

Figure 12. Directional stability, C_{n_β}.

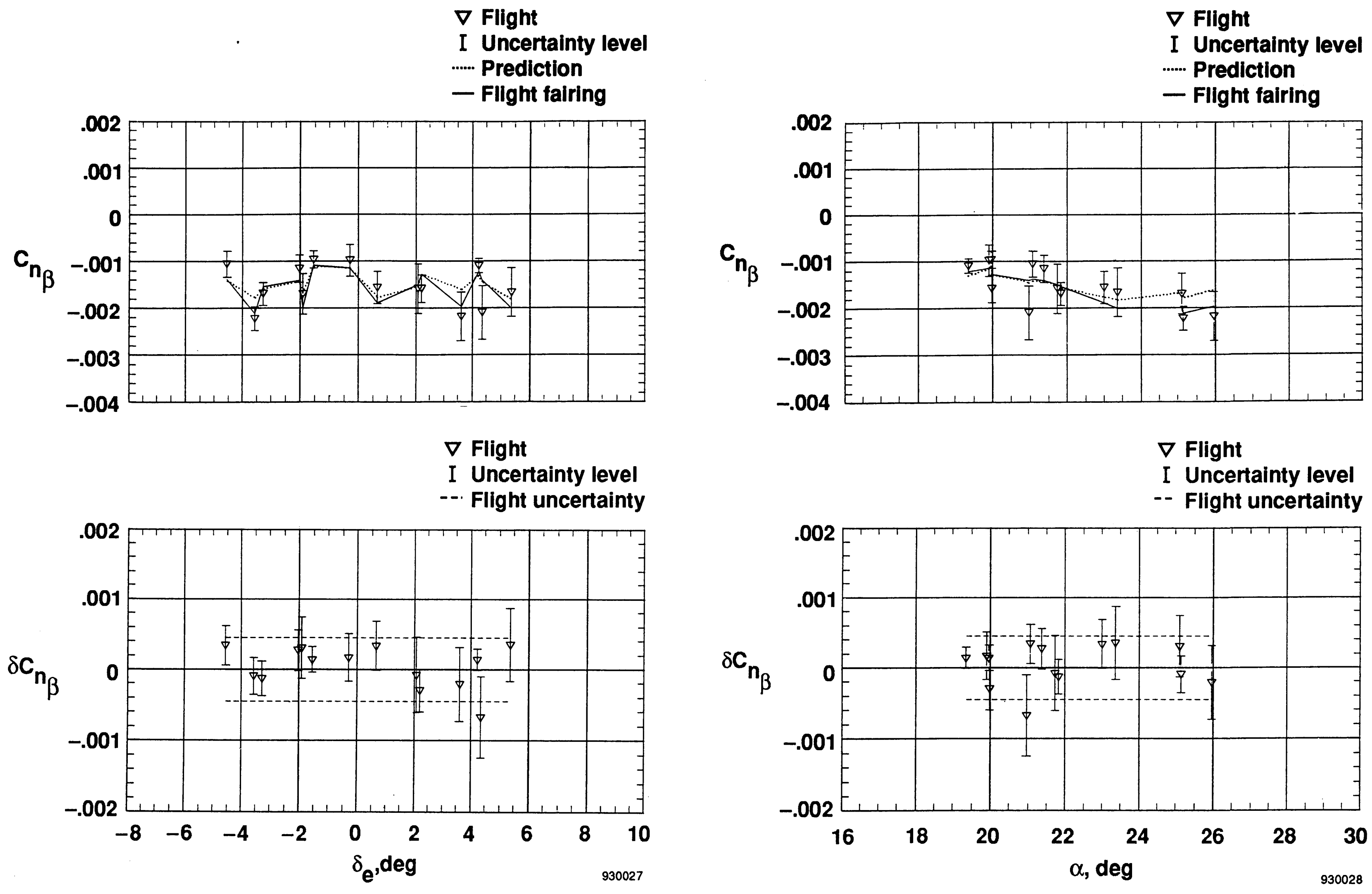

(c) The C_{n_β} and δC_{n_β} as a function of elevon position, δ_e, $4 \leq M \leq 5$.

(d) The C_{n_β} and δC_{n_β} as a function of α, $4 \leq M \leq 5$.

Figure 12. Concluded.

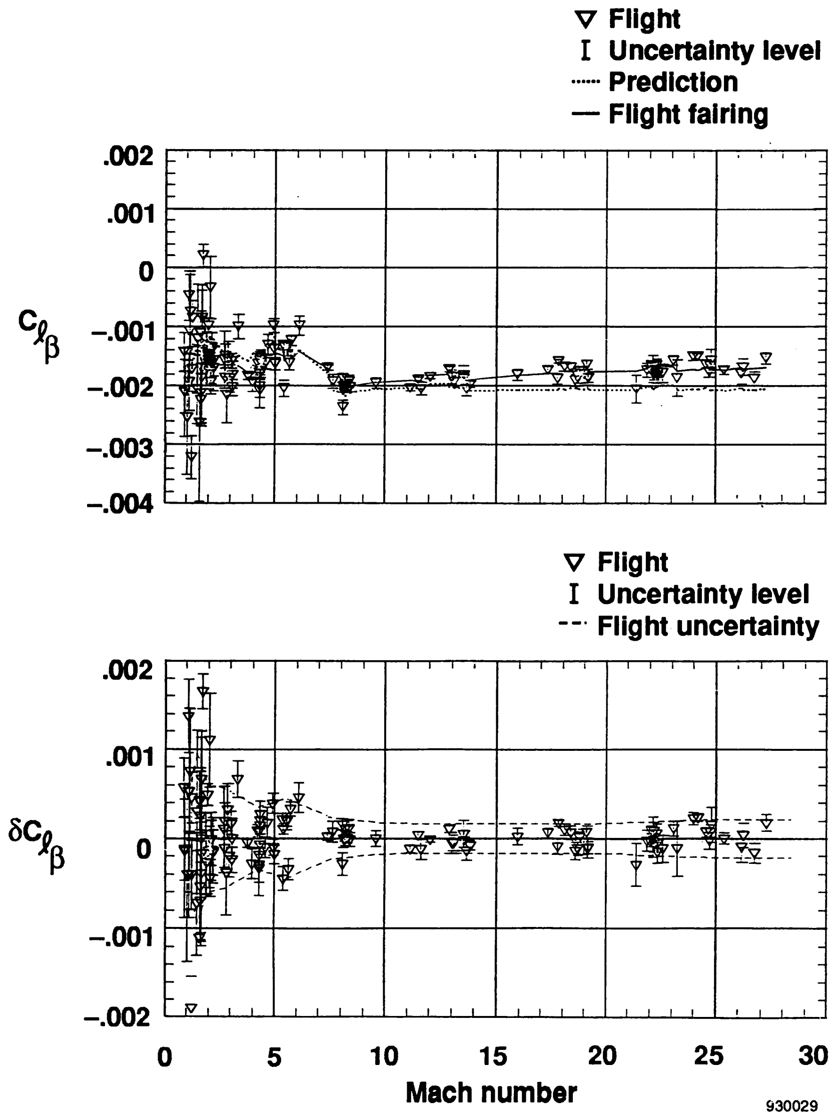

Figure 13. Dihedral effect, C_{l_β}, as a function of Mach number.

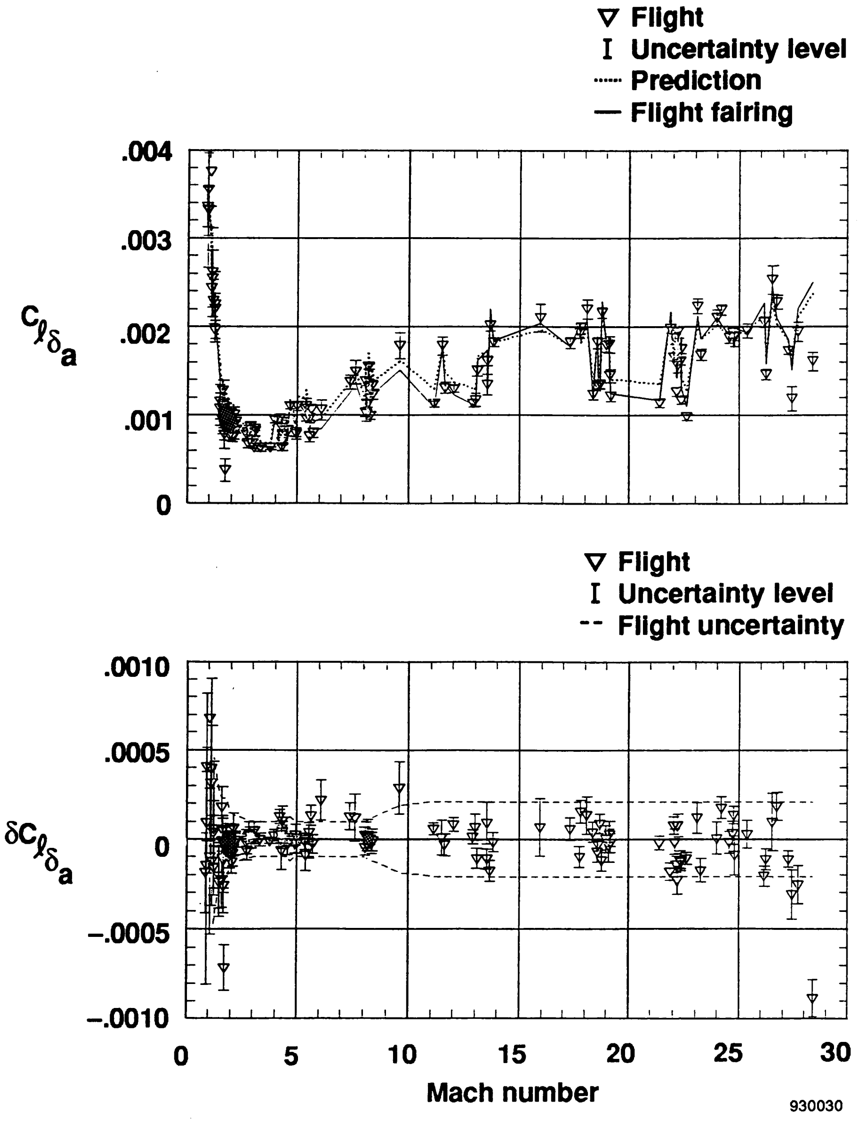

(a) The $C_{l_{\delta_a}}$ and $\delta C_{l_{\delta_a}}$ as a function of Mach number.

Figure 14. Roll control power, $C_{l_{\delta_a}}$.

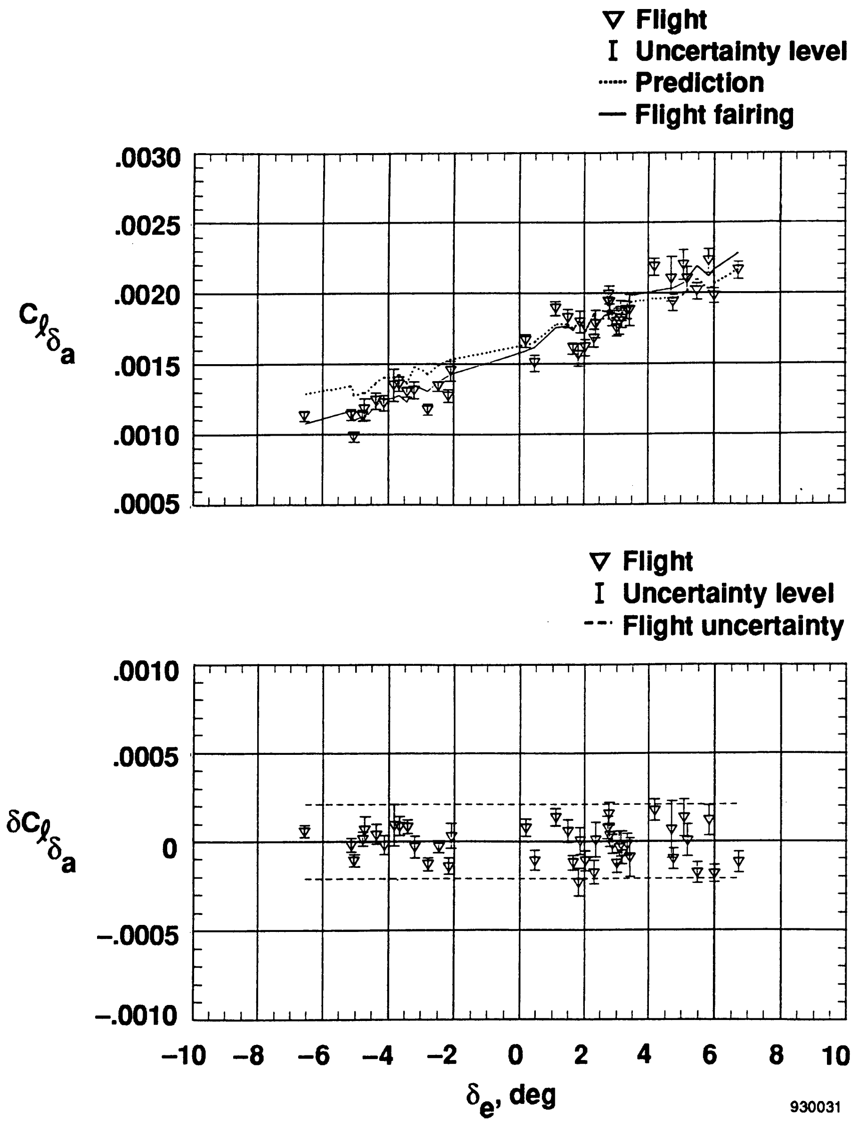

(b) The $C_{l_{\delta_a}}$ and $\delta C_{l_{\delta_a}}$ as a function of elevon position, δ_e, $10 \leq M \leq 25$.

Figure 14. Concluded.

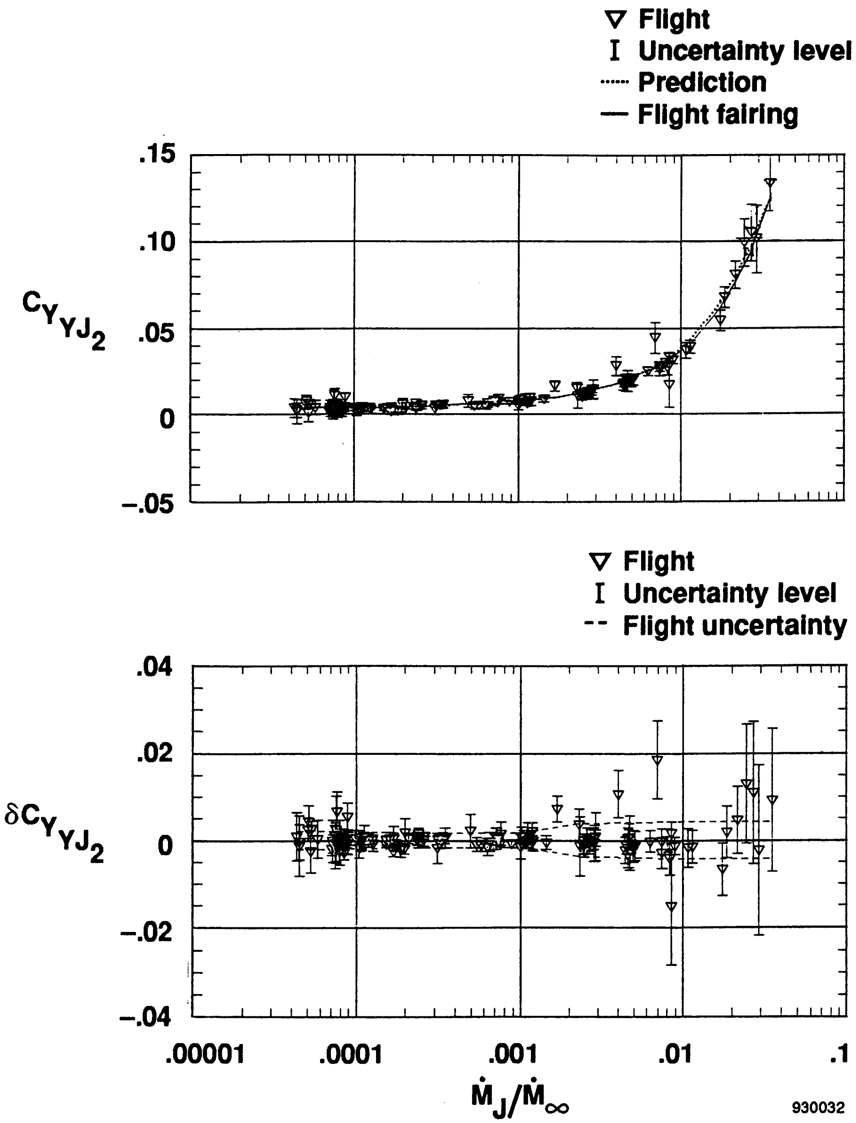

Figure 15. Coefficient of side force due to two yaw jets, $C_{Y_{YJ_2}}$, as a function of mass-flow ratio, $\dot{M}_J/\dot{M}_\infty$.

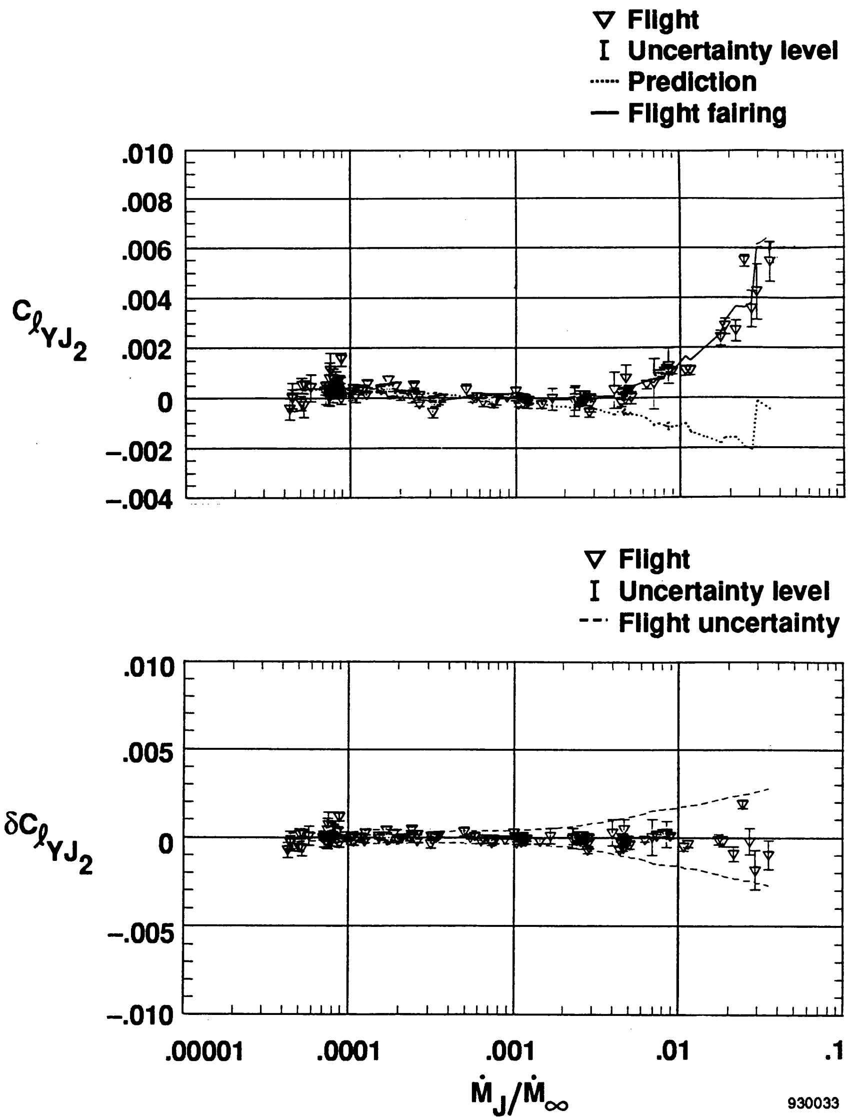

Figure 16. Coefficient of rolling moment due to two yaw jets, $C_{l_{YJ_2}}$, as a function of mass-flow ratio, $\dot{M}_J/\dot{M}_\infty$.

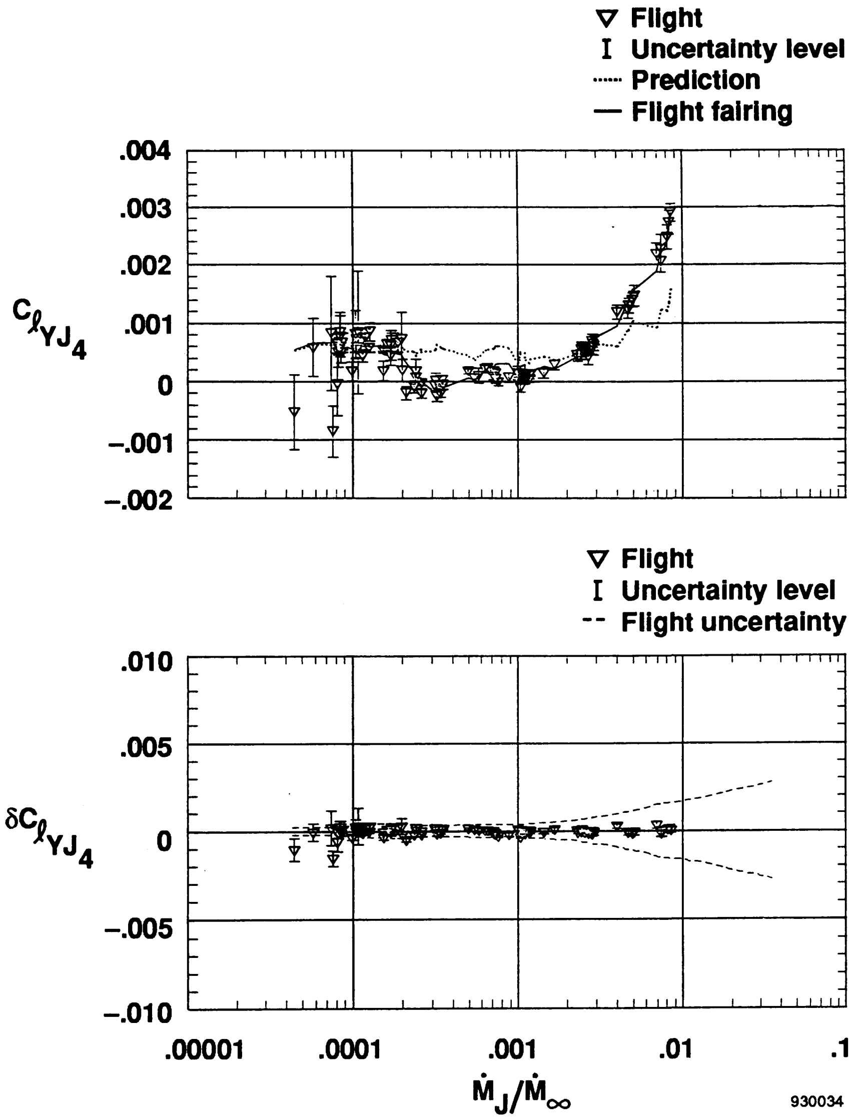

Figure 17. Coefficient of rolling moment due to four yaw jets, $C_{l_{YJ_4}}$, as a function of mass flow ratio, $\dot{M}_J/\dot{M}_\infty$.

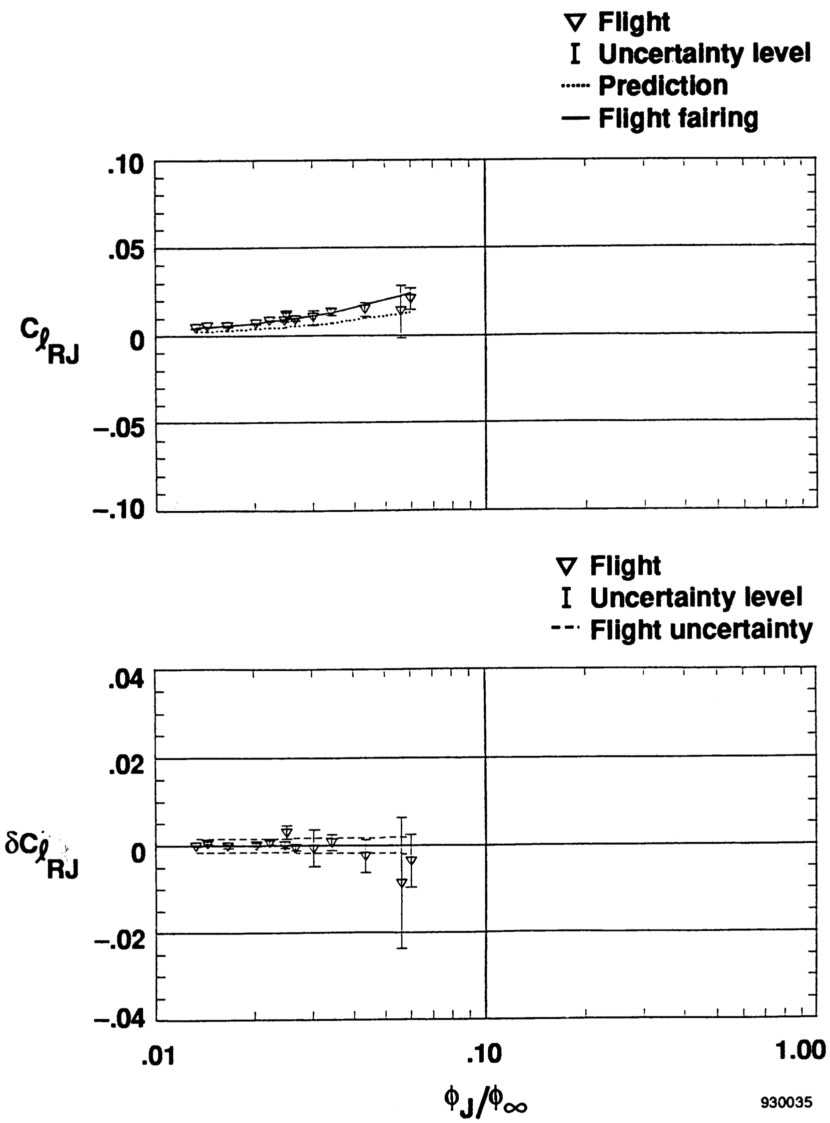

Figure 18. Coefficient of rolling moment due to roll jets, $C_{l_{RJ}}$, as a function of jet momentum ratio, ϕ_J/ϕ_∞.

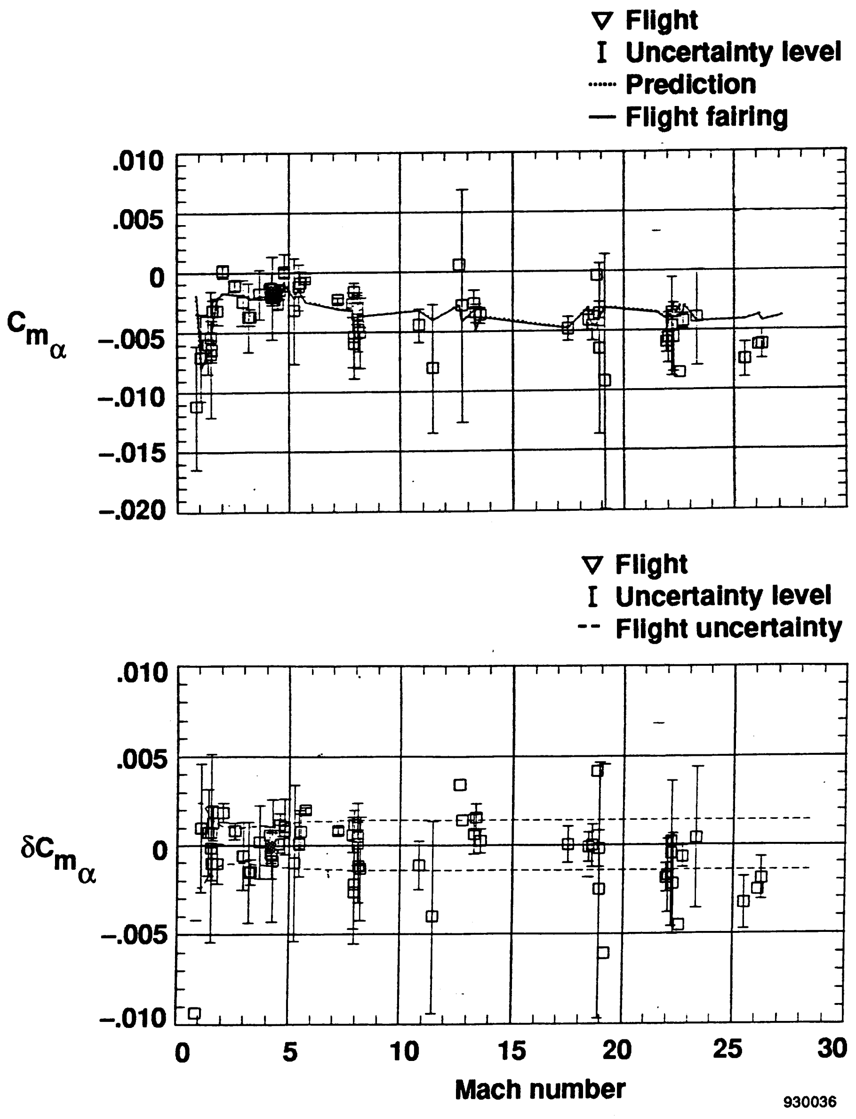

Figure 19. Longitudinal stability term, C_{m_α}, as a function of Mach number, M.

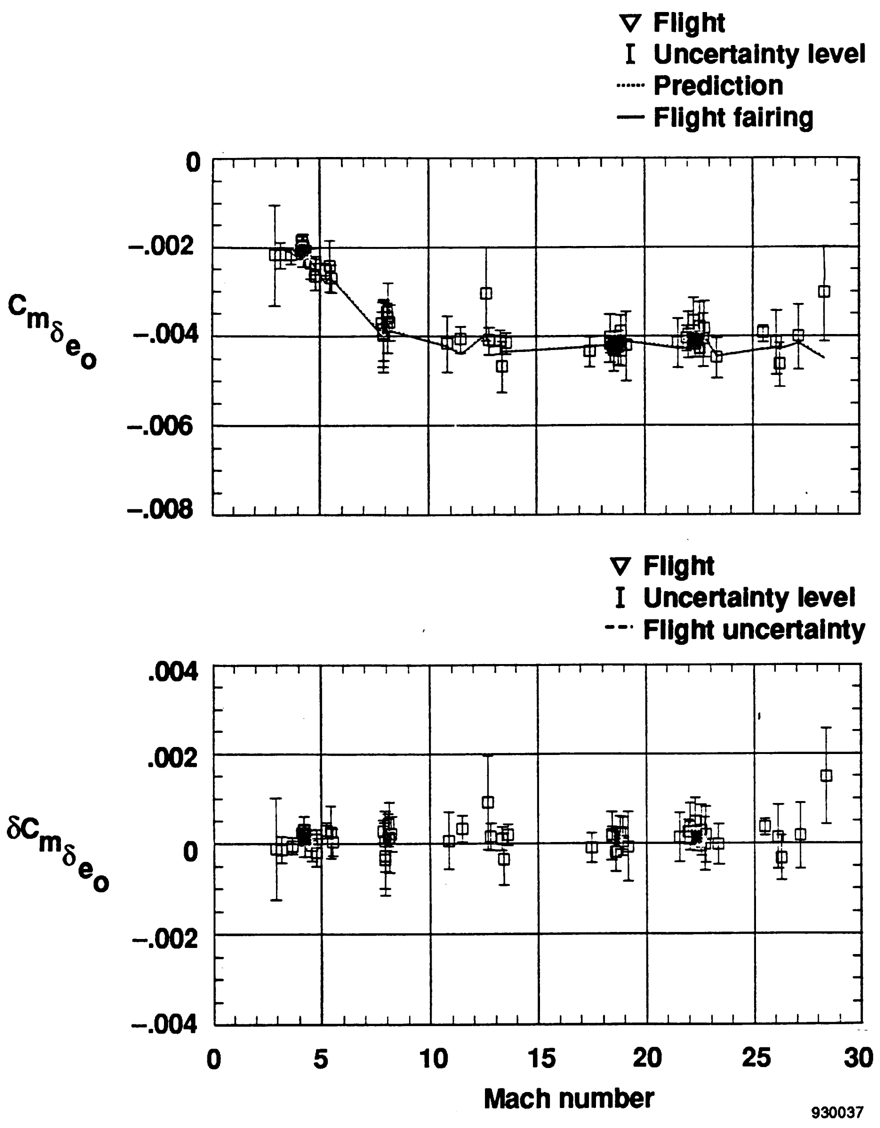

Figure 20. Coefficient of pitching moment due to elevon position, $C_{m_{\delta_{e_0}}}$, as a function of Mach number, M.

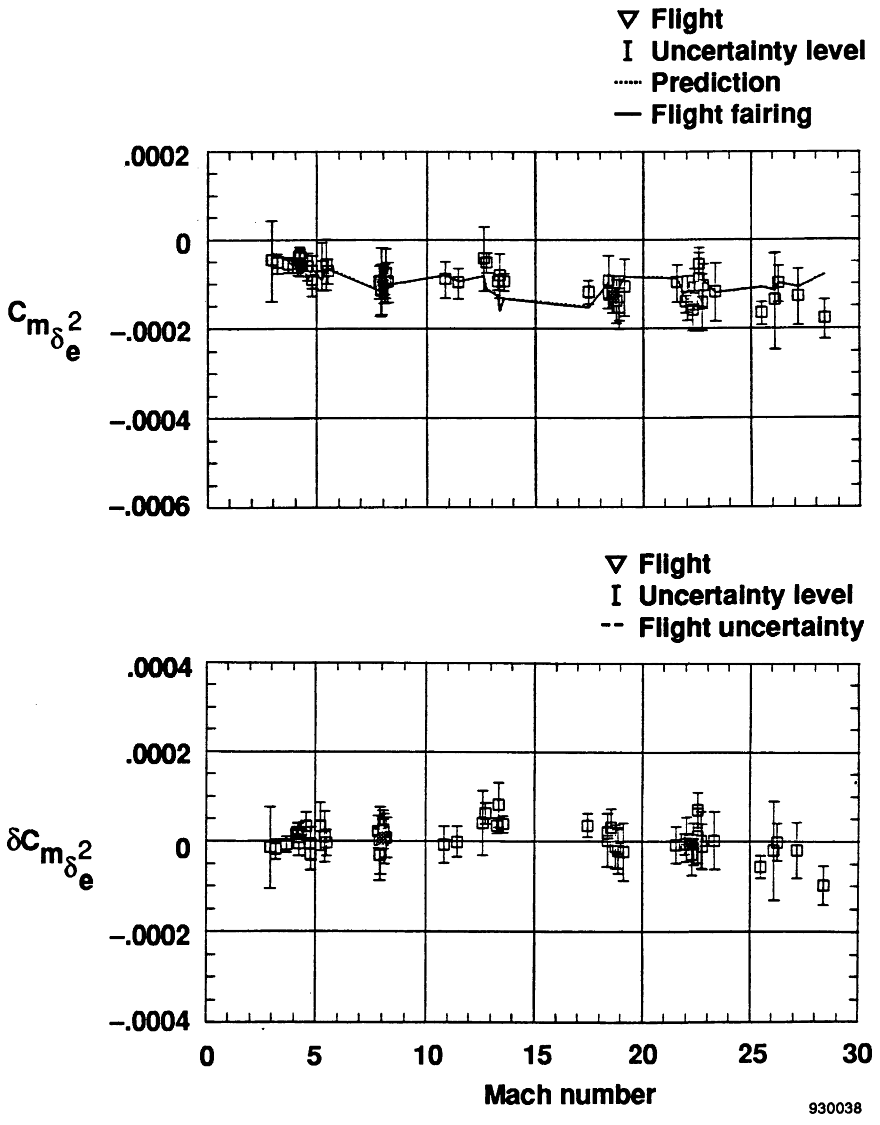

Figure 21. Coefficient of pitching moment due to elevon position squared, $C_{m_{\delta_e^2}}$, as a function of Mach number, M.

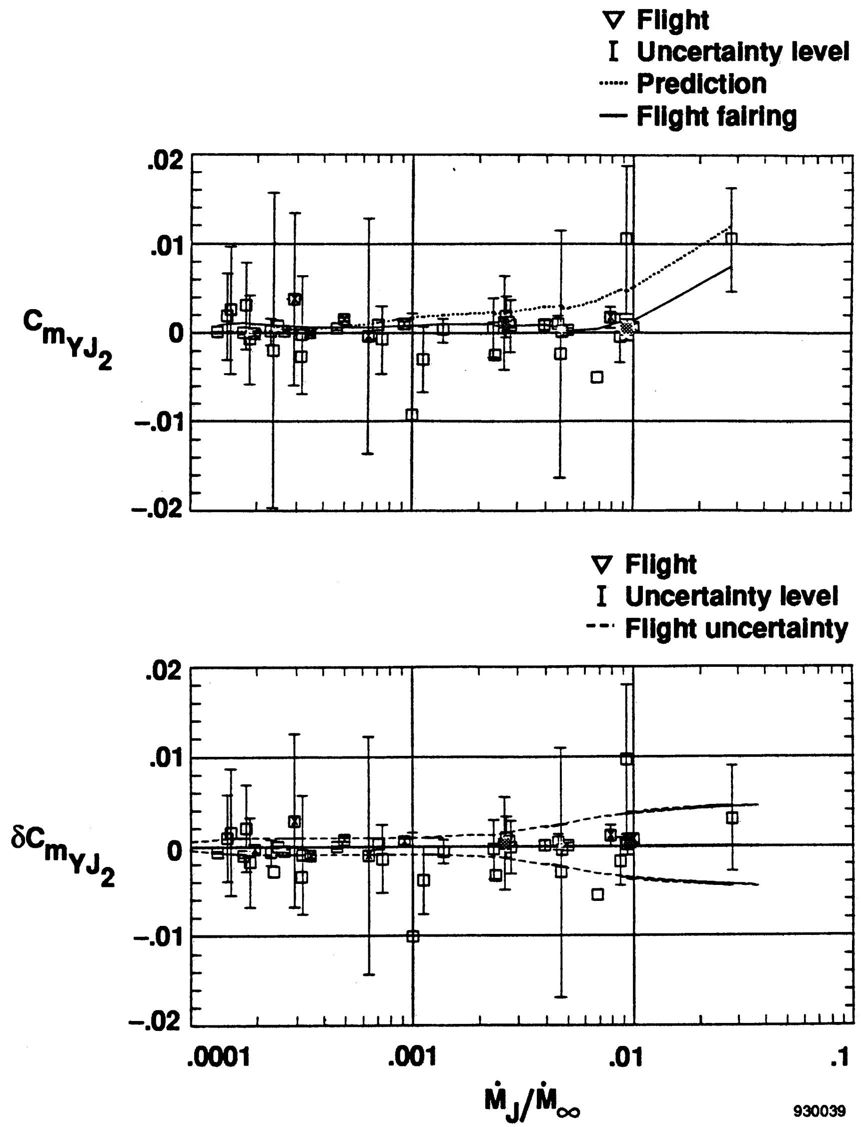

Figure 22. Coefficient of pitching moment due to two yaw jets, $C_{m_{YJ_2}}$, as a function of mass-flow ratio, $\dot{M}_J/\dot{M}_\infty$.

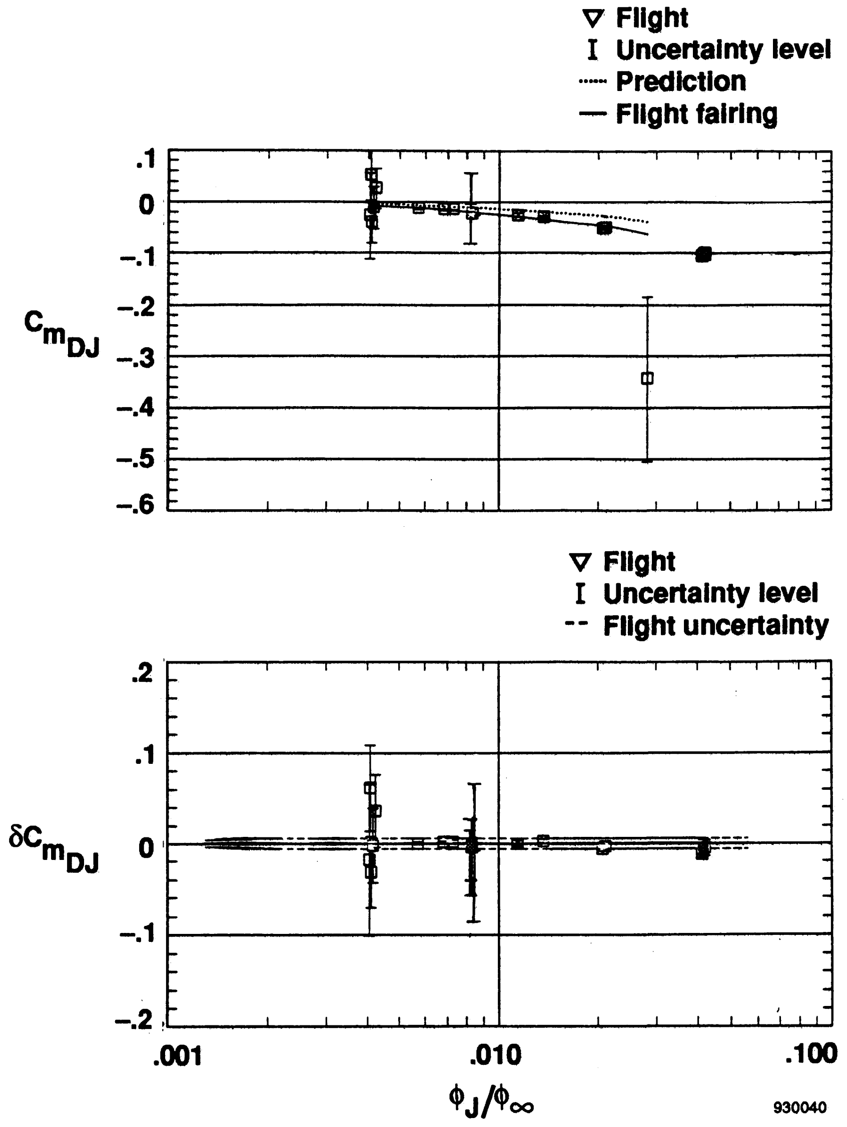

Figure 23. Coefficient of pitching moment due to down-firing jets, $C_{m_{DJ}}$, as a function of mass-flow ratio, $\dot{M}_J/\dot{M}_\infty$.

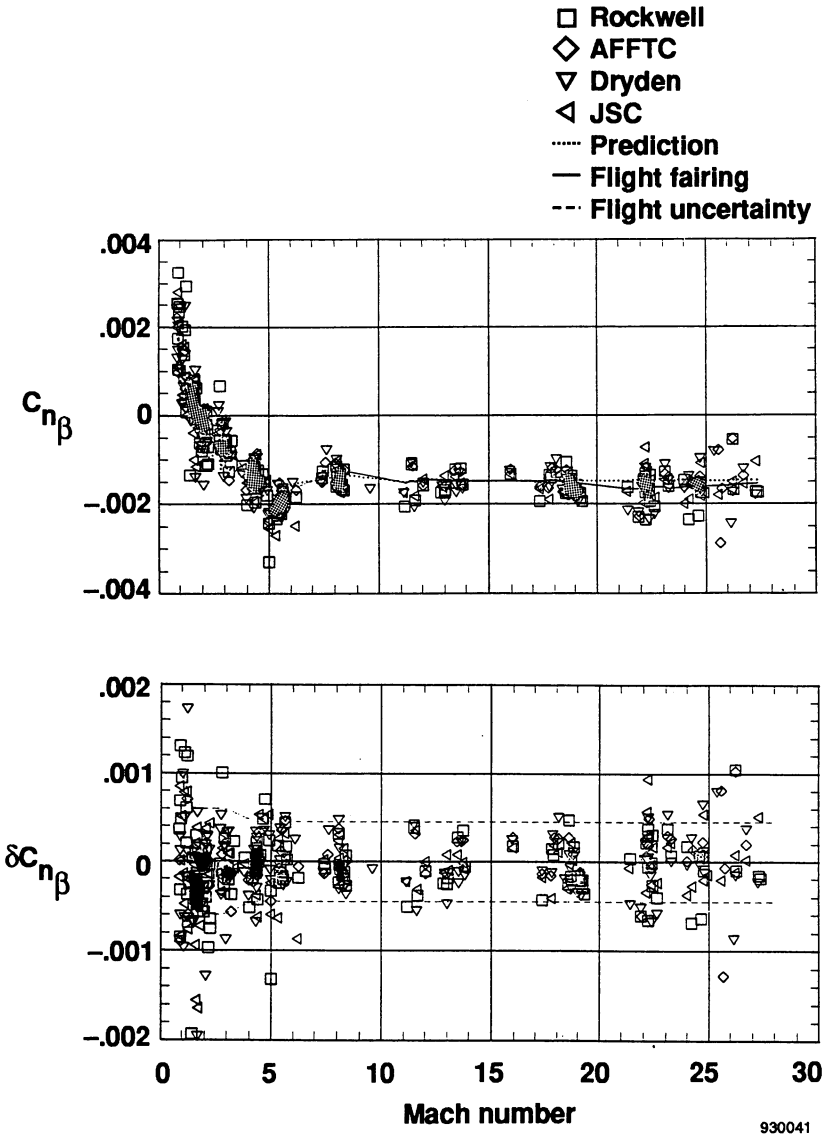

Figure 24. Directional stability, C_{n_β}, as a function of Mach number, M.

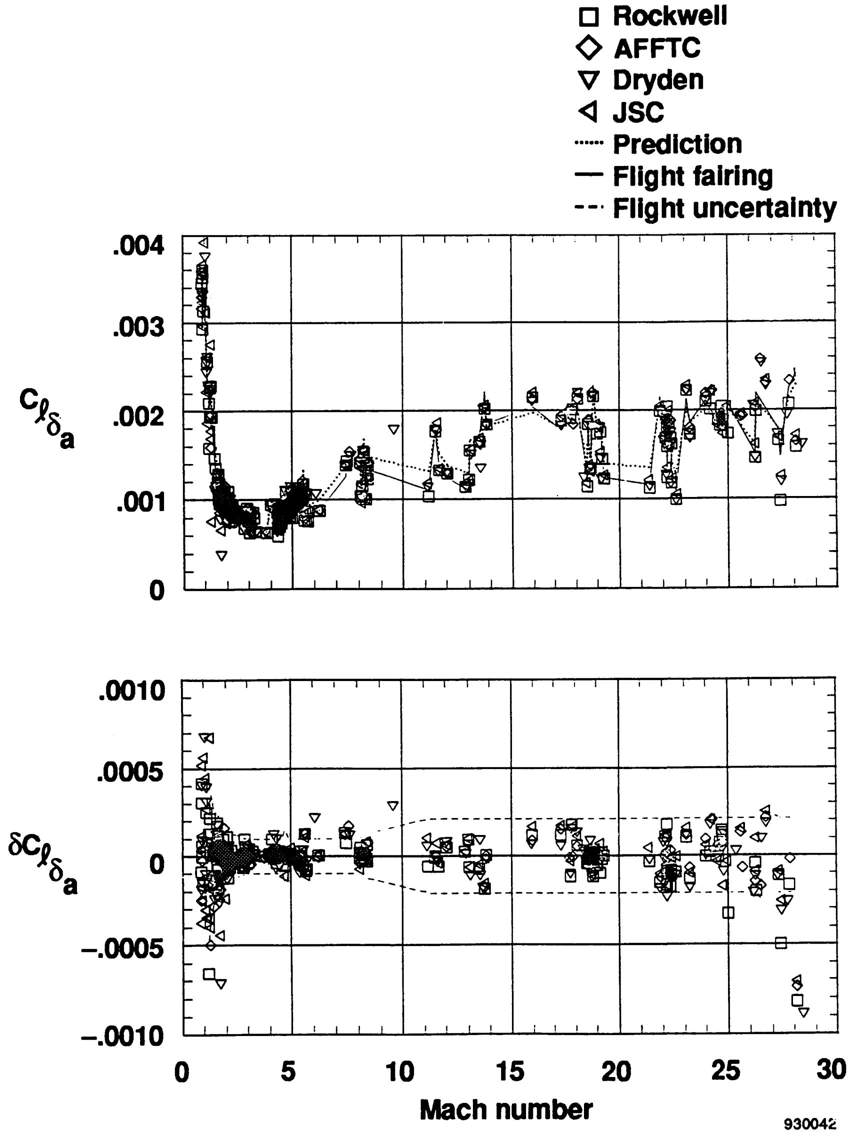

(a) The $C_{l_{\delta_a}}$ and $\delta C_{l_{\delta_a}}$ as a function of Mach number.

Figure 25. Roll control power, $C_{l_{\delta_a}}$, from all sets of analysts.

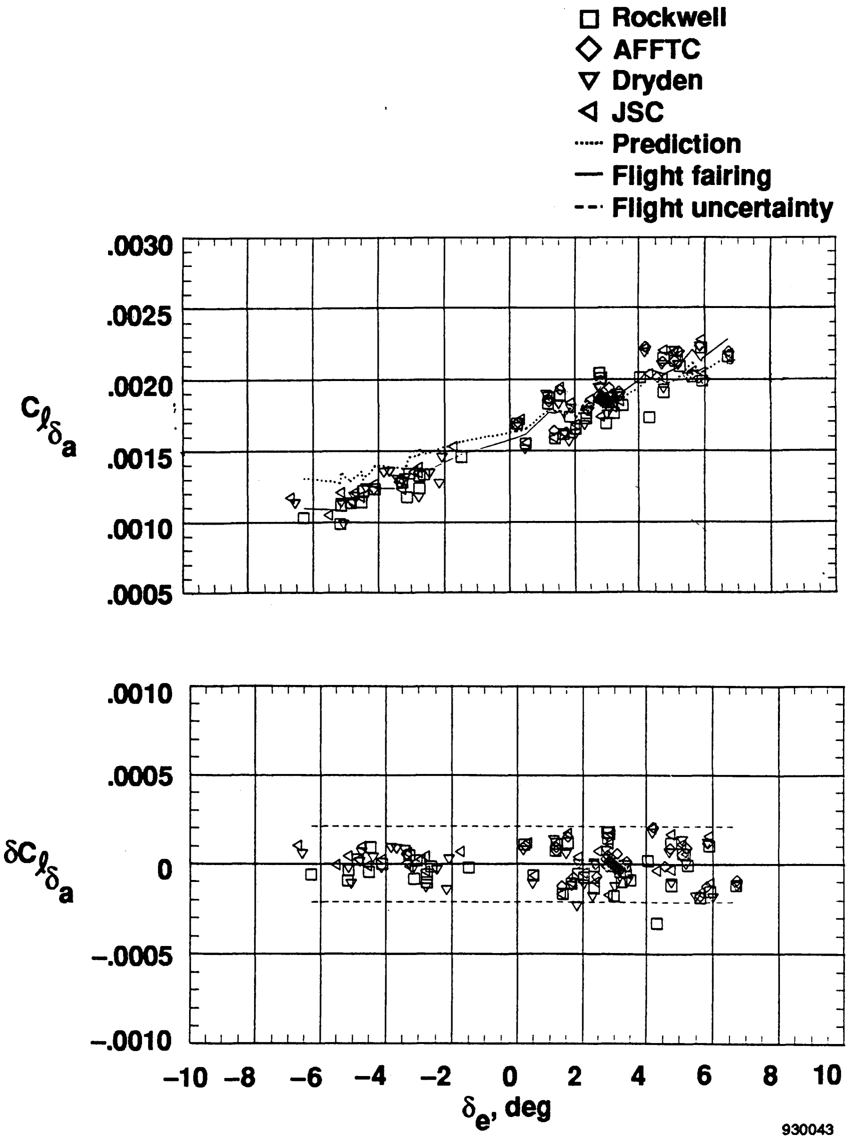

(b) The $C_{l_{\delta_a}}$ and $\delta C_{l_{\delta_a}}$ as a function of elevon position, δ_e, $10 \leq M \leq 25$.

Figure 25. Concluded.

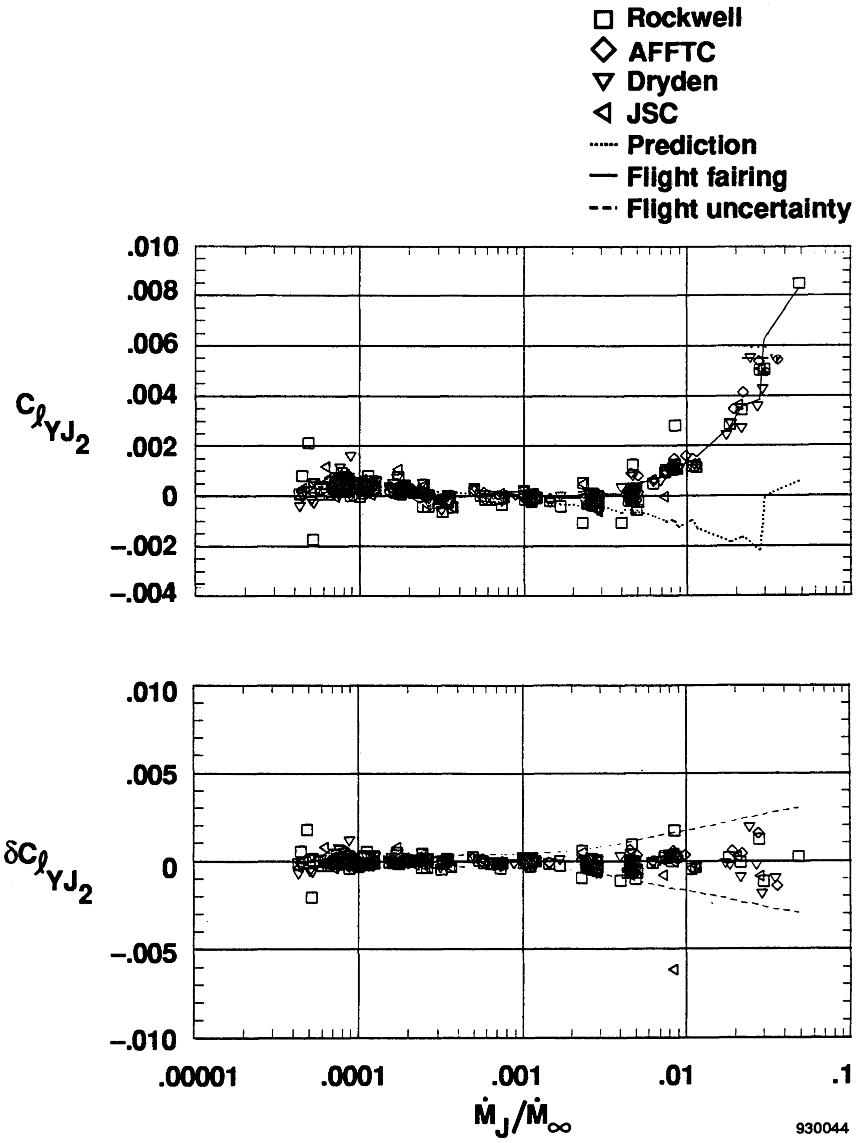

Figure 26. Coefficient of rolling moment due to two yaw jets, $C_{l_{YJ_2}}$, as a function of mass-flow ratio, $\dot{M}_J/\dot{M}_\infty$.

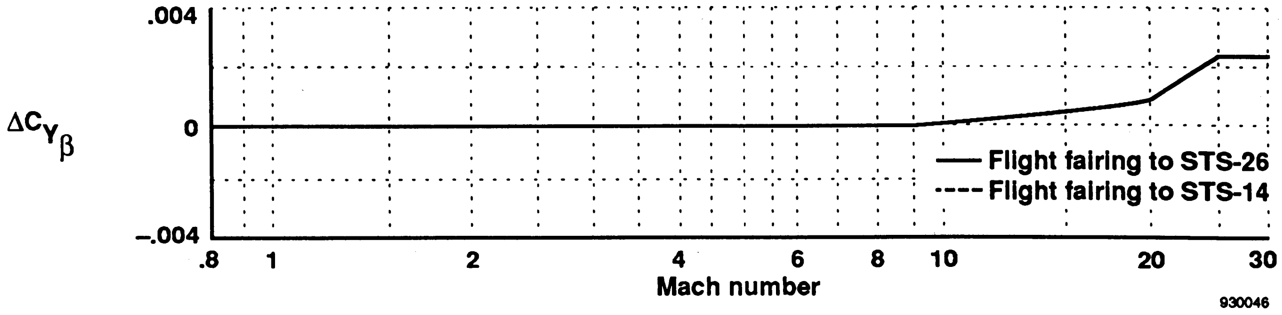

(a) Fairings of ΔC_{Y_β} as a function of Mach number.

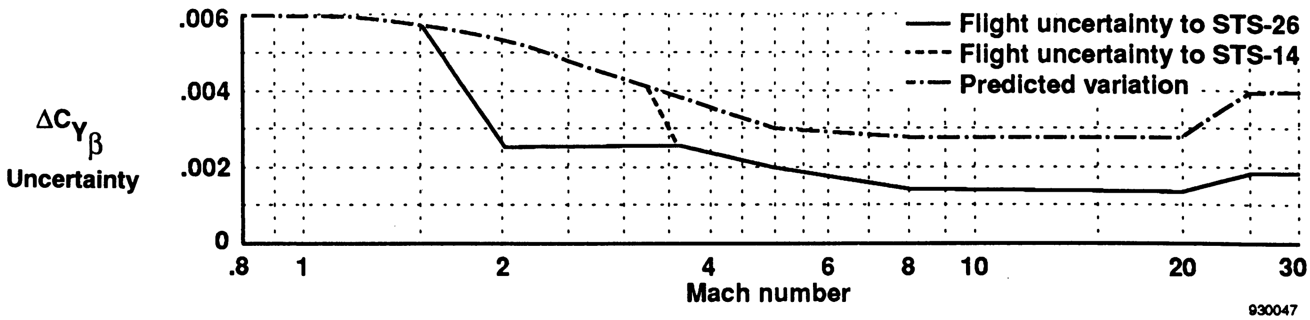

(b) Fairings of ΔC_{Y_β} uncertainty as a function of Mach number.

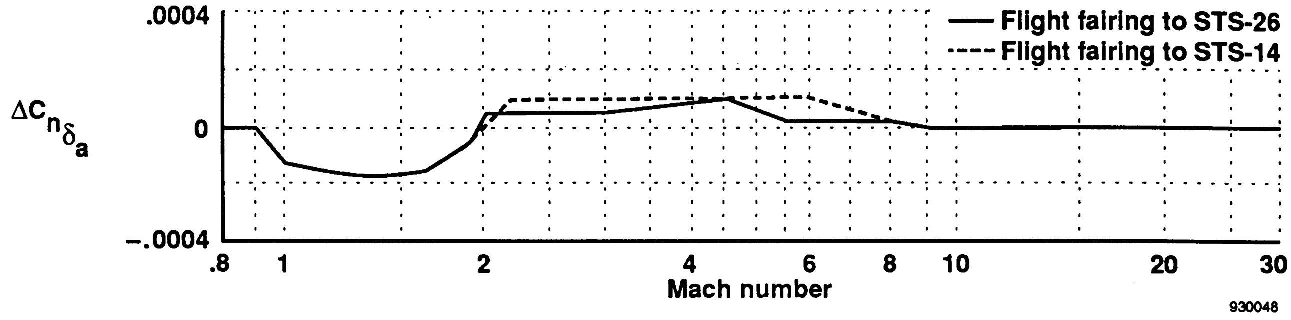

(c) Fairings of $\Delta C_{n_{\delta_a}}$ as a function of Mach number.

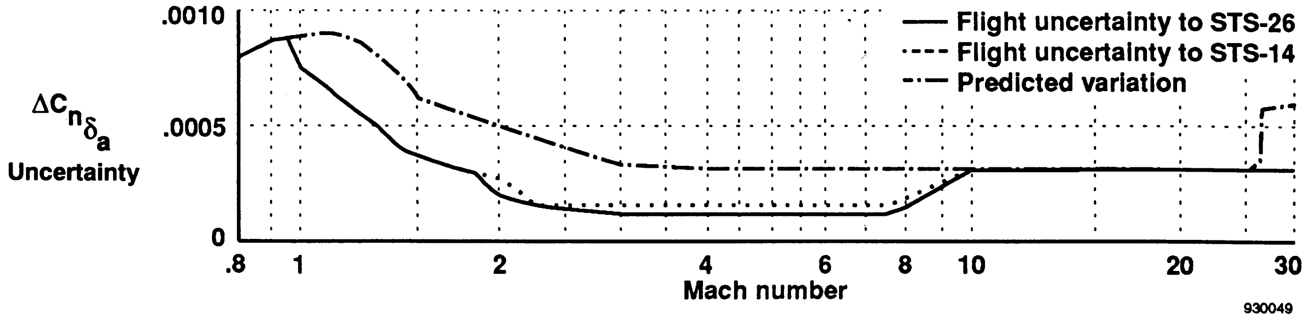

(d) Fairings of $\Delta C_{n_{\delta_a}}$ uncertainty as a function of Mach number.

Figure 27. The FAD–14 and FAD–26 fairings.

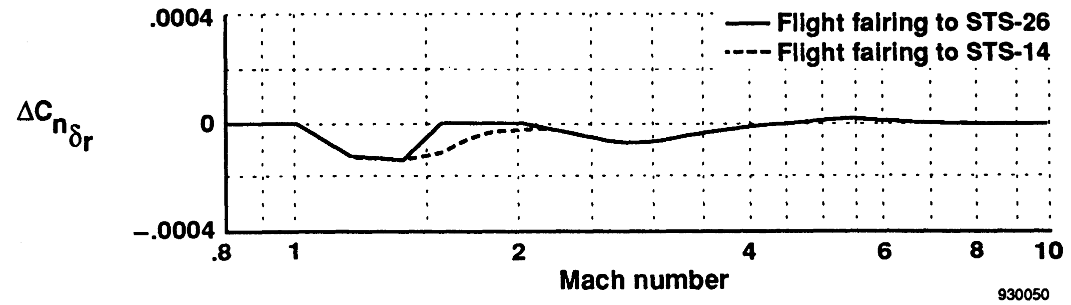

(e) Fairings of $\Delta C_{n_{\delta_r}}$ as a function of Mach number.

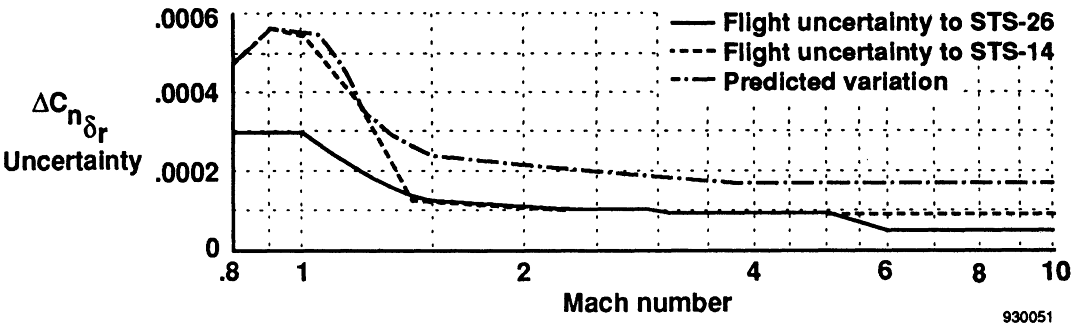

(f) Fairings of $\Delta C_{n_{\delta_r}}$ uncertainty as a function of Mach number.

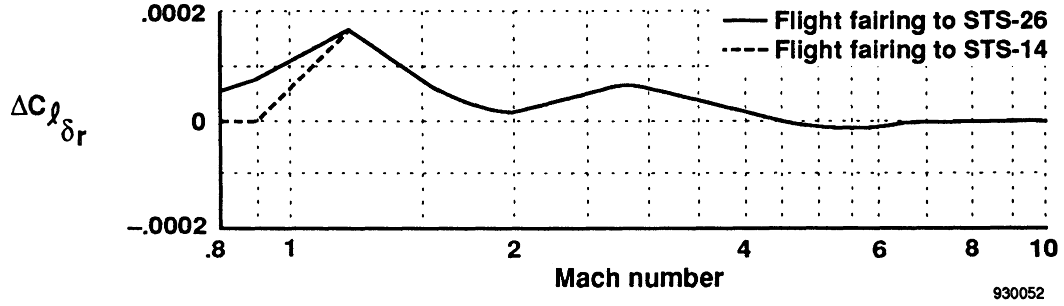

(g) Fairings of $\Delta C_{l_{\delta_r}}$ as a function of Mach number.

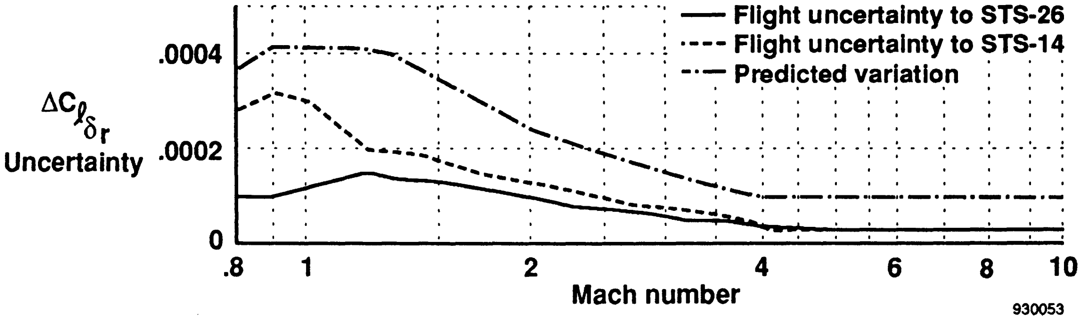

(h) Fairings of $\Delta C_{l_{\delta_r}}$ uncertainty as a function of Mach number.

Figure 27. Continued.

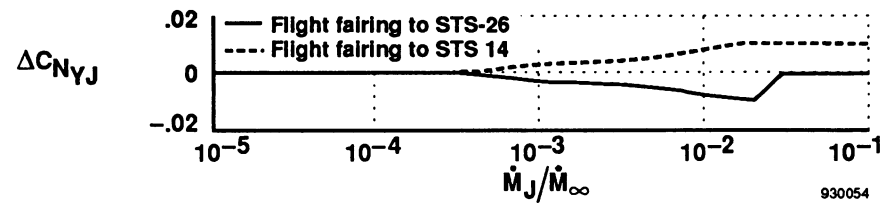

(i) Fairings of $\Delta C_{N_{\mathrm{YJ}}}$ as a function of $\dot{M}_J/\dot{M}_\infty$.

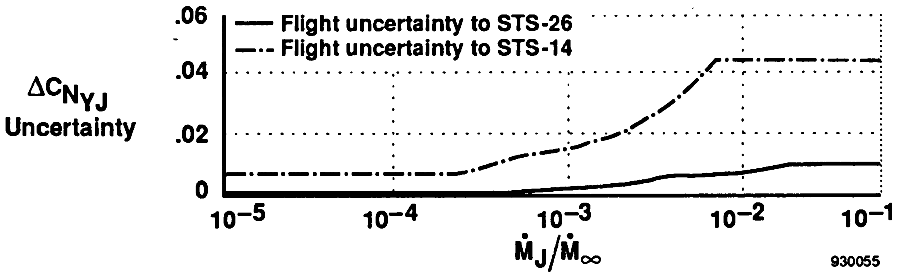

(j) Fairings of $\Delta C_{N_{\mathrm{YJ}}}$ uncertainty as a function of $\dot{M}_J/\dot{M}_\infty$.

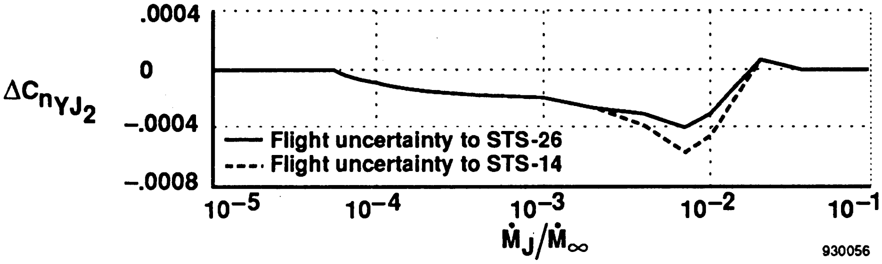

(k) Fairings of $\Delta C_{n_{\mathrm{YJ}_2}}$ as a function of $\dot{M}_J/\dot{M}_\infty$.

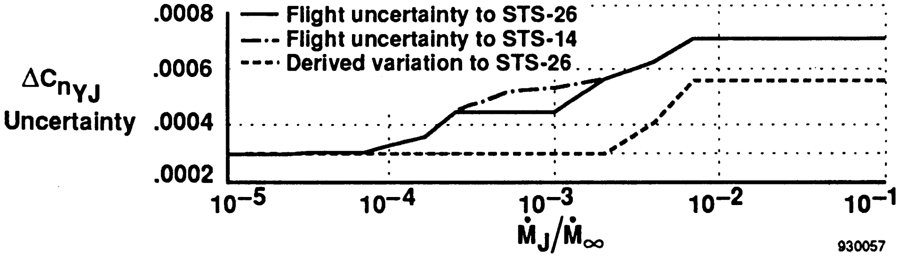

(l) Fairings of $\Delta C_{n_{\mathrm{YJ}}}$ uncertainty as a function of $\dot{M}_J/\dot{M}_\infty$.

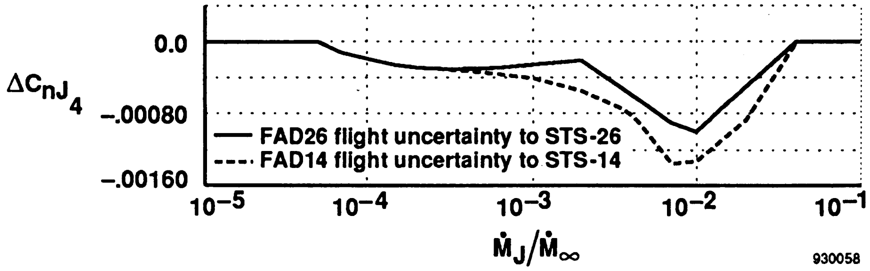

(m) Fairings of $\Delta C_{n_{\mathrm{YJ}_4}}$ as a function of $\dot{M}_J/\dot{M}_\infty$.

Figure 27. Continued.

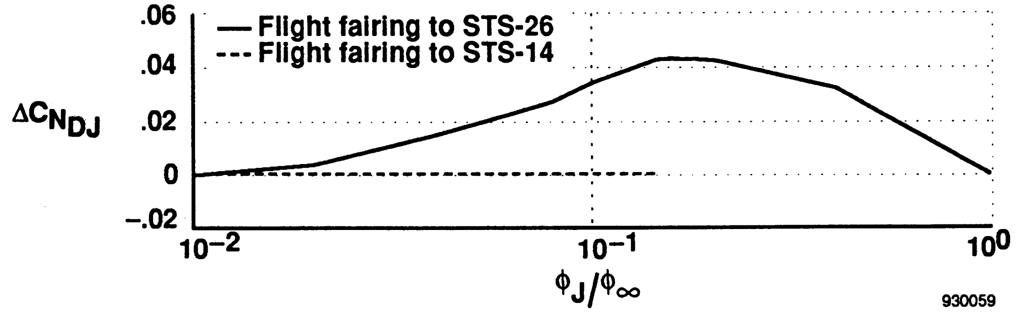

(n) Fairings of $\Delta C_{N_{\rm DJ}}$ as a function of ϕ_J/ϕ_∞.

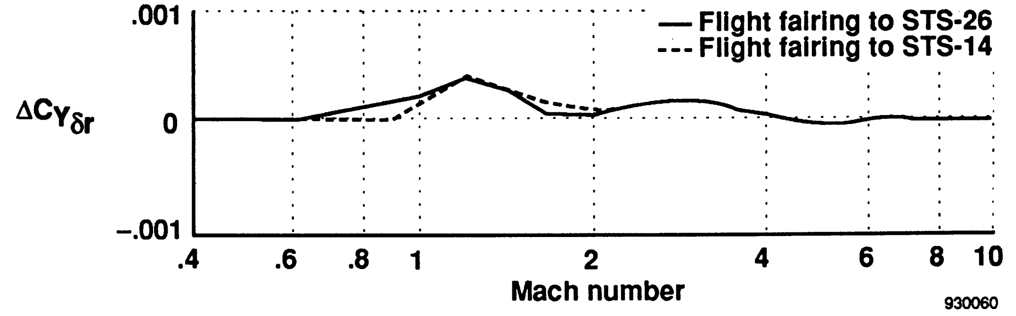

(o) Fairings of $\Delta C_{Y_{\delta_r}}$ as a function of Mach number.

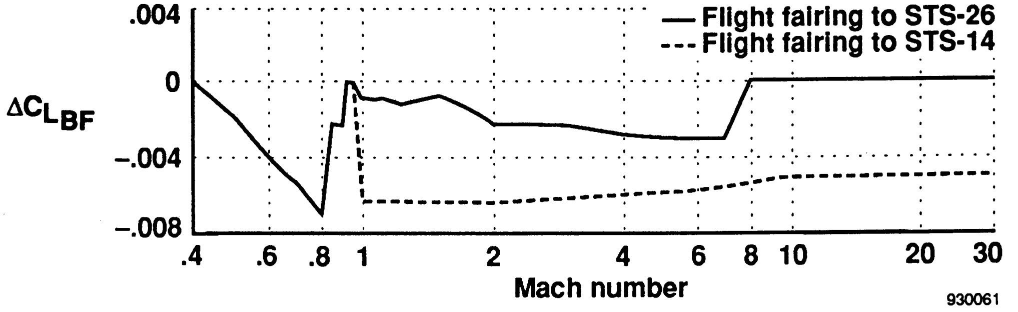

(p) Fairings of $\Delta C_{L_{\rm BF}}$ as a function of Mach number.

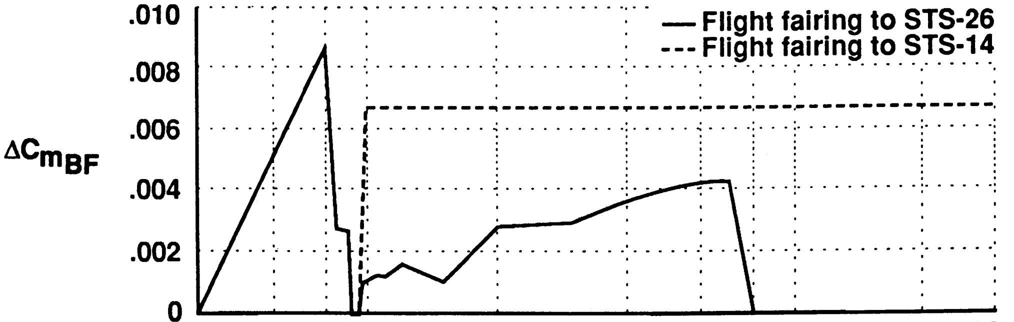

(q) Fairings of $\Delta C_{m_{\rm BF}}$ as a function of Mach number.

Figure 27. Concluded.

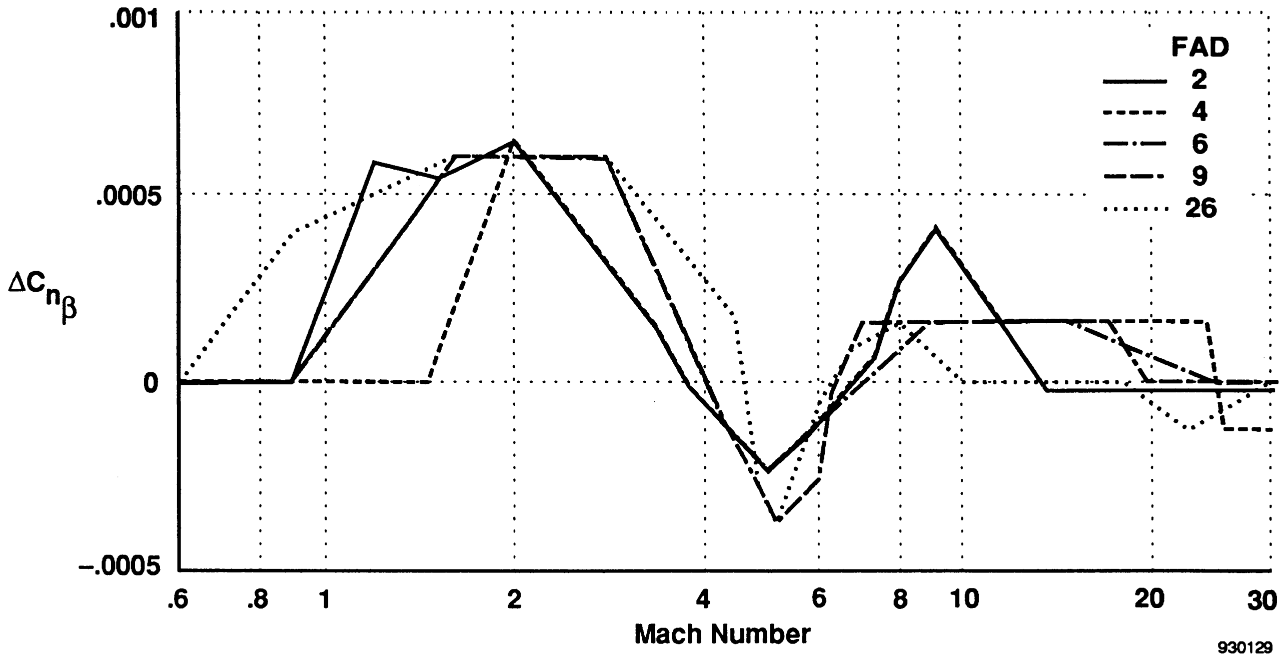

Figure 28. Fairings of ΔC_{n_β} as a function of Mach number for several FAD's.

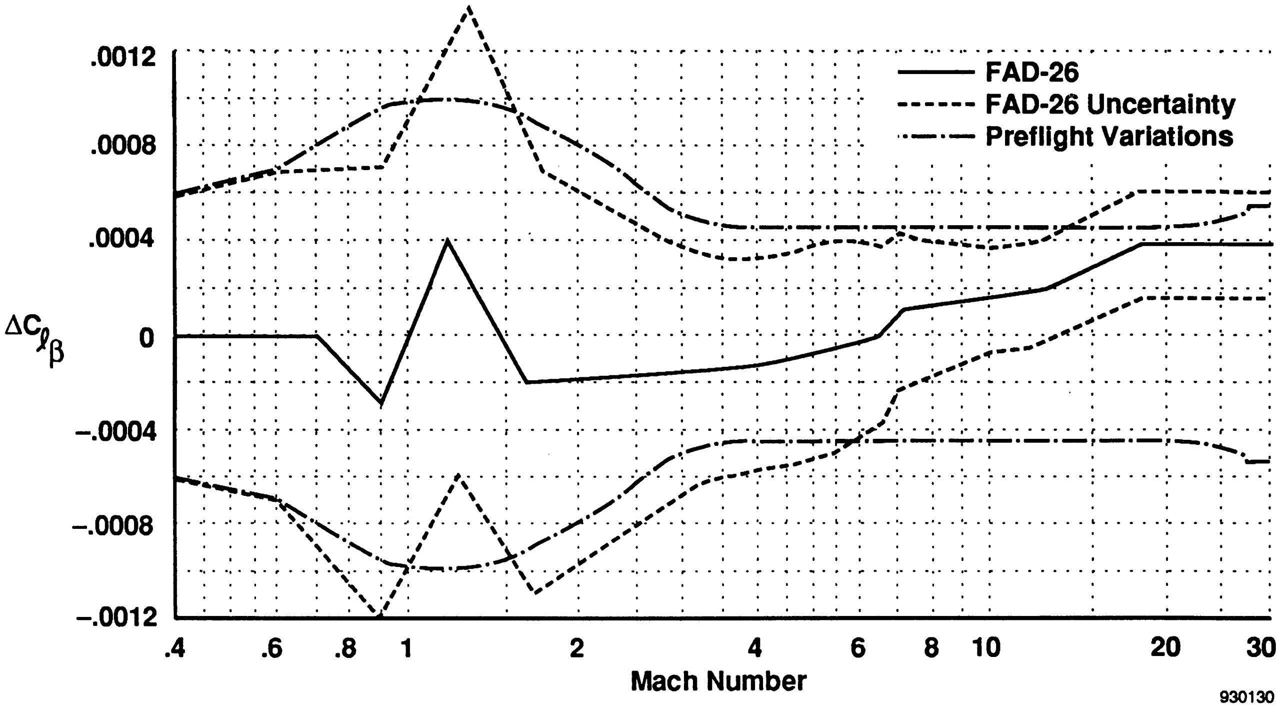

Figure 29. Fairings of ΔC_{l_β} as a function of Mach number for FAD–26 and the preflight aerodynamic data book.

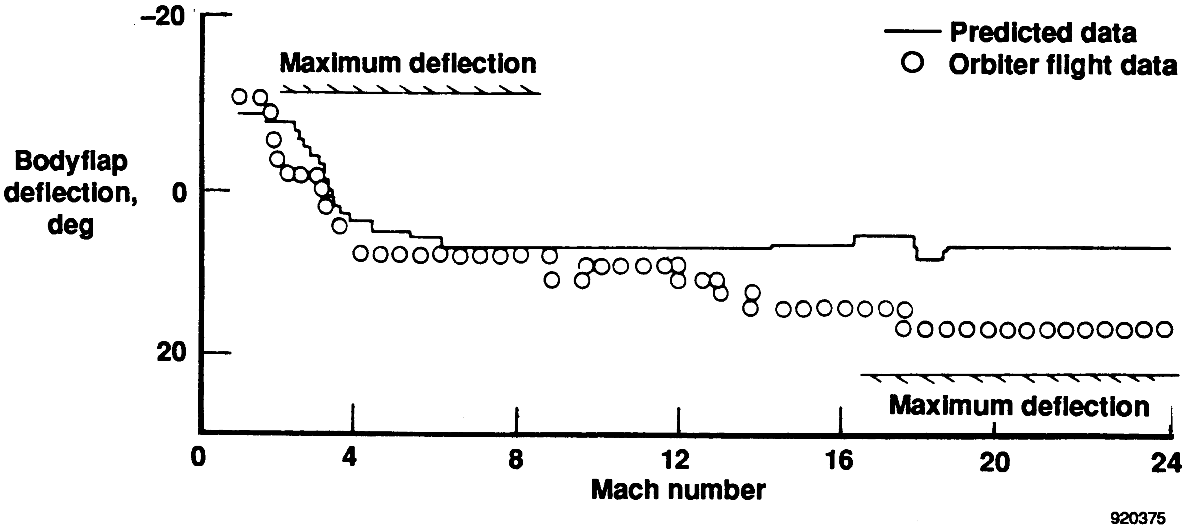

Figure 30. Longitudinal trim characteristics from STS-1 (from ref. 14).

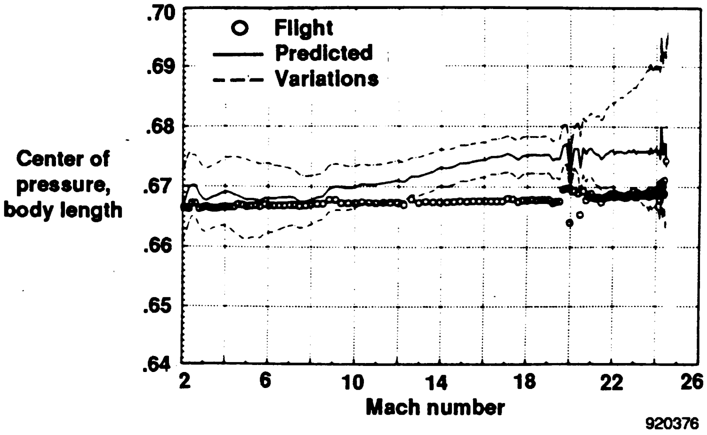

Figure 31. The STS-2 longitudinal aerodynamic center-of-pressure location comparison (from ref. 20).

SPACE SHUTTLE REACTION CONTROL SYSTEM - FLOW FIELD INTERACTIONS DURING ENTRY

William I. Scallion
NASA Langley Research Center
Hampton, VA

ABSTRACT

The results of an ongoing experimental study of reaction control system (RCS) jet plume/lee side flow field interactions on the Space Shuttle Orbiter at an entry angle of attack of 40° are presented. The purpose of the study is to gain a better understanding of the RCS/flow field interaction phenomena in order to develop improved methods for the prediction of the RCS interactions encountered in flight. The study is based on the utilization of flight data, preflight and post-flight wind-tunnel data and the results of computational fluid dynamic simulations of the lee side flow fields. The existence of an extensive flight data base offers an opportunity not previously available to assess wind-tunnel-to-flight correlation parameters in detail. The wind tunnel and flight data are compared in terms of momentum ratio and calculated exit plume shape, and the degree of correlation is discussed. The calculated leeside flow fields are assessed and their influence on the relationships between the wind tunnel and flight results are discussed. An example of the application of the results of the flow field calculations to the RCS/flow field interactions problem is presented and an approach to the prediction of RCS interactions for future space vehicles is suggested.

INTRODUCTION

The control of spacecraft during atmospheric entry is generally accomplished with a combination of movable aerodynamic surfaces and reaction controls. The Space Shuttle Orbiter, a lifting configuration with large aerodynamic surfaces utilizes an aft-mounted reaction control system (RCS) for yaw control during atmospheric entry until the velocity decreases to about Mach 1. The complex flow field generated by the RCS exhaust plume interacting with the external flow about a vehicle of this type at entry flight conditions is little understood, and requires experimental data for definition. This was the case for the shuttle orbiter, where a series of experimental studies were performed to define the RCS/flow-field interactions the vehicle would encounter during entry (references 1-8).

Two primary effects of interaction between the RCS exhaust plume and the flow about the vehicle are involved. First, the exhaust affects the flow next to the surface from which it emanates, separating the flow ahead of the nozzle and changing the local pressure distribution. This type of interaction has been studied extensively, and considerable data exists in the literature for both laminar and turbulent flows (see reference 9, for example). Secondly, the exhaust plume interacts with the external, leeside flow field which alters the surface pressures on adjacent surfaces, in the present case, the leeside of orbiter wing. Very little information existed for the latter type of interaction prior to the orbiter experimental aerodynamic test program, and an exhaustive analysis was conducted on the data generated in these tests (reference 10) to determine the most applicable set of correlation parameters. The correlated data were documented in reference 11 for use in preflight guidance and control system analyses and application.

During the first flight of the Space Shuttle (STS 1), the initial orbiter navigation bank maneuver resulted in damped yaw oscillations in excess of the expected values (reference 11) and excess usage of RCS propellant. Flight data analyses (references 12-15) indicated that the rolling moments produced by interaction of the side-firing RCS exhaust plumes with the leeside flow field were much smaller than predicted by the preflight wind tunnel data base.

As a result of the number of flights that have occurred since the first flight, a large amount of data on the RCS interactions has been obtained. These data have been processed, analyzed, and incorporated in the orbiter Operational Aerodynamic Data Book (OADB), reference 16, and implemented in the flight control system. Although the magnitude of the RCS aerodynamic interactions are relatively well known, little is understood about the physical phenomena involved.

Accordingly, a study was initiated at the Langley Research Center to gain a better understanding of the RCS aerodynamic interaction phenomena and to determine methods that would provide improved predictions of the RCS interactions encountered in flight. The existence of an extensive flight data base offers an opportunity not available before to examine wind-tunnel-to-flight correlation parameters . The emphasis was placed on the RCS/flow-field interaction that influenced the loading on the orbiter wing, that is, the rolling-moment interaction. The study is based on the utilization of flight data, preflight wind-tunnel data, and post-flight wind-tunnel data. This report summarizes the results of the study to date.

Symbols

A_j	nozzle exit area
C_D	ratio of measured nozzle thrust to theoretical nozzle thrust
$\Delta C_{l_{JI}}$	RCS incremental rolling-moment coefficient caused by interaction
$C_{n_{JI}}$	RCS incremental yawing-moment coefficient caused by interaction
$\Delta C_{y_{JI}}$	RCS incremental side-force coefficient caused by interaction
M	Mach number
m	mass-flow rate
m_j/m_∞	nozzle-to-free stream mass flow ratio
mV_j/mV_∞	nozzle-to-free stream momentum ratio
N	number of nozzles
p	pressure

q	dynamic pressure
R	gas constant
R_e	Reynolds number based on mean aerodynamic chord
S_{ref}	reference area
T	temperature
α	angle of attack
γ	ratio of specific heats
λ	conical nozzle divergence correction to momentum at exit, $1/2(1 + \cos \theta j)$
θj	nozzle exit lip angle

Subscripts:

c	nozzle chamber conditions
j	nozzle exit plane conditions
ι	local flow conditions
∞	free stream conditions

SIMULATION OF INTERACTION EFFECTS

The RCS interactions occurring during entry are produced by the aft side-firing thrusters as shown in figure 1. The up-and-down-firing thrusters are de-activated when the elevons become effective in pitch and roll control which occurs when the dynamic pressure rises to about 20 psf. The side-thrusters remain active for yaw control during entry down to Mach 1. A sketch of the individual thruster and its characteristics are shown on the left-hand side of the figure. The nozzles are contoured and have an exit angle of about 12°. Because of the cross-section shape of the OMS pod, the nozzle exit is scarfed at about 15°. At high altitudes, the exhaust plumes from the thrusters are large, and they interact with the flow along the surface of the OMS pods and with the leeside flow field over the wing. The classical jet interaction with supersonic flow along the surface is illustrated in figure 2(a) as taken from reference 9. This type of interaction occurs on the orbiter OMS pod surface when the RCS side-firing thrusters are active. As this type of interaction is reasonably well understood, the emphasis in this study was placed on the effects of the interaction of the nozzle plume with the leeside flow field on an adjacent surface parallel with the thrust axis as shown in figure 2(b). The plume/flow-field interaction increases the pressure on the adjacent surface, in this case the orbiter wing, and results in an increment in rolling moment. Although corresponding increments in normal force and pitching moment are also produced, the largest error in predicting the flight interactions occurred with the rolling moment.

A review of the preflight aerodynamic design substantiation report, reference 17, indicated that the preflight nozzles were designed to simulate mass-flow rate, momentum, thrust, exit pressure, and plume shape. As these properties cannot be properly scaled, the ratios between them and free-stream properties were used as test parameters. During entry flight, the vehicle encounters continuously changing atmospheric free stream conditions (because of changes in attitude and velocity) and consequently, the leeside flow field properties are also changing. The nozzle exit conditions, static pressure, temperature, mass flow, and momentum remain constant during entry (with the exception of exit plume shape which varies with altitude) because the thrusters are either full-on or off. The ratios of mass flow, momentum, and exit pressure to the corresponding free stream properties are therefore functions of the entry trajectory. In the wind tunnel at a given Mach number and Reynolds number, the free-stream properties are constant, and simulation of the ratio of mass flow or momentum is accomplished by varying the model nozzle chamber pressure, and by using nozzles of different designs. The difficulty in simultaneously simulating these parameters in the wind tunnel is illustrated in figure 3, where the variations of mass-flow ratio and exit pressure ratio are presented as functions of momentum ratio for a preflight nozzle and for the flight nozzle during nominal entry. Note that the flight curves are nonlinear (because of the nature of the entry trajectory) and the wind-tunnel curves are linear. The wind-tunnel mass-flow ratio curve compares favorably with the flight curve through a large range of momentum ratio, but the exit pressure ratio matches flight at only one point. (Note the circled intersections on the figure). These same nozzles would match with flight at another point on the curve if the model were tested at a different Mach number. Both the preflight and post-flight data were obtained at a maximum Mach number of 10 and the effects of Mach number above this value in the wind tunnel are not known.

FLIGHT DATA

At this writing some 50 entry flights have been flown since the first orbital flight, STS-1. Many of these flights were made with vehicles (Columbia and Challenger) that were equipped with a high data rate Aerodynamic Coefficient Identification Package (ACIP) that provided high quality acceleration and angular rate measurements from which aerodynamic data could be extracted. An example of the increments in rolling-moment coefficient, $\Delta C_{l_{JI}}$, resulting from the firing of the RCS side thrusters extracted from the data from entry flights STS-2 and STS-3 is shown in figure 4 along with the curve representing OADB rolling-moment interactions based on data extracted from the first 26 shuttle entry flights. The OADB (flight) data are presented as a function of total momentum ratio without regard for the number of nozzles firing. When the data are applied to predict the interaction coefficients for a given flight condition, the momentum ratio for a single nozzle at that condition is multiplied by the number of active nozzles to arrive at a total momentum ratio. This is supported by the flight data (reference 16) which have shown that the RCS interaction coefficients are a function of the number of active nozzles.

ANALYSES AND DISCUSSION

The analysis of the preflight wind-tunnel data base incorrectly predicted the RCS/leeside flow field interaction effects on the Space Shuttle Orbiter aerodynamic characteristics, and one of the first steps toward developing an improved method of prediction is to understand the interaction effects as revealed by the data. To this end, the preflight wind tunnel RCS interaction data have been reviewed and reanalyzed. The post-flight wind-tunnel data have also been analyzed and compared with the preflight wind-tunnel data and the flight data. The following sections of this paper discuss the analyses.

Preflight Data

The preflight data base as taken from reference 11 is listed in table I. The majority of the data used to predict the flight RCS interactions came from test MA22 (reference 5), and the analysis reported herein is limited to those data. This test, as well as several others (ref. 1-4), utilized a force and moment model with a nonmetric nozzle block. The five different nozzle configurations, (fig. 5) used in the test of ref. 5 were designed to simulate mass-flow ratio and plume shape, or momentum ratio, exit pressure ratio, and plume shape. The nozzles varied considerably in shape and in exit diameter with the exception of nozzles N51 and N85. These nozzles are identical except that the N51 configuration contains 4 nozzles whereas N85 contains 2 nozzles as do the other configurations. A scaled model flight nozzle is shown for comparison only; unfortunately, it was not built and tested. The basic preflight RCS interaction data from test MA22 are presented in figures 6 to 8 as a function of momentum ratio. It is obvious that the data do not correlate well with momentum ratio and a better way to correlate the data was necessary to more accurately predict the RCS interactions for flight. This task was accomplished and documented in reference 10.

The side-firing RCS data were correlated by assuming that the RCS interactions were not a function of the number of thrusters firing, and by correcting the mass flow for the nozzle C_D (ratio of actual thrust to ideal thrust) and compensating for the differences in nozzle exit cone angles by the square root of the sine of the exit cone half-angle (ref. 10). The data correlated in this manner (figures 9 to 11) were used to predict the interactions for the first flight entry. Comparison of these curves with curves derived from actual flight measurements (denoted in figures 9 to 11 as 91 OADB) indicates that the wind-tunnel data predicted much larger side-firing RCS interactions than actually occurred in flight. These incorrectly predicted interactions produced the detrimental effects on vehicle controllability reported in reference 11.

In the analysis reported herein, the preflight data were assessed with a view toward understanding the relationships between the differences in $\Delta C_{l_{JI}}$ for a given momentum ratio to the differences in the model nozzle physical parameters. The diversity in these parameters offered an opportunity to identify the common factor or factors that produced the results. An obvious factor is the number of active nozzles or total momentum ratio as illustrated in figures 6, 7, and 8 for nozzles N85 (2 nozzles) and N51 (4 nozzles). For example, in figure 8, the rolling-moment interaction coefficient, $\Delta C_{l_{JI}}$, is about the same for nozzles N85 at a given momentum ratio as for nozzle N51 at twice the momentum ratio. This occurs because the nozzles are identical and in this example, are operating at the same chamber pressure. This supports the conclusion in reference 10 that the number of nozzles do not affect the end result. This subject will be addressed in a later section. The other nozzle configurations are different except for having the same number of nozzles (2). As in reference 10, the difference in nozzle exit cone angles must be accounted for, and additionally, the design exit Mach numbers have to be considered. The approach taken herein was to relate the preflight model nozzle physical parameters to those of the scaled flight model nozzle shown in figure 4. The preflight data are shown to correlate reasonably well by using the normalizing ratios of Mach number and exit half-angle cosines to modify either mass-flow ratio or momentum ratio as shown in figures 12 to 15. The number of nozzles was also factored out. The exponent applied to the cosine ratios was varied to obtain the narrowest spread of the data, and the value shown is about an optimum. The parameter ratio of actual to ideal thrust, C_D, was not used with the mass-flow ratio parameter, since experience with post-flight nozzle tests indicated that it primarily affected the momentum. Although the data are more closely correlated, the curves do not adequately predict the flight RCS rolling-moment interactions. The modified curves do reasonably predict the flight RCS side-force and yawing-moment interactions (figures 14 and 15). The side-force and yawing-moment interactions are essentially the classical surface interactions whereas the rolling-moment interaction involves the leeside flow field over the wing.

The correlation of the wind-tunnel data indicates factors common between the individual nozzle effects on the leeside flow field. The wind-tunnel data were correlated with exit Mach number and exit cone half angle, both of which have a strong influence on the shape of the exit plume. The relationship between nozzles N85 and N51 discussed previously also indicates that the plume is a primary influence on the leeside flow field. This idea was explored by using the method of reference 18 to calculate plume shapes for nozzle configurations N85, N51, N37, and N61 for free stream conditions corresponding to two values of the rolling-moment interaction coefficient, $\Delta C_{l_{JI}}$ as taken from figure 8. It must be noted that the fluid dynamics of the highly 3-D leeside flow field of the model is unknown and the only means available to compare the plume shapes of the various model nozzles is by calculating them for ambient, quiescent conditions using the nozzle exit-to-free-stream pressure ratios. The good agreement for the calculated plume shapes corresponding to four different nozzles that produce the same rolling-moment interaction (figures 16 and 17) implies that the preflight data from different nozzles can be physically correlated in this way.

What is needed is to determine if the correlation of RCS rolling-moment interaction with plume shape can be extended to RCS interaction data from other ground facilities such as those used in obtaining the post-flight data. Such a correlation, if applicable to all wind tunnel RCS interaction data, could be used to establish a link between wind tunnel and flight data.

Post-Flight Data

The post-flight wind-tunnel data were obtained from force and moment tests at Mach 6 and pressure distribution tests at Mach 10 with a 0.0125 scale model (figures 18 to 21). The same nozzle configurations (figure 18) were used in both tests. The Mach 6 data (figures 19 and 20) afforded an opportunity to assess the effect of multiple, identical nozzles on the rolling-moment interactions. At low values of momentum ratio (< 0.015), the data may be approximated by a single curve (figure 19) without regard for the number of active nozzles. The preflight data (figure 8) do not show this but the range of momentum ratio where this occurs is below the lowest value for which preflight data were obtained. At the higher momentum ratios, the Mach 6 data show the same trends as the preflight data; that is, the curves for different numbers of nozzles begin to diverge into separate curves. Since the individual nozzles are identical, this suggests that the nozzle exit plumes have become large enough such that an increase in the number of nozzles begins to have less effect on the resulting interaction. Figure 20 shows that at the higher chamber pressures there is little variation in $\Delta C_{l_{JI}}$ with the number of active nozzles. Apparently, at the lower momentum ratios (below 0.015), the plumes are smaller, and an increase in the number of nozzles indicates that the increase in momentum ratio is predominant in this range, or the increase in the number and longitudinal extent of the smaller plumes are relevant since the leading plume is not large enough to blank out the effect of the following plumes. Schlieren photographs of the plumes emanating from side-by-side nozzles (reference 19) showed a merged plume shape with a shear layer between the two in the plane containing the centerlines of the nozzles and the size of the boundary in this plane was about the same as for a single nozzle at the same exit to ambient pressure ratio. In the plane where one nozzle is aligned behind the other, no plume boundary could be distinguished, which indicated that the exit flow was diffuse and was expanding at a greater rate in this plane.

The Mach 10 integrated pressure data (figure 21) indicate that the rolling-moment interactions, like those of flight, correlate with momentum ratio, and are insensitive to the number of active nozzles. This is substantiated in figure 22, where chordwise pressure distributions at a single spanwise station are compared for the same momentum ratio with 1, 2, and 4 nozzles.

These Mach 10 data indicate an entirely different set of results than the post-flight Mach 6 data even though the model and nozzles are the same. The measurement techniques are different (force and moment at Mach 6 and surface pressures at Mach 10), but the measurements were consistent and repeatable. The major differences were in the test free stream flow conditions at Mach 6 and Mach 10. The Mach 10 pressure distribution test was conducted at twice the free-stream Reynolds number as the Mach 6 tests, and in viscous-dominated regions such as the orbiter leeside flow field, local Reynolds number and Mach number effects are expected to be significant. The free stream static pressures were nearly identical in both test facilities and a given chamber pressure would be expected to produce essentially the same plume shape and size for either case (under quiescent ambient conditions), but the Mach 10 free stream momentum is nearly three times the momentum in the Mach 6 facility. Conversely, the momentum ratio at Mach 6 test conditions was nearly three times that at Mach 10 test conditions for a given nozzle configuration and chamber pressure. This will always be the case when identical nozzles are tested in facilities designed for a different Mach number; it is not possible to match both momentum and free stream pressure at the same time. It is, therefore, not probable that the Mach 6 and 10 post-flight plumes would correlate the data in the same manner. The plume shapes calculated for the post-flight nozzles for the respective ambient, quiescent tunnel static pressures for a given rolling-moment interaction coefficient are compared in figure 23. The Mach 6 plumes are closely grouped, showing a correlation similar to the preflight case (figure 16). The chamber pressures for this case were sufficiently high to be in the region where the number of active nozzles was becoming less significant (see figure 20). Although the Mach 10 plumes fall in the same area, they do not appear to correlate in the same manner. They show a difference between the 4-nozzle case and the two-nozzle case.

The comparisons between the plumes calculated for quiescent conditions corresponding to the preflight and post-flight wind-tunnel conditions and entry flight conditions at the same rolling-moment interaction coefficient (figure 24) show that the flight plumes are considerably larger than the wind-tunnel plumes. The flight data of figure 24 reveal the same relationship between 2 and 4 nozzles as do the post-flight Mach 10 plumes (see figure 23). The preflight wind tunnel plumes are also larger than the post-flight plumes. The free stream static pressure of the preflight test was about half that of the post-flight tests, but the free stream momentum was equal to that of the post-flight Mach 6 test. On this basis, it would be expected that the preflight plume generated would be larger for a given momentum ratio. Moreover, the preflight nozzles were designed to produce a large plume (seeking to duplicate the flight plume), and as a result, these nozzles produced the larger plumes shown in the figure with a much smaller momentum ratio than either the post-flight or the flight nozzles (see table in figure 24). This is the major reason for the overestimation of the rolling-moment interactions by the preflight results.

Leeside Flow Field Calculations

Given the complexity of the leeside flow fields, it is not likely that the wind-tunnel data can correctly predict the flight RCS/flow field interactions without first understanding the differences in the respective flow fields themselves. Recent calculations of the complete, fully viscous, laminar, chemically reacting flow field of the shuttle orbiter for several entry flight conditions have been made by Gnoffo and Weilmuenster (reference 20). Examples of the leeside contours of local-to-free-stream static pressure ratios at a station at the wing trailing edge (just ahead of the aft-mounted side-firing RCS nozzles) taken from the simulation results of reference 20 is shown in figure 25.

At Mach 23.68 the leeside local pressures are higher than free stream static pressure (figure 25 (a)). A rocket exhaust plume in this flow field would be smaller than one exhausting into free stream ambient conditions. The static pressure ratios tend to decrease with Mach number and the calculations of reference 20 show that the leeside local-to-free-stream pressure ratios at Mach 24 flight conditions are about four times those at Mach 12.86 conditions. The calculations of reference 20 also show that the ratio of leeside local momentum to free stream momentum at Mach 12.86 decreases to about two-thirds of the ratios at Mach 23.68. It is apparent that early attempts to match flight momentum ratios and plume shapes in the wind tunnel based on free stream conditions were not appropriate for conditions where the rocket or model nozzle is exhausting into a separated, highly viscous leeside flow field.

A more rigorous approach must take into account the characteristics of the local leeside flow fields for both flight and wind-tunnel conditions and use them to determine the appropriate test parameters and conditions, and to design the model. In the case of data already in hand, the question arises as to whether it can be adjusted by the information gained from the flow field calculations discussed herein. Because, like the flight data, the Mach 10 post-flight rolling-moment interaction data correlate with momentum ratio, they were used in an example of this type of adjustment. The momentum ratio values of the Mach 10 data from figure 21 were adjusted by dividing them by two thirds (from the previously discussed change from Mach 23.68 to Mach 12.86 of reference 20). This can only be a first-order approximation because it is assumed that the two-thirds deduced from the CFD calculations is applicable to the ratio between wind-tunnel and flight local-to-free stream momentum ratios. The result of this exercise (figure 26) shows a more favorable comparison with the flight curve. This is only a single case, and it is not conclusive, but it illustrates that future analyses should consider the relationships between local flow environments in the wind tunnel and flight. Consideration of the differences in momentum ratios between wind tunnel and flight should be accompanied by scaling the plume size to accommodate the differences between flight and wind-tunnel ratios of leeside local-to-free-stream static pressures as indicated by the CFD simulations. The approach described herein, while considered appropriate, cannot be firmly established until the flow-field calculations include the modeling of the RCS thruster plume. In addition, the wind-tunnel data must be better understood. The differences in the data from different facilities as discussed herein need to be isolated in terms of Reynolds number, Mach number, and in tunnel characteristics themselves. The viscous interaction parameter, V'_∞, may be significant in relating the wind-tunnel results to flight. Future wind-tunnel tests must include studies of these effects as well as surface and leeside flow field visualizations and leeside flow field surveys for computational fluid dynamics (CFD) code validation.

Because the RCS/flow field interaction effects are strongly configuration dependent, the results of the ongoing study presented herein cannot be directly applied to another entry vehicle configuration, but the general approach taken herein, can. Since the space shuttle entry data are the only flight data available, the current effort, reinforced by CFD simulations and additional wind-tunnel tests, will continue to utilize the shuttle data base for analysis and solution of the RCS/leeside flow field interaction problem.

CONCLUDING REMARKS

The preflight prediction of the Space Shuttle Orbiter side-firing RCS/flow field interactions over-estimated their effects on the orbiter entry lateral aerodynamic characteristics. A subsequent investigation of these effects was initiated at the Langley Research Center on a time available basis, and although the work is still ongoing, a better understanding of the effects of a side-firing jet discharging into the separated, highly viscous leeside flow field of the orbiter during hypersonic entry has been gained. The preflight data overestimated the RCS interactions because the large exit plumes generated during the tests (in simulating the flight nozzle plumes) produced large interactions for relatively small values of momentum ratio. These effects were magnified by the way in which the data were correlated to generate the predictions of the flight RCS interactions. The preflight and post-flight wind tunnel results correlated with either momentum ratio or plume shape, but no uniform correlation was found between them. Different tunnel test conditions (Mach number, Reynolds number, and free stream static pressure) did not permit identical momentum ratios and plume shapes to be simultaneously simulated. The flight RCS interaction data correlated with momentum ratio, and only the post-flight Mach 10 test results followed this trend. The reasons for the above wind-tunnel results are unknown, and warrant further investigation. The Reynolds number of the Mach 10 post-flight test was double that of the preflight Mach 10 and post-flight Mach 6 test, which indicates that Reynolds number may be a contributing factor to the differences observed, but several other parameters may have also contributed. For instance, the preflight test was conducted at the same Mach number (10) and the Reynolds number was about half, thus reinforcing the previous statement, but this proposition is clouded by the fact that the much larger plumes generated in the preflight tests greatly influenced the results. The other post-flight test was conducted at Mach 6 and the mismatching of plume shape and momentum ratio with respect to the Mach 10 post-flight test conditions probably had a greater influence on the results than the difference in Reynolds number. The effects of Reynolds number cannot be isolated with the existing wind-tunnel data and this, along with the effects of Mach number (extending the Mach number range above 10) needs to be explored. The post-flight Mach 10 data correlation with momentum ratio may have been the result of a combination of momentum ratio with a smaller plume shape, and this seems to be supported by the trends shown in the leeside flow field characteristics generated by the CFD simulations. Based on the lessons learned from the study to date, additional wind-tunnel investigations should include leeside flow field surveys to aid in understanding the results and in validating the computational codes. Neither leeside nor surface flow characteristics over the shuttle models were obtained during the preflight or the post-flight RCS ground test programs. Leeside surface pressure distributions were obtained only in the post-flight Mach 10 test. The pressure distributions need to be known in greater detail than were obtained in that test and future tests may make use of the emerging global pressure measurement technology. Such tests should be accompanied by comprehensive flow visualization for both surface and flow field; for example, surface streamline patterns may be obtained using oil-flow techniques and infrared techniques used to observe jet plumes (using gases opaque to infrared light). Future flow field surveys will utilize advanced optical laser systems to provide nonintrusive planar measurements of the flow field quantities. All of the aforementioned will increase the understanding of the jet interaction phenomena in the wind tunnel but this must be reinforced by calculations of the leeside flow fields for the wind-tunnel test conditions to establish the relationships between wind-tunnel and shuttle orbiter flight conditions. Ultimately, the complete understanding of the jet interaction effects leading to development of reliable prediction methods will require that the exit plumes for both the shuttle flight and wind-tunnel cases be modeled in the computational fluid dynamics simulations of the orbiter flow fields.

REFERENCES

[1] Dziubala, T. J.; Marroquin, J.; Cleary, J. W.; and Mellenthin, J. A.: "Effects of Reaction Control System Jet Simulation on the Stability and Control Characteristics of a 0.015-Scale Space Shuttle Orbiter Model in the Ames Research Center 3.5-Foot Hypersonic Wind Tunnel," NASA CR-128-800, November 1972.

[2] Daileda, J. J.; and Marroquin, J.: "Effects of Reaction Control System Jet Simulation on the Stability and Control Characteristics of a 0.015-Scale Space Shuttle Orbiter Model Tested in the Langley Research Center Unitary Plan Wind Tunnel," NASA CR-134.070, February 1974.

[3] Blackstock, T. A.; Daileda, J. J.; and Marroquin, J.: "Effects of Reaction Control System Jet Flow Field Interactions on the Aerodynamic Characteristics of a 0.010 Scale Space Shuttle Orbiter Model in the Langley Research Center 31-Inch CFHT," NASA CR-134-111, October 1974.

[4] Thornton, D. E.: "Results of Test OA82 in the NASA 31-Inch CFHT on a 0.010-Scale Model (32-0) of the Space Shuttle Configuration 3 to Determine RCS Jet Flow Field Interaction and to Investigate RT Real Gas Effects," NASA CR-134.442, January 1975.

[5] Kanipe, D. B.: "Results of Test MA22 in the NASA/LaRC 31-Inch CFHT on a 0.010-Scale Model (32-0) of the Space Shuttle Configuration 3 to Determine RCS Jet Flow Field Interaction," NASA CR-147.605, May 1976.

[6] Daileda, J. J.; and Marroquin, J.: "Results of Tests Using a 0.0125-Scale Model (70-0T) of the Space Shuttle Vehicle Orbiter in the AEDC VKF Tunnel B (OA 169)," NASA CR-151.391, January 1978.

[7] Daileda, J. J.; and Marroquin, J.: "Results of Wind-Tunnel RCS Interaction Tests on a 0.010-Scale Space Shuttle Orbiter Model (51-0) in the Calspan Corporation 48-Inch Hypersonic Shock Tunnel," NASA CR-141.847, November 1976.

[8] Covell, P. F.: "Interference Effects of Aft Reaction-Control Yaw Jets on the Aerodynamic Characteristics of a Space Shuttle Orbiter Model at Supersonic Speeds," NASA TM 84645, June 1983.

[9] Spaid, F. W.; and Cassel, L. A.: "Aerodynamic Interference Induced by Reaction Controls," AGARD-AG-173, December 1973.

[10] Rausch, J. R.: "Space Shuttle Orbiter Rear Mounted Reaction Control System Jet Interaction Study," General Dynamics Report No. CASD-NSC-77-003, May 1977.

[11] Stone, J. S.; Baumbach, J. J.; and Roberts, B. B.: "Space Shuttle Orbiter Reaction Control Subsystem Flight Data Anomalies," Shuttle Performance: Lessons Learned, NASA CP-2283, Part 1, pp. 381-395, March 1983.

[12] Iliff, K. W.; Maine, R. E.; and Cooke, D. R.: "Selected Stability and Control Derivatives from the First Space Shuttle Entry," AIAA Paper 81-2451, November 1981.

[13] Office of Advanced Manned Vehicles, Air Force Flight Test Center: "Evaluation of the Space Shuttle Orbiter First Flight Descent Phase," AFFTL-TR-81-21, July 1981.

[14] Compton, H. R.; Scallion, W. I.; Suit, W. T.; and Schiers, J. R.: "Shuttle Entry Performance and Stability and Control Derivatives Extraction From Flight Measurement Data," AIAA Paper 82-1317, August 1982.

[15] Scallion, W. I.; Compton, H. R.; Suit, W. T.; Powell, R. W.; Blackstock, T. A.; and Bates, B. L.: "Space Shuttle Third Flight (STS-3) Entry RCS Analysis," AIAA Paper 83-0116, January 1983.

[16] Anon: "Operational Aerodynamic Design Data Book, Vol. II, Orbiter Vehicle," Space Division, Rockwell International Report No. STS85-0118-2, November 1991.

[17] Anon: "Aerodynamic Design Substantiation Report, Orbiter Vehicle," Space Division, Rockwell International Report No. SD74-SH-0206, Vol. 11, December 1978.

[18] Salas, M. D.: "The Numerical Calculation of Inviscid Plume Flow Fields," AIAA Paper 74-523, June 1974.

[19] Dye, Thomas P.; and Scallion, William I.: "Experimental Simulation of Reaction Control System Thruster Plume Shapes and Comparison with Prediction." NASP Technical Memorandum 1096, January 1990.

[20] Gnoffo, P. A.; and Weilmuenster, K. J.; S. Alter: "A Multiblock Navier Stokes Analysis for Shuttle Orbiter Entry Heating from Mach 24 to Mach 12," AIAA Paper 93-2813, April 1993.

TABLE I. - RCS TEST DATA BASE FOR ENTRY

Test No.	Test Type	Model	Scale	Test Facility	Remarks
MA 7	Force and heat transfer	PRR	0.015	LaRC/UPWT	Convair test
OA 70	Force	139B	0.015	LaRC/UPWT	Yaw RCS data only
OA 73	Force	139B	0.015	ARC 3.5 ft	--
OA85	Force and limited pressure	139B	0.010	LaRC/CFHT	Tabulated pressure only
LA25	Force	139B	0.010	LaRC/CFHT	Jet location and cant angle study
OA82	Force	139B	0.010	LaRC/CFHT	--
MA22	Force	139B	0.010	LaRC/CFHT	--
OA99	Force and limited pressure	139	0.0175	LaRC/vacuum	On-orbit impingement
OA93	Force	140A/B	0.010	Calspan	High Mach no.
OA169	Force	2C	0.0125	AEDC/VKF B	Forward and aft jets
OA-255	Force and limited base pressure	2C	0.0125	LaRC/UPWT	Aft side jets

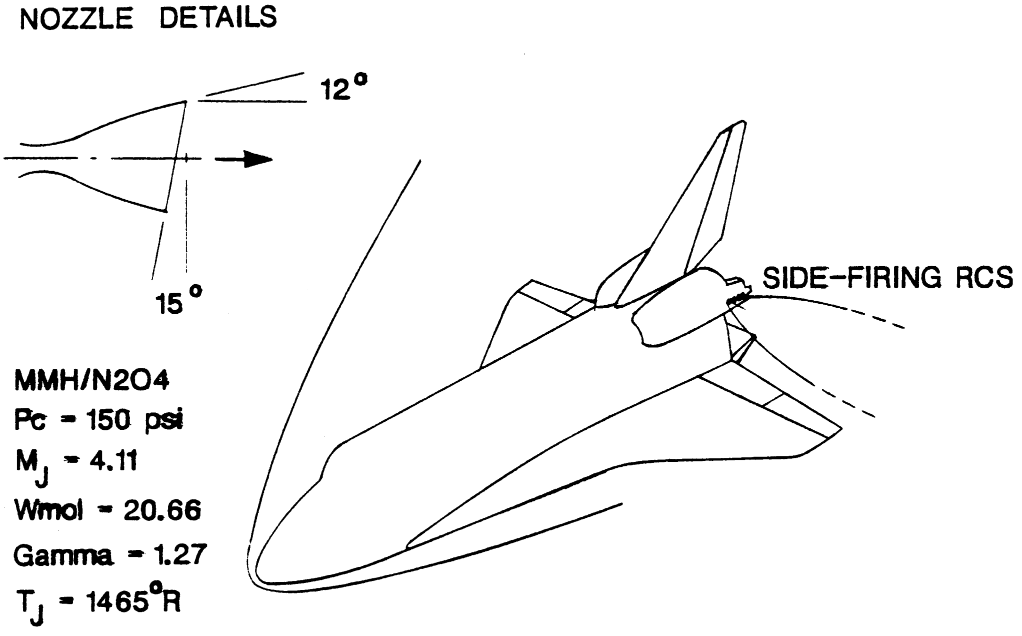

Figure 1. Sketch of the Orbiter showing the location of the aft side-firing RCS thrusters.

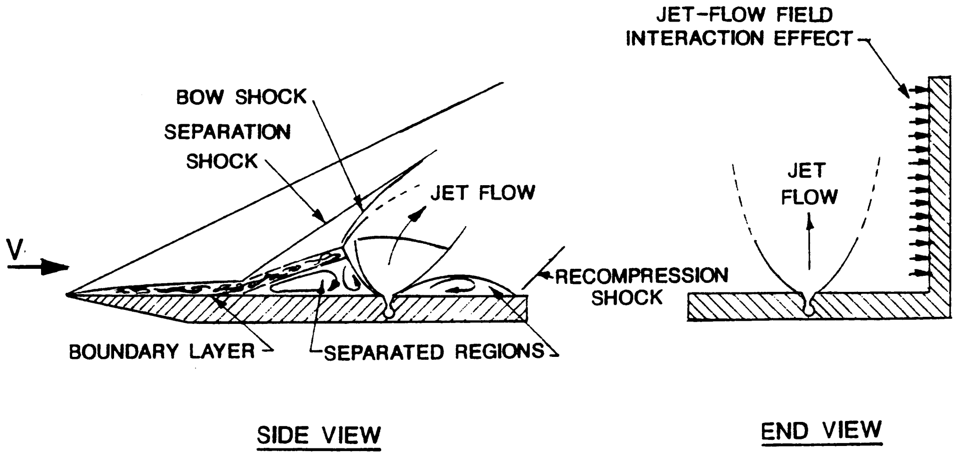

(a) Classical jet-surface interaction (as taken from reference 9)

(b) Jet-flow field interaction on adjacent surface

Figure 2. Interactions caused by a jet exhausting perpendicular to a supersonic flow.

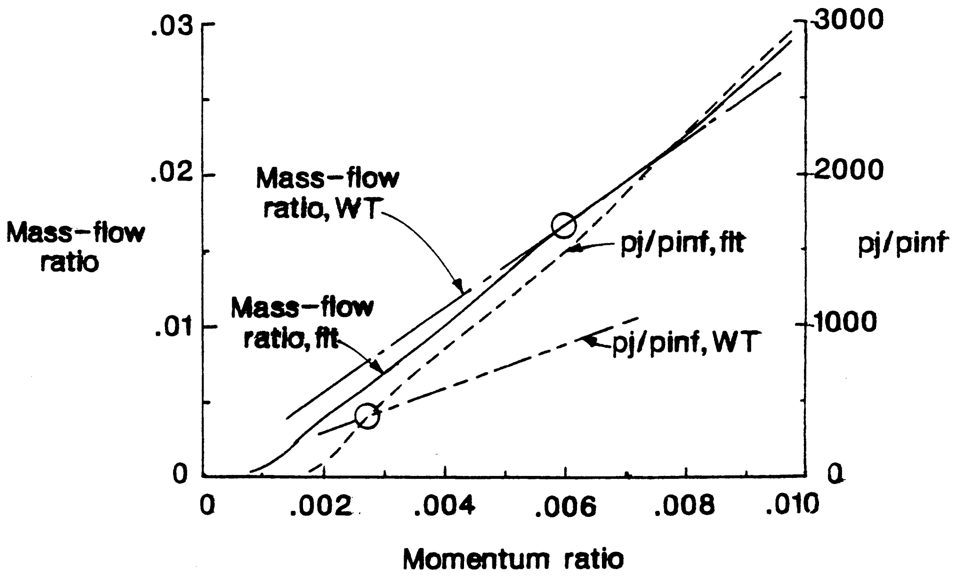

Figure 3. Variation of mass-flow and exit-pressure ratios with momentum ratio for a preflight model nozzle and the flight RCS nozzle.

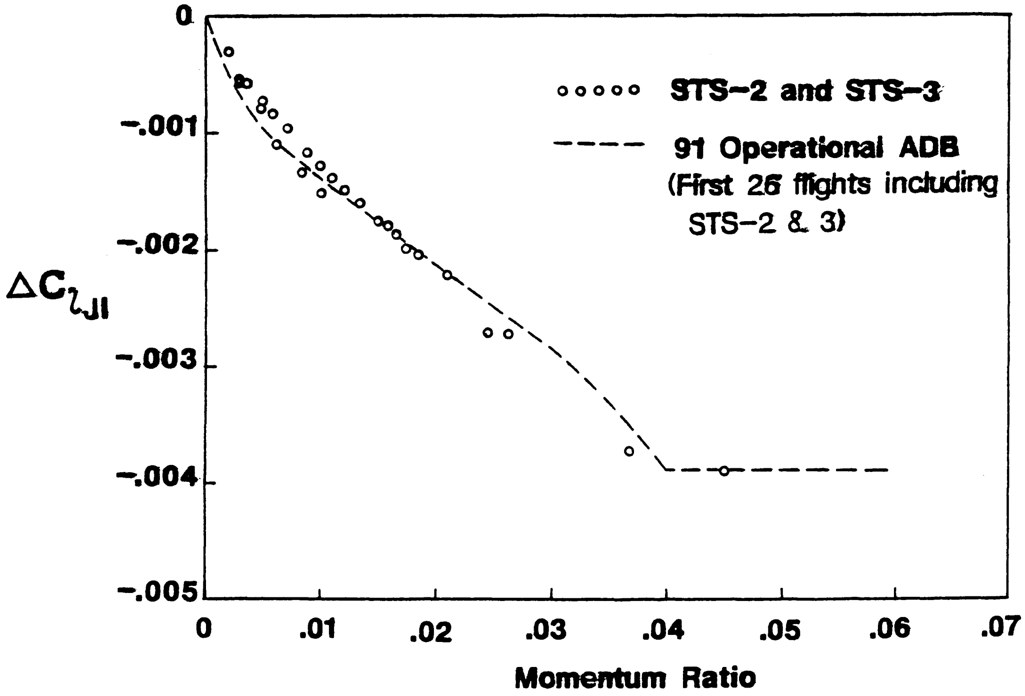

Figure 4. Variation of the rolling-moment interaction coefficients with momentum ratio for entry flights 2 and 3 and the flight operational databook.

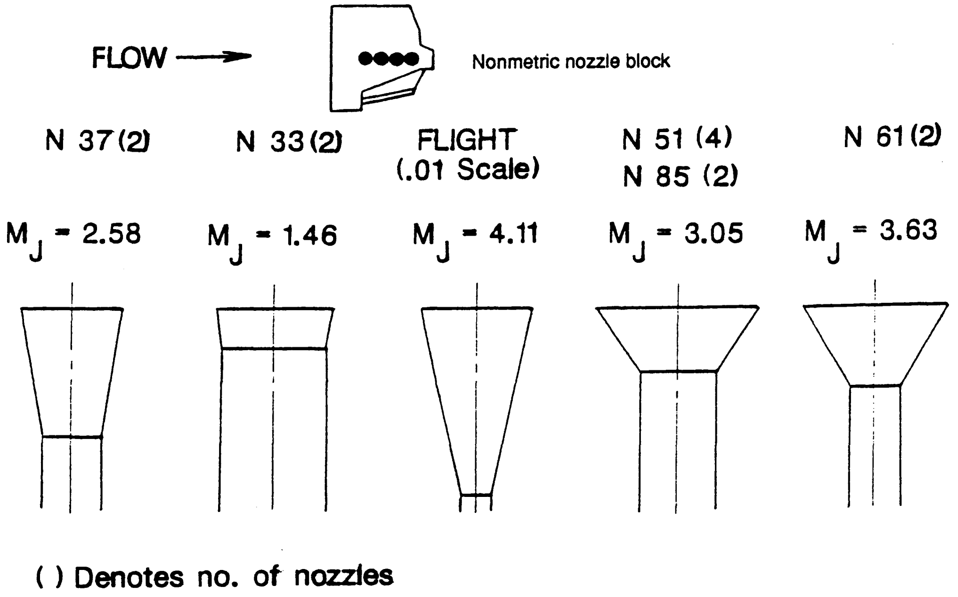

Figure 5. The model nozzle configurations used to develop the data base for the first entry flight.

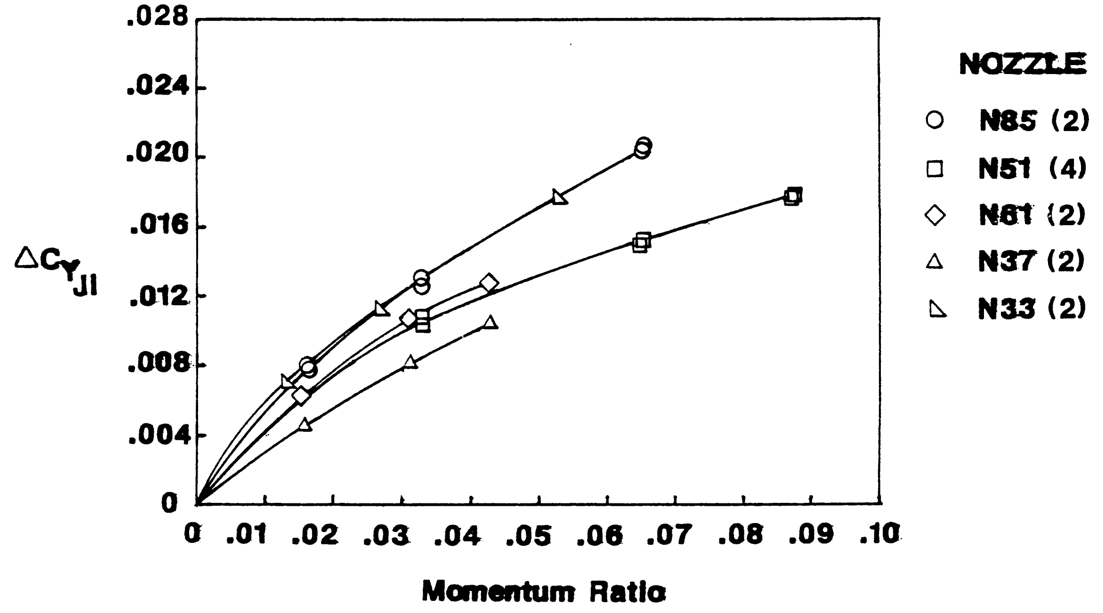

Figure 6. Variation of side-force interaction coefficient with momentum ratio as obtained from preflight wind-tunnel tests at Mach 10. Re = 0.396 x 10^6, α = 36°.

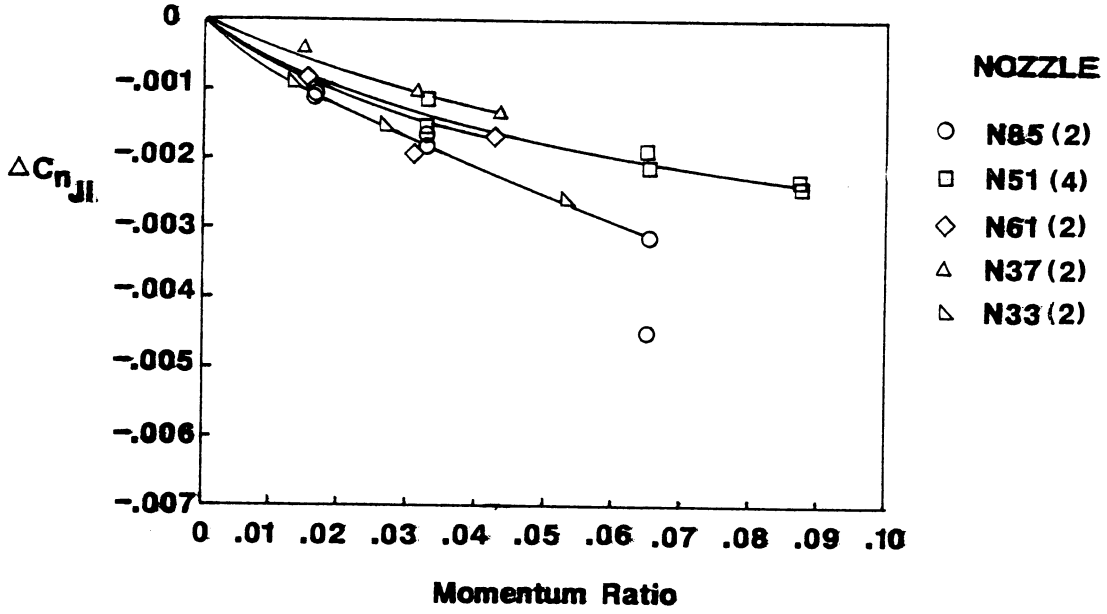

Figure 7. Variation of yawing-moment interaction coefficient with momentum ratio as obtained from preflight wind-tunnel tests at Mach 10. Re = 0.396 x 10^6, α = 36°.

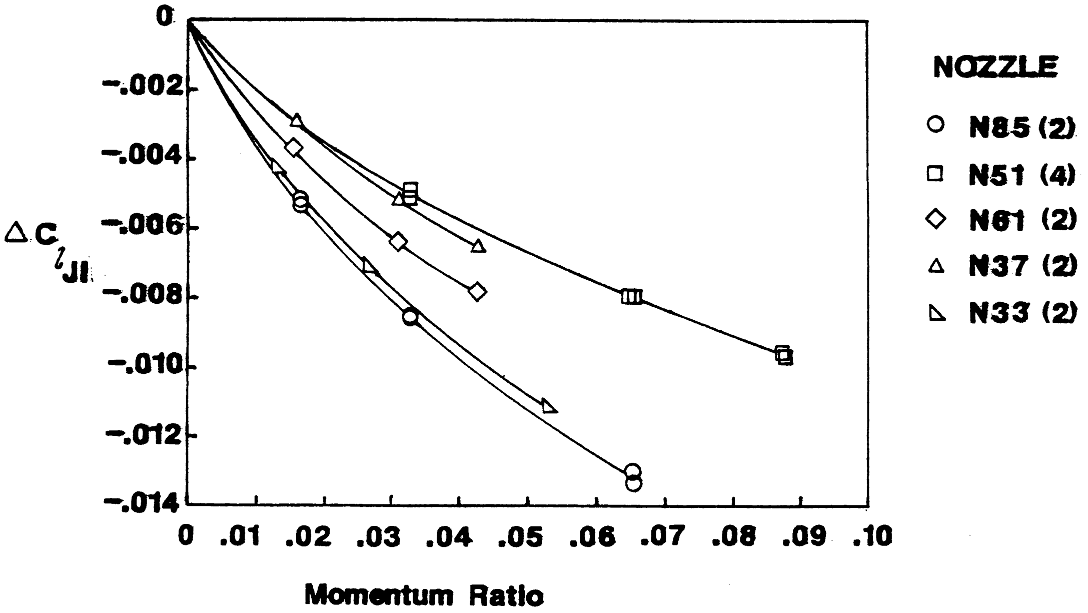

Figure 8. Variation of rolling-moment interaction coefficient with momentum ratio as obtained from preflight wind-tunnel tests at Mach 10. Re = 0.396 x 10^6, $\alpha = 36°$.

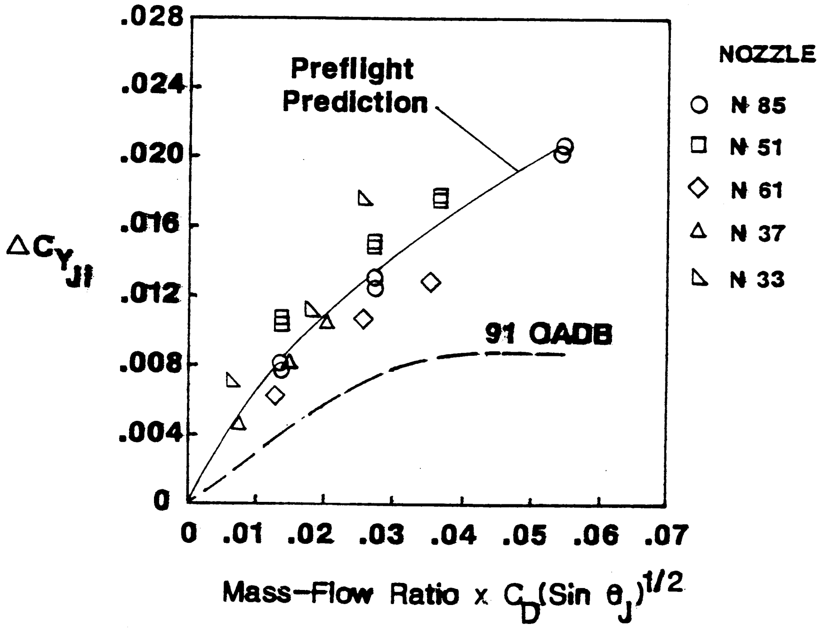

Figure 9. The preflight predicted side-force interaction coefficients compared with flight-derived values.

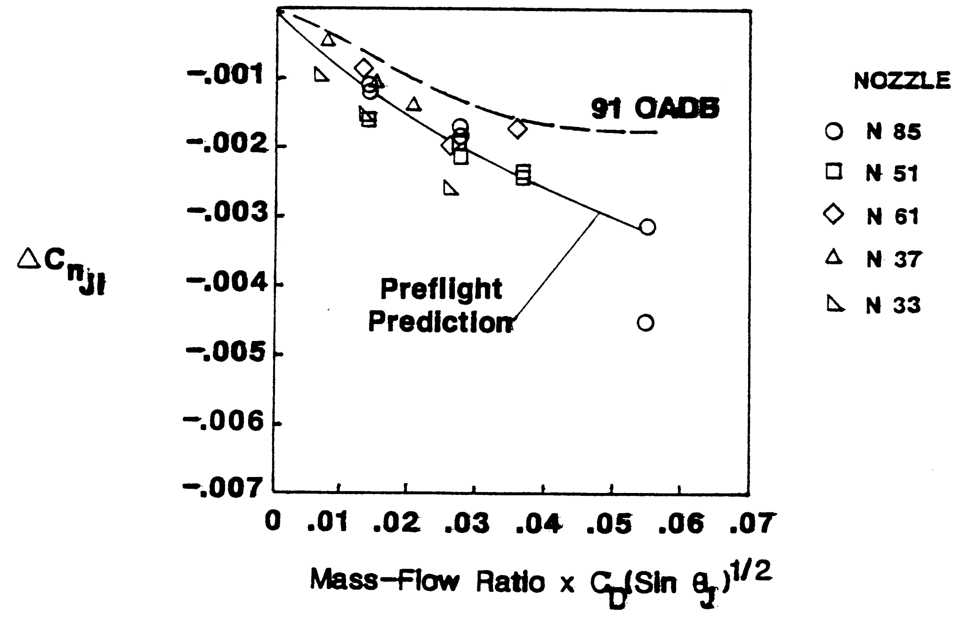

Figure 10. The preflight predicted yawing-moment interaction coefficients compared with flight-derived values.

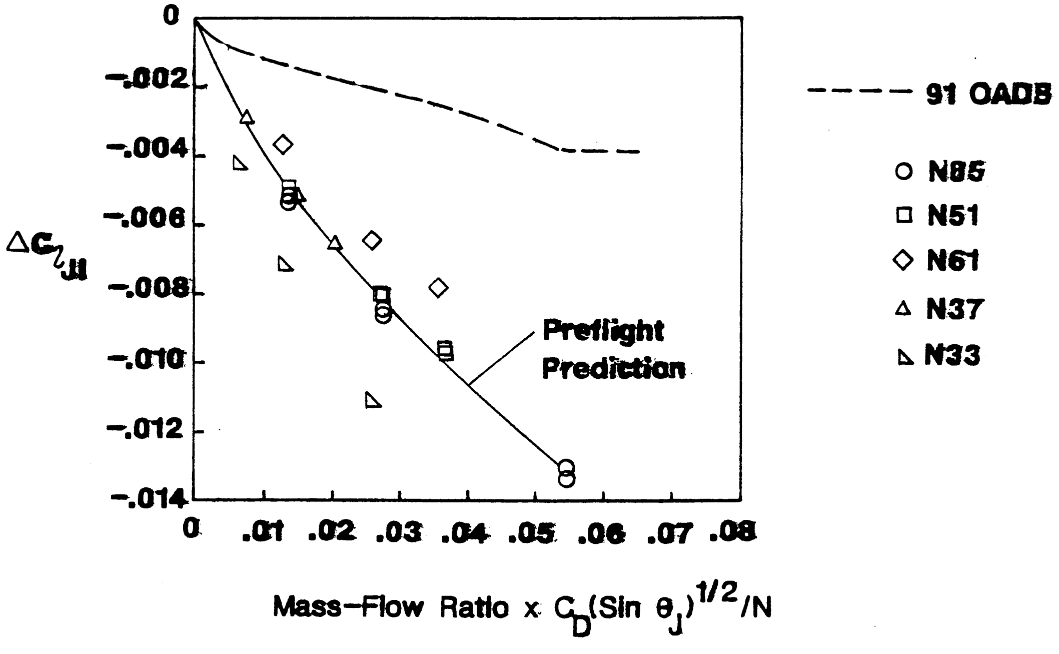

Figure 11. The preflight predicted rolling-moment interaction coefficents compared with flight-derived values.

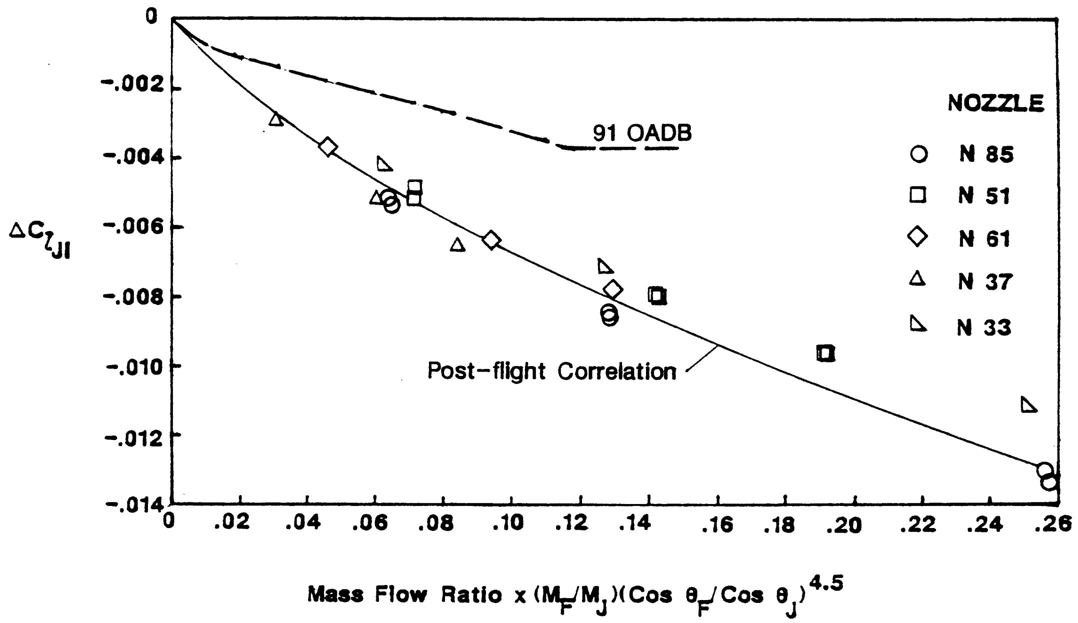

Figure 12. Post-flight correlation of the preflight rolling-moment interaction coefficients as a function of mass-flow ratio.

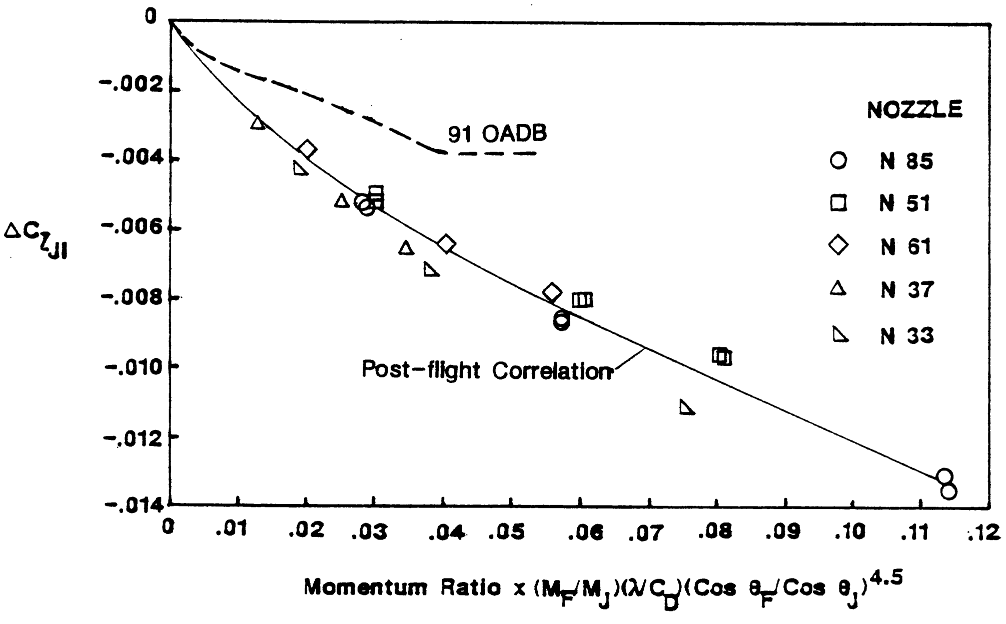

Figure 13. Post-flight correlation of the preflight rolling-moment interaction coefficients as a function of momentum ratio.

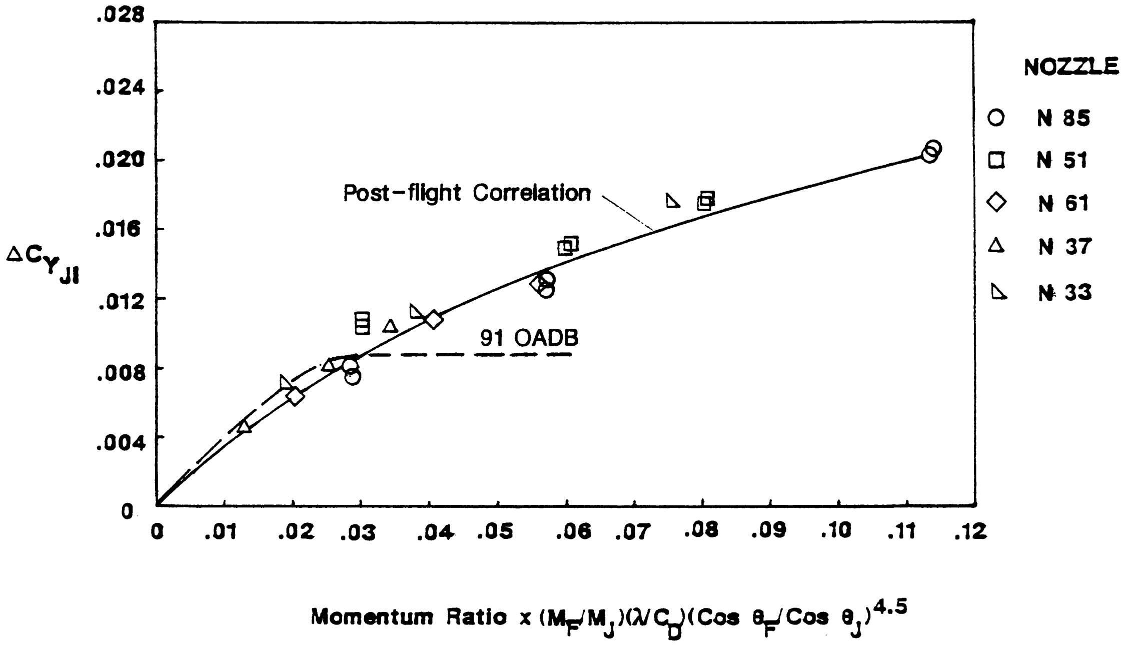

Figure 14. Post-flight correlation of the preflight side-force interaction coefficients as a function of momentum ratio.

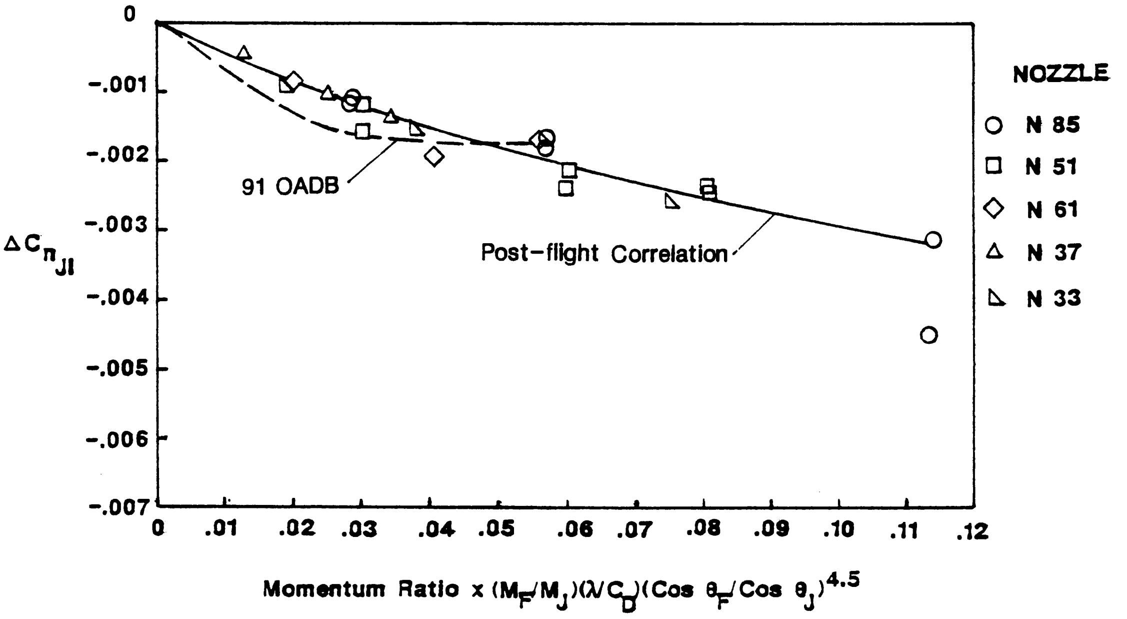

Figure 15. Post-flight correlation of the preflight yawing-moment interaction coefficients as a function of momentum ratio.

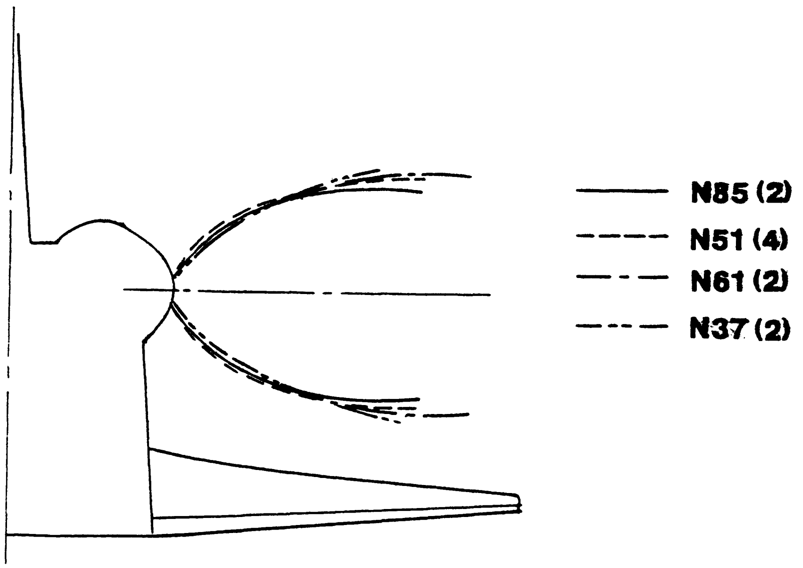

Figure 16. Calculated preflight nozzle plume shapes for a constant rolling-moment interaction coefficient of 0.0021. Calculations based on exit-to-free stream static pressure ratios. Mach 10, $\alpha = 36°$.

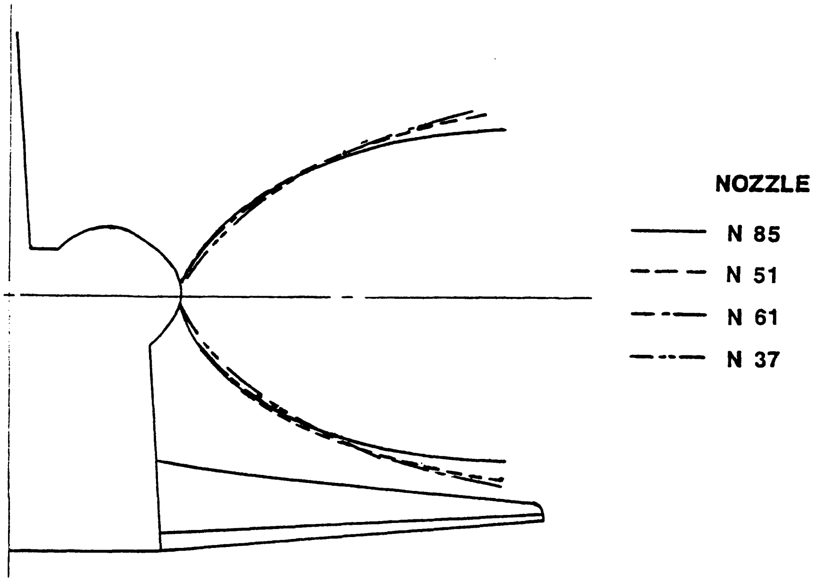

Figure 17. Calculated preflight nozzle plume shapes for a constant rolling-moment interaction coefficient of 0.0043. Calculations based on exit-to-free stream static pressure ratios. Mach 10, $\alpha = 36°$.

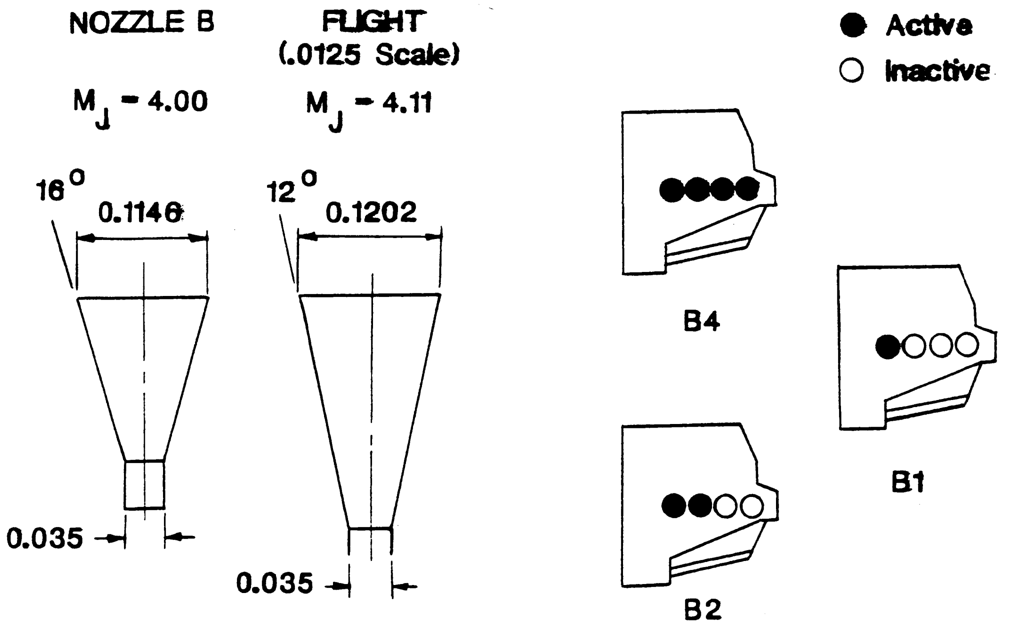

Figure 18. Nozzle configurations used with 0.0125-scale model tested in AEDC tunnels B and C at Mach 6 and 10, respectively.

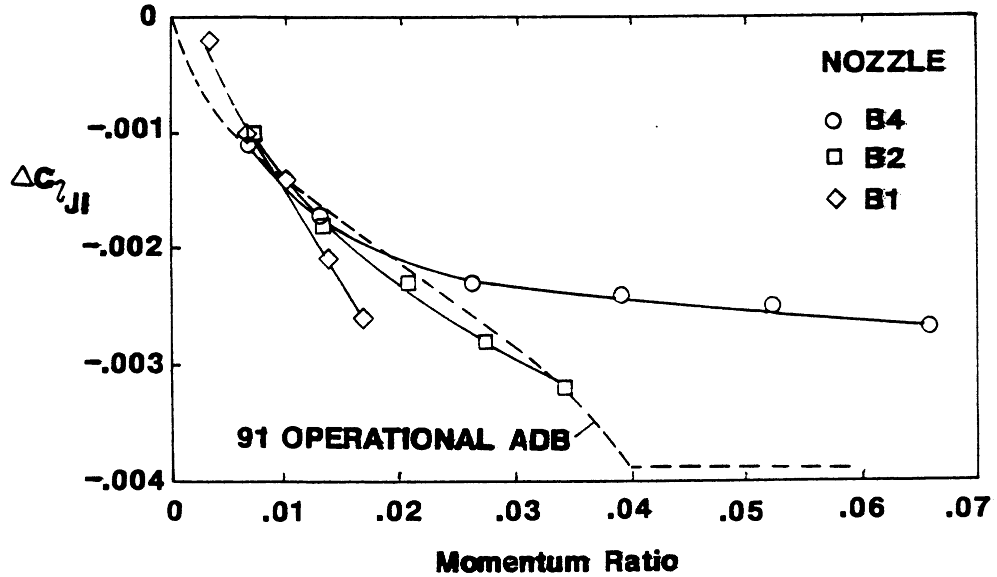

Figure 19. Variation of rolling-moment interaction coefficient with momentum ratio obtained from post-flight tests at Mach 6. Re = 0.368 x 10^6, α = 40°.

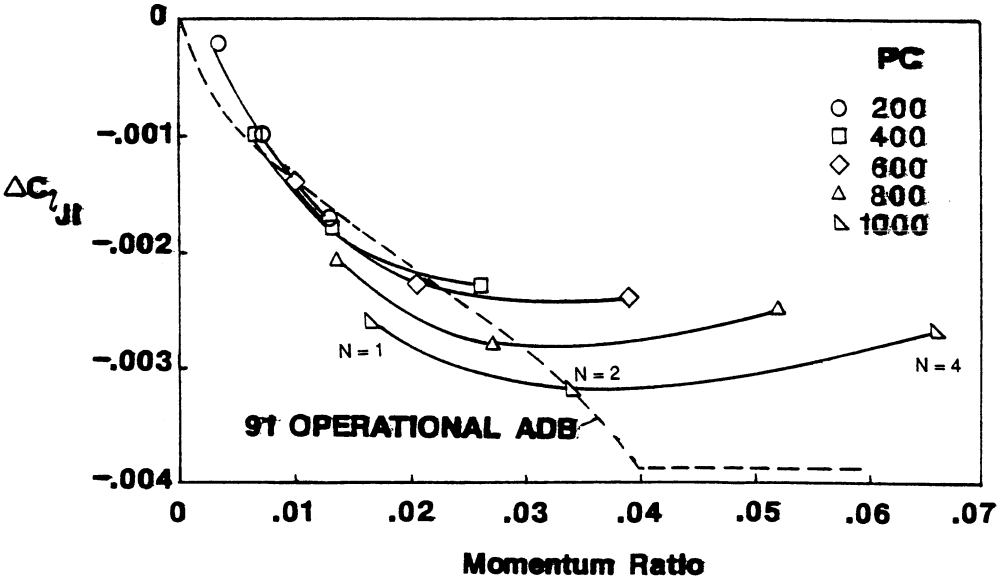

Figure 20. Variation of rolling-momentum interaction coefficient with momentum ratio at constant chamber pressure. Mach 6, Re = 0.368 x 10^6, α = 40°.

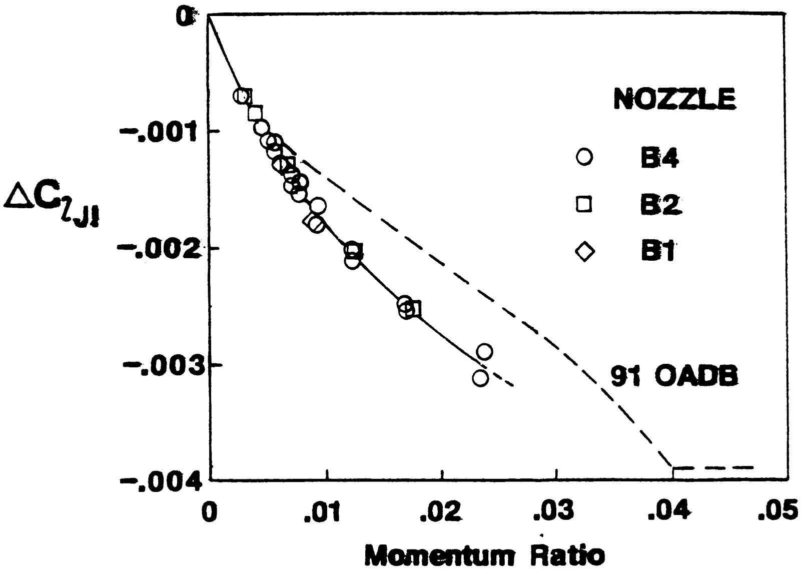

Figure 21. Variation of rolling-moment interaction coefficient with momentum ratio obtained from post-flight tests at Mach 10. Re = 0.736 x 10^6, α = 40°.

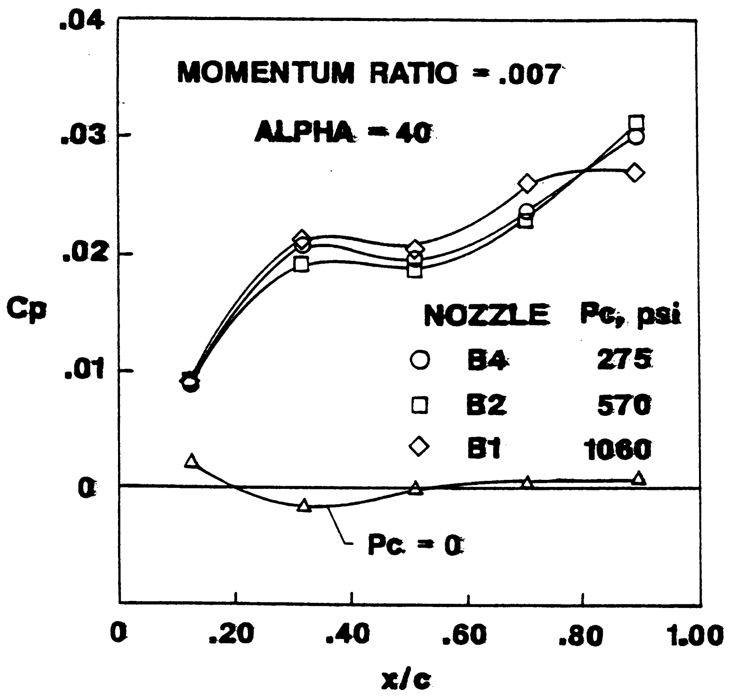

Figure 22. Chordwise pressure distributions at wing semi-span station Y/(b/2) = 0.378 at a constant momentum ratio for 1, 2, and 4 active nozzles. Mach 10.

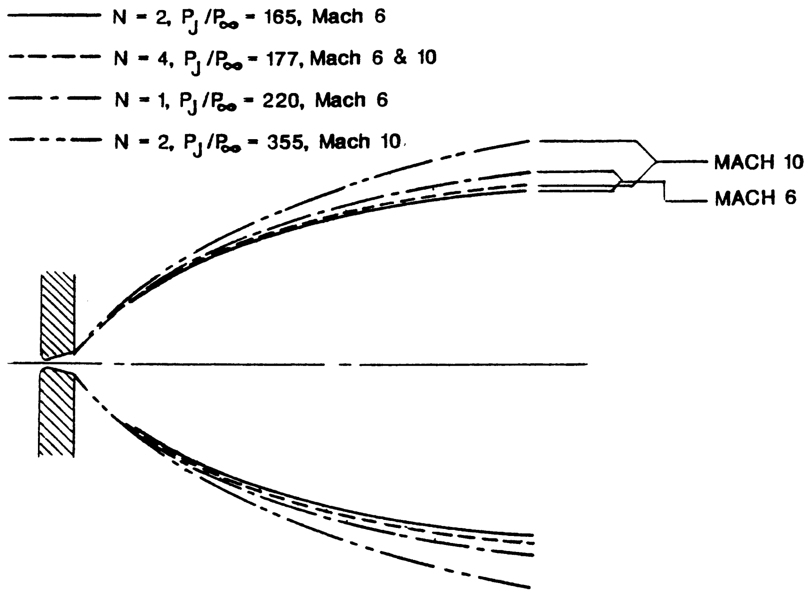

N = 2, P_J/P_∞ = 165, Mach 6
N = 4, P_J/P_∞ = 177, Mach 6 & 10
N = 1, P_J/P_∞ = 220, Mach 6
N = 2, P_J/P_∞ = 355, Mach 10
MACH 10
MACH 6

Figure 23. Comparison of model plumes for the same rolling-moment interaction, $\Delta C_{l_{Jl}} = -0.0025$, as obtained from post-flight tests at $\alpha = 40°$.

Mach	Jet	N	Mom. Ratio
10	N85	2	0.0060
	N71	4	0.0122
	N37	2	0.0127
	N61	2	0.0092
↓	B2	2	0.0177
10	B4	4	0.0170
6	B1	1	0.0160
↓	B2	2	0.0232
6	B4	4	0.0484
26.9	Flt.	2	0.0250
25.9	Flt.	4	0.0250

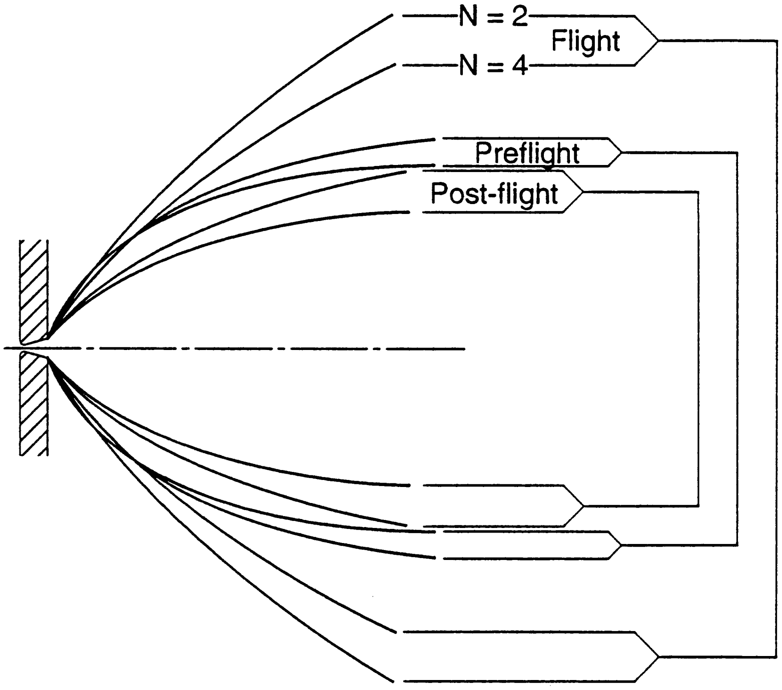

Figure 24. Comparison of wind-tunnel model and flight plumes for the same rolling-moment interaction, $\Delta C_{l_{JI}} = -0.0025$ at $\alpha = 40°$.

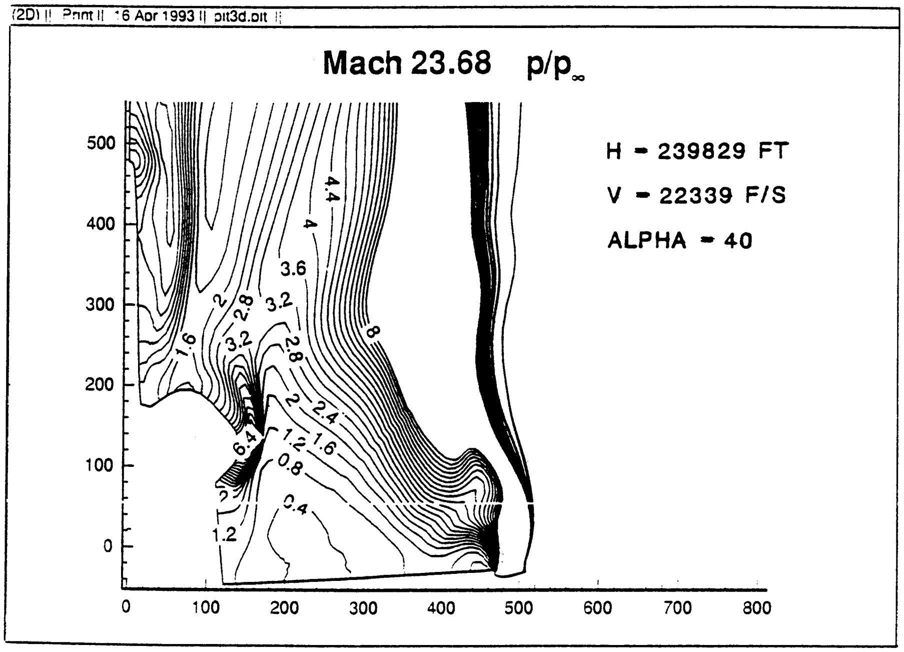

(a) Ratio of local-to-free stream static pressure at Mach 23.68.

Figure 25. Shuttle leeside flow fields in the region of the side-firing RCS as taken from reference 20.

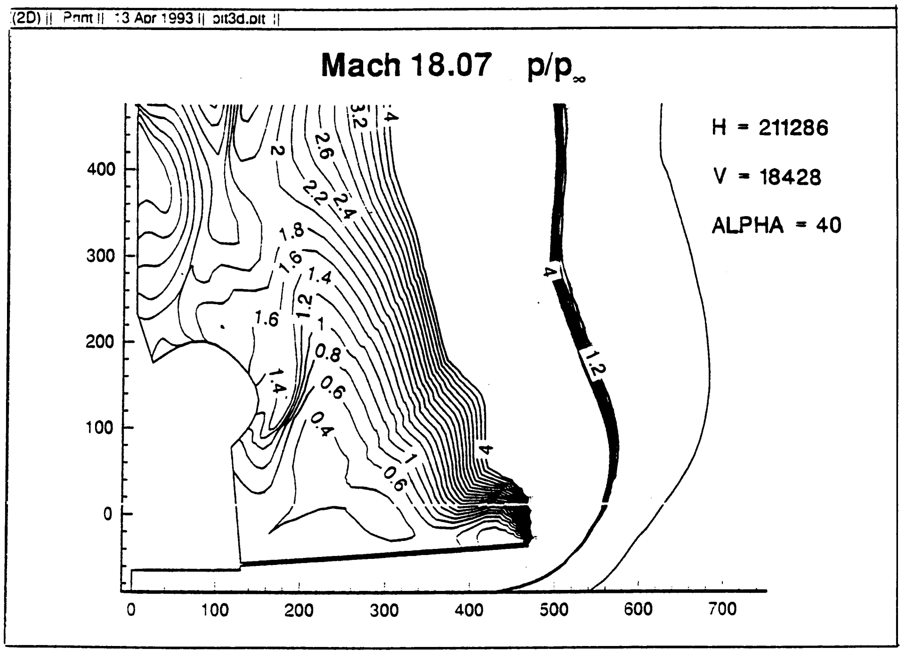

(b) Ratio of local-to-free stream static pressure at Mach 18.07.

Figure 25. Continued.

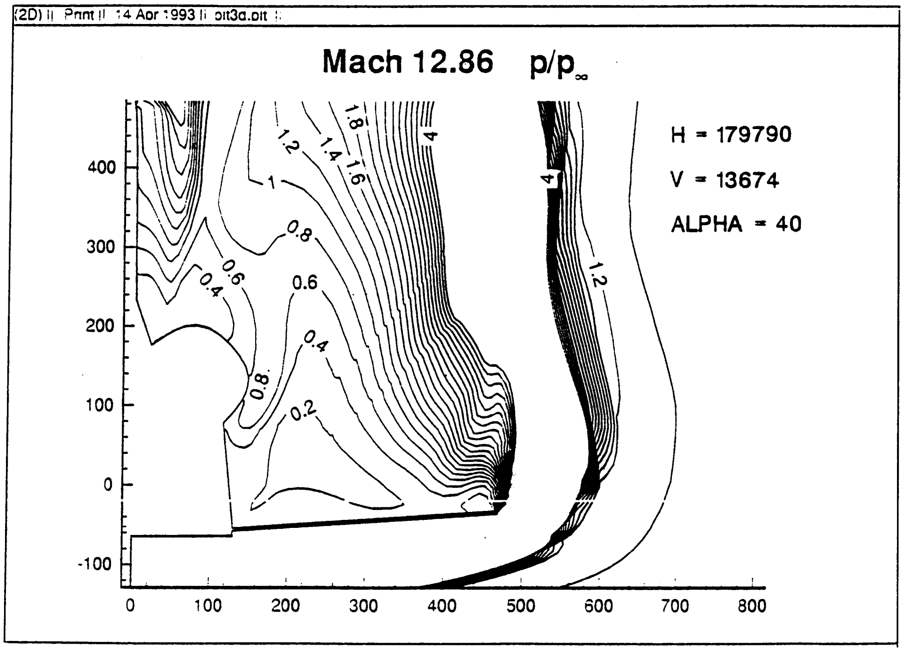

(c) Ratio of local-to-free stream static pressure at Mach 12.86.

Figure 25. Concluded.

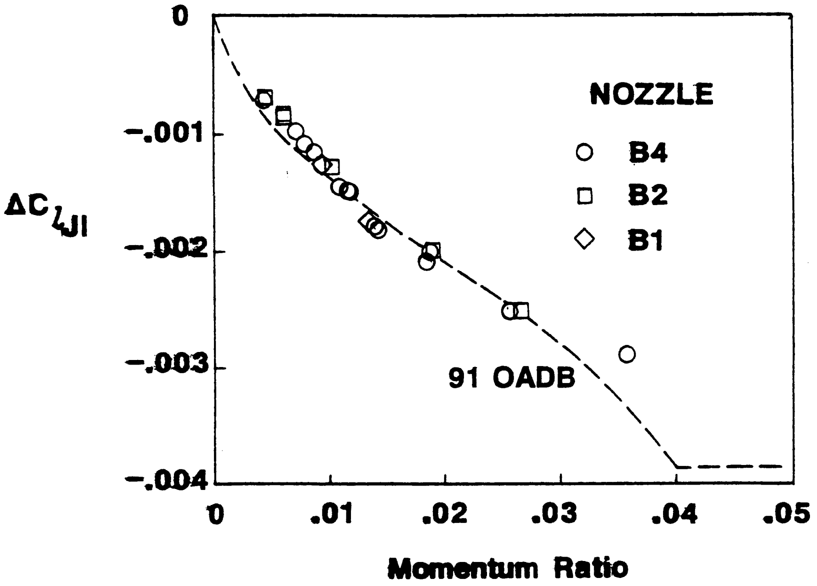

Figure 26. Post-flight rolling-moment interaction coefficients plotted as a function of momentum ratio adjusted by the ratio of local-to-free stream momentum ratio at Mach 23.68 to that at Mach 12.86 as taken from reference 20.

SHUTTLE ORBITER AERODYNAMICS - COMPARISON BETWEEN HYPERSONIC GROUND-FACILITY RESULTS AND STS-1 FLIGHT-DERIVED RESULTS

W. C. Woods and R. D. Watson
NASA Langley Research Center
Hampton, VA

INTRODUCTION

The first Shuttle flight, STS-1 on April 14, 1981, was unique in the history of American manned aerospace vehicle development in that no graduated flight test program was performed to perfect the wind tunnel based aerodynamic data book prior to flight. (The only flight tests were the five approach and landing tests, ALT 1-5.) A sub scaled flight vehicle or an unmanned first flight were rejected due to schedule constraints and expense. There was a high level of confidence in the subsonic through supersonic aerodynamic data base, since the subsonic data were explicitly supported by the approach and landing tests and the transonic/supersonic data were implicitly supported by the historical development of U.S. supersonic airplanes. However, there was a lower level of confidence in the hypersonic regime due to uncertainties related to real gas, viscous interaction, and low density effects and the overall influence of boundary layer transition (when and how it would occur) on aerodynamic performance. This country had three conventional hypersonic blowdown facilities (Aronld Engineering and Development Center Tunnel B, Naval Surface Warfare Center Tunnel 9 and Langley Research Center 22-Inch Helium Tunnel) capable of simultaneous Mach number and Reynolds number simulation for Shuttle entry but for ideal gas flow fields. Analytical codes, in the 1970's, lacked the capabilities provided by current computational fluid dynamic computer codes and were generally limited to viscous flows on simple shapes (such as cones) and inviscid flows on simplified 3-dimensional geometries at angles of attack less than the Shuttle entry angle of attack.

NASA attempted to bound these aerodynamic uncertainties in the hypersonic regime by several methods. In general, configuration screening was conducted in NASA's hypersonic research facilities (relatively small, inexpensive blowdown tunnels) and benchmark performance, stability, and control characteristics in hypersonic continuum flow were determined in the Department of Defense's relatively large hypersonic facilities (refs. 1, 2). Heavy gas simulation of real gas effects (lower ratio of specific heat than ideal air) was attempted using the Langley 20-inch Mach 6 CF_4 Tunnel. This facility and corresponding test techniques were quite immature at that time and the results were subject to question. Analytical methods were used to calculate both ideal gas and equilibrium air chemistry effects on a simplified orbiter shape at Mach numbers of 10 and 26 and an angle of attack of 25° (ref. 3) in an effort to deduce real gas influences on aerodynamic coefficients. There was no effect on axial force coefficient (the solution was inviscid) but normal, lift, and drag coefficients were reduced about 10% along with a nose up increment of about 0.03 in pitching moment coefficient, all attributed to real gas effects. The magnitude of this real-gas effect was within the scatter of the wind tunnel data base. Therefore, a decision was made to correlate the wind tunnel data in terms of Mach number up to a Mach number of 15, emphasizing the high fidelity model data in the large DOD facilities, and correlate in terms of the viscous parameter, V'_∞, for Mach number greater than 15 or $V'_\infty \geq 0.01$, emphasizing results from low density impulse facilities. This approach produced a preflight data book that indicated for the expected vehicle center of gravity location and elevon deflection during entry (2° up to protect them from possible excessive heating), that about 8° of body flap would trim the vehicle in the high Mach number domain. During STS-1, approximately 16° of body flap was required for trim at Mach numbers greater than 17. This difference between what occurred during the first flight and what was predicted by the preflight data book is commonly referred to as the "Shuttle trim anomaly."

In 1983, there was a "Lessons Learned" conference at the Langley Research Center with Shuttle flights STS-1 through 5 as the focus (ref. 4). Five presentations at this conference discussed some aspect of the trim anomaly (refs. 3, 5-8) and the literature contains on the order of 8 to 10 other publications (for example, refs. 9 and 10) on the subject. Although some consideration was given to the possible influences of compressibility or Mach number (ref. 6) and boundary layer transition (ref. 3) on trim, the general consensus was that real-gas effects (as indicated by the mid 70's calculations) were the primary cause of the trim anomaly. However the cause(s) of the trim anomaly were not unconditionally resolved at the "Lessons Learned" conference and have continued to be a topic for discussion and debate. That is, were real-gas effects the primary contributor to the anomaly, or were other first order effects, such compressibility, viscous interaction, or low density effects (e. g. ref. 10) responsible.

The present paper represents a revisit to the pre-flight wind tunnel data base and Shuttle flight data in an effort to determine why differences occurred between these data. Added to this information are post-flight wind tunnel data obtained using improvements in testing techniques and additional Shuttle flights which augment the flight data base. The emphasis is on STS-1 because it was the first flight, with the design hypersonic aerodynamics based only on wind tunnel data without the benefit of previous flight information for adjustments to the data base. One additional flight (STS-28) is of particular interest because boundary layer transition occurred earlier (higher Mach number and altitude) than other flights. The objective of this revisit is to determine if the preflight data base was adequate, from hindsight, to explain the anomaly. Was it incapable of defining the anomaly or was the anomaly contained in the data base and overlooked. The approach is to identify principal tests and hypotheses, review contributing test data and compare to flight, and examine inconsistencies between specific wind tunnel data and flight to determine possible causes. New test results conducted to support this symposium (ref. 11) are included in the analysis.

SYMBOLS AND ABBREVIATIONS

B	Arnold Engineering and Development Center Tunnel B
b	wing span, ft (78.051 ft full scale)
C'	Chapman-Rubesin viscosity coefficient based on reference temperature conditions, $(\mu'/\mu)(T/T')$
CALSPAN	CALSPAN 48" Shock Tunnel
C_A	axial-force coefficient, axial force/$q_\infty S$
C_D	drag coefficient, drag/$q_\infty S$
CF_4	Langley Research Center 20" Mach 6 CF_4 Tunnel
C_L	lift coefficient, lift/$q_\infty S$
C_m	pitching-moment coefficient, pitching moment/$q_\infty Sc$
C_N	normal-force coefficient, normal force/$q_\infty S$
c	mean aerodynamic chord, ft (39.567 ft full scale)
H(TO), H	heat transfer coefficient, fig. 2 (ref. 12), fig 3 (ref. 13).respectively BTU/ft^2-sec-°R

HREF, Ho	reference heat transfer coefficient based on Fay-Riddel theory, fig. 2 (ref. 12), fig 3 (ref. 13).respectively BTU/ft^2-sec-°R
L	reference length, feet (107.525 ft full scale)
L/D	lift-to-drag ratio, C_L/C_D
M	Mach number
MH2A, 2B & OH4A	Shuttle wind tunnel heating tests, fig. 2(c) (ref. 12)
q	dynamic pressure
R	Reynolds number, $\rho VL/\mu$
S	reference area, ft^2 (2690 ft^2 full scale)
T	temperature, °R
T'	reference temperature, °R
V	velocity
V'	viscous parameter, $M\sqrt{C'}/\sqrt{R}$
X_o	longitudinal distance along shuttle fuselage, inches

Y_o, Y	lateral distance from shuttle fuselage centerline, inches
y	vertical distance through the boundary layer, inches
Z_o	vertical distance from shuttle fuselage waterline, inches
α	angle of attack, degrees
δ	control deflection
γ	ratio of specific heats (gamma)
γ_e	isentropic exponent (effective gamma)
μ	viscosity
ρ	density
8A	Naval Surface Warfare Center Tunnel 8A
9	Naval Surface Warfare Center Tunnel 9
20"	Langley Research Center 20" Mach 6 Air Tunnel
22"	Langley Research Center 22" Mach 20 Helium Tunnel

Subscripts:

BF	body flap
E	elevon
e	boundary layer edge conditions
o, t	total
w	wall
∞	free stream

Abbreviations:

ADDB	Aerodynamic Design Data Book (ref. 17)
AEDC	Arnold Engineering Development Center
CALSPAN	Arvin Calspan Advanced Technology Center
c. g.	center of gravity
EI	entry interface, 400,000 ft altitude
LaRC	Langley Research Center

NSWC	Naval Surface Weapons Center
RCS	reaction control system
STS-1, 28	Shuttle flights
WT	wind tunnel

DISCUSSION

STS-1

Flight results from STS-1 are presented in fig. 1(a) with Reynolds number, angle of attack, and body flap deflection plotted vs Mach number. Also shown are the broad ranges of flight conditions that the orbiter experiences from non continuum low density through continuum real gas to ideal gas flows. In addition, the boundary layer was expected to be laminar initially and to transition to turbulent sometime during entry. A domain for each of these conditions is indicated on the figure, but, the actual points where each occur was not known prior to STS-1. Due to unknowns in the pre flight data, a relatively benign entry trajectory was proposed with angle of attack being maintained near 40° until $M_\infty \approx 12$, and the body flap being the aerodynamic control responsible for maintaining trim.

The flight results indicate that above $M_\infty \approx 26$, where q_∞ is extremely low, the body flap appears to be oscillating and eventually maintains trim at a deflection of about 16° where it remains constant until about Mach 18 when it decreases to 14°. At $M_\infty \approx 14$, the body flap deflection starts stepping down until at $M_\infty \approx 9$ it reaches a value of approximately 7°. From entry interface (400,000 ft altitude, $q_\infty \approx 0.02$ psf) to about 299,000 ft. altitude ($q_\infty \approx 2$ psf) control is provided by RCS. From this point, blended RCS and aerodynamics provide control until dynamic pressure increases to 20 psf (about 248,000 ft. altitude). Then longitudinal control depends only on aerodynamics (RCS provides directional control until $M_\infty \approx 1.5$).

A detailed examination of the region of mixed aero and RCS control is presented in fig. 1(b) where α, δ_E, and δ_{BF} are presented as functions of V'_∞. The range in V'_∞ from 0.1 to 0.001 corresponds to $M_\infty \approx 27$, 315,000 ft. altitude and $M_\infty \approx 5.5$, 125,000 ft. altitude respectively. The values of dynamic pressure that define the domain of blended control ($2 < q_\infty < 20$) are indicated on the figure and coincide with $0.07 > V'_\infty > 0.02$ (reference 3). Although it is not obvious from the figure, there is little, if any, aerodynamic control until q_∞ increases to near 20 psf. This is illustrated in fig. 1(b) where α, responding to RCS thrusters firing in alternating directions, oscillates from 41° to 39° and the control surfaces appear to wander ($-5° \leq \delta_E \leq 5°$ and $8.5° \leq \delta_{BF} \leq 19°$). As aerodynamic control became predominant ($q_\infty \rightarrow 20$ psf) the elevons remained negative and the body flap remained near 16°. In the hypersonic regime angle of attack ($\alpha \approx 40°$) and elevon position ($\delta_E \approx -2°$) were predetermined and the body flap was responsible for maintaining those settings. The data book indicated $\delta_{BF} \approx 7°$ would be sufficient. The fact that it wasn't and this condition persisted through many regimes (low density, real gas, continuum, laminar and turbulent flow) produced the trim anomaly.

Preflight Data

Prior to examining shuttle flight results it is beneficial to look at specific wind tunnel results to establish the basis of the preflight data base. Pitching moment as a function of angle of attack for various values of Reynolds number and body flap deflection as measured in AEDC Tunnel B on a 0.02-scale high fidelity shuttle model at Mach 8 in air is presented in fig. 2(a),. (ref. 1). For zero control deflection ($\delta_{BF} = 0°$), increasing Reynolds number from 1.3×10^6 to 4.3×10^6 caused a positive increment (nose up) in pitch as might be anticipated due to an expected decrease in skin friction on the lower surface with increasing Reynolds number. But an additional increase in Reynolds number to 5 x 10^6 showed no additional effect. This implies no further reduction in skin friction and suggests the possible onset of transition or some mixed flow (laminar, transitional, turbulent) condition. It is admitted that some of the differences shown are within experimental data uncertainty and therefore this analysis is speculation. The body flap is effective, producing substantial nose down pitching moment for both 16.4° and 22.6° deflections. At $\alpha = 40°$, $\delta_{BF} = 16.4°$, a nose down increment of $\Delta C_m \approx -0.04$ is produced relative to $\delta_{BF} = 0°$. Body flap deflections, at $M_\infty = 8$, were only tested at the higher Reynolds number of 5 x 10^6 (compared to 7.5 x 10^6 in flight).

Results from heating tests conducted in Tunnel B to determine the location of transition on a 0.0175 scale model with simulated randomly misaligned thermal protection system tiles are presented in figs. 2(b) and 2(c) (ref. 12). These tests show, for $T_w/T_t \approx 0.44$ and a Reynolds number of 1.9 x 10^6 (a unit Reynolds number of 1 x 10^6/ft, fig. 2(b)), laminar heating profiles occurred regardless of roughness . However, for a Reynolds number of 7 x 10^6 (a unit Reynolds number of 3.7 x 10^6/ft, fig. 2(c)) transition occurred near $X/L \approx 0.5$ for a range of roughness. These test conditions bracket the force test results of fig. 2(a) suggesting the possibility of mixed flow conditions influencing the force measurements as was inferred by analysis of the force results. However, in general, the force test results of fig. 2 exhibit the expected response to Reynolds no. and control deflection effects.

Force results at $M_\infty = 13.5$, in Nitrogen, from NSWC Tunnel 9, are presented in fig. 3(a) (ref. 2). During this test Reynolds number was varied for all three body flap deflections (0°, 16.4°, and 22.6°). The higher test Reynolds number (4.1 x 10^6) duplicates full scale flight Reynolds number at $M_\infty \approx 13.5$. Increasing Reynolds number from 1.2 x 10^6 to 4.1 x 10^6 tends to have opposite results depending upon angle of attack and control deflection. For example, for 0° controls increasing Reynolds number produces nose up C_m when $\alpha < 37°$ and nose down C_m

when $\alpha > 37°$. For deflected controls the C_m curves cross for $\alpha < 19°$ so increasing Reynolds number produces nose down pitch for $\alpha > 19°$ and $\delta_{BF} > 0°$. These variations could indicate mixed flow conditions. For example, for all laminar flow on the lower surface increasing Reynolds number accompanied by a reduction in skin friction coefficient should result in a nose up pitching moment coefficient. But the onset of transition, possibly due to increasing α can reverse this trend. Fortuitously, at $\alpha \approx 40°$ for both 0° and 16.4° body flap the values of C_m at both the low and high Reynolds number are in close proximity so Reynolds number appears to have little effect on control effectiveness at $\alpha \approx 40°$, $\delta_{BF} \approx 16.4°$. To quantify this for comparison to the other results, for flight Reynolds number ($R = 4.1 \times 10^6$), at $\alpha = 40°$, $\delta_{BF} = 16.4°$ produces nose down pitching moment of $\Delta C_m \approx -0.053$.

Results obtained in tests conducted in NSWC tunnel 9, in Nitrogen, to extend the heating wind tunnel data base to $M_\infty \approx 14$, $R_\infty \approx 7 \times 10^6$ are presented in fig. 3(b) (ref. 13). Similar to the $M_\infty \approx 8$ tests, the heating model was .0175 scale so the test Reynolds numbers of 3.3×10^6 (unit Reynolds number. of 1.75×10^6/ft) and 7.2×10^6 (unit Reynolds number. of 3.85×10^6/ft) bound the force results at flight Reynolds number (4.1×10^6). For both Reynolds numbers at $\alpha = 40°$ these results exhibit a departure in surface heating from what appears to be a laminar distribution by $x/L < 0.6$. Therefore the heating tests appear to support the conclusion that non laminar surface flow conditions existed ahead of the body flap hinge line for the $M_\infty = 13.5$, $R_\infty = 4.1 \times 10^6$ force tests.

The data of figs. 2 and 3 were considered the best continuum ideal air and Nitrogen results available. To simulate aerodynamic performance at lower densities corresponding to higher altitudes, tests were conducted in the CALSPAN 48" shock tunnel (ref. 14). An example of these results is shown in fig. 4 for $M_\infty = 15$, $R_\infty = 0.05 \times 10^6$ and 0.26×10^6, and body flap deflections of 0° and 16.4°. The results were on the whole similar to the $M_\infty = 13.5$ continuum results in that for 0° body flap C_m vs α curves for two different Reynolds numbers coincidentally cross at $\alpha = 40°$ while for 16.4° body flap the curves are essentially parallel. This creates the appearance, similar to the lower Mach number/Reynolds number continuum results, that variation in Reynolds number at $\alpha = 40°$ had little effect on the magnitude of pitching moment produced by the deflected body flap. Moreover, like the Mach 8 results, 16.4° of body flap produces a nose down pitching moment increment on the order of -0.04 at $\alpha = 40°$.

The Shuttle aerodynamic test data base developed used tests in facilities that could match or bound the expected extremes the vehicle would encounter in Mach number, Reynolds number, and V'_∞. Figures 2 through 4 presented results referenced to the data base reference center of gravity of 0.65L. Figure 5 presents the results of figs. 2 - 4 transferred to the STS-1 reference center of gravity (0.667L) for $\delta_{BF} = 0°$ (fig. 5(a.)) and 16.4° (fig 5(b.)). In addition, data from the data base, acquired in the LaRC 22-Inch Mach 20 Helium Tunnel at flight Reynolds (ref. 15) and in NSWC Tunnel 8A at $M_\infty \approx 18$, low Reynolds number ($R_\infty = 0.26 \times 10^6$), continuum conditions (ref. 16) are included. These results show a range of C_m for $\delta_{BF} = 0°$ at $\alpha \approx 40°$ of $\Delta C_m \approx 0.03$ ($0 \leq C_m \leq 0.03$) and a range of C_m (fig. 4(b)) for 16.4° body flap of $\Delta C_m \approx 0.034$ ($-0.045 \leq C_m \leq -0.011$). In all cases, the data implied something less than 16.4° of body flap would provide trim. The fundamental dilemma was, with the exception of refs. 11 and 12, there was no diagnostic pressure and heating data (global or otherwise) to support a rationale for which, if any, hypersonic wind tunnel results best predicted flight stability and control.

The scatter in the wind tunnel data and the vague projections of when transition would occur in flight (see e.g., ref. 12, table 3, range of probable transition, $2{,}610 \leq R/ft \leq 44{,}194$, or $0.28 \times 10^6 \leq R_\infty \leq 4.75 \times 10^6$) added to the uncertainties in preflight trim predictions. Calculations on simple shapes such as cones provided some guidance on the possible influence of low density, viscous, and real-gas effects (ref. 3). In addition calculations on cones provided a means of comparing boundary layer thickness at both flight and wind tunnel conditions to assess the possible influence of the boundary layer on control effectiveness. Boundary layer profiles on 30°

cones calculated, using the methods of ref. 17, at both flight conditions and wind tunnel conditions, are presented in fig. 6. The ratio of vertical height in the boundary layer to the distance from the nose (y/L) is plotted against the ratio of local dynamic pressure to the dynamic pressure at the edge of the boundary layer (q/q_e). The physical quantity L represents a surface distance equal to the distance from the nose to the body flap hinge line on the Shuttle. The sketch in the upper right corner indicates where along the surface length the profile is calculated. The relative height of the trailing edge of the Shuttle body flap divided by the distance from the nose to the body flap hinge line for $\delta_{BF} = 7°$ and 14° is denoted on the right border of each plot to indicate the location of the body flap relative to boundary layer thickness and local dynamic pressure. These calculations indicate that for the relatively low density test environments produced by NSWC Tunnel 8A (fig. 6(a)), which generally induce laminar boundary layers, the body flap could be submerged in a thick boundary layer where the local dynamic pressure is less than 10 percent of the edge dynamic pressure ($q/q_e < 0.1$). The heating data of figs. 2 and 3 indicated possible mixed boundary layers for tests in AEDC Tunnels B and NSWC Tunnel 9 where high density testing conditions are present. Therefore laminar, transitional, and turbulent boundary layer calculations are shown for these conditions in fig. 6(b). These results indicate that regardless of boundary layer state, higher dynamic pressures (q/q_e between 0.3 and 0.8 instead of less than 0.1) should exist in the vicinity of the body flap in these higher density facilities as compared to those from Tunnel 8A. Both laminar and turbulent calculations are presented for flight environments at Mach 18 and Mach 8 in fig. 6(c) showing boundary layer profiles similar to those determined for Tunnels B & 9, shown in fig. 6(b). These calculations support a possible explanation for the body flap being less effective in tests in Tunnel 8A as compared to tests in higher density facilities. Also these results could be considered an indication that results from ideal gas tunnels AEDC B and NSWC 9 and flight could exhibit similar body flap effectiveness and support a decision to base continuum body flap effectiveness on Tunnels B & 9 test data.

Missing from the ground-based aerodynamic data base was information addressing high temperature gas chemistry commonly referred to as "real gas effects." Inviscid analytical calculations, that were limited in terms of vehicle geometry and angle of attack, indicated for a modified geometry at $\alpha \approx 25°$ that high temperature gas chemistry effects reduced normal, lift, and drag coefficients about 10 percent and produced a nose up increment in pitching moment on the order of $\Delta C_m \approx 0.034$ (ref. 3, fig. 27). Heavy gas tests were conducted in the LaRC 20-Inch Mach 6 CF_4 Tunnel to simulate these effects. At that time this facility was still in development, was not well calibrated, and testing techniques were quite immature. As a result, the data obtained on models of the Shuttle orbiter in this facility were inconclusive (i.e. did not establish a definitive trend). The shuttle data book was formulated using all available wind tunnel data, emphasizing the data from AEDC Tunnel B and NSWC Tunnel 9 for the continuum portion of flight ($V'_\infty < 0.01$) and the CALSPAN Shock Tunnel data for the low density portion of flight ($V'_\infty > 0.01$). The nose up bias predicted from real-gas calculations was added to the tolerance and variation band built into the control system to insure the vehicle could handle out of trim moments of that magnitude. This philosophy basically produced the hypersonic portion of the preflight Aerodynamic Design Data Book (ADDB, ref. 18). Prior to the first shuttle flight concerns that the elevons might experience excessive heating resulted in the elevons being deflected up 2° ($\delta_E = -2°$). Based on aerodynamics in the ADDB (ref. 18), for the flight center of gravity and the guidelined elevon deflection, about 7° to 8° of body flap deflection was expected to be required in the hypersonic regime during STS-1.

Comparison Between STS-1 and Wind Tunnel Data

To compare wind tunnel data to flight results a common basis is required in terms of center of gravity and vehicle configuration. While this is obvious, it should be recognized that certain liberties must be taken with the data to provide commonality. All wind tunnel data and the data book used a reference c. g. located within the shuttle coordinate system at $X_O = 1076.68$ in., $Y_O = 0$ in., $Z_O = 375$ in. During entry, the actual shuttle c. g. varies as RCS fuel is used. At entry interface (EI), the c. g. location was calculated to be, $X_O = 1097.80$ in., $Y_O = 0.2$ in., $Z_O = 372.8$ in. When the vehicle was at Mach 3 it was calculated to be, $X_O = 1096.40$ in., $Y_O = 0.7$ in., $Z_O = 372.4$ in. The c. g. location assumed for comparing wind tunnel data to STS-1 was constant at $X_O = 1096.7$, $Y_O = 0$ in., $Z_O = 372.4$ in. Since the assumption of linearity for body flap and elevon effectiveness was also made, linear interpolation was used to calculate wind tunnel aerodynamic coefficients for observed flight control deflections for direct comparison with flight. For example see equation (1):

$$C_{N,WT/Flight} = C_{N,WT} + \left(\Delta C_{N,WT}/\Delta\delta_{BF,WT}\right)\left(\delta_{BF,\ Flight}\right) + \left(\Delta C_{N,WT}/\Delta\delta_{E,WT}\right)\left(\delta_{E,\ Flight}\right) \tag{1}$$

Selected wind tunnel data are compared to STS-1 flight results on the basis of compressibility effects (Mach number) in fig. 7. The wind tunnel data was taken from the references (refs. 1, 2, 11, 14, 15, 16) and the flight data was provided by Johnson Space Center. The letters and/or numbers near the data points identify the facility that produced the data (see symbols list). At Mach numbers of 6 and 8, the tunnel values of C_N agree with flight but at $13.5 \leq M_\infty \leq 21$ agreement varied from good to the wind tunnel results being 5 percent high (fig. 7(a)). Agreement between values of C_A measured in wind tunnel and flight varied from quite good to poor; they were generally within 10 percent except for the low density facilities (CALSPAN and Tunnel 8A) where viscous interaction effects cause larger C_A than would be experienced at the same Mach number in flight (fig. 7(b)). For the flight c.g. and control deflection, the preflight wind tunnel results determined that C_m varied from -0.008 (AEDC Tunnel 8A) to -0.035 (NSWC Tunnel 9) (fig. 7(c)). The recently conducted $M_\infty = 6$ test in air (20") agreed with flight and the recently conducted $M_\infty = 6$ test in CF_4 produced a positive C_m of +0.01. However this recent test data could not be adjusted for flight elevon settings because only $\delta_E = 0°$ was tested. It is important to note that the largest difference of -0.035 was the same as was indicated by early real gas calculations on a modified geometry, and that the low density test results from NSWC Tunnel 8A produced the preflight data closest to flight results. The pitch-up anomaly that occurred for STS-1 is clearly indicated in fig. 7(d) where the body flap required for trim is presented. At Mach numbers above 13 at least 14° of body flap was required. Only the recent CF_4 results and the low density results from Tunnel 8A required $\delta_{BF} > 10°$ for trim.

Stability axis data versus Mach number is shown in fig. 7 (e through g). Differences in lift and drag typically follow the same trend as normal coefficient. Agreement between wind tunnel and flight lift to drag ratio is good as should be expected since differences in lift and drag generally cancel in the ratio.

Aerodynamic coefficients are shown as a function of Reynolds number in fig. 8. At Reynolds numbers less than 1×10^6 when the flight attitude oscillated, the low density facilities appear to trace the flight data. For $R_\infty > 1 \times 10^6$ wind tunnel C_N was generally 5% greater than flight even for the 20" and AEDC Tunnel B results. This is mainly because at flight values of Reynolds number, the flight Mach number is greater than 10 and possible high temperature gas chemistry may still have a significant influence on the flight data. The low density tunnel results (CALSPAN, 8A), which should model to some extent viscous interaction effects, more closely follow the variation of C_A (fig. 8(b)) than when previously compared on the basis of Mach number (fig 7(b)). This should be expected. The agreement in C_m (fig. 8(c)) is no better than when Mach number was the basis for comparison. Only the CF_4 data comes close to the body flap deflection needed for trim. The stability axis data again follow the trends dictated by normal force coefficient with agreement between flight and wind tunnel varying from good to approximately 5% (figures 8(e-g)).

Wind tunnel and flight aerodynamic coefficients plotted vs. viscous interaction parameter $\overline{V}'_\infty$ ($= M_\infty\sqrt{C'}/\sqrt{R_\infty}$) is presented in fig. 9. The results exhibit similar trends as were shown with Reynolds number with the exception of $\delta_{BF,\ trim}$ where only the low density results from NSWC Tunnel 8A approximated flight body flap deflection (fig. 9(d)).

Reference 3 speculated that the boundary layer remaining laminar later than expected on STS-1 had as much influence on the trim anomaly as possible real gas effects. On subsequent flights transition occurred at different times (Mach numbers), generally in the $M \approx 9$ to 13 range until STS-28. On STS-28, lower surface centerline thermocouples indicated transitional and turbulent heating at $M \approx 18$. Figure 10 compares the data from AEDC Tunnel B and NSWC Tunnel 9 to STS-28 results using the same approach as the previous comparisons (referencing tunnel data to flight c. g. and using linear control effectiveness to interpolate tunnel data to the flight configuration). These comparisons are similar to those obtained from STS-1. Tunnel B data tends to agree with flight while Tunnel 9 C_N is about 10 percent higher than flight and C_m is about 0.025 nose down. The effect of boundary layer transition appears minor and this indirectly leads to the conclusion that real gas chemistry existing down to $M_\infty < 10$ is the predominant cause of the trim anomaly.

SUMMARY

In summary there was no wind tunnel data in the Shuttle pre-flight data base which conclusively indicated that a body flap deflection of approximately 16° would be required for trim during the first Shuttle entry. At the time state of the art in both wind tunnel testing and CFD was not capable of a conclusive determination of the effects of high temperature gas chemistry on specific vehicle stability and control. A direct comparison between wind tunnel and flight results for the Shuttle orbiter at high hypersonic conditions is not possible because all pertinent flight parameters (compressibility, viscosity, viscous interaction, real gas) cannot be simultaneously simulated or duplicated in ground based facilities. Comparison between wind tunnel and flight aerodynamic data, when the Mach number in flight is greater than eight, shows a difference in magnitude and direction bounded by the influence of real gas effects calculated for a modified geometry prior to the first flight (STS-1). Mach 6 and 8 wind tunnel data compared reasonably with $M_\infty = 6$ and 8 flight results. In addition, recent $M_\infty = 6$ data in heavy gas (CF_4) accurately modeled the pitch characteristics exhibited by the orbiter in flight. Agreement between data from low density facilities and flight at high Mach numbers is considered fortuitous. Low control effectiveness was seen in the tunnel data and the agreement occurred prior to the body flap becoming set at a fixed trim position. The only model that fits all contingencies is the influence of high temperature real gas chemistry affecting aerodynamics throughout the continuum regime to Mach numbers below 10. Considering the state of the art that existed in the 1970's, the ADDB did a commendable job of predicting pre-STS-1 aerodynamics. Improvements in test techniques and CFD discussed in references 11, 19, and 20 that are verified by flight results have provided NASA with the ability to determine preflight aerothermodynamics of future systems to an accuracy that did not exist when present operational systems were designed.

REFERENCES

1. Daileda, J. J.: Results of Tests Using A 0.02 Scale Model (105-0) of the Space Shuttle Orbiter in the Arnold Engineering Development Center Von Karman Facility Supersonic Tunnel A (OA 209) and Hypersonic Tunnel B (OA 208), NASA CR-151, 785, November 1979.

2. Daileda, J. J.: Results of Tests Using A 0.020 Scale Model (105-0) of the Space Shuttle Vehicle Orbiter in the Naval Surface Weapons Center Hypervelocity Tunnel 9. NASA CR-151764, October 1978.

3. Woods, W. C.; Arrington, J. P.; and Hamilton, H. H.: "A Review of Preflight Estimates of Real Gas Effects on Space Shuttle Aerodynamic Characteristics," Shuttle Performance Lessons: Learned, NASA C P 2283, Part 1, pp. 309-346, March 1983.

4. Arrington, J. P.; and Jones, J. J.: Shuttle Performance: Lessons Learned, NASP CP 2283, October 1983. Proceedings of a conference held at Langley Research Center, Hampton, Virginia, March 8-10, 1993.

5. Romere, Paul O.; and Whitnah, A. Miles: "Space Shuttle Entry Longitudinal Aerodynamic Comparisons of Flights 1-4 with Preflight Prediction," Shuttle Performance: Lessons Learned, NASP CP 2283, Part 1, pp. 283-307, March 1983.

6. Griffith, B. J.; Maus, J. R.; and Best, J. T.: "Explanation of the Hypersonic Longitudinal Stability Problem - Lessons Learned," Shuttle Performance: Lessons Learned, NASA CP 2283, Part 1, pp. 347-380, March 1983.

7. Compton, H. R.; Schiess, J. R.; Suit, W. T.; Scallion, W. I.; and Hudgins, J. W.: "Stability and Control Over the Supersonic and Hypersonic Speed Range," Shuttle Performance: Lessons Learned, NASA CP 2283, Part 1, pp. 473-507, March 1983.

8. Kirsten, P. W.; Richardson, D. F.; and Wilson, C. M.: "Predicted and Flight Tests Results of the Performance, Stability, and Control of the Space Shuttle From Reentry to Landing," Shuttle Performance: Lessons Learned, NASA CP 2283, Part 1, pp. 509-524, March 1983.

9. Young, James C.; and Findlay, John T.: An Analysis of the Space Shuttle Hypersonic Entry Trim Anomaly. AIAA Paper No. 85-1764-CP. Presented at the AIAA 12th Atmospheric Flight Mechanics Conference, Snowmass, Colorado, August 19-21, 1985.

10. Koppenwallner, Georg: "Low Reynolds Number Influences on Aerodynamic Performance of Hypersonic Lifting Vehicles", AGARD Fluid Dynamics Symposium on Aerodynamics of Hypersonic Lifting Vehicles, Bristol, U. K., April 6-9, 1987

11. Paulson, John W., Jr.; and Brauckmann, Gregory J.: Recent Ground Facility Simulations of Shuttle Orbiter Aerodynamics. Presented at Orbiter Experiments (OEX) Aerothermodynamics Symposium, Williamsburg, Virginia, April 22-30, 1993.

12. Wannenwetsch, G. D.; and Martindale, W. R.: Roughness and Wall Temperature Effects on Boundary-Layer Transition on A 0.0175 Scale Space Shuttle Orbiter Model Tested at Mach Number 8. AEDC-TR-77-19, August 1976.

13. Ragsdale, W. C.: Space Shuttle Heat Transfer Tests in the NSWC Hypervelocity Tunnel, NSWC MP 80-423, September 1980.

14. Burrows, R. R.; and Rogers, C. E.: Wind Tunnel Tests OA 113 of the 0.010-Scale Space Shuttle Orbiter Model 51-0 in the CALSPAN Hypersonic Shock Tunnel (48-Inch Leg), NASA-CR-141,S47, July 1975.

15. Hawthorne, P. J.: Results of A 0.004-Scale 140C Modified Configuration Space Shuttle Vehicle Orbiter Model (74-0) in the Langley Research Center Hypersonic Helium Tunnel. NASA CR-141532, May 1975.

16. Keel, A. G., Jr.; and Knott, J.: Static-Stability Testing of the 0.004-Scale Space Shuttle Orbiter in the White Oak Mach 18 Hypervelocity Research Tunnel. Naval Surface Weapons Center, White Oak Laboratory Wind-Tunnel Report No. 109, January 1976.

17 Harris, J. E.: Computer Program for Solving Laminar, Transitional or Turbulent Compressible Boundary-Layer Equations for Two Dimensional and Axisymmetric Flow. NASA TM-83207, February 1982.

18. Aerodynamic Design Data Book. Volume I - Orbiter Vehicle 102, Report No. SD72-SH-0060-Il, Rockwell International, October 1978.

19. Weilmuenster, K. J. and Gnoffo, P. A.: Navier-Stokes Simulations of Orbiter Aerodynamic Characteristics. Presented at Orbiter Experiments (OEX) Aerothermodynamics Symposium, Williamsburg, Virginia, April 22-30, 1993, NASA CP-3248.

20. Gnoffo, P. A. and Weilmuenster, K. J.: A Multiblock Navier-Stokes Analysis for Shuttle Orbiter Entry Heating from Mach 24 to Mach 12. Presented at Orbiter Experiments (OEX) Aerothermodynamics Symposium, Williamsburg, Virginia, April 22-30, 1993, NASA CP-3248.

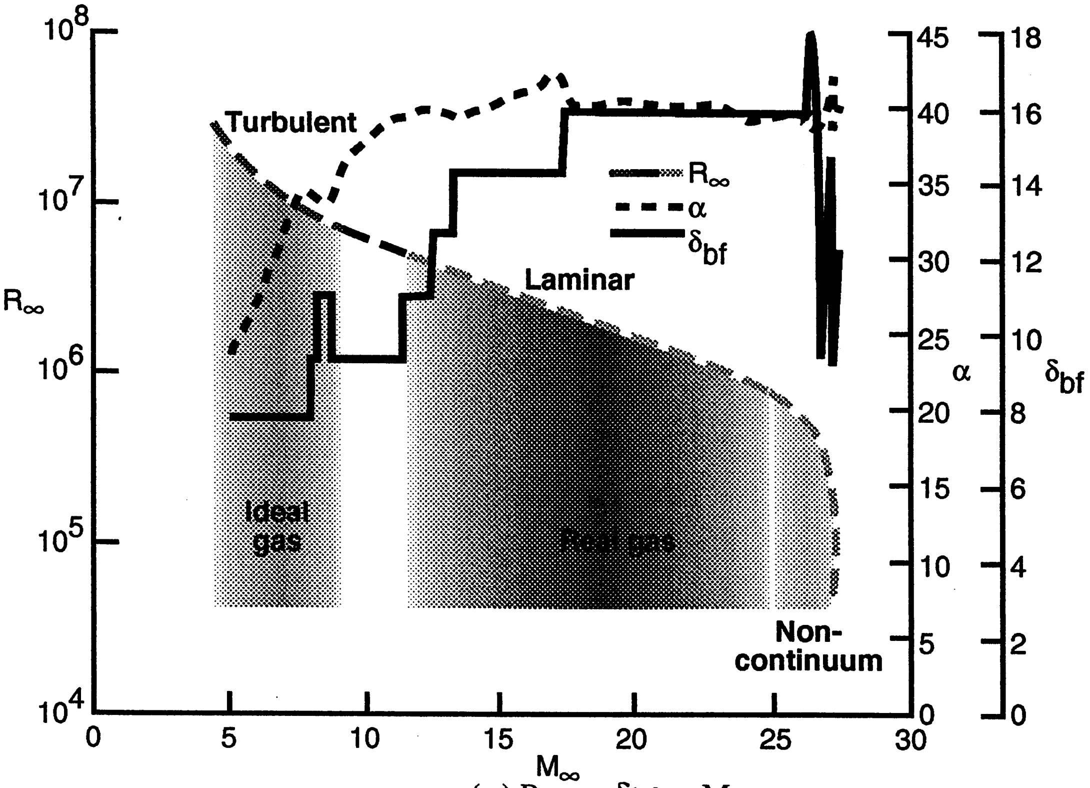

(a.) R_∞, α, δbf vs M_∞

Figure 1. - Variation of vehicle attitude, control configuration, and simulation parameters during STS-1.

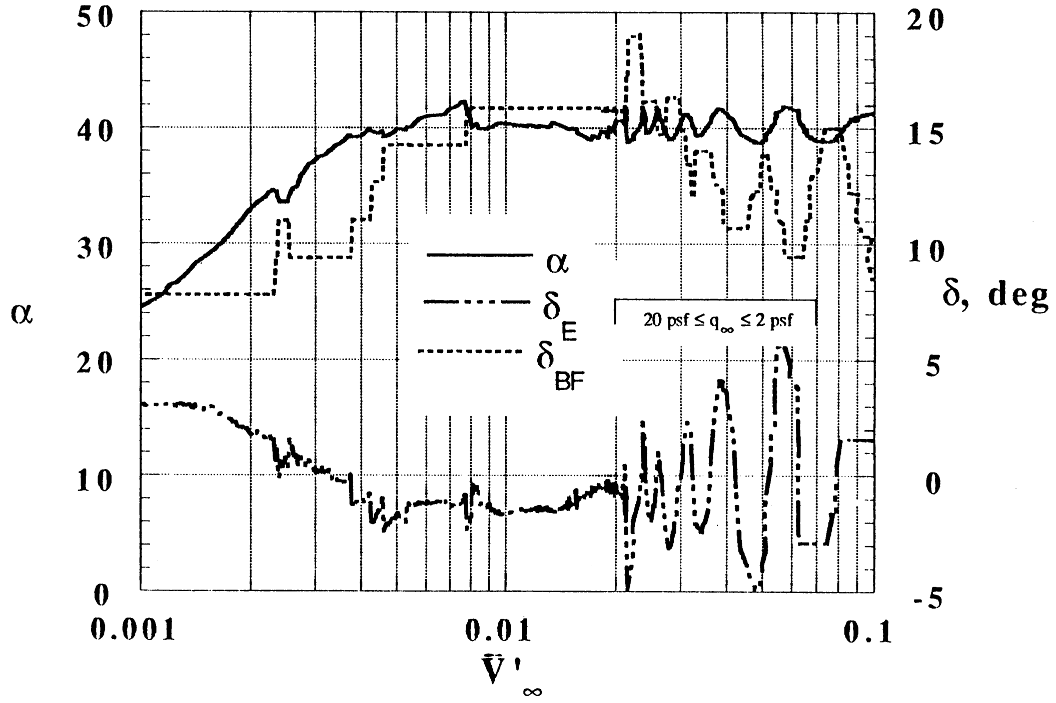

(b) α, δ_{BF}, and δ_E vs $\bar{V}'_\infty$

Figure 1. - Concluded

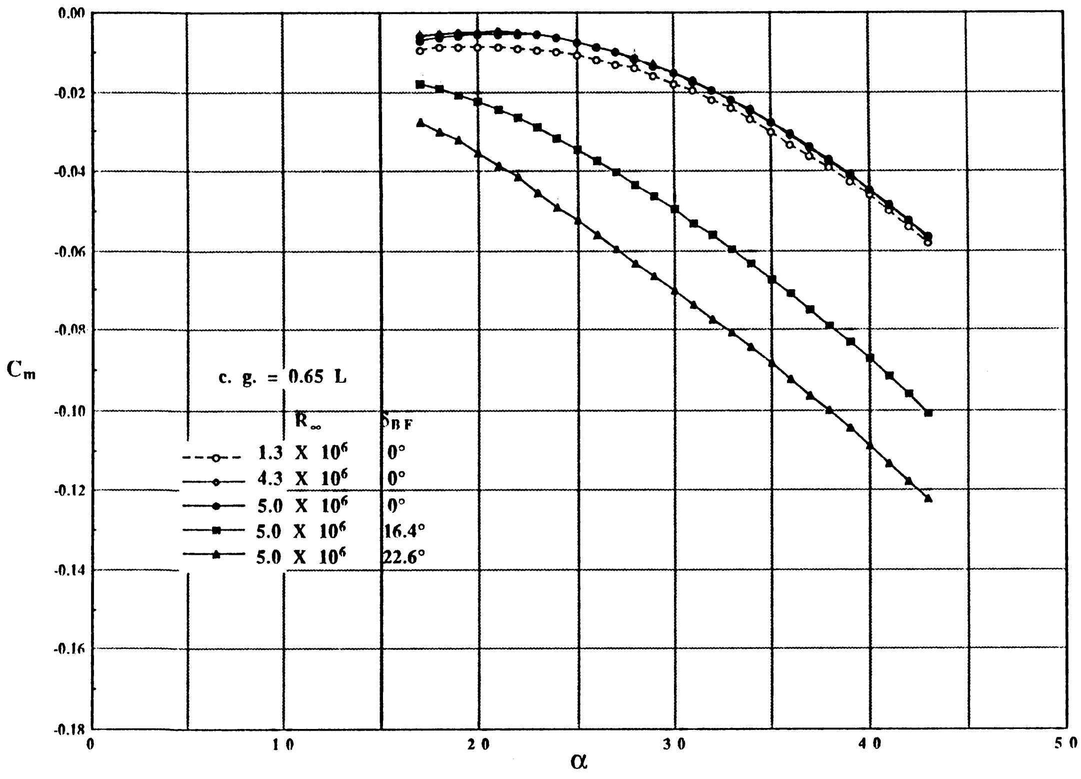

(a) Effect of Reynolds no. and body flap on pitching moment

Figure 2. - Shuttle Experimental Aerothermodynamic Measurements at M = 8 in AEDC Tunnel B (ref. 1).

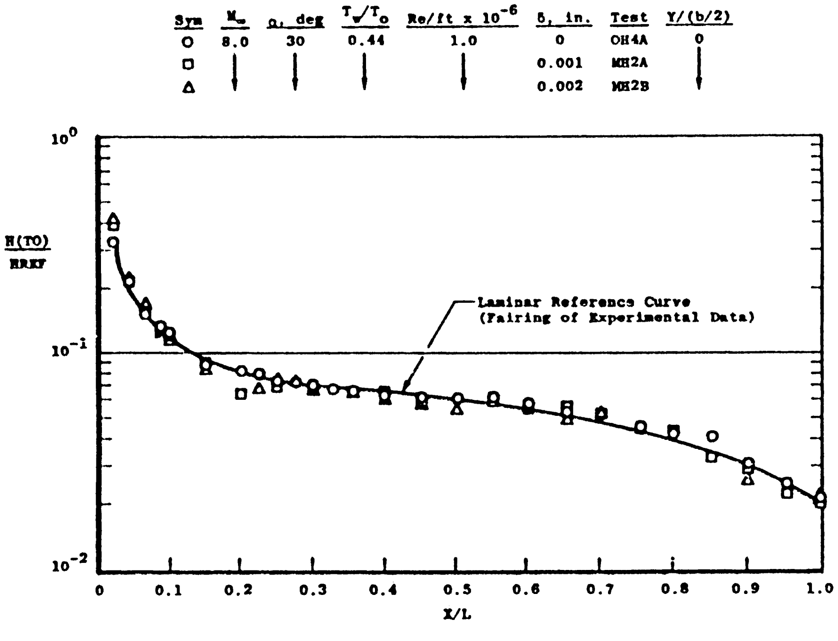

(b) Effect of roughness on Shuttle centerline heating, reference 12, figure 6 (laminar).

Figure 2 - Continued

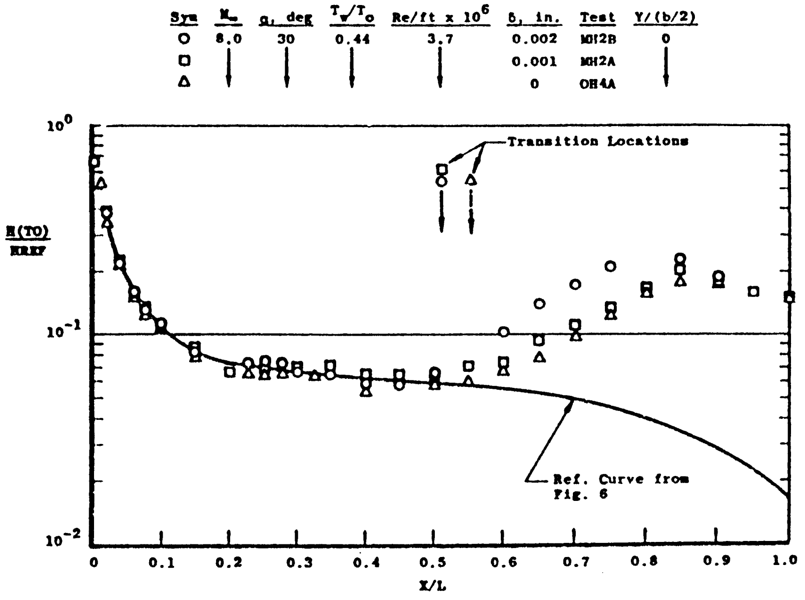

(c) Effect of roughness on Shuttle centerline heating, reference 12, figure 10 (transitional).

Figure 2. - Concluded

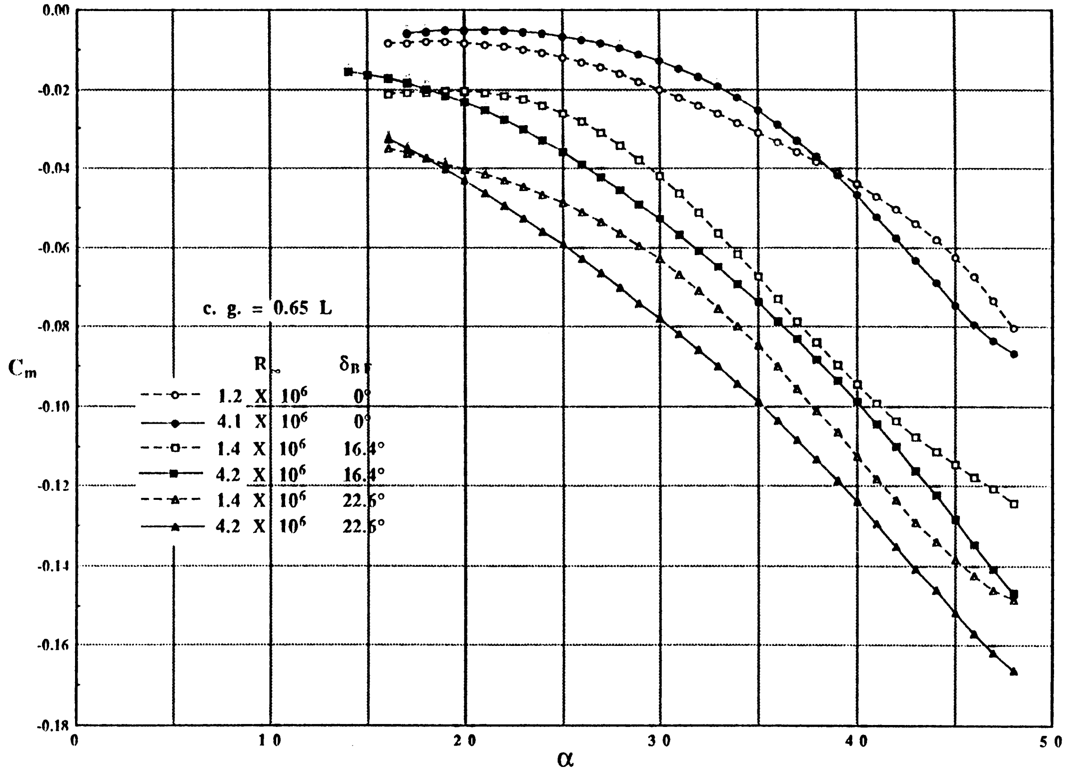

(a) Effect of Reynolds no. and body flap on pitching moment

Figure 3. - Shuttle Experimental Aerothermodynamic Measurements at M = 13.5 in NSWC Tunnel 9 (ref. 2).

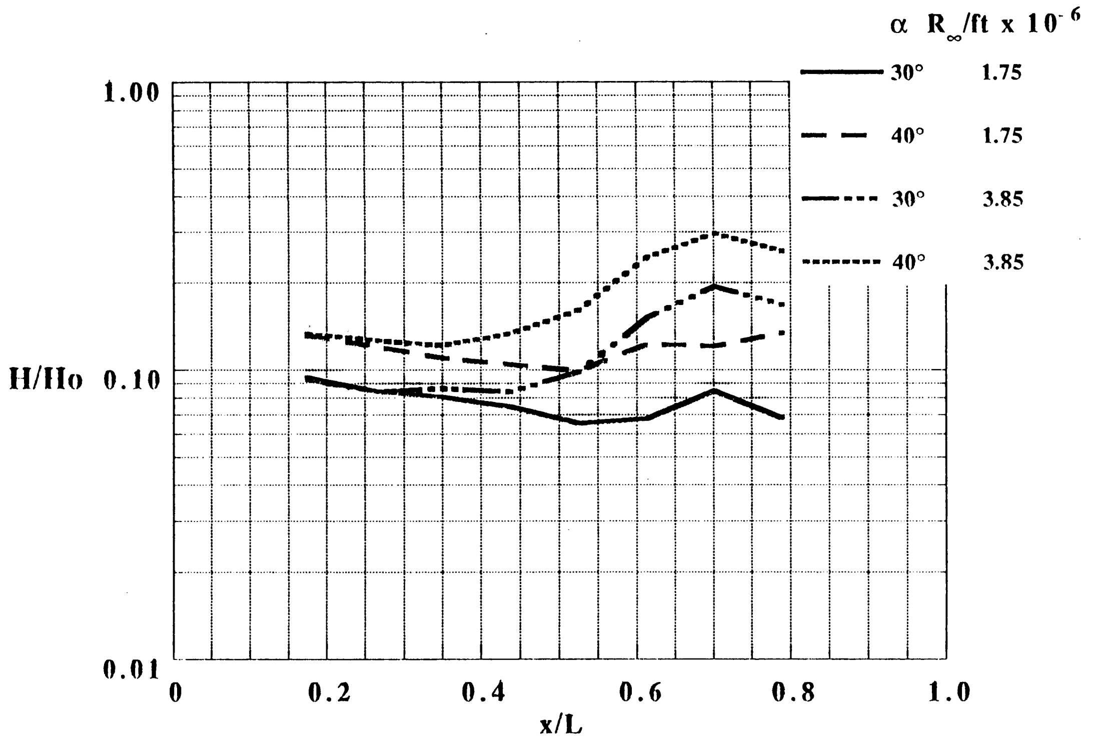

(b) Effect of Reynolds no. and α on centerline heating.

Figure 3. - Concluded

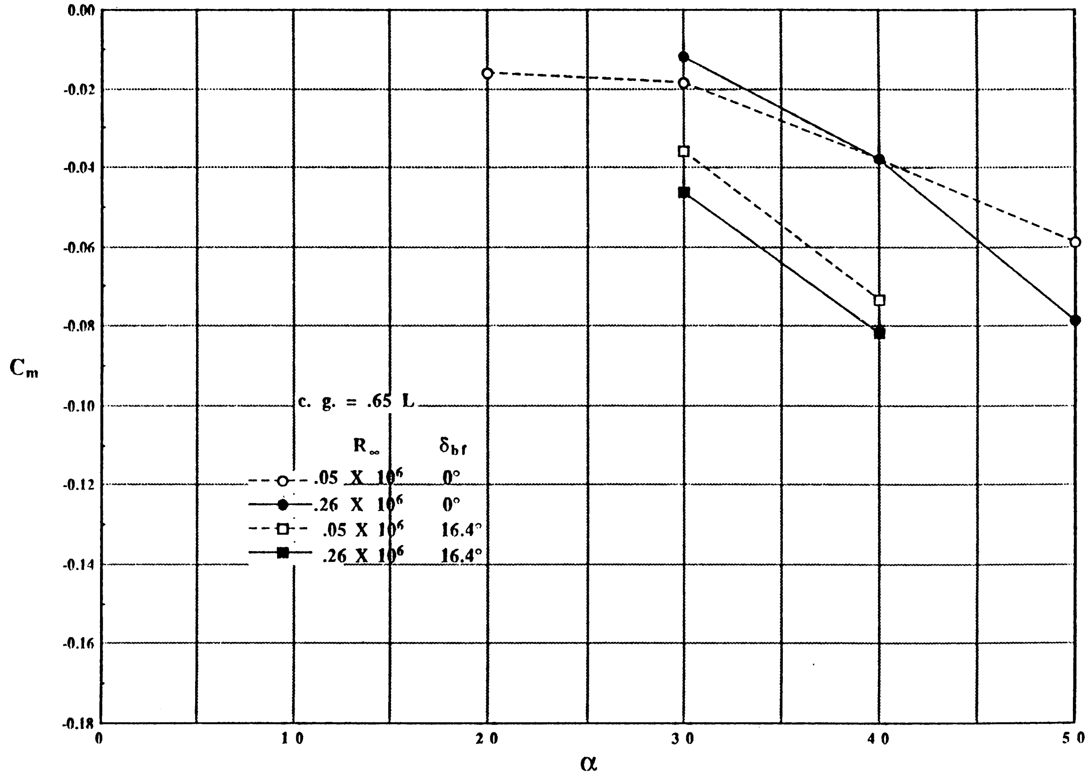

Figure 4. - Effect of Reynolds no. and body flap on pitching moment at $M \approx 15$ in CALSPAN 48" Shock Tunnel (ref. 14)

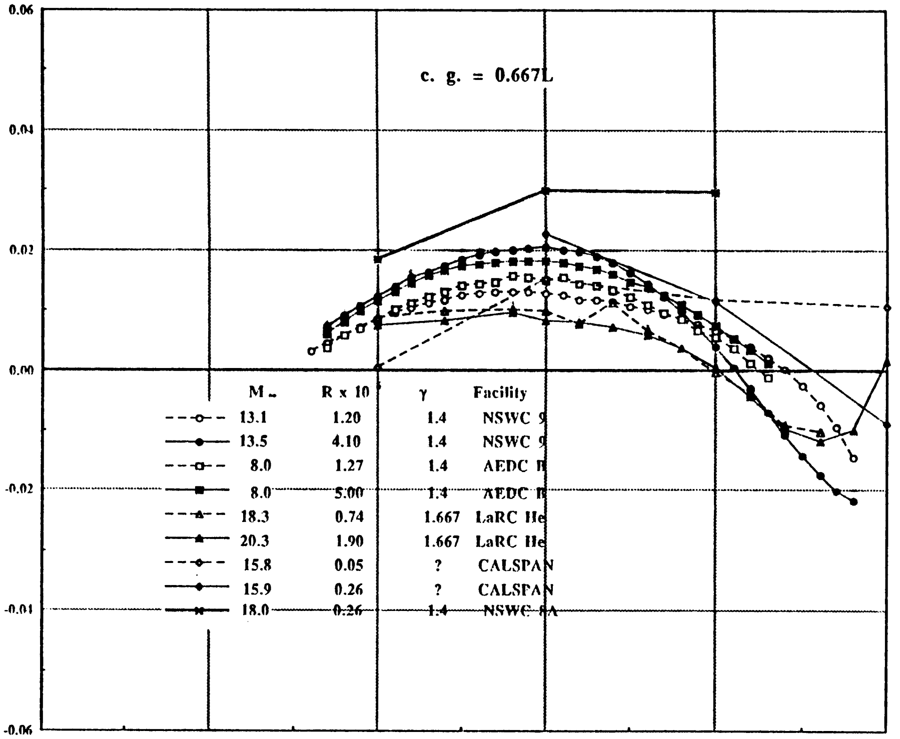

(a) $\delta_{BF} = 0°$

Figure 5. - Effect of Mach no., Reynolds no., and body flap on Shuttle pitching moment determined by hypersonic wind tunnel data

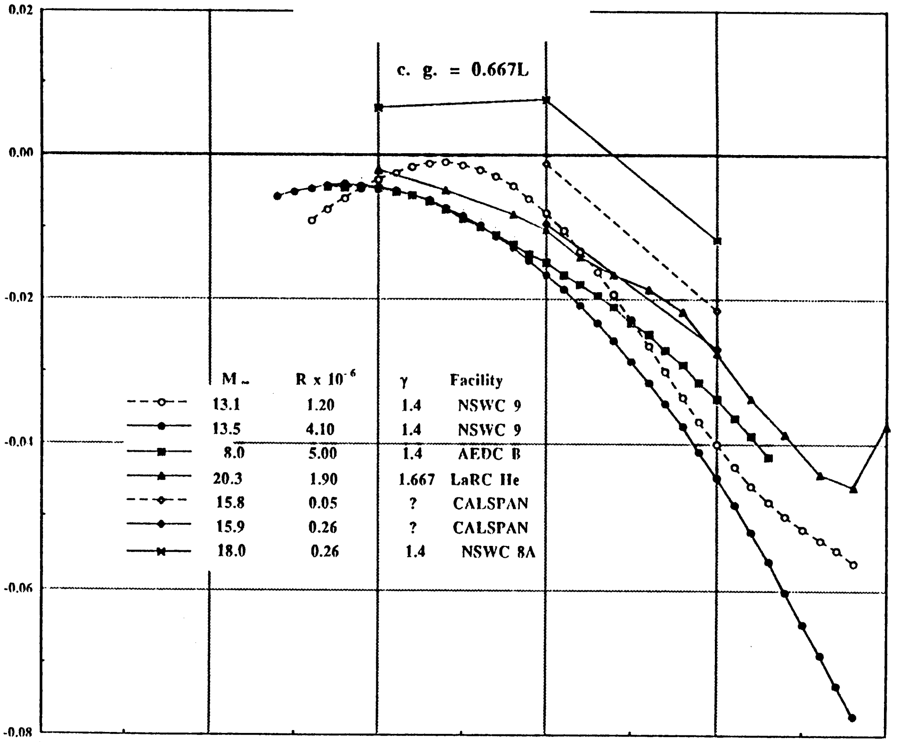

(b) $\delta_{BF} = 16.4°$

Figure 5. - Concluded

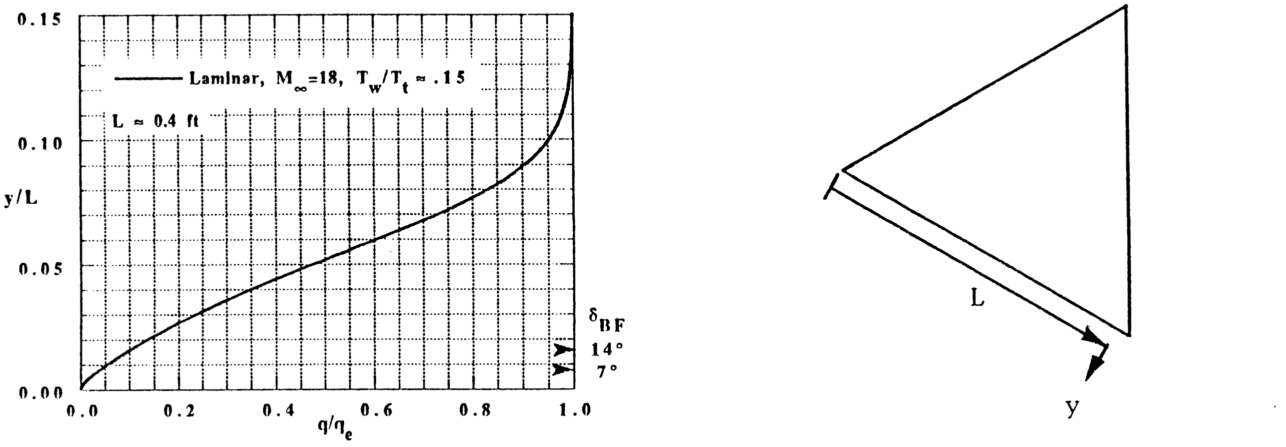

(a) Tunnel 8A Conditions

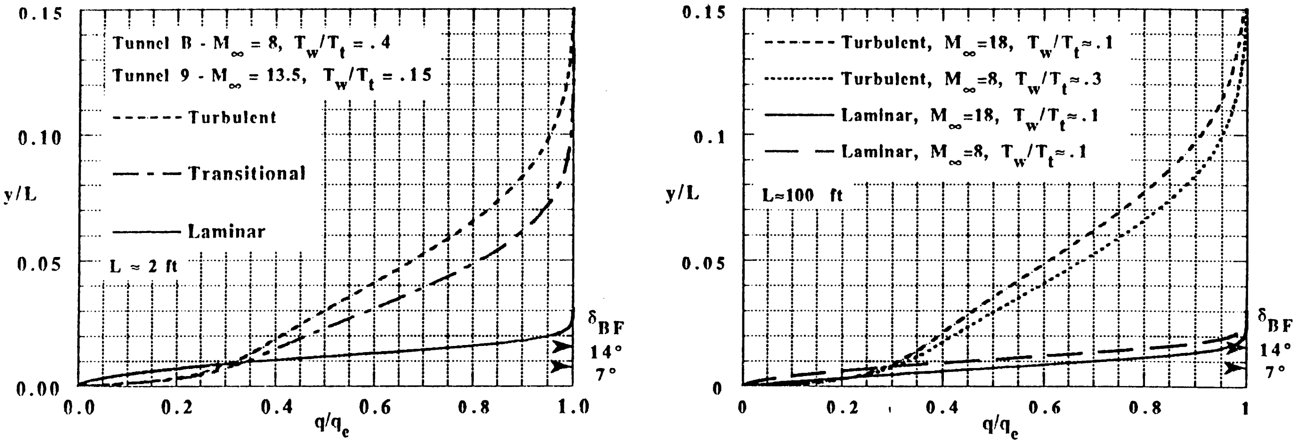

(b.) Tunnels B & 9 Conditions

(c) Shuttle Flight Conditions

Figure 6. Ideal gas boundary layer profiles on a 30° cone

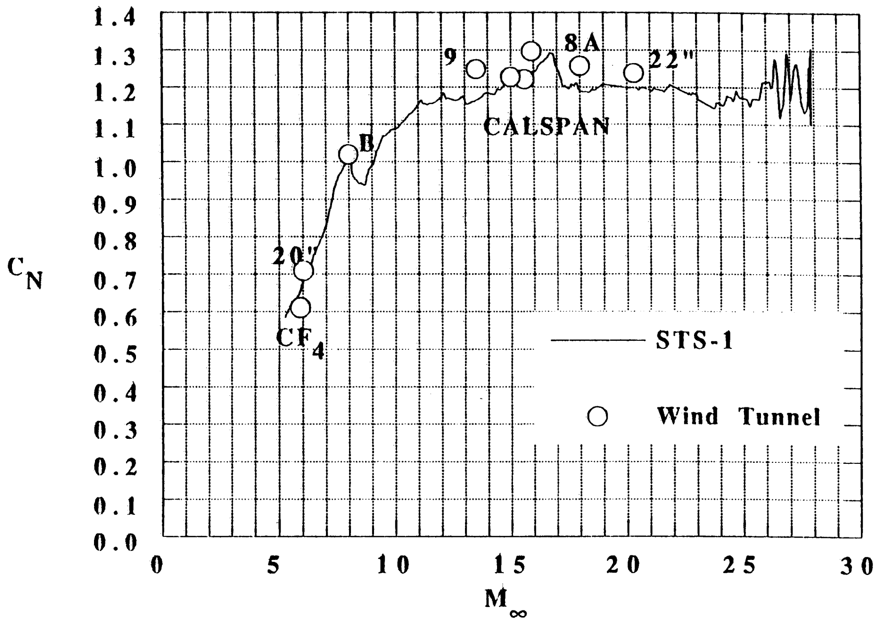

(a) C_N vs Mach No.

Figure 7. - Comparison between wind tunnel and STS-1 on the basis of compressibility effects.

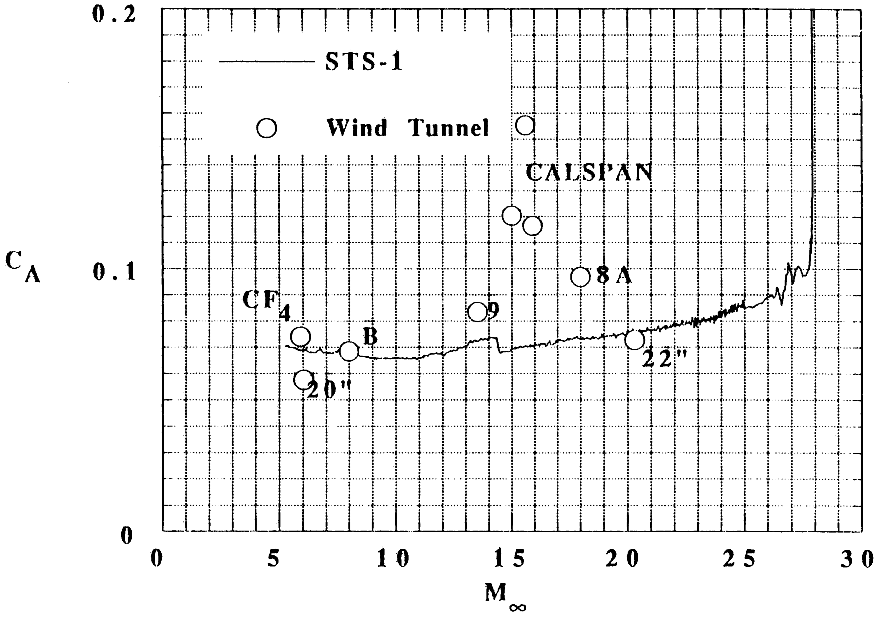

(b) C_A vs Mach No.

Figure 7. - Continued

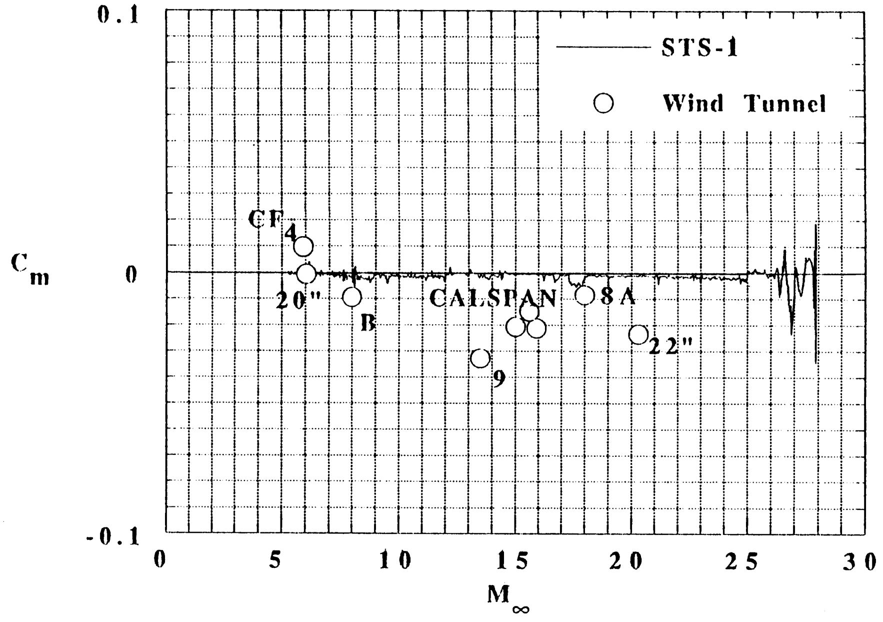

(c) C_m vs Mach No.

Figure 7. - Continued

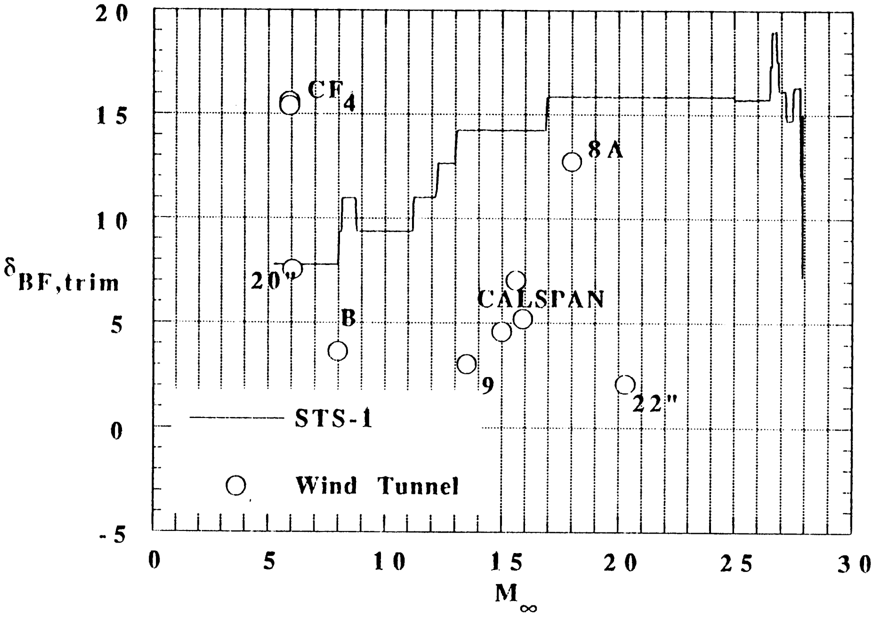

(d) $\delta_{BF,trim}$ vs M_∞

Figure 7. - Continued

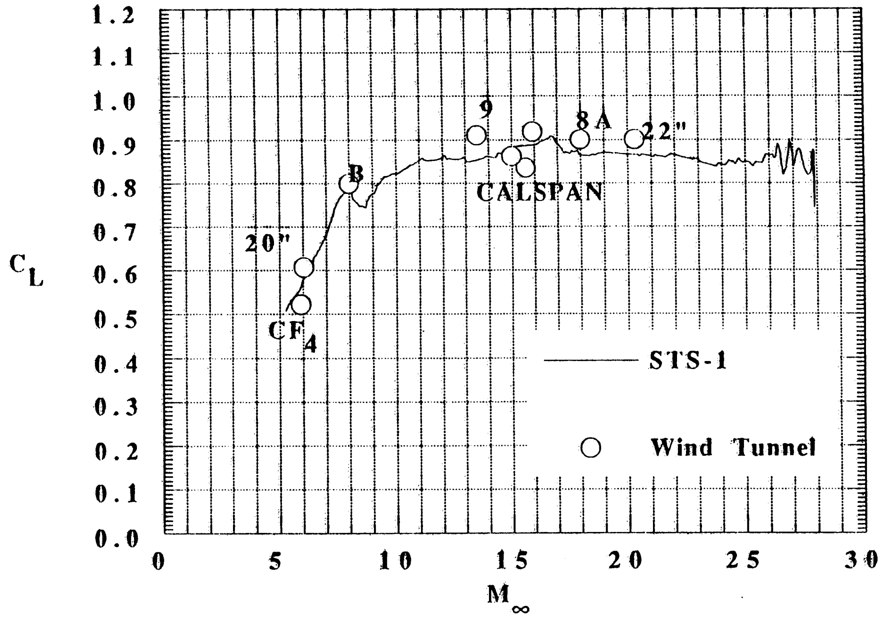

(e) C_L vs Mach No.

Figure 7. - Continued

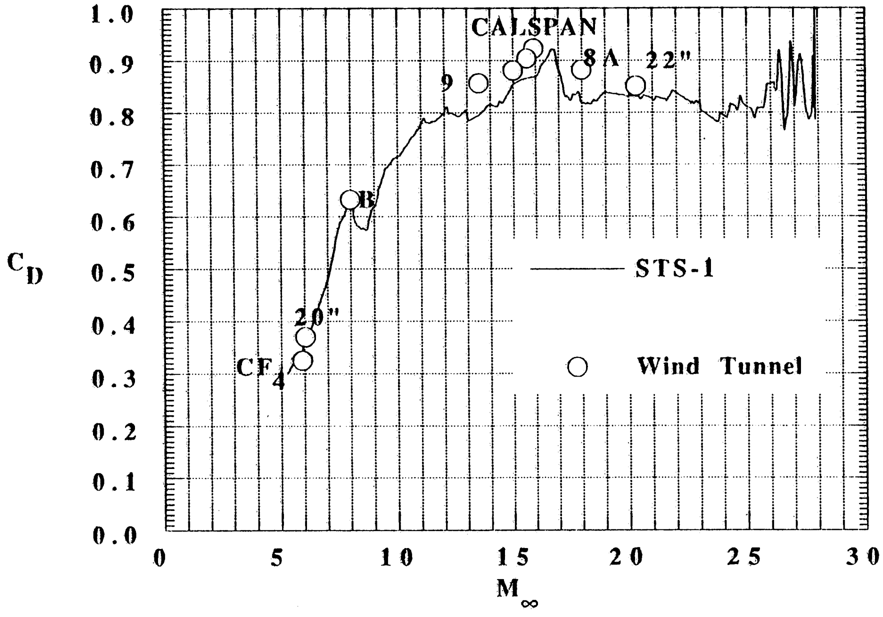

(f) C_D vs Mach No.

Figure 7. - Continued

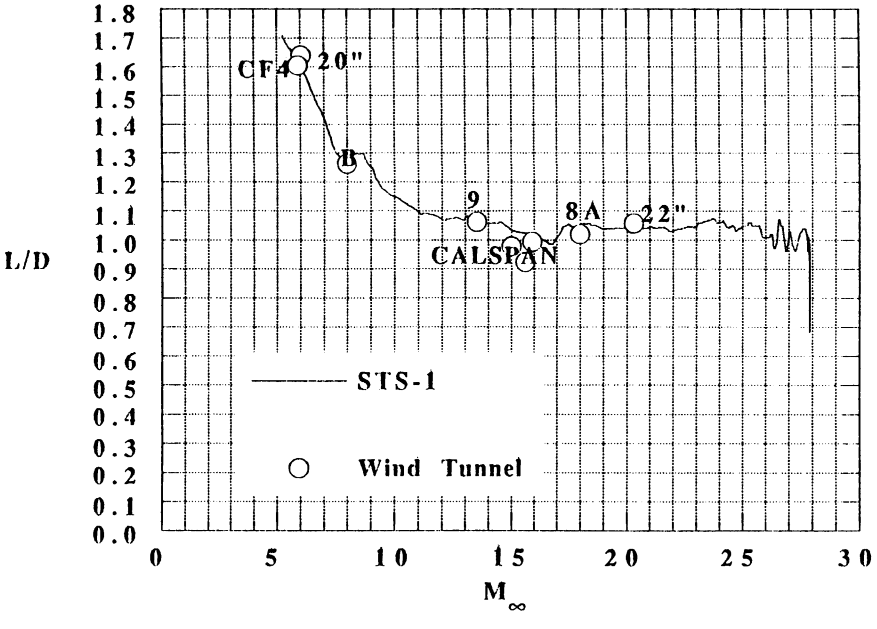

(g) L/D vs Mach No.

Figure 7. - Concluded

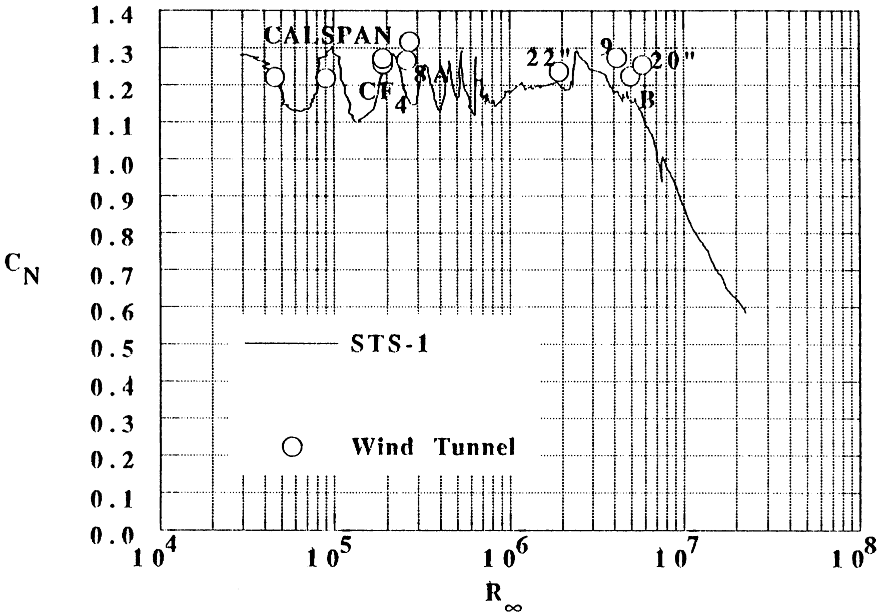

(a) C_N vs Reynolds No.

Figure 8. - Effect of Reynolds no. on comparisons between wind tunnel and STS-1.

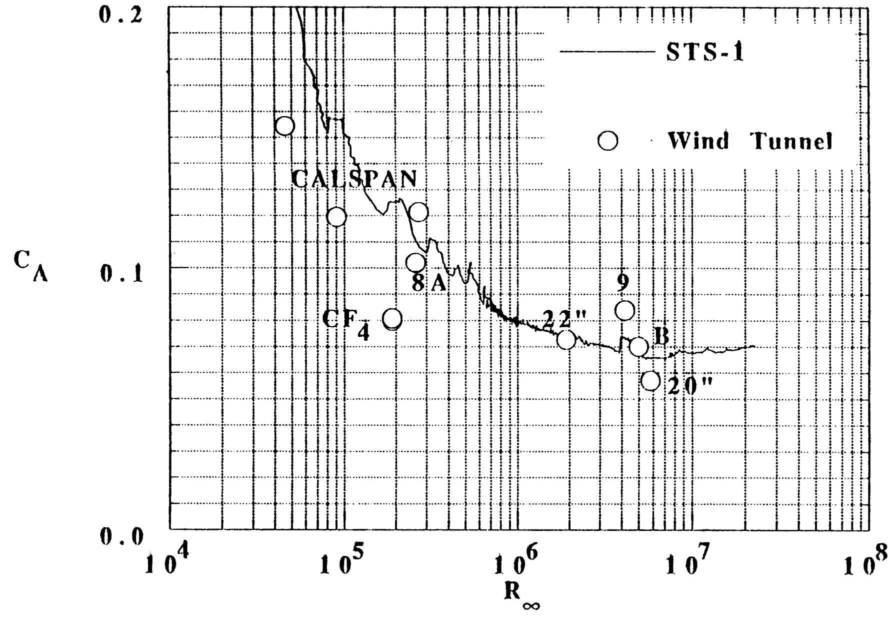

(b) C_A vs Reynolds No.

Figure 8. - Continued

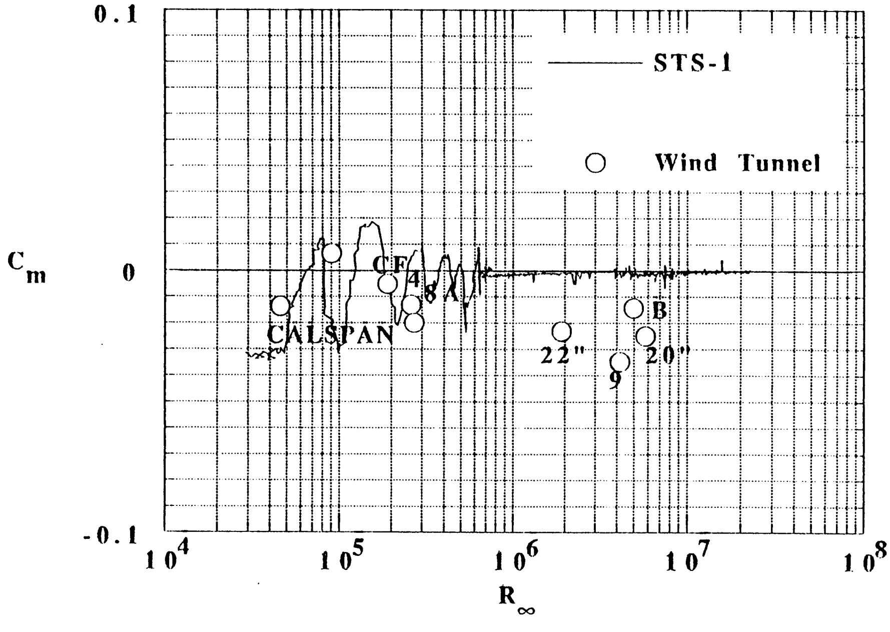

(c) C_m vs Reynolds No.

Figure 8. - Continued

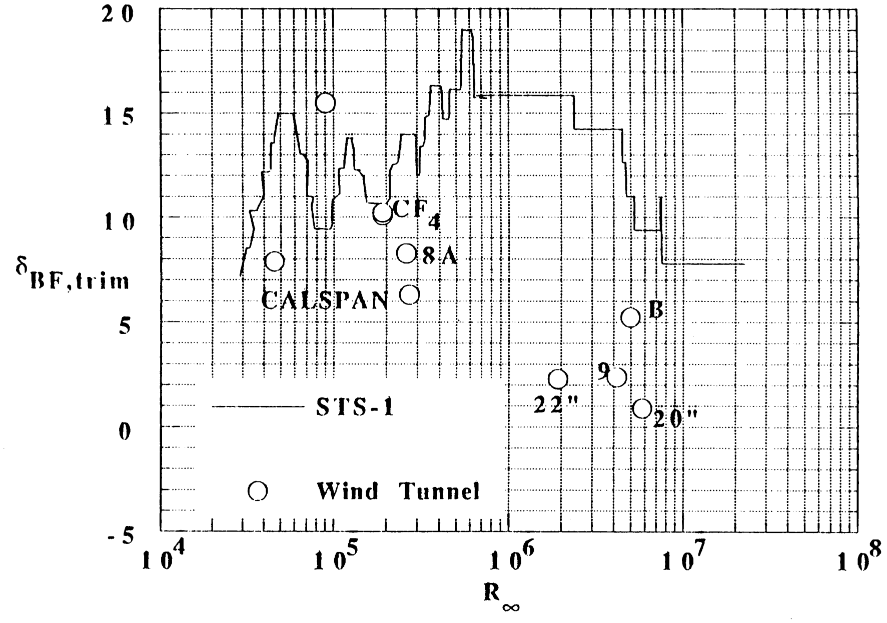

(d) $\delta_{BF,trim}$ vs Reynolds No.

Figure 8. - Continued

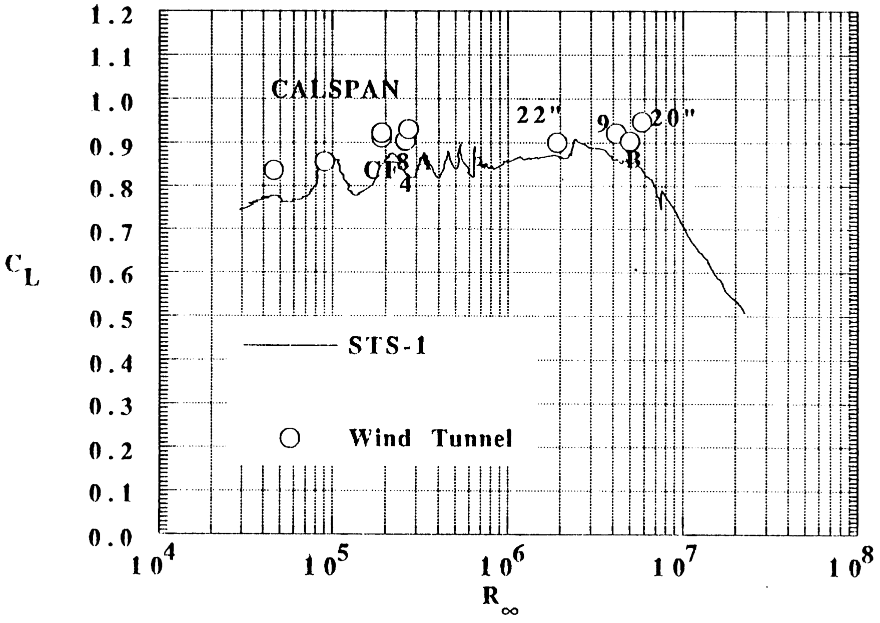

(e) C_L vs Reynolds No.

Figure 8. - Continued

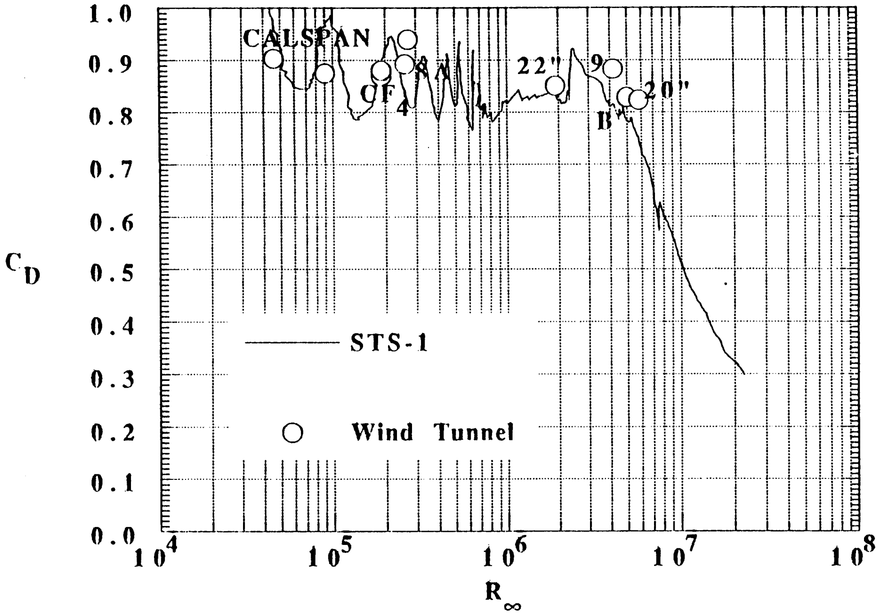

(f) C_D vs Reynolds No.

Figure 8. - Continued

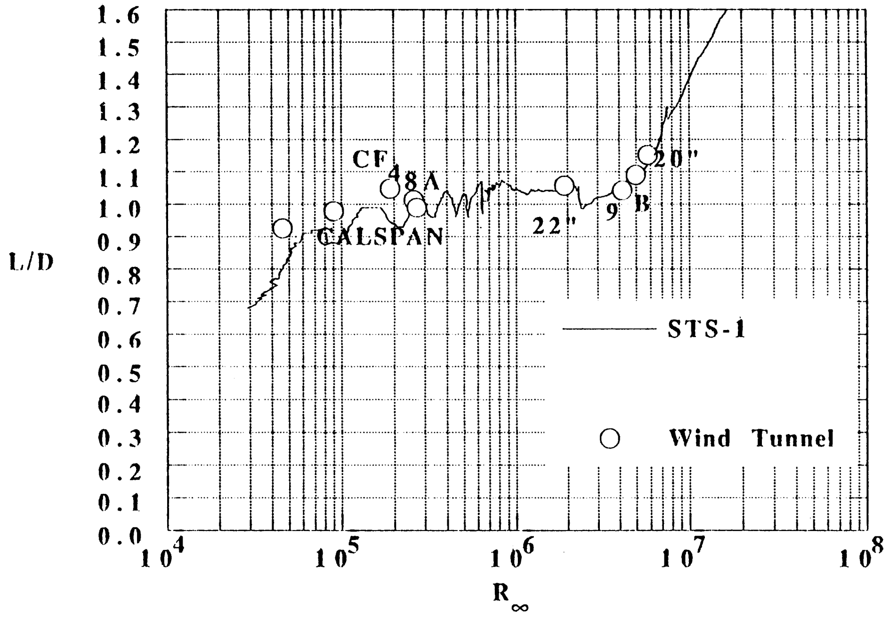

(g) L/D vs Reynolds No.

Figure 8. - Concluded

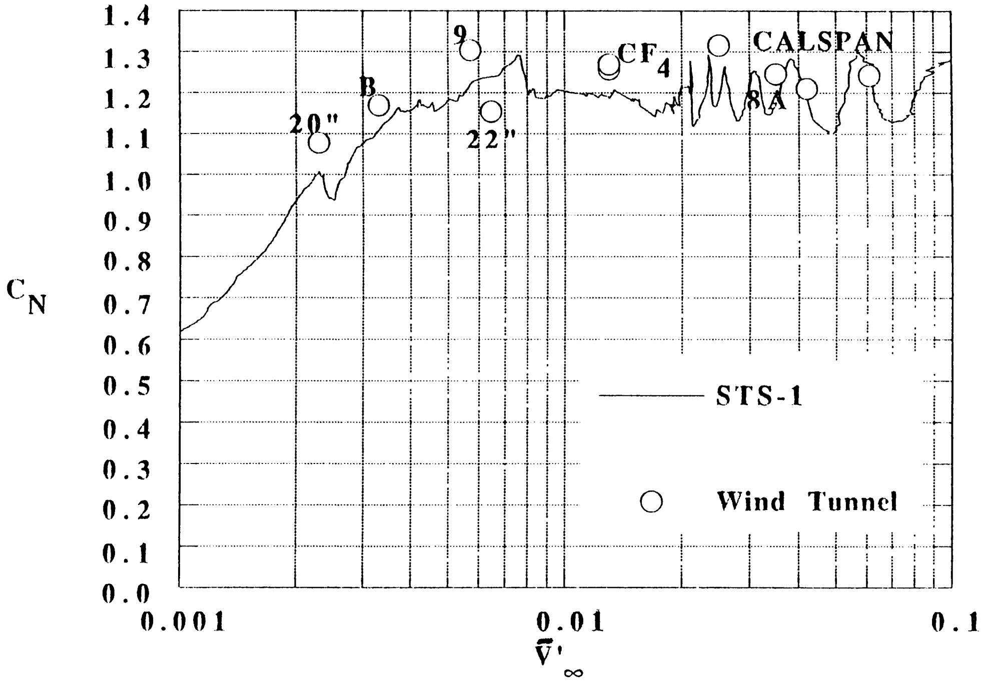

(a) C_N vs $\bar{V}'_\infty$

Figure 9. - Effect of viscous interaction on comparisons between wind tunnel and STS-1

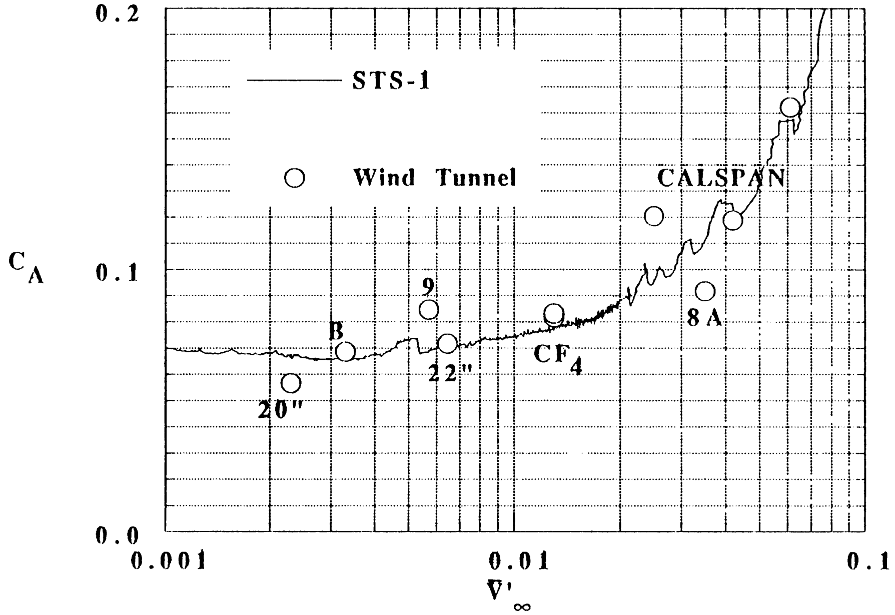

(b) C_A vs $\bar{V}'_\infty$

Figure 9. - Continued

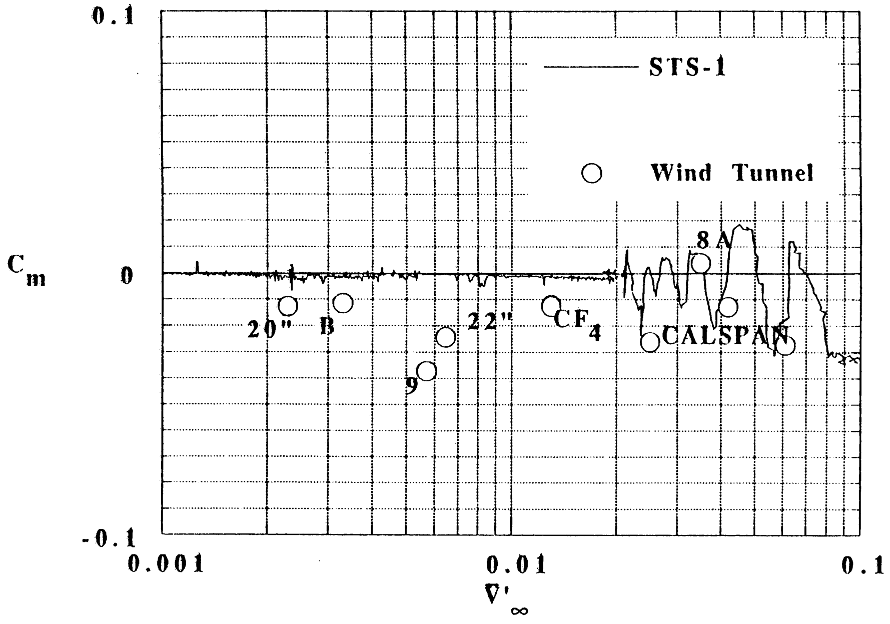

(c) C_m vs $\bar{V}'_\infty$

Figure 9. - Continued

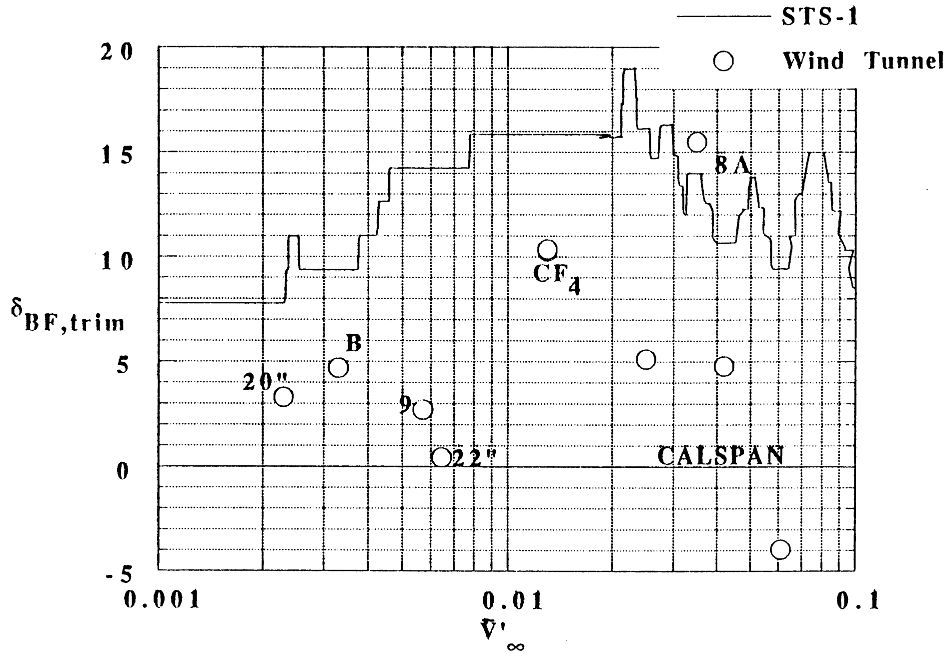

(d) $\delta_{BF,trim}$ vs $\bar{V}'_\infty$

Figure 9. - Continued

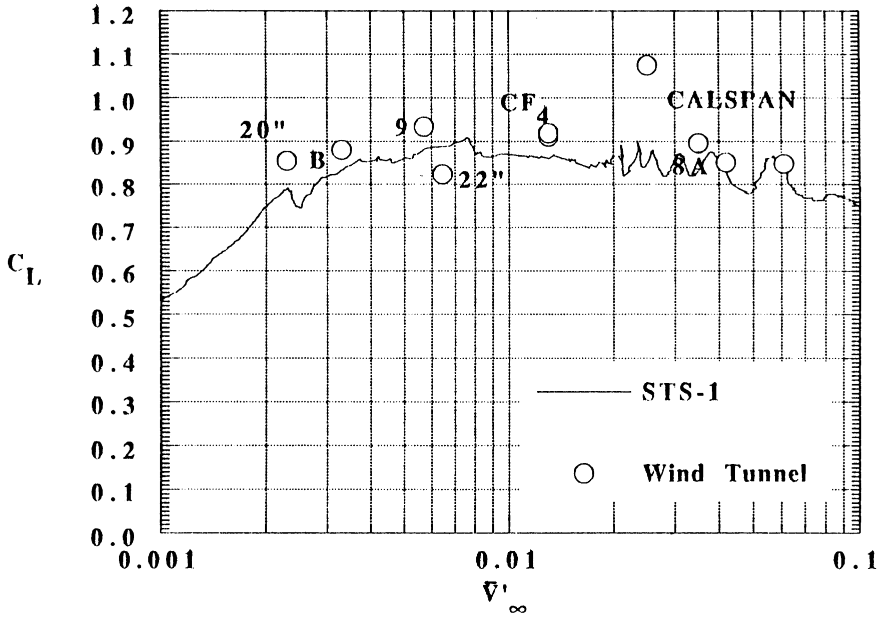

(e) C_L vs $\bar{V}'_\infty$

Figure 9. - Continued

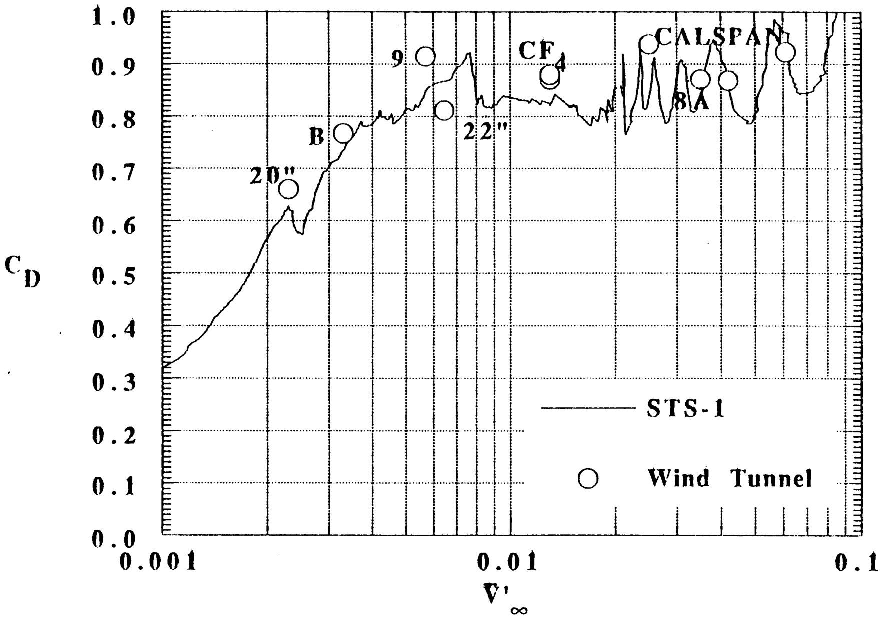

(f) C_D vs $\bar{V}'_\infty$

Figure 9. - Continued

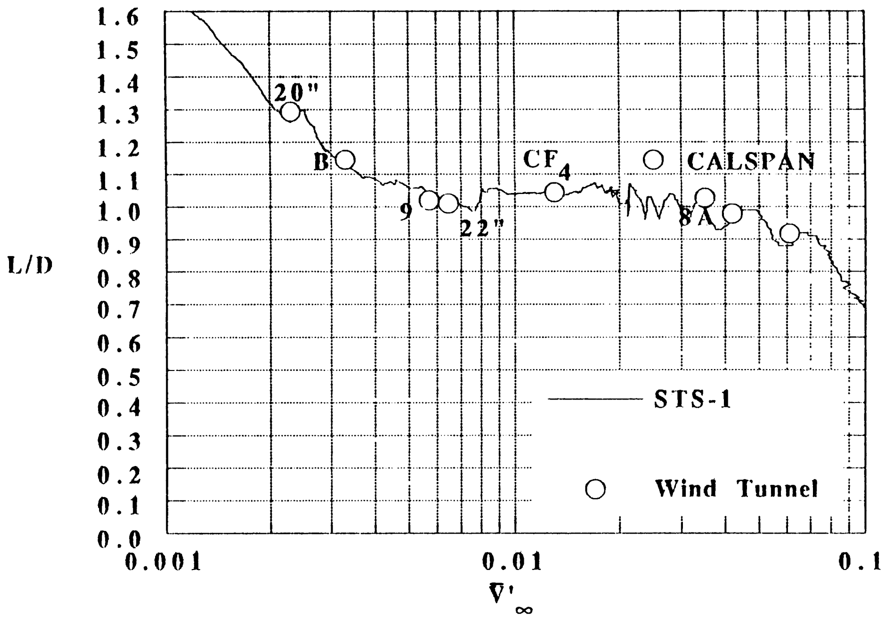

(g) L/D vs $\overline{V}'_\infty$

Figure 9. - Concluded

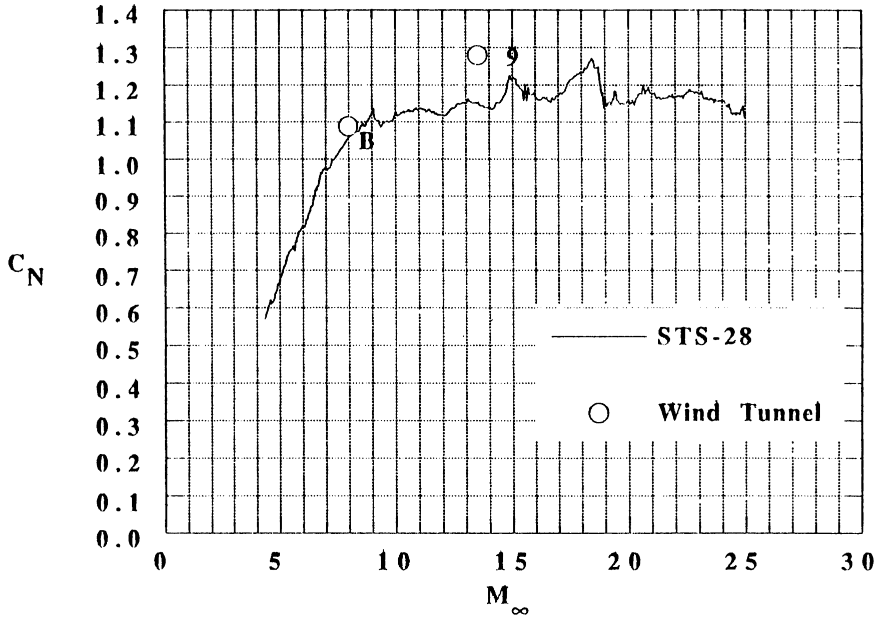

(a) C_N vs Mach No.

Figure 10. - Effect of Mach no. on comparison of wind tunnel data to STS-28.

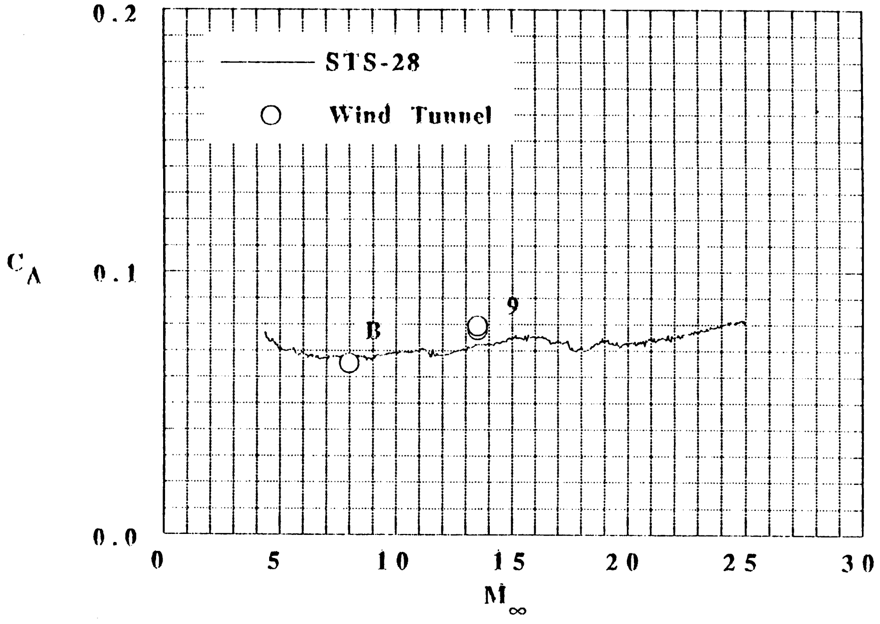

(b) C_A vs Mach No.

Figure 10. - Continued

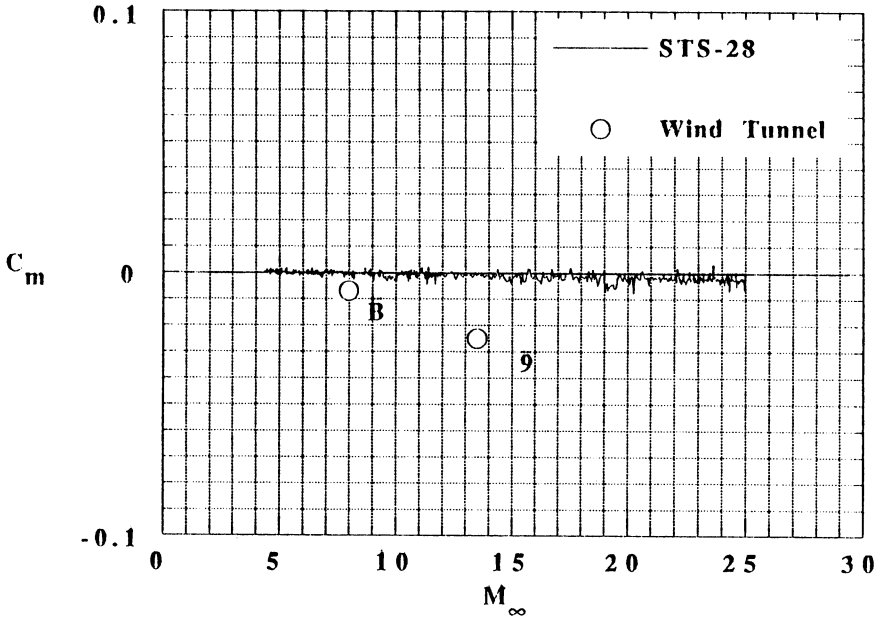

(c) C_m vs Mach No.

Figure 10. - Concluded

RECENT GROUND-FACILITY SIMULATIONS OF SPACE SHUTTLE ORBITER AERODYNAMICS

John W. Paulson, Jr., and Gregory J. Brauckmann
NASA Langley Research Center
Hampton, VA

SUMMARY

Hypersonic wind tunnel tests have been conducted in four NASA Langley Research Center facilities in an effort to determine the cause of the so-called "pitch-up anomaly" of the Space Shuttle Orbiter. The "pitch-up anomaly" occurred during the first flight of the orbiter (STS-1) because of a significant difference between the preflight estimated pitching moment and that experienced during the first entry from orbit. The result was that the body flap required to provide longitudinal trim during the high Mach number portion of the STS-1 entry was over twice that which was expected.

Tests were conducted at Mach 6 and 10 in air using 0.004 and 0.0075 scale orbiter models to obtain baseline aerodynamics, body flap control effectiveness, support interference effects, and tunnel-to-tunnel and model-to-model comparisons over a range of free stream Reynolds numbers from 0.5 to 7 $\times 10^6$ per foot and angles of attack from 0° to 45°. Most importantly, tests were also conducted at Mach 6 in a heavy gas (carbon tetrafluoride, CF_4) having a low ratio of specific heats. These tests using the 0.004 scale orbiter model determined aerodynamics and body flap effectiveness at Reynolds numbers from 0.05 to 0.5 $\times 10^6$ per foot and angles of attack of 30°, 35°, 40°, and 45°. When the results of these tests in CF_4 were compared with the results obtained in air, the nose up difference in pitching moment observed between pre-STS-1 estimates and flight was matched almost exactly by the results obtained in CF_4. Testing in a heavy gas, with a low ratio of specific heats which approximates the values found during entry flight at high Mach number, does appear to simulate the real gas effects on pitching moment found in flight.

INTRODUCTION

Prior to the first flight of the Space Shuttle (STS-1), the entry aerodynamics of the orbiter were estimated from data obtained using then state-of-the-art ground based facilities and engineering analysis. The planned trajectory called for the orbiter to trim at an angle of attack of 40° during the high Mach number portion of the entry but because of concern over possible high heating on the elevons, they were not to be deflected downward as a trimming control surface. Instead, the body flap, which originally was planned to act as heating protection for the engine nozzles and which could be replaced more easily if over heated, was to provide pitch trim. The nominal predicted deflection for the body flap was 7°. However, during the first flight, the body flap was actually deflected about 16°, more than twice that anticipated, in order to maintain longitudinal trim at Mach numbers above about 14 or 15 (Reference 1). An example of the predicted orbiter pitching moment is shown in figure 1 (figure 14, reference 1). The predicted pitching moment is based on the basic body pitching moment corrected for the observed control deflections, using the Aerodynamic Design Data Book (ADDB, reference 2) values for control effectiveness and, of course, the trimmed, flight pitching moment is zero. The variation, or the maximum allowable differences (for design purposes) between flight and preflight prediction, is indicated to be ±0.01 up to a Mach number of 18 and then grows for higher Mach numbers. The difference between the flight and predicted pitching moment is about 0.03 at Mach numbers above 14. Therefore, the actual flight pitching moment was higher by a factor of three than the predicted value. At Mach numbers below 14 the difference between the predicted and flight values reduces, almost linearly, to the point where there is only a small difference between predicted and flight values at a Mach number of eight or less. While the flight pitching moment was considerably outside of the variations placed on the predicted values, it was within the trim capability of the body flap and, obviously, the orbiter completed a successful first flight. This so called "pitch anomaly" was easily handled on subsequent flights as flight results showed that elevon heating was not as severe as predicted and the control laws were modified to include use of the elevons as trimming devices. After the first five flights, the aerodynamics of the orbiter were very well defined for the entry trajectory and there have been only minor changes to the operational data book in the ensuing decade of operation. However, the cause or causes of the discrepancies noted in the original estimates of the orbiter aerodynamics, particularly pitching moment, have never really been settled.

The fact that the body flap deflection required for trim on STS-1 was greater than predicted has generally been attributed to either an error in the basic configuration pitching moment or an error in body flap effectiveness. Both of these possibilities will lead to a larger than predicted body flap deflection. The proposed causes of this "pitch anomaly" have included real gas effects, viscous effects, a combination of real gas and Mach number effects, simple scale effects (i.e., model fidelity), all giving incorrect basic pitching moment. Also the state of the boundary layer on the windward surface, its thickness and whether or not it is laminar or turbulent, could affect the body flap effectiveness. Finally, there was very little information at Mach numbers greater than ten. (References 3 to 7).

During the period of the aerodynamic development and assessment of the orbiter, the capability to simulate real gas effects in the wind tunnels effectively did not exist. An effort was made to simulate real-gas effects via testing in the Langley Research Center 20-Inch Mach 6 CF_4 Tunnel. However, the facility was still under development at the time and considered a laboratory facility as compared to a productive hypersonic research facility and the results were not considered valid at the time.

Recent improvements in the flow quality of the hypersonic facilities at Langley Research Center (Reference 8) and in Computational Fluid Dynamics (CFD), which was essentially in its infancy about fifteen years ago, provided the opportunity for a new assessment of orbiter aerodynamics. In addition, the 20-Inch Mach 6 CF_4 Tunnel is now a fully operational, calibrated facility which should allow simulating the low gamma aspect of real gas effects by testing in a heavy gas. The purpose of this paper is to describe the experimental research conducted over this past year in an effort to re-examine hypersonic orbiter aerodynamics in continuum flow facilities.

An existing pair of high fidelity orbiter models, shown in figure 2, were refurbished and used for the majority of this testing. In addition, a modified orbiter model representing the complete windward surface, including the body flap, but having a simplified leeward surface was used for comparison and to provide force and moment data for CFD code calibration. The two high fidelity orbiter models of 0.004 and 0.0075 scale were tested in four separate facilities at Mach numbers from 6 to 10, at Reynolds numbers from 0.05-7 x 10^6 per foot and free stream ratio of specific heats of 1.22 and 1.4. The modified orbiter was tested at Mach 10, at Reynolds numbers from 0.5 to 2.0 x 10^6 per foot and a ratio of specific heats of 1.4.

SYMBOLS

C'_∞	Chapman-Rubensin viscosity coefficient
C_A	axial force coefficient
C_m	pitching moment coefficient
C_N	normal force coefficient
M_∞	Mach number
m.c.	moment center
P_0	stagnation pressure, psi
q_∞	free stream dynamic pressure, lb_f/ft^2
R_e	Unit Reynolds number, per foot
$R_{e,L}$	length Reynolds number, based on reference body length
T_0	stagnation temperature
$\bar{V}'_\infty$	viscous interaction parameter, $\frac{M_\infty \sqrt{C'_\infty}}{\sqrt{Re,L}}$
x	longitudinal dimension, inches
z	vertical dimension, inches
Subscripts	
α	angle of attack, degrees

γ	ratio of specific heats
δ_{BF}	body flap deflection, degrees
ρ_2/ρ_∞	normal shock density ratio
ΔC_m	increment in pitching moment coefficient between body flap deflections of 0° and 16° (or 16.3°)

MODELS AND TEST HARDWARE

Two existing, high fidelity shuttle orbiter models were refurbished and used in this investigation to provide aerodynamic data on identical configurations in several facilities. In addition, a modified orbiter model, which accurately modeled the full windward surface including the body flap, was fabricated and tested at Mach 10 in air to provide wind tunnel results for calibration of CFD calculated results, as well as a "sanity check" on the orbiter wind tunnel results.

These existing models, one of 0.004 scale and the other of 0.0075 scale, shown in figure 2 with reference dimensions in Table 1, were part of the stable of models from the original shuttle orbiter testing and were chosen so that the same configuration could be tested in all facilities. Both models were checked for fidelity and the results are shown in figure 3 where contours were scaled to the length of the 0.0075 scale model for comparison. These contours are in good agreement with the outer mold line coordinates of the shuttle orbiter geometry and with each other back to about 90-percent of body length. At this point, the region around the flap section does differ as the 0.004-scale model does not accurately represent the fairing over the flap hinge line on the full scale orbiter which is included on the 0.0075-scale model. The modified orbiter model was also checked for fidelity and matches the shuttle orbiter lines very well. The coordinates for the wind tunnel model were obtained from those described in the CFD grid of the modified orbiter. This ensured that the wind tunnel model and computer model were identical so that comparisons of predicted and experimental results would be for the same geometry. All models had a removable body flap, which could be replaced to provide nominal body flap deflections of 0°, 12°, 16°, and 20°. The modified orbiter body flap was attached from inside the aft body so that the external surface was extremely smooth, i.e., no screw holes required filling when the flap was changed.

Each model was set up to be tested on both a straight sting mount and a blade mount as shown in figure 2. In addition, there were two cast, 0.004 scale models which were originally used for blade-versus-sting support interference testing. This allowed support effects on overall configuration aerodynamics and body flap effectiveness to be determined. Due to tunnel installation restrictions, the 0.0075-scale model was tested at Mach 10 only on the blade and a bent sting, also shown in figure 2. The bent sting setup allowed the upper limit of the angle of attack range to be increased from 42° to 45°.

Since each model was tested over a wide range of conditions (e.g., q_∞ and α) in several facilities, the actual loads experienced varied significantly from test to test. In order to optimize accuracy, several different balances, designed for different loads, were used to match balance load capability with the expected aerodynamic loads for the conditions being tested. These balances were water cooled and the temperature difference across the balance was monitored to ensure that no significant temperature gradients were encountered during a wind tunnel run. Also, each model installation included base pressure measurements which were corrected to free stream pressure on the base and this incremental pressure times the base area was applied to axial force.

FACILITIES

31-Inch Mach 10 Tunnel

The 31-Inch Mach 10 Tunnel is a blow down facility with a run time of about one minute. This is sufficient time for obtaining "pitch pause" aerodynamic data over an angle of attack range from 0° to 45°. Tests of the 0.004 and 0.0075-scale orbiter and the 0.0075-scale modified orbiter models were conducted by establishing the tunnel flow conditions, injecting the model at zero angle of attack, pitching through a set of points at various angles of attack, from 0° to 45° and back to 0°, and retracting the model prior to tunnel shut down.

This facility provides a uniform free stream flow at a nominal Mach number of 10. Stagnation pressure can be varied from 350 to 1450 psia, while the temperature is usually maintained at about 1350°F, to provide a range of free stream Reynolds numbers from $0.5\text{x}10^6$ to $2.1\text{x}10^6$ per foot. A detailed description of the facility and calibration information may be found in reference 8.

20-Inch Mach 6 Tunnel

The 20-inch Mach 6 Tunnel is a blow down facility with a nominal run time of about two minutes. Like the 31-Inch Mach 10 Tunnel, this run time is sufficient for pitch pause force and moment testing, with a testing procedure nearly identical to that of the Mach 10 facility. The 0.0075 scale orbiter model was tested in this facility over an angle of attack range of 0° to 45°.

This facility provides a uniform free stream flow at a nominal Mach number of 6. Stagnation pressure can be varied from 30 to 500 psia while temperature can be varied from 760°R to 1000°R to give a range of free stream Reynolds numbers from $0.5\text{x}10^6$ to $9\text{x}10^6$ per foot. This range of conditions allows a direct comparison of Mach number effects by testing identical models at both the 20-Inch Mach 6 and 31-Inch Mach 10 Tunnels while maintaining constant Reynolds number. A detailed description of the facility and calibration information may be found in reference 8.

20-Inch Mach 6 CF_4 Tunnel

The 20-Inch Mach 6 CF_4 Tunnel is a blow down facility with a run time of 20-30 seconds. This short run time coupled with a slow pitch drive necessitated that data be obtained one angle of attack at a time. That is, once the tunnel flow was established, the model was injected at a fixed angle of attack and about 15 seconds of data were obtained, ensuring steady loads and base pressures, before the model was retracted and the tunnel shut down. Between tunnel runs the angle of attack was changed and test procedure would be repeated. Discrete angles of attack tested were 20°, 30°, 35°, 40° and 45°.

This facility provides a uniform free stream flow at a nominal Mach number of six. Stagnation pressure can be varied from 100 to 2000 psia while temperature can be varied from 1100°R to 1400°R to give a range of Reynolds numbers from 0.04 x 10^6 to 0.7 x 10^6 per foot. The unique feature of this facility is its ability to simulate real gas effects through a high normal shock density ratio. At Mach 6 the CF_4 gas has a density ratio of 12, compared to 5.3 in Mach 6 air. This higher density ratio, and corresponding lower ratio of specific heats (γ of 1.22 in CF_4 compared to 1.4 in air), more closely matches the values experienced in air at high velocities (enthalpy) typical of entry flight. Use of a heavy gas of relatively low enthalpies for blunt and moderately blunt bodies simulates the high ρ_2/ρ_∞, low γ aspect of a real gas. This will be discussed further in a later section of the paper. A detailed description of the facility and calibration information may be found in reference 8.

15-Inch Mach 6 High Temperature Tunnel

The 15-Inch Mach 6 High Temperature Tunnel is a blow down tunnel with a run time of about one minute. Presently, the model injection system does not allow model attitude to be changed for "pitch pause" testing; thus, tests performed in this tunnel were similar to those performed in the 20-Inch Mach 6 CF_4 Tunnel. That is once the tunnel flow was established, the model was injected into the test section, 5-10 seconds of data were obtained, the model was retracted and the tunnel shut down.

This facility provides a uniform flow at a nominal Mach number of 6. Stagnation pressure can be varied from 30 to 300 psia while temperature can be varied from 760°R to 1000°R to give a range of free steam Reynolds numbers from 0.5 x 10^6 to 6 x 10^6 per foot. A detailed description of the facility and calibration information may be found in reference 8.

PLANS, PRELIMINARY TESTING, AND FINAL TEST PROGRAM

The original planned experimental approach was to conduct a systematic investigation, using existing high fidelity shuttle orbiter models, to determine the cause(s) of the "pitch-up anomaly." Testing was to be conducted in the 15-Inch Mach 6 High Temperature Tunnel, the 31-Inch Mach 10 Tunnel, the 20-Inch Mach 6 CF_4 Tunnel, the 20-Inch Mach 17 N_2 Tunnel and the 22-Inch Mach 20 Helium Tunnel. These five hypersonic facilities, managed by the Experimental Hypersonics Branch, would provide a large range in simulation parameters including Mach numbers from 6-20, free stream unit Reynolds numbers from 0.05-25 x 10^6 per foot, and free stream ratio of specific heats (γ) from 1.22-1.67. In addition, new 0.0075 scale modified orbiter models were to be tested in the 31-Inch Mach 10 Tunnel to provide force and moment, surface pressure, and heat transfer information for CFD code calibration.

Because of model and facility availability, some preliminary testing to determine support interference effects using the 0.0075 scale model was conducted in the Unitary Plan Wind Tunnel at a Mach number of 4.6 and using two 0.004 scale cast stainless steel models in the 31-Inch Mach 10 Tunnel. These tests, along with others at Mach 6, indicated that there were no significant support effects on the 0.0075 scale models. An example from this support interference study is presented in figure 4 where a comparison of the Mach 6 aerodynamics of the 0.0075 scale orbiter with the straight sting versus blade support shows no significant effects. Similar tests on the smaller 0.004 scale cast orbiter models showed larger support effects because the sting size relative to the model size was larger than for the 0.0075 scale models. However, inspection of the cast models revealed geometry fidelity problems, and these models were dropped from the test plan. The remaining machined steel, high fidelity model could only be mounted using a straight sting, so there were no further support interference tests conducted.

There was some concern about the 0.0075 scale model causing blockage problems in the 15-Inch Mach 6 Tunnel. Therefore, a blockage test using an existing 0.006 scale stycast, heating model was conducted and results indicated that at angles of attack of 40°-45° the model caused tunnel unstart as soon as it was injected into the tunnel flow. The planned test of the large 0.0075 scale model had to be changed to the larger 20-Inch Mach 6 Tunnel managed by the Supersonic/Hypersonic Aerodynamics Branch.

There were also problems in getting all of the EHB facilities, some of which were undergoing Major Construction of Facilities Project upgrades, on line at the same time. Tests in the 20-Inch Mach 17 N_2 and 22-Inch Mach 20 Helium Tunnels were postponed and have not been conducted at the time of this writing. Also while conducting the second force and moment run of the 0.004 scale model in the 31-Inch Mach 10 Tunnel, the heater element failed and brought an end to this phase of testing. After completing the test program for the 0.004 scale model in the 20-Inch Mach 6 CF_4 Tunnel, this tunnel was being prepared for the first force and moment run with the 0.0075 scale orbiter model when the line which carries the CF_4 through the lead-bath heater failed. At the time of this writing, the damaged heater is under repair and testing of the larger model is scheduled immediately following the reactivation of the facility. The final set of testing completed and reported in this paper is indicated in figure 5. The remaining tests will be completed as soon as tunnel availability permits.

DISCUSSION OF RESULTS

The results of the experimental program will be presented in the following format. First to be presented are the basic aerodynamics, including body flap effectiveness and effect of Reynolds number, for the 0.0075 scale orbiter models at Mach 6 and 10. Second will be a comparison of the aerodynamics obtained using the 0.004 and 0.0075 scale orbiter models at both Mach 6 and 10. Finally, a comparison of the aerodynamic results obtained using the 0.004 scale orbiter model at Mach 6 in both ideal air and carbon tetrafluoride (CF_4) will be presented. There is also a discussion on the simulation of real gas effects by using a heavy gas as the testing medium. The results from the Mach 10 tests of the modified orbiter model are presented in reference 9 and as such are not discussed herein.

Aerodynamics of 0.0075 Scale Orbiter Model at Mach 6 and 10

The basic aerodynamics of the 0.0075 scale orbiter model obtained in the 20-Inch Mach 6 Tunnel are presented in figures 6, 7, and 8. The effect of Reynolds number on C_N, C_A, and C_m for body flap deflections of 0° and 16° is presented in figures 6 and 7, respectively, and the body flap effectiveness, represented as ΔC_m, the increment in C_m between a body flap deflection of 0° and 16° is presented in figure 8. As expected, varying the length Reynolds number from 0.8 to 5.8×10^6, when the body flap was undeflected, had a measurable but small effect on C_N and C_m, with a decrease in C_N with increasing $R_{e,L}$. Also as expected, C_A decreased as $R_{e,L}$ increased and the amount of decrease was minimal above $R_{e,L} = 3.2 \times 10^6$ implying that a departure from laminar flow had occurred. When the body flap was deflected 16° similar trends were present for C_N and C_A but there was a significant increase in nose down C_m which increased with increasing Reynolds number. The effect of increasing Reynolds number on C_m can be more clearly observed by examining the increment in pitching moment produced by deflecting the body flap from 0° to 16° as presented in figure 8. The increment in pitching moment, around $\alpha = 40°$, increases as Reynolds number increases. However, as Reynolds number approaches 5×10^6 the rate of increase begins to drop off. That is, the increment in ΔC_m between a Reynolds number of 3.2×10^6 and 5.8×10^6 is considerably less than the increment at lower Reynolds numbers. Insight to the reason for these trends is provided by the oil flow photographs of figures 9 to 12. In these photos the separation region on and in front of the deflected body flap is clearly visible at the lowest free stream Reynolds number of 0.5×10^6 per foot. As the free stream Reynolds number increases, the reattachment point on the flap moves forward, diminishing the separation region, which increases the flap effectiveness and hence the increment in pitching moment as indicated in figure 8. When the free stream Reynolds number is 4×10^6 per foot the flow over the flap appears to be fully attached as the boundary layer flow has enough energy to push through the adverse pressure gradient ahead of the flap. Once the flow on the flap is fully attached, further large increases in flap effectiveness would not be expected and the relatively small increment in pitching moment at the highest Reynolds numbers, in figure 8, would support this conclusion. Data from the ADDB, shown as the solid symbols in these figures, indicates that the present low hypersonic Mach number wind tunnel results accurately represent the predicted flight aerodynamics, particularly at the highest Reynolds number tested (closest to flight value).

Similar trends in aerodynamics, for Reynolds number from 0.5 to 2.1 x 10^6, for data obtained in the 31-Inch Mach 10 Tunnel, are presented in figures 13 to 16. When the body flap is undeflected, the only significant Reynolds number effect is the reduction in C_A as Reynolds number increases. When the body flap is deflected 16°, the body flap effectiveness is increased as Reynolds number is increased. The oil flow photographs of figure 16 clearly show the separation region upstream of the deflected body flap and this region diminishes as Reynolds number increases. However, for the conditions tested at Mach 10, the Reynolds number could not be increased to the point that the separation was eliminated as at Mach 6. As with the Mach 6 data, at the highest Reynolds number tested, the Mach 10 data is in good agreement with the ADDB data. An additional point is also evident in the incremental pitching moment data presented in figure 15. That is, there is no effect of Mach number on the body flap effectiveness, for these laminar flow conditions, as the increments in pitching moment are the same for constant Reynolds numbers at Mach 6 and 10.

Comparison of Aerodynamics from 0.004 and 0.0075 Scale Orbiter Models

A comparison of the aerodynamics obtained on the 0.004 and 0.0075 scale orbiter models in two facilities at Mach 6 and one facility at Mach 10 is presented in figures 17 and 18. The data presented in figure 17 are for the 0.004 and 0.0075 scale models at constant length Reynolds number of about 1.6 x10^6 in the 15-Inch Mach 6 and 20-Inch Mach 6 Tunnels for body flap deflections of 0° and 16°. The data in figure 18 are for the large and small models at a constant length Reynolds number of 0.5 x 10^6 in the 31-Inch Mach 10 Tunnel with the body flap deflected 16°. These comparisons between models and tunnels indicate that the differences in C_N and C_m

are small. There are differences in C_A that are not explained, but they are not large. The important point is that the differences in aerodynamic C_N and C_m from variations in Mach number, model support, and/or model and tunnel differences are relatively small.

Comparison of Results Obtained in Mach 6 Air and CF_4

In an effort to simulate real gas effects in a ground based facility, tests were conducted in the 20-Inch Mach 6 CF_4 Tunnel, where the test medium is carbon tetraflouride (CF_4), with a molecular weight equal to 88. During entry, sufficient energy is imparted to the shock layer flow that molecules of air are vibrationally excited, dissociated and even ionized and no longer behave as ideal gases. The result is that γ no longer equals 1.4 as found in ideal air, but in fact is a lower value, and the normal shock density ratio is increased. This increase in density ratio causes the shock stand off distance to be reduced, as shown in the schlieren photographs of figure 19, and the gas compresses to higher pressures and expands to lower pressures than would occur for an ideal gas case.

For the shuttle orbiter, the increased compression of the flow in the nose region due to real-gas effects would yield an increase in lift and nose up pitching moment when compared to ideal gas results. However, because of the relatively small increase in pressure level due to a real gas in compression and the small area involved, these increments would be expected to be small. This is not the case on the aft of the orbiter where there is a significant expansion which covers a very large area, not only ahead of the body flap but also across the entire wing span. The resulting lower pressures should cause a reduction in total lift and produce a significant nose up increment in pitching moment. The question that must be addressed, in this effort to simulate real gas effects via a heavy test gas in a lower Mach number facility, is: do values of γ found within the shock layer for CF_4 at Mach 6 approximate the values for flight?

In order to address this question, the computed variation of γ within the shuttle orbiter windward flow field was provided by J. K. Weilmuenster (Reference 9) and is presented in figure 20. It can be seen that for this Mach 24 flight condition γ varies from about 1.12 behind the normal portion of the bow shock to about 1.18 near the expansion at the aft end of the body, with the majority of the flow field having a nearly constant value of γ around 1.18 to 1.20. Since the post normal shock value of γ in the CF_4 tunnel for present operating conditions (i.e., P_o, T_o) is about 1.12 to 1.15 and the free stream value is 1.22, it would appear that the low γ aspect of the real gas shock layer flow field is reasonably well simulated by using CF_4.

The effect of γ on aerodynamic characteristics is presented in figures 21 and 22. The comparison of the aerodynamics, obtained by testing the same model (0.004 scale), at the same Mach number (6), with the same Reynolds number (0.5×10^6 per foot), in ideal air and CF_4, shows the expected loss in normal force and significant nose up increment in pitching moment. The pitching moment data are replotted to a more sensitive scale in figure 22 to indicate that the difference in pitching moment found between the pre-flight estimates and the STS-1 flight results of about 0.03 is well represented by testing in ideal air and CF_4. As mentioned previously, possible causes of the "pitch-up anomaly" were errors in basic C_m and/or body flap effectiveness. It was shown in figure 15 that the body flap effectiveness was not affected by Mach number for Mach 6 and 10 air. Now it is shown in figure 23 that body flap effectiveness is not affected by testing medium (air versus CF_4). In addition, these low Reynolds number results fall within the range of the existing data indicated on the figure, which included most if not all of the results conducted prior to flight and incorporated into the ADDB predicted values. There does not appear to be any significant effect which changes the body flap effectiveness, except for Reynolds number, and the difference between predicted and flight C_m is well matched by testing in air and CF_4. This would tend to support the premise that the "pitch-up anomaly" is a real gas effect on basic configuration pitching moment rather than on body flap effectiveness.

When comparing the data for air and CF_4 in order to examine real gas effects, the effect of the viscous interaction parameter, $\overline{V}'_\infty$, should not be ignored. Testing the 0.004 scale model in CF_4 at Mach 6 yields a $\overline{V}'_\infty$ of 0.015 which is very near the orbiter flight value at Mach 23 and is different from the value in Mach 6 air. In addition, when testing at this condition in CF_4 the length Reynolds number of 0.2×10^6 is lower than the Mach 23 flight condition, where $R_{e,L} = 1 \times 10^6$.

Therefore, more than one variable has been changed (i.e., γ and $\overline{V}'_{\infty}$ as well as $R_{e,L}$) in going from air to CF_4 and it cannot be categorically stated that the nose up increment in pitching moment was caused exclusively or solely by the low γ simulation of CF_4. However, it has been shown in reference 7 that $\overline{V}'_{\infty}$ is the proper correlation factor between entry and wind tunnel data and of course the Space Shuttle program has always used $\overline{V}'_{\infty}$ at Mach numbers greater than 15. It has also been shown in this paper that the primary effect of $R_{e,L}$ is an increase in body flap effectiveness and not a significant change in basic pitching moment. This would indicate that $R_{e,L}$ is not the cause of the large nose up increment in C_m between wind tunnel and flight.

Testing of the 0.0075 scale model in CF_4 will maintain the low γ with about a 1.38 decrease in $\overline{V}'_{\infty}$ to 0.011 and testing the 0.004 scale model in Mach 17 nitrogen will maintain $\overline{V}'_{\infty}$ at 0.015 with $\gamma = 1.4$. These tests will provide a definitive answer to whether or not this effect is caused by γ or $\overline{V}'_{\infty}$. As mentioned, the tests of the larger scale model in CF_4 and either scale model nitrogen have been delayed. A primary effect of larger $\overline{V}'_{\infty}$ (i.e., more viscous) is to thicken the boundary layer which may cause a reduction in body flap effectiveness. Because this ΔC_m is shown to be about the same in air and CF4 (Figure 23) and since the computed increment in pitching moment from reference 9, based on a flow field γ distribution simulated in Mach 6 CF_4, so closely matches the wind tunnel results it is believed that the effects are due to γ and not $\overline{V}'_{\infty}$ or $R_{e,L}$.

The CF_4 results are presented again in figure 24 whereby C_m has been reduced about the flight center of gravity of 66.7 percent of body length compared to the previous value of 65 percent. The data of figure 24 show that configuration trims at an angle of attack of 40° when the body flap is deflected 12.5°. This wind tunnel model was tested with the elevons deflected 0° where STS-1 had them deflected about -2° to -3°. This would, of course, require an increase in the body flap deflection to maintain trim and move the body flap deflection to around 15°, very close to the 16° found on STS-1, if the ADDB values for control effectiveness are used.

SUMMARY REMARKS

Hypersonic wind tunnel tests have been conducted in four NASA Langley Research Center facilities in an effort to determine the cause of the so-called "pitch-up anomaly" of the Space Shuttle Orbiter. These tests were conducted at Mach 6 and 10 in air in order to determine baseline aerodynamics, control effectiveness, support interference effects and model to model and tunnel to tunnel comparisons. Tests at Mach 6 in a heavy gas (carbon tetrafluoride CF_4) simulated the low ratio of specific heats found in a real gas at entry flight conditions. This program is continuing as of this writing but has provided significant insight into the cause of the anomaly.

There are no significant support interference effects, at least for the range of models, blade and sting supports and test conditions investigated, which could be construed as having been the cause of the anomaly. The orbiter basic aerodynamics from ideal gas facilities agree well with 1977 Aerodynamic Design Data Book which was based on ideal gas results. Body flap effectiveness increased with increasing Reynolds number and also reasonably agrees with the 1977 Aerodynamic Design Data Book. In addition, at low Reynolds numbers the body flap effectiveness does not change with either Mach number or γ. These findings imply that a poor estimate of the body flap effectiveness was not the cause of the anomaly. Testing in a heavy gas, in this case CF_4 (molecular weight equals 88) at Mach 6, to simulate the low γ aspect of a real gas, very closely approximates the nose up increment in pitching moment found in flight. The testing in CF_4 not only simulates the low γ aspect of a real gas but also, for the small model, provides a match of the flight viscous interaction parameter, $\overline{V}'_\infty$ at Mach 23, however, at a low value of $R_{e,L}$. Since this represents a change of more than one variable, when testing in air and CF_4, it cannot be stated categorically that the cause of the "pitch-up anomaly" is the low γ aspect of real gases. However, it has been shown that the major effect of $R_{e,L}$ is on body flap effectiveness and not on basic pitching moment. This and testing of the larger model at Mach 6 in CF_4 to change $\overline{V}'_\infty$ at constant $\gamma = 1.22$ as well as testing the small model at Mach 17 in nitrogen, to match flight

$\overline{V}'_{\infty}$, at $\gamma = 1.4$ will allow a final statement as to the accuracy of simulating the low γ aspect of a real gas on configuration aerodynamics.

After conducting a series of tests in four hypersonic facilities, it is believed that the cause of the shuttle orbiter "pitch-up anomaly" has been shown to be due, to a large extent, to the low γ aspect of a real gas, which causes the shock layer flow to expand on the aft portion of the body to lower pressure levels than for an ideal gas. The lower pressure on the aft section results in a loss in normal force and a significant nose up increment in pitching moment which corresponded to the differences between preflight data and the STS-1 flight results.

References

1. Compton, H. R.; Schiess, J. R.; Suit, W. T.; Scallion, W. I.; and Hudgins, J. W.: Stability and Control Over the Supersonic and Hypersonic Speed Range." Shuttle Performance: Lessons Learned, NASA Langley Research Center, Hampton, Virginia. March 1983.

2. Aerodynamic Design Data Book, Rockwell International, Space Division, ADDB; SD74-SH-0206-1K.

3. Wada, Y.; and Kubota, H.: "Numerical Simulation of Re-Entry Flow around the Space Shuttle with Finite-Rate Chemistry." International Symposium on Space Technology and Science, Tokyo. May 20-25, 1990.

4. Romere, P. O., and Whitnah, A. M.: "Space Shuttle Entry Longitudinal Aerodynamic Comparisons of Flights 1-4 with Preflight Predictions." Shuttle Performance: Lessons Learned, NASA Langley Research Center, Hampton, Virginia. March 1983.

5. Griffith, B. J.; Maus, J. R.; and Best, J. T.: "Explanation of the Hypersonic Longitudinal Stability Problem - Lessons Learned." Shuttle Performance: Lessons Learned, NASA Langley Research Center. March 1983.

6. Illif, K. W.; and Shafer, M. F.: "Space Shuttle Hypersonic Flight Research and the Comparison to Predicted Results." AIAA Paper No. 92-3988, July 1992.

7. Woods, W. C.; Arrington, J. P.; and Hamilton, H. H. II: "A Review of Preflight Estimates of Real-Gas Effects on Space Shuttle Aerodynamic Characteristics. Shuttle Performance: Lessons Learned, NASA Langley Research Center, March 1983.

8. Miller, C. G. III: "Hypersonic Aerodynamic/Aerothermodynamic Testing Capabilities at Langley Research Center." AIAA Paper No. 92-3937, July 1992.

9. Weilmuenster, J. K.; and Gnoffo, P.: "Navier-Stokes Simulations of Orbiter Aerodynamics Characteristics." Orbiter Experiments (OEX) Aerothermodynamics Symposium, Williamsburg, Virginia. April 27-30, 1993.

Table 1. Full and model scale Space Shuttle Orbiter reference dimensions.

Reference Dimension	Full	Scale 0.0075	0.004
Wing Area	2690.00 ft^2	21.7890 in^2	6.2288 in^2
Wing Span	936.68 in	7.0251 in	3.7561 in
Mean Aerodynamic Chord	474.81 in	3.5611 in	1.9040 in
Body Length	1290.30 in	9.6773 in	5.1741 in

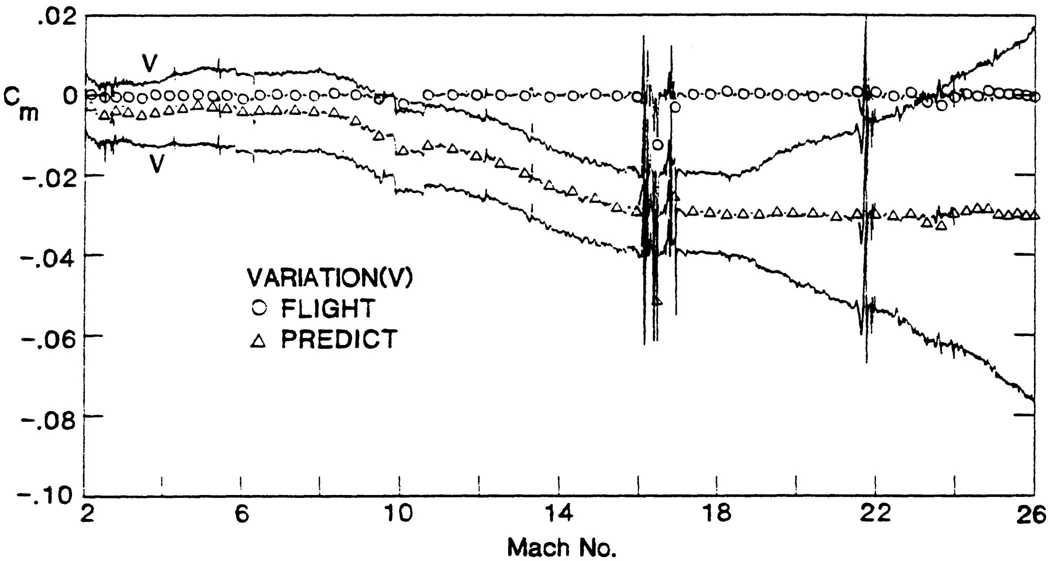

Figure 1. Example of Space Shuttle Orbiter predicted pitching moment based on observed entry control deflections and estimated control effectiveness (from Reference 1).

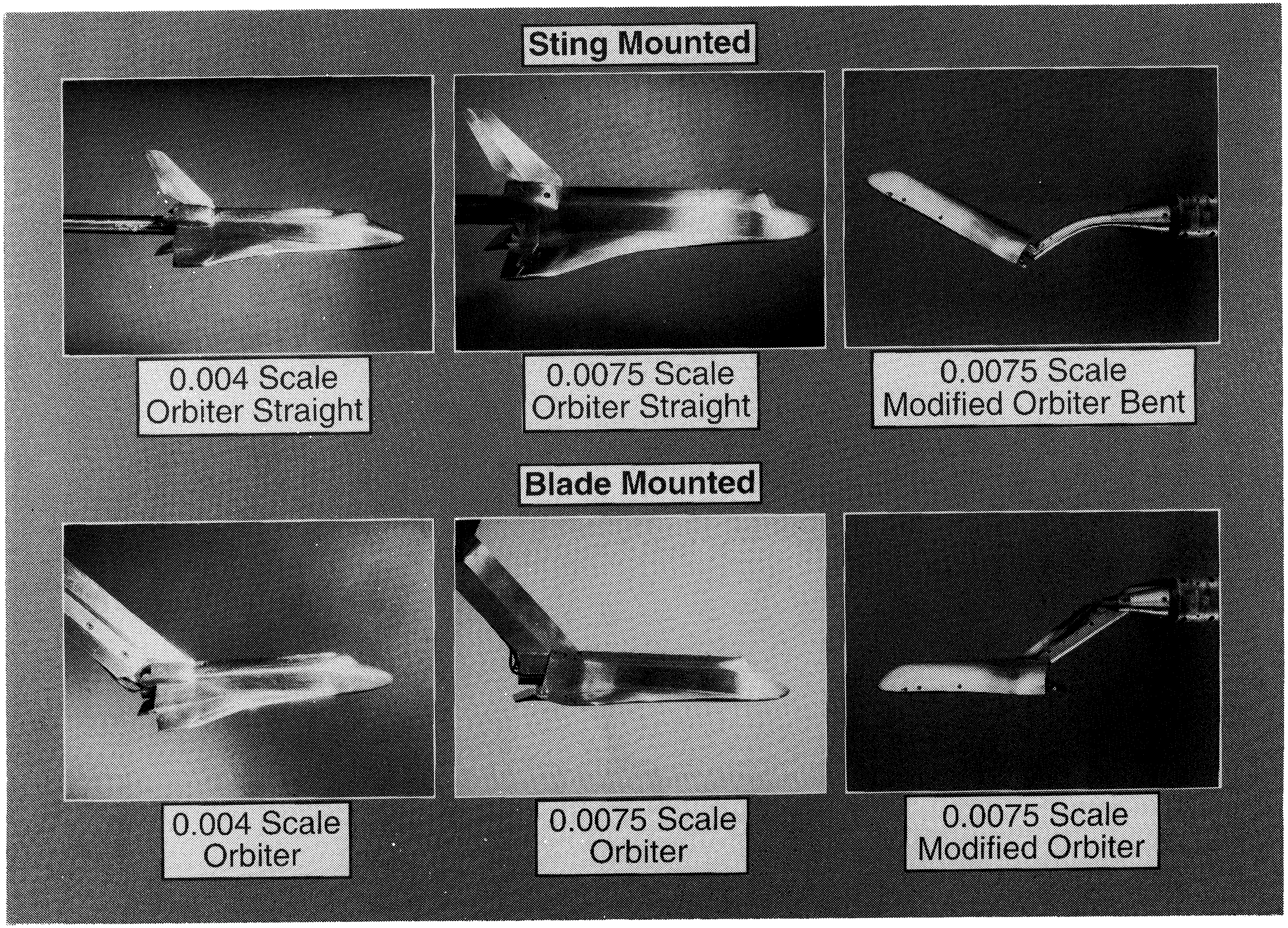
Sting Mounted
0.004 Scale Orbiter Straight
0.0075 Scale Orbiter Straight
0.0075 Scale Modified Orbiter Bent
Blade Mounted
0.004 Scale Orbiter
0.0075 Scale Orbiter
0.0075 Scale Modified Orbiter

Figure 2. Photographs of 0.004 and 0.0075 scale Space Shuttle Orbiter models and 0.0075 scale modified orbiter model with various sting and blade model support systems.

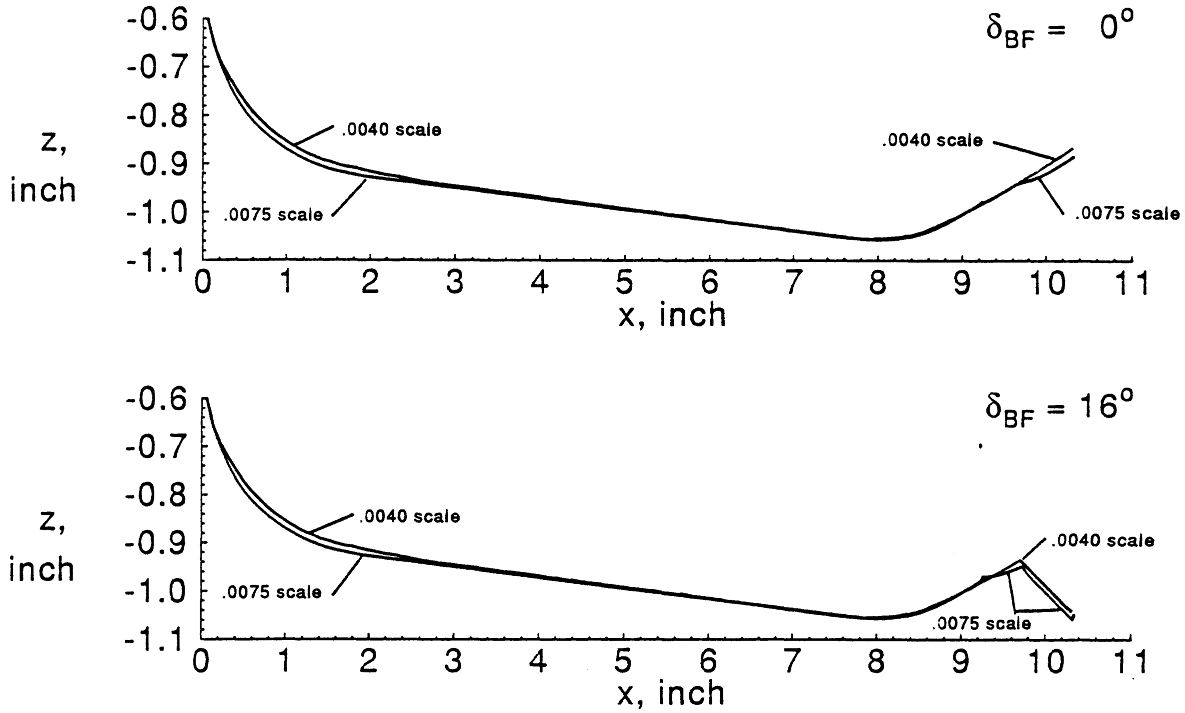

Figure 3. Example of Space Shuttle Orbiter center line coordinates compared with both the 0.004 and 0.0075 scale model coordinates, all values scaled to the length of the 0.0075 scale model.

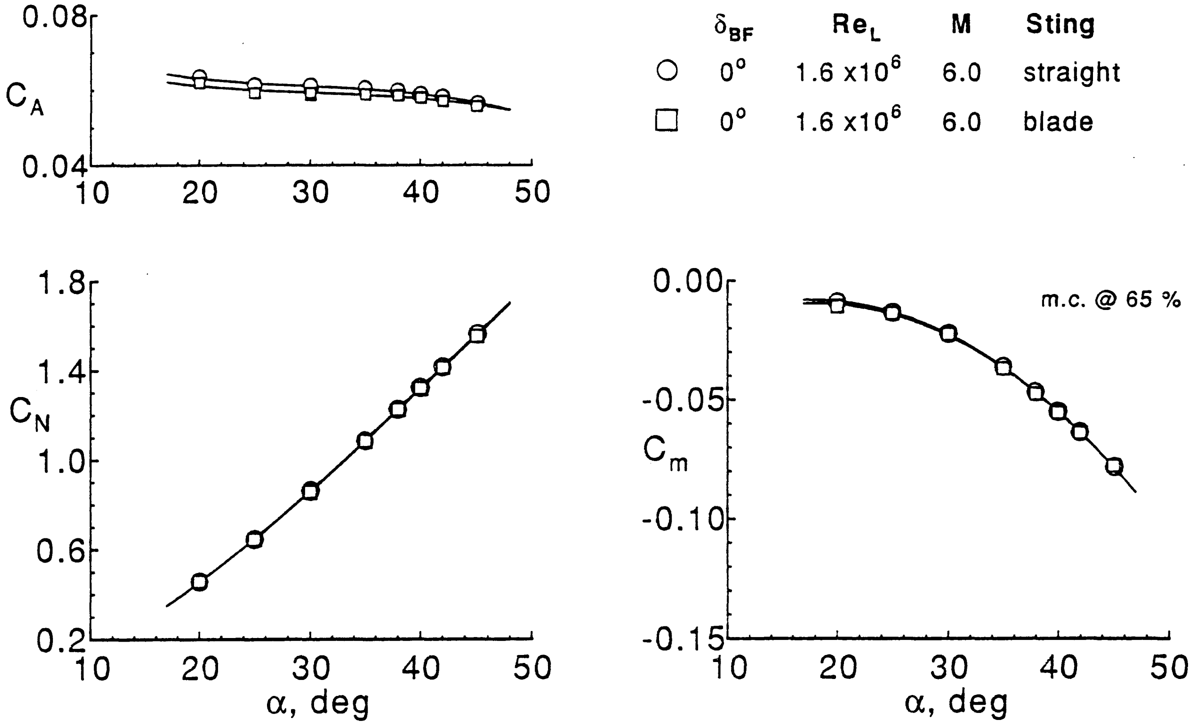

Figure 4. Effect of support arrangement on 0.0075 scale Space Shuttle Orbiter longitudinal aerodynamic characteristics obtained in the 20-Inch Mach 6 Air Tunnel, $M_\infty = 6$, $\delta_{BF} = 0°$.

Model / Facility	15-Inch Mach 6	20-Inch Mach 6	20-Inch Mach 6 CF4	31-Inch Mach 10
0.004 scale orbiter	Re = 0.5, 1.0, 4.0 sting δ_{BF} = 0°, 12.5°, 16.3° F&M, schlieren	Unavailable	Re = 0.5 sting δ_{BF} = 0°, 12.5°, 16.3° F&M, schlieren	Re = 1.0 (1 run) sting δ_{BF} = 16.3° F&M heater failure & water leak ended test
0.0075 scale orbiter	Resulted in Tunnel Blockage	Re = 0.5, 1.0, 2.0, 4.0, 7.6 blade/sting δ_{BF} = 0°, 16°, 20° F&M, oil flow, schlieren	Tunnel heater damaged on first run with 0.0075 model	Re = 0.5, 1.0, 2.0 blade/bent sting δ_{BF} = 0°, 16°, 20° F&M, oil flow
"HALIS - II" 0.0075 scale modified orbiter	Resulted in Tunnel Blockage	Unavailable	Heater damage prevented test	Re = 0.5, 1.0, 2.0 blade/bent sting δ_{BF} = 0°, 16° F&M, oil flow

NOTE: Re x 10^{-6}/ft

Figure 5. Actual test matrix completed to date.

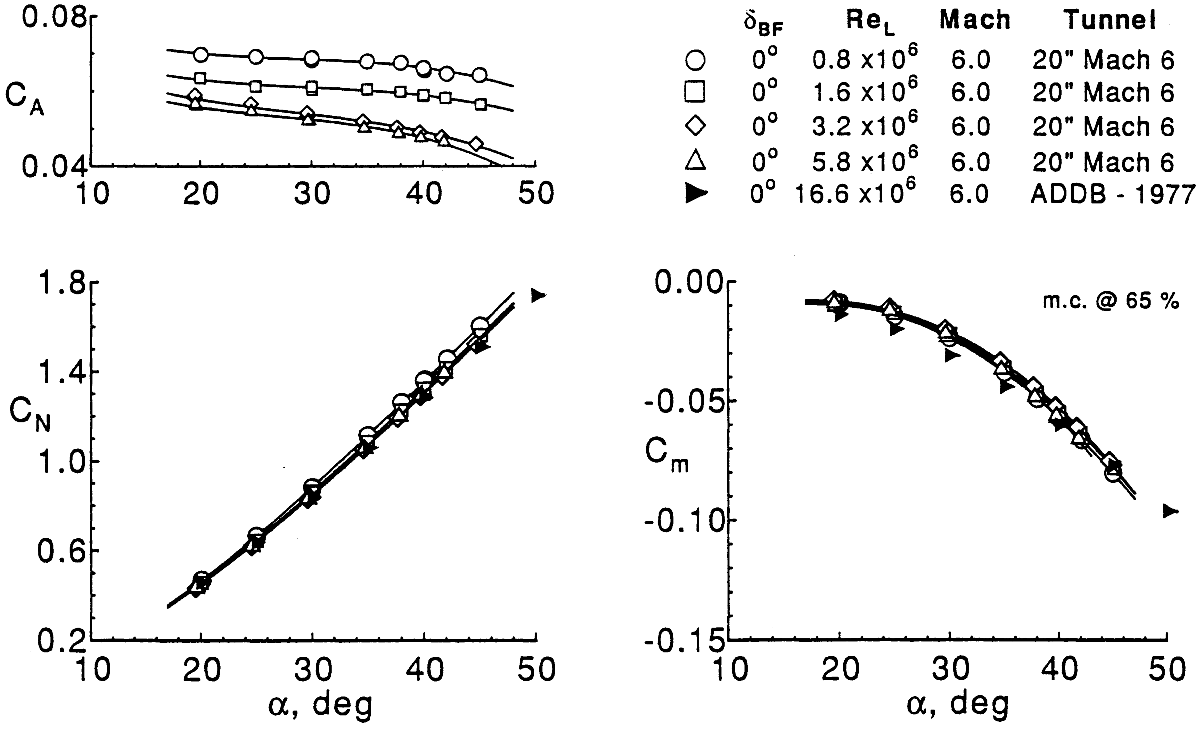

Figure 6. Effect of Reynolds number on 0.0075 scale Space Shuttle Orbiter longitudinal aerodynamic characteristics obtained in the 20-Inch Mach 6 Air Tunnel, $M_\infty = 6$, $\delta_{BF} = 0°$.

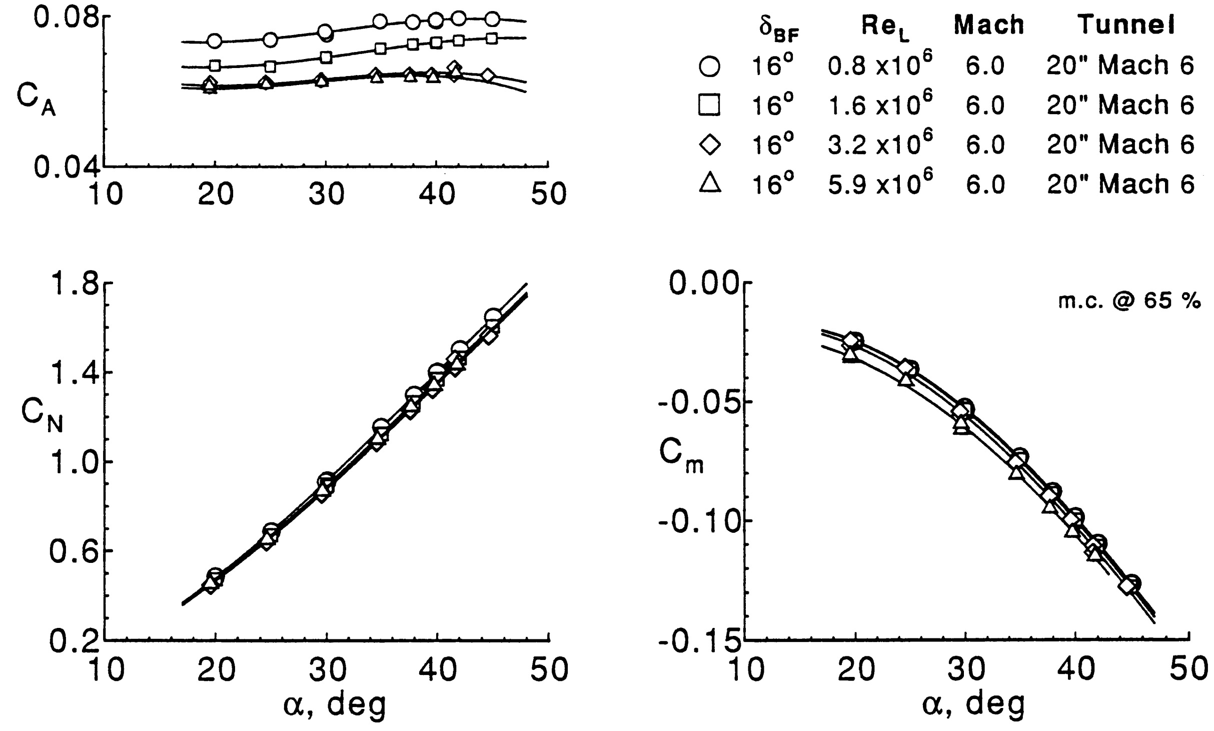

Figure 7. Effect of Reynolds number on 0.0075 scale Space Shuttle Orbiter longitudinal aerodynamic characteristics obtained in the 20-Inch Mach 6 Air Tunnel, $M_\infty = 6$, $\delta_{BF} = 16°$.

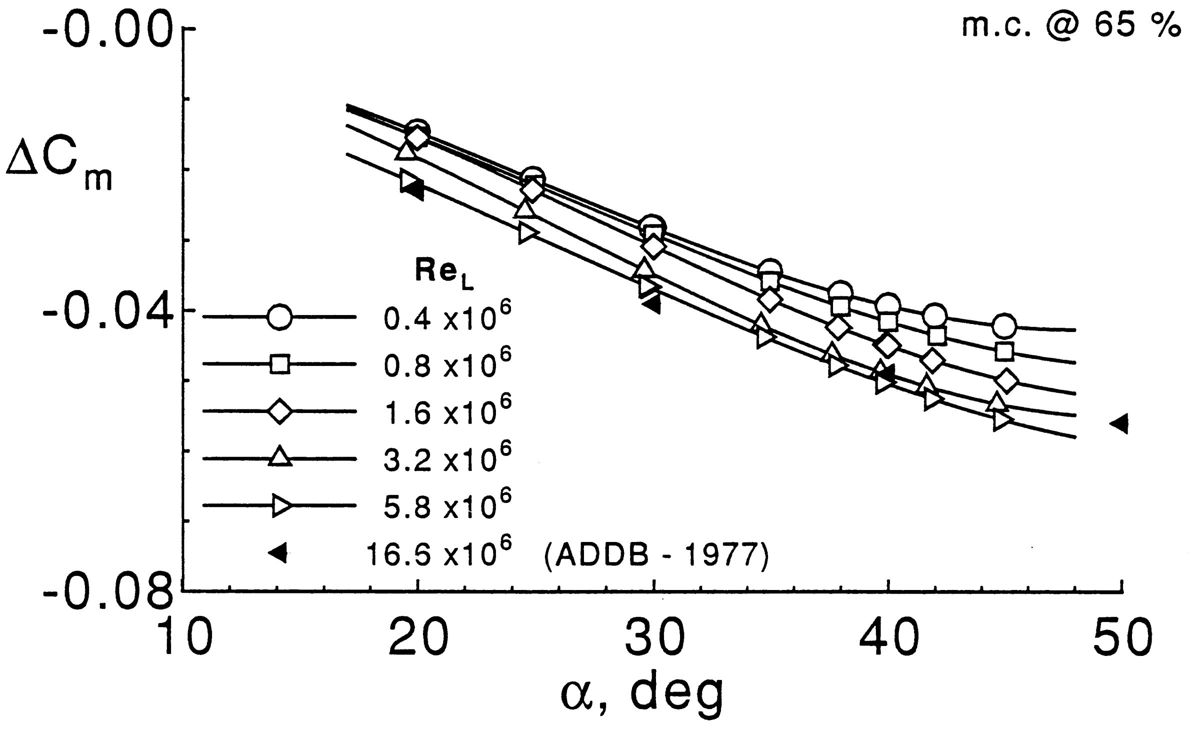

Figure 8. Effect of Reynolds number on 0.0075 scale Space Shuttle Orbiter body flap effectiveness obtained in the 20-Inch Mach 6 Air Tunnel, $M_\infty = 6$, $\Delta C_m = C_m|_{\delta_{BF=16°}} - C_m|_{\delta_{BF=0°}}$.

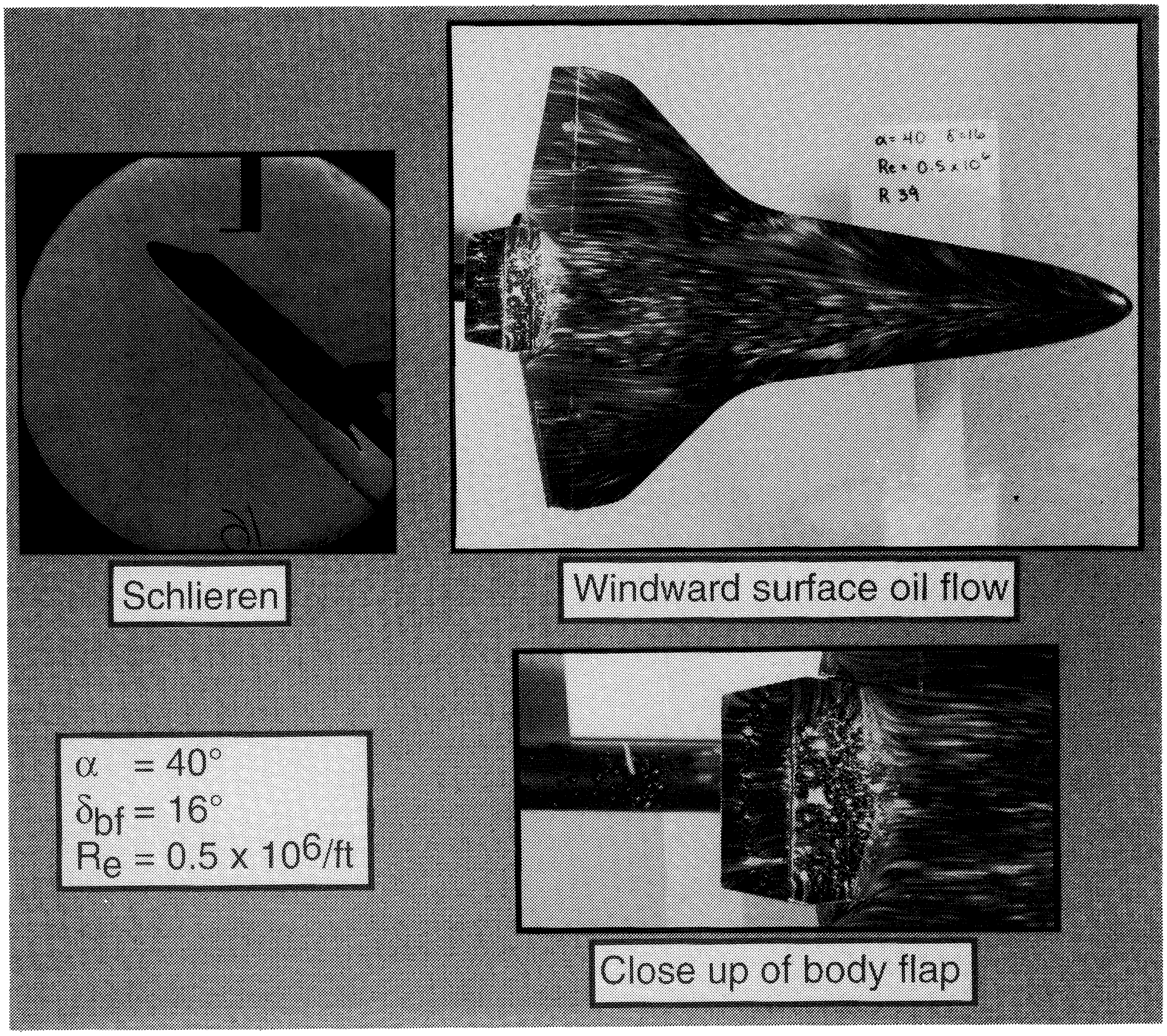

Figure 9. Visualization of windward surface flow field on 0.0075 scale Space Shuttle Orbiter obtained in the 20-Inch Mach 6 Air Tunnel, $M_\infty = 6$, $R_e = 0.5 \times 10^6$.

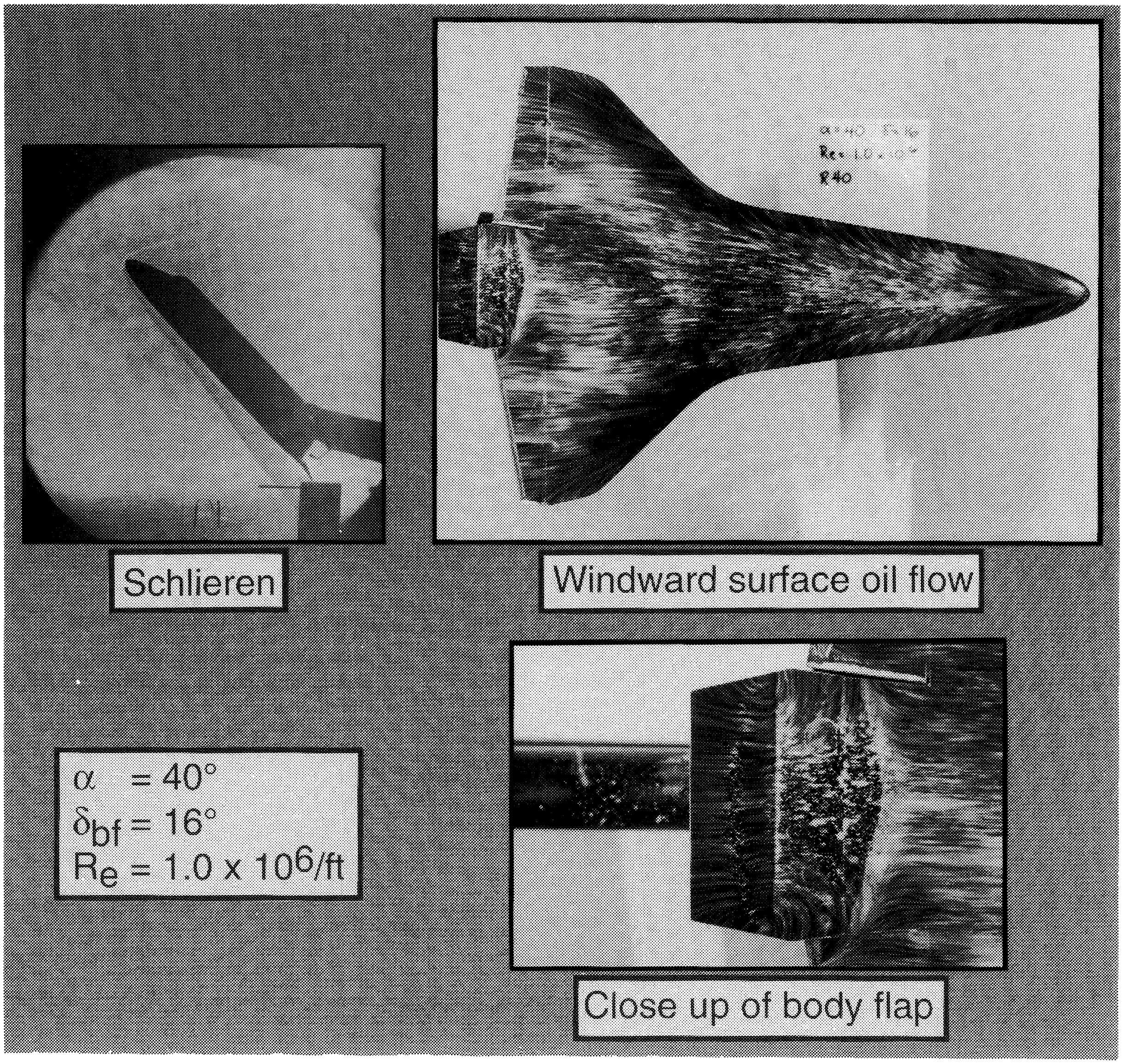

Figure 10. Visualization of windward surface flow field on 0.0075 scale Space Shuttle Orbiter obtained in the 20-Inch Mach 6 Air Tunnel, $M_\infty = 6$, $R_e = 1.0 \times 10^6$.

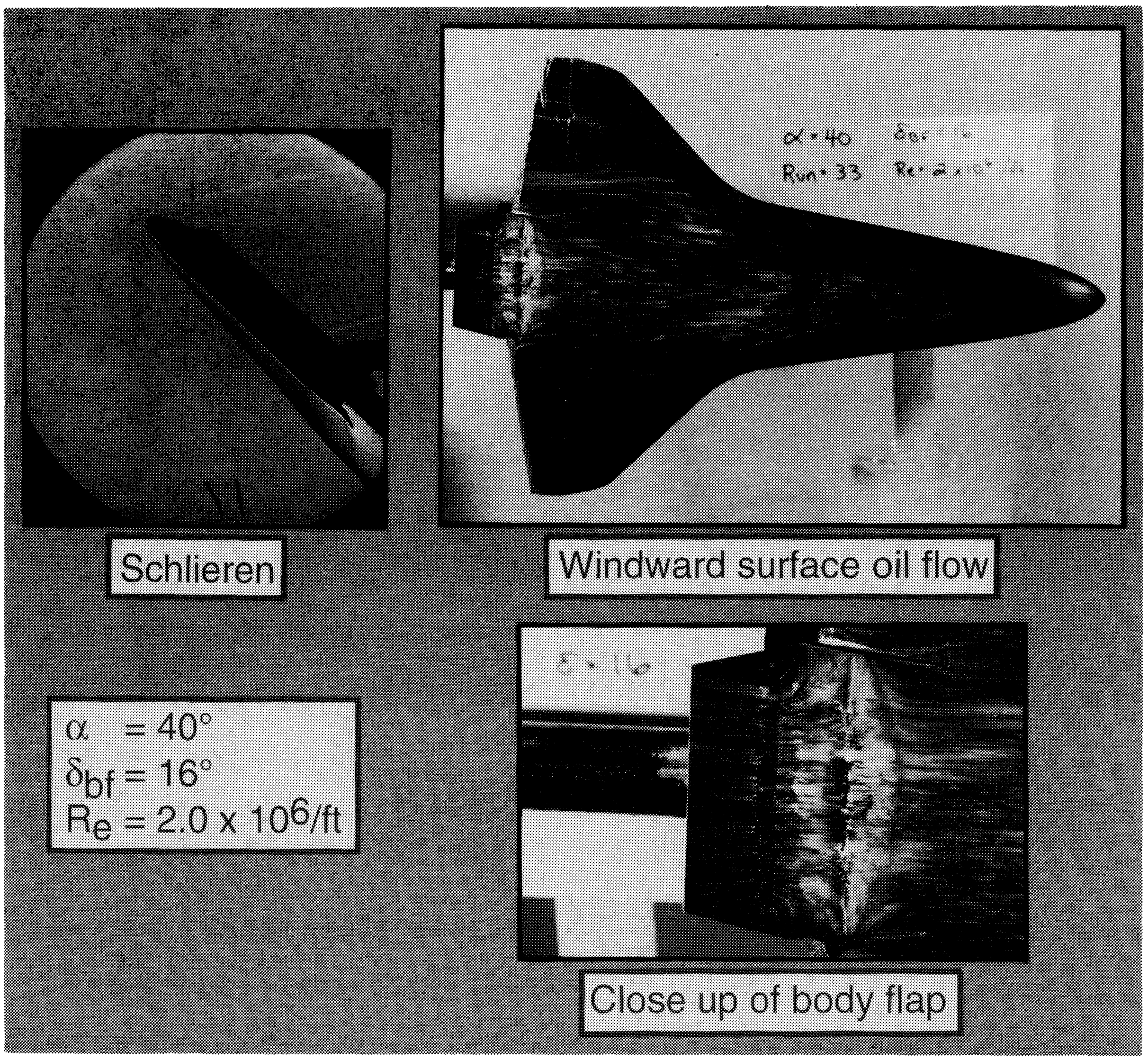

Figure 11. Visualization of windward surface flow field on 0.0075 scale Space Shuttle Orbiter obtained in the 20-Inch Mach 6 Air Tunnel, $M_\infty = 6$, $R_e = 2.0\text{x}10^6$.

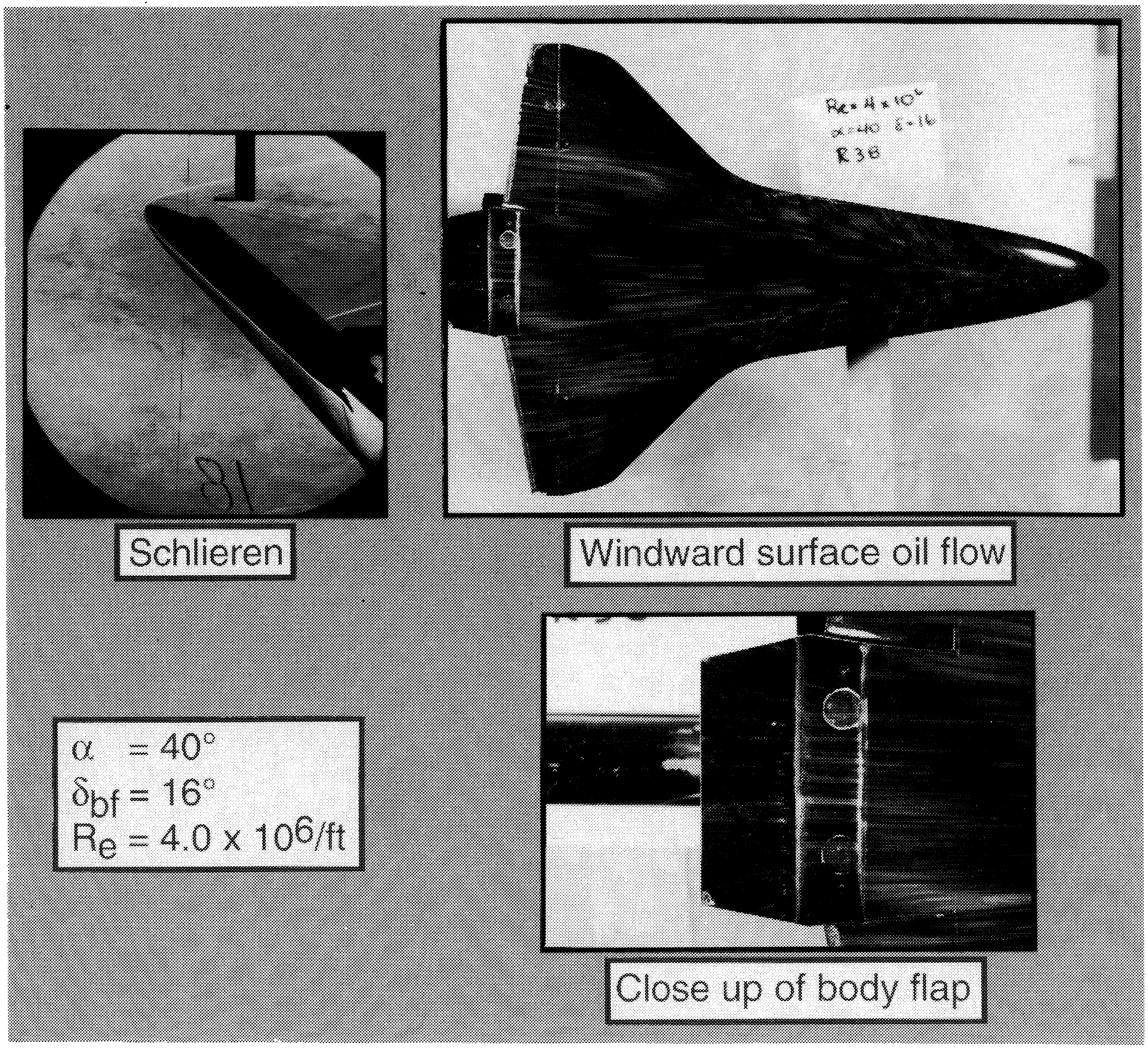

Figure 12. Visualization of windward surface flow field on 0.0075 scale Space Shuttle Orbiter obtained in the 20-Inch Mach 6 Air Tunnel, $M_\infty = 6$, $R_e = 4.0x10^6$.

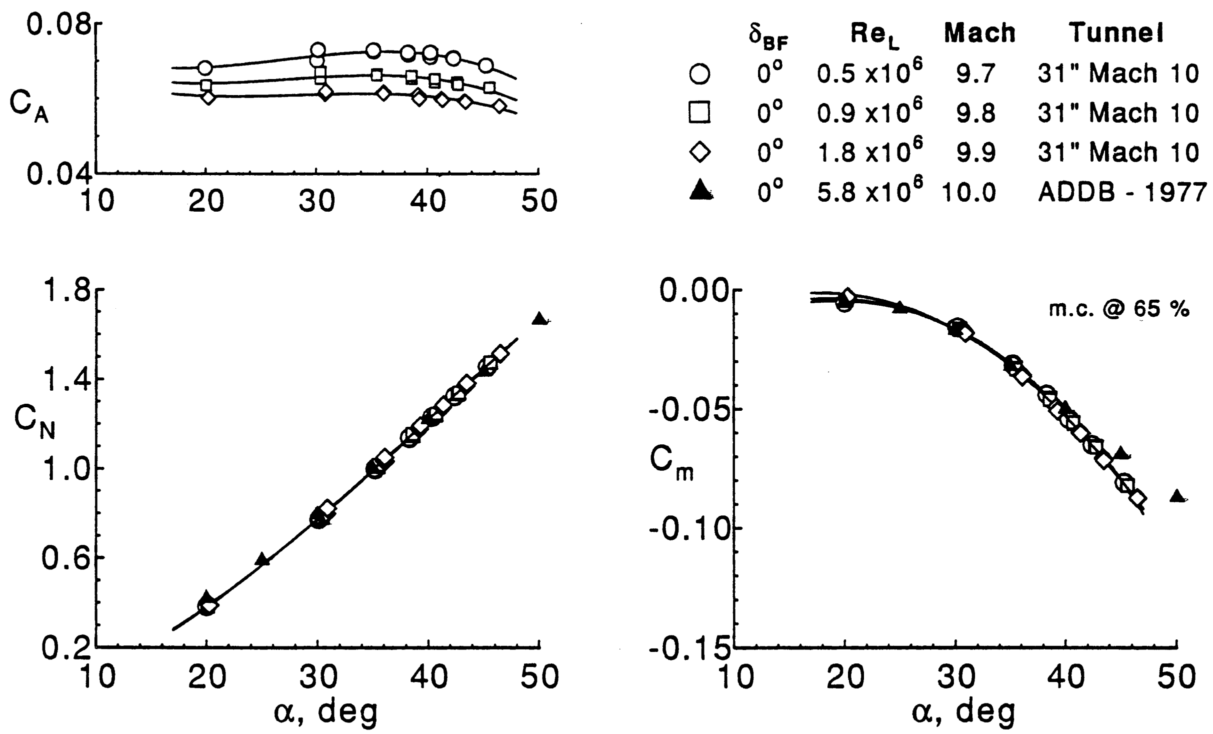

Figure 13. Effect of Reynolds number on 0.0075 scale Space Shuttle Orbiter longitudinal aerodynamic characteristics obtained in the 31-Inch Mach 10 Air Tunnel, $M_\infty = 10$, $\delta_{BF} = 0°$.

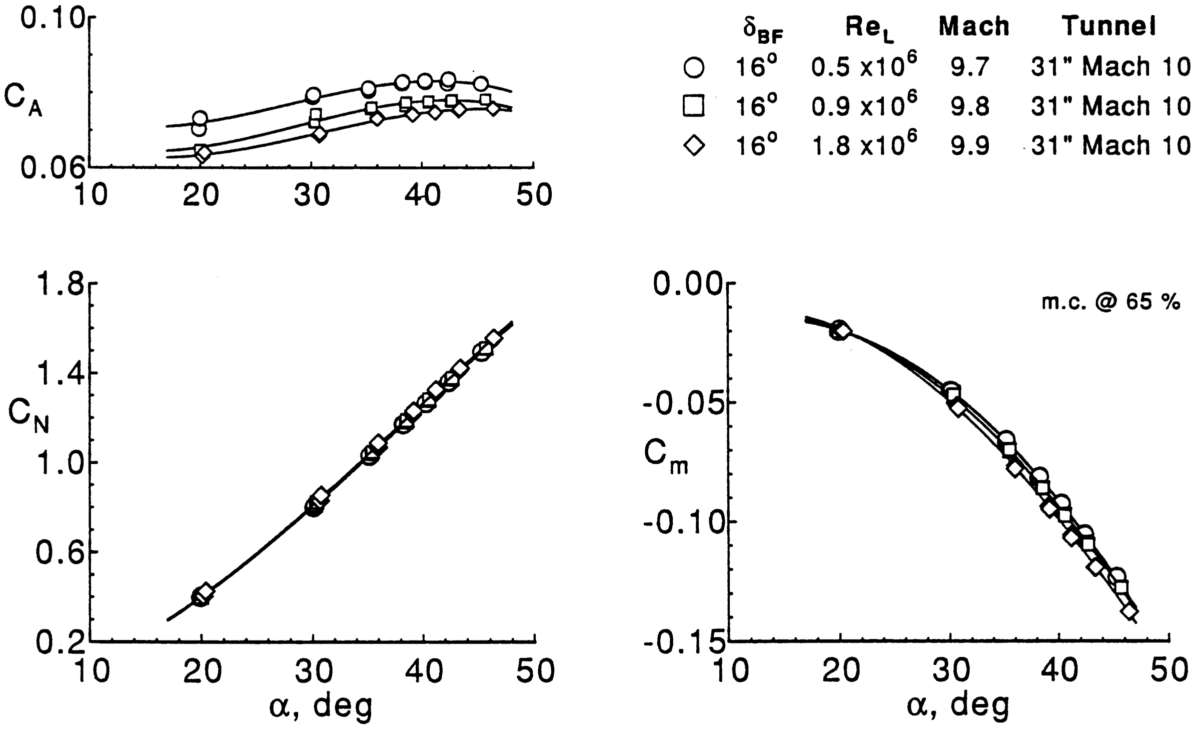

Figure 14. Effect of Reynolds number on 0.0075 scale Space Shuttle Orbiter longitudinal aerodynamic characteristics obtained in the 31-Inch Mach 10 Air Tunnel, $M_\infty = 10$, $\delta_{BF} = 16°$.

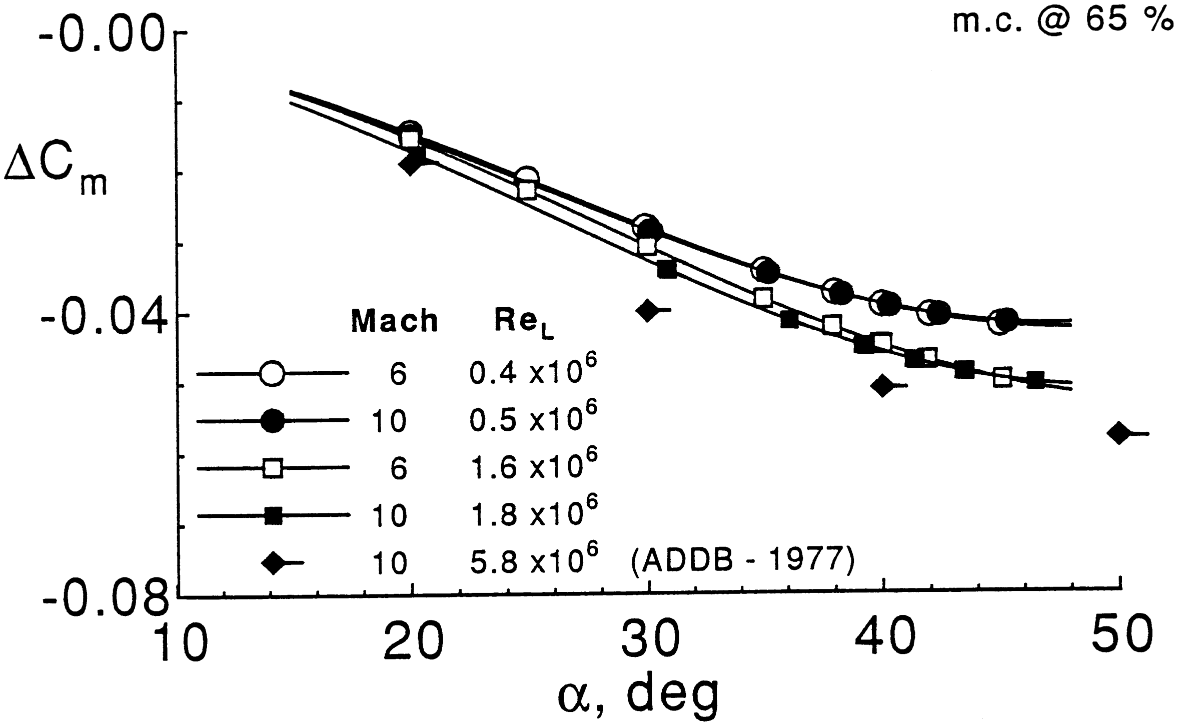

Figure 15. Effect of Mach and Reynolds numbers on 0.0075 scale Space Shuttle Orbiter body flap effectiveness obtained in the 20-Inch Mach 6 and 31-Inch Mach 10 Air Tunnels, $M_\infty = 6$ and 10, $\Delta C_m = C_m|_{\delta_{BF=16^\circ}} - C_m|_{\delta_{BF=0^\circ}}$.

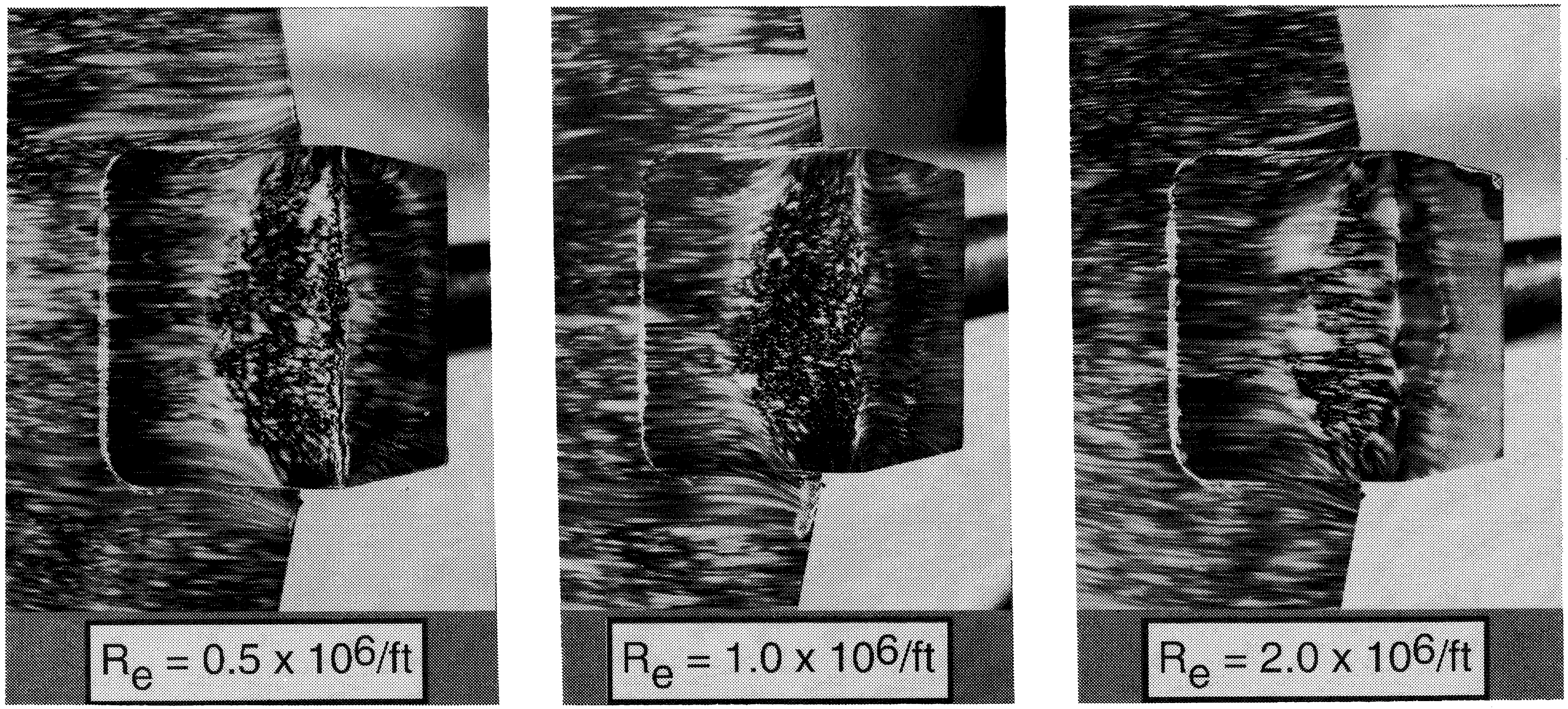
$R_e = 0.5 \times 10^6$/ft
$R_e = 1.0 \times 10^6$/ft
$R_e = 2.0 \times 10^6$/ft

Figure 16. Visualization of body flap surface streamlines obtained in the 31-Inch Mach 10 Air Tunnel.

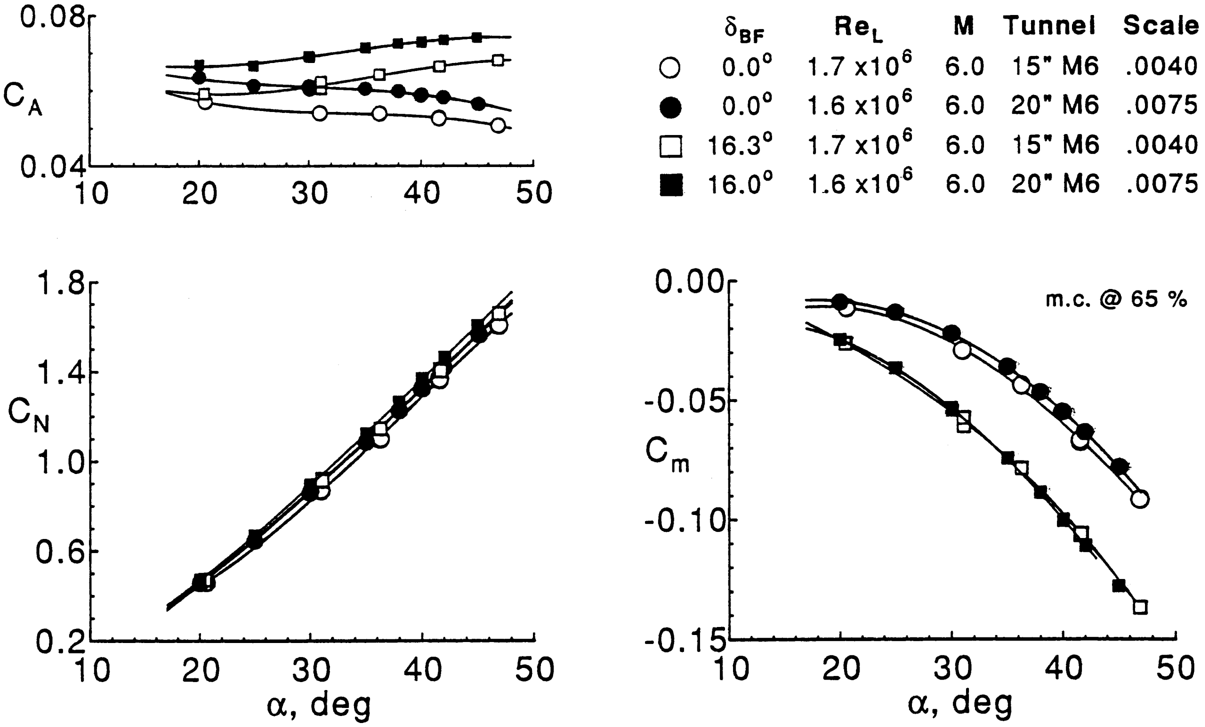

Figure 17. Comparison of 0.004 and 0.0075 scale Space Shuttle Orbiter longitudinal aerodynamics obtained in the 15-Inch and 20-Inch Mach 6 Air Tunnels at constant Reynolds number, $M_\infty = 6$, $\delta_{BF} = 0°$ and 16°.

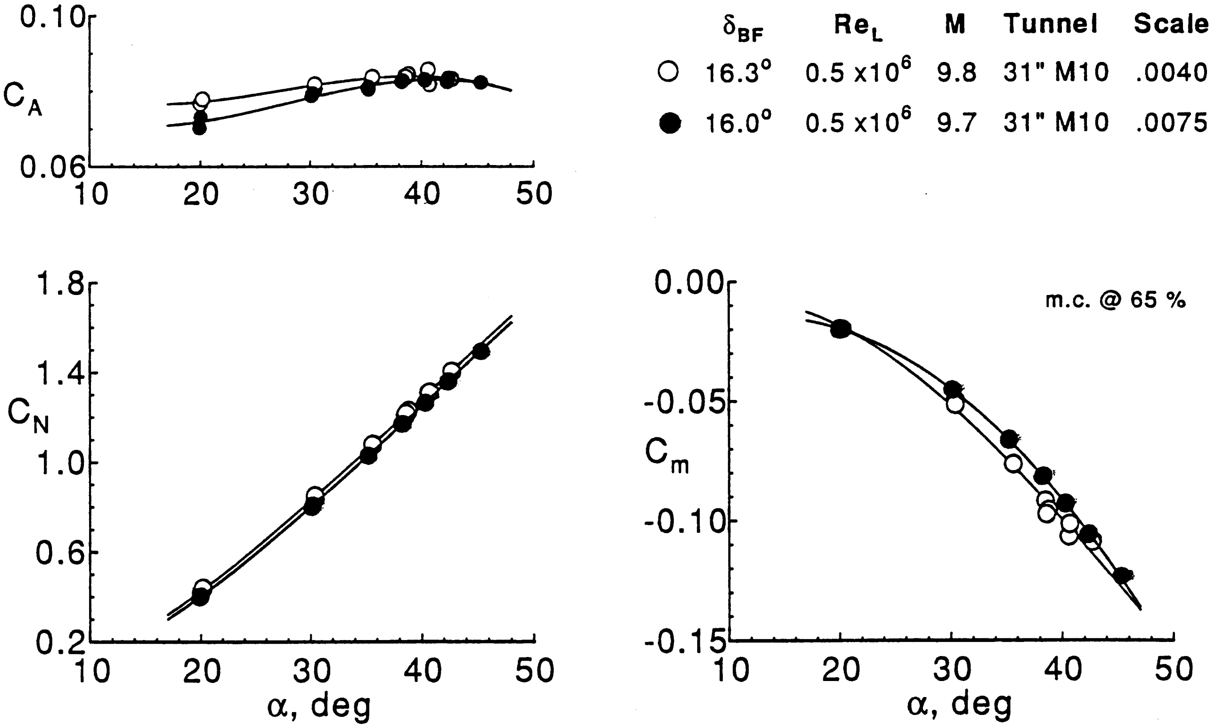

Figure 18. Comparison of 0.004 and 0.0075 scale Space Shuttle Orbiter longitudinal aerodynamics obtained in the 31-Inch Mach 10 Air Tunnel at constant Reynolds number, $M_\infty = 10$, $\delta_{BF} = 16°$.

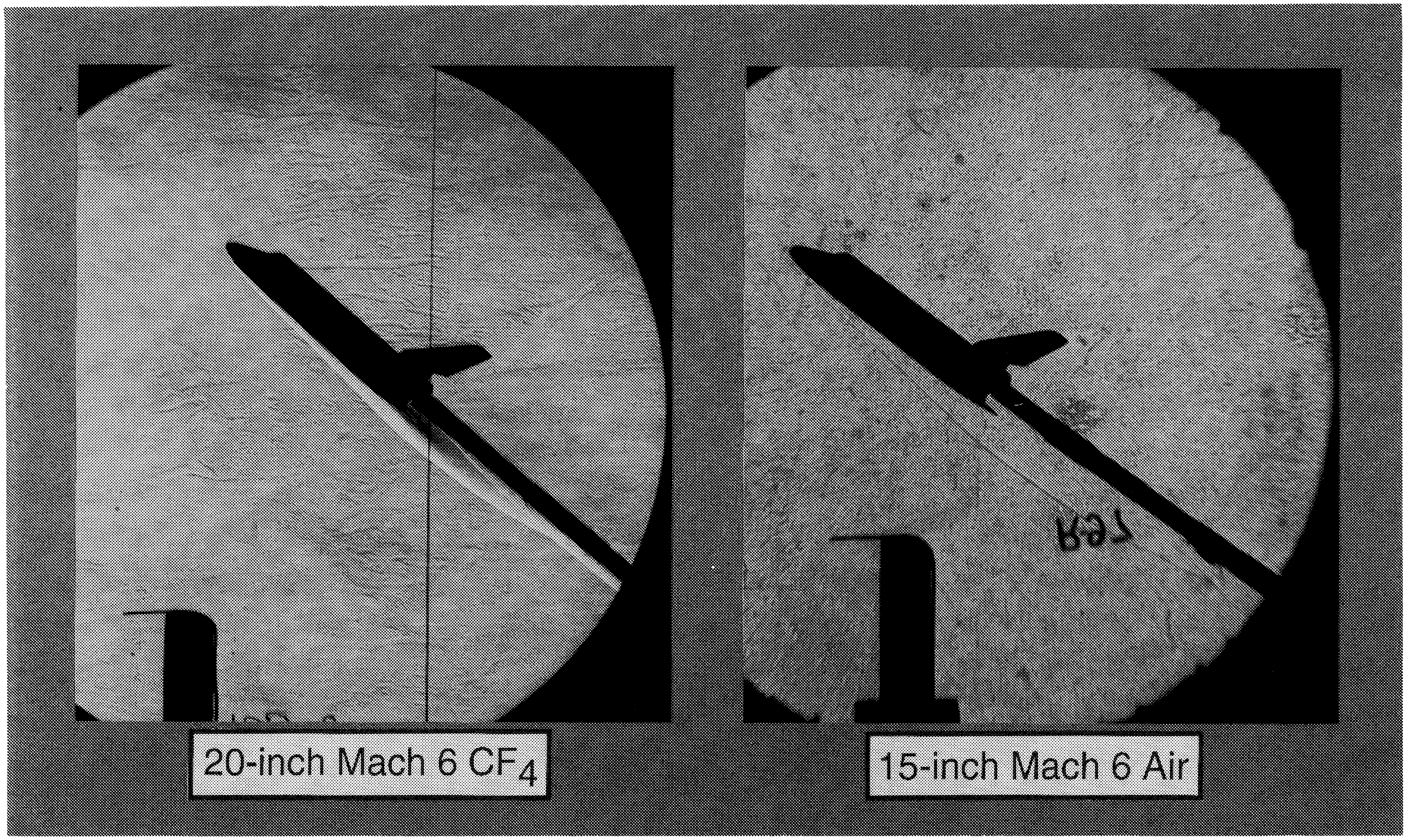

Figure 19. Schlieren photographs comparing the flow field obtained on 0.004 scale Space Shuttle Orbiter in Mach 6 Air and Carbon Tetrafluoride (CF4).

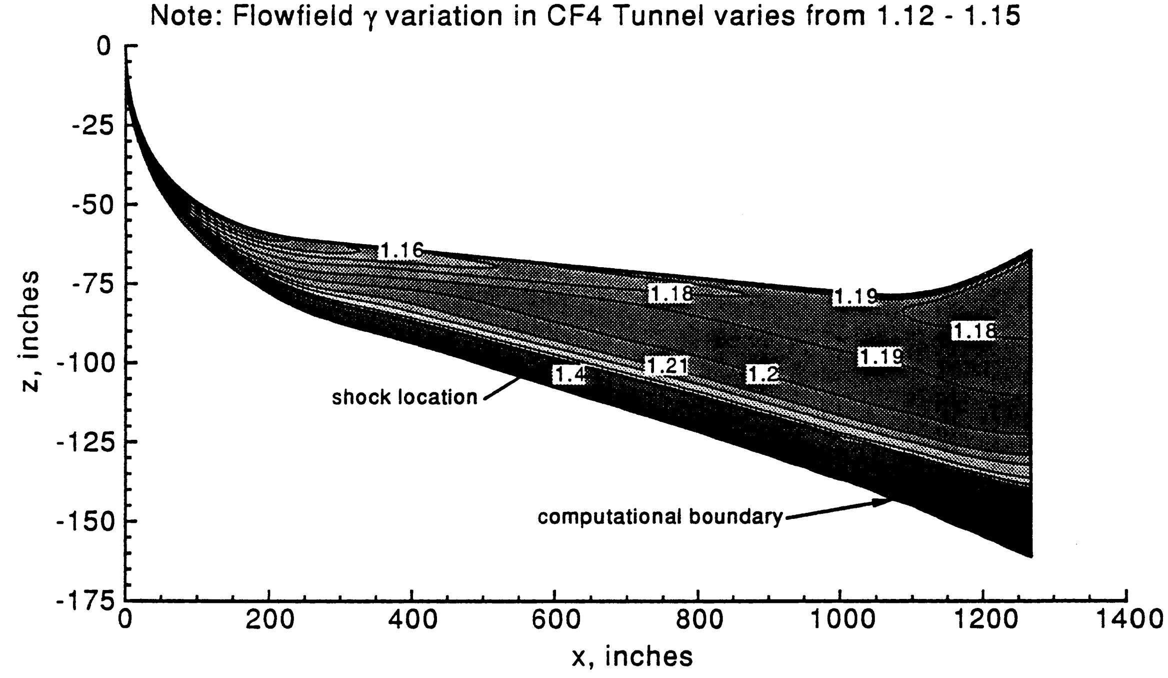

Figure 20. Computed variation of gamma within Space Shuttle Orbiter windward flow field for entry conditions, $M_\infty = 24.3$, $V_\infty = 6.92$ km/sec, $\alpha = 39.4°$.

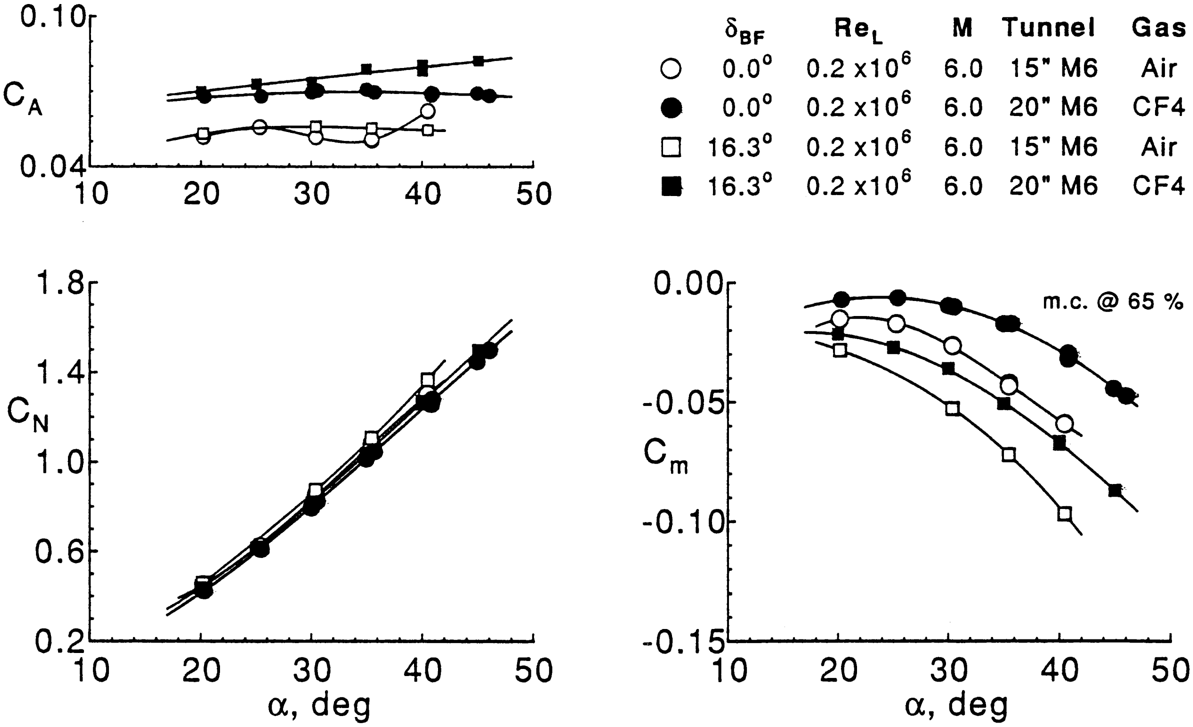

Figure 21. Effect of change in gamma on 0.004 scale Space Shuttle Orbiter longitudinal aerodynamic characteristics obtained in the 15-Inch Mach 6 Air and 20-Inch Mach 6 CF_4 Tunnels, $M_\infty = 6$, $\delta_{BF} = 0°$ and 16.3°.

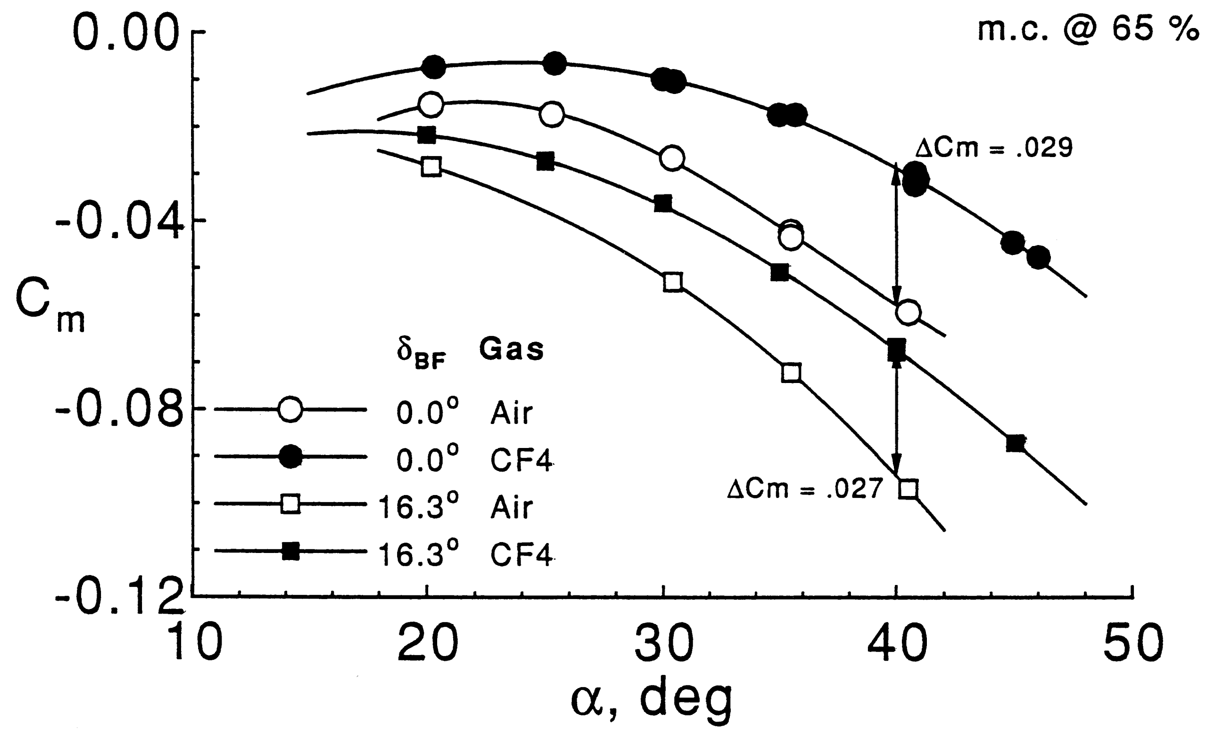

Figure 22. Effect of change in gamma on 0.004 scale Space Shuttle Orbiter pitching moment characteristics obtained in the 15-Inch Mach 6 Air and 20-Inch Mach 6 CF_4 Tunnels, $M_\infty = 6$, $\delta_{BF} = 0°$ and 16.3°.

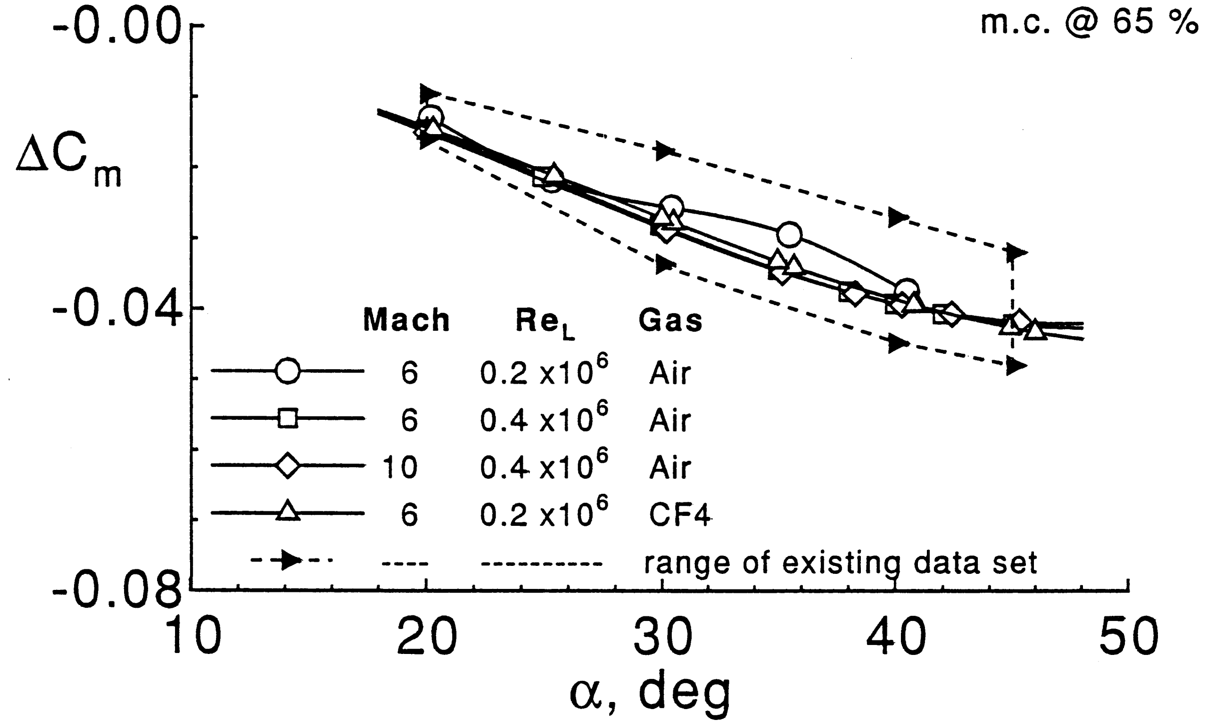

Figure 23. Effect of Mach and Reynolds numbers and gamma on 0.0075 scale Space Shuttle Orbiter body flap effectiveness obtained in the 20-Inch Mach 6 and 31-Inch Mach 10 Air Tunnels and the 20-Inch Mach 6 CF_4 Tunnel, $M_\infty = 6$ and 10, $\Delta C_m = C_m|_{\delta_{BF=16°}} - C_m|_{\delta_{BF=0°}}$.

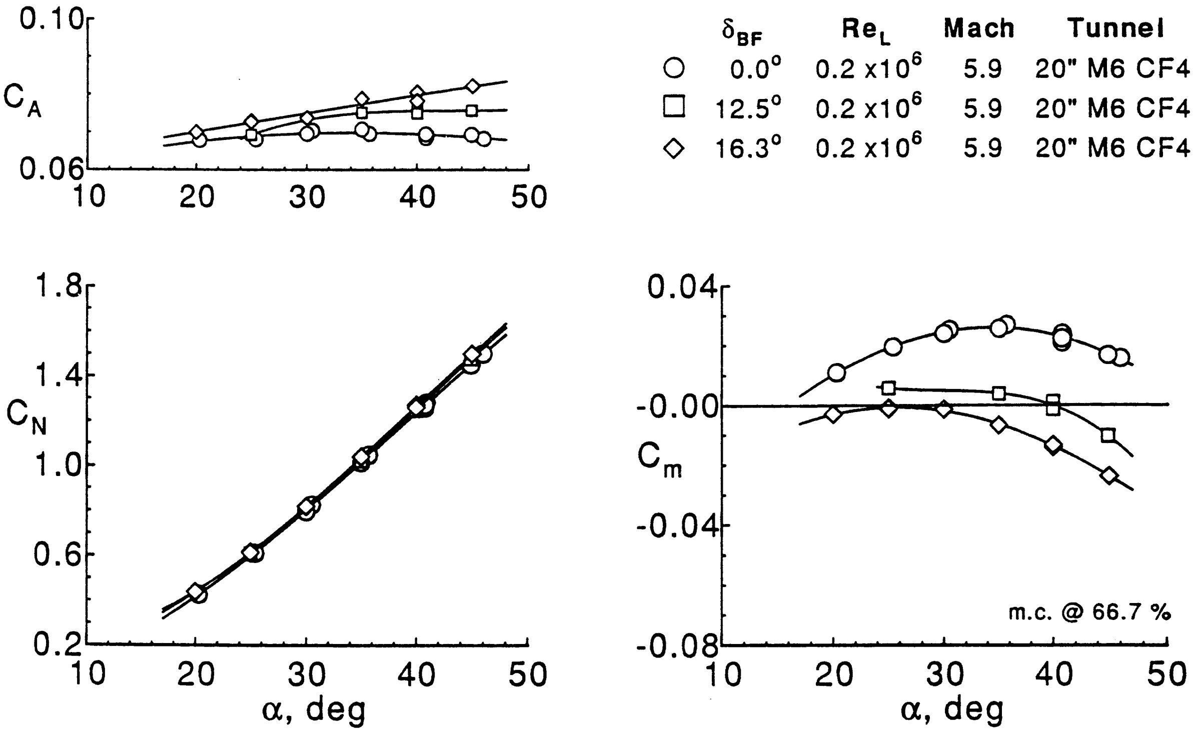

Figure 24. Longitudinal aerodynamic characteristics of 0.004 scale Space Shuttle Orbiter obtained in the 20-Inch Mach 6 CF_4 Tunnel referenced to the flight center of gravity, $M_\infty = 6$.

NAVIER-STOKES SIMULATIONS OF ORBITER AERODYNAMIC CHARACTERISTICS

K. James Weilmuenster, Peter A. Gnoffo, and Francis A. Greene
NASA Langley Research Center
Hampton, VA

NOMENCLATURE

A	reference area, 2690 ft^2
C_A	axial-force coefficient, F_A/Aq_∞
C_M	pitching-moment coefficient, $M_0\sqrt{c}Aq_\infty$
C_N	normal-force coefficient, F_N/Aq_∞
CG	center of gravity
$\bar{c}$	reference chord length, 474.8 in.
F_A	axial force
F_N	normal force
M	Mach number
M_o	total moment about CG
P	pressure
Q	heat-transfer rate
q	dynamic pressure
Re	free-stream Reynolds numbers per foot
$Re_{\infty,L}$	free-stream Reynolds number based on length
T	Temperature
V	velocity
x,y,z	Cartesian coordinates
α	angle of attack
Δ	difference
δ	deflection angle
γ	specific heat ratio
ρ	density

Subscripts

base	vehicle base
bf	body flap

el	elevon
f	leeside flap surface
trim	trim angle
w	wall
∞	freestream

INTRODUCTION

On the entry phase of its first flight, STS-1, the hypersonic pitching moment characteristics exhibited by the Shuttle Orbiter were significantly different from those derived from preflight predictions. As a result, in order to maintain trim, the vehicle's bodyflap had to be deflected to an angle over twice that predicted prior to the flight.

The aerodynamic performance characteristics of the Orbiter were determined by extensive testing in ground-based facilities. Since real-gas effects could not be fully simulated in ground-based facilities, some analytical assessments were made of real-gas effects on Orbiter aerodynamics. These analytical assessments of real-gas effects were not viewed with a great deal of confidence and thus were applied to the uncertainty in the aerodynamics of the vehicle rather than its expected aerodynamic performance. Because of the large uncertainty assigned to these predicted aerodynamics in the hypersonic speed range, ample control power was built into the system to overcome the anomaly in the flight pitching moment. Still, the large bodyflap deflection required to trim the vehicle raised concerns for the structural and thermal integrity of the body flap. However, the inability to predict the hypersonic pitching moment characteristics of the Orbiter--despite extensive wind tunnel testing--was of more fundamental concern. The pitching moment anomaly has been attributed to any number of phenomenon including viscous effects, diminished body flap effectiveness, Mach number effects and real-gas effects. In 1983, a conference was held at NASA Langley Research Center to review the performance of the complete Shuttle launch system during its initial flights. The proceedings from this conference[1] contain a number of papers that compare and analyze the aerodynamic performance of the vehicle relative to predictions in the preflight data book. One paper in the proceedings by Griffin, et al.[2] used a computational fluid dynamic (CFD) approach to analyze the pitching moment anomaly. Their analysis was quite thorough considering the state of the flow solvers and computer hardware available to them at that time. These limitations forced them to make approximations to the vehicle geometry and the gas chemistry models. They were, however, able to make a plausible argument that the pitching moment anomaly was not predicted by ground-based facilities because they could not simulate Mach number and real-gas effects.

It is the purpose of this paper to once again address the hypersonic aerodynamic characteristics of the Shuttle Orbiter through the use of CFD. Now, however, due to increased sophistication and robustness of flow solvers and a several order of magnitude increase in computer power, the exact Orbiter configuration and proper gas chemistry models can be used. The problem will be approached through two parallel investigations. First, solutions of flow about the complete Orbiter vehicle will be made at a point on the STS-1 trajectory and points on the STS-2 trajectory. The vehicle aerodynamics derived from these solutions will be compared with the flight aerodynamics of the vehicle. In addition, solutions for a modified Orbiter configuration which retains the windside Orbiter geometry while greatly modifying the leeside topology of the vehicle will be made at wind tunnel and flight conditions so that the aerodynamics and flowfield characteristics of a model at tunnel conditions can be compared with those that would occur in flight on a full scale vehicle.

GEOMETRIES AND GRIDS

The coordinate system in which the geometries and grids are described, along with the convention for the aerodynamic coefficients, is shown in Fig. 1.

Shuttle Orbiter: The full Orbiter geometry as used in this study is shown in Fig. 2. Slideslip is not considered in this report, only half the configurations is used in the computations. The surface geometry was constructed from CAD surfaces provided by Rockwell International using the ICEM surface modeling software. Control surfaces are rotated within the surface modular so that the flight configuration of the vehicle can be matched.

The configuration differs slightly from the actual vehicle. To facilitate surface and volume grid generation, the three motor nozzles on the base of the vehicle along with the reaction control jets on the aft end of the OMS pods have been removed. In addition, the elevon gaps have not been modeled. These alterations should not impact the information sought in this study. The surface grid which has dimensions 151x110 along with selected planes from the volume grid where there are 61 points between the surface and the outer boundary are shown in Fig. 3 when every other grid line has been removed for visual clarity. A closer view of the near body grid shown in Fig. 4 illustrates the complexity of the volume grid required to complete the flow about this vehicle. The surface of the vertical tail is embedded in the upper symmetry plane as shown in Fig. 5. The surface grid was created using ICEM and the volume grid using the GRIDGEN[3] software. For computational purposes, the bodyflap is treated as a separate entity. As described in a later section of the paper, only a portion of the lower surface of the vehicle needs to be included when making bodyflap calculations. The surface blocks used in the flap calculation are outlined on the vehicle in Fig. 6(a). The corresponding surface geometry and grid used in the body flap calculations is shown in Figs. 6(b-c).

Modified Orbiter: The complete modified Orbiter configuration is shown in Fig. 7. As with the Orbiter, only half the geometry is used for the computations. This configuration has exactly the same wind surface geometry as the Orbiter vehicle. In a profile view, the tail and OMS pods have been removed and the area between the nose and top of the canopy has been faired in as indicated by the dashed line in Fig. 8. The leeside surface is then constructed by fitting elliptic curve segments between the strake and wing leading edges and the line defining the surface in the upper symmetry plane as shown in the section A-A, Fig. 8. This results in a reduced surface grid of 151 x 81 while 61 points are still used between the surface and outer boundary in the volume grid. Also, no provision has been made for elevon deflection in this model. The surface grid and selected planes from the volume grid are shown in Fig. 9. Bodyflap calculations for the modified orbiter use the same surfaces as those shown in Figs. 6(a) - 6(b) for the full Orbiter configurations.

COMPUTATIONAL TECHNIQUE

Code: The formulation of the Langley Aerothermodynamic Upwind Relaxation Algorithm (LAURA) is presented in detail in Refs. [4-6] The LAURA code as used here is set up for a solution of the thin-layer Navier-Stokes algorithm. The inviscid first-order flux is constructed using Roe's flux-difference-splitting[7] with second-order corrections based on Yee's symmetric total variation diminishing scheme.[9]

Chemistry: A 7-species chemical reaction model is used in the code for these computations. The species N, O, N_2, NO, NO^+, and e^- are accounted for in the model.

Boundary Conditions: The usual no-slip boundary condition for viscous flow is applied at the wall while freestream conditions are set at points on the outer boundary of the computational domain. The exit plane is set such that the inviscid outflow is supersonic.

Numerous studies have shown that the catalytic property of the Shuttle Orbiter thermal protection system (TPS) has an effect on surface heating that persists to approximately 160,000 ft. Thus a catalytic wall boundary condition has been included for this study. The implementation of this boundary condition is based on the work of Thompson[11] who assumed that only nitrogen and oxygen recombine at the surface. Thompson also found that the best comparisons with shuttle flight data were obtained when Scott's[12] recombination rates for nitrogen and Zoby's[13] recombination rates for oxygen were used. Therefore, these rates were chosen for use in the present study.

Computations presented account for a variable wall temperature. The variable wall temperatures are based on the radiation equilibrium temperature at the wall, and when determining these temperatures, the dependency of emissivity on temperature was included.

DATA

Experimental: A force and moment model for the modified Orbiter has been tested in the Langley 31-Inch Mach 10 Tunnel.[14] Tests have been made at vehicle angles-of-attack of 35, 40, and 45 degrees and body flap deflections of 0 and 16 degrees at each angle of attack. In addition, experimental Orbiter data from Ref. 15 has been utilized.

Flight: To thoroughly investigate the pitching moment anomaly, it is important to know not only the flight aerodynamics of the vehicle, but also information about surface properties such as temperature and pressure. During its first five flights, the Orbiter was fitted with the Development Flight Instrumentation (DFI) data acquisition system to record surface temperatures and pressure on the vehicle during the ascent and decent phases of flight. On STS-1, this system did not function over the hypersonic portion of the flight trajectory. However, there is a complete set of surface data for STS-2. On the other hand, flight aerodynamics are available for both STS-1 and 2. Flight data were obtained from the Johnson Space Center. The authors would like to thank Paul Romere of JSC for his assistance in obtaining and interpreting the flight data.

Computational Data Points: The computational data points used for this study are given in Table 1. Case 1 is taken from the STS-1 trajectory and was chosen because it corresponded to a maximum body flap deflection at a Mach number and altitude where nonequilibrium chemistry was important. Cases 2-4 represent points on the STS-2 trajectory for which both the flight aerodynamics and DFI data base are available. The choice of the three points was based on the desire to cover as much of the hypersonic flight regime as possible, the onset of leeside and windside transition and the expected thermodynamic state of the flowfield. Case 2 closely replicates the condition of Case 1. Case 3 represents a point on the entry trajectory just prior to the time at which DFI thermocouples indicated transition on the leeside of the vehicle. Case 4 corresponds to the flight conditions just prior to the onset of transition on the windside of the vehicle. The nominal Langley 31-Inch Mach 10 Tunnel freestream conditions used for the included computations are given as Case 5. These conditions were chosen to insure high quality flow in the facility as well as laminar flow over the model.

SOLUTION TECHNIQUE

A multiblock solution strategy is applied in two stages. The first stage may be regarded as a space marching solution, like the Parabolized-Navier-Stokes (PNS) methods, except that three-dimensional data blocks are employed rather than two-dimensional data planes. The second stage is a conventional, global relaxation which uses the first stage solution as an initial condition. The advantages of the three-dimensional block-marching over two-dimensional block-marching are that solution robustness is not sacrificed when employing second-order discretization in the streamwise direction and embedded subsonic pockets and shock/boundary layer interactions are easily computed--provided that the outflow boundary of the sub-domain is intelligently chosen. The sub-domain boundaries are easily tailored to the physics of a given application. The advantage of the two-dimensional block-marching is that if the flow is sufficiently well behaved (i.e., supersonic streamwise flow above the boundary-layer and insignificant perturbations moving upstream through the boundary layer) then the stage one computation can be an order of magnitude faster. A detailed description of this solution technique can be found in Ref. 16.

RESULTS

A determination of the difference in Orbiter aerodynamics derived from tests in ground based facilities and those occurring in hypersonic flight along with the flow phenomena responsible for this difference is the first issue to be addressed in this section. The modified Orbiter configuration was chosen for this study as its simplified leeside geometry and the associated reduction in computational resources allowed parametric studies to be carried out. The second issue to be addressed is the comparison of the computed aerodynamics for the Orbiter with those measured in flight. All aerodynamic coefficients are based on standard Orbiter area and mean aerodynamic chord and a q_∞ derived from Table 1. The default nominal moment reference center is taken as the forward CG location as described in the Shuttle Operational Aerodynamic Data Book. In the Orbiter coordinate system, this point is at x = 1076.7 in. and z = 375.0 in. and in the coordinate system used in this report, at z = -841.7 and x = 37.0 in. When a direct comparison of tunnel and flight flowfield characteristics is made, the physical dimensions of the wind tunnel model are expanded to the size of the full scale vehicle.

Modified Orbiter Computations. Computations have been made for flow conditions in the Langley 31-Inch M=10 wind tunnel for two reasons. First, force and moment data from this tunnel is available to establish the validity of the aerodynamics derived from computations. Secondly, this tunnel is used for establishing vehicle aerodynamics at hypersonic speeds and as such it can serve as a baseline for the differences in tunnel and flight aerodynamics.

Calculations have been made for a 0.0075 scale model of the modified orbiter at the case 5, Table 1 freestream conditions. Flowfield solutions have been obtained for this model at angles-of-attack of 35, 40, and 45 degrees at bodyflap deflections of 0, 5, 10, 15, and 20 degrees. The aerodynamics derived from these solutions along with corresponding tunnel data are shown in Figs. 10(a-c). In these figures, the axial and normal force coefficients and the moment coefficient are plotted as a function of angle of attack for bodyflap deflections of 0 and 16 degrees. The computed results are represented by the filled symbols while tunnel data at the same bodyflap deflection are represented by a corresponding open symbol. The tunnel data represents measurements from multiple tests for a given bodyflap deflection. The tunnel data only covers an angle-of-attack range from 30 to approximately 42.5 degrees as the sting configuration used in these tests prevented the model from being pitched up to 45 degrees. The overall comparison of the computed results with the tunnel data, even though it contains considerable scatter, is quite good as both the levels and trends derived from the computed results are supported by the tunnel data. C_A and C_N are in the best agreement with the tunnel data. The computed pitching moment shows a persistent nose down moment relative to the tunnel data while the slope of the two sets of data are essentially the same for both bodyflap deflections. Moments measured on very small models are highly sensitive to very small differences in balance centers and transfer distances used in data reduction. Only a few thousandths of an inch uncertainty in these numbers will produce large differences in the measured moment. Given this sensitivity, the computed and measured pitching moment are in reasonably good agreement.

Case 2, Table 1 was chosen as a representative flight condition to use when comparing tunnel and flight aerodynamics. The aerodynamics derived from these computations are plotted in

Fig. 11(a-c) along with the computed tunnel results. Here, each aerodynamic coefficient is plotted vs bodyflap deflection for a constant angle-of-attack. The open symbols refer to the tunnel case, while the corresponding filled symbols refer to the flight case. For C_A, the magnitude and slope of the curves for both cases are similar for bodyflap deflections less than 10 degrees. At higher bodyflap deflections, the curves diverge rapidly. The magnitude of C_N is different for the two cases, but the slope of the curves is almost identical. Both the magnitude and slope of the C_m curves are significantly different for both cases.

Bodyflap effectiveness can be extracted from the data in Fig. 11(a-c) by zeroing the data base to the baseline configuration (zero bodyflap deflection). These results are shown in Fig. 12(a-c) where significant differences in tunnel and flight incremental aerodynamics are shown, especially for bodyflap deflections greater than 10 degrees. Of particular interest is the incremental pitch curve, Fig. 12(c), where, in flight, the nose down pitch control can be as much as 50 percent greater than that for the tunnel condition at the same bodyflap deflection.

In order to make a meaningful analysis of Orbiter aerodynamics and bodyflap effectiveness at tunnel and flight conditions, modified orbiter aerodynamics should be similar to that for the Orbiter. However, as will be shown, the above results only offer a good approximation of C_N for the Orbiter. Wind tunnel tests and flight data both show that the computed and measured values of C_A for the modified Orbiter are approximately twice that which would be expected for the Orbiter. This increment in C_A difference also results in large differences in pitching moment for the two configurations. Figures 13(a-c) show the running integration of each modified Orbiter aerodynamic coefficient as a function of N, the number of incremental surface areas around the body, where N=1 represents the first strip of cells next to the windward centerline. This integration is made over the body only and does not include the bodyflap. Referring to Figs. 3 and 9, the grid on the windward surface for both the Orbiter and modified Orbiter is represented by 41 points in the circumferential direction. The locus of the 41 point on the surface lies along the leading edge of the wing and strake, is common to both configurations and effectively divides the bodies into wind and leeside surfaces. Again referring to Figs. 13(a-c) , C_A and C_m are greatly influenced by the leeside surface ($N > 40$) while the same surface has virtually no effect on C_N. If for the Orbiter, integrating the computed modified orbiter surface properties over the windside only should produce aerodynamics that are consistent with those for the Orbiter. This can be demonstrated computationally by comparing the integrated aerodynamics for the modified Orbiter and Orbiter at the flight condition given as case 2 in Table 1. Before examining these comparisons, two points need to be made. First, the Orbiter calculation is for a configuration with elevon deflected per case 2, Table 1. Second, each geometry has 41 points describing the windward surface, but the distribution of the points on the surface is different for each configuration. Thus, the only point in the running integration at which the aerodynamics should converge is at $N = 40$. The integrated aerodynamics are shown in Figs. 14(a-c). For each coefficient, the value at $N = 40$ for the modified Orbiter is good approximation of the final Orbiter value. C_N is in excellent agreement while C_m appears to be off some. However, C_m for the Orbiter without elevons deflected would be more positive which would bring the modified Orbiter value at $N = 40$ into better agreement with the final Orbiter value. As shown in Fig. 14(a), integrating over the windward surface only will result in a C_A which is smaller than the final Orbiter C_A. This difference is due to an incomplete integration of forces over the nose of the body.

The veracity of only integrating over the windside can also be demonstrated by comparison of computed modified Orbiter and experimental Orbiter aerodynamics at the case 5, Table 1 wind tunnel condition. For these tests, the Orbiter model was configured with zero elevon and bodyflap deflections. The results of this comparison are shown in Figs. 15(a-c). The computed values of C_N and C_m are in excellent agreement with the tunnel data while the computed values of C_A are, as expected, slightly lower than the tunnel data.

The above results have established the validity of the computational approach and the use of the lower surface of the modified Orbiter to simulate Orbiter aerodynamics. In the following, the differences in Orbiter aerodynamics at tunnel and flight conditions will be investigated and the flowfield characteristics responsible for these differences will be identified.

In order to evaluate the trim characteristics of the Orbiter at tunnel and flight conditions, the moment reference center was moved to the STS-2 entry interface CG location ($x = 1096.6$ in. and $z = 372.3$ in. in the Orbiter Structural Reference System) as given in Ref. 18. The set of transferred moment coefficients is shown in Fig. 16 for both the tunnel and flight case. The bodyflap deflections required to trim the vehicle at a given angle-of-attack have been extracted from these curves and are plotted as a function of angle-of-attack in Fig. 17 for both tunnel and flight conditions. At ≈40 degrees in the tunnel, the vehicle will not trim at a positive bodyflap deflection. The trim bodyflap deflection plotted in Fig. 17 for this condition was determined by extrapolation of the $C_m - \alpha$ curve in Fig. 16. The large difference shown here between the bodyflap deflection required to trim at a tunnel condition and that required to trim in flight is comparable to the difference between the STS-1 preflight prediction of 7.5 degrees bodyflap deflection to trim at hypersonic speeds and the 16 degree deflection actually experienced in flight. To determine the cause of these large differences in bodyflap trim requirements, the aerodynamics of the basic body and the bodyflap will be addressed separately.

The moment coefficient, for tunnel and flight, based on a body with no flap, as well as the corresponding increment in C_m are listed as a function of angle-of-attack in Table 2. The incremental values of C_m are quite large at all three angles-of-attack and these differences are due primarily to different surface pressure distributions for the two cases. As an example, the windward centerline distribution of nondimensional surface pressure for both the tunnel and flight case are shown in Fig. 18. Forward of 500 in., the two pressure distributions vary very little, diverge slowly to the 1000 in. station and then separate at a more rapid rate over the expansion at the aft end of the vehicle. Although these differences in pressure appear to be small, they will produce large differences in moment when integrated over the vehicle's wind surface area. Fig. 18 does not describe all of the windside surface pressure differences for the tunnel and flight cases. Figure 19 shows color* contour plots of the nondimensional windside surface pressure. The pressures in each plot are referenced to the same color scale where red represents the highest pressure and dark blue the lowest pressure. The differences in the overall surface pressure patterns are suttle, but again, because of the large surface areas involved, they are important. The most obvious differences are at the wing leading edge, where the high pressure region extends back over the wing for the tunnel case, as opposed to the flight case, where the high pressure region is confined to the leading edge, and at the aft end of the vehicle, where pressures for the flight case are lower, especially along the inboard elevons, than those for the tunnel case. The effects of these pressure differences can be seen in Figs. 20(a-c) which show the running axial integration of the vehicle aerodynamics.

These figures reflect the results that would be expected from an examination of the pressure distributions shown in Figs. 19 and 20. Namely, the differences in aerodynamics of the vehicle at tunnel and flight conditions are caused by dissimilar surface pressures on the vehicle aft of the 900 in. station.

The contribution of pressure and viscous forces to any aerodynamic coefficient can be isolated in a CFD analysis. For the two cases shown here, where the Reynolds number based on vehicle length is approximately 10^5, viscous forces contribute 25 percent to C_A, 2 percent to C_m and nothing to C_N.

The fact that the viscous effect on the aerodynamics is the same in the wind tunnel as in flight is probably fortuitous and it should not be inferred that these effects can be scaled from tunnel to

---

* Color photographs appear in a special section of this document.

flight conditions. The purpose here is to illustrate that viscous forces have little impact on the overall aerodynamics of the vehicle at these particular conditions.

Since viscous effects have no significant impact on the aerodynamics of the vehicle at either tunnel or flight conditions, differences in the aerodynamics are due to differences in surface pressures, and, in particular, to those pressures on the surface aft of the 900 in station (see Fig. 20), where the vehicle becomes an expansion surface. At the flight condition, the value of g in the shock layer is much less than the 1.4 value in the perfect gas $M_\infty = 10$ wind tunnel, and in the expansion region, the smaller values of g will result in lower levels of pressure. Thus, the difference in aerodynamics for the vehicle without the bodyflap is an effect which, of course, reflects the state of the gas chemistry in the shock layer.

Flow over the forward part of the vehicle for both tunnel and flight cases is similar and characterized by relatively small pressure differentials. Flow over the bodyflap, particularly at large deflections, becomes much more complex as flow separation and internal shocks come into play.

Figure 21 shows color contour plots of nondimensional pressure in the symmetry plane of the flap geometry configuration, Fig. 6(b), for both the tunnel and flight cases. For both cases, the pressures are referenced to the same scale where red and blue correspond, respectively, to the highest and lowest pressures. These plots show the effect of different shock density ratios on shock standoff distance as well as the curvature of the bow shock due to the shock interaction with the expansion at the aft end of the vehicle. Also, the inclination of the flap shock in flight is lower than that for the tunnel case due to the higher Mach number in the shock layer. For the deflected flap plots, the pressure on the flap is higher in flight than in the tunnel. This is most evident for the 20 degree bodyflap deflection plots. In addition to the flap shock, there is a second oblique shock whose origin is the leading edge of the separation bubble in front of the flap. This shock is most obvious in the 20 degree deflection tunnel plot, but is also present to varying degrees in the 10 degree tunnel and 10 and 20 degree flight condition plots. The extent of the separation can be seen in the combination streamline and surface heating plots shown in Fig. 22. Because the levels of surface heating for the tunnel and flight conditions are quite different, red and blue colors correspond to the maximum and minimum heating for each case. The most striking feature in this set of plots is the small amount of separation seen for the flight cases when compared to the tunnel cases at an equivalent bodyflap deflection. The extent of the separation in the symmetry plane is shown in Fig. 23 where streamlines have been superimposed on a pressure field in the vicinity of the bodyflap hinge line. The small separation regions seen in Fig. 22 for the 10 degree bodyflap deflection do not have enough vertical extent to be picked up in this figure. Referring back to

Fig. 21, flow over the 20 degree bodyflap at the tunnel condition will be processed by two well defined oblique shocks. At the flight condition, the flow will also be processed by two oblique shocks, although the first shock appears to be quite weak. The overall centerline surface pressure for these two cases is shown in Fig. 24 where the nondimensional pressure is plotted as a function of axial length. For the tunnel case, the effect of the large axial separation on the surface pressure is clear. The highest pressure on the flap is very close to the stagnation value which is due to the flow being processed by multiple shocks. For the flight case, the pressure rise through the first shock can be seen along with the pressure jump across the flap shock to a level of 15 percent higher than the stagnation line. For this case, the pressure in front of the flap is lower than that for the tunnel case, yet the pressure on the flap ends up being much higher than that for the tunnel case.

Unlike the flow over the vehicle forward of the bodyflap, the different pressure signatures due to a single bodyflap deflection at tunnel and flight conditions cannot be attributed to a single parameter. The pressure rise, p_2/p_1, across an oblique shock is a function of upstream Mach number, M_1, shock inclination, θ and δ as given by

$$\frac{P_2}{P_1} = \frac{2\gamma M_1^2 \sin^2\theta - (\gamma-1)}{\gamma + 1}$$

For example, Mach number, inclination angle and γ have the following values just in front of the flap shock for $\alpha = 40$ and $\delta_{bf} = 20$.

	M_1	θ	γ
Tunnel	2.13	40^o	1.4
Flight	3.45	26^o	1.2

Here, γ is the ratio of static enthalpy to internal energy. Analysis of the above equation shows that for a given normal shock Mach number, $M_1 \sin\theta$, the pressure rise will decrease with decreasing γ. However, in the above example, the difference in normal shock Mach number between the flight and tunnel case is enough to overcome this effect. Using the above equation and the listed preshock conditions, the predicted pressure ratio across the flap shock is 2.0 for the tunnel case and 2.4 for the flight case, which is in good agreement with the pressure rise on the bodyflap shown in Fig. 24.

Now that the flow over the body and bodyflap has been analyzed, some conclusions can be drawn about the relationship between tunnel derived aerodynamics and those occurring in flight and how they relate to the perceived pitching moment "anomaly" on STS-1. For the cases shown here, the computed tunnel case did not correctly predict the aerodynamics for flight. At $\alpha = 40^o$, computed tunnel aerodynamics underpredicted C_A by a factor of 1.07 and overpredicted C_N by a factor of 1.04. C_m, however, was underpredicted by a factor of 1.7. The large differences in C_m and the smaller differences for the other coefficients are, as has been demonstrated, due to the inability of the perfect gas tunnel to properly model the chemical state of the gas in the shock-layer at a flight condition. In addition, the difference between the surface pressures and tunnel and flight conditions occurred over the aft end of the vehicle where the pressure increments would have the greatest impact on the pitching moment. On the other hand, the bodyflap in flight is more effective than in the tunnel (see Fig. 12). The reason for this increased efficiency is not clear cut, but appears to be Mach number driven. Even though the bodyflap offered more control power in flight, it was still not enough to overcome the large increase in nose up pitching moment encountered in flight.

Orbiter Computations: In this section, aerodynamic characteristics of the Orbiter derived from CFD solutions based on the geometry shown in Fig. 2 will be compared with flight data. Computations have been made at freestream conditions corresponding to a point on the STS-1 (case 1, Table 1) and points on the STS-2 (cases 2-4, Table 1) entry trajectories. As discussed in the geometries section, some aspects of the Orbiter geometry such as elevon gaps and base configuration have either been omitted or not modeled. In addition, no attempt has been made to computationally address the base flow problem. The rationale for correcting the computed aerodynamics for the inconsistencies cited above is given below.

The bodyflap deflections given in Table 1 are for values measured at the bodyflap hinge line. For the computations, these deflections have been corrected for aeroelastic effects which range from .3 degrees at $M_\infty = 24$ to 1.15 degrees at $M_\infty = 12.85$.

Treating the inboard and outboard elevon gaps is outside the capabilities of the computational resources used in this report. Initially, it was felt that the elevon gaps would have little effect on the vehicle aerodynamics. However, after solutions had been obtained, the gap effect was further investigated. The incremental aerodynamics due to the gaps were determined by integrating surface properties over the gap areas. The results are shown in Table 3 for the case 2 condition. As would be expected, C_A is not measurably affected while there is a very small effect on C_N. The increment is C_m, on the other hand, amounts to about 5 percent of the flight value. Once again, small changes in surface properties at the aft end of the vehicle, while not having much impact on C_A and C_N, result in non-trivial changes in C_m. The increments given in Table 3 are insensitive to flight condition and are valid for all the flight cases given in Table 1.

Flight base pressure for the orbiter is given by the correlation shown in Fig. 25 which was taken from Ref. 17. This expression gives P_{base}/P_∞ as a function of Mach number for flight at $\alpha = 40^o$. Also, unpublished data for a matrix of pressure transducers on the base of the Orbiter indicate that pressure is nearly constant over this area. The result of integrating pressure over the base geometry (without nozzles) which corresponds to the flight cases in Table 1 is given in Table 4. Only at $M_\infty = 24$, and then only for CA, does the base pressure have any significant effect on the vehicle aerodynamics at hypersonic speeds.

One other area could contribute to the vehicle aerodynamics. Pressures on the leeside of the bodyflap should be quite low, although there is no flight data available to establish a pressure level, and there is a large surface area associated with the bodyflap. If it is assumed that the pressure on the leeside of the bodyflap is at the same level as it is on the base, the aerodynamic increments due to leeside body flap pressure are given in Table 5. For all of the corrections given above, the nominal forward CG location has been used for the moment increment. The above corrections have been applied to all the computed flight aerodynamics given below. Where appropriate, the moment correction has been transferred to the current moment CG.

The comparison of computed and measured STS-1 aerodynamics are given below for the corrected bodyflap deflection of 15.6 degrees. The moment center is at the STS-1 entry interface value (x = 1096.7 in. and z = 372.4 in. in the Orbiter Structural Reference System) as given in Ref. 18.

	C_A	C_N	C_m
computed	.0904	1.193	-.0062
flight	.0866	1.226	.0005
ΔC_i	4 %	-2.7%	--

The computed value of C_A is 4 percent higher than the flight value while the computed value of C_N is 2.7 percent lower than that measured in flight. The computed value for C_m indicates a nose down moment that is close to zero. The aerodynamics of the vehicle at this flight condition as a function of bodyflap deflection are shown in Figs. 26(a-c). The trim bodyflap deflection and associated aerodynamics derived from these curves are

$$\delta_{bf} = 14.1^o$$
$$C_A = .088$$
$$C_N = 1.187$$

which is a 1.5 degree difference in bodyflap trim angle. Iliff[19] gives the expected accuracy in the flight CG location as +1.0 in. The effect of applying this delta CG to the computed STS-1 pitch values is shown in Fig. 27 and results in a potential ± .6 degree shift in trim bodyflap angle for the computed cases. Even when this uncertainty is applied, the computed trim bodyflap deflection would be less than that indicated by the flight data.

The comparison of the STS-2 computed and flight aerodynamics is presented in Figs. 28 (a-c). In this figure, the solid line represents the predicted aerodynamics based on the STS-2 trajectory and the latest addition of the Operational Aerodynamic Data Book. The dashed lines represent the uncertainty in these predicted values based on wind tunnel and flight data. The open symbols designate the actual flight data and the filled symbols correspond to the computed results. The moment center is at the data book forward CG location. The computed, measured and predicted values of C_A and C_N are in good agreement over the Mach number range. As with the STS-1 results, the computed results show a nose down pitching moment relative to the flight data at the bodyflap deflection required to trim in flight. This increment in C_m translates into a nominal 1.5 degree decrease in the bodyflap deflection required to trim the vehicle based on the computed results.

In addition to the results shown here, some additional work has been done to determine the effect of using different flow chemistry models. Preliminary results indicate that using an equilibrium chemistry model at the $M_\infty = 12.87$ condition does not materially affect the computed aerodynamics and that using a thermal nonequilibrium model at the $M_\infty = 24.3$ condition may result in a more positive moment than indicated in Fig. 28(c) for that condition.

In general, the computed results are in good agreement with the flight data and all of the computed results lie within the uncertainty band on the flight data. Also, there are enough uncertainties associated with both the flight and computed results to compensate for the differences shown in Figs. 28(a-c). From a computational standpoint, the greatest concern is for the fidelity of the surface geometry. There is no guarantee, nor reasonable way to determine if the computational surface geometry and the flight hardware are the same. Given the high sensitivity of the pitching moment to small pressure differentials as demonstrated in this paper, small differences in surface slope or planform area could have a significant impact on the pitching moment. Also, the size of the problem has precluded any grid refinement studies to insure grid converged solutions. For instance, the authors feel that 60 points in the shock-layer represents minimum number for this type of calculation. Finally, since the grid is not sufficiently dense in the axial and crossflow directions, the thin-layer approximation to the Navier-Stokes equations has been used which could result in some loss of accuracy, especially in high gradient areas.

CONCLUDING REMARKS

Computations using a modified Orbiter configuration have been used to establish that real-gas effects account for the different aerodynamic characteristics of the Orbiter at tunnel and flight conditions. The aerodynamics of the basic body and the bodyflap were investigated independently and it was shown that most of the increment can be attributed to the basic body. The bodyflap has been shown to be as much as 1.5 times as effective in flight as in the wind tunnel which contradicts assertions that the Orbiter pitching moment "anomaly" was due to reduced bodyflap effectiveness in flight. In fact, had the bodyflap exhibited the same effectiveness in flight as in the tunnel, the vehicle may not have trimmed at all. All evidence presented here leads to the conclusion that the so called "pitching moment anomaly" which occurred on STS-1 was due to the inability of perfect-gas ground-based facilities to simulate the real-gas chemistry encountered by the vehicle in hypersonic flight.

The results presented here should not be generalized to other vehicles as the geometry of the Orbiter plays a major role in the aerodynamic increments between tunnel and flight conditions. Certainly, at tunnel and flight conditions there are differences in surface pressures in stagnation and near-stagnation regions such as the nose and wing leading edges of the vehicle, but the surface area over which these pressures act is a very small fraction of the wetted surface of the vehicle. As shown in this paper, the aerodynamic increments between tunnel and flight conditions are due to a relatively small pressure differential acting on an expansion surface at the aft end of the vehicle which has a very large surface area. For example, computations[20] for the HL-20 vehicle carried out at the same tunnel condition used in this paper and at hypersonic speeds indicate almost no real-gas effect on vehicle aerodynamics. While these two vehicles share no geometric similarities, the major difference on the windside of the HL-20 is that it contains no expansion surface outside of the immediate vicinity of the nose.

The computed aerodynamics for the complete vehicle are in good agreement with the flight data considering the possible uncertainties in both data sets. Even with the differences between the flight and computed aerodynamics, the computed flight aerodynamics are far superior to those stated in the pre STS-1 Operational Aerodynamic Data Book. In fact, if CFD results such as these had been available prior to STS-1 there would not have been an "STS-1 pitching moment anomaly."

REFERENCES

1. Shuttle Performance: Lessons Learned, NASA Conference Publication 2283, Parts 1 and 2, 1983.

2. Griffith, B. J.; Maus, J. R.; and Best, J. T.: Explanation of the Hypersonic Longitudinal Stability Problem - Lessons Learned. NASA CP-2283, March 1983.

3. Steinbrenner, J.; Chawner, J.; and Pouts, C.: Multiple Block Grid Generation in the Interactive Environment. AIAA Paper 90-1602, June 1990.

4. Gnoffo, P. A.; Gupta, R. N.; and Shinn, J.: Conservation Equations and Physical Models for Hypersonic Air Flows in Thermal and Chemical Nonequilibrium. NASA TP-2867, February 1989.

5. Gnoffo, P. A.: Upwind-Biased, Point-Implicit Relaxation Strategies for Viscous Hypersonic Flows. AIAA Paper 89-1972, June 1989.

6. Gnoffo, P. A.: An Upwind Point Implicit Relaxation Algorithm for Viscous Compressible Perfect-Gas Flows. NASA TP 2953, February 1990.

7. Roe, P. L.: Approximate Riemann Solvers, Parameter Vectors, and Difference Schemes. *Journal of Computational Physics*, Vol. 43, 1981, pp. 357-372.

8. Harten, A.: High Resolution Schemes for Hyperbolic Conservation Laws. *Journal of Computational Physics*, Vol. 49, No. 3, 1983, pp. 357-393.

9. Yee, H. C.: On Symmetric and Upwind TVD Schemes. NASA TM-86842, September 1985.

10. Wang, Z. and Richards, B. E.: High Resolution Schemes for Steady Flow Computation. *Journal of Computational Physics*, Vol. 79, No. 1, November 1991, pp. 53-72.

11. Thompson, R. A.: Comparison of Nonequilibrium Viscous-Shock-Layer Solutions with Shuttle Heating Measurements. *Journal of Thermophysics and Heat Transfer*, Vol. 4, No. 2., April 1990.

12. Scott, C. D.: Catalytic Recombination of Oxygen and Nitrogen in High-Temperature Surface Insulation. Progress in Astronautics and Aeronautics: Aerothermodynamics and Planetary Entry, Vol. 77, edited by A. L. Crosbie, AIAA, New York, 1981, pp. 192-212.

13. Zoby, E. V.; Gupta, R. N.; and Simmonds, A. L.: Temperature Dependent Reaction Rate Expressions for Oxygen Recombination. *Progress in Astronautics and Aeronautics: Thermal Design of Aeroassisted Orbital_Transfer Vehicles*, Vol. 96, edited by H. F. Nelson, AIAA, New York, 1985, pp. 445-465.

14. Miller, C. G. III: Measured Pressure Distributions, Aerodynamic Coefficients, and Shock Shapes on Blunt Bodies at Incidence in Hypersonic Air and CF4. NASA TM-84489, 1982.

15. Paulson, J. W. Jr.; and Brauckmann, G. J.: Recent Ground-Facility Simulations of Shuttle Orbiter Aerodynamics," Orbiter Experiments (OEX) Aerothermodynamics Symposium, NASA CP-3248, 1994.

16. Gnoffo, P. A.; Weilmuenster, K. J.; and Alter, S. A.: A Multiblock Navier-Stokes Analysis for Shuttle Orbiter Entry Heating from Mach 24 to Mach 12. Orbiter Experiments (OEX) Aerothermodynamics Symposium, NASA CP-3248, 1994.

17. Bancraft, S. A.; Engel, C. D.; and Pond, J. E.: REMTECH SSME Nozzel Design TPS Final Report, Volume I. RTR 113-03, September 1990, NASA Contract NAS8-36151.

18. Findaly, J. T.; and McConnell, J. G.: A Summary of STS-1 and STS-2 Flight Derived and Aerodynamic Data Base Comparisons - A Data Package for ACME Investigations. AIAA Report No. 82-16, NASA Contract No. NAS1-16087, April 1982.

19. Iliff, K. W.; and Shafer, M. F.: Space Shuttle Hypersonic Flight Research and the Comparison to Ground Test Results (Invited)," AIAA Paper 92-3988, July 1992.

20. Weilmuenster, K. J.; and Greene, F. A.: A CFD Analysis of the HL-20/PLS," to be published in the *Journal of Spacecraft and Rockets*.

Table 1. Computational Points

Case	Flight	Altitude km	V_∞, km/s	$\rho_\infty x10^5$ kg/m^3	p_∞, N/m^2	T_∞, K	GMT s	α deg	δ_{bf}, deg	δ_{el} deg	M_∞
1	STS-1	73.1	6.81	5.29	3.13	205	64758	39.4	15.973	-0.4444	23.68
2	STS-2	72.4	6.92	5.75	3.33	202	75620	39.4	14.914	1.7436	24.3
3	STS-2	64.4	5.62	16.26	11.22	241	75950	41.2	13.54	1.511	18.07
4	STS-2	54.8	4.17	53.30	39.98	261	76130	39.7	12.92	0.74	12.85
5	Tunnel	--	1.42	788.00	113.10	50	---	40^o	---	--	10.00

Table 2. Basic Body Moment Coefficient - No Flap

α	C_m Tunnel	C_m Flight	Δ C_m Flight-Tunnel
35	.0487	.0725	.0238
40	.0472	.0784	.0312
45	.0457	.0827	.0370

Table 3. Elevon Gap Aerodynamics Corrections for Flight Cases

$\Delta C_A \approx .0$

$\Delta C_N = -.0036$

$\Delta C_m = +.0028$

Table 4. Aerodynamic Increments Due to Base Pressure

$M_\infty = 24 \qquad P_{base}/P_\infty = 10$

$\Delta C_A = -.00014$
$\Delta C_N \approx .0$
$\Delta C_m = +.00017$

$M_\infty = 18 \qquad P_{base}/P_\infty = 3.5$

$\Delta C_A = -.0007$
$\Delta C_N \approx .0$
$\Delta C_m = +.00085$

$M_\infty = 12 \qquad P_{base}/P_\infty = 1.5$

miminal values

Table 5. Aerodynamic Increments Due to Leeside Flap Pressure

$M = 24 \qquad P_f/P_\infty = 10$

$\Delta C_A \approx .0$
$\Delta C_N = -.0014$
$\Delta C_m = +.0014$

$M = 18 \qquad P_f/P_\infty = 3.5$

$\Delta C_A \approx .0$
$\Delta C_N = -.0072$
$\Delta C_m \doteq +.00072$

$M = 12 \qquad P_f/P_\infty = 1.5$

miminal values

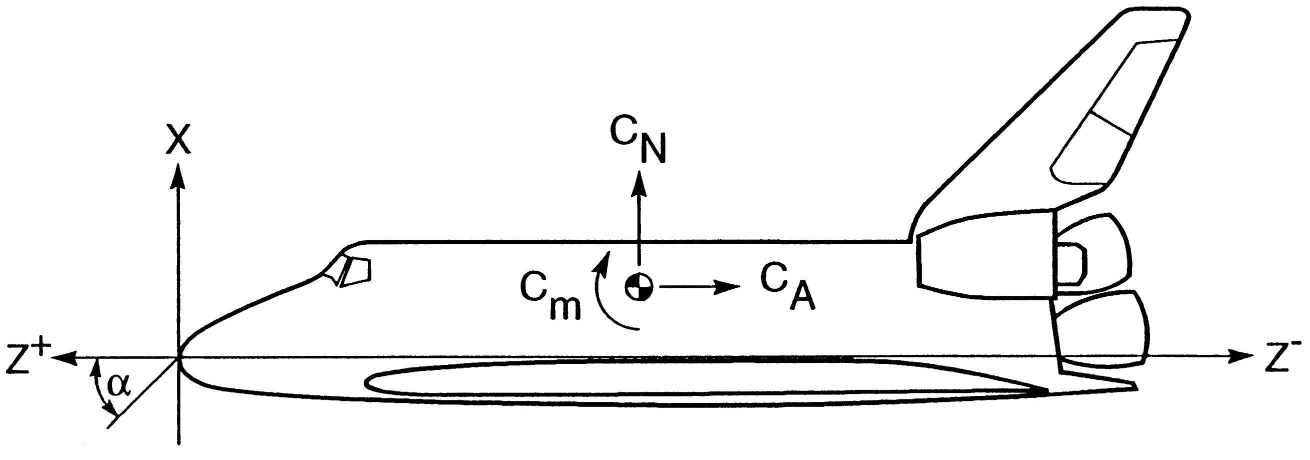

Fig. 1 Coordinate system and aerodynamic convention.

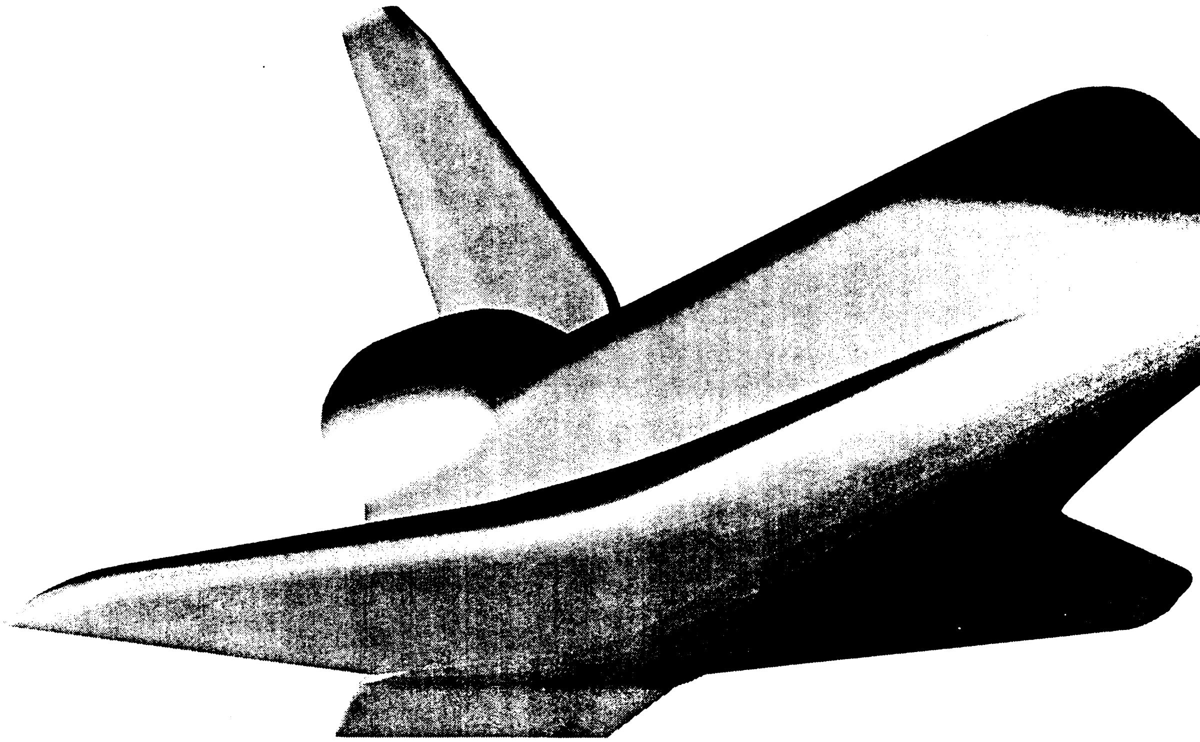

Fig. 2 Complete Shuttle Orbiter geometry.

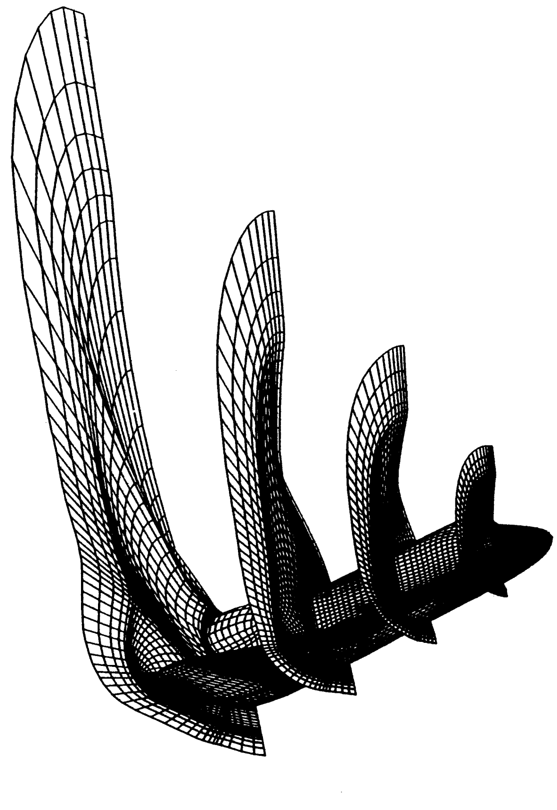

Fig. 3 Shuttle Orbiter surface and volume grid.

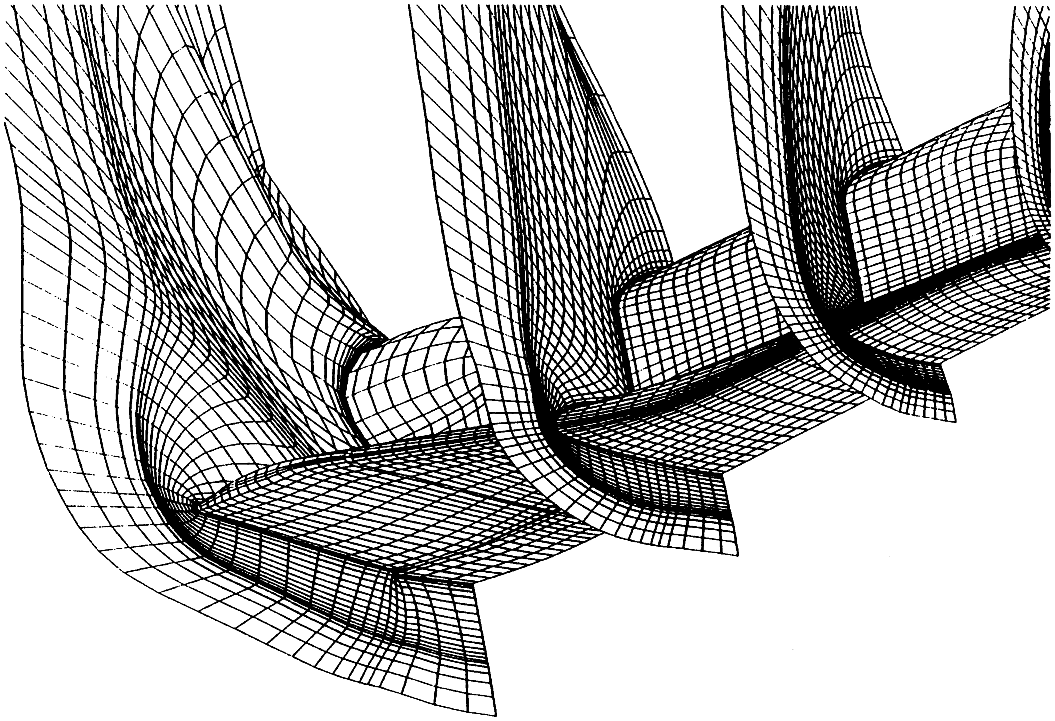

Fig. 4 Expanded view, Shuttle Orbiter surface and volume grid.

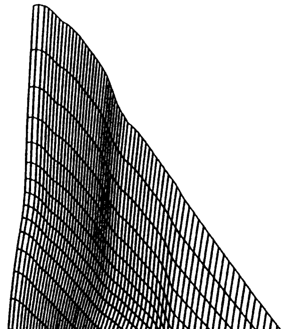

Fig. 5 Shuttle Orbiter upper-symmetry plane grid.

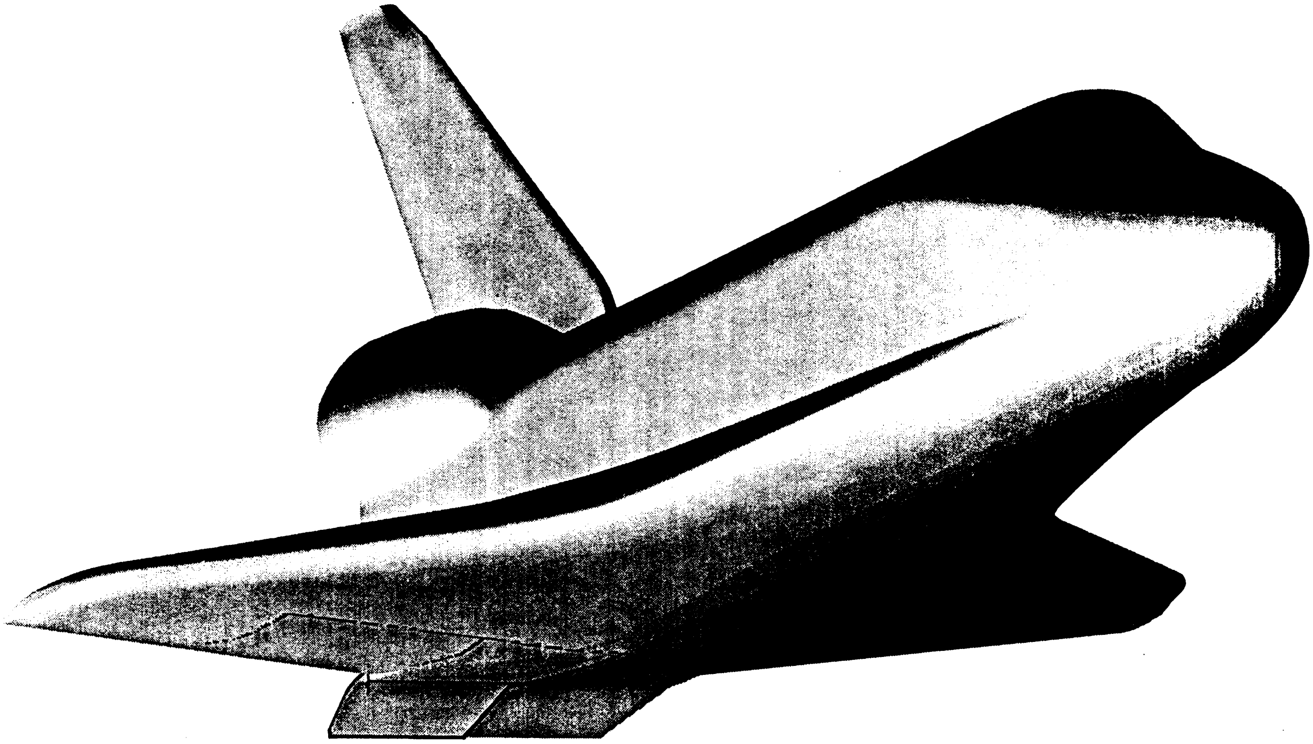

Fig. 6 (a) Shuttle Orbiter and bodyflap computational surface.

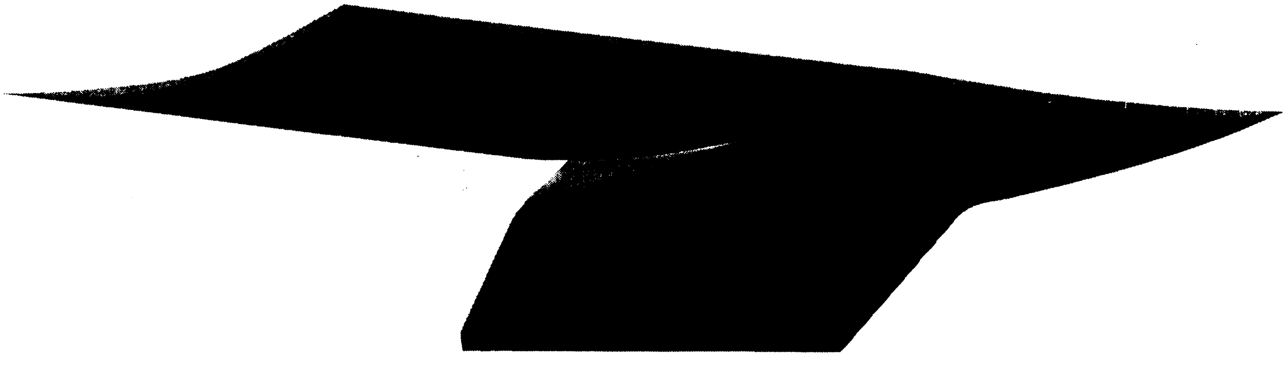

Fig. 6 (b) Bodyflap computational surface.

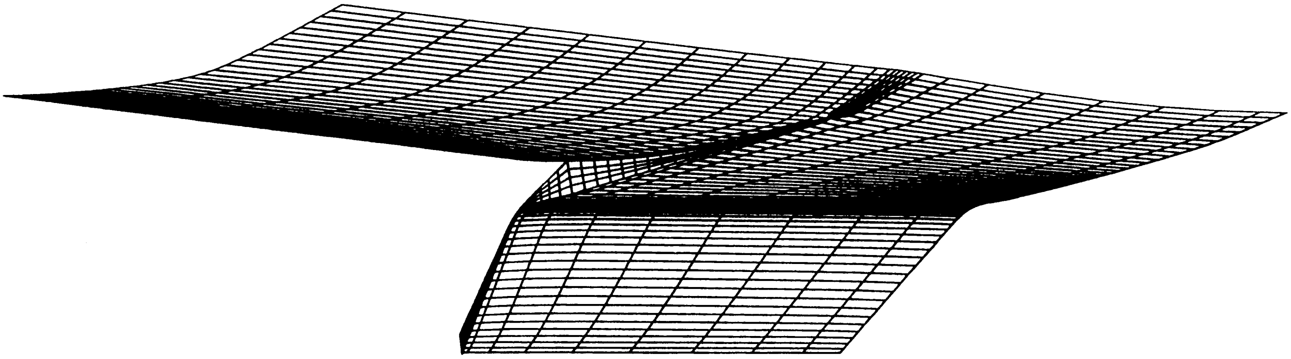

Fig. 6 (c) Surface grid, bodyflap computational surface.

Fig. 7 Complete modified Orbiter and bodyflap computational surface.

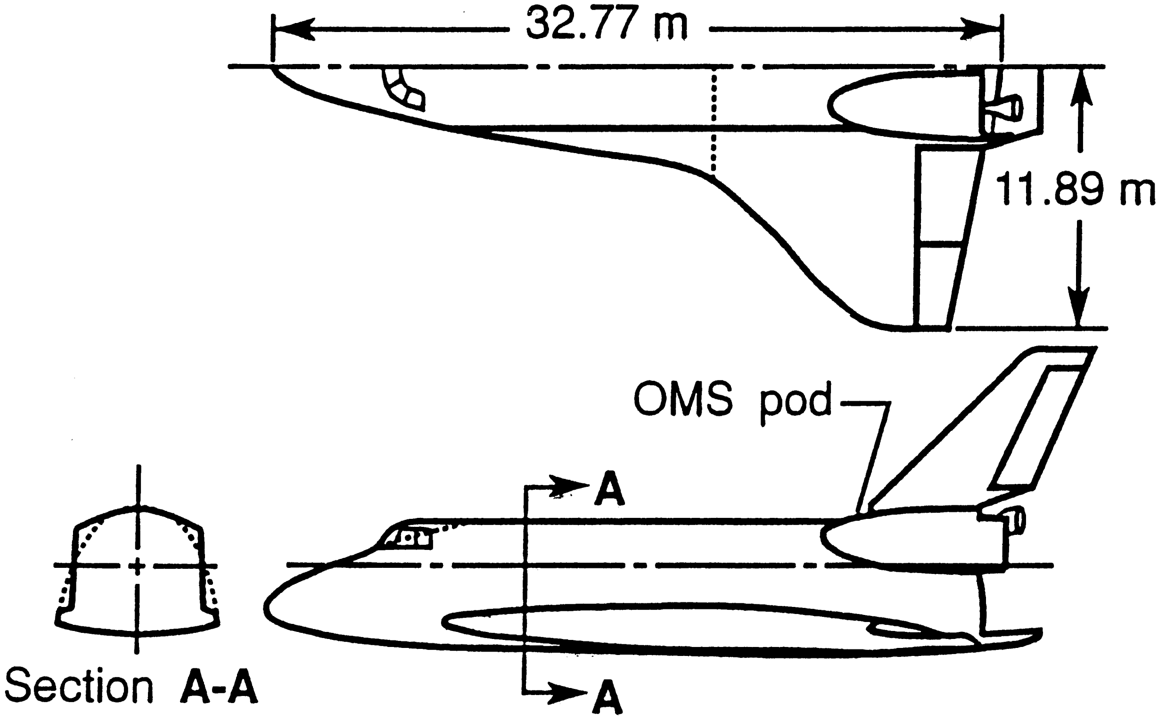

Fig. 8 Shuttle Orbiter modification.

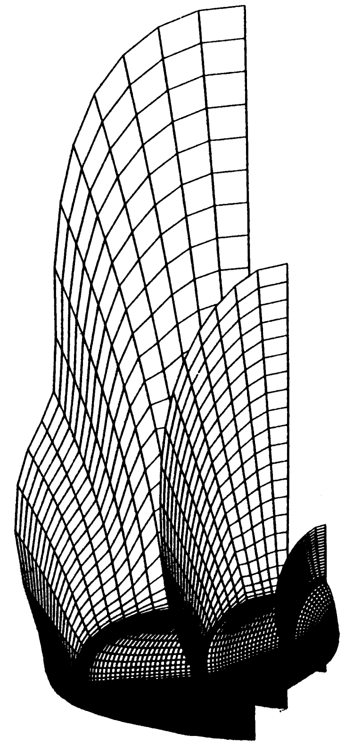

Fig. 9 Modified Orbiter surface and volume grid.

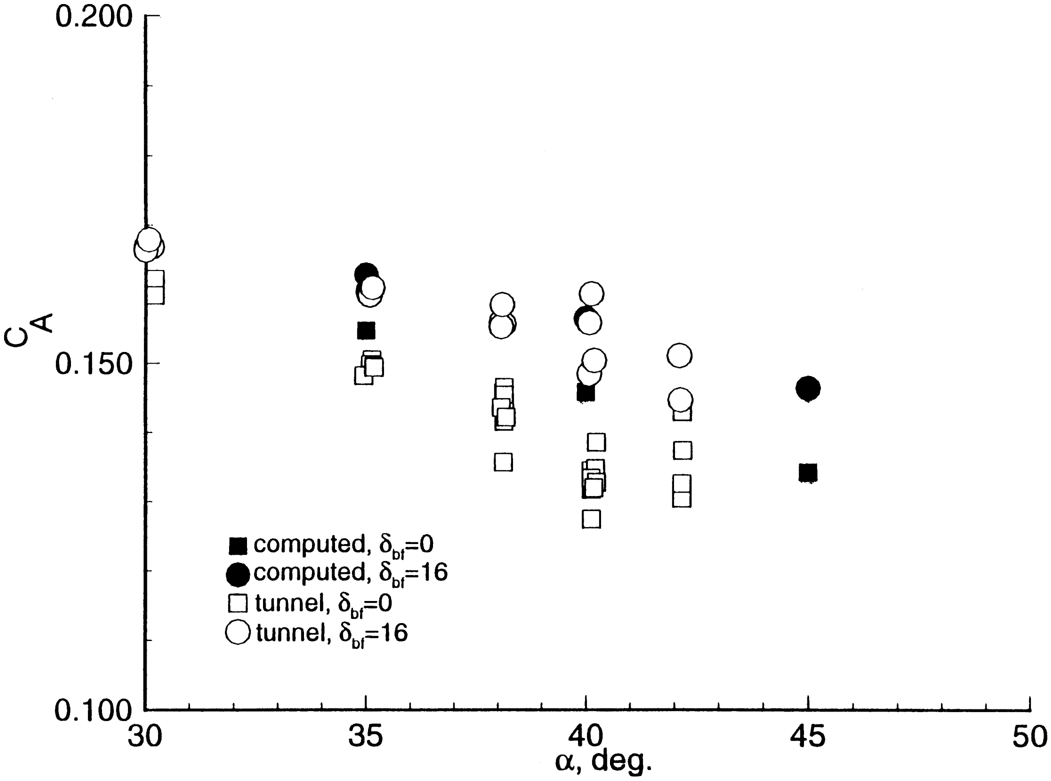

(a) C_A

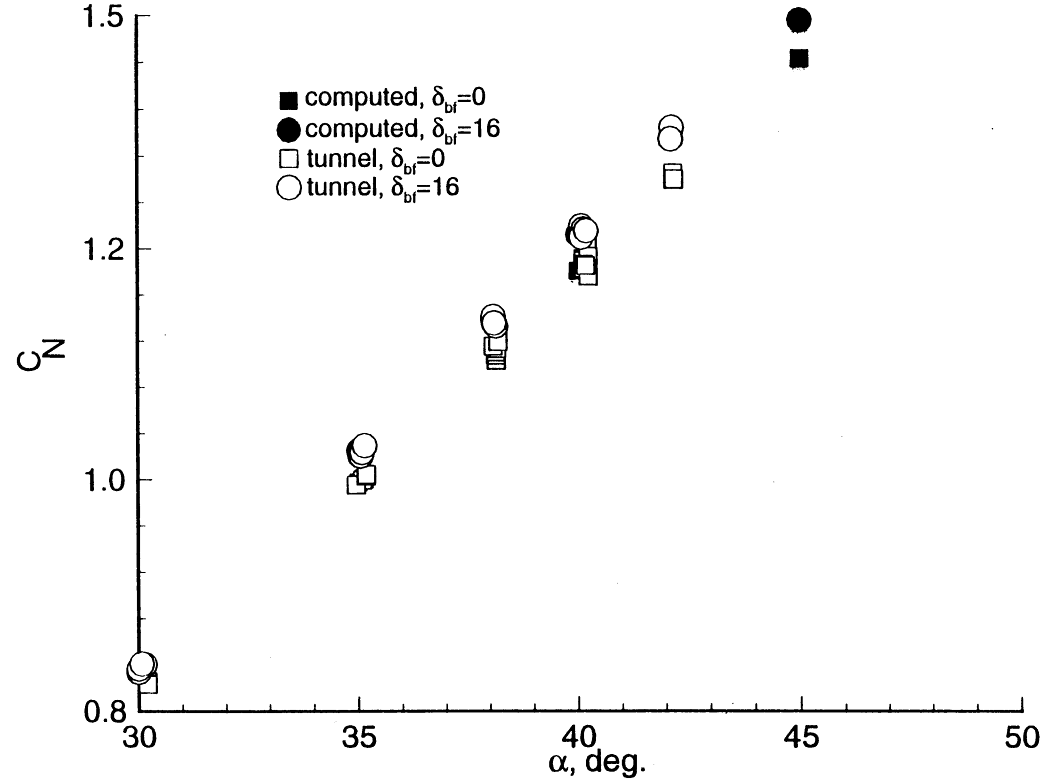

(b) C_N

Fig. 10 Comparison of computed and measured aerodynamics for the modified Orbiter configuration at $M_\infty = 10$ and $Re_\infty = 1.07x10^6$.

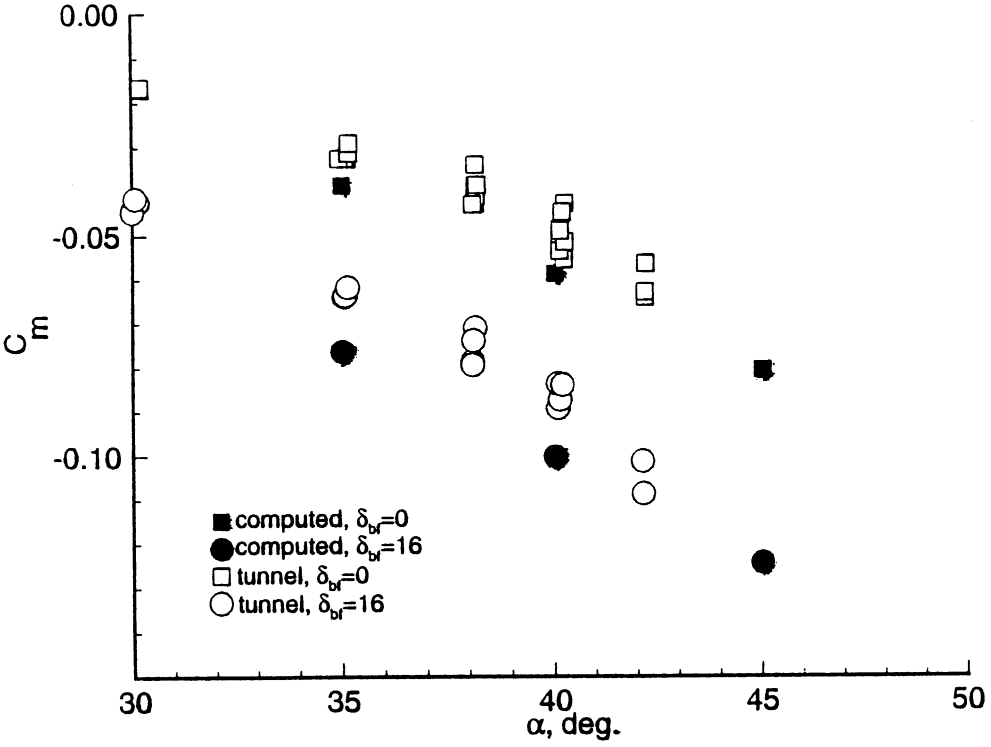

(c) C_m

Fig. 10 Comparison of computed and measured aerodynamics for the modified Orbiter configuration at $M_\infty = 10$ and $Re_\infty = 1.07 \times 10^6$.

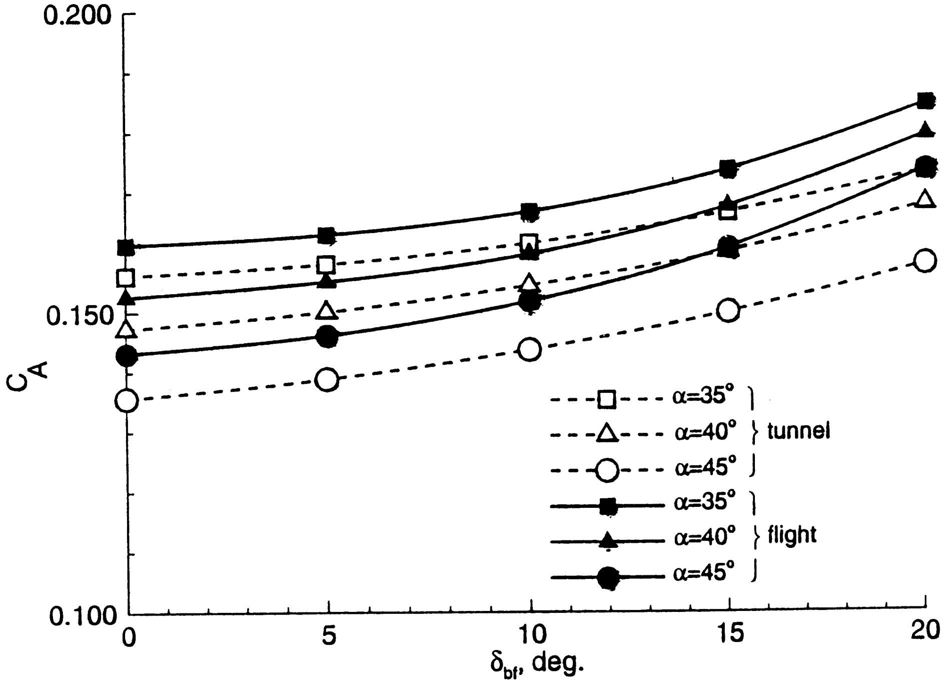

(a) C_A

Fig. 11 Comparison of computed aerodynamics for the modified Orbiter configuration at a $M_\infty = 10$ tunnel condition and at a $M_\infty = 24$ flight condition.

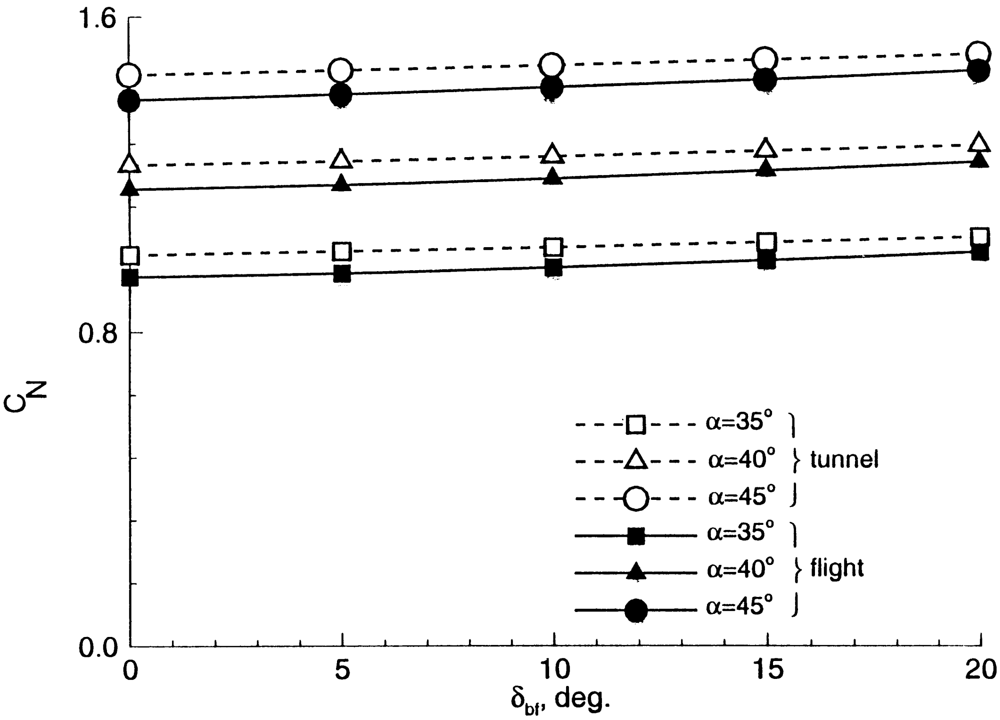

(b) C_N

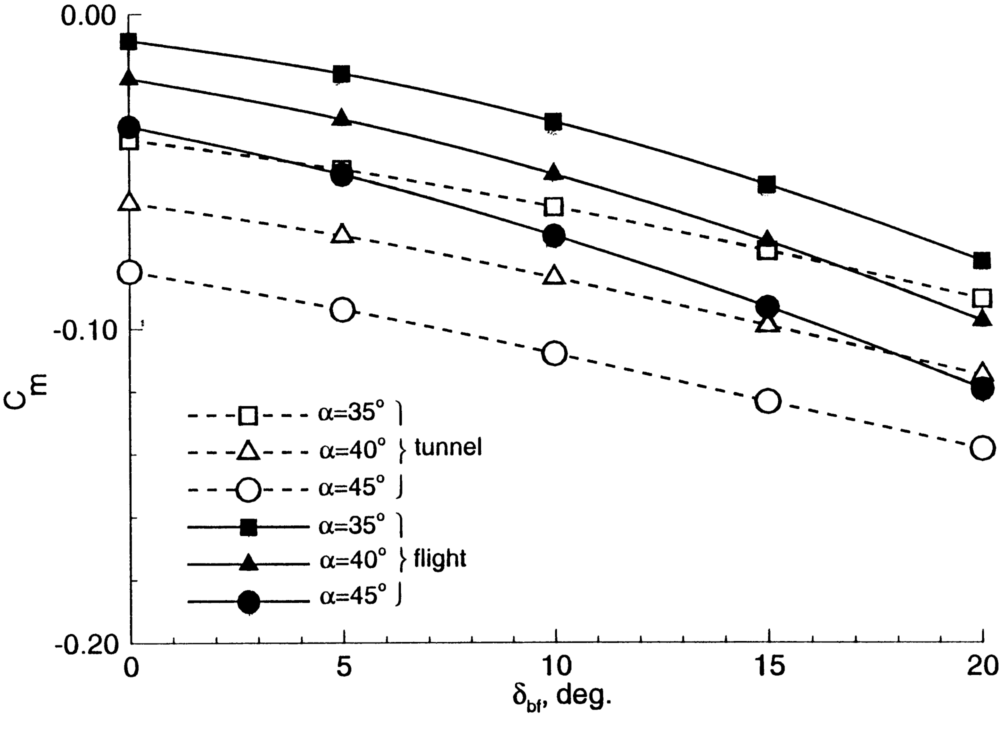

(c) C_m

Fig. 11 Comparison of computed aerodynamics for the modified Orbiter configuration at a $M_\infty = 10$ tunnel condition and at a $M_\infty = 24$ flight condition.

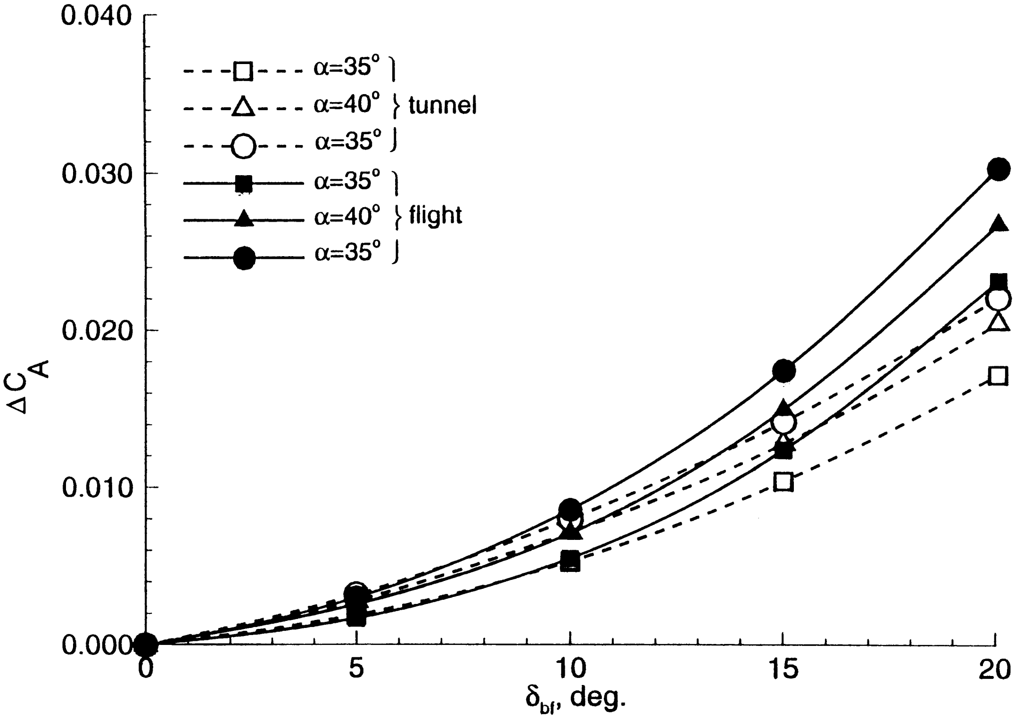

(a) C_A

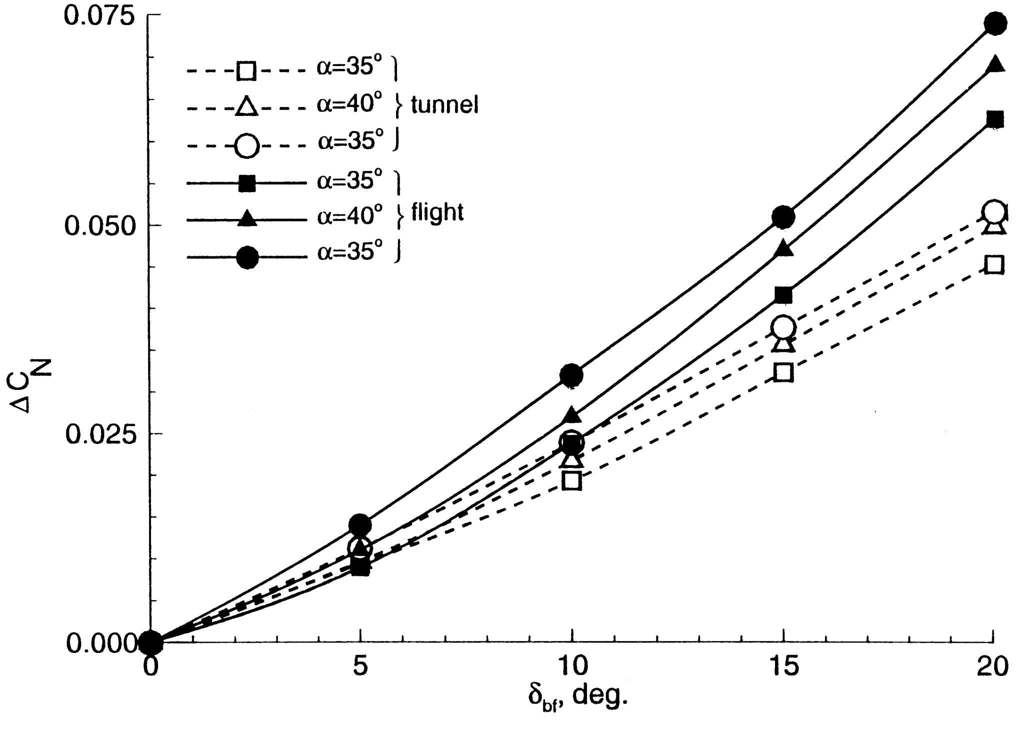

(b) C_N

Fig. 12 Comparison of computed incremental aerodynamics for the modified Orbiter configuration at a $M_\infty = 10$ tunnel condition and at a $M_\infty = 24$ flight condition.

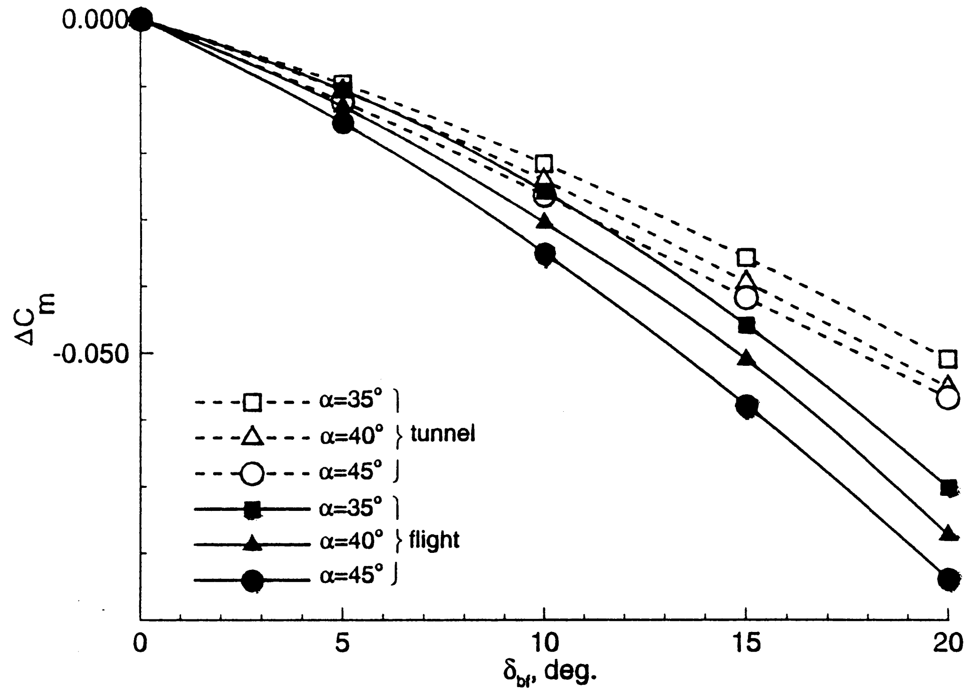

(c) C_m

Fig. 12 Comparison of computed incremental aerodynamics for the modified Orbiter configuration at a $M_\infty = 10$ tunnel condition and at a $M_\infty = 24$ flight condition.

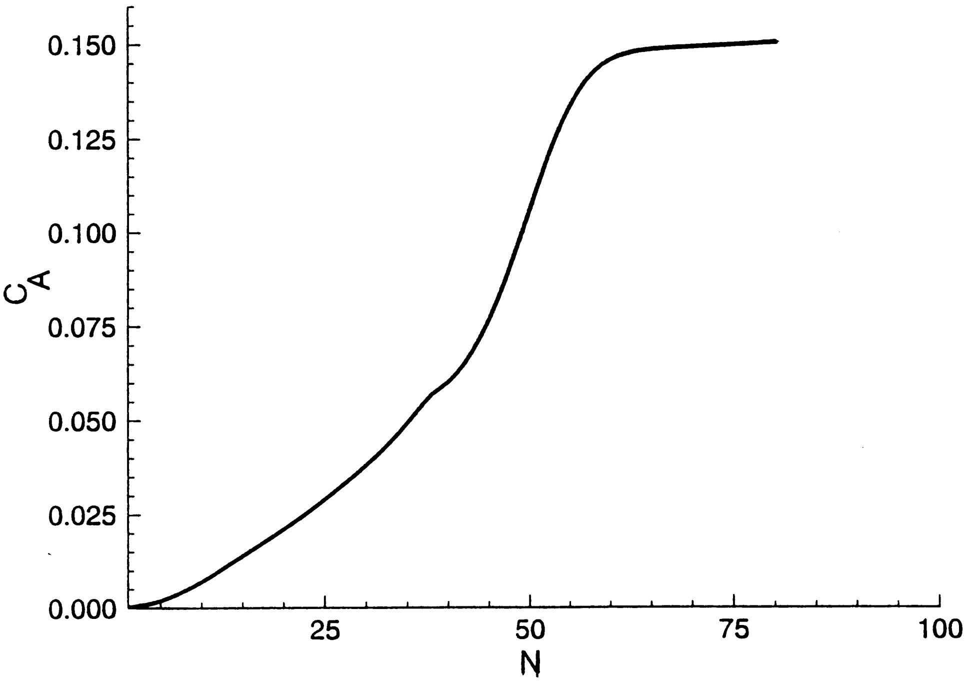

(a) C_A

Fig. 13 Circumferentially integrated (no bodyflap included) aerodynamic coefficients for the modified Orbiter configuration at a $M_\infty = 10$ tunnel condition and 40 degrees angle-of-attack.

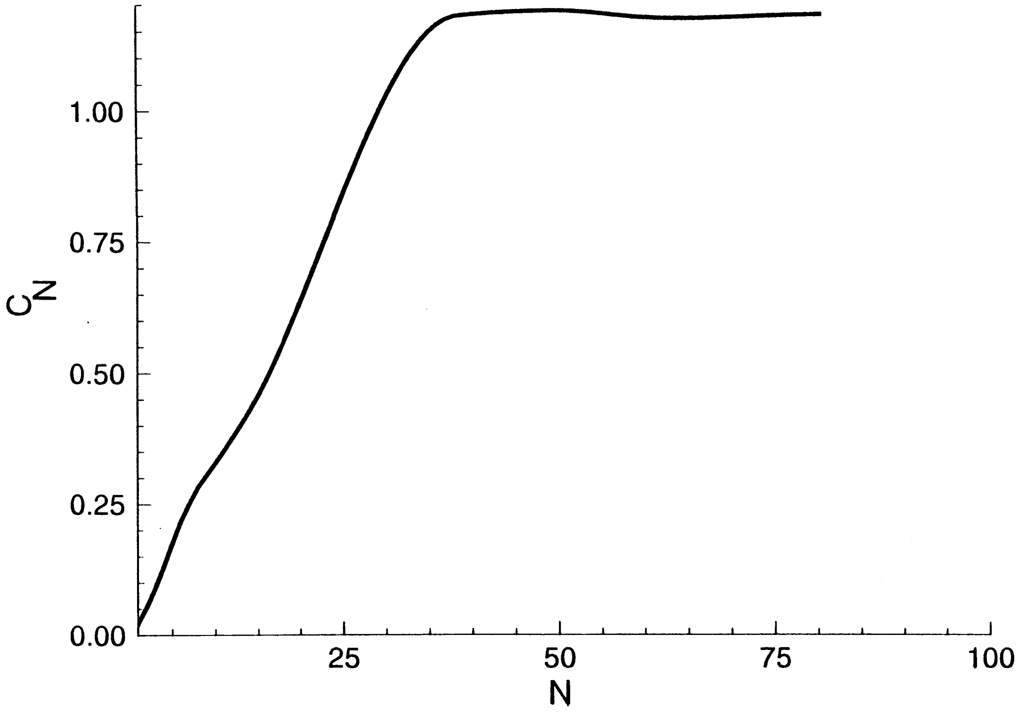

(b) C_N

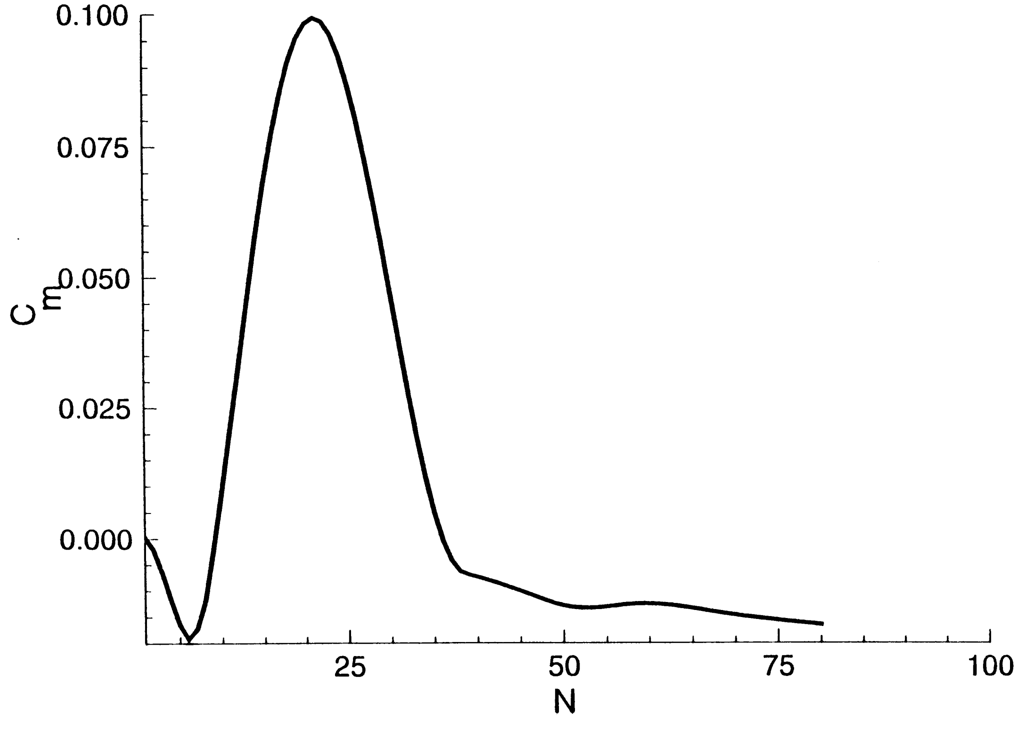

(c) C_m

Fig. 13 Circumferentially integrated (no bodyflap included) aerodynamic coefficients for the modified Orbiter configuration at a $M_\infty = 10$ tunnel condition and 40 degrees angle-of-attack.

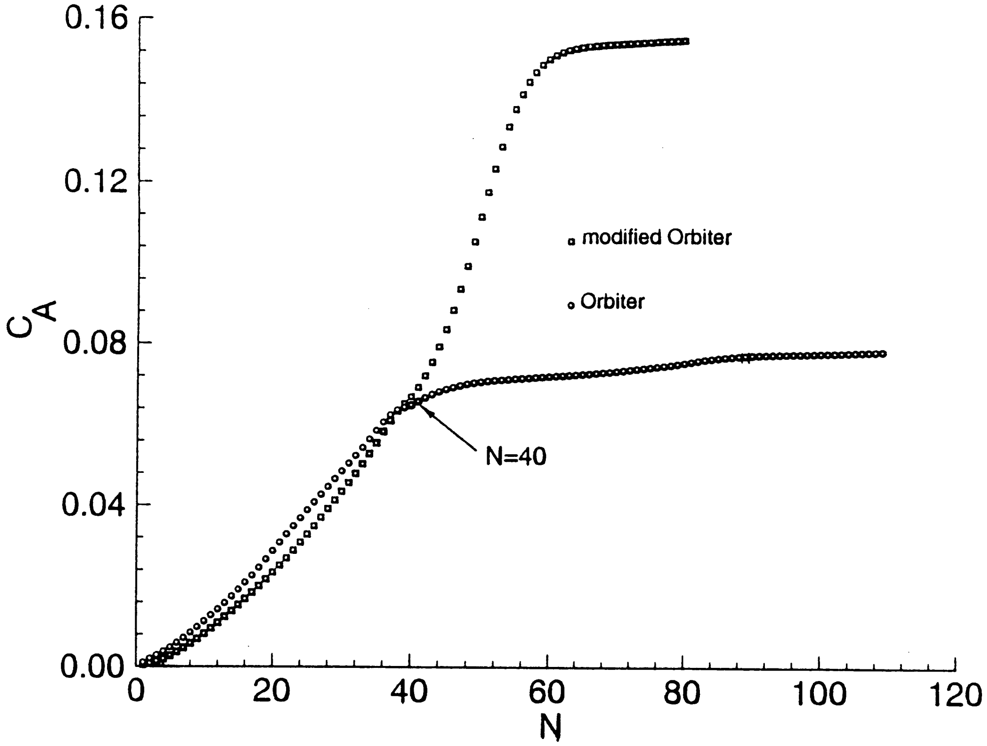

(a) C_A

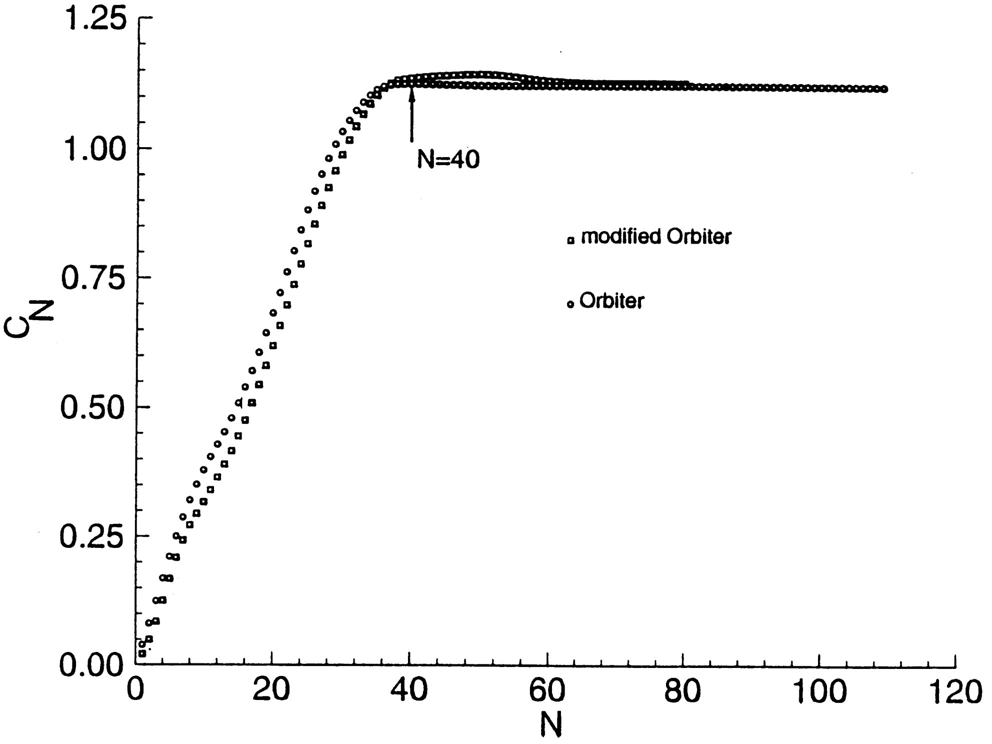

(b) C_N

Fig. 14 Comparison of circumferentially integrated (no bodyflap included) aerodynamic coefficients for the modified Orbiter and complete Orbiter configurations at a $M_\infty = 24$ flight condition and 40 degrees angle-of-attack.

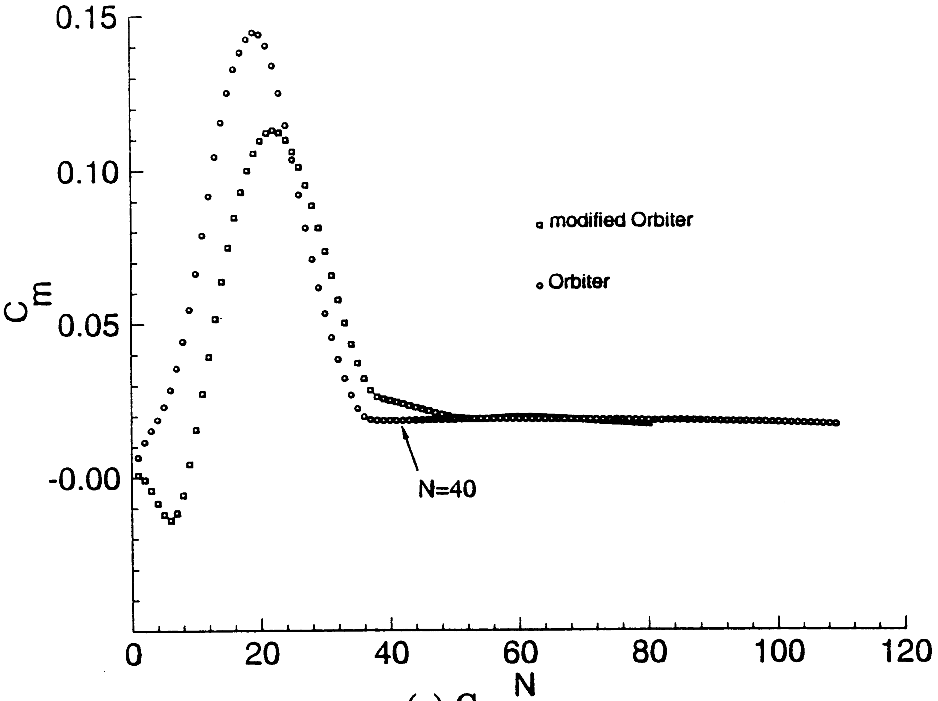

(c) C_m

Fig. 14 Comparison of circumferentially integrated (no bodyflap included) aerodynamic coefficients for the modified Orbiter and complete Orbiter configurations at a $M_\infty = 24$ flight condition and 40 degrees angle-of-attack.

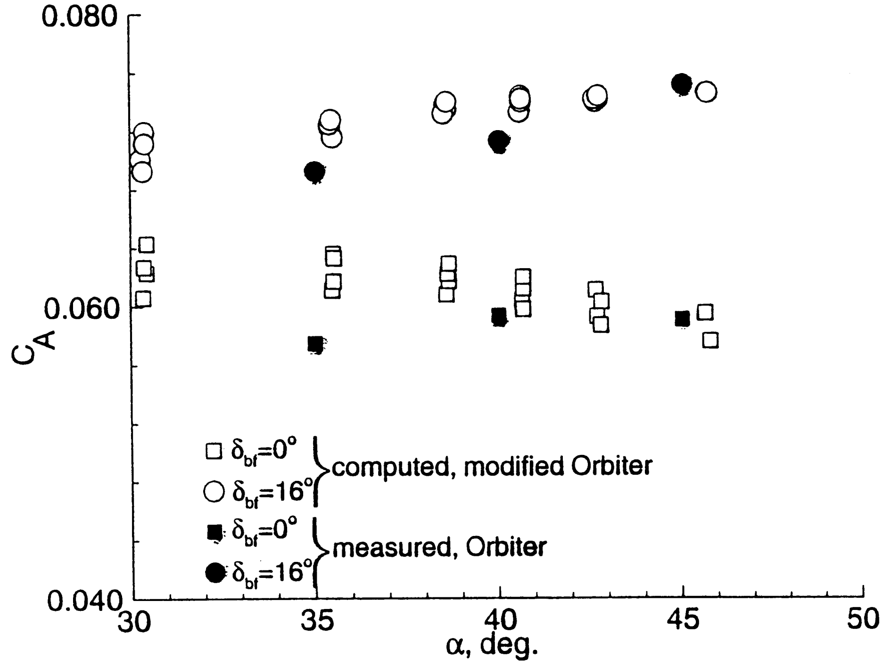

(a) C_A

Fig. 15 Comparison of modified Orbiter aerodynamics based on lower surface properties and measured aerodynamics for the complete Shuttle Orbiter configuration at a $M_\infty = 10$ tunnel condition and 40 degrees angle-of-attack.

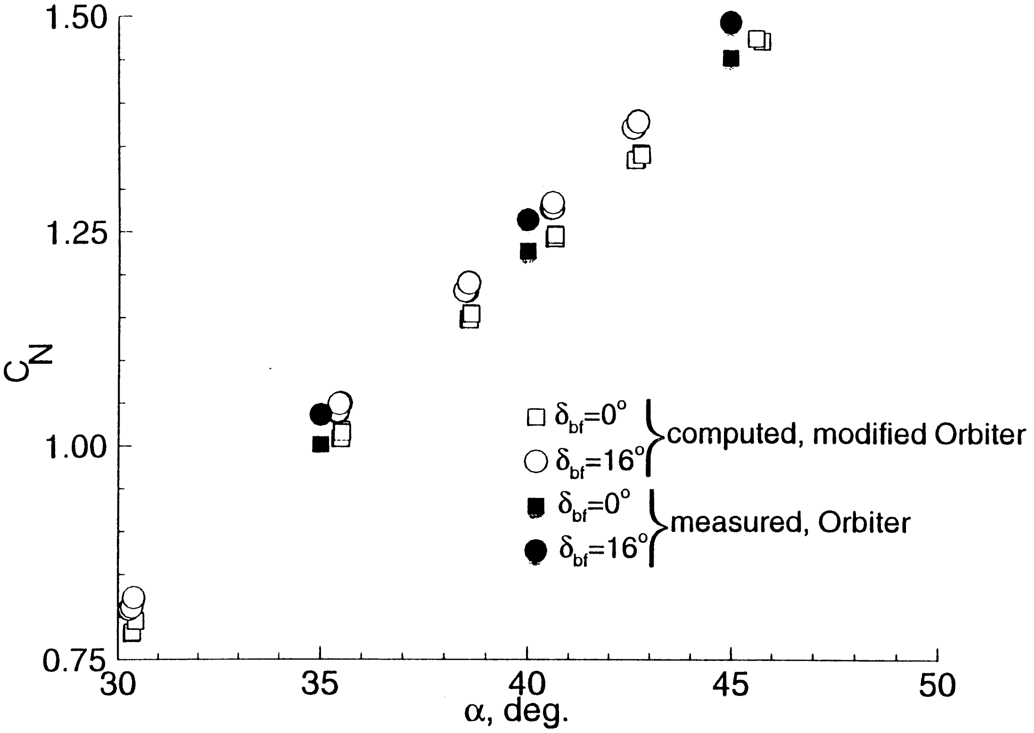

(b) C_N

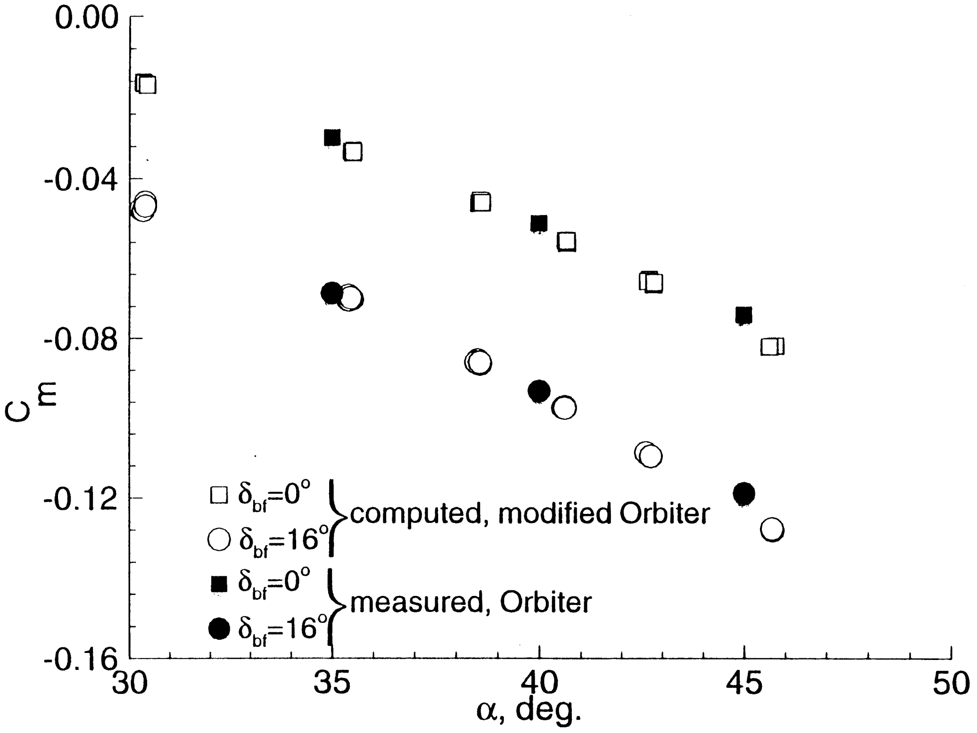

(c) C_m

Fig. 15 Comparison of modified Orbiter aerodynamics based on lower surface properties and measured aerodynamics for the complete Shuttle Orbiter configuration at a M_∞ = 10 tunnel condition and 40 degrees angle-of-attack.

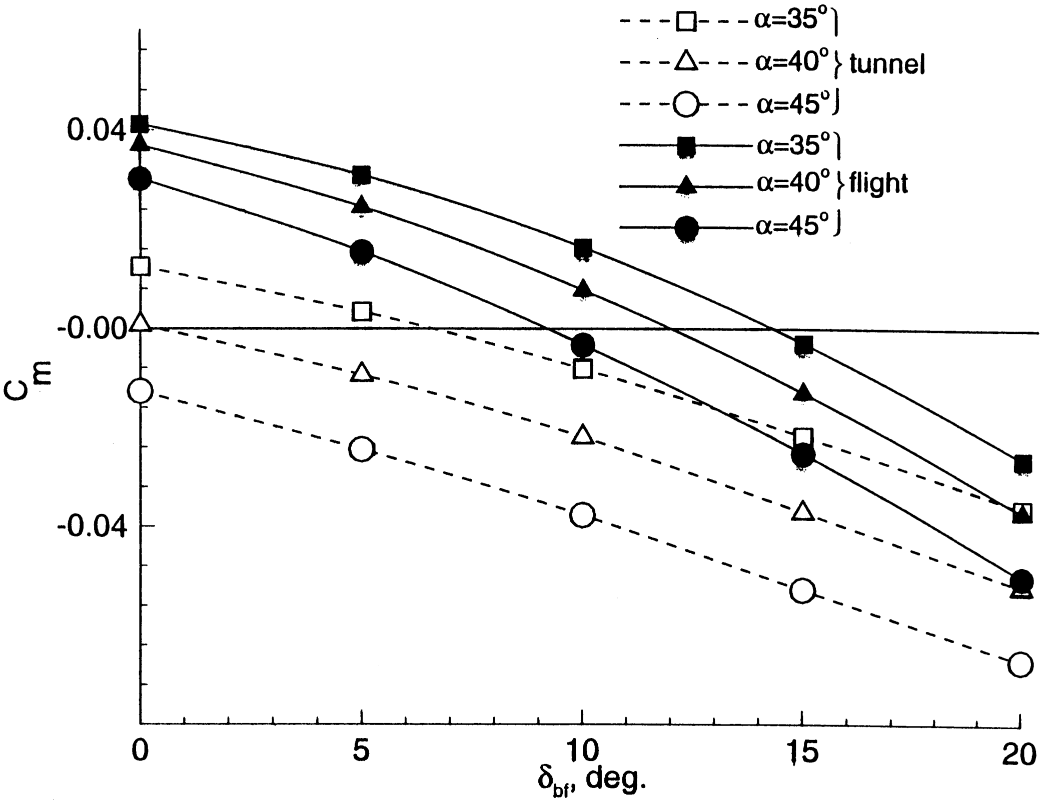

Fig. 16 Comparison of computed pitching moment based on STS-2 entry interface CG location for the modified Orbiter lower surface at a $M_\infty = 10$ tunnel condition and at a $M_\infty = 24$ flight condition.

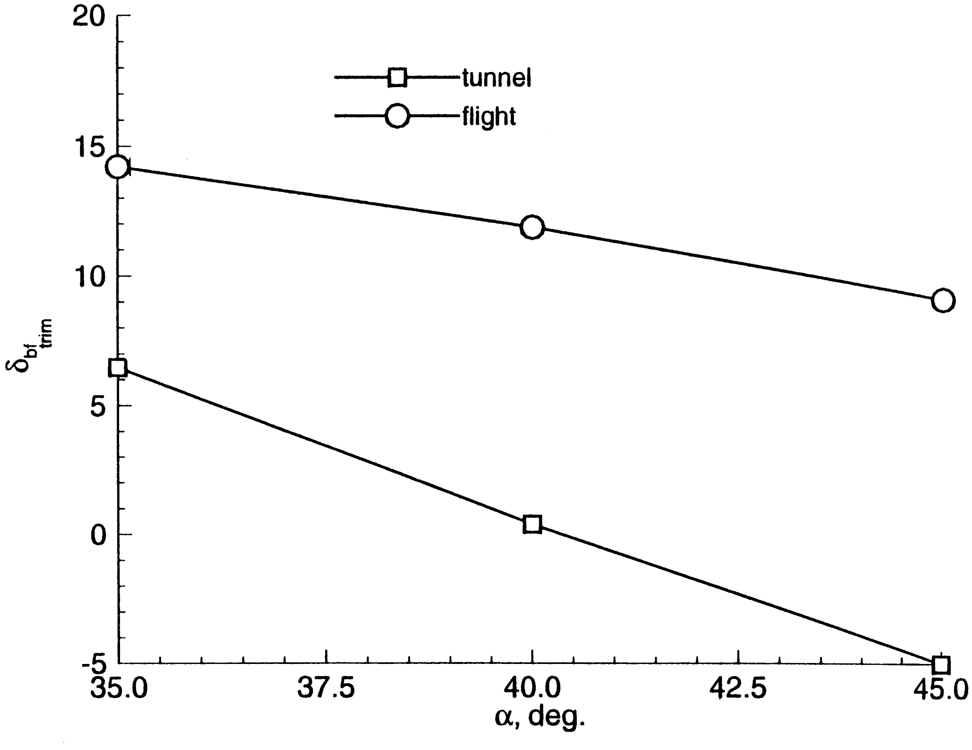

Fig. 17 Computed bodyflap trim angle as a function of angle-of-attack for a $M_\infty = 10$ tunnel condition and a $M_\infty = 24$ flight condition.

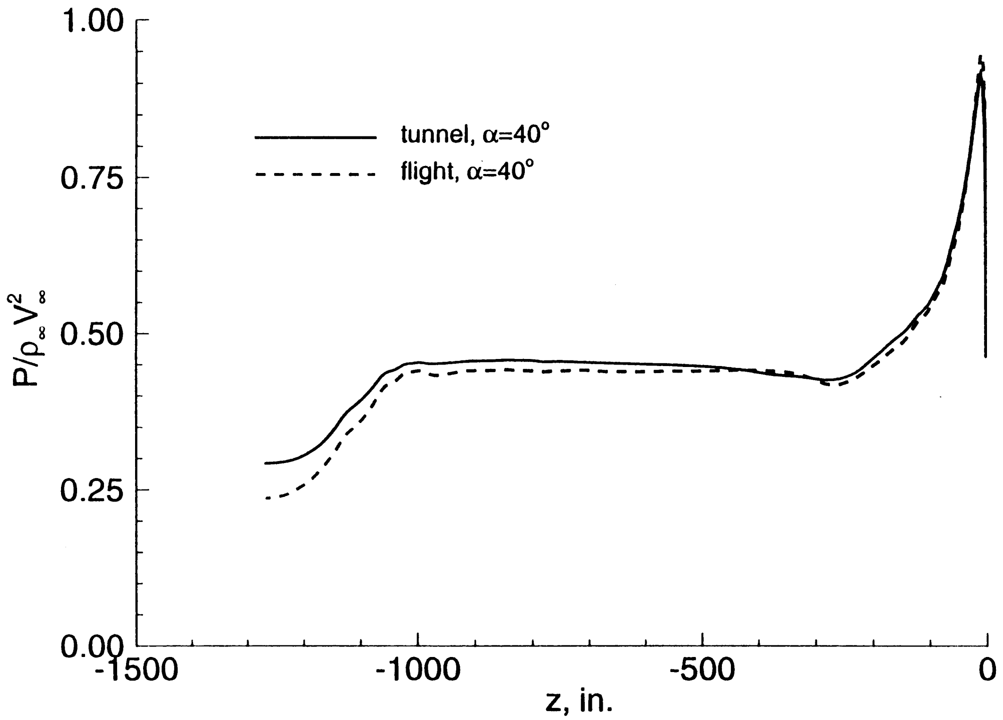

Fig. 18 Computed windward centerline surface pressure plot (bodyflap not included) for a $M_\infty = 10$ tunnel condition and a $M_\infty = 24$ flight condition at 40 degrees angle-of-attack.

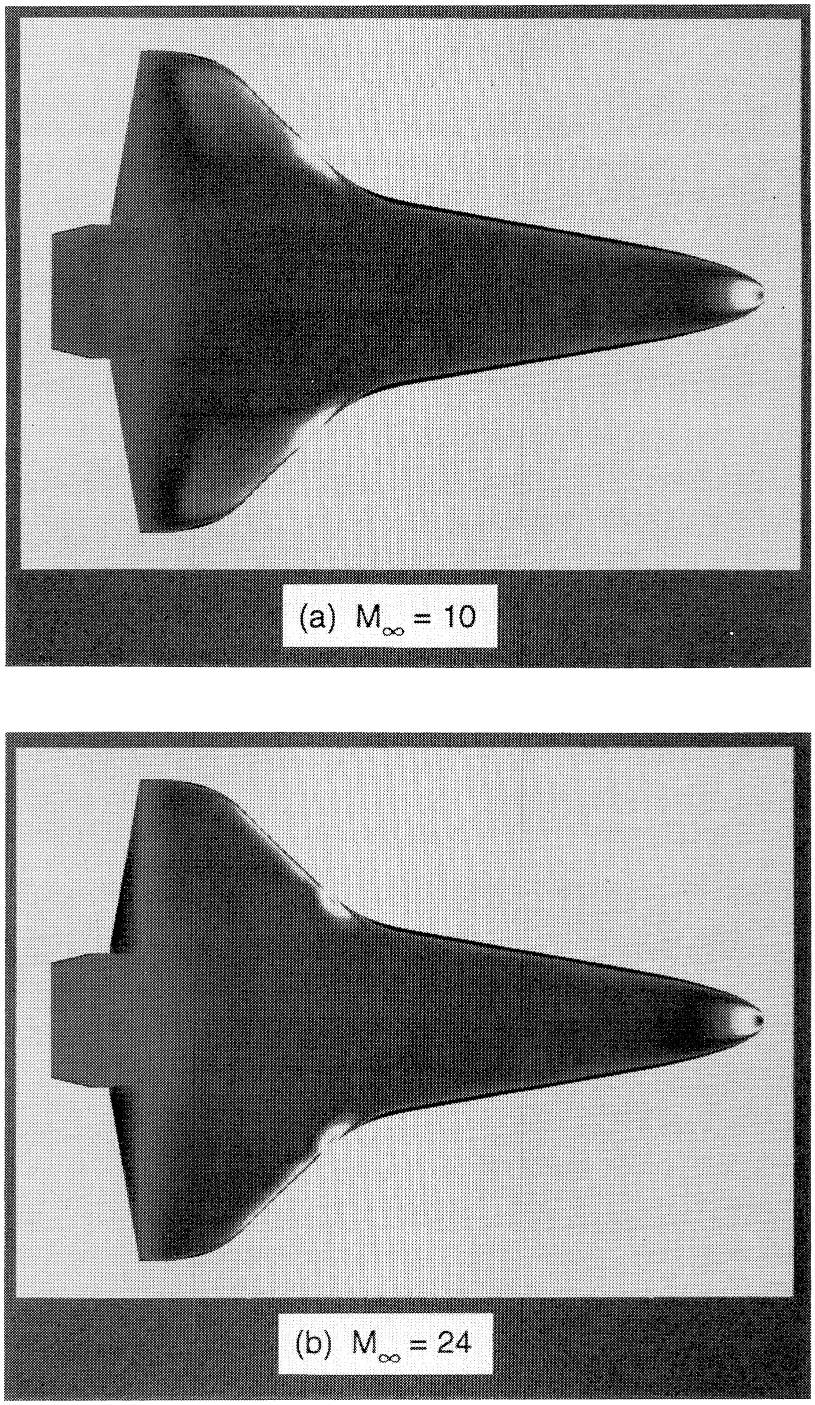

Fig. 19 Computed windward surface color contour plots of pressure at 40 degrees angle of attack and 0 degree bodyflap deflection.

(The color versions of figures 19a and 19b are shown on page 498.)

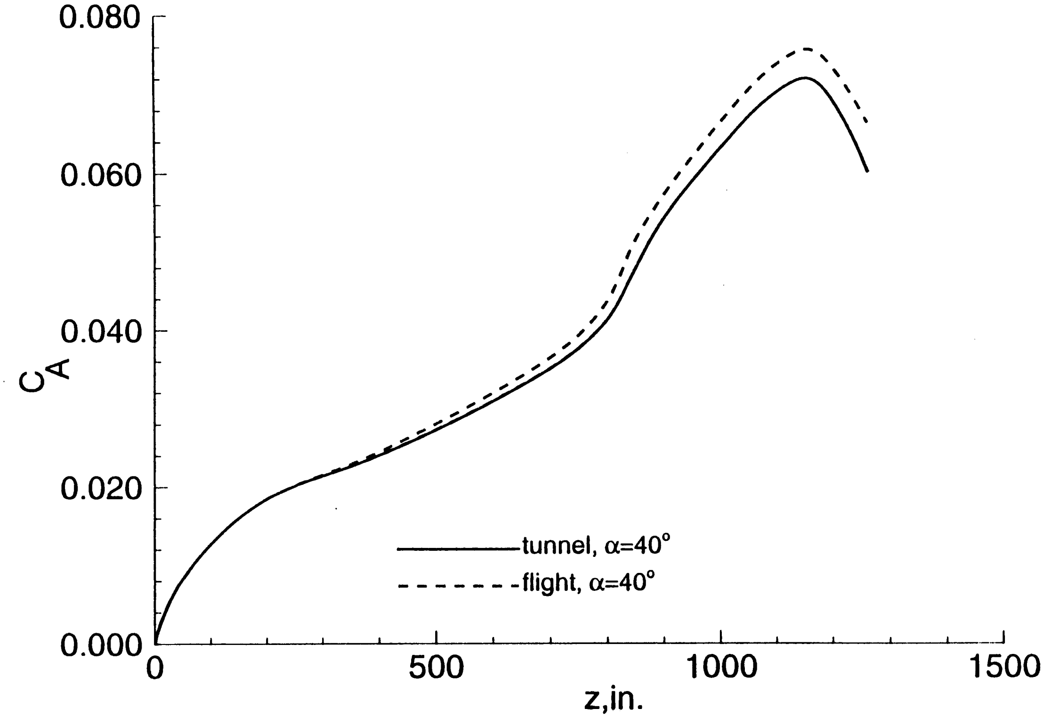

(a) C_A

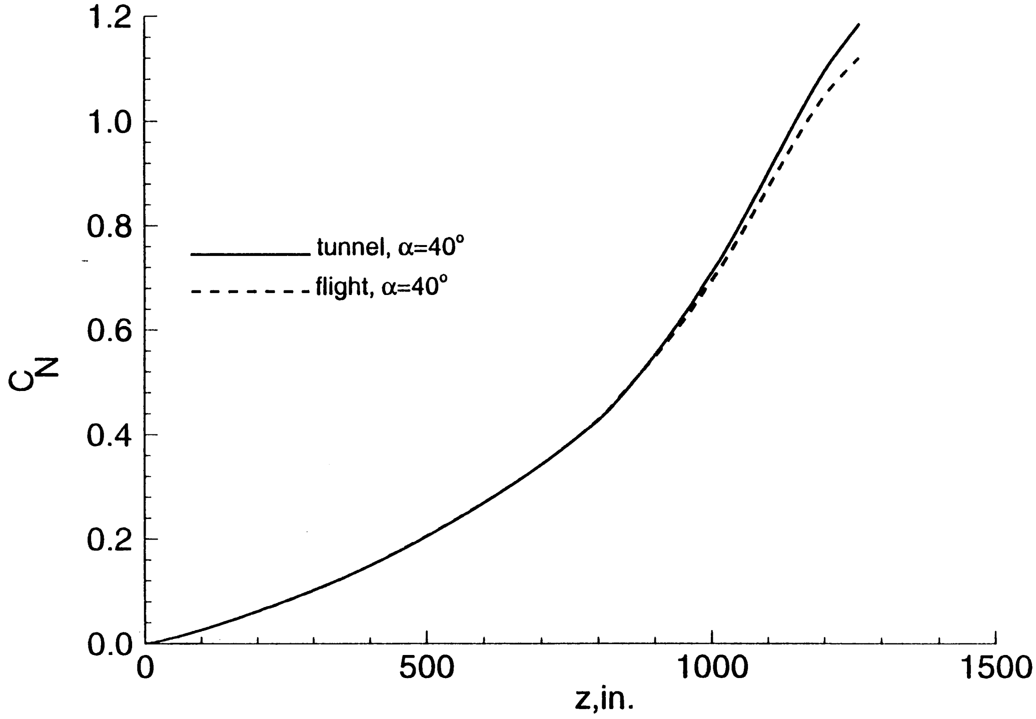

(b) C_N

Fig. 20 Comparison of axially integrated (bodyflap not included) aerodynamic coefficients based on modified Orbiter lower surface for a $M_\infty = 10$ tunnel condition and a $M_\infty = 24$ tunnel condition at 40 degrees angle of attack.

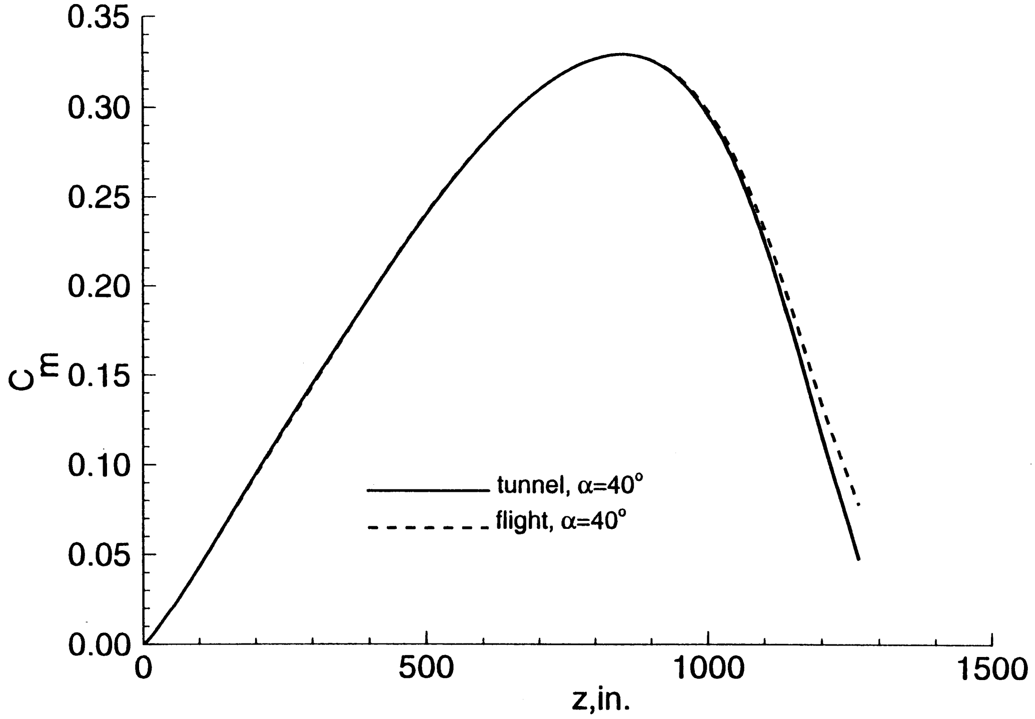

(c) C_m

Fig. 20 Comparison of axially integrated (bodyflap not included) aerodynamic coefficients based on modified Orbiter lower surface for a $M_\infty = 10$ tunnel condition and a $M_\infty = 24$ tunnel condition at 40 degrees angle of attack.

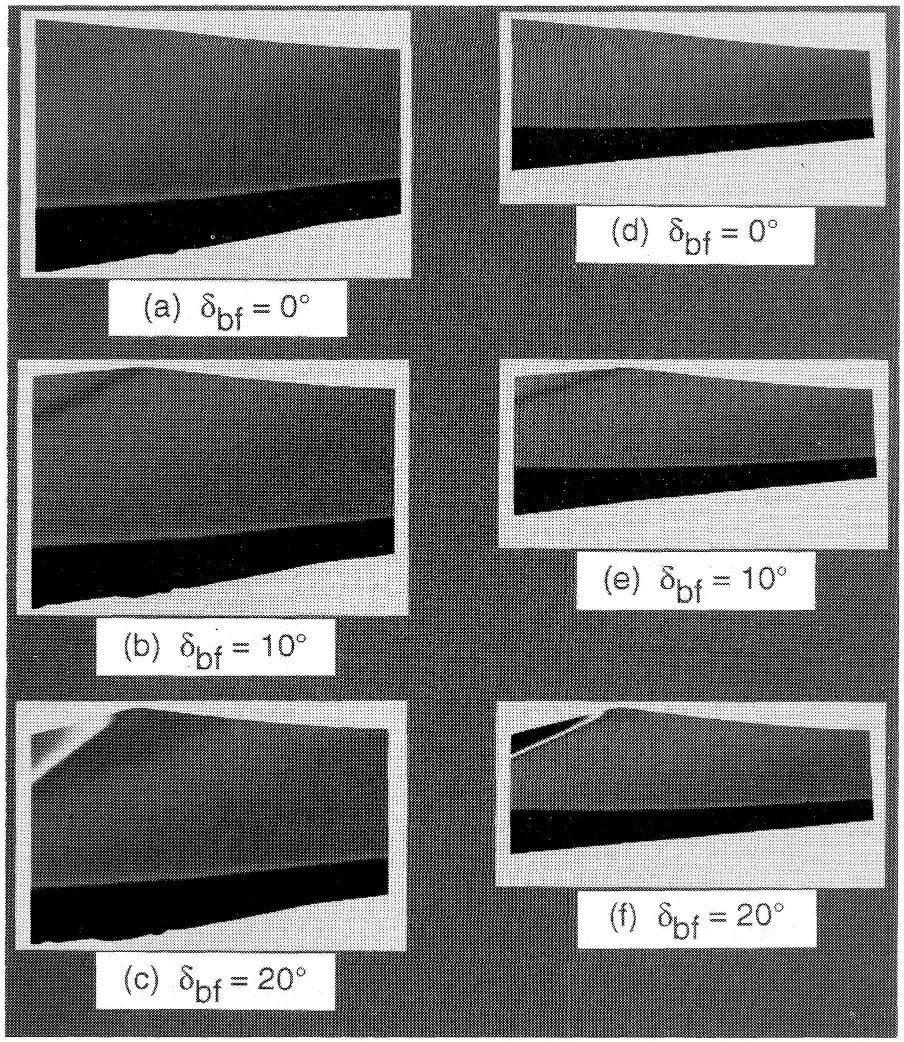

(a) $\delta_{bf} = 0°$

(b) $\delta_{bf} = 10°$

(c) $\delta_{bf} = 20°$

(d) $\delta_{bf} = 0°$

(e) $\delta_{bf} = 10°$

(f) $\delta_{bf} = 20°$

Fig. 21 Comparison of symmetry plane color contour plots of pressure in the vicinity of the bodyflap at a $M_\infty = 10$ tunnel condition and a $M_\infty = 24$ flight condition at 40 degrees angle of attack and bodyflap deflections of 0, 10, and 20 degrees.

(The color version of Figure 21 is shown on page 499.)

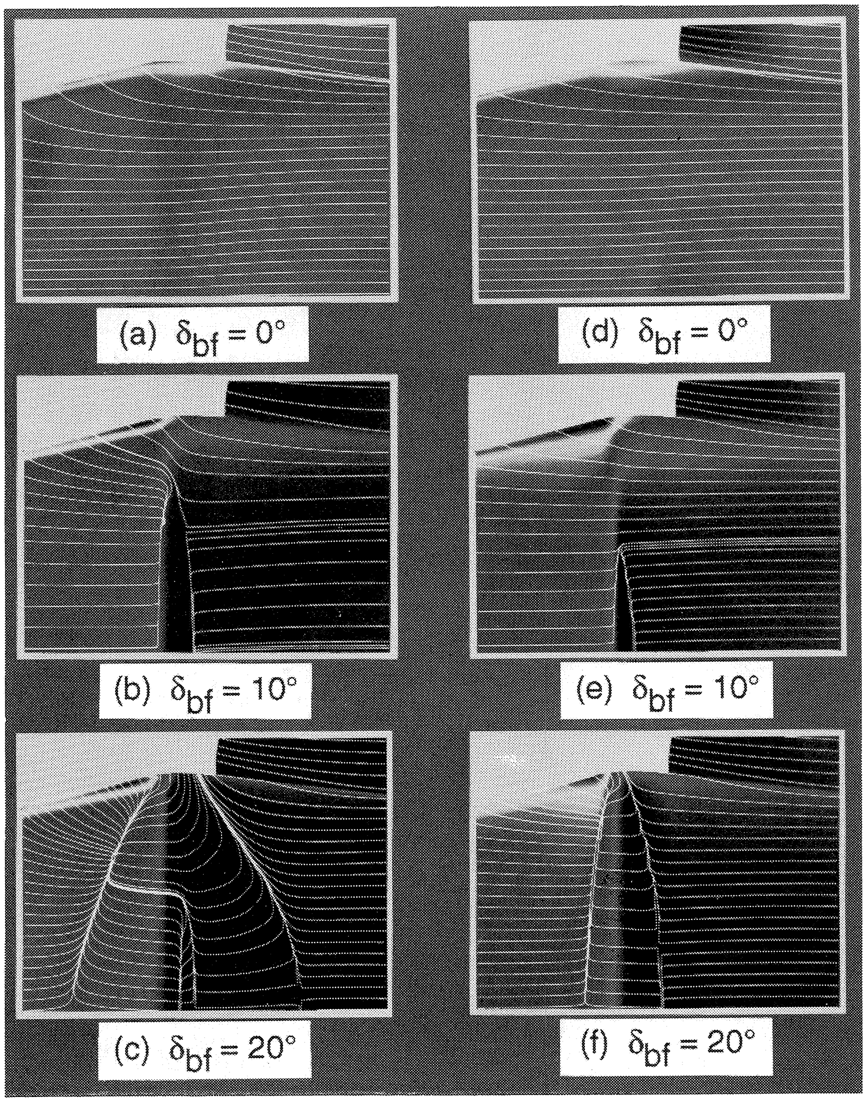

Fig. 22 Surface streamlines superimposed on color contour plots of surface heating in the vicinity of the bodyflap hinge line for a $M_\infty = 10$ tunnel condition and a $M_\infty = 24$ flight condition at 40 degrees angle of attack and bodyflap deflections of 0, 10, and 20 degrees.

(The color version of Figure 22 is shown on page 500.)

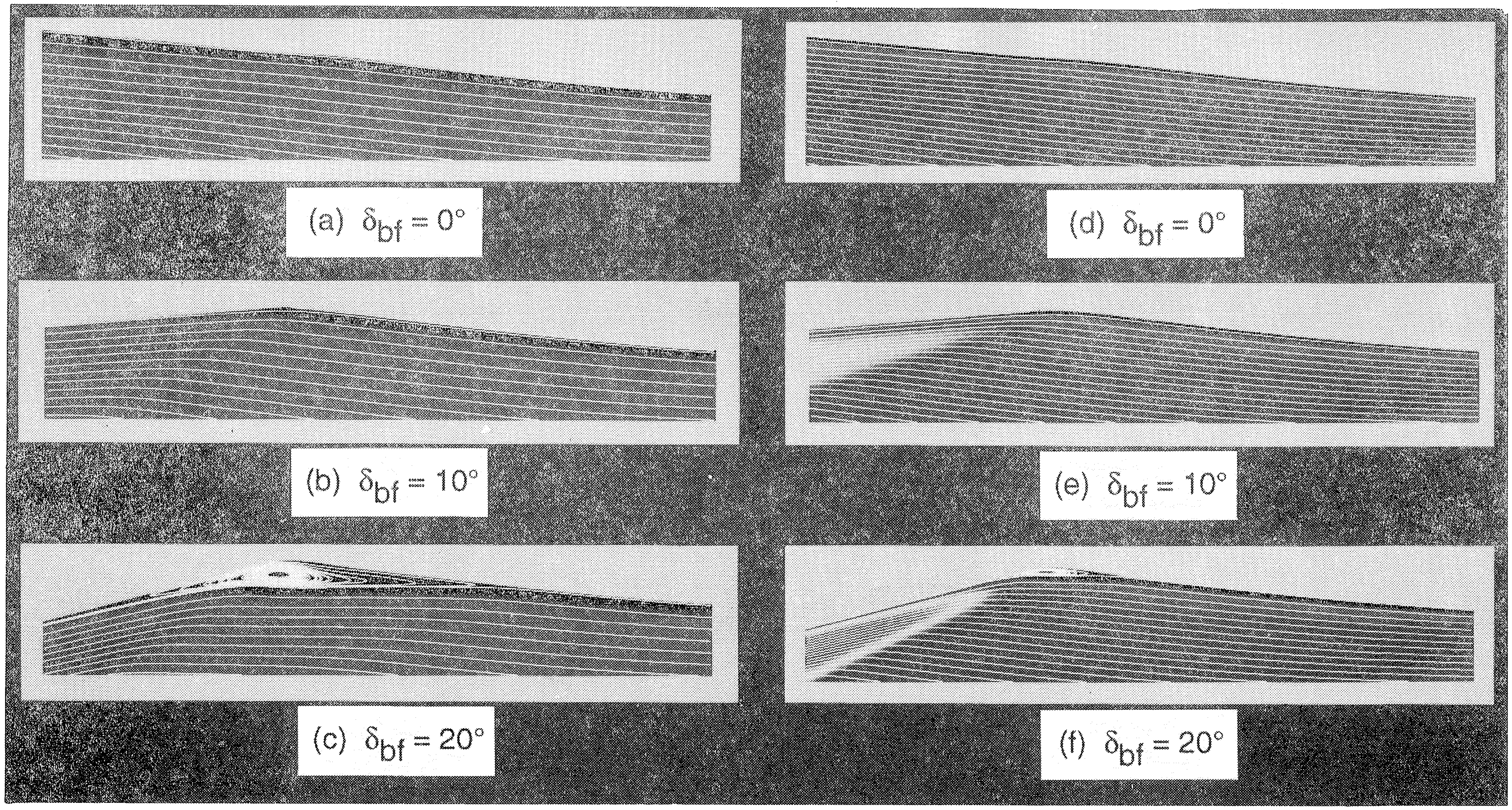

Fig. 23 Streamlines in the windward symmetry plane superimposed on color contour plots of pressure for a $M_\infty = 10$ tunnel condition and a $M_\infty = 24$ flight condition at 40 degrees angle of attack and bodyflap deflections of 0, 10, and 20 degrees.

(The color version of Figure 23 is shown on page 501.)

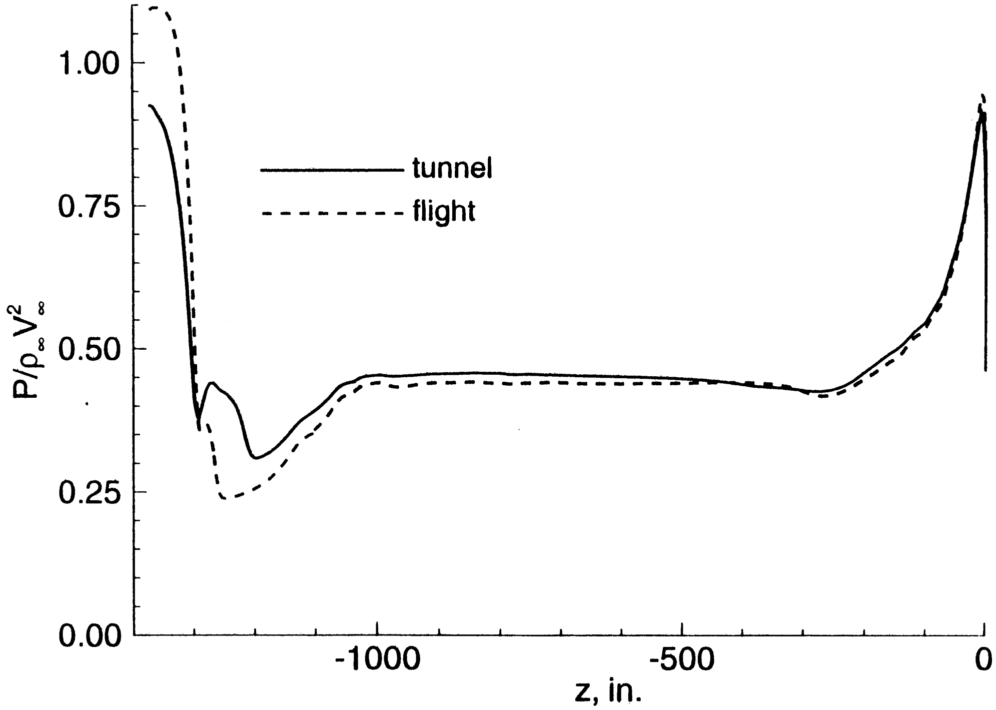

Fig. 24 Computed windward centerline distribution of pressure for a $M_\infty = 10$ tunnel condition and a $M_\infty = 24$ flight condition at 40 degrees angle of attack and a 20 degree bodyflap deflection.

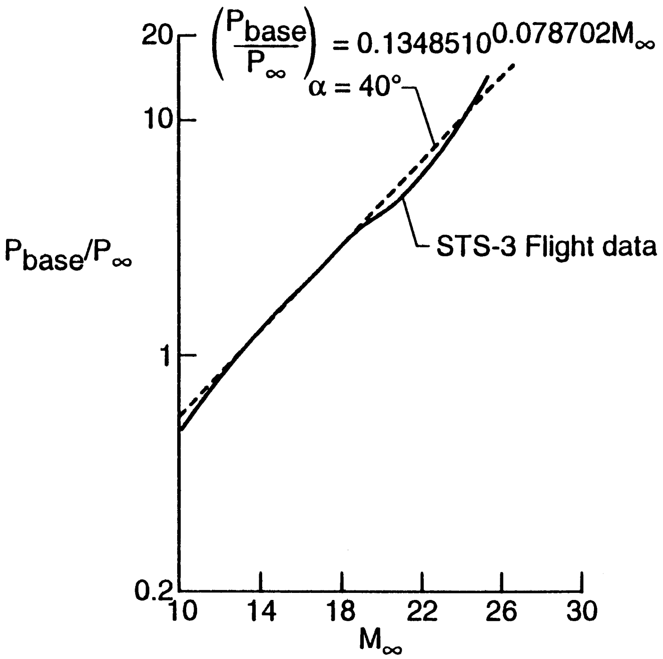

Fig. 25 Correlation of Shuttle Orbiter base pressure as a function of Mach number.

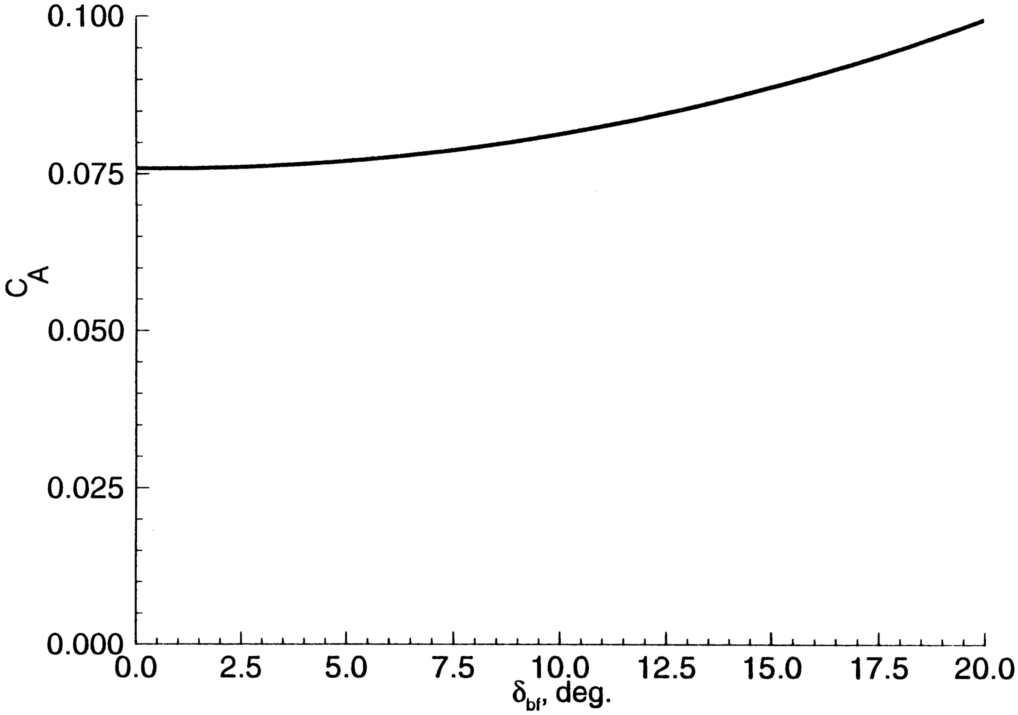

(a) C_A

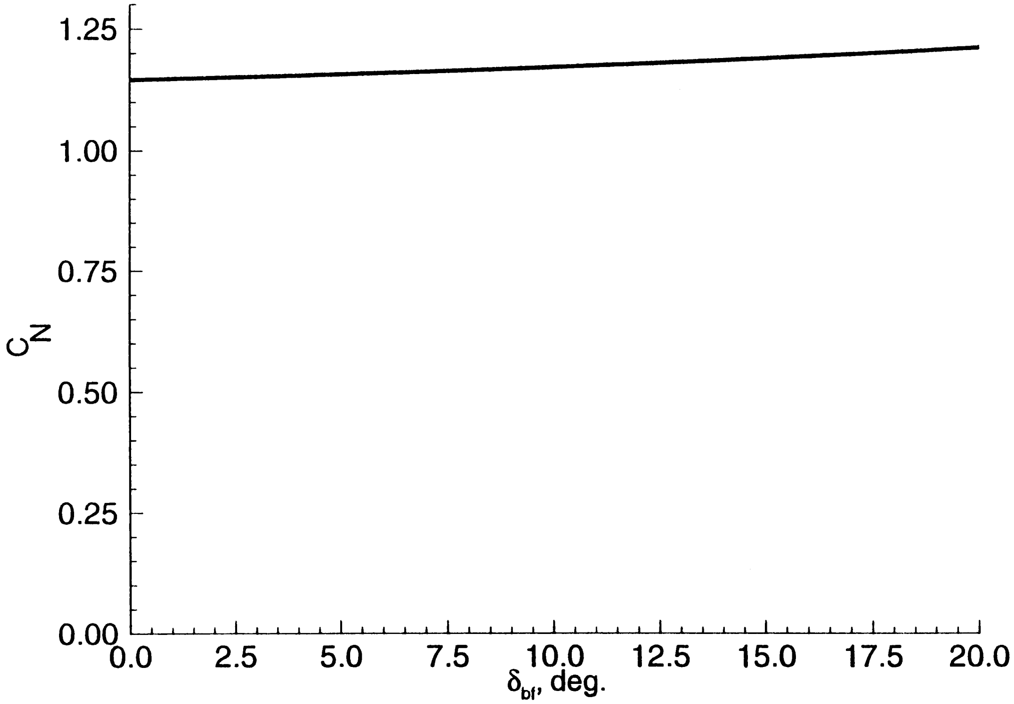

(b) C_N

Fig. 26 Effect of bodyflap deflection on computed STS-1 aerodynamic coefficients.

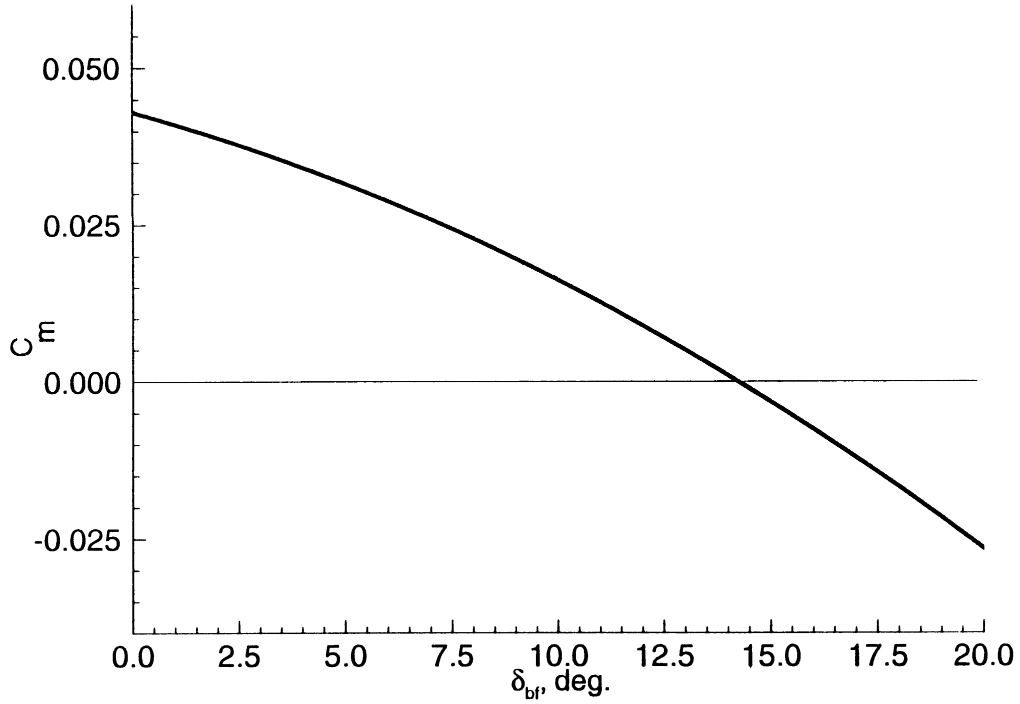

(c) C_m

Fig. 26 Effect of bodyflap deflection on computed STS-1 aerodynamic coefficients.

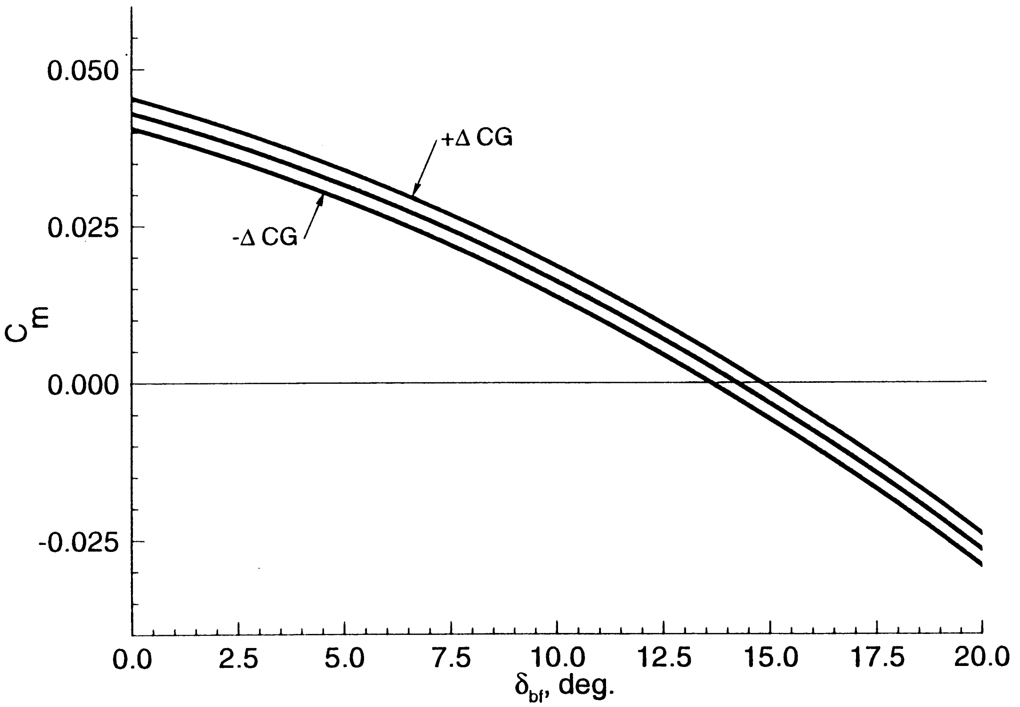

Fig. 27 Effect of CG shift on computed STS-1 bodyflap trim angle at 40 degrees angle of attack and $M_\infty = 23$.

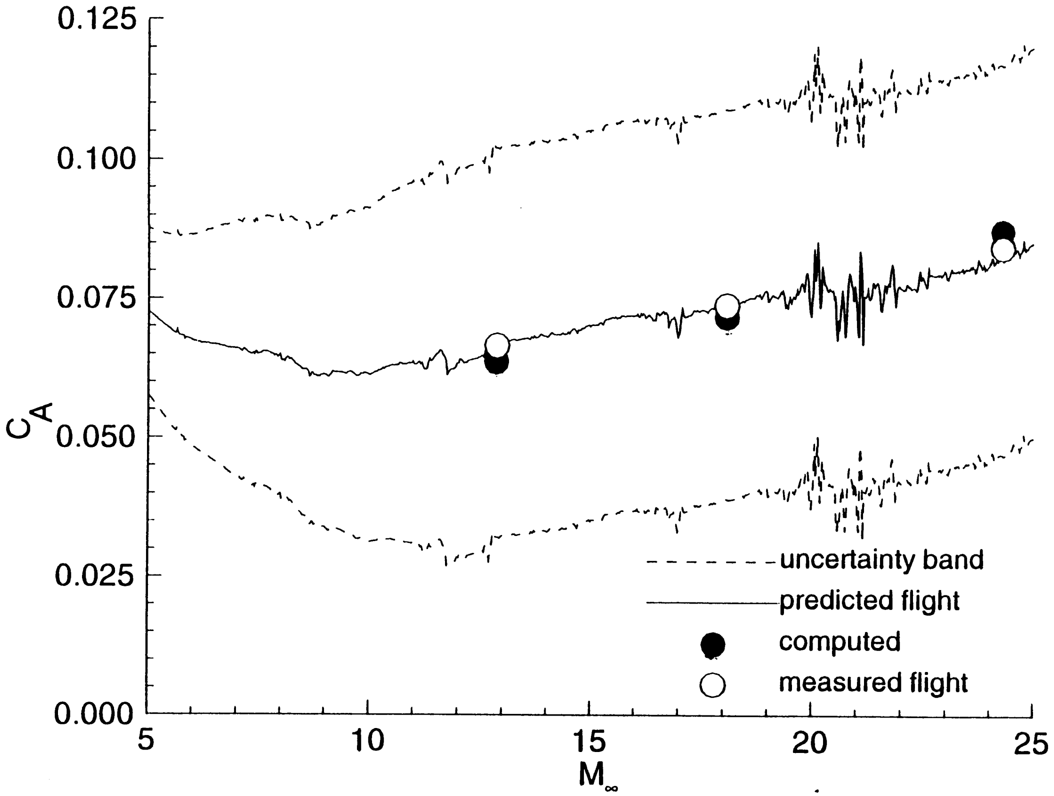

(a) C_A

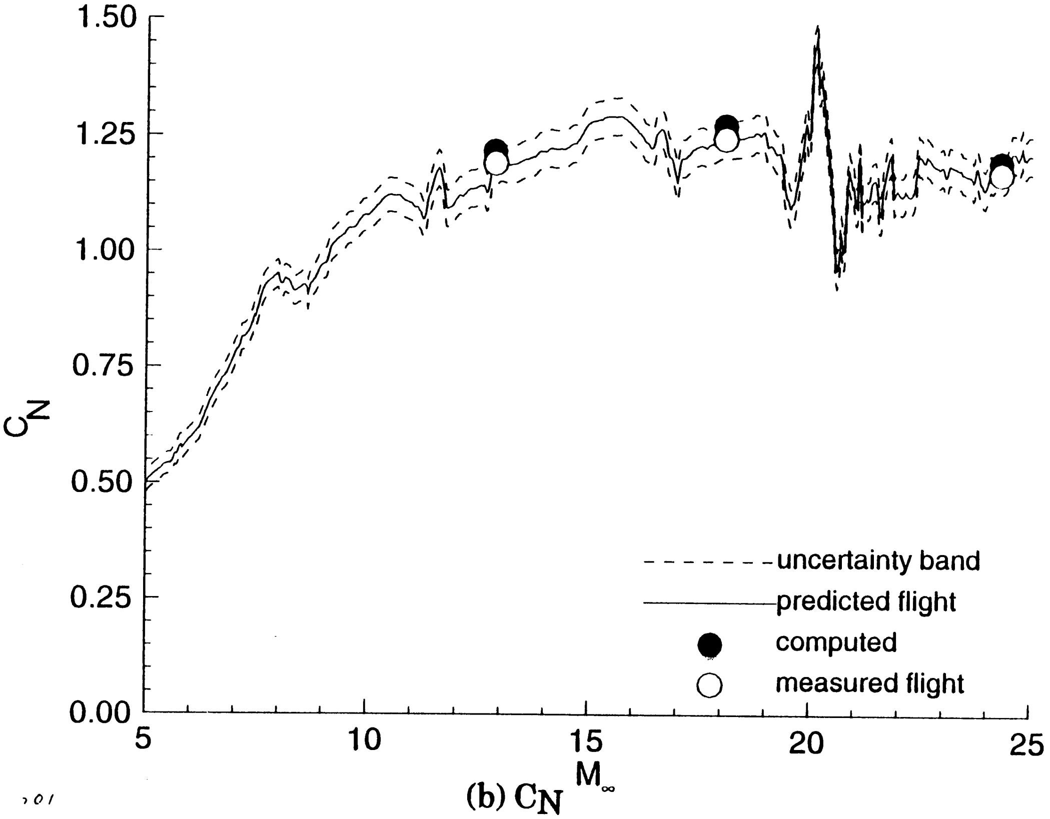

(b) C_N

Fig. 28 Comparison of predicted, measured and computed aerodynamic coefficients over the hypersonic portion of the STS-2 entry trajectory.

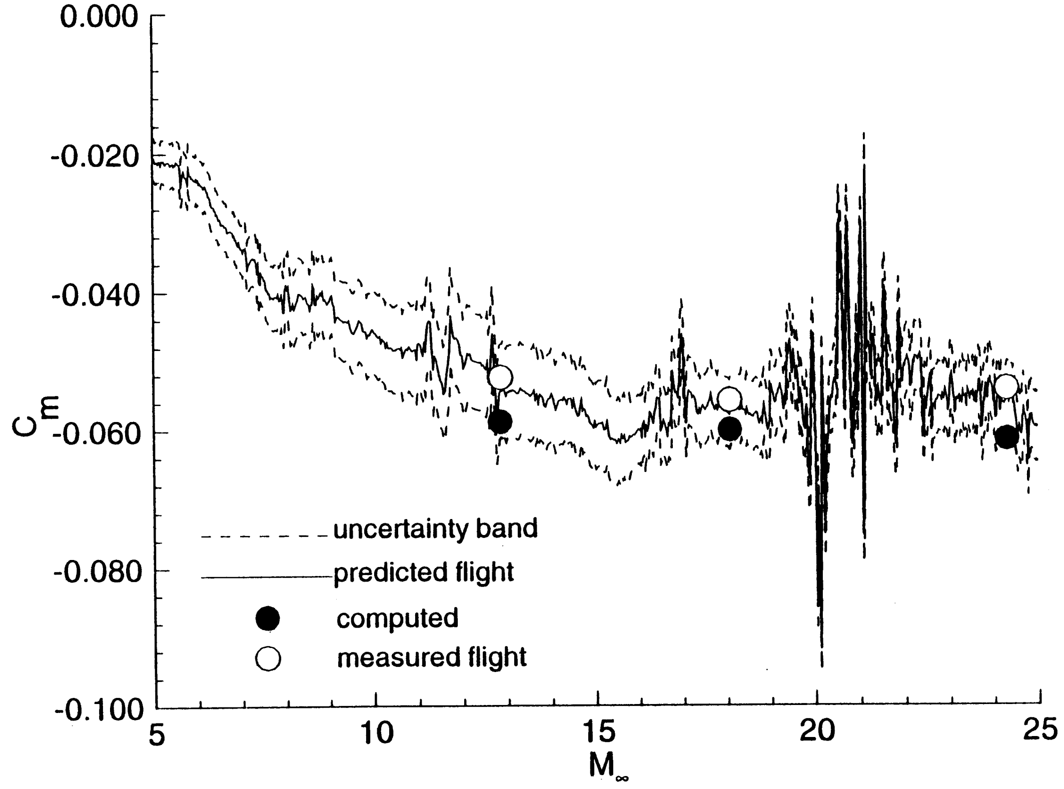

(c) C_m

Fig. 28 Comparison of predicted, measured and computed aerodynamic coefficients over the hypersonic portion of the STS-2 entry trajectory.

Printed on Recycled Paper

U.S. GOVERNMENT PRINTING OFFICE: 1995–841-250/12

COLOR FIGURES

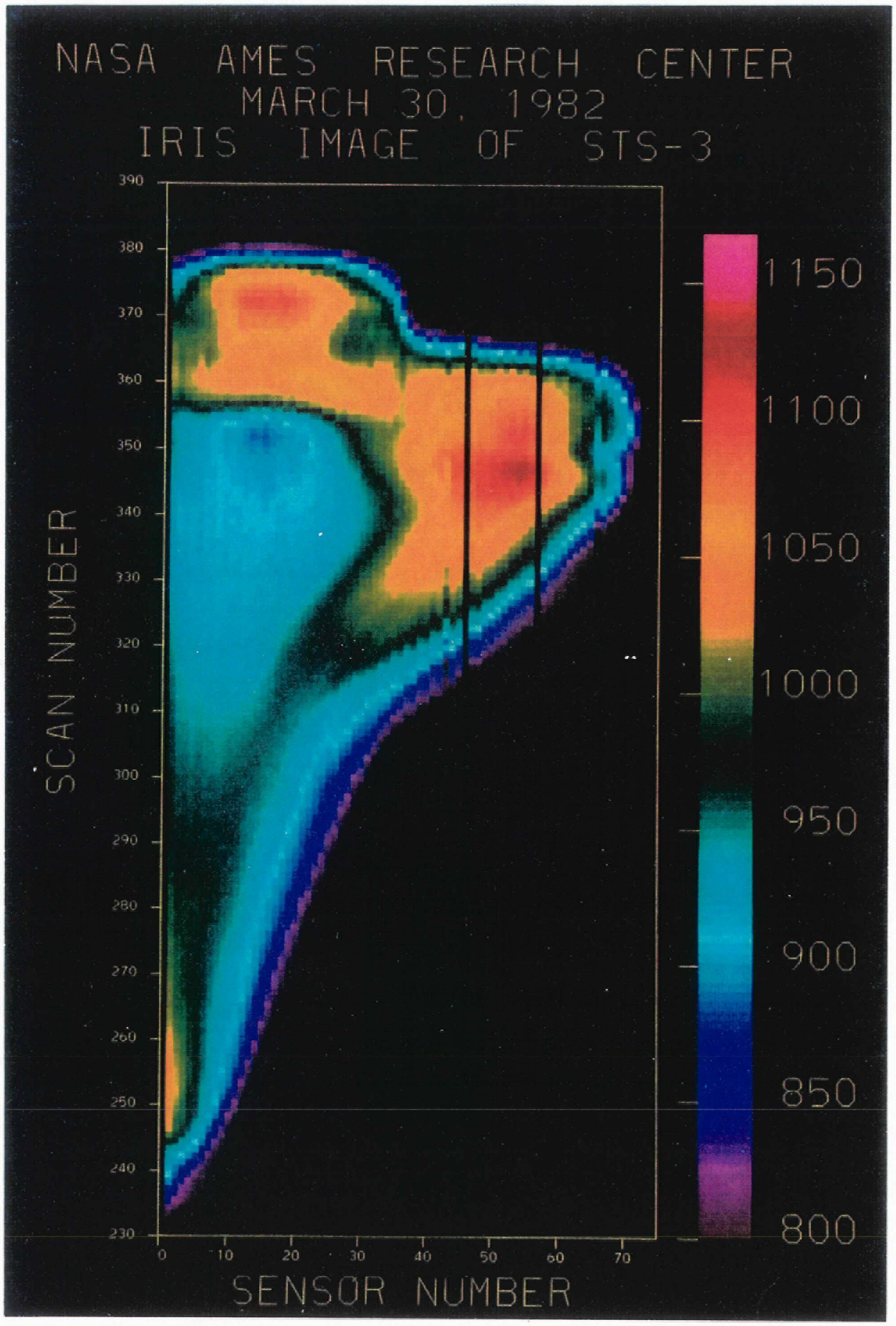

Figure 5. IRIS focal plane image of STS-3.

(Color version of black and white photograph shown on page 229.)

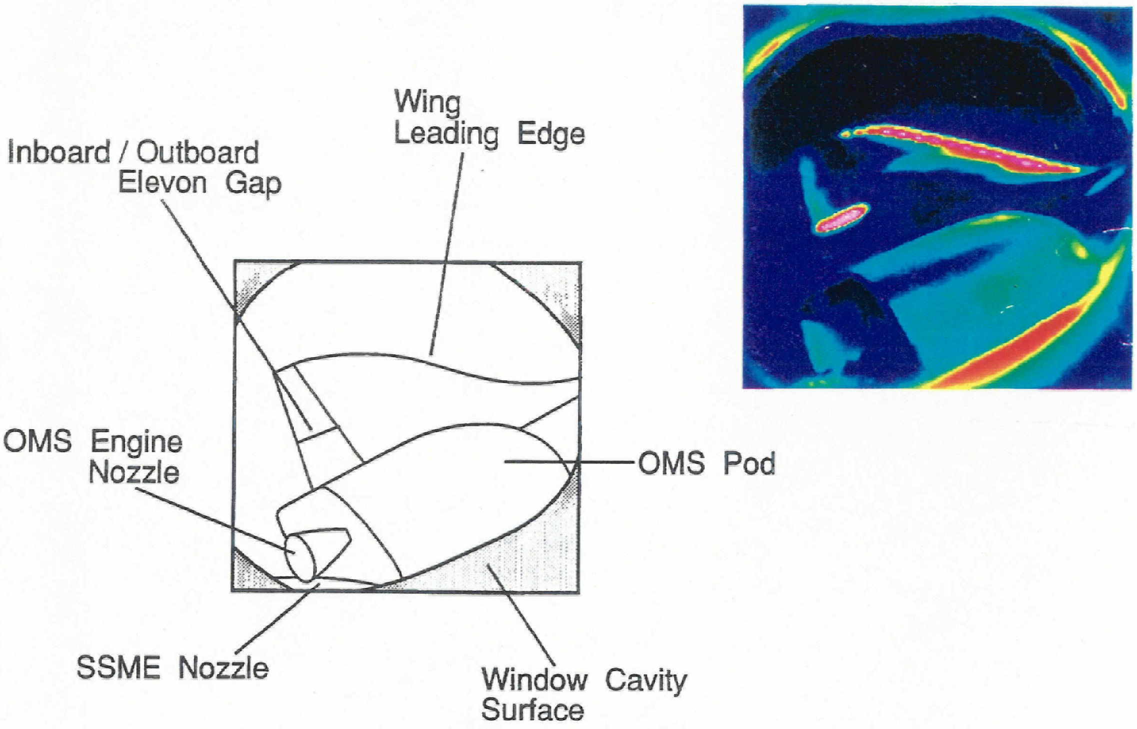

Figure 7–Typical SILTS wing-data image (from STS-28).

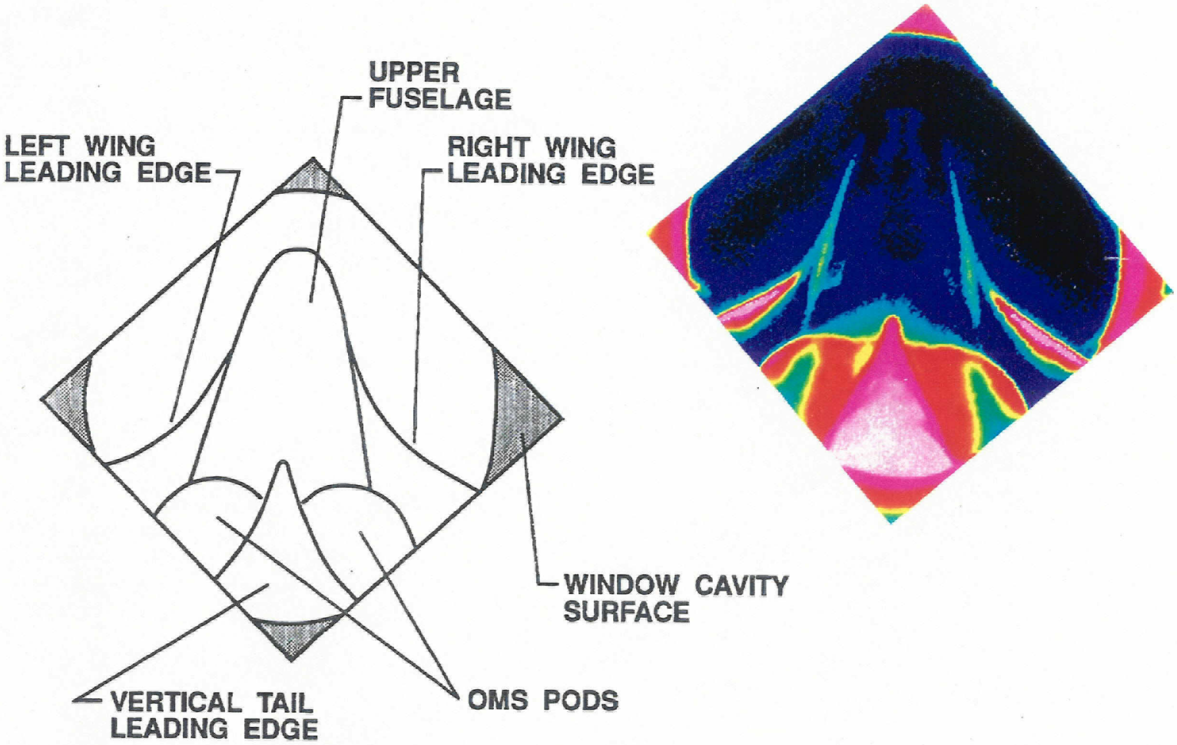

Figure 8– Typical SILTS fuselage-data image (from STS-35).

(Color versions of black and white figures shown on page 247.)

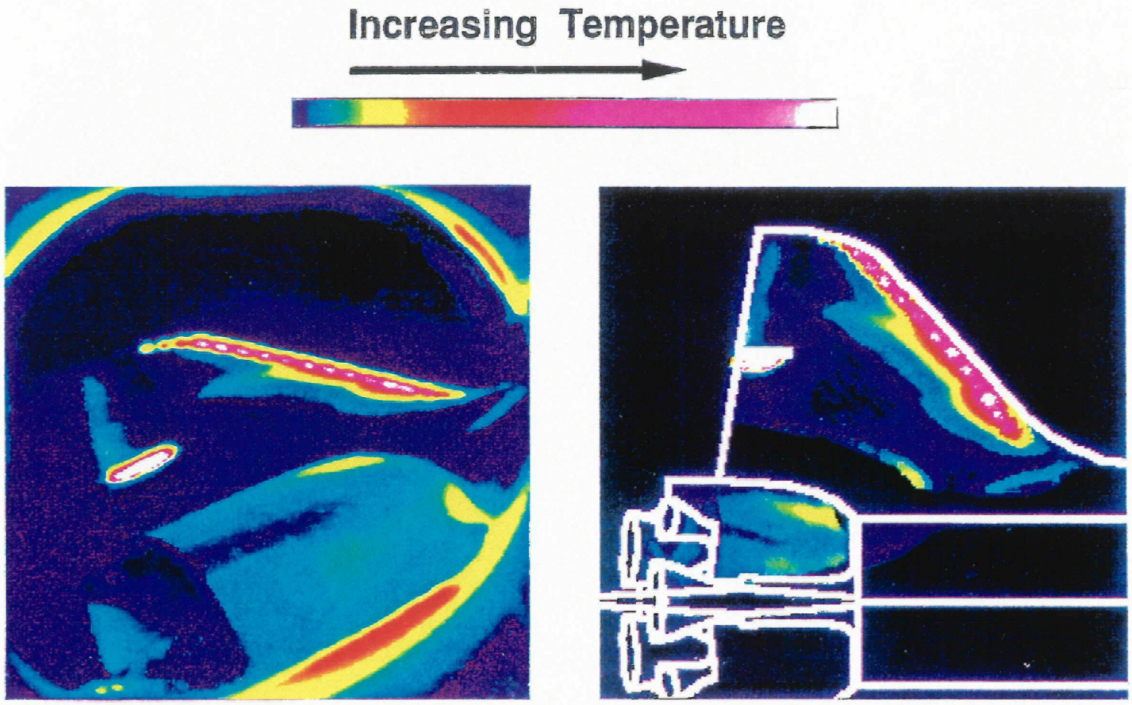

Camera View

Projection to Planview

Figure 9 – Typical data projection to orbiter planview.
(Color version of black and white photographs shown on page 248.)

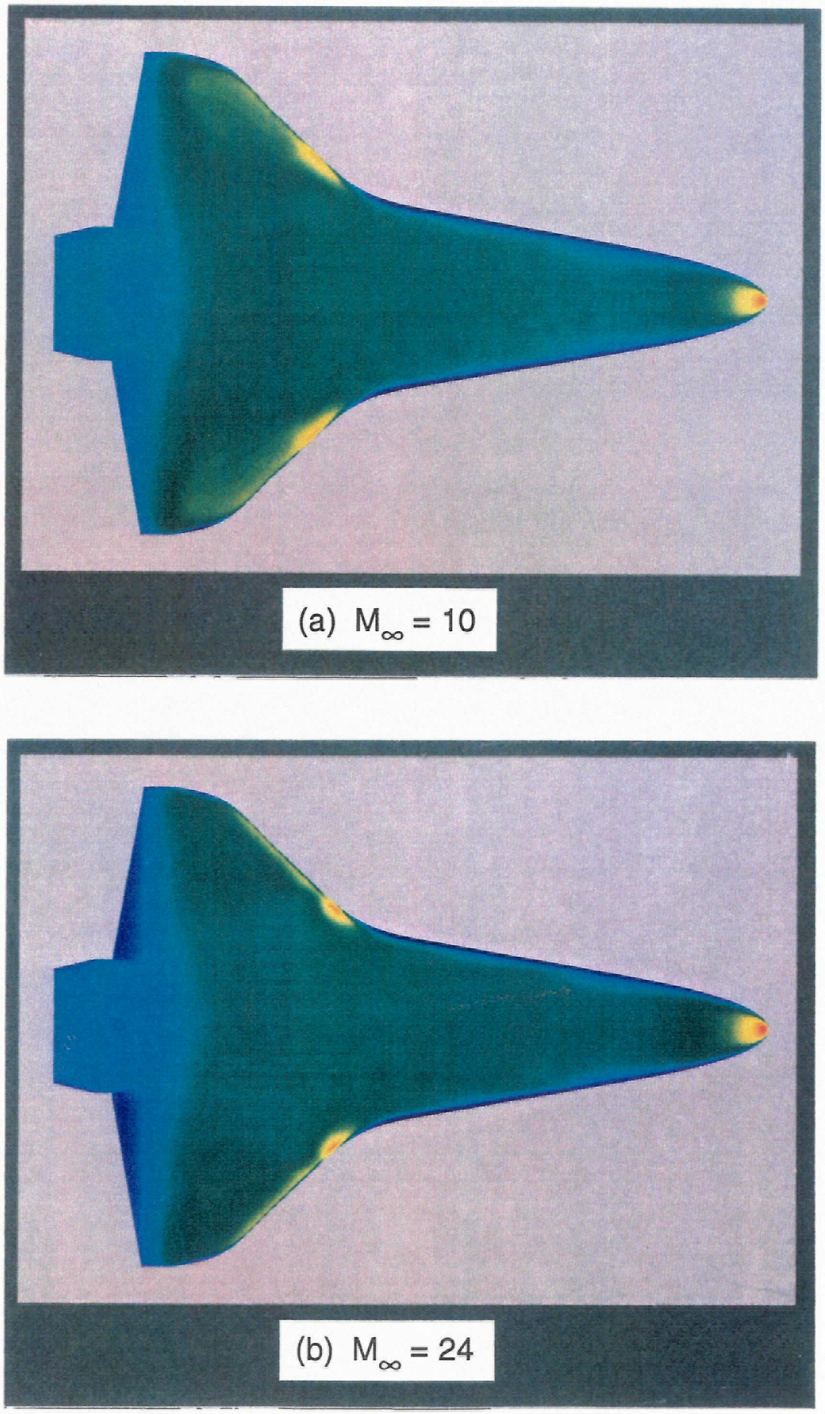

(a) $M_\infty = 10$

(b) $M_\infty = 24$

Fig. 19 Computed windward surface color contour plots of pressure at 40 degrees angle of attack and 0 degree bodyflap deflection.

(Color versions of black and white photographs shown on page 484.)

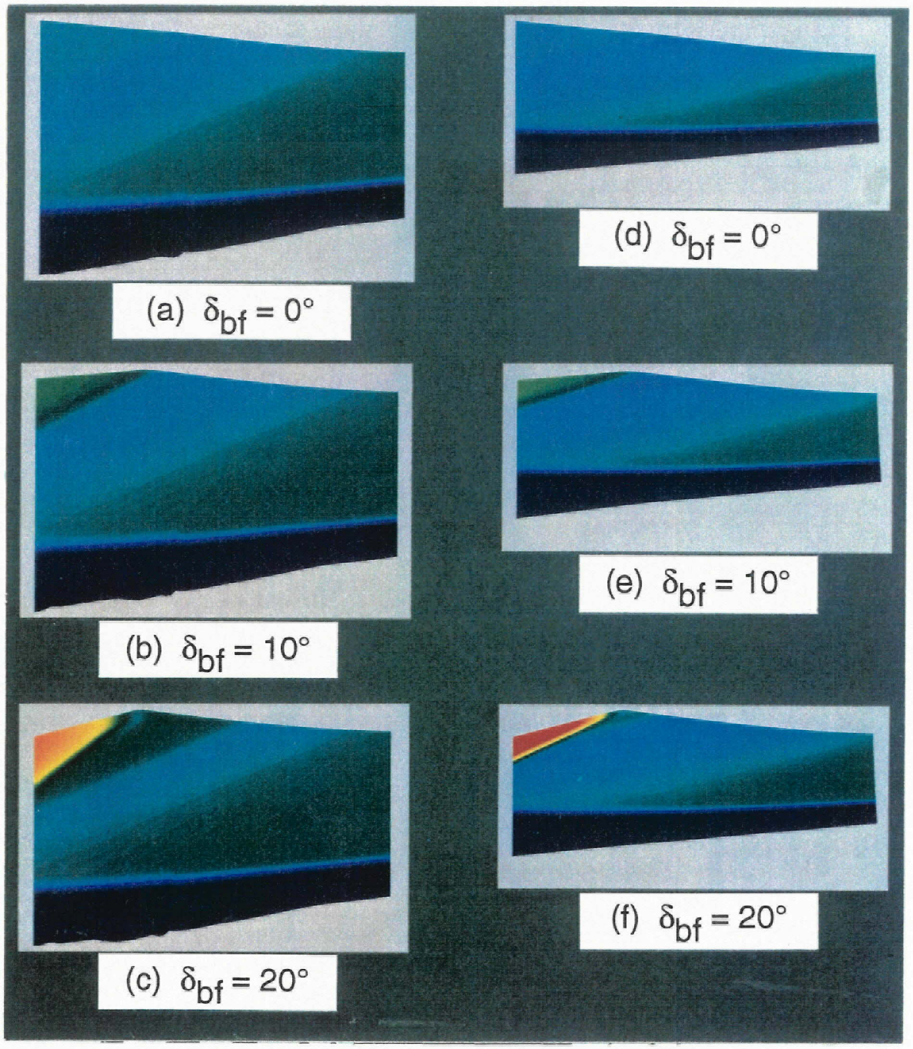

(a) $\delta_{bf} = 0°$

(b) $\delta_{bf} = 10°$

(c) $\delta_{bf} = 20°$

(d) $\delta_{bf} = 0°$

(e) $\delta_{bf} = 10°$

(f) $\delta_{bf} = 20°$

Fig. 21 Comparison of symmetry plane color contour plots of pressure in the vicinity of the bodyflap at a $M_\infty = 10$ tunnel condition and a $M_\infty = 24$ flight condition at 40 degrees angle of attack and bodyflap deflections of 0, 10, and 20 degrees.

(Color version of black and white photograph shown on page 487.)

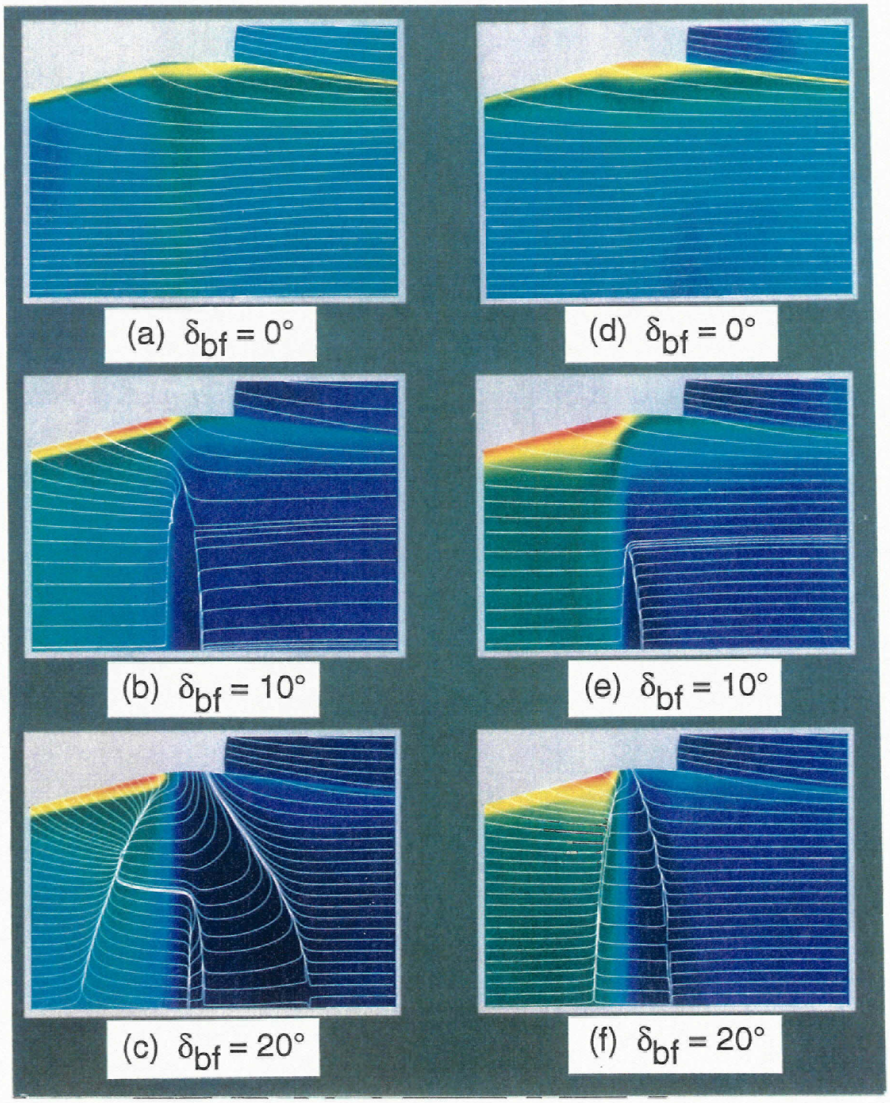

Fig. 22 Surface streamlines superimposed on color contour plots of surface heating in the vicinity of the bodyflap hinge line for a M = 10 tunnel condition and a M = 24 flight condition at 40 degrees angle of attack and bodyflap deflections of 0, 10, and 20 degrees.

(Color version of black and white photograph shown on page 488.)

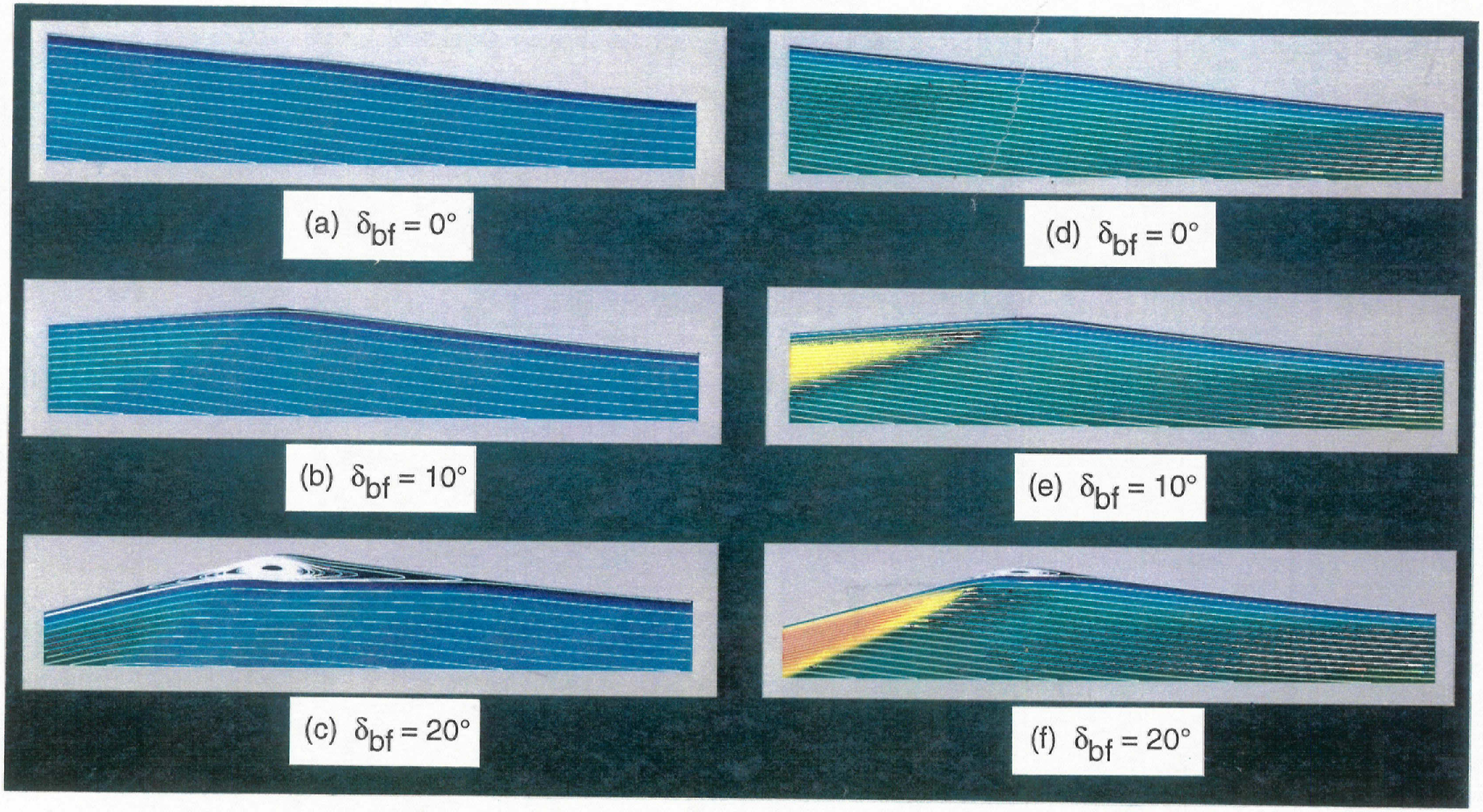

(a) $\delta_{bf} = 0°$

(b) $\delta_{bf} = 10°$

(c) $\delta_{bf} = 20°$

(d) $\delta_{bf} = 0°$

(e) $\delta_{bf} = 10°$

(f) $\delta_{bf} = 20°$

Fig. 23 Streamlines in the windward symmetry plane superimposed on color contour plots of pressure for a $M_\infty = 10$ tunnel condition and a $M_\infty = 24$ flight condition at 40 degrees angle of attack and bodyflap deflections of 0, 10, and 20 degrees.

(Color version of black and white photograph shown on page 489.)

REPORT DOCUMENTATION PAGE

Form Approved
OMB No. 0704-0188

Public reporting burden for this collection of information is estimated to average 1 hour per response, including the time for reviewing instructions, searching existing data sources, gathering and maintaining the data needed, and completing and reviewing the collection of information. Send comments regarding this burden estimate or any other aspect of this collection of information, including suggestions for reducing this burden, to Washington Headquarters Services, Directorate for Information Operations and Reports, 1215 Jefferson Davis Highway, Suite 1204, Arlington, VA 22202-4302, and to the Office of Management and Budget, Paperwork Reduction Project (0704-0188), Washington, DC 20503.

1. AGENCY USE ONLY *(Leave blank)*

2. REPORT DATE
April 1995

3. REPORT TYPE AND DATES COVERED
Conference Publication

4. TITLE AND SUBTITLE
Orbiter Experiments (OEX) Aerothermodynamics Symposium

5. FUNDING NUMBERS
WU 506-40-91-01

6. AUTHOR(S)
David A. Throckmorton, Editor

7. PERFORMING ORGANZATION NAME(S) AND ADDRESS(ES)
NASA Langley Research Center
Hampton, VA 23681-0001

8. PERFORMING ORGANIZATION REPORT NUMBER
L-17373 A

9. SPONSORIING/MONITORING AGENCY NAME(S) AND ADDRESS(ES)
National Aeronautics and Space Administration
Washington, DC 20546-0001

10. SPONSORING/MONITORING AGENCY REPORT NUMBER
NASA CP-3248, Part 1

11. SUPPLEMENTARY NOTES

12a. DISTRIBUTION/AVAILABILITY STATEMENT
[redacted] Publicly Available
Subject Categories 34 and 16

12b. DISTRIBUTION CODE

13. ABSTRACT *(Maximum 200 words)*

Initiated in the mid-1970's, the NASA Orbiter Experiments (OEX) Program provided a mechanism for utilization of the Shuttle Orbiter as an entry aerothermodynamic flight-research vehicle, as an adjunct to its normal operational missions. OEX experiment instrumentation obtained in-flight measurements of the requisite parameters for determination of the Orbiter's aerodynamic characteristics over the entire entry flight regime, as well as the aerodynamic-heating rates imposed upon the vehicle's thermal protection system during the hypersonic portion of atmospheric entry. Data derived from the OEX complement of experiments comprise benchmark hypersonic flight data. These data are being used in a continual process of validation of state-of-the-art methods, both experimental and computational, for simulating/predicting the aerothermodynamic characteristics of advanced space transportation vehicles. This Orbiter Experiments Aerothermodynamics Symposium provided a forum for the dissemination of OEX experiment results, and for demonstration of the manner in which OEX data are being used for validation of advanced vehicle aerothermodynamic design tools.

14. SUBJECT TERMS
Space shuttle; Flight data; Aerodynamics; Aerothermodynamics

15. NUMBER OF PAGES
516

16. PRICE CODE
A22

17. SECURITY CLASSIFICATION OF REPORT
Unclassified

18. SECURITY CLASSIFICATION OF THIS PAGE
Unclassified

19. SECURITY CLASSIFICATION OF ABSTRACT
Unclassified

20. LIMITATION OF ABSTRACT

NSN 7540-01-280-5500

Standard Form 298 (Rev. 2-89)
Prescribed by ANSI Std. Z39-18
298-102